Galactic Molecular Dust Clumps using SCUBA-2 - Effects of HII Regions on Star Formation

by

George Bobotsis

A thesis presented to
the University of Waterloo
in fulfillment of the thesis requirement
for the degree of
Masters of Science in
Physics

Waterloo, Ontario, Canada, September 2018

Examining Committee Membership

The following served on the Examining Committee for this thesis. The decision of the Examining Committee is by majority vote.

Supervisor(s):	Michel Fich Professor, Dept. of Physics and Astronomy, University of Waterloo
Committee Members:	Niayesh Afshordi Professor, Dept. of Physics and Astronomy, University of Waterloo
	Michael Balogh Professor, Dept. of Physics and Astronomy, University of Waterloo
	Michel Fich Professor, Dept. of Physics and Astronomy, University of Waterloo
Internal-External Member:	Michael Hudson Professor, Dept. of Physics and Astronomy, University of Waterloo

I hereby declare that I am the sole author of this thesis. This is a true copy of the thesis, including any required final revisions, as accepted by my examiners.

I understand that my thesis may be made electronically available to the public.

Abstract

I present findings from a broad array of SCUBA-2 observations. The sample consists of 38 SCUBA-2 images targeted near mature, galactic, HII regions of the Sharpless "Sh-2" or Blitz-Stark-Fich "BFS" catalogue. In 31 of those images, dusty molecular clumps are identified by-hand using SCUBA-2 450μm and 850μm data and HII regions are identified using VLA 1.46/4.89 GHz data. Photometry and derivative properties are obtained using scripted routines.

In total, 185 molecular clump composites hosting 333 cores are identified in the SCUBA-2 images. After segregation takes place for their association with nearby HII regions, a total of 176 clumps and 315 cores continue into analysis. A full property dataset is obtained for these clumps and their components as well as their associated HII regions.

The SCUBA-2 clump identification process leads to strong evidence in support of increased clump condensation occurring near HII region boundaries. In addition, the HII regions are found to have a compressing effect on the outer layers of their associated clumps due to the pressure differential between the two.

Average temperature analysis reveals that the portion of cores that are hotter than their surrounding cloud medium (i.e potentially collapsing and star forming) is comparable to the portion of cores colder than their surrounding cloud medium (i.e stable).

Cloud segments are found to become cooler with increasing column and number density, suggesting they are not significantly heated by external mechanisms and are able to cool more efficiently at denser states. Cores are also found to be cooler with increasing column density and depict no significant temperature change with increasing number density, suggesting that most of their heating is coming from internal processes such as gravitational contraction and that the heating from this process is on the same order as the convective cooling taking place. No correlation is found between the average temperature of a cloud segment and the accumulated mass of its embedded cores.

HII regions as well as OB stars are observed to have a mild heating effect on the cores and cloud segments of this molecular clump sample. The mildness of the OB star heating effect is expected to occur due to the very low incident fluxes encountered in this sample of clumps ($\leq 1\ W/m^2$).

HII regions themselves show a rapid decrease in electron number density with increas-

ing radial size. The opposite trend is observed for their total mass.

The few HII region systems for which a complete description was obtained suggested a mean Star Formation Efficiency (SFE) of 4.82%, with a max of 38.72% and a min of 0.216%. However, most of the analyzed systems have an SFE value $\leq 1\%$.

Finally, significant effort was made in identifying the greatest uncertainty contributors to SCUBA-2 data. Out of all, atmospheric emission and absorption were found to be by far the most dominant. Furthermore, a stochastic Monte-Carlo technique was developed for tending to the asymmetric nature of uncertainty in all SCUBA-2 temperature-dependent properties. This helped better understand the uncertainty introduced from a prescribed opacity model as well as the use of a non-linear temperature model.

Acknowledgments and Dedications

I would like to first and foremost dedicate this thesis to my two kind and caring parents, as I acknowledge their continuous support through my undergrad struggles, and now, my graduate degree perseverance. None of this would have been possible without them and I'm very grateful for their love and support during this difficult process that has lead to a successful master's degree completion.

An enormous shout-out to my dedicated friends who stuck with me through major lows and highs in this turbulent time of my life, even while residing half-way across the world from my current location.

A big thank you to my supervisor Dr. Fich, who trusted me with this project and was constantly engaged with me, offering his expertise and wisdom when tackling challenging problems that would occasionally arise.

An additional big thank you to my committee members Dr. M.Balogh and Dr. N.Afshordi who were very supportive and insightful when discussing new ideas, goals and eventually the findings of this project.

Another big thanks to my colleagues, in particular, Mollie Conrad and Chuchong Ni, with whom I collaborated closely during my master's studies.

Finally, I've saved a special thank you for Dr. Rohan Jayasundera, who pushed me to experiment with teaching physics at the beginning of this thesis, and, although extremely hesitant at the start, I have now found a true calling for physics education. Words cannot describe how much I enjoyed working with you for the entirety of my 2 year master's degree.

Preface

I would like to point out that this thesis addresses several topics regarding the role of HII regions in sequential star formation as well as particulars pertaining to the "dusty" nature of this investigation. I list these topics below, as well as the location where they are discussed in detail:

- Clump Photometry and Derivative Properties (Ch. 2.1-2.5, Ch 3.2-3.3)
- Association of Cores to HII Regions (Ch. 3.4)
- Association of OB stars to HII Regions (Ch. 3.5)
- Major Uncertainty Contributors (Ch. 4.1-4.2)
- Effects of HII regions (Including Heating) on Molecular Clumps (Ch. 5.3)
- Clump Heating from Nearby OB stars (Ch. 5)
- Star Formation Efficiency for HII region Systems (Ch. 5.6)

For the first time, an in depth uncertainty treatment is performed throughout all SCUBA-2 measurements and derivative properties. Due to the massive investigation held to tackle this topic, the determination of uncertainty is discussed on its very own chapter (Ch. 4), away from the measurements (Ch. 2) and calculations (Ch. 3) themselves.

It should be noted that this thesis deals extensively with very noisy data, particularly in the 450μm band. Calculated properties and overall results are prone to substantial future improvement from the use of less noisy data.

Nonetheless, I hope that this thesis sheds further light in dusty molecular systems and provides a useful tool to the reader in support of their endeavor in star formation astrophysics.

Let's begin.

Table of Contents

List of Tables

List of Figures

Chapter 1

Introduction

Interstellar space may seem empty, but is indeed buzzing with activity. From particle-anti-particle pair creation/annihilation, to dark energy generation from expanding space, all the way out to the more intuitive, but complex interplay between gas and dust molecules, which gracefully leads to the exciting process of star formation.

Star formation is a dynamic field, which, as the name suggests, is concerned with the origin and phase evolution of interstellar material into the orderly structure of a star. Unfortunately, almost all experimental aspects of this field are technologically impeded. More often than not, large noise levels in measurements lead to lack of robust evidence, allowing several theories with differing claims to potentially coexist.

However, instrumentation technology is continuously improving and the number of identified prestellar objects is steadily increasing, allowing claims of different theories to be leveraged through the power of statistics. In fact, several claims in this thesis, require some type of statistical treatment in order to bring forth a desired property out of a sea of noise, by making meaningful combinations of measurements of that property across a number of different objects.

Allow me then to begin discussion of the star formation process from a very general stance, while progressively driving the focus toward the specific branch of the theory that will be the "bread and butter" of this thesis. This will be done in a story-telling fashion, where the quantitative specifics will be immediately accessible through the referenced works in order to avoid redundancy and maintain a simple flow that is comprehensible to specialized and non-specialized readers alike.

1.1 Star Formation

The basic physics behind the formation of a star in ideal conditions is well known. An instability at some particular region of a molecular cloud leads to the collapse of that region under the action of gravity. This collapse takes place through several different phases, which can in turn trigger further star formation in nearby regions. Overall, gravitational potential energy is converted to heat, and as temperature rises, the core of the collapsed clump eventually becomes hot enough to support nuclear fusion of hydrogen into helium. A star is born!

This simple picture becomes increasingly complicated as simplifying assumptions begin being replaced by realistic descriptions. Let's begin discussing such complexities starting with the molecular cloud itself. A molecular cloud is never composed exclusively from a single molecular compound, and as such, is much better described through the use of abundance levels. These abundance levels are variable, as material is injected into a cloud through processes such as stellar winds and supernovae that enrich the cloud with atomic species generated by fusion in stellar cores, but also, ejected from processes such as cloud-cloud collisions. In addition, changes in the physical parameter space of the cloud (e.g temperature, density etc) can lead to interesting chemical interplays between the already-contained constituents. This variability is why molecular clouds are described using chemical abundances, where essentially the abundance of one species against that of a standard species (typically hydrogen) is tracked through time.

In addition, a molecular cloud is never perfectly smooth, as it is embedded in a space full of activity. Incident radiation and the movement of massive bodies can give rise to lumpiness and inhomogeneities. In fact, as was previously mentioned, molecular clouds can merge, but also fragment, with both processes altering their chemical abundance levels and further destabilizing their structure.

It is important to be aware that the formation of a star is a process uniquely tied to the initial conditions of the star forming environment itself. Clearly, those conditions can and do change, altering the specifics of star formation as well, where now some phases can become brief or non-occurring, while others can become pronounced and even prolonged. As an example, a low-mass molecular cloud originating from a fragmentation event cannot support the production of massive stars. In such a molecular cloud, the protostellar stage of disk formation will be commonly observed in the almost-exclusive low-mass star population. On the contrary, Giant Molecular Clouds (GMCs) do host the formation of

massive stars as well as low-mass stars. However, massive stars produce very strong stellar winds which in turn cause the disk formation stage to be suppressed and very shortlived. It should be clear then that which stages of star formation are observed is something that is closely tied to the location that the star formation process takes place.

Additional complexities are introduced from mechanisms that act in aid of, or in prevention of clump formation and collapse inside molecular clouds themselves. This list is certainly incomplete and an active area of astronomical research today.

For example, inhomogeneities in the molecular cloud's density make the collapse non-uniform, assisting in the rise of turbulence, which can in turn prevent the collapse from reaching completion. The presence of a permeating magnetic field can interact with the content of a clump (particularly the dusty component), and lead to the retardation or complete prevention of the entire collapse. A nearby star can provide radiation that heats molecular material, raising its internal pressure, and consequently supporting it against collapse. The same star can also deposit ionizing radiation to the clump, which, if sufficient, can lead to the complete evaporation of the clump before it has a chance to collapse. All these mechanisms acting to prevent the collapse of a molecular clump are commonly referred to as "support mechanisms".

On the other hand, highly energetic processes, such as supernovae, can yield shockwaves that propagate inside a molecular cloud. The induced pressure differential from a passing shockwave sweeps up material, packing it close together. With a little luck the proximity and accumulated mass of material is great enough for gravity to dominate over all support mechanisms, leading the accumulation into collapse. This process, in which a propagating front can trigger clump formation and collapse sequentially is commonly referred to as the "collect-collapse" (CC) model of star formation, though this particular terminology for the process is more commonly associated with HII regions rather than supernovae.

Besides supernovae however, there exist other processes capable of generating shockwaves. One of those is the evolution of HII regions inside a molecular cloud. HII regions are created from massive OB stars. A substantial amount of radiation produced by these types of stars lies in the Lyman continuum, and as such, is capable of ionizing atomic hydrogen. This ionization takes place sequentially through a propagating ionization front, accompanied by a pressure wave. Without diving into the specifics yet, the ionization front and pressure wave eventually meet, at which point the pressure wave evolves rapidly into a full-fledged shockwave. The ionization front then traces closely the propagation of the shockwave. Between the two, a sharp pressure differential acts as a "cradle" that sweeps up and com-

presses molecular material along the way. Eventually the accumulation is great enough that it collapses under its own gravity to form a protostar, closely tracing the specifics of the CC process. A graphic to aid the visualization of this version of CC star formation is presented in figure 1.1 (Elmegreen,1977 [11]).

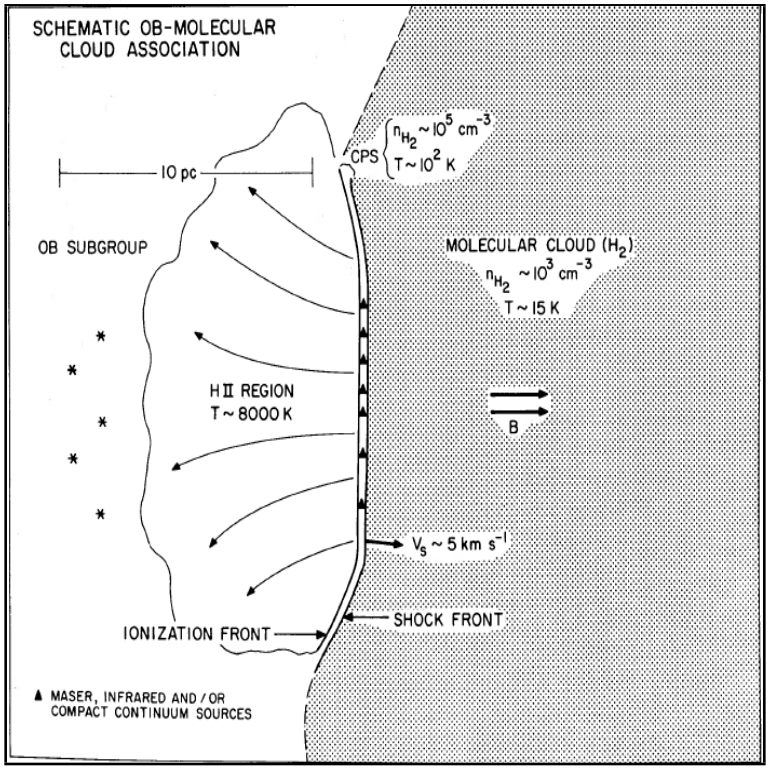

Figure 1.1: From left to right, an OB subgroup generating an expanding HII region. Accumulation of mass is occurring between the ionization and shockwave fronts as both expand into deeper layers of the neutral molecular cloud. (Elmegreen,1977 [11])

However, these accumulations are typically expected to be more massive than those that form in the unshocked part of the same molecular cloud. This is due to the strong temperature dependence of the protostar mass function, combined with the fact that temperatures in the region between the ionization front and shockwave will be much warmer than the rest of the unshocked cloud. This is why HII regions are believed to trigger almost exclusively the formation of massive OB stars. (Elmegreen,1977 [11])

The star formation capabilities of HII regions do not only extend to the formation of

clumps in the smooth component of a molecular cloud. They can also lead pre-existing, stable clumps into collapse through a process commonly referred to as "Radiation-Driven Implosion" (RDI). Here, the scenario is essentially the same, however the ionization front propagates into a stable, dense clump of molecular material instead of a smooth, low-density molecular bedding. Much like the smooth case, the material becomes ionized, however due to the much higher density, the ionization happens gradually over the clump structure. At the same time, when the accompanying shockwave passes over the clump, it has the potential of destabilizing it enough through sufficient compression and leading a portion of it into collapse.

Numerical simulations show that for RDI to take place, the ionizing flux from the OB star must lie within a specific, moderate range, where the ionization front will erode the clump slowly enough so that the generated shockwave has enough time to destabilize it into collapse before the clump is evaporated. A graphic from six different RDI simulations is presented in figure 1.2, where it is evident that the ionization layer evolves from a "U" shape into an increasingly narrower "V" shape while evaporating the clump at an increasingly faster pace. (Bisbas,2011 [55])

Adding to the above, simulations of clumps undergoing RDI have pointed to RDI decreasing the free-fall time of clumps due to the compression caused by the eroding ionization front. This compression also drives up the accretion rate of protostars, making them significantly more luminous than their non-imploded counterparts. Finally, the simulations show that stars formed due to RDI end up being less massive than other spontaneously formed stars due mass losses from ionization. However, the difference is not found to be significant, and even less-so as the density of the imploded object is increased. (Motoyama,2007 [29])

So far one can see why HII regions are considered valuable mediators in the star formation process. It will prove very useful to maintain a picture of star formation in molecular clouds, such as the one presented in figure 1.3 that depicts the components involved in star formation taking place at the Eagle Nebula while venturing further into the next chapters, where the beautiful interplay between dust, gas and massive OB stars will be further unfolded.

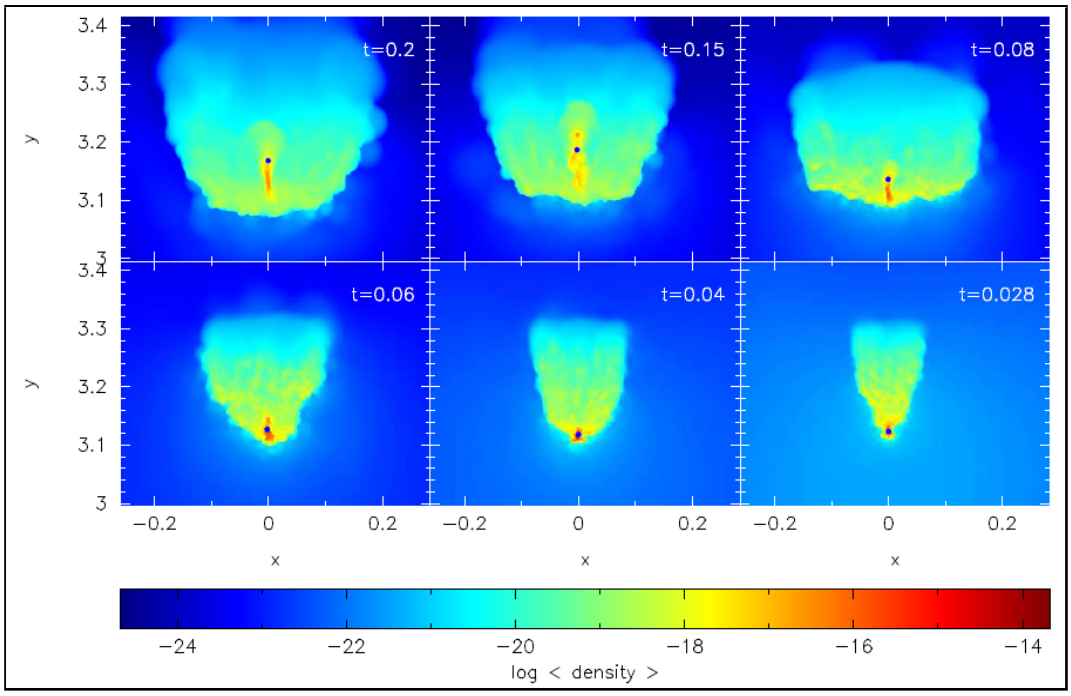

Figure 1.2: Six RDI simulations of a molecular clump using different ionization fluxes. The ionization flux is gradually increased from top-left to bottom right. The color coding indicates surface density levels in g/cm^2. The position of the formed protostar is indicated by a blue dot and the time of creation is indicated on the top right in Myr. (Bisbas,2011 [55])

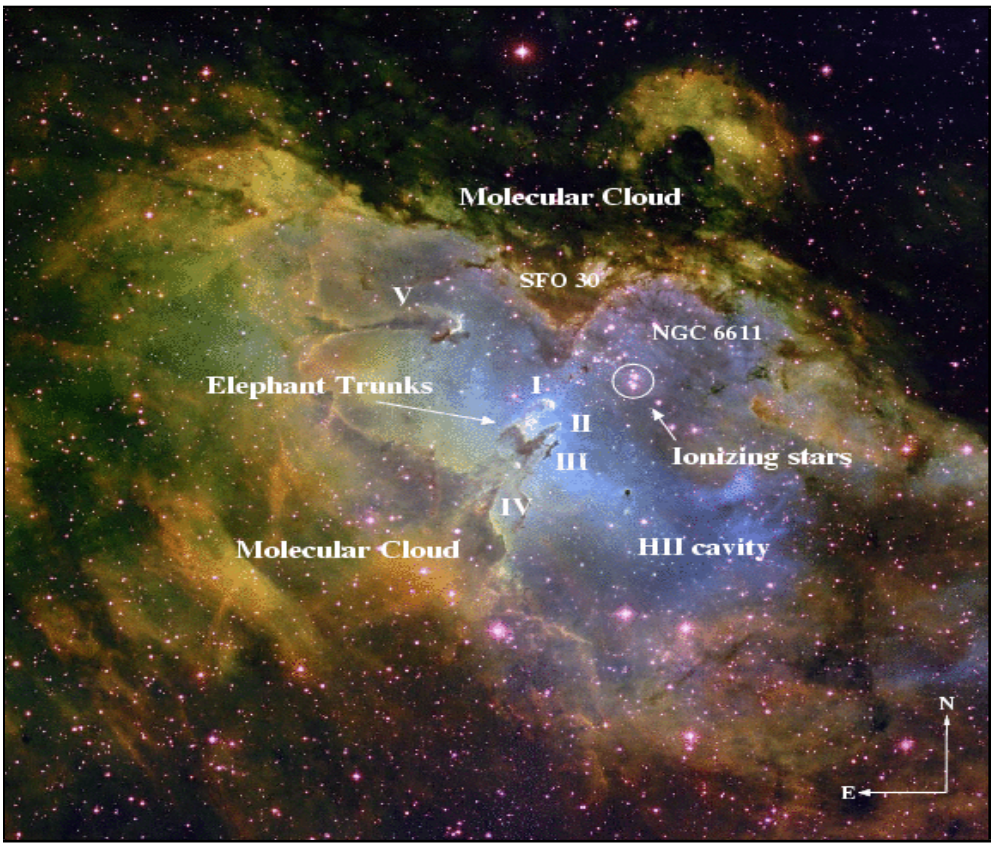

Figure 1.3: Wide-field ($\approx 40'$) image of the Eagle Nebula. The image combines H (green), OIII (blue) and SII (red) images to display the HII region created by the massive stars in NGC6611 as well as the dusty pillars near the center (labeled from I to V) of the GMC. (Oliveira,2008 [28])

1.2 Sequential Star Formation

HII regions are just a single link in a complex star formation chain process known as "Sequential Star Formation" (SSF). This theory is concerned with massive giant molecular cloud structures (GMCs) with typical masses ($\geq 10^5\ M_\odot$), which are capable of hosting the formation of massive OB stars. The ionizing radiation and strong stellar winds produced by these stars are the two defining triggers behind this process. I describe this theory in detail below while following closely C.J Lada's work on the subject [13].

The chain begins when the first population of low-mass stars is formed spontaneously inside the GMC. The strong stellar winds produced during the outflow stages of the stars comprising this population significantly alter the gas conditions in their neighboring region, favoring the formation of high-mass stars there.

Eventually, the first massive OB subgroup emerges. Each member is capable of producing large amounts of photons that can ionize hydrogen (Lyman continuum photons), but also heavier atomic elements after it departs the "Main-Sequence" (MS) phase of its evolution. Accompanying these stars are very strong stellar winds that gradually dissipate molecular material from their subgroup region.

The ionization process takes place progressively, in the form of a propagating ionization front, accompanied by a slower-moving pressure wave. The expansion of the ionization front will cease star formation locally as it dissipates molecular material in the smooth portion of the GMC and evaporates pre-existing clumps through ionization. A small portion of these pre-existing clumps may evolve into low-mass stars through the aforementioned RDI process.

When the ionization front expands out to a radius at which all the ionizing radiation from the host OB subgroup is used up in its maintenance, it gradually slows down to a near-halt, giving time to the pressure that is still traveling at the local speed of sound to reach up to it and overpass it. When this happens, the pressure wave evolves into a full-fledged shockwave, sweeping up and compressing material along its way. The ionization front traces closely the shockwave's passage, providing a second pressure gradient that acts so as to disallow accumulated material from falling behind. Essentially, the two fronts act collectively as a cradle that stores molecular material swept up by the shockwave's passage. This leads to the sequential formation of more high-mass stars deeper in the GMC structure through the aforementioned CC process.

As subsequent OB subgroups arise, the process is repeated all over again. Eventually, the GMC structure becomes completely dissipated of molecular material on a relatively short timescale of 10^6 years, with an unbound association or a bound cluster left behind, the outcome being tied to the star formation and gas clearance efficiencies.

It is useful to distinguish the term "association" and "cluster" at this point. An association pertains to a group of stars originating from a common GMC nursery which are not gravitationally bound, yet share a common direction of motion. A cluster on the other hand is essentially an association that is gravitationally bound. Generally, denser GMC structures experience a smaller yield of OB stars which take longer to clear the structure of its gaseous component, and consequently lead the structure to evolve into a cluster rather than an association. A graphic depicting the different stages of star formation in massive GMCs is presented in figure 1.4.

Having investigated the large-scale picture of SSF theory, it's important to address its small-scale particulars as well, namely, the specific stages of low-mass star formation. After all, low-mass stars are the initial triggers in this process, therefore an improved understanding of their formation specifics will lead to an improved understanding of the SSF theory as a whole.

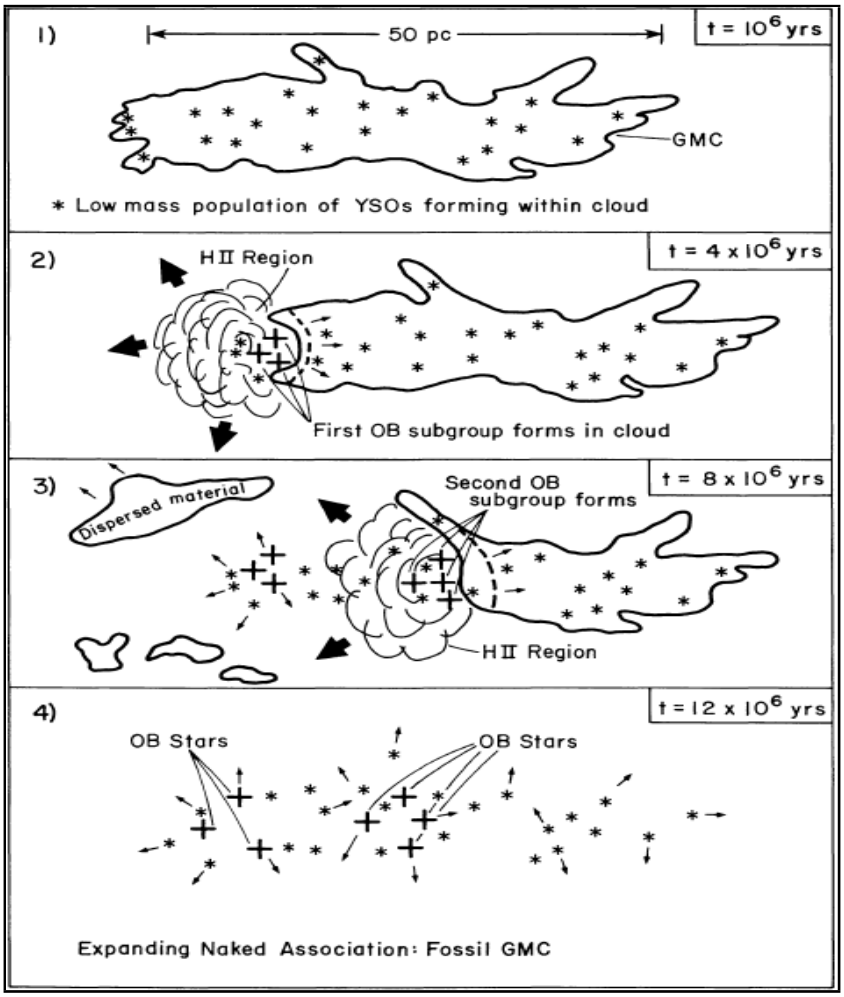

Figure 1.4: Sequential Star Formation (SSF) taking place inside a massive Giant Molecular Cloud (GMC). (Lada, 1987 [13])

1.3 Star Formation Stages

A discussion of low-mass star formation is important if one is to understand at what point the stellar winds from these types of stars develop into the initial triggers of SSF. To begin, it is important to mention that star formation, regardless of mass, is believed to occur predominantly inside GMC structures. A typical GMC structure is permeated by an array of neutral molecules, of which hydrogen is by far the most common. The low temperature and high density of these structures make for very favorable conditions for clump forma-

tion and subsequent collapse. GMC structures are also gravitationally bound, since the turbulent pressure of a GMC has been observed to always dwarf the thermal pressure of the surrounding Inter-Stellar Medium (ISM), yet the structure remains intact.

The types of clumps that can form inside a GMC structure can be summarized in 3 broad categories:

1. Non-Collapsed, Stable Clumps (inert clumps, filaments etc.)
2. Collapsed, Stable Clumps (cold cores)
3. Collapsed, Star Forming Clumps (hot cores)

Members of category 1 remain in this state until some support mechanism gives way (e.g cloud cools down), or a large trigger is set in place (e.g a passing shock-wave) in which case they can move either to category 2 or 3. Members of category 2 also remain in the same state but can potentially move to category 3 by similar means as their category 1 counterparts.

Members of category 3 however, progressively pave their path toward the main sequence through a number of phases whose characteristics are summarized under the term "class". These can differ slightly between low-mass ($\leq 2\ M_{\odot}$) and high-mass stars ($\geq 10\ M_{\odot}$).

High-mass stars typically do not form a circumstellar dust ring unlike low-mass stars which always do so. They also require higher initial clump temperatures and densities for a more efficient collapse that utilizes a larger portion of the clump's mass. Also, high-mass stars demonstrate much higher accretion rates and a rapid clearance of star forming material when compared to their low-mass counterparts.

Focusing on low-mass stars, their evolution journey may be summarized in 4 such phase classes, of which classes I, II and III are first discussed in detail by C.J Lada [13] and Class 0 is introduced later on by P. Andre et al [47]. Each class is qualitatively and quantitatively distinct from others.

Class 0 encompasses the inside-out collapse of the clump to progressively form a rapidly rotating, hot core with a steep density gradient. These objects are engulfed in an opaque, envelope, where the high opacity is a consequence of the dusty component. This opaque nature makes it very difficult to infer what is happening inside the envelope, making class

0 objects the least understood in the evolution sequence.

Class I encompasses the infall phase, where the core is now a structure comprising of a hot, dense center with an accreting envelope and a luminous, thin dust ring. Gravitational energy lost from the envelope's accretion makes this class of objects quite luminous. Objects at this stage are commonly referred to as "Protostars".

Class II encompasses the first outflow phase, in which the luminosity output of the object is large enough to reverse the infall of the envelope into an outflow. Here, the envelope is being driven away, while the dust ring, although being compromised as well, is still intact. Objects at this stage are commonly referred to as "Pre-Main Sequence Objects" (PMSOs).

Class III encompasses the second outflow phase, where the protostar has completely compromised its disk, with the remaining structure being a naked, contracting, T-tauri-type star, becoming hotter through the loss of gravitational potential energy and eventually becoming self-sustainable by Lithium burning through the P-P chain. Objects at this stage are commonly referred to as "Young Stellar Objects" (YSOs).

A graphic depicting the four evolution stages is shown in figure 1.5. Beyond class III, the YSO continues to contract and heat up. Its trip to the main sequence ends when it either develops a radiative zone (low-mass star) or begins fusing hydrogen (all other stars). Objects that reach either of these outcomes are commonly referred to as "Zero-Age Main Sequence Objects" (ZAMSOs).

When the ZAMSO clears its vicinity entirely from star forming material and dust, its emission spectrum traces closely that of a perfect blackbody with temperature equal to that of the object's surface temperature. At this point, the object has finally evolved to a "Class V" or "Main-Sequence" (MS) star.

If the formed MS star is massive, its birth will be accompanied with the generation of an expanding HII region as well. It is now time then to dive deeper into the evolution specifics of HII regions in order to understand the timescale and nature of the events taking place in SSF theory.

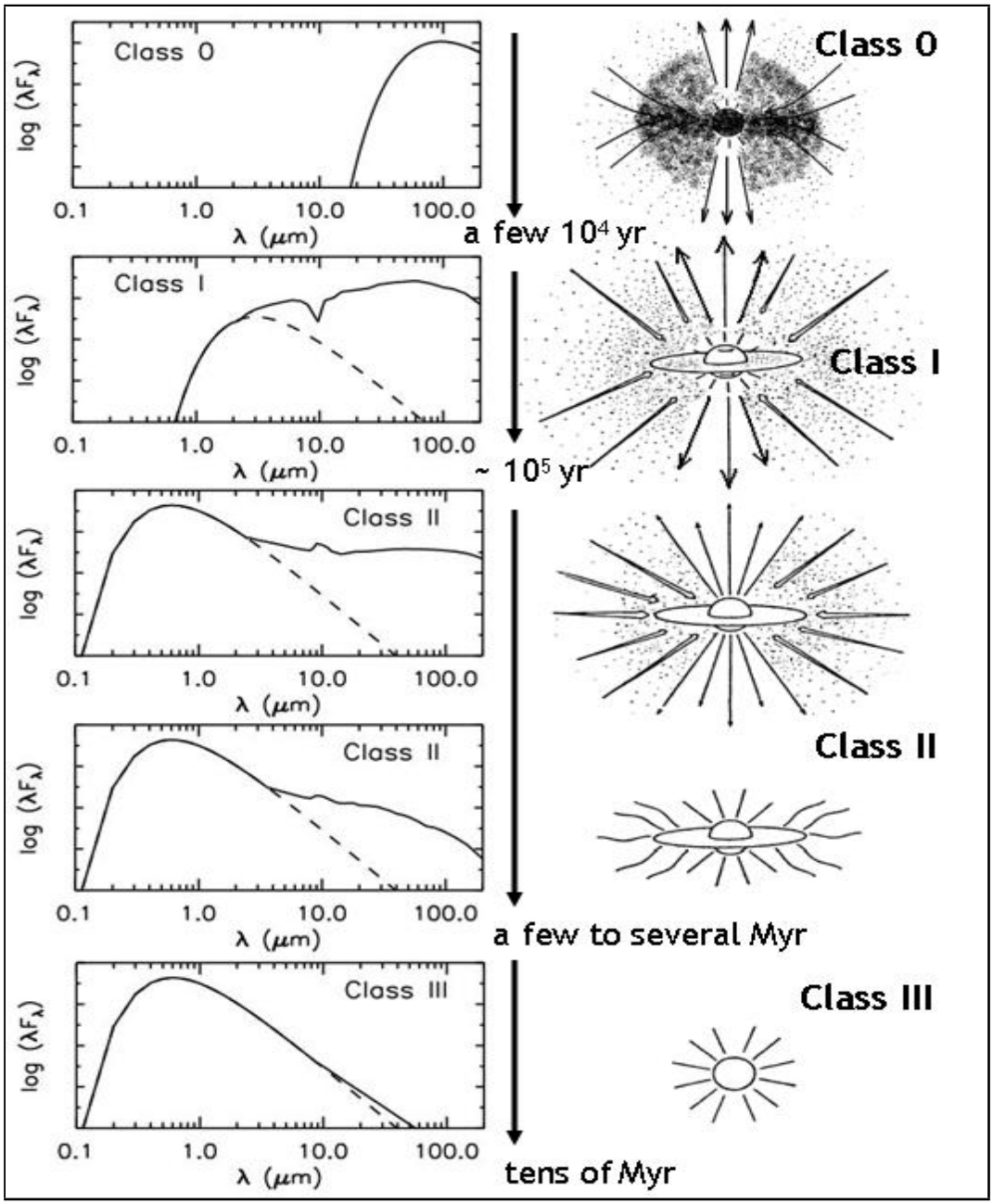

Figure 1.5: Star formation stages for low-mass stars. This is a modified figure of the one found in Wilking,1989 [62], where class 0 objects are now also incorporated. Presented are the spectral distribution of each stage in the infrared (Left) along with a graphic summarizing the associated evolution stage (Right).

1.4 HII Regions

HII regions are central to this thesis, and as such, deserve a thorough discussion. So far, their origin and role in sequential star formation has been clearly established. In this subsection I dive further into the physical processes behind these structures and their evolutionary specifics while closely following Professor *R. Pogge's* lecture notes [3] for the former and *T. Wilson's* quantitative description for the latter [56].

1.4.1 Physical Processes and Spectral Emission Characteristics

As the name suggests, HII regions are created through the ionization of atomic hydrogen. A common approximation regards all such ionizations as occurring exclusively from the ground state. This is because the probability of ionization occurring from a non-ground state level is extremely low, a consequence of the very short lifetime of excited states as compared to the average time for an encounter between a Lyman continuum photon and a hydrogen atom in a molecular cloud. This assumption is often referred to as the "nebular approximation".

Now, during such a photo-ionization event, if the incident Lyman continuum photon carries an energy greater than the ionization potential of a ground state hydrogen atom (13.6 eV), the difference is invested in the form of kinetic energy to the released electron. This excess energy is essentially the main heating mechanism of the HII region's electron plasma. Collision events between free electrons are very frequent and efficient. As a consequence, the electrons of an HII region plasma reach local thermodynamic equilibrium (LTE) very quickly and their kinetic energies as well as associated velocities are well described by a Maxwellian distribution.

The reverse process of recombination, involves a free electron becoming re-captured by a free ion in the HII region plasma. This process ends with the electron reaching the ground state either directly, or via a cascade through a number of energy states, the former being much more probable than the latter option. This means that the majority of recombinations lead to the emission of a Lyman continuum photon, ready to ionize another Hydrogen atom in the nebula. However, in an expanding HII region, the timescale of recombination events is several orders of magnitude larger than that of photo-ionization events, meaning that recombinations drive much more weakly the expansion, especially in the initial stages. The situation flips near ionization equilibrium, where photo-ionization and recombination timescales approach equality. Recombinations end up enriching an HII

region's emission spectrum with spectral lines spanning the meter to millimeter range, with the strongest line being the one generated through direct transition to the ground state, as it is the most probable. Recombinations also act as a cooling mechanism for the HII region itself in two different ways. The first occurs when an electron recombines with a proton but doesn't return to the ground state directly, but rather in a cascade fashion. Each of the stops in this cascade produces a photon that is not able to re-ionize Hydrogen and can therefore travel freely in the HII nebula and eventually completely depart from it. This is due to the very small probability for this non-ionizing radiation to be absorbed by other constituents of the nebula. The second occurs when recombinations take place near the boundary of an HII region. A portion of the produced photons are directed outward from the nebula and as a consequence are lost to interstellar space.

However, a free electron may approach a free ion without ending up being captured in a recombination event, but rather scattered in what is commonly referred to as "thermal bremsstrahlung". In this process, an electron is accelerated as it approaches an ion. The perpendicular component of this acceleration produces a radiation pulse with a certain frequency spectrum. The ion is presumably inert during this interaction due to its much larger mass. The acceleration's magnitude depends on the separation at closest approach (i.e impact parameter), while its duration on both the impact parameter and electron velocity. Both the impact parameters and electron velocities define continuous variable distributions. The impact parameters are typically represented by a truncated Gaussian between the maximum and minimum possible values. The upper limit is typically taken to be the Debye length, while the lower limit comes from asserting the quantum mechanical uncertainty principle. The velocities on the other hand are assumed a Maxwellian distribution based on the aforementioned fact that HII regions reach local thermodynamic equilibrium very fast. The resulting emission spectrum arises from a convolution of the two distributions through the radiative transfer equation. Overall, this spectrum follows a $\propto v^2$ power law in the deep radio range, peaks around 1.0 GHz at which point the HII region turns from optically thick to optically thin, and then roughly follows a $\propto v^{-0.1}$ power law.

Even though Hydrogen is the primary constituent of an HII region nebula, other atomic species are present as well, albeit at much lower abundances. These include, but are not limited to, Helium, Carbon, Nitrogen, Oxygen, Neon, Iron and Silicon in decreasing order of abundance. The presence of heavier elements in a molecular cloud ends up giving it a resulting onion-like ionization structure as will be discussed later on. Although such heavier elements carry a larger number of electrons that can be potentially ionized, their abundances are typically several orders of magnitude smaller than that of Hydrogen. Essentially the greatest contributor of free electrons in an HII region is always Hydrogen.

Dust grains and aggregates also exist in HII regions at very small abundances, yet their presence has dramatic effects on their emission spectrum. Dust grains tend to absorb UV radiation produced by an HII region's host star(s), a process that heats them up. The grains then glow thermally in the submillimeter range, their emission spectrum tracing closely the Rayleigh-Jeans blackbody emission limit. In addition, this UV absorption tendency of dust grains contributes considerably to the opacity that goes into the radiative transfer equation describing an HII region's emission spectrum as a whole.

Collisional excitations and de-excitations also take place inside an HII region. Typically the rate of occurrence of the two is the same. Their importance lies in their ability to act as a second and much inferior cooling mechanism to the HII region in a very specific way. If an electron collides with an ion and excites it, while shortly after a second electron re-collides with the excited ion, de-exciting it to the ground state, energy is conserved. However, if the excited ion becomes de-excited through spontaneous emission instead, the incident electron's kinetic energy is lost from the nebula in the form of radiation that is highly unlikely to be absorbed by any of the nebula's constituents. It should be noted however that the probability of such an interaction taking place is extremely small and this is why this method of cooling is not particularly important for the HII region system as a whole.

1.4.2 Evolution

The simplest, yet surprisingly accurate model of an HII region involves one massive OB star embedded in an atomic hydrogen cloud of uniform density. Once the star "turns on", it begins generating Lyman continuum photons ($E \geq 13.6\ eV$) which in turn ionize atomic hydrogen in the cloud. The barrier formed between hydrogen that has been ionized and hydrogen that is still neutral is referred to as an "ionization front". A pressure wave accompanies this ionization front. This is due to the induced increase in both temperature and number density as the Lyman continuum photons progressively ionize hydrogen atoms in the nebula. Specifically, the temperature climbs from roughly 100 K to 10000 K while the number density is doubled as electrons and protons are now two separate particles in the system.

The existence of molecular hydrogen in the GMC structure however begs the question of how it complicates the simple picture constructed above. Since the dissociation energy for atomic hydrogen is roughly 4.8 eV, and the population of photons with $E \geq 4.8\ eV$ will

be much greater than that with $E \geq 13.6\ eV$, a dissociation front is expected to propagate much further ahead than the ionization front of the atomic hydrogen.

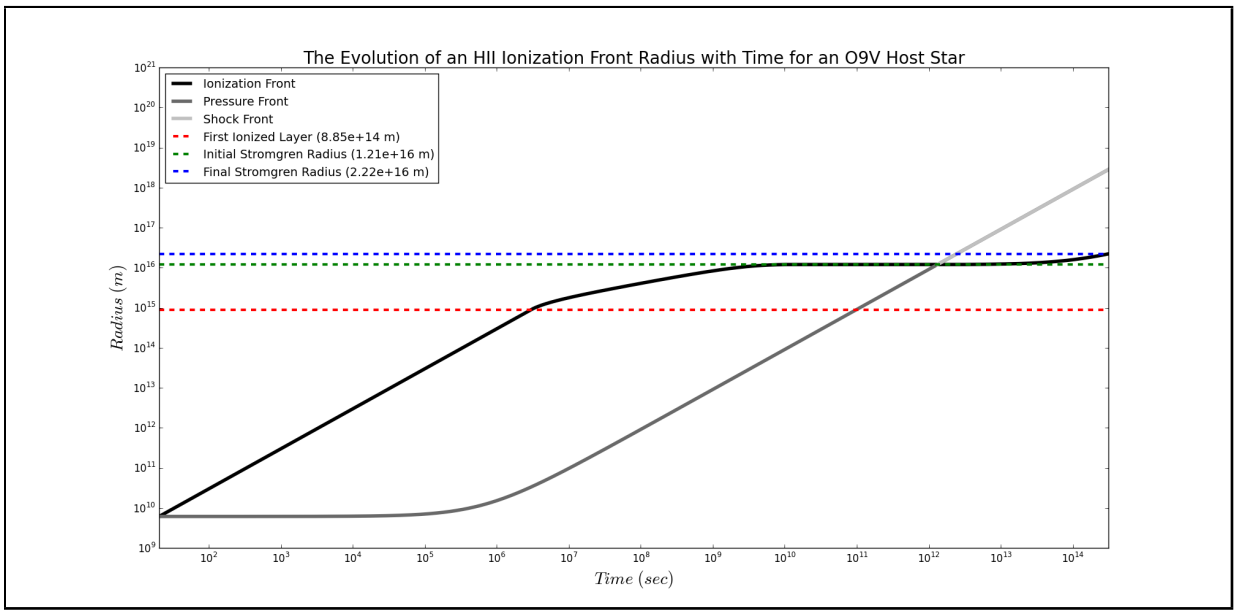

Figure 1.6: A plot depicting the radius evolution of the ionization, pressure and shock fronts for an ideal HII region under the influence of a single O9V host star as a function of time. This model is constructed using T.Wilson's quantitative description [56]

The pressure wave that accompanies the initial ionization front can develop into a shock-wave through one of two ways, depending on the density profile of the GMC. The first involves the pressure wave propagating in a GMC neighborhood with a significantly negative density gradient, something that is not very common. The second occurs when the pressure wave meets the ionization front. The sharp and almost discontinuous change in number density significantly slows down the rarefaction component, while the compression component catches up, to the point where the two almost overlap.

This meeting however does not happen for quite a while, as the ionization front initially moves at the speed of light, while the induced pressure wave travels at the local, isothermal speed of sound. At some point however, the ionization front reaches a size with a radius such that the time it takes ionizing photons originating from the OB star to traverse it becomes comparable to the recombination time of hydrogen atoms themselves. This radius defines what is commonly referred to as the "First Ionized Layer". The ionization

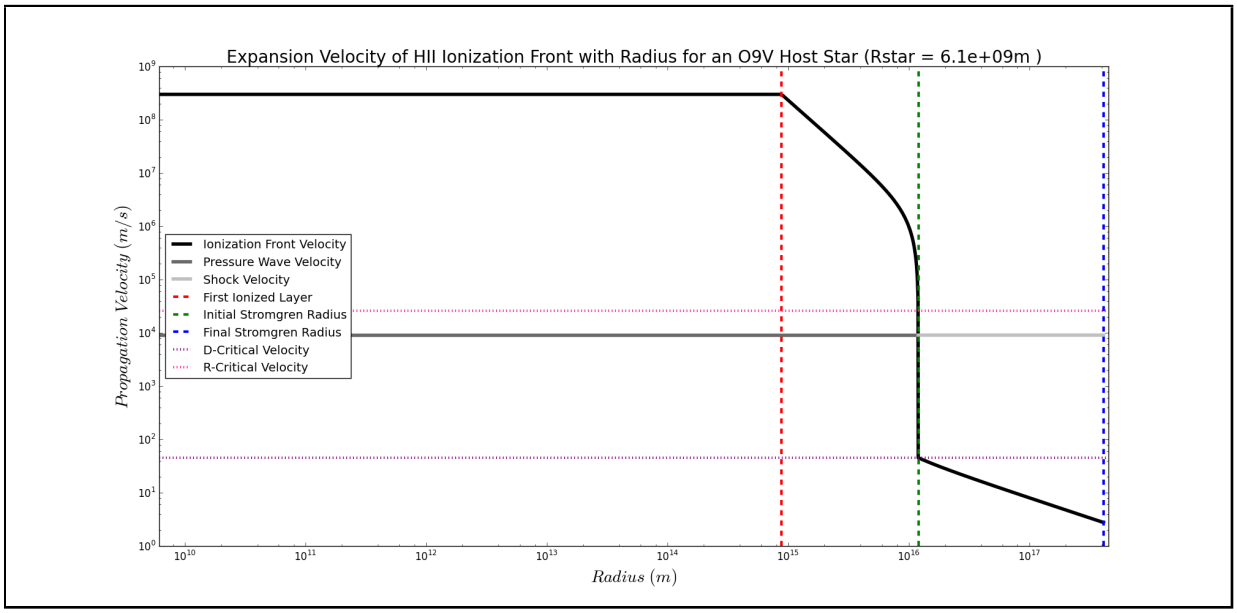

Figure 1.7: A plot depicting the evolution of the expansion velocity of the ionization, pressure and shock fronts for an ideal HII region under the influence of a single O9V host star as a function of radius. The D-Critical and R-Critical turnover velocities are also displayed. This model is constructed using T.Wilson's quantitative description [56]

front gradually slows down from this point onward, while the accompanying pressure wave continues propagating at its original speed.

At a timescale of $\approx 10^{10}$ seconds, the ionization front becomes sonic, then quickly becomes subsonic with an ever-decreasing expansion velocity. It is at this point where the HII region temporarily achieves ionization equilibrium at a radius commonly refereed to as the "Initial Stromgren Radius". However, the pressure wave continues propagating at its original pace, gradually catching up to the ionization front.

At a timescale of about $\approx 10^{12}$ seconds, the pressure wave overtakes the ionization front, and evolves into a shockwave. The overall effect of this overpass is to decrease the number density of particles ahead of the ionization front. This allows the ionization front to proceed moving outward at some initial subsonic pace that is continuously slowing down ever after.

The expansion of the ionization front can end in one of two ways. If the cloud is small,

then the OB star eventually completely ionizes it and the ionization front traces the cloud's boundary. If the cloud is large, the ionization front continues to expand throughout the lifetime of the OB star, which typically lasts around $10^{\approx 13-14}$ seconds ($\approx 1 - 10\ Myr$). The final, and largest radius that the ionization front reaches through either of these two scenarios is commonly referred to as the "Final Stromgren Radius".

An overall graphic of the expansion of an ideal ionization front supported by an O9V type star is presented in figure 1.6. Note the initial light speed expansion up to the first ionized layer, then the continuous slow-down until the initial Stromgren radius. The ionization front spends on the order of 100000 years near this radius as the pressure wave catches up. When the two meet, the ionization front once again expands at a subsonic and continuously retarding rate.

The same situation may be seen from a different perspective using figure 1.7. Here, expansion velocity is plotted against radius instead in order to clearly depict the four stages of the ionization front's expansion (light-speed, supersonic, sonic and subsonic). Note also the unchanging velocity of the pressure wave and its derivative shockwave. The "Dense" and "Rarefied" expansion velocities (D-critical and R-critical) essentially mark turnover points for the ionization front as it transitions between supersonic-sonic, then sonic-subsonic expansion velocities. These two points strongly depend on the GMC environment as well as the spectral class of the host star.

1.4.3 Complications

It is important to point out that these models reflect only the ideal case, which is founded over several assumptions. The list of major assumptions includes:

- A uniform GMC density profile
- A single, massive OB star with unchanging luminosity output
- No effect from recombinations
- A strictly HI GMC composition

Below, I discuss the effect of each of these complications on the HII region's evolution.

A variable GMC density profile means that the HII region will expand in a non-uniform

fashion, as the ionization front encounters different amounts of neutral hydrogen at different regions of the GMC. A denser region of the GMC will require a larger number of ionizing photons to become ionized and the ionization front will spend more time at that location as a consequence. The evolution then becomes spatially dependent and the geometry of the HII region is no longer resembles a simple sphere.

When two or more massive OB stars exist in the same vicinity, they will each initialize their own ionization front and accompanying pressure wave. When the boundaries of two ionization fronts meet, they will merge together into a larger front that will now be fueled by the combined ionizing radiation of both host stars. The pressure waves will also merge in a similar fashion, producing a pressure wave of larger amplitude. In the limit of an OB subgroup then, the individual ionization fronts will merge to give rise to a much larger ionization front that is fueled by the combined ionizing photons of all involved members.

Recombinations in essence will increase the total number of ionizing photons present in the system. A small, yet considerable amount of HII recombinations will comprise the capture of an electron followed by a direct drop to the ground state. This results in the emission of a photon with energy equal to that required for re-ionizing HI. Consequently, consideration of recombinations leads to a slightly larger initial Stromgren radius.

Having elements in the GMC other than HI introduces interesting new features. As an example, Helium is the second most common ingredient of a GMC. If the massive OB star is capable of producing radiation that can singly-ionize HeI to HeII, an HeII ionization front is formed with its own pressure wave. Due to the fact that HeI-ionizing photons are less populous than HI-ionizing photons, the size of the HeII Stromgren radius will always be smaller than that of its HII counterpart. It shouldn't then come as a surprise that a massive enough star can also form a doubly-ionized helium (HeIII) ionization front with an even smaller Stromgren radius than its HeII counterpart. In general then, additional elements give an onion-like ionization structure to the molecular cloud, provided that the host star can produce photons capable of ionizing these elements.

However, although gas constitutes the majority of a molecular cloud's mass, the dusty component, comprising a little over 1% of the total mass, has significant consequences on the cloud's dynamics and spectral characteristics as will be seen in the following section.

1.5 Dust

Dust grains typically comprise a little over 1% of a molecular cloud's total mass, yet it would be impossible to talk about star formation without a discussion of its effects. Dust is a crucial tool for scoping the chemical, dynamical and thermal processes behind molecular material and in particular, its dense phases that ultimately lead to star formation. In fact, thermal dust emission in the millimeter and submillimeter regime enables us to infer the presence of a collapsing clump, as the dust is well mixed with the gas component everywhere in the cloud.

Cosmic dust is a multi-component system, composed of different types of grain subunits. The compositions one can find are many and depend strongly on the environment the dust exists. In the work of Ossenkopf [58] and Henning [21], a total of six characteristic dusty regimes are identified, namely:

1. Dust in the ISM
2. Dust in Stellar Outflows
3. Dust within Cold Molecular Clouds
4. Dust in YSO Envelopes and Circumstellar Disks
5. Dust in Hot YSO Cores
6. Dust in Cold Protostar Cores

The properties that change between these categories are the type of coagulating material, the size of a typical grain, as well as the presence of ice mantles. As an example, dust in the low-density ISM environment is composed of more coarse, denser dust aggregates, while dust inside a dense molecular cloud experiences more collisional and chemical interactions that allow coagulation and ice mantle formation respectively (Henning,1995 [21]).

Clearly, these are not the only places where dust exists in the cosmos, however, these regimes define six distinct dust grain populations, which can be found in other places with similar conditions. In fact, one of these places of interest is within HII regions themselves where dust is observed in the form of small, low-density cavities, whose presence is given away from observations of light scattering taking place. The characteristics of the dust

grains found in HII regions trace those of dust found in YSO envelopes, however, a particular trait of HII region dust is that it progressively diminishes as one observes closer and closer to the ionizing OB star. (Akimkin et al, 2015 [59]).

However, although different, a common characteristic across all dusty compounds is their large opacity. This opaque nature of dust has tremendous consequences in star formation. Arguably the greatest of these consequences involves a molecular cloud's energy budget where dust plays both a heating and cooling role. The heating aspect of dust may be seen in action through dust grains present near sources of radiation spanning the UV to near-IR range. Such radiation tends to be absorbed by dust, introducing additional internal energy to the dusty system, while a portion of this energy ends up being re-emitted thermally in the far-infrared. The cooling aspect of dust on the other hand may be seen through its dynamic interactions with the gas component. Collisions between dust and gas particles lead to stimulated emission from collisional de-excitations, where emitted photons carry energy away from the cloud system, leading to its gradual cooling. (Savage,1979 [9]).

Another effect from this large opacity is the extinction of light emitted from sources surrounded by, or mixed with dust. The energy budget estimates of such sources may become significantly skewed if this extinction remains unaccounted for. Dust also affects the emission spectrum of such sources, as dusty emission drowns out features introduced from other components of the system. (Savage,1979 [9]).

The mere presence of dust in star forming clumps has been found to directly limit accretion of mass during the YSO stage of star formation. (Henning,1995 [21]) In addition, it has been shown through numerical simulations that it acts in a destabilizing manner both during the inflow and outflow stages of star formation. (Noh,1993 [20]). Dust particles are also easily charged and as such can become polarized, but also interact with permeating magnetic fields, leading to the introduction of dynamic effects on the dust itself as well as its coupled gas component. (Henning,1995 [21])

Overall, the goal of dust astrophysics remains two-fold. The first involves the development of accurate extinction curves that span the widest possible wavelength range for each type of dust grain. The second, involves the matching of astrophysical environments to specific dust grain populations based on the environment's physical properties. The first goal is achievable through a consolidation between chemistry, solid-state physics and quantum physics, while the second through pure astrophysical observations. Developments in the modeling of interstellar dust, as well as a discussion about the goals of a unified dust model can be found in Zubko's work [63].

1.6 Instrumentation

So far the physical systems involved in sequential star formation have been explored, however there has been no discussion of the manner in which they will be observed. It is then time to take a closer look at the instruments used to obtain the data that will be analyzed in this thesis.

The most commonly used tool for investigating molecular clumps is spectral emission from various molecular CO transitions. However, many of the CO spectral lines are optically thick, making their interpretation quite difficult. Optically thick emission means that only the outer layers of a clump may be investigated. This in turn means that any mass estimates stemming from CO observations are prone to underestimation. However, dust emission is almost always optically thin at submillimeter wavelengths. This allows the mass problem discussed above to be circumvented.

Therefore, the thermal submillimeter emission of the dusty component of clumps is assessed in this thesis. The submillimeter data necessary for this is provided by the "Submillimeter Common-User Bolometer Array 2" (SCUBA-2) instrument. At the same time, in order to identify the position of Sharpless HII regions and overlay them on the SCUBA-2 images, the radio flux from the free-free and thermal radio emission of the HII regions is assessed. The radio data necessary for this is provided by the "Very Large Array" (VLA).

In the following subsections I introduce the two telescope configurations and discuss some of their associated features.

1.6.1 SCUBA-2

SCUBA-2 is a camera part of the JCMT telescope that operates simultaneously at 450μm and 850μm wavelengths. These two wavelengths are located at the position of two significant atmospheric transmission windows in the submillimeter regime. Each wavelength band uses a total of 5120 chained bolometers, with amplifiers that use the "Superconducting Quantum Interference Device" (SQUID) architecture. This dense setup allows SCUBA-2 to construct sufficiently detailed, wide-field observations of some of the coldest structures the universe has to offer.

The two operating wavebands of SCUBA-2 align well with two big atmospheric transparency windows in the submillimeter regime. They are also close (but not exactly at) the

peak emission of cold and hot molecular clumps. This enables SCUBA-2 to have a great chance at observing the earliest stages of star formation. These types of observations will aid researchers in determining how star formation rates change with redshift, and potentially, when galaxy formation started taking place in the early universe!

The JCMT is located near the summit of Mauna Kea in Hawaii, at an altitude of $\approx 4200\ m$. This is done in order to minimize the detrimental effects of water vapor on atmospheric transmission. However, even at this altitude, weather conditions can occasionally become non-cooperative. An in depth discussion of the SCUBA-2 transmission sensitivity to atmospheric conditions is presented in chapter 3, with particular focus on the 450μm band which suffers the most.

SCUBA-2 observations are performed using distinct scan patterns that are developed with 2 main goals in mind. The first goal is to minimize effects due to variable atmospheric transmission from bulk motions of the atmosphere itself but also variable water content between different patches of the sky. The second goal is to tend best to each type of source, treating bright, compact sources differently than their dimmer, extended counterparts.

To accommodate the first goal, each pattern consists of a base-pattern design that is rotated in a circular fashion until the telescope reaches its starting slewing position. This allows each location of the sky to be sampled from several different directions, giving a better sense of the sky's variability, which in turn can be used to remove its effect on data during the data reduction stage.

To accommodate the second goal, two distinct base-patterns are developed to suit each type of source. The first pattern is called "PONG" and is optimized for scanning a large area while maintaining a relatively constant exposure time. "PONG" scans are typically used to cover extended sources up to 2 degrees in diameter. The second pattern is called "DAISY" and is optimized for maximizing exposure time near the center of the image. "DAISY" scans are typically used to cover compact sources of order 3-6 arcminutes in diameter. Both scan patterns and their base-patterns are presented in figure 1.8. This summarizes the SCUBA-2 essentials for this thesis. For further details on SCUBA-2's design, data reduction pipeline, calibration tests as well as SQUID and other technologies, refer to the MNRAS publication on SCUBA-2. [61].

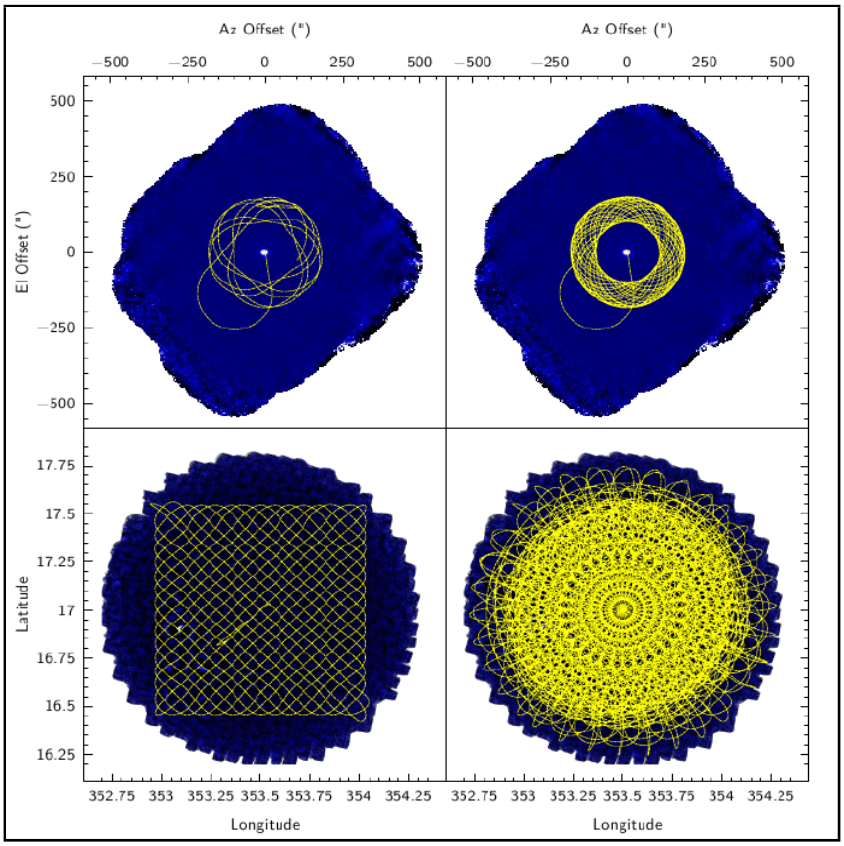

Figure 1.8: The DAISY (Top) and PONG (Bottom) scan patterns. A single iteration of each pattern is displayed on the left panels, while a complete rotation of each pattern is displayed on the right panels.

1.6.2 VLA

The VLA is essentially a radio telescope consisting of 27 individual radio antennas. It uses aperture synthesis in order to achieve the resolving power of a single, massive antenna using multiple smaller antennas instead. Incoming signals are stamped with a time provided by a precise atomic clock, then mixed and finally amplified before reaching a computer for processing. The result is a view of resolving power equivalent to that of a single dish of diameter equal to the separation between the furthest members in the antenna arrangement.

Each antenna consists of a 25 m diameter dish and is mounted on movable rails. The antennas are arranged in a "Y" orientation to maximize spanned area. Through the year,

each arm is lengthened from 1 km out to 37 km as the antennas are moved using a special transporter vehicle to achieve a different compromise between light sensitivity and resolving power.

The telescope array is located in New Mexico. The reasoning behind the choice of this location is three-fold. First, it is a flat desert, and as such, makes the geometry, but also the placement and movement of the components, a straightforward task. Second, the dry desert climate minimizes effects from atmospheric water vapor on observations. Finally, this area lies far from any urban centers and is surrounded by a wall of natural rock formations that provides considerable shelter from the constant bombardment of man-made radio signals.

The VLA operates at 10 different radio bands spanning the MHz and low GHz range (74MHz - 43GHz). This makes it ideal for observing continuum spectra from thermal-bremsstrahlung (free-free), synchrotron and pure thermal emission, and consequently, ideal for observing HII region nebulae.

Finally, although the antennas were built and assembled in the early 1970s, they are well maintained with no report of any significant downgrade in performance over the years. In addition, the electronics of the assembly are continuously updated. Incoming signals are currently fed through fiber-optic wires into a powerful central processing computer that uses a recently developed architecture for interferometric data processing called "Wide-band Interferometric Digital Architecture" (WIDAR).

This summarizes the VLA essentials for this thesis. For more information regarding details of the array's design, interferometry, and WIDAR technology, refer to the NRAO website [4].

1.7 Thesis Motivation

At this point, I've discussed star formation with a particular focus on sequential star formation and the role of HII regions and dust in this process. The instruments used for investigating these were also introduced. It is time then to discuss the particular research motivating the construction of this thesis, as I slowly conclude its introductory segment.

Theories regarding HII regions triggering star formation through the CC and RDI pro-

cesses have been circulating since the early 1980's. Eventually, the ideas forwarded by these theories began being tested through multiwavelength studies of HII region objects. These studies were dedicated in finding evidence of extensive clump formation near the boundaries of HII regions.

One of the first HII regions to be studied for this purpose (also part of this thesis) was Sh-2 104 by Deharveng and her team in 2003 [33]. Evidence for massive condensations along the rim of Sh-2 104 was inferred from the elevated fluxes of the CO^{12}(2-1) line emission there. An image from a more recent study of Sh-2 104 is presented in figure 1.9, where the H_2 column density map reveals the extensive clump formation along the HII region's rim.

The findings from the Sh-2 104 study stimulated investigation of more HII region objects for the same purpose. Below, I present a list of a number of such studies that confirm extensive molecular condensation near the rim of the HII region under study.

- Sh-2 104 (Deharveng,2003 [33]), (Zavango,2005 [6]), (Xu,2017 [27])
- RCW 79 (Zavagno,2005 [6])
- Sh-2 219 (Deharveng,2006 [34])
- RCW 120 (Zavagno,2007 [7])
- Sh-2 212 (Deharveng,2008 [36])
- Sh-2 254 - Sh-2 258 Complex (Chavarria,2008 [38])
- Sh-2 217 (Brand,2011 [24])
- Sh-2 90 (Samal,2014 [43])
- Sh-2 39 (Duronea,2017 [45])
- Sh-2 242 (Dewangan,2017 [39])

This is not a complete list, and is simply intended to motivate the beginning of this thesis by placing it in a proper scientific context, as well as allow the reader to refer to other studies of similar nature. Most of these studies investigate molecular CO emission and near-to-mid infrared (IR) observations. Very few investigate dust in the far-IR regime. Below, I summarize the results obtained in the study of each of these objects. Remember that all listed objects present evidence for the "collect-collapse" process taking place.

Sh-2 104

Sh-2 104 is a 7' diameter HII region, ionized by an O6V star and located at a distance of 4.0 kpc. Studies of $^{12}CO(2-1)$ emission revealed 4 extended molecular condensations, with CS, $HCO+$, ^{13}CO and $C^{18}O$ revealing several denser core fragments of sizes 0.4 to 0.6 pc in diameter and average column and number densities of $3-3.5\times10^{15}$ cm^{-2} and $1.6-2.8\times10^{5}$ cm^{-3} respectively, implying total masses of 70-100 $M_{\odot}$. (Deharveng,2003 [33])

The total mass of the extended condensations was estimated to be 6000 $M_{\odot}$. A cluster was visible inside the largest condensation, one or more stars of which are suspected to be ionizing a smaller, compact HII region. The regular spacing of the molecular condensations allowed several theories regarding its creation to be discarded, including that the cluster was a result of a spontaneous molecular clump collapse, that it was a consequence of a collision between two clumps and that it was the result of a post-shock as the clump material was propagating supersonically through a turbulent interstellar medium. (Deharveng,2003 [33])

The star formation efficiency of the brightest fragment (670 $M_{\odot}$) was calculated to be 40%, using a standard initial mass function for low-mass stars and accounting for the presence of a B0V exciting star. (Zavango,2005 [6])

A more recent $^{12}CO(1-0)$, $^{13}CO(1-0)$ and $C^{18}O(1-0)$ study of Sh-2 104 revealed an almost completely 2-dimensional, double ring structure, with radii 2.9 pc and 4.4 pc for the inner and outer ring respectively. The ring structure was found to have an average column density of 6.8×10^{21} cm^{-2} and a total mass of roughly 2.2×10^{4} $M_{\odot}$. Column density maps using Hi-GAL survey data revealed the presence of 21 clumps, of which roughly 90% are expected to give rise to low-mass stars. (Xu,2017 [27])

RCW 79

RCW 79 is a 12' diameter HII region located roughly at a distance of 4.2 kpc. Studies in the 843 MHz band revealed a shell-like structure overlapping with this HII region. A study of 8.3 μm emission revealed the presence of a dust ring around RCW 79. An overlay of 1.2 mm and H_{α} emission data revealed 7 extended molecular clumps that were regularly spaced in an annular structure. The three most massive fragments had masses between 400 and 1400 $M_{\odot}$. (Zavango,2005 [6])

Near-IR studies revealed several sources, all of which are very massive and observed to be forming at the boundary of the molecular clump fragments. The star formation efficiency was estimated at 45%, using an initial mass function for the low-mass stars and accounting for an ionizing O6.5V star. (Zavango,2005 [6])

Sh-2 219

Sh-2 219 is a roughly 3' diameter HII region, ionized by an O9.5V star and located at a distance of 5 kpc. It is highly spherically symmetric and almost perfectly surrounds its exciting star. The study of $^{12}CO(2-1)$ emission revealed a very massive ($\approx$ 2000 $M_{\odot}$) molecular cloud at the S-W border of the region. The molecular cloud is found to be present before the creation of Sh-2 219, leading to no satisfactory explanation for the massive star formation in the area. (Deharveng,2006 [34])

At the boundary between this molecular cloud and Sh-2 219, 2 molecular condensations can be found whose shape is elongated and traces the ionization front of Sh-2 219. Near-IR emission reveals a cluster that is found between this interaction region, containing an early B-type star which is exciting an ultracompact HII region. (Deharveng,2006 [34])

A chimney-like structure can be seen, at one end of which Sh-2 219 is located. The existence of this feature was attributed to a bright H_{α} star at the rim of Sh-2 219. (Deharveng,2006 [34])

RCW 120

RCW 120 is a 7' diameter HII region, ionized by an O8V star and located at a distance of 1.34 kpc. The ionization front of this HII region is almost perfectly circular. A N-S density gradient appears to be in place, where density increases toward the south. The ionized sphere of RCW 120 appears to open in the direction of lower density (North) where the ionized gas can be seen escaping, in what appears to be the start of a "champagne flow". (Deharveng,2007 [7])

The study of 1.2 mm continuum observations traced the cold dust in the region and revealed 8 fragments, five of which are in direct contact with the borders of RCW 120. Near-IR data from 2MASS and mid-IR data from GLIMPSE are used to locate warm IR sources in the region. The largest fragment had a mass of 370 $M_{\odot}$. However, no YSO activity was seen in these fragments. (Deharveng,2007 [7])

On the other hand, many class I and II YSOs were observed throughout the rest of the area inside and around RCW 120, some of which were quite far from its ionization front. This indicated the importance of the interaction of escaping radiation from the HII region and the surrounding ISM. This radiation can warm the surface layers of distant, pre-existing clumps and lead them to a slow collapse through the RDI process. In fact, the existence of a large portion of YSOs in this study was attributed to RDI. (Deharveng,2007 [7])

Sh-2 212

Sh-2 212 is a 5' diameter HII region, ionized by an O5.5V star and located at a distance of 6.5 kpc. It is another highly symmetric case, consisting of an ionization front encircling its exciting star to a near perfect extent. (Deharveng,2018 [36])

Near-IR observations reveal a large cluster near the center of Sh-2 212 and a bright reflection nebulosity at its border. An 8.3 μm image revealed a bright source at the direction of this nebulosity, later determined to be a massive (14 $M_{\odot}$) YSO. (Deharveng,2018 [36])

Radio continuum observations reveal the presence of an ultracompact HII region at the same location as the nebulosity, likely being ionized by the massive YSO there. This HII region has opened toward the low-density gas outside the condensation and is another great example of a "champagne flow" taking place. (Deharveng,2018 [36])

Observations in the millimetre reveal a thin molecular, half-ring structure that engulfs the brighest region of Sh-2 212 which is expanding and fragmenting. The most massive of these fragments had a mass of 200 $M_{\odot}$. The fact that the ultracompact HII region and the inhomogeneity of the environment haven't inhibited the accumulating molecular material portrays evidence that collect-collapse can work in non-homogeneous mediums as well. (Deharveng,2018 [36])

Sh-2 254 - Sh-2 258 Complex

Sh-2 254-258 defines a complex of 5 HII regions, located at distances 2 to 3 kpc. Sh-2 254 is ionized by an O9V star, Sh-2 255 by a B0V star, Sh-2 256 by a B2.5V star and Sh-2 257 by a B0.5V star. Sh-2 254 is located behind Sh-2 255 and Sh-2 257, while the latter two appear to be on the same plane. Star formation appears to be propagating in a backwards direction behind Sh-2 255 and Sh-2 257 and toward Sh-2 254. (Chavarria,2008 [38])

Study of column density maps revealed that Sh-2 254 has depleted all its gas and dust, while a moderate amount still remains in Sh-2 255 and Sh-2 257 all-while Sh-2 256 and Sh-2 258 appear to be completely embedded in the original molecular cloud. This is mostly because each of these HII regions is at a different age. (Chavarria,2008 [38])

The study of IR data has identified clusters of stars inside Sh-2 256 and Sh-2 258 as well as one inside Sh-2 254. A massive cluster with lots of near-IR sources is also present between Sh-2 255 and Sh-2 257 and is part of a dense, dusty, molecular filament. Roughly 1' north from this cluster, another bright far-IR source is present without any evident near-IR peaks, as this cluster is likely at an earlier evolution stage. (Chavarria,2008 [38])

Near-IR SPITZER, IRAC and Flamingos observations revealed 510 YSOs, of which 87 were class I and 165 were class II. Another 6 YSO clusters were discovered between Sh-2 255 and Sh-2 257. Roughly 80% of the 510 identified YSOs were part of a cluster while the rest were isolated. (Chavarria,2008 [38])

Sh-2 217

Sh-2 217 is an elongated HII region with dimensions 9.3' x 7.5', ionized by an O9.5V star and located at a distance of 4.2 kpc. It's brightness in the radio continuum is uneven, with the brightest part extending from a S-W to a N-W direction. An ultracompact HII region of diameter ≈ 0.9 pc also exists at the S-W border of Sh-2 217 and is being ionized by a cluster of stars there. (Brand,2011 [24])

Studies of CO emission attribute roughly 1.7×10^4 $M_\odot$ of molecular mass to Sh-2 217 and its immediate vicinity. Four large molecular complexes are also identified with masses between $1.5 - 6 \times 10^3$ $M_\odot$. The east complex is inside Sh-2 217, while the north and south-east complexes are in the immediate exterior of Sh-2 217. (Brand,2011 [24])

The fourth complex forms a distinct ring structure with an accompanying dense rim. This complex interacts with the S-W border of Sh-2 217 and incorporates the ultracompact HII region mentioned previously. At the east portion of this ring, a cluster is identified along with evidence for a molecular outflow and a water maser. More water masers are found at two other locations along this ring structure. (Brand,2011 [24])

Three additional large molecular condensations are found, with masses $\geq 330 - 1100$ $M_\odot$ in-

side which several smaller cores are embedded with tens of solar masses worth of molecular material in each. (Brand,2011 [24])

Sh-2 90

Sh-2 90 is an irregularly shaped HII region with a 4.8' diameter, consisting of two bubbles, at a distance of roughly 2.3 kpc. The source of ionization has not been found, although its existence can be attributed to an O9.5V-O8V star. Its electron number density is established at roughly 144 cm^{-3} and its mass at 55 $M_{\odot}$. An ultracompact HII region is also found near its border. (Samal,2014 [43])

The study of CO(3-2) emission reveals that Sh-2 90 is inside an elongated molecular cloud of mass $\approx 1.0 \times 10^4$ $M_{\odot}$. Neutral material forms a shell surrounding the entire HII region. A total of 9 clumps are identified in this shell, 7 of which are situated at the border of Sh-2 90. (Samal,2014 [43])

Mid-IR observations reveal 4 large IR blobs and 129 low-mass YSOs which are distributed in regions of high column density. In these 129 YSOs, 4 are class 0 candidates, 21 are class I and 34 are class II YSOs. Far-IR observations revealed 5 cold dust clumps whose temperature varied between 18-27 K. (Samal,2014 [43])

Sh-2 39

Sh-2 39 is a roughly 8' diameter HII region, located at a distance of 4.1 kpc away. Sh-2 39 is coincident with a large IR bubble that has a very characteristic arc-shape with an open morphology. The ionizing source is unknown but the existence of Sh-2 39 is estimated to be the product of a single B0V star. (Duronea,2017 [45])

The study of CO(3-2) emission revealed a concentration of molecular material toward the west and south borders of the IR nebula. Sh-2 39 was also found to be ionization-bounded to the west and density-bounded to the east, pointing to it being a case of a "blister-type" HII region. (Duronea,2017 [45])

Furthermore, 4 molecular clumps were identified toward the west border, with total masses between $1.4 - 2.2$ $M_{\odot}$ and average number densities between $1.5 - 3.3$ cm^{-3}. Virial analysis of these clumps showed that 2 of them were gravitationally unstable. (Duronea,2017 [45])

Studies in the IR lead to the identification of 28 YSOs, whose position is projected to be adjacent to the IR bubble coincident with Sh-2 39. Finally, 2 clusters were also identified, one of which overlaps with the position of one of the molecular clumps and hosts a young O8-9V star. (Duronea,2017 [45])

Sh-2 242

Sh-2 242 is an 8' diameter HII region, ionized by a B0V star and located at a distance of 2.1 kpc. (Dewangan,2017 [39])

Herschel column density maps in the vicinity of Sh-2 242 identified a large, elongated molecular cloud associated with Sh-2 242, whose extent is far beyond its boundary. In addition, the map revealed the presence of 18 molecular clumps, 11 of which are found to be regularly distributed along this extended filamentary structure (EFS). (Dewangan,2017 [39])

The average mass per unit length of the EFS is 200 $M_{\odot}/pc$, which exceeds by far the critical value of 16 $M_{\odot}/pc$ (Assuming T=10K throughout it). The identified clumps have total masses ranging from $150 - 1020$ $M_{\odot}$ with the most massive being located near the ends of the EFS. (Dewangan,2017 [39])

GPS-2MASS and GLIMPSE360 data are used to identify a total of 192 class I and 153 class II YSOs, with an additional 101 YSOs being identified through an H-K color magnitude diagram. This brings the total number of identified YSOs to 293, all of which are mostly distributed along the EFS. Class I YSOs are almost exclusively found at locations of high column density. Finally, clusters of YSOs are seen exclusively at the ends of the EFS. (Dewangan,2017 [39])

What's Next?

In this thesis, I am attempting to find similar such evidence in a large, galactic HII region sample. However, rather than taking the traditional molecular CO approach, I divert my attention to the thermal emission from the dusty component. The reason behind this choice is to study such systems in a band that is optically thin to the systems themselves. This will allow much better estimates of total mass as well as mass-dependent properties

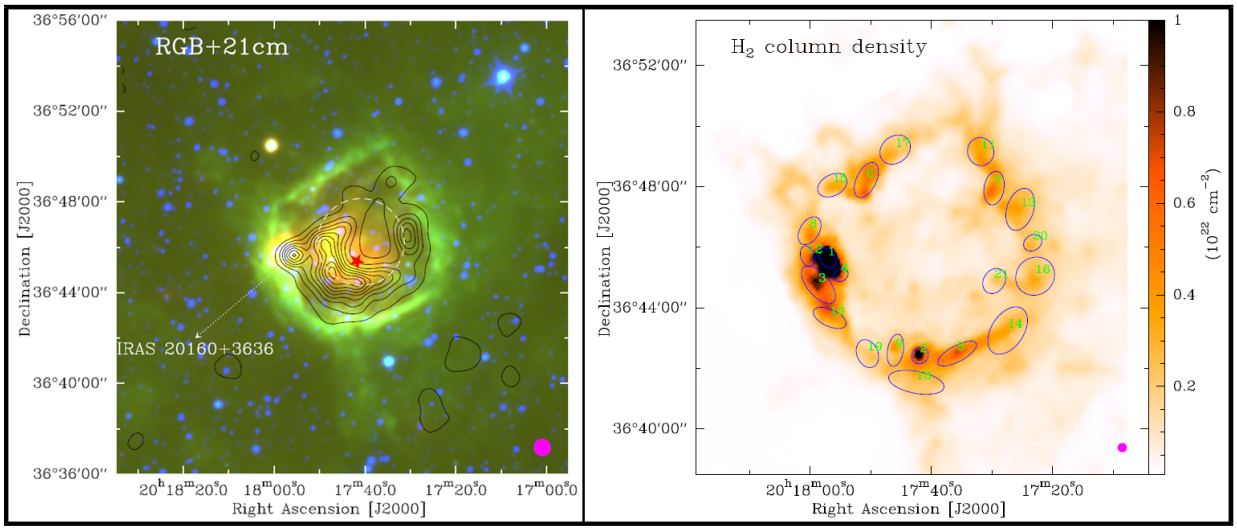

Figure 1.9: A multi-wavelength composite displaying WISE 3.4μm, 12μm, 22μm in blue, green and red respectively along with an overlay of 1.4 GHz VLA contours (Left). An H_2 column density map derived from Hi-Gal survey data (Right) (Xu,2017 [27])

such as number and column density.

In addition, I would like to test claims regarding molecular clump heating from nearby associated OB stars and HII regions as well as claims regarding the compression of these clumps from the HII regions themselves. I would also like to investigate claims for small overall star formation efficiencies ($< 3\%$) in HII region systems. I would also like to determine the effectiveness of HII regions at inducing star formation and how important their role is in sequential star formation theory by conducting a census of HII region associated cores in order to establish what fraction of these cores are likely to be star-forming.

The images to be analyzed for achieving these goals are presented and discussed in detail in section 5.1. It is about time then to begin unraveling this "dusty" approach to the study of molecular clumps!

Chapter 2

Data and Measurements

In this chapter I will be discussing the progressive reduction of raw data into meaningful measurements. The discussion will begin with the origin of the raw data and the manner in which it was reduced into usable images. This will be followed by a thorough discussion of the manner in which sources were identified and subsequently measured.

It is important to note that raw data from both telescope configurations has been reduced to image form prior to the creation of this thesis. The SCUBA-2 images in particular were reduced immediately before the beginning of this thesis by an undergraduate summer assistant. I only created variations of the SCUBA-2 images of objects G115 and G182 for the purpose of investigating the effects of different data reduction parameter settings on photometric measurements (see Ch.4).

2.1 Data Reduction

The raw data used in the construction of the VLA images was originally obtained from the VLA during April, 1987 while the telescope array was in the "D" configuration (shortest baseline setup) and operating in "snapshot" mode (4-5 minute exposure time). This project originally surveyed 109 HII regions. Of these, 53 were observed in the 1.46 GHz band and 61 in the 4.89 GHz band, with 5 being observed at both bands. The data was cleaned and reduced into image form in July, 1992. For further information regarding the sample and its data reduction, refer to *M. Fich's* work using the VLA [15] [16] and citations within.

The raw data used in the construction of the SCUBA-2 images stems from projects part

of the public archives available in the "Canadian Astronomical Data Center" (CADC). Specifically, data under the project names *M12BC12*, *M12AC10*, *M13AU03*, *M13AC21*, *MJLSY02*, *MJLSJ14B*, *M12BD04* and *M11BGT01* was used. However, these projects had different goals in mind which did not necessarily align well with the goal of this thesis. This leads to a major shortcoming, as a selection bias of complicated nature is in place and the list of galactic HII regions investigated is directly tied to the data that was available in these project archives.

The data itself was obtained from the CADC archives using queries for SCUBA-2 450μm and 850μm observations in a search engine. First, the names of every "Sharpless" (Sh-2) and "Blitz-Stark-Fich" (BFS) galactic HII region were inputted in order to see if any SCUBA-2 project had targeted them. If a result occurred, the data was downloaded and stored for future data reduction. However, more times than not, a name query was not fruitful, and a coordinate query needed to be used instead. Results from these queries were typically not part of a single project and/or telescope observation. Data was selected for further data reduction on the basis of proximity to the inputted coordinates and area coverage.

Regardless of the query method, raw data was always downloaded for storage on a local server named *eclipse*. Data reduction was then performed using a specific pipeline whose particulars can be found in a detailed article by *H.S Thomas* and *M.J Currie* [22]. The steps involved in running this pipeline are outlined in detail within *S. Beaulieu's* manuscript [10]. In summary, the process begins with an unmasked, "raw" run for the purpose of creating a base image to work with and identify structure. This is followed by the construction of a mask that is supplied to the pipeline for a subsequent "final", masked run. There are several parameters available for tweaking, which do influence the final product both quantitatively and qualitatively. A closer look at two of the most influential such parameters will be made in chapter 4.

2.2 Source Identification

Both VLA and SCUBA-2 images were converted to *.fits* format, and downloaded to a local machine for analysis. The software package *SAOImageDS9* was used for viewing these final images as well as a means of identifying sources within them. Identification of sources was done manually for both datasets, with the procedure being quite similar, although differing in some particulars.

In the VLA dataset, it is fairly straightforward to identify the extended structure of the contained HII regions. This is because the signal-to-noise ratios (SNRs) are typically high, there is no crowding and the HII regions themselves consist of a single, continuous and most often compact structure. Typically each VLA image is home to a single HII region, with the exception of a few cases where HII regions formed a tight group such as in the case of S254-S258.

In the SCUBA-2 dataset, the identification process is more involved. Each SCUBA-2 image typically contains several clump composites. These composites consist of a diffuse, cloud-like filament, which itself contains one or more bright cores. The high level of crowding, particularly in the case of cores, makes the identification difficult at times. Nonetheless, since the identification is done manually, a workaround can always be found for difficult cases.

For example, the overlapping of sources makes it unclear if they comprise a single source, or two sources that simply happen to be very close to eachother. This issue is alleviated through use of the *line-tool* provided by *SAOImageDS9*. This tool plots the flux registered at each pixel along a line defined by the user against the distance of that pixel from the line's origin. This can be used to view the variation of received flux along different paths across a source. As a rule-of-thumb, when this profile depicted two peaks that differed more than $\approx 50\%$ in flux, it was established that each peak belonged to a separate source.

Another common complication arises from "hot-spots" that resemble cores but are too asymmetric for a conclusive judgment. Once again, the *line-tool* can be used to monitor the flux profile across different paths through such hot-spots. If this profile resembles a Gaussian bell-curve whose peak is distinct from peaks found in the surrounding background emission, the hot-spot is deemed a source, and vise versa.

Finally, certain sources had to be automatically excluded from identification purely due to their location in an image. These include sources very near or at the noisy edge of their SCUBA-2 image, as well as sources lying too far from any HII regions to justify any potential association between the two.

2.3 Measurement Techniques

VLA measurements are used in order to obtain some important physical properties for the entire HII region sample of this thesis. These properties include the central coordinates, angular size, distance, physical size and integrated flux. Later on, these will allow the determination of properties such as electron number density and total mass.

The central coordinates and angular sizes of the HII regions are crucial for their association to cores and massive OB stars later on in this thesis. For this reason, I determine them manually using a robust approach. The approach begins with the generation of a flux contour plot for each VLA image. In this plot, the contour corresponding to 10% of the maximum pixel flux is identified, as it is a good approximation to the HII region's boundary. This is similar to considering the ≈ 2.0 SNR contour, and is used purely because it is slightly simpler to work with in a scripting environment.

This contour is then fitted with a circular aperture whose radius and central coordinates are stored and used as the best estimates of the HII region's radius and central coordinates respectively. An example of how this approach is carried through is presented in figure 2.1.

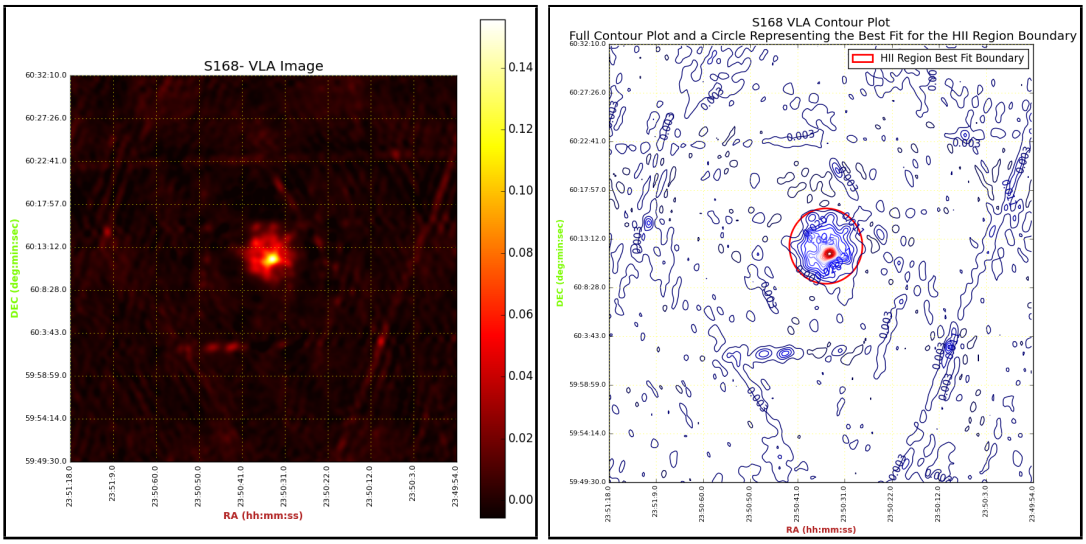

Figure 2.1: The VLA image of HII region "S168" (Left) and its associated flux contour plot with the circular aperture of best fit to the 10% contour (Right).

For the very small number of HII regions for which VLA data is unavailable, I obtain their central coordinates and angular sizes through *M. Fich's* VLA [16] and IRAS [12] survey papers, whose claims I manually verify through queries on SIMBAD and observation of results from the *Digital Sky Survey* (DSS).

Distance information is collected from three literature works, specifically, *M. Fich's* work on VLA [16] and IRAS [12] surveys as well as *T. Foster's* [54] work on HII region and massive, OB star association. Modern distances to HII regions are determined from spectrophotometric measurements of all massive OB stars that fall inside the boundary of each HII region's ^{12}CO emission. The mean distance of these stars is established and any star whose distance is 3 or more standard deviations further from this mean is dropped from the calculation. The mean is then re-taken and the result is used as the best estimate to the HII region's radial distance. While *M. Fich* covers the entirety of my HII region sample, distances from *T. Foster* make use of a larger number of associated stars with more sophisticated spectral observations, and are therefore preferred when available.

Physical sizes are obtained using simple trigonometry combined with the previously collected distance and angular size information. Finally, integrated flux measurements are collected once again from *M Fich's* work on VLA [16] and IRAS [12] surveys. The fluxes will not be part of calculations in this thesis and are only presented for the purpose of forming a complete, self-consistent list of physical properties for the HII region sample. The results are contained in table 5.

Now, measurements of the SCUBA-2 data will lead to the 450μm and 850μm photometric description of each and every dusty source near the HII region sample. This can technically be performed exclusively by-hand through the use of best-fit apertures on a proper software package, such as *SAOImageDS9*. In principle, this is the most precise approach. However, the sheer number of calculations that need to take place and the volume of data that needs to be stored requires the use of an automated routine.

For this purpose, the *.astropy* package in *Python 2.7* is employed. Scripted routines are developed to handle the various measurement tasks that would otherwise have to be done by-hand. The way in which these routines operate and the manner in which they obtain photometric quantities will be discussed in detail below. It may prove useful to refer to figure 2.2 in order to be aware of the common jargon used and the logic behind steps taken in the measuring process.

To begin, in order to measure the flux of a SCUBA-2 source, an aperture that fits best

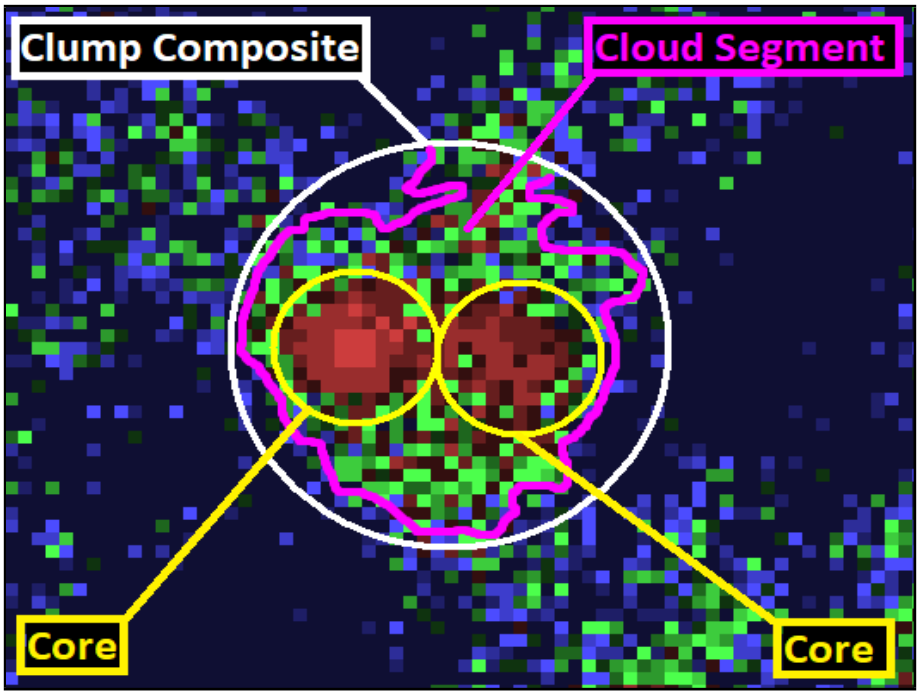

Figure 2.2: A graphic showing a particular "clump composite" in image G115. The composite consists of a diffuse "cloud" that spans the area denoted by the pink contour and two bright "cores" indicated by yellow circles.

its dimensions is required. The ideal such aperture is composed from a set of linear segments that together constitute a complicated, irregular polygon. Elliptical apertures are an excellent second choice for this purpose and circular ones a close third. Manipulating irregular polygonal shapes and ellipses in a scripted routine is a rather tedious task for the small gain in precision. Therefore, I choose to use circular apertures and investigate the consequences of this choice in chapter 4.

Care needs to be taken when translating the dimensions of these circular apertures between the 450μm and 850μm images, as the pixels in each band correspond to different physical scales. Specifically, 1 pixel in the 450 μm image corresponds to a 2x2 arcsecond area in the sky while 1 pixel in the 850 μm image corresponds to a 3x3 arcsecond area in the sky. Therefore one can translate each dimension of an aperture from a 450μm to an 850μm image via multiplication by 3/2, and vice versa.

As mentioned earlier, SCUBA-2 sources are composed of a cloud segment and one or

more embedded cores, which together comprise the clump composite as may be seen in figure 2.2. The main photometric goals include obtaining the pure, integrated fluxes of all cloud segments and their embedded cores, with "pure" being a term used to distinguish a flux measurement directly off the image from the same flux measurement after all known backgrounds have been subtracted.

There are two main backgrounds affecting both 450μm and 850μm photometry. The first is a rather uniform emission from the warm cloud segments themselves. The second is also a rather-uniform "virtual absorption" commonly referred to as the "Negative Bowl Background" (NBB). A third, relatively non-uniform background affects only the 850μm photometry and arises from the molecular CO(3-2) transition. Other molecular transitions pollute the 850μm emission as well, however the scale of the pollution is very insignificant when compared to the scale of the 850μm emission itself (less than 1%).

To treat these three backgrounds, I describe them using a mean "flux per pixel" (fpp) value. This presupposes that the backgrounds are uniform, an assumption that fits well the cloud and negative bowl backgrounds, but can be potentially misleading for the CO(3-2) background if the CO is not well-mixed within a SCUBA-2 source. Below is a closer look at these backgrounds, how they are measured and eventually how they are removed for the purpose of obtaining a pure cloud and core photometry.

2.3.1 Negative Bowl Background (NBB)

Negative bowls appear around bright sources as a result of filtering of spatial structure on various scales due to a complex interplay between detector array size, scanning rate, the filtering spatial scales used to remove the atmospheric variations and more. The data reduction pipeline takes out an average value over some time and if there is a bright source in the data stream, then that average is a bit too high. When that elevated average is subtracted from the data, the "no-signal" background pixels may venture into the negative flux territory as a result. Masking bright sources and using a variety of filtering parameters reduce this effect but do not completely eliminate it.

The NBB is by far the trickiest background to measure. This stems from the fact that the pixels that need to be used for its estimation are coupled to those of the source itself, with no obvious way of decoupling. It is known however that the NBB extends significantly far from a clump's boundary. This means that pixels outside a clump's boundary (and hence not associated with it) can be used in order to roughly estimate the NBB. This is possible

because the expectation for the flux of these exterior pixels is zero, or positive but close to zero, yet the presence of the negative bowl draws their values below zero.

It is known that the depth of a clump's NBB strongly depends on the total flux contained within that clump. Observation of mean fpp versus distance plots, such as the one presented in figure 2.4, suggest that the bowl's behavior outside a clump resembles a parabola, as it gradually deepens when moving away from the boundary of a clump, reaches a local minimum, then rises back near the level it was just outside the clump. Remember that it is not meaningful to extend this plot inside the clump boundary, as there the source's emission is strongly coupled with the negative bowl.

It is suspected that the negative bowl resembles a step function and the parabolic behavior is just an artifact introduced from a small, positive background emission, which decreases when moving away from a clump, (thus the bowl deepens) but increases when approaching a neighboring clump or warm filament (thus the bowl rises). For the purposes of this thesis, the NBB is approximated as a step function whose depth will be the minimum value encountered in the mean fpp versus distance plot.

To find this minimum, mean fpp value, a scripted routine is used. This routine creates a set of 8 circular apertures at a small distance from the clump's boundary. The mean flux per pixel of each aperture is evaluated as follows:

$$\bar{f}_j = \frac{\sum_{i=1}^{n} F_i}{n} \tag{2.1}$$

Where $\bar{f}_j$ indicates the mean fpp of a particular aperture in the set of 8, F_i its integrated flux and n its total number of pixels. The mean fpp of the NBB at that distance is calculated to be the mean fpp across all apertures of the set:

$$\bar{f}_{NBB} = \frac{\sum_{j=1}^{n} \bar{f}_j}{N} \tag{2.2}$$

Where $\bar{f}_{NBB}$ refers to the mean fpp estimate of the NBB and N to the number of apertures used. N is used instead of 8, as some apertures from the set may be deemed inappropriate for use as I will discuss shortly.

When the above calculation is completed for one set of apertures, a new set of apertures is produced at a slightly larger distance, leading to a new estimate of $\bar{f}_{NBB}$. When

the distance range provided by the user is covered, it is parsed again using a larger radius for each aperture in the set. After all aperture sizes provided by the user are parsed, the best estimate of the mean fpp of the NBB is taken to be the most negative value in the measurement set.

There are two main uncertainty sources contributing to this estimate. The first is the standard error introduced from using only 8 apertures in the mean fpp calculation. The second is the error introduced from the slightly different mean fpp estimates produced when using different radii for the aperture set.

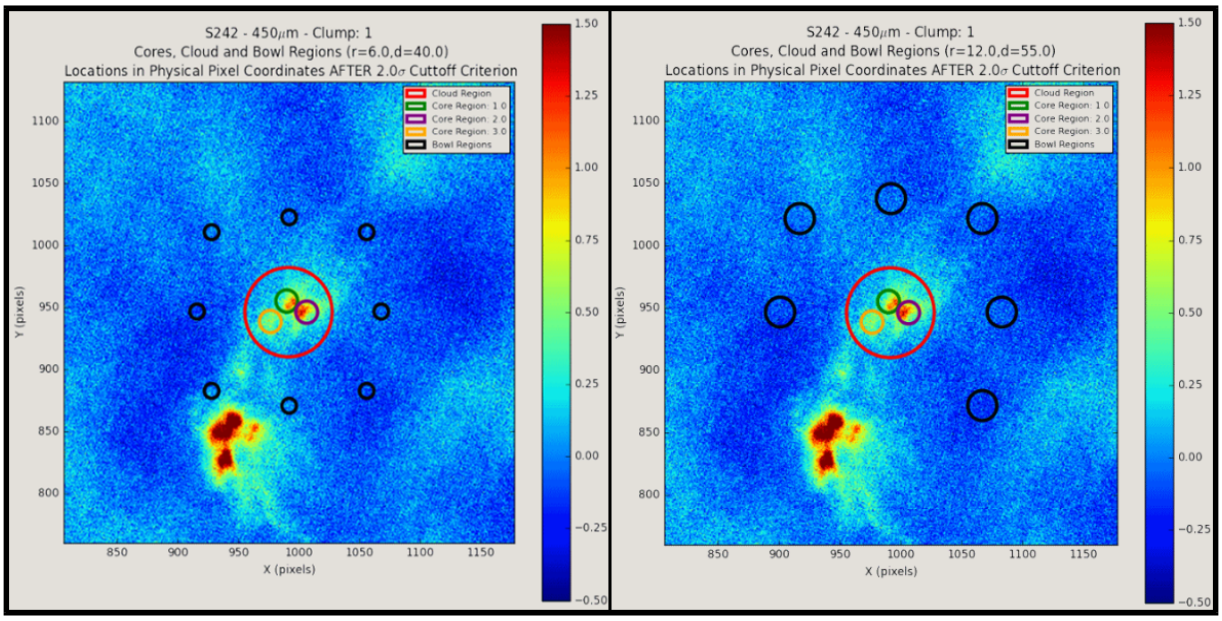

Figure 2.3: Two different bowl aperture sets for estimating the NBB of clump G182-1. The first set is lies at a distance of 40 pixels from the clump boundary using apertures of radius 6 pixels (Left). The second set lies at a distance of 55 pixels and uses apertures of radius 12 pixels (Right). Note the exclusion of the 2 lower-left apertures in the second set as they happen to be crossing another clump, making them inappropriate for the calculation.

Complications can arise however due to the automatic manner in which the bowl apertures are generated. As mentioned earlier, some of these apertures can be inappropriate for use in this calculation by virtue of their non-ideal placement location. Common such locations include near/inside a warm filament and near/inside a neighboring clump. If these apertures are not filtered out of the calculation, they will introduce an unwanted

positive skew to the mean fpp estimate.

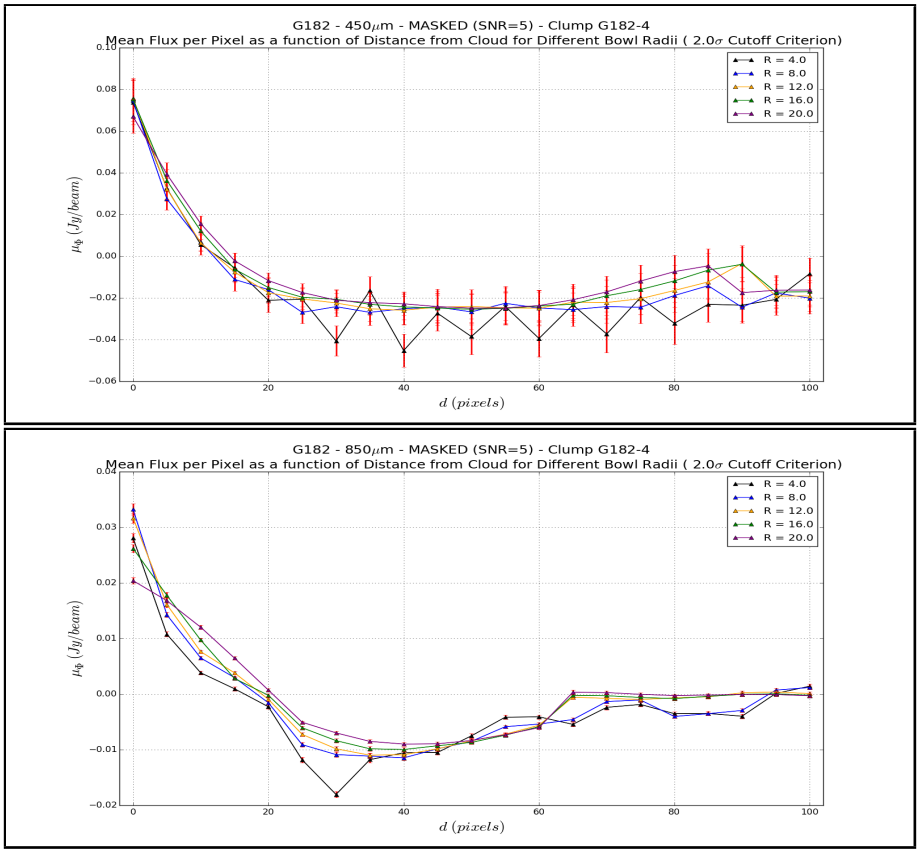

Figure 2.4: Estimating the mean fpp of the NBB for clump G182-4 in the 450μm (Top) and 850μm (Bottom) band. The mean fpp is evaluated at increasing distances from the clump boundary and with apertures of varying radius. The most negative measurement is used as the best description of the NBB.

To prevent this from happening, such apertures are dropped from their initial set of 8 under the application of a cutoff criterion. First, the overall mean fpp and standard deviation are calculated using all 8 apertures of a set. Then, for an aperture to be considered in the calculation of the final mean fpp for that set, it needs to have a mean fpp that differs less than 2σ from the mean fpp determined using all 8 apertures. More formally, the requirement reads:

$$\bar{f}_j \leq \bar{f} + 2\sigma \tag{2.3}$$

Where $\bar{f}_j$ indicates the mean fpp of a particular aperture out of the set of 8 and $\bar{f}$, σ respectively refer to the mean fpp and standard deviation calculated using all 8 apertures.

After this cutoff criterion is imposed, the remaining apertures are used for the calculation of the final mean fpp for the set. It is worth noting that the NBB is calculated on a clump-clump basis, which means that all cores belonging to a particular clump are treated using the same NBB estimate.

A snapshot of two different bowl aperture sets used for the evaluation of the NBB around G182's first clump is presented in figure 2.3. This clump case is chosen in order to display the cutoff criterion in effect through the exclusion of the two lower-left apertures of the second set as they happen to be generated in the vicinity of a neighboring clump.

I also present the consecutive measurements made for establishing the mean fpp of the NBB around G182's fourth clump in figure 2.4. This clump case is chosen as it is relatively isolated, and as such, provides a better view of what is happening outside the clump, where the flux is expected to be zero or positive and near zero.

2.3.2 CO Emission Background

As mentioned earlier, all flux measurements made in the 850μm band suffer unwanted contamination from the molecular CO(3-2) transition. The emission from this transition is treated as a background, even though the validity of this simplification depends strongly on how well mixed the CO is in a particular clump. The level of CO is something that also varies from clump to clump. Ideally, the spatial distribution of CO needs to be precisely known so that its subtraction from 850μm flux measurements may be done on a pixel-to-pixel basis. However, data regarding the CO(3-2) emission is only available for few SCUBA-2 targets, for which sometimes it does not cover a fraction of the SCUBA-2 image.

To circumvent the lack of CO data and to treat the CO(3-2) contamination in SCUBA-2 850μm photometric measurements, the average polluting effect of the CO(3-2) transition is established. This is done by using SCUBA-2 images that possess complete or partial CO data coverage, then comparing the CO flux against that from the SCUBA-2, 850μm band on a pixel-to-pixel basis. This comparison requires proper alignment of the SCUBA-2 and CO pixels, a complicated process incorporating both a rotation and up/down scaling of either image's pixel grid.

The overall average ratio of CO to SCUBA-2, 850μm pixel flux becomes obtainable. This average has not yet been published as it is part of ongoing research taking place at the same time as the construction of this thesis. The current best unpublished estimate for this average is:

$$\bar{f}_{CO} = (0.1 \pm 0.02)\bar{f}_{850} \tag{2.4}$$

This can be converted for use with integrated flux measurements simply by multiplying with the number of pixels comprising the SCUBA-2 source of interest.

It is then straightforward to remove the CO(3-2) contamination from SCUBA-2 850μm measurements, however, this is by no means a complete treatment of the problem, rather a first approach using the current available data, and as such, is open to future improvement.

2.3.3 Cloud Background

A cloud segment is comprised of warm gas filaments that surround a hotter and denser phase of the same gas that is defined under the term "core". The flux profile of a cloud segment is nearly constant, something that allows its description by a mean fpp value. Determination of this mean fpp value allows the removal of the cloud emission from that of its embedded cores later on. However, clouds are constituents of a clump composite, and as such, need to have a complete, pure photometric description as well.

The first issue that must be circumvented when trying to measure the photometry of a cloud is the coupling of the flux emission to that of the embedded cores. Decoupling the two is done through a two-stepped scripted routine. In the first step, the cloud integrated flux is determined by summing up the fluxes of pixels inside the clump boundary but outside the core boundaries as follows:

$$F_{Cloud} = \sum_{i=1}^{n} f_i \tag{2.5}$$

Where F_{Cloud} indicates the cloud's integrated flux, f_i the flux of each cloud pixel and n the total number of pixels belonging solely to the cloud. The mean flux per pixel can then be naturally obtained as follows:

$$\bar{f}_{Cloud} = \frac{F_{Cloud}}{n} \tag{2.6}$$

Where $\bar{f}_{Cloud}$ indicates the cloud's mean fpp, F_{Cloud} its integrated flux and n the total number of pixels belonging solely to it. Having the cloud mean fpp makes it straightfor-

ward to subtract its emission from that of its embedded cores as will be displayed in the following section. However, we're still interested in obtaining the pure photometry of the cloud.

Assuming at this stage knowledge regarding the CO emission background and the NBB, it becomes possible to obtain the pure 450μm and 850μm cloud, integrated fluxes as follows:

$$450: \quad F_{Cloud}^{Pure} = F_{Cloud} - n(\bar{f}_{NBB}) \tag{2.7}$$

$$850: \quad F_{Cloud}^{Pure} = F_{Cloud} - n(\bar{f}_{NBB} - \bar{f}_{CO}) \tag{2.8}$$

$$\tag{2.9}$$

Where n once again indicated pixels belonging solely to the cloud.

The calculation of the pure, 450μm and 850μm mean fpp involves simply the division of the above values by n as follows:

$$\bar{f}_{Cloud}^{Pure} = \frac{F_{Cloud}^{Pure}}{n} \tag{2.10}$$

2.4 Cores

A core is a very distinguishable feature inside a clump composite. Unlike clouds, cores are very bright and their flux profile has a very characteristic Gaussian-like shape. The radial size of a core is taken to be the radius at which this Gaussian-like flux profile stops changing significantly. This is done visually, however, the determined boundary always ends up tracing an SNR of ≈ 2.

In order to calculate the pure, integrated flux of a core, its unprocessed, integrated flux must be first obtained by simply summing the flux of each pixel within the core's boundary as follows:

$$F_{Core} = \sum_{i=1}^{n} f_i \tag{2.11}$$

Where f_i indicates the flux of pixels belonging solely to the core. Assuming at this stage full knowledge of the CO background, the NBB, as well as the cloud background, the pure

450μm and 850μm core integrated fluxes are obtainable as follows:

$$450: \quad F_{Core}^{Pure} = F_{Core} - n(\bar{f}_{NBB} - \bar{f}_{Cloud}^{Pure}) \tag{2.12}$$

$$850: \quad F_{Core}^{Pure} = F_{Core} - n(\bar{f}_{NBB} - \bar{f}_{Cloud}^{Pure} - \bar{f}_{CO}) \tag{2.13}$$

$$\tag{2.14}$$

Where n indicates the number of pixels belonging solely to the core. It is not meaningful to talk about a core's mean fpp, as the core is not a background. However, if fitting to some emission model presents the need for this value, it can be obtained simply by dividing the above integrated fluxes by n as follows:

$$\bar{f}_{Core}^{Pure} = \frac{F_{Core}^{Pure}}{n} \tag{2.15}$$

2.5 Summary

At this point, all photometric quantities of importance have been obtained. These include:

- The 450μm/850μm Clump Negative Bowl Background → figure 2.5/2.6
- The 450μm/850μm Cloud Background → figure 2.7/2.8
- The 450μm/850μm Cloud Pure Integrated Flux → figure 2.9/2.10
- The 450μm/850μm Core Pure Integrated Flux → figure 2.11/2.12

The aforementioned figures can be used as a guideline for what to expect regarding the 450μm and 850μm photometry of molecular clump systems. The negative bowl background histograms convey the magnitude of the negative bowl introduced from the data reduction pipeline. Roughly, an average drop of 12.46 mJy and 0.85 mJy per pixel is expected for measurements made in the 450μm and 850μm band respectively.

In addition, the cloud background histograms convey how influential the cloud medium is in the 450μm and 850μm photometry measurements. On average, in a single 450μm and 850μm SCUBA-2 pixel, 17.34 mJy and 3.08 mJy are contributed solely by the warm cloud background.

Another way to view the significance of the cloud background is using the integrated flux histograms for the clouds and cores. On average, core emission in both bands accounts for only $\approx 27\%$ of the total emission, while cloud emission accounts for the rest. This is important, as mass is proportional to integrated flux. Provided the cores share a similar temperature with the clouds, they will only account on average for $\approx 27\%$ of the total clump mass.

This concludes the photometry portion of this thesis. The focus now shifts to derivative properties that are obtainable through use of the measurements made in this section. For a complete list of all core and cloud physical properties obtained, refer to tables 1 and 3 respectively.

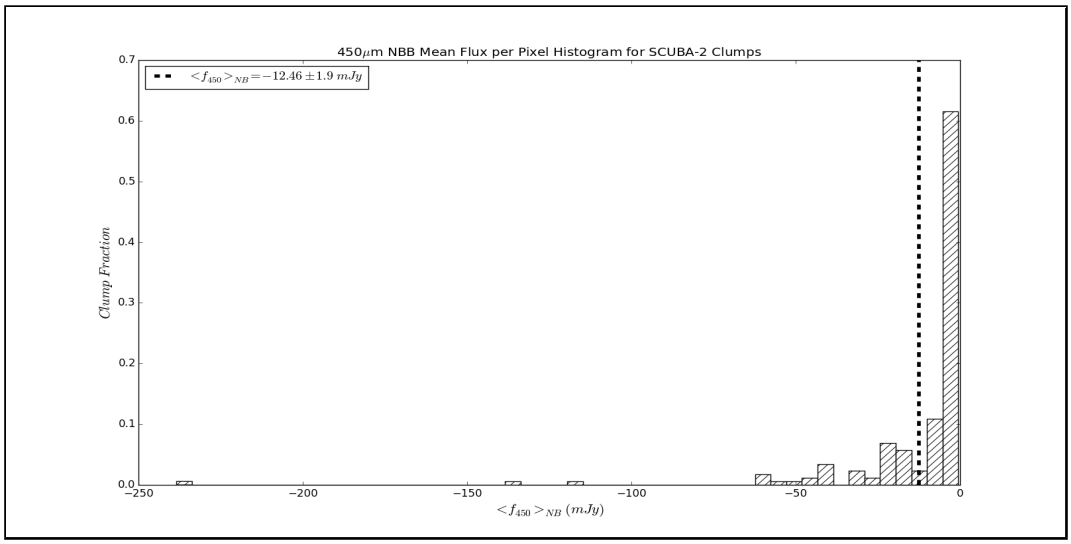

Figure 2.5: Histogram of the mean fpp estimates for the NBB around SCUBA-2 clumps in the 450μm band. A linear scale is used on the x-axis and the y-axis is normalized so that the sum of the bins equals unity. The mean is indicated using a black, dashed line.

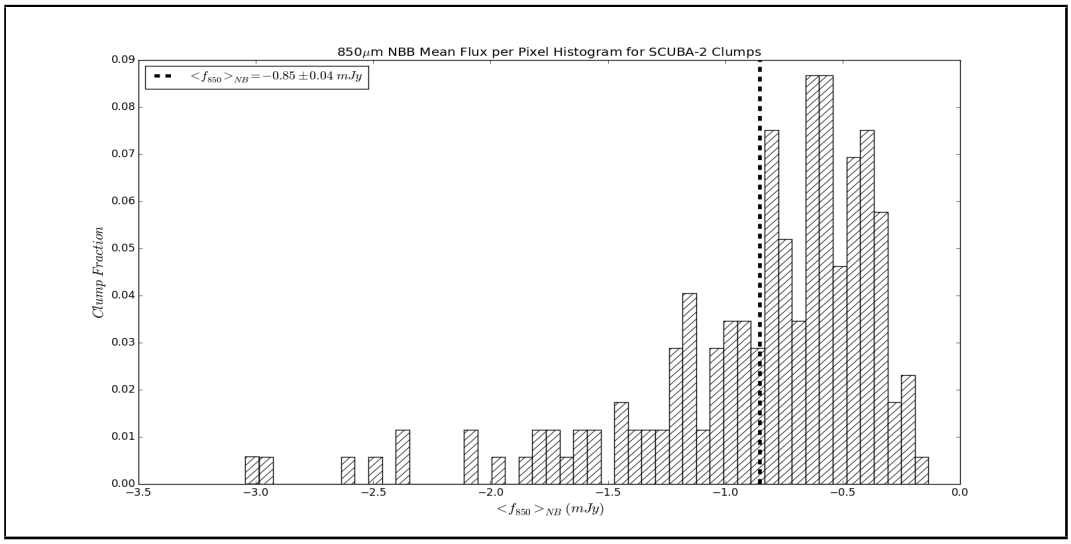

Figure 2.6: Histogram of the mean fpp estimates for the NBB around SCUBA-2 clumps in the 850μm band. A linear scale is used on the x-axis and the y-axis is normalized so that the sum of the bins equals unity. The mean is indicated using a black, dashed line.

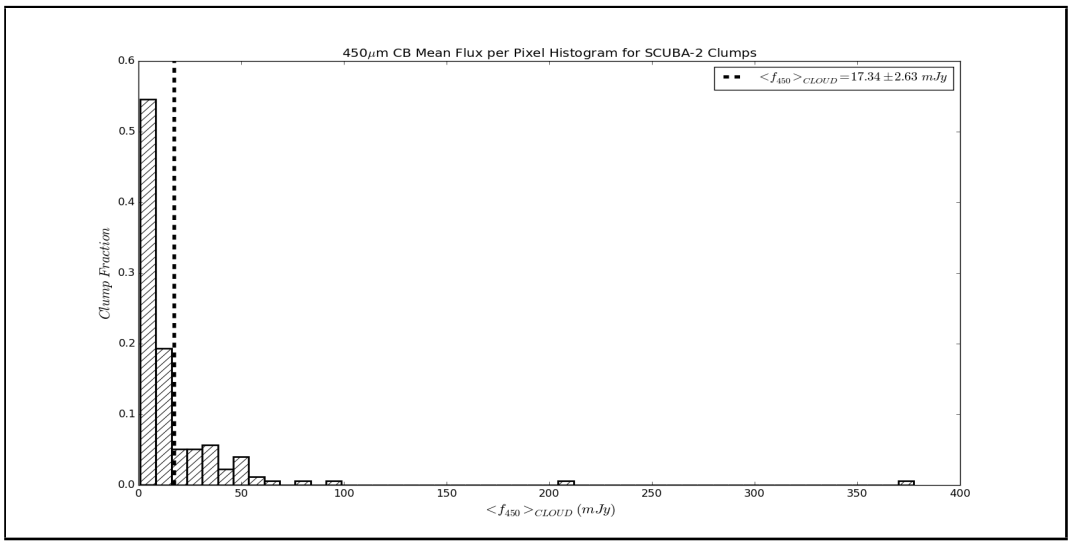

Figure 2.7: Histogram of the cloud mean fpp values for SCUBA-2 clumps in the 450μm band. A linear scale is used on the x-axis and the y-axis is normalized so that the sum of the bins equals unity. The mean is indicated using a black, dashed line.

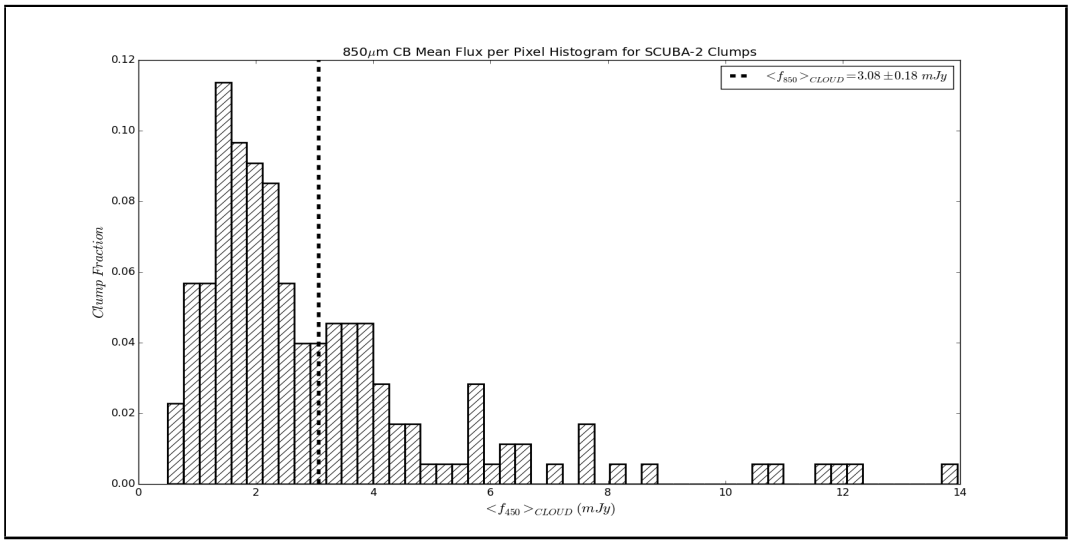

Figure 2.8: Histogram of the cloud mean fpp values for SCUBA-2 clumps in the 850μm band. A linear scale is used on the x-axis and the y-axis is normalized so that the sum of the bins equals unity. The mean is indicated using a black, dashed line.

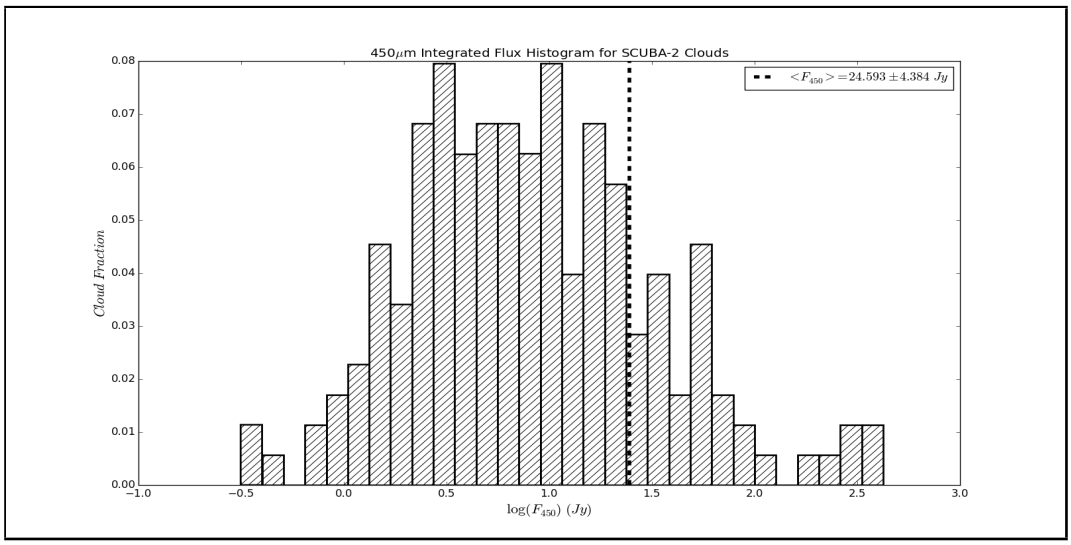

Figure 2.9: Histogram of the pure cloud integrated fluxes in the 450μm band. A logarithmic base-10 scale is used on the x-axis and the y-axis is normalized so that the sum of the bins equals unity. The mean is indicated using a black, dashed line.

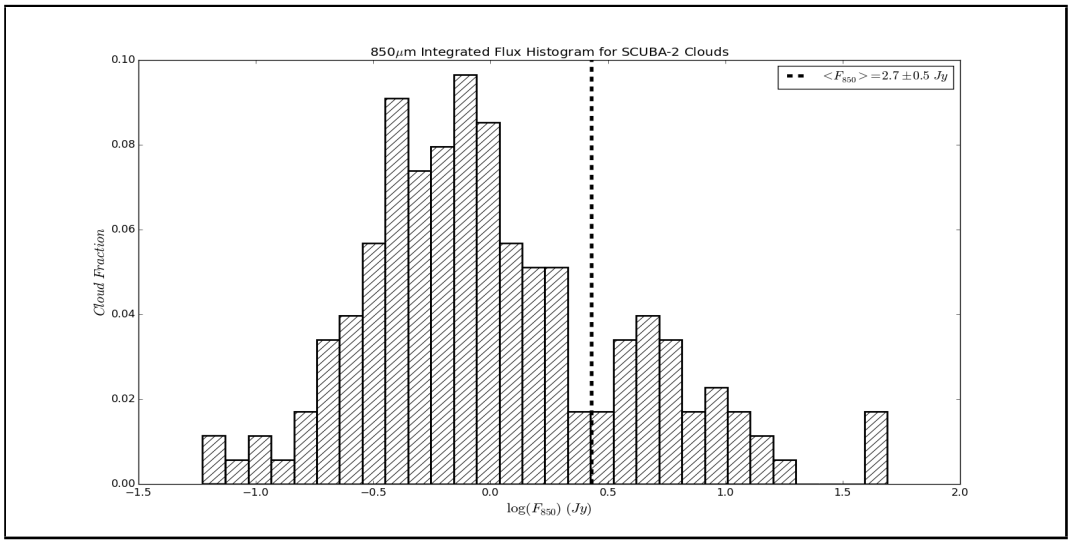

Figure 2.10: Histogram of the pure cloud integrated fluxes in the 850μm band. A logarithmic base-10 scale is used on the x-axis and the y-axis is normalized so that the sum of the bins equals unity. The mean is indicated using a black, dashed line.

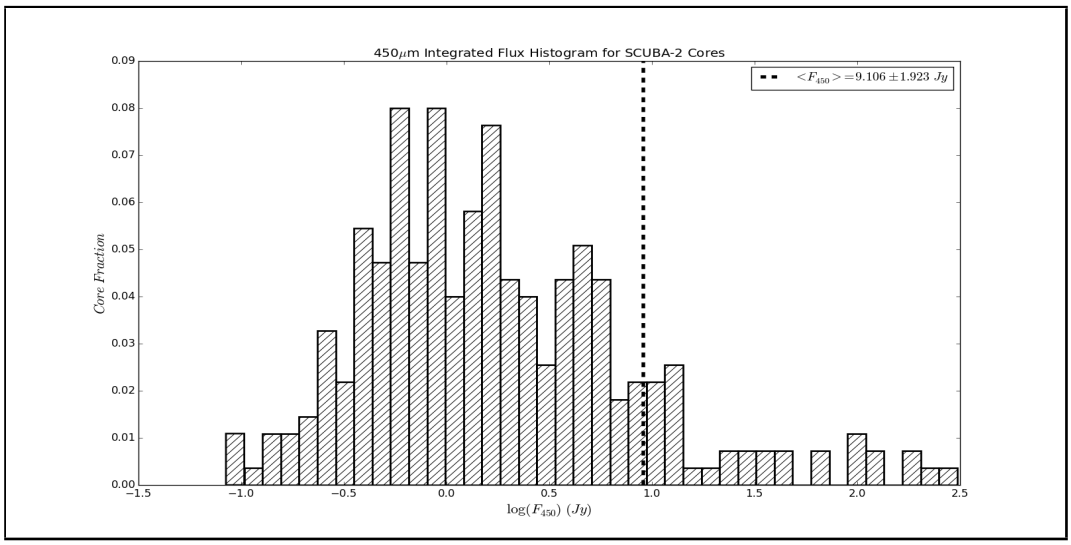

Figure 2.11: Histogram of the pure core integrated fluxes in the 450μm band. A logarithmic base-10 scale is used on the x-axis and the y-axis is normalized so that the sum of the bins equals unity. The mean is indicated using a black, dashed line.

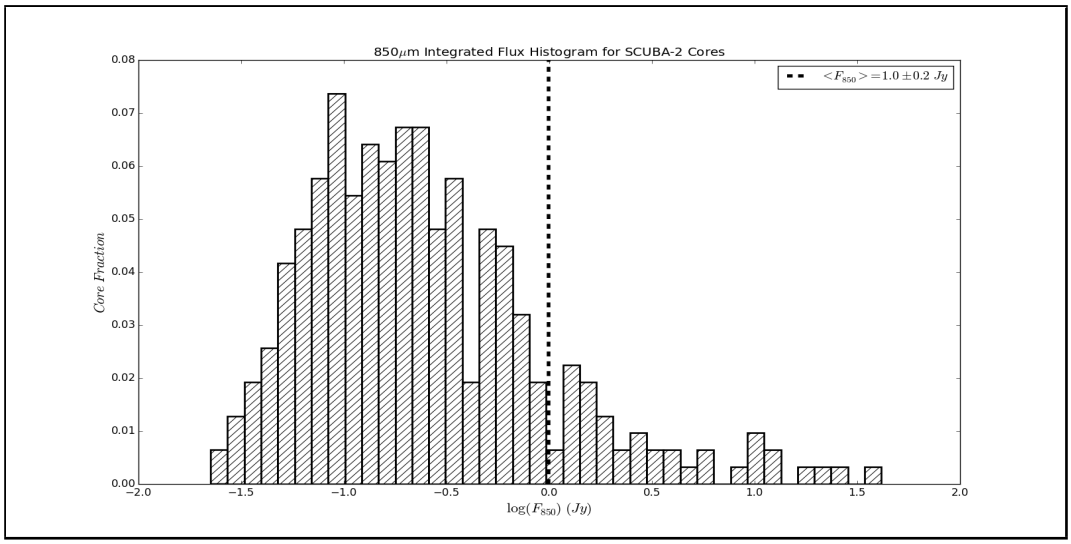

Figure 2.12: Histogram of the pure core integrated fluxes in the 850μm band. A logarithmic base-10 scale is used on the x-axis and the y-axis is normalized so that the sum of the bins equals unity. The mean is indicated using a black, dashed line.

Chapter 3

Calculations

In this chapter I will be discussing how the physical properties determined in the previous chapter will be used for the determination of important derivative properties. I begin by presenting some prerequisite quantities that are to be used throughout this calculation section.

I then proceed to address temperature and non-temperature dependent derivative properties separately. This is done due to the very different and statistically dense manner in which the uncertainty of temperature dependent quantities will be calculated in chapter 4.

The obtained results for each property are displayed in a histogram fashion. The values included are all quantities with an SNR ≥ 1.0. Later on in this chapter the requirements for a quantity to continue into analysis will become tighter. The reason why this is necessary will become apparent in the flux ratio section of this chapter.

Finally, after all the properties of interest and their calculation recipes are presented, I take a closer look at how the association of HII regions to cores and OB stars is performed.

3.1 The Prerequisites

3.1.1 Flux Conversion Factors

A "Flux Conversion Factor" (FCF) is used for converting flux received by the detectors in the telescope array in pW to flux received by the telescope in Jy. Its value is simply

obtained by comparing the expected flux from a source against the actual signal received by the telescope. FCFs are only used for SCUBA-2 photometry, as no original VLA photometry is performed in this thesis. A detailed discussion regarding the establishment of SCUBA-2 FCFs can be found in the SCUBA-2 calibration paper from *T. Jenness* et al [25]. The parts of this paper relevant to this thesis are summarized below.

First, when dealing with an integrated flux calculation, the expected integrated flux from the source is compared against the actual signal received by the detectors of the telescope array and their area as follows:

$$FCF_{arcsec} = \frac{F}{I_0 A} \quad \frac{Jy}{pW\ arcsec^2} \tag{3.1}$$

Where F indicates the known integrated flux in janskys, I_0 the measured pixel signal in picowatts and A the pixel angular area in squared arcseconds.

Now, if the peak flux of a source is of interest, the comparison involves a single pixel, leading to the simplification of the above expression to the following:

$$FCF_{peak} = \frac{F_{peak}}{I_{peak}} \quad \frac{Jy}{pW} \tag{3.2}$$

Where F_{peak} indicates the known peak flux in janskys and I_{peak} the measured peak signal in picowatts.

SCUBA-2 FCFs are established through calibration of the SCUBA-2 camera against sources of known flux emission. These sources are observed using a DAISY scan pattern with each scan iteration lasting $\approx$ 4 minutes. The two primary sources used are Uranus and Mars. However, a handful of secondary sources are used as well of which the most prominent are CRL 618 and CRL 2688.

The values of the FCFs are not constant, as they strictly depend on the telescope's performance which may change over time. The value of the FCFs needs to be periodically re-determined in order to make sure that conversion between different flux units is as

precise as can be. The FCF values used in this thesis are the following:

$$FCF^{450}_{arcsec} = 4.71 \pm 0.5 \quad \frac{Jy}{pW\ arcsec^2} \tag{3.3}$$

$$FCF^{850}_{arcsec} = 2.34 \pm 0.08 \quad \frac{Jy}{pW\ arcsec^2} \tag{3.4}$$

$$FCF^{450}_{peak} = 491 \pm 67 \quad \frac{Jy}{pW} \tag{3.5}$$

$$FCF^{850}_{peak} = 537 \pm 26 \quad \frac{Jy}{pW} \quad [25] \tag{3.6}$$

The calibration tests for the determination of the above set were made throughout 2012. The performance of the JCMT showed strong evidence against any kind of deterioration over this timespan, and, since all SCUBA-2 raw data that is used in this thesis was originally obtained between 2012 and 2015, it is deemed reasonable to use solely this set for its treatment.

3.1.2 Opacity

An accurate opacity model is one of the biggest challenges in star formation astrophysics. As mentioned earlier in the introductory chapter, dust grains vary in composition and size, while some develop mantles and others do not. These properties are typically functions of a dusty system's environmental physical parameter space (temperature, density etc), however, they also depend on the time allowed for its evolution. Simulations for different such parameters and evolution times have been performed and tables of opacity values against wavelength have been constructed for various dust populations.

The dust population encountered in this thesis comprises of dust inside hot and cold molecular clumps. Studies of dust in these conditions describe its submillimeter emission as optically thin. The opacity of such a system is well represented by a power-law of the following form:

$$\kappa_\nu = \kappa_{\nu_0} \left(\frac{\nu}{v_0} \right)^\beta \quad [58] \tag{3.7}$$

Where κ_ν indicates the opacity at some frequency v, while κ_{ν_0} indicates the opacity at some reference frequency v_0 and β the opacity power-law index. If one has knowledge about β for the type of source being observed, as well its opacity for some reference frequency, it is possible to obtain the opacity for any other frequency desired.

To accommodate the type of sources in this thesis, a β value of 1.8 is assumed, following closely arguments in studies of similar nature, such as the Gould Belt Survey using the SCUBA-2 instrument [26] [30]. As for the reference opacity, $\kappa_{300} = 0.01\ m^2\ kg^{-1}$ at a frequency of $v_0 = 1.0 \times 10^{12}\ Hz$ is used from consideration of the molecular clumps investigated in the Gould Belt using the Herschel instrument [57]. Combining these two pieces of information, the resulting, simplified opacity model used in this thesis reads as follows:

$$\kappa_\nu = \kappa_{300}\left(\frac{\nu}{1.0 \times 10^{12}}\right)^{1.8} \tag{3.8}$$

Where v indicates the desired frequency in Hz. The 450μm and 850μm opacities are then be easily obtained from the above equation:

$$\kappa_{450} = 4.81 \times 10^{-3} \quad m^2\ kg^{-1} \tag{3.9}$$

$$\kappa_{850} = 1.53 \times 10^{-3} \quad m^2\ kg^{-1} \tag{3.10}$$

3.1.3 Pixel Solid Angle

The solid angle subtended by 450 and 850 array pixels can be calculated for use in converting between different flux units, namely $Jy\ arcsec^{-1}$ to Jy. The 450μm pixels have a side of angular size equal to 2 arcseconds while their 850μm counterparts have a side of 3 arcseconds. Conversion of these areas to steradians is done as follows:

$$\Omega_{450} = (2\ arcsec)^2\left(2.35x10^{-11}\frac{ster}{arcsec^2}\right) = 9.40x10^{-11}\quad ster \tag{3.11}$$

$$\Omega_{850} = (3\ arcsec)^2\left(2.35x10^{-11}\frac{ster}{arcsec^2}\right) = 2.115x10^{-10}\quad ster \tag{3.12}$$

3.2 Non-Temperature Dependent Quantities

The recipes for the derivative properties in this section do not incorporate temperature. As such, they do not suffer from the asymptotic nature of the temperature model and are therefore Gaussian in nature. Consequently, these properties will have symmetric uncertainties attached, which will be determined using standard error propagation rules in Chapter 4.

3.2.1 Spectral Index

The spectral index α is essentially the index of the frequency versus flux power-law typically denoted as $F_v \propto \nu^{\alpha}$. This index can vary significantly between different frequency ranges. In the case of SCUBA-2 sources, it describes the average steepness of this power-law between the 450μm ($6.6620 \times 10^{11}\ Hz$) and 850$\mu$m ($3.5270 \times 10^{11}\ Hz$) wavelengths. Its calculation is carried as follows:

$$\alpha = \frac{\ln\left(F_{450}\right) - \ln\left(F_{850}\right)}{\ln\left(850\right) - \ln\left(450\right)} \tag{3.13}$$

Where α indicates a source's spectral index, and F_{450} and F_{850} its respective, pure, integrated 450μm and 850μm flux. Spectral indices with symmetric uncertainty greater than 100% are excluded from the results.

3.2.2 In-Band Luminosity

The luminosity of a SCUBA-2 source can be calculated using its pure, integrated flux along with its radial distance from the telescope array. SCUBA-2 emission is assumed to have no preferred direction (isotropic), therefore the equivalent area of the emission sphere of the source is used without any correction for polarization effects. Thus, the luminosity in the 450μm and 850μm band can simply be calculated as follows:

$$v_{450}L_{450} = 4\pi d^2 F_{450} v_{450} \tag{3.14}$$

$$v_{850}L_{850} = 4\pi d^2 F_{850} v_{850} \tag{3.15}$$

Where $v_{450}L_{450}$ and $v_{850}L_{850}$ indicate a source's respective 450 and 850 in-band luminosity, F_{450} and F_{850} its respective pure, 450μm and 850μm integrated flux, v_{450} and v_{850} the 450μm and 850μm equivalent frequencies and d the radial distance to the source. In-band luminosities with symmetric uncertainty greater than 100% are excluded from the results. A histogram of the 450μm cloud and core in-band luminosities is presented in figure 3.1, while a similar histogram is displayed for the 850μm in-band luminosities in figure 3.2 with the mean luminosity values displayed using a vertical dashed line.

3.2.3 Surface Brightness

The surface brightness of a SCUBA-2 source can be obtained through a comparison of its pure, integrated flux to its spanned area. The area can either be in physical or angular

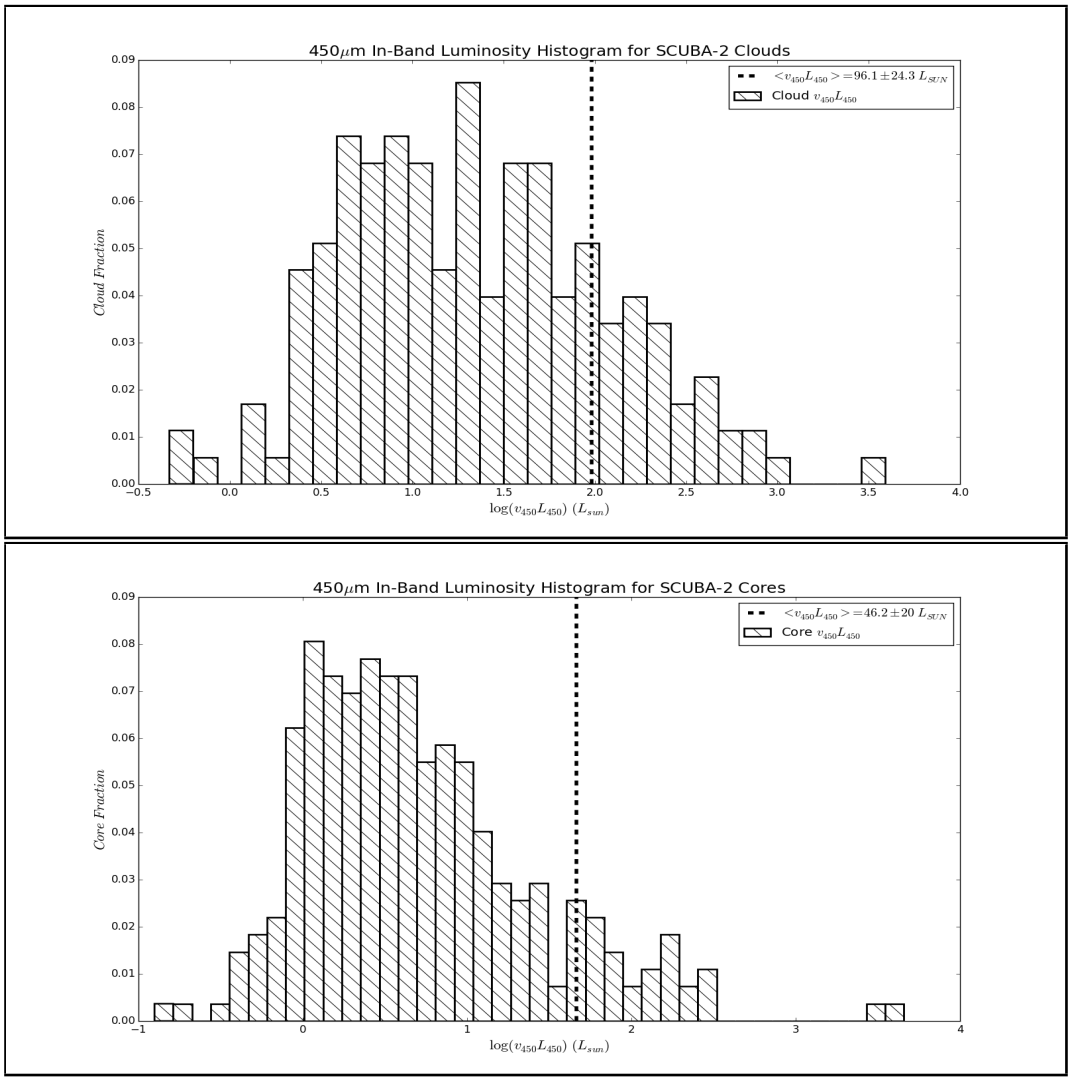

Figure 3.1: Histogram of the cloud (Top) and core (Bottom) 450μm in-band luminosities. A logarithmic base-10 scale is used on the x-axis and the y-axis is normalized so that the sum of the bins equals unity. The mean is indicated using a black, dashed line.

units, however the latter choice is used here. It is worthy to note that the area used in the surface brightness calculation is that of the aperture used to identify and measure its flux. Due to the fact that simplified circular apertures are used for this purpose, this area is a close, but not an exact approximation of the source's area. A polygonal aperture would provide a better approximation to the source boundary.

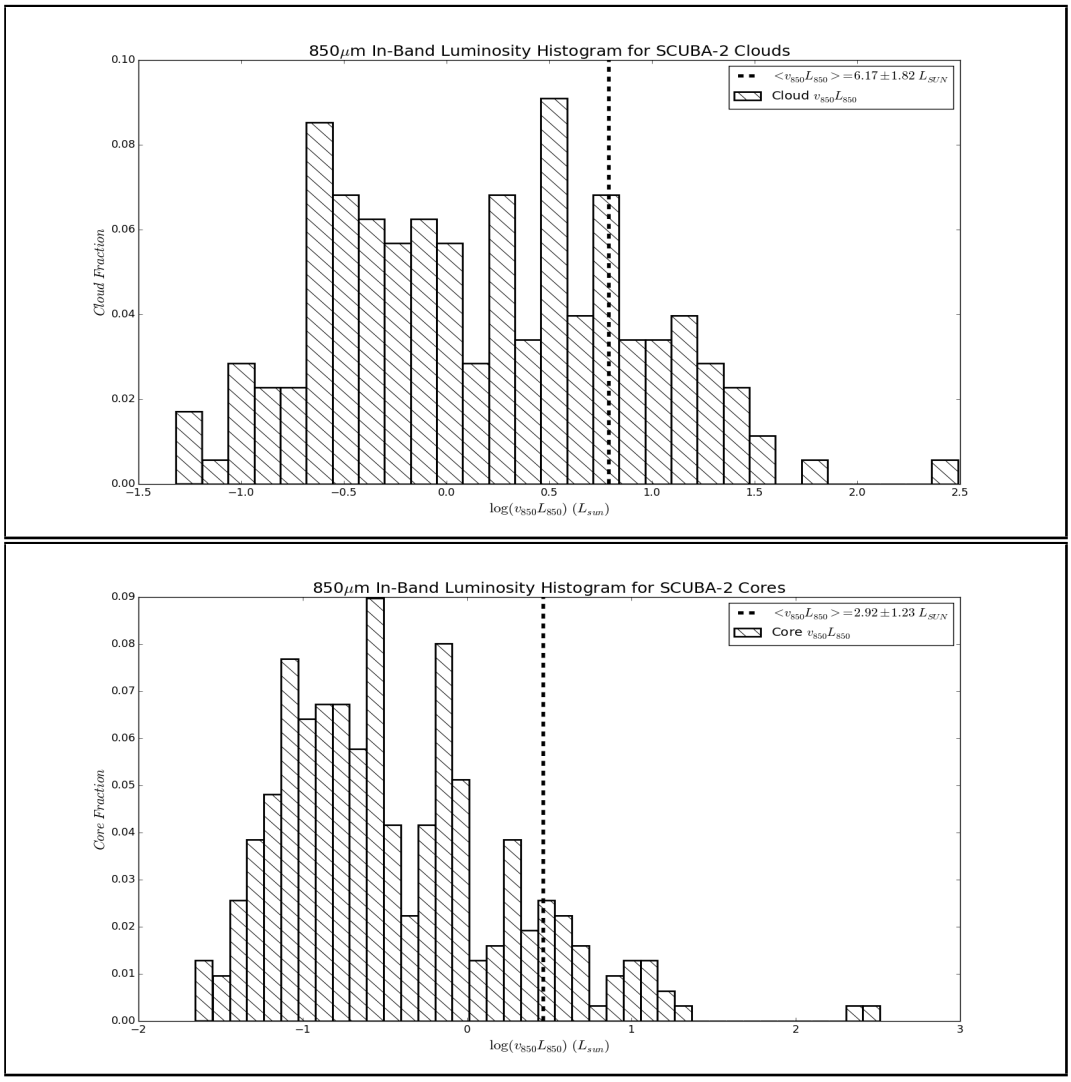

Figure 3.2: Histogram of the cloud (Top) and core (Bottom) 850μm in-band luminosities. A logarithmic base-10 scale is used on the x-axis and the y-axis is normalized so that the sum of the bins equals unity. The mean is indicated using a black, dashed line.

The surface brightness in the 450μm and 850μm band can be obtained as follows:

$$S_{450} = \frac{F_{450}}{A} \tag{3.16}$$

$$S_{850} = \frac{F_{850}}{A} \tag{3.17}$$

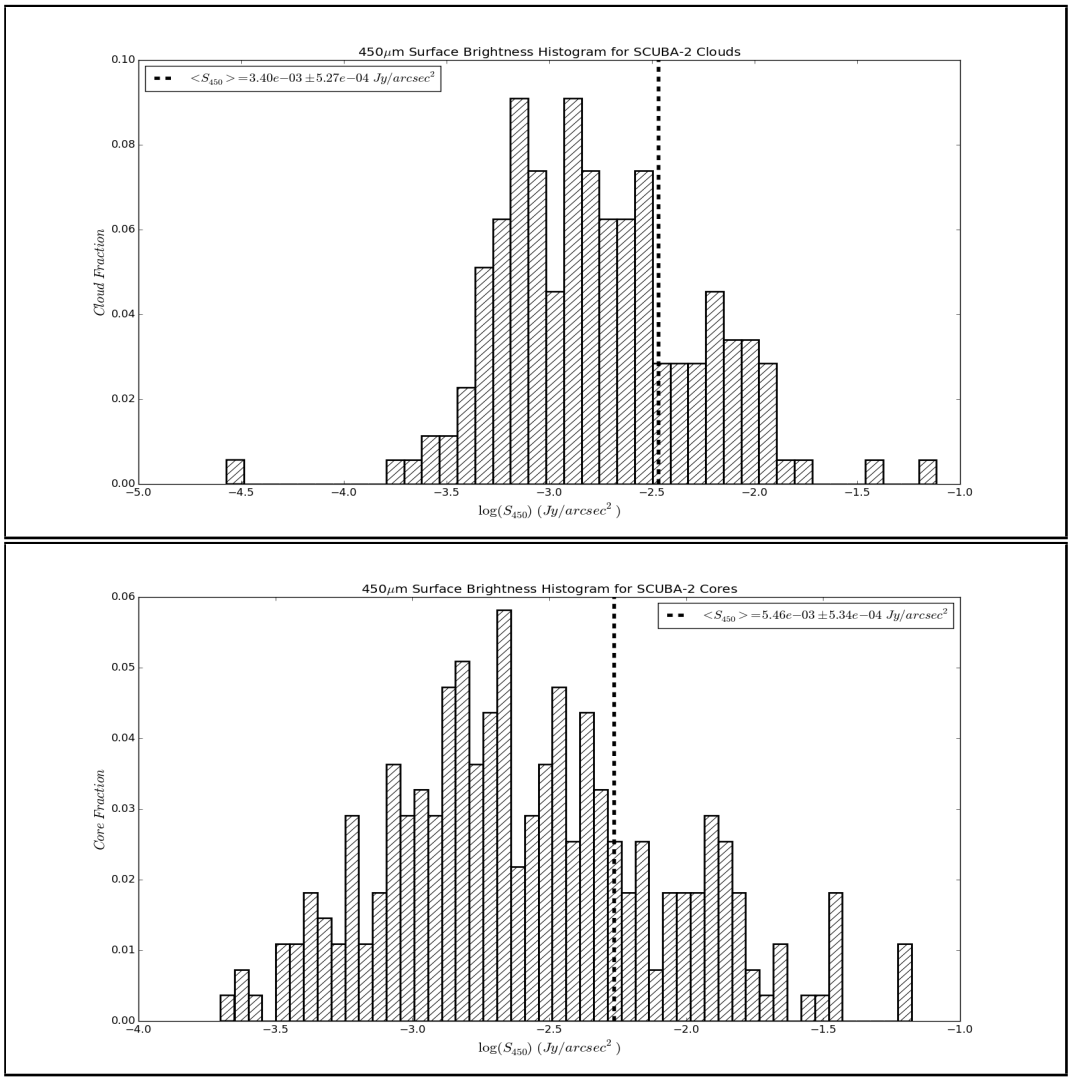

Figure 3.3: Histogram of the cloud (Top) and core (Bottom) 450μm surface brightnesses. A logarithmic base-10 scale is used on the x-axis and the y-axis is normalized so that the sum of the bins equals unity. The mean is indicated using a black, dashed line.

Where S_{450} and S_{850} indicate a source's respective 450 and 850 surface brightness, F_{450} and F_{850} its respective pure, 450μm and 850μm integrated flux and A its angular surface area. Surface brightnesses with symmetric uncertainty greater than 100% are excluded from the results. A histogram of the 450μm cloud and core surface brightnesses is presented in figure 3.3, while a similar histogram is displayed for the 850μm equivalents in figure 3.4 with the

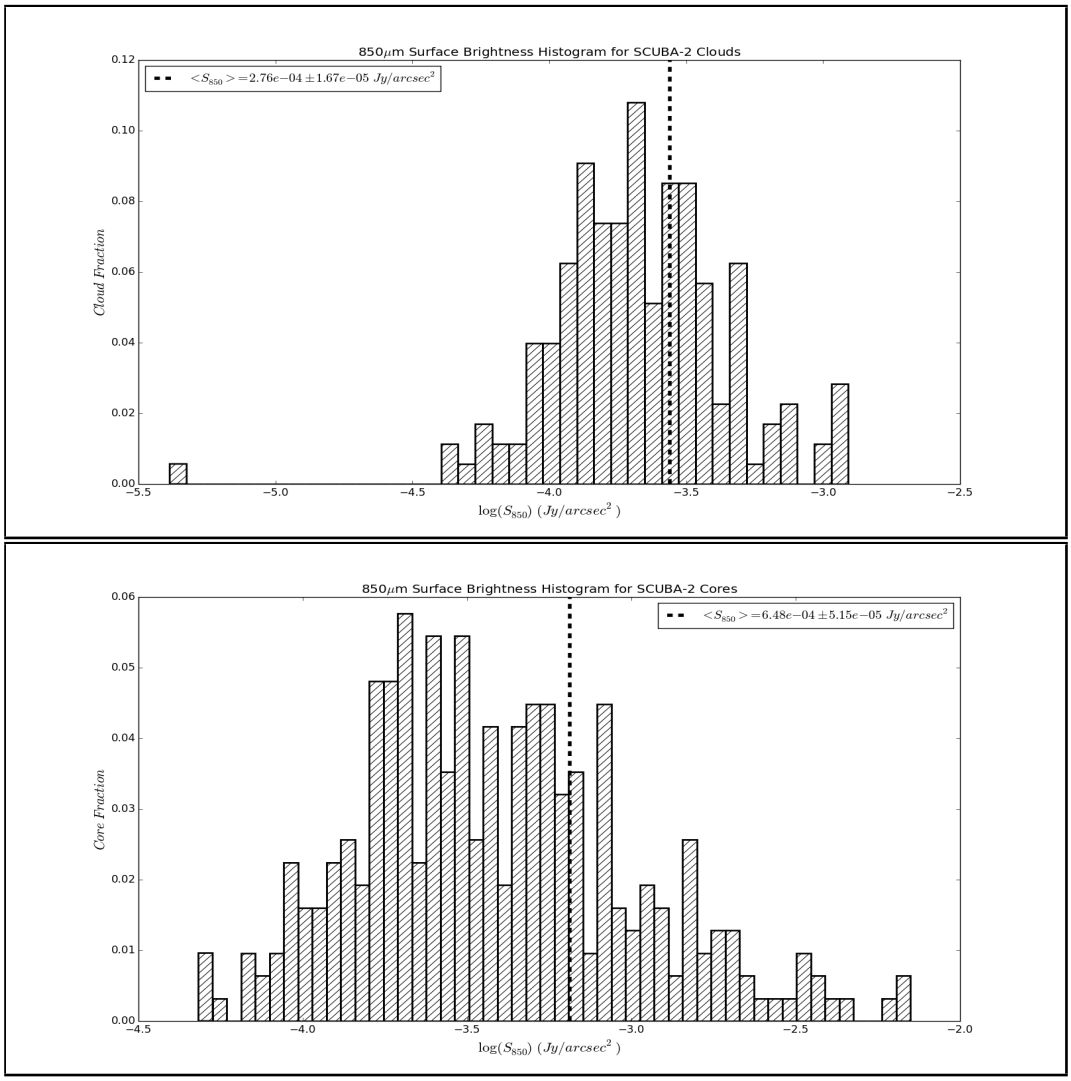

Figure 3.4: Histogram of the cloud (Top) and core (Bottom) 850μm surface brightnesses. A logarithmic base-10 scale is used on the x-axis and the y-axis is normalized so that the sum of the bins equals unity.The mean is indicated using a black, dashed line.

mean surface brightness values displayed using a vertical dashed line.

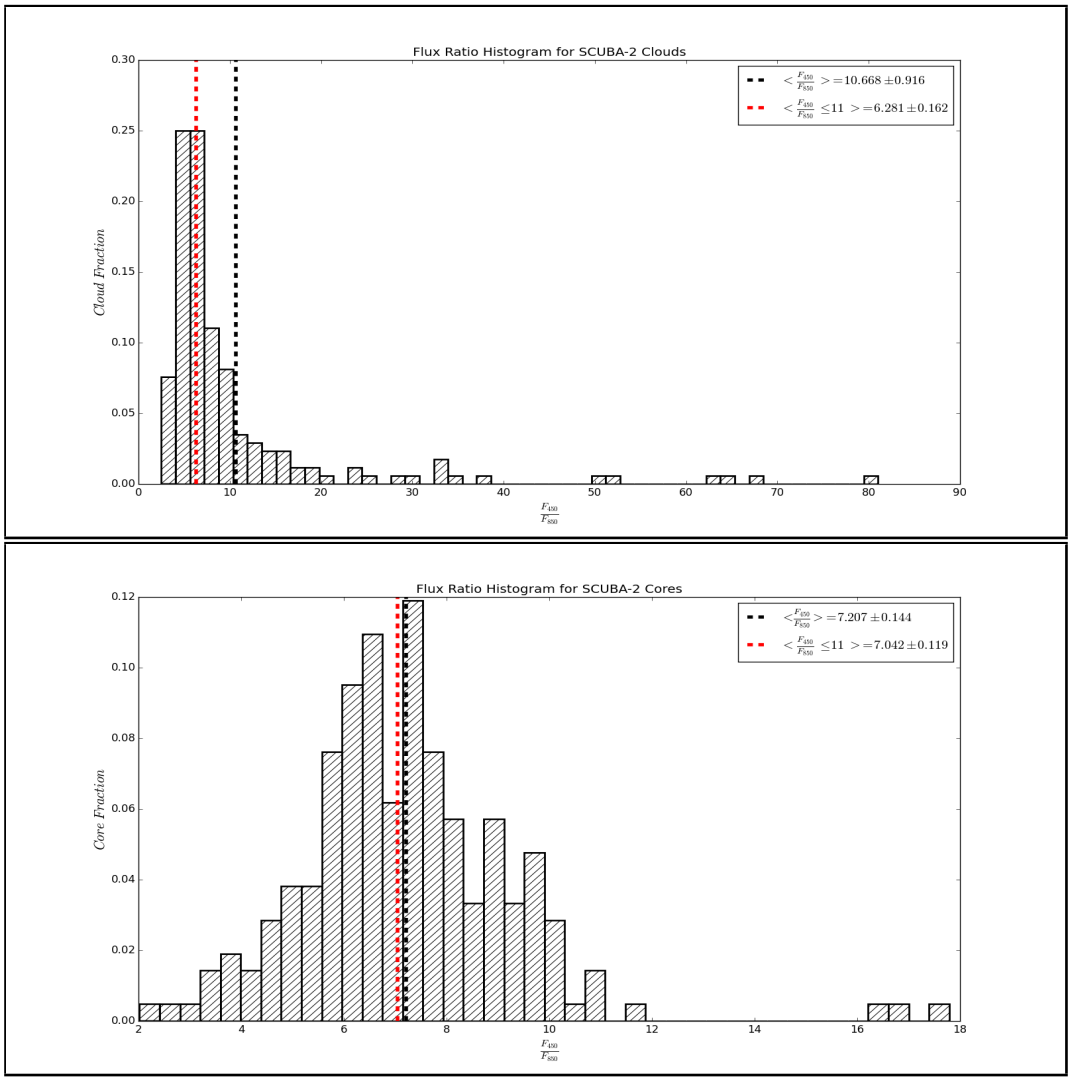

Figure 3.5: Histogram of the cloud (Top) and core (Bottom) ratios of the pure, integrated 450μm to 850μm fluxes. A linear scale is used for the x axis and the y-axis is normalized so that the sum of the bins equals unity. The overall mean is indicated using a black, dashed line while the mean of all physical flux ratios (i.e $\leq$ 11) is indicated using a red dashed line.

3.2.4 Flux Ratio

A flux ratio is simply a direct comparison between a source's pure, 450μm integrated flux to its 850μm counterpart. This ratio is the crucial input for the source's average temperature estimate. In preparation of this calculation, it is important that the fluxes going into the flux ratio calculation are pure, meaning all known backgrounds have been properly subtracted beforehand. Also, it is crucial that care has been taken to express both fluxes in comparable units. Here, both 450μm and 850μm fluxes are expressed in units of Jy. The flux ratio of a source can then be simply calculated using:

$$R = \frac{F_{450}}{F_{850}} \tag{3.18}$$

Where R indicates a source's flux ratio and F_{450} and F_{850} its respective, pure, 450μm and 850μm integrated flux. Determined flux ratios with a symmetric uncertainty over 100% are excluded from the results. However, as I will show in a later section, a stricter prerequisite will be enforced to flux ratios for the purpose of performing effective quality control on the data. A histogram of the cloud and core flux ratios is presented in figure 3.5. The mean of all obtained flux ratios is displayed using a black dashed line. The mean of all physical flux ratios (i.e ≤ 11) is displayed using a red dashed line.

Taking a look at the overall mean flux ratios, it appears that the cloud mean is much greater than its core equivalent. The reason for this involves the large number of outliers present in the cloud flux ratios which tend to drag the average value up. Recall that the 450μm band is much more prone to the level of atmospheric water vapor than the 850μm band. The integrated flux measurements in both bands suffer inflation as a consequence but the 450μm measurement is always inflated more than the 850μm equivalent. At the same time, the apertures used for the measurement of the cloud's integrated flux are always much larger than those used for any of the embedded cores. Due to this size difference, it is expected that the cloud flux ratios will be even more skewed than the core ones as the proportion of 450μm to 850μm noise will be much greater for the clouds.

On the contrary however, when considering physical flux ratios (i.e ≤ 11) which result from reliable 450μm and 850μm data, the reverse occurs. Clouds now have on average a lower flux ratio than their embedded cores, meaning that they are on average cooler than them. Objects with unphysical flux ratios (≥ 11) are dropped from data analysis and the manner in which this segregation takes place is discussed in section 3.6.2.

3.3 Temperature Dependent Quantities

The recipes for the derivative properties in this subsection do incorporate temperature. As such, they do suffer from the asymptotic nature of the temperature model and are therefore skewed-Gaussian in nature. Consequently, these properties will have asymmetric uncertainties attached, which will be calculated using Monte-Carlo simulations in Chapter 4.

3.3.1 Average Temperature

The average temperature of a SCUBA-2 source can be obtained once its ratio of 450μm to 850μm pure, integrated flux has been calculated. The temperature model for dust grains is an implicit, non-linear function of this ratio and is adopted from the SCUBA-2 studies of the Gould belt [26]. This model relationship can be expressed as follows:

$$R = \left(\frac{e^{\frac{hc}{k_B \lambda_{850} T}} - 1}{e^{\frac{hc}{k_B \lambda_{450} T}} - 1}\right)\left(\frac{850}{450}\right)^{3+\beta} \quad [26] \tag{3.19}$$

Where T indicates a source's average temperature, R its pure F_{450} to F_{850} integrated flux ratio, β its opacity power-law index and λ_{450} and λ_{850} the 450 and 850 wavelengths in meters respectively. Substituting all physical constants and a β of 1.8, the above expression can be simplified to:

$$R = 21.17\left(\frac{e^{\frac{16.96}{T}} - 1}{e^{\frac{32.00}{T}} - 1}\right) \tag{3.20}$$

Determined temperatures with asymmetric uncertainty above 100% on both sides are excluded from the results. A histogram of the determined core and cloud average temperatures is presented in figure 3.6.

It is worthy to note that the temperature model behaves asymptotically beyond a particular flux ratio, yielding an infinite temperature estimate. The flux ratio value at which this happens strongly depends on the choice of β. Using a value of 1.8 for β as was done above will result in an infinite temperature estimate above a flux ratio of ≈ 11.

Care must be taken as a minority of sources is not well described by this choice of β and/or its accompanied opacity model. A portion of this minority is simply associated with tremendously noisy 450μm images. High uncertainty in the 450μm photometry can

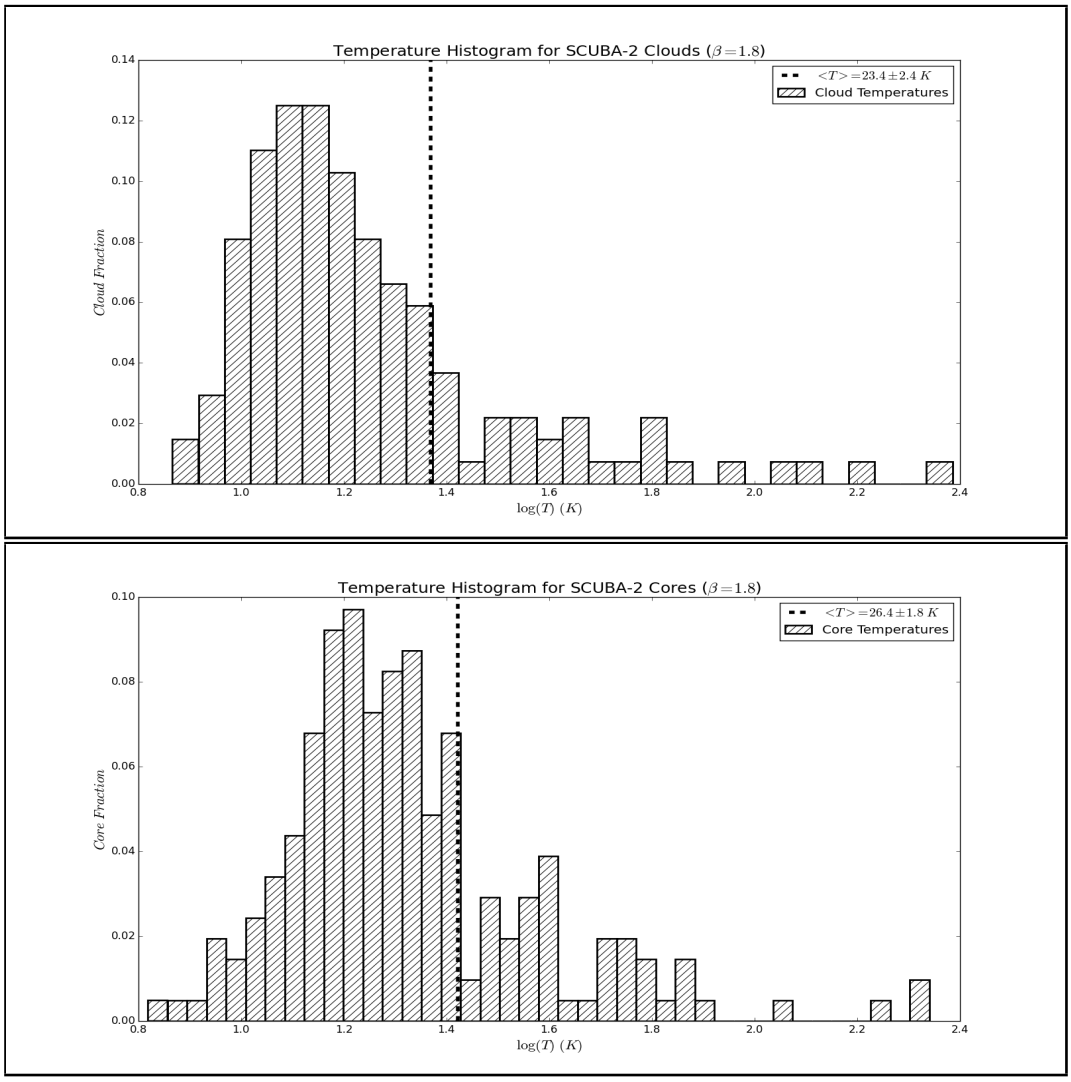

Figure 3.6: Histogram of cloud (Top) and core (Bottom) average temperatures. A logarithmic base-10 scale is used on the x-axis and the y-axis is normalized so that the sum of the bins equals unity. The mean is indicated using a black, dashed line.

easily skew the flux ratio upwards and into the highly asymptotic regime. However, a small portion of this minority comprises of clumps whose photometry is good, yet their determined average temperatures and subsequent derivative properties are highly unphysical. This suggests that the composition of a small number of SCUBA-2 clumps is vastly different than the one assumed, indicating a later stage of star formation, or simply a more

complicated environment at play. A threshold is put in place to segregate such unphysical results later on in section 3.6.2.

3.3.2 Cumulative Mass

The cumulative mass of a SCUBA-2 source can be calculated using either its 450μm or 850μm photometric description. The latter is preferred due to the fact that 850μm photometric measurements are by nature less noisy than their 450μm counterparts.

The recipe for the calculation of the total mass is adopted from SCUBA-2 studies of the Gould Belt [26] without any modifications. The recipe requires a radial distance, which is taken to be the radial distance of the HII region in the vicinity of a SCUBA-2 source. In the case where multiple HII regions exist in the vicinity, an average of their radial distances is used instead. Overall, the mass can be calculated as follows:

$$M = \frac{F_{850} d^2}{\kappa_{850} B(\lambda = 850\mu m, T)} [26] \tag{3.21}$$

With:

$$B(\lambda, T) = \frac{2hc^2}{\lambda^5} \frac{1}{e^{\frac{hc}{\lambda kT}} - 1} \tag{3.22}$$

Where M indicates a source's total mass, F_{850} its pure, 850μm integrated flux, κ_{850} its opacity in the 850μm band, d its radial distance and T its average temperature. Total masses with asymmetric uncertainty above 100% on both sides are excluded from the results. A histogram of the determined core and cloud total masses is presented in figure 3.7.

3.3.3 H_2 Column Density

The column density of a SCUBA-2 source, similarly to the mass, can be determined using either the 450μm or 850μm photometric description, however the less noisy 850μm parameters are preferred.

The column densities calculated here are overall averages as they use an integrated flux measurement and the average temperature of the source at hand. Column densities are expected to rise as one moves toward the center of a source, where they are expected to become roughly a factor of 10 greater than the established averages presented here.

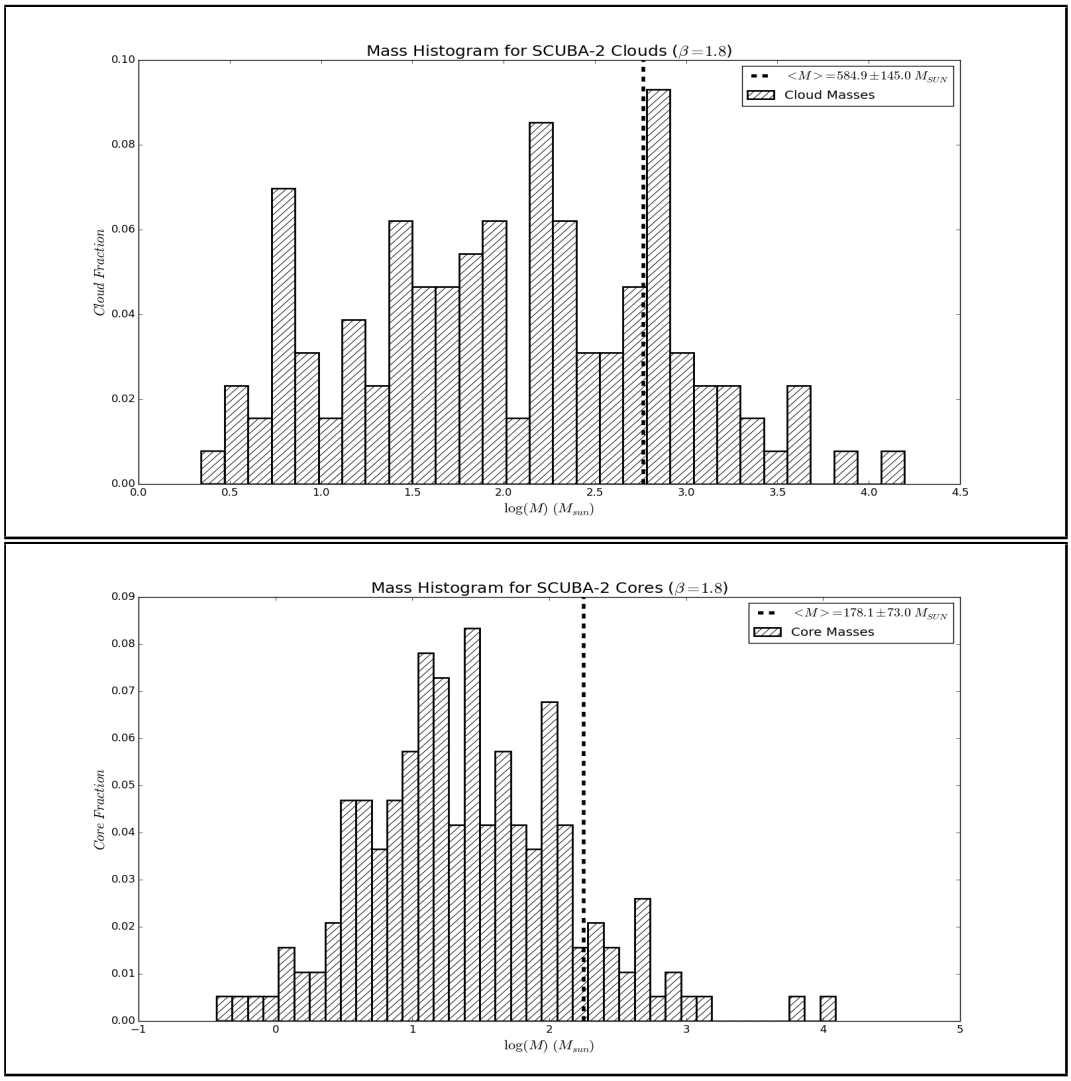

Figure 3.7: Histogram of cloud (Top) and core (Bottom) cumulative masses. A logarithmic base-10 scale is used on the x-axis and the y-axis is normalized so that the sum of the bins equals unity. The mean is indicated using a black, dashed line.

The H_2 column density recipe is also adopted from the SCUBA-2 Gould Belt study [30]. However, in order to minimize the propagated uncertainty, the quantities involved in this recipe are broken down into their constituents to permit cancellation of highly uncertain factors such as radial distance.

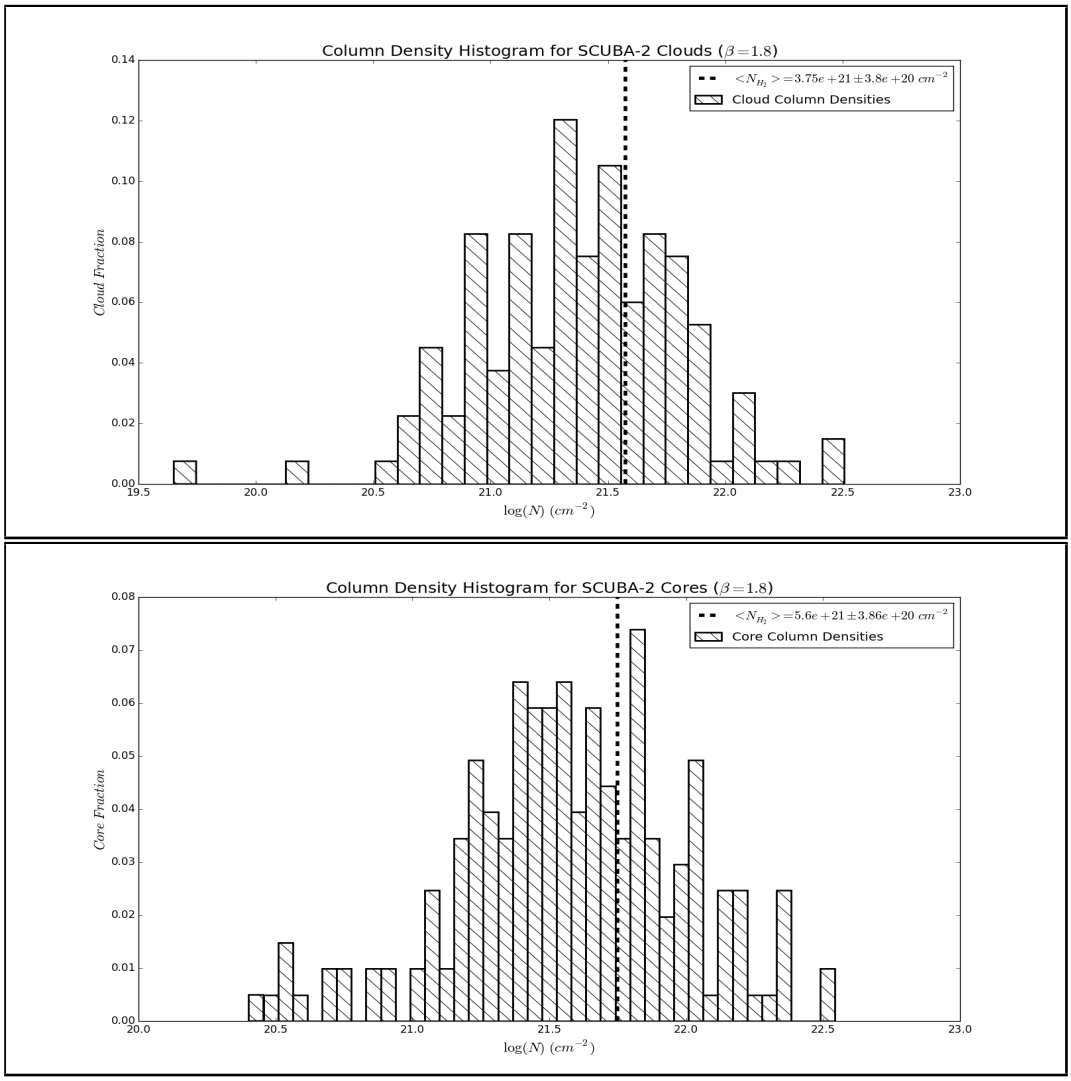

Figure 3.8: Histogram of cloud (Top) and core (Bottom) H_2 column densities. A logarithmic base-10 scale is used on the x-axis and the y-axis is normalized so that the sum of the bins equals unity. The mean is indicated using a black, dashed line.

The mean molecular weight is also required for this calculation, and it is taken to be ≈ 2.86. This number assumes a composition of $\approx 70\%$ H_2 by mass, a mean particle mass of ≈ 2.3 amu and a sufficient mixture of the dusty and gaseous components. The modified

H_2 column density recipe reads as follows:

$$N_{H_2} = \frac{F_{850}}{\pi \kappa_{850} \mu m_H B(\lambda = 850\mu m, T) \tan^2\left(\frac{\pi R('')}{648000}\right)} \text{ [30]} \tag{3.23}$$

Where N_{H_2} indicates a source's H_2 column density, F_{850} its pure, 850μm integrated flux, κ_{850} its opacity in the 850μm band, $B(\lambda = 850\mu m, T)$ its Planck blackbody emission, T its average temperature, $R('')$ its angular radius in arcseconds and μ its mean molecular weight. H_2 column densities with asymmetric uncertainty above 100% on both sides are excluded from the results. A histogram of the determined core and cloud column densities is presented in figure 3.8.

3.3.4 H_2 Number Density

The H_2 number density of a SCUBA-2 source can be calculated through a simple comparison of its mean particle mass to its previously determined total mass. However, this maximizes propagated uncertainty, and instead, in a similar manner to the column density calculation, the involved quantities are broken down to their constituents.

Like the column densities, number densities calculated here are also overall averages as an integrated flux measurement and an average temperature is used for their calculation. Number densities are also expected to rise as one moves toward the center of a source by roughly 10 to 100 times the value of the established average.

The choice to use 850μm photometric parameters and the values used for the mean molecular weight and radial distance follow directly from the previous sections. The original H_2 number density recipe can be found in the SCUBA-2 Gould Belt study [30] and is a simple modification of the column density recipe. The final H_2 number density recipe reads as follows:

$$n_{H_2} = \frac{3F_{850}}{4\pi \mu m_H \kappa_{850} B(\lambda = 850\mu m, T) d \tan^3\left(\frac{\pi R('')}{648000}\right)} \text{ [30]} \tag{3.24}$$

Where n_{H_2} indicates a source's H_2 number density, F_{850} its pure, 850μm integrated flux, κ_{850} its opacity in the 850μm band, $B(\lambda = 850\mu m, T)$ its Planck blackbody emission, T its average temperature, d its radial distance and $R('')$ its angular radius in arcseconds. H_2 number densities with asymmetric uncertainty over 100% on both sides are excluded from results. A histogram of the determined core and cloud number densities is presented in figure 3.9.

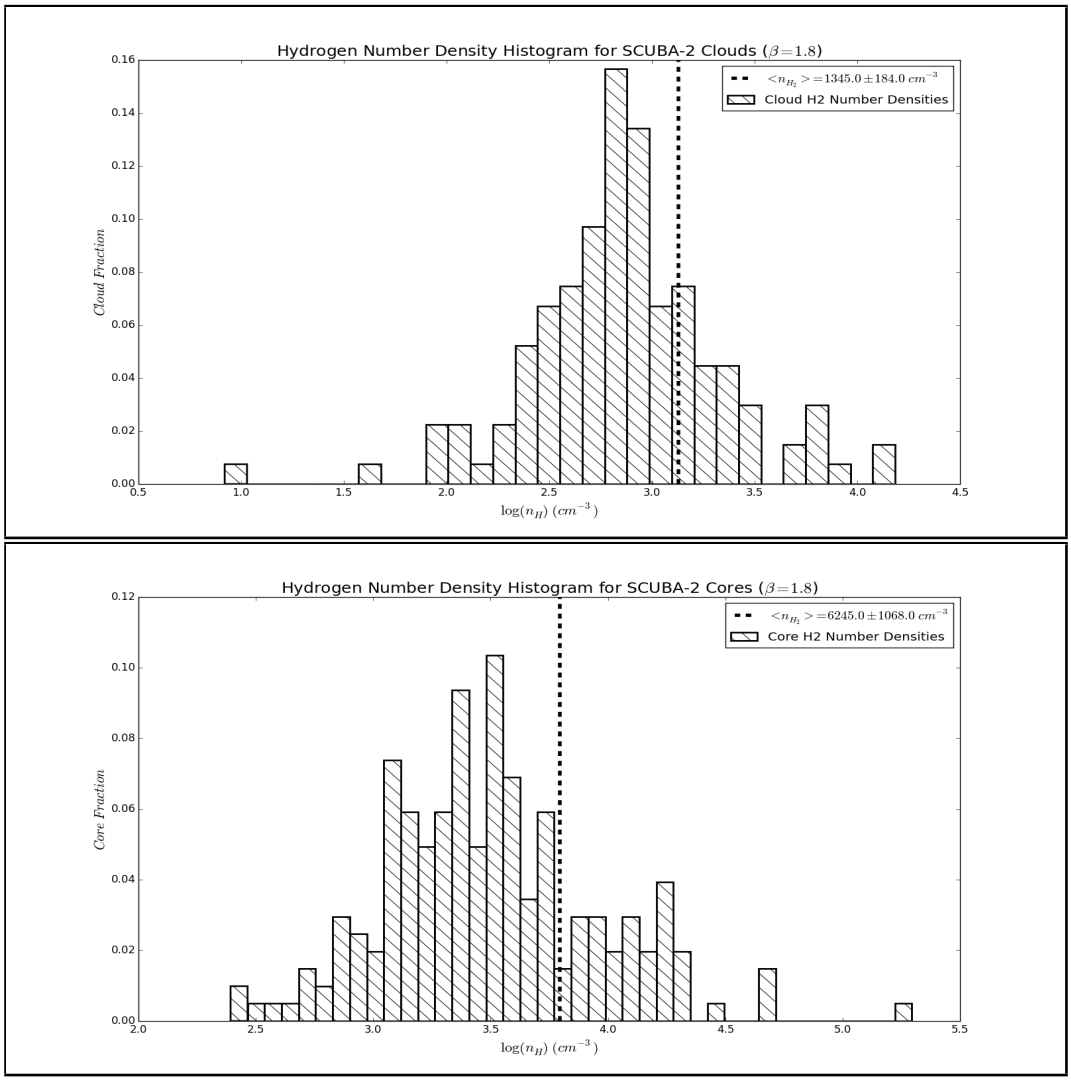

Figure 3.9: Histogram of cloud (Top) and core (Bottom) H_2 number densities. A logarithmic base-10 scale is used on the x-axis and the y-axis is normalized so that the sum of the bins equals unity. The mean is indicated using a black, dashed line.

It is of great interest to note that the majority of cores ($\approx 90\%$) have an average number density $\geq 1000\ cm^{-3}$ while a large majority of clouds ($\approx 70\%$) have an average number density $\leq 1000\ cm^{-3}$.

Finally, if desired, the H_2 number density can be converted to the overall particle number density through multiplication of 1.24 under the assumptions made earlier regarding the mean molecular weight of SCUBA-2 sources. This is useful for calculating the average pressure below:

3.3.5 Pressure

The average pressure of a SCUBA-2 source can be estimated by assertion of the ideal gas law as follows:

$$P = k_B \sum_{i=1}^{n} n_i T_i \tag{3.25}$$

Where n_i indicates the number density of each particle species and T_i its average temperature. If the assumptions that the dust is strongly coupled to the gas and that the clump is comprised of $\approx 70\%$ H_2 by mass hold, then the conversion between n_{H_2} and n can be performed via:

$$n = 1.24 n_{H_2} \tag{3.26}$$

and the average temperatures for the different species can be approximated to be the same, leading to the following approximation to the average pressure:

$$P \approx \frac{3.72 k_B T F_{850}}{4\pi \mu m_H \kappa_{850} B(\lambda = 850\mu m, T) d \tan^3\left(\frac{\pi R('')}{648000}\right)} \tag{3.27}$$

Where P indicates a source's average pressure, T its average temperature, F_{850} its pure, 850μm integrated flux, μ its mean molecular weight, κ_{850} its opacity in the 850μm band, $B(\lambda = 850\mu m, T)$ its Planck blackbody emission, d its radial distance and $R('')$ its angular radius in arcseconds. Pressures with asymmetric uncertainty over 100% on both sides are excluded from results. A histogram of the determined core and cloud average pressures is presented in figure 3.10.

Note that core average pressures are on average much greater than those of clouds. I will explore this interesting feature in more depth in section 5.3.2.

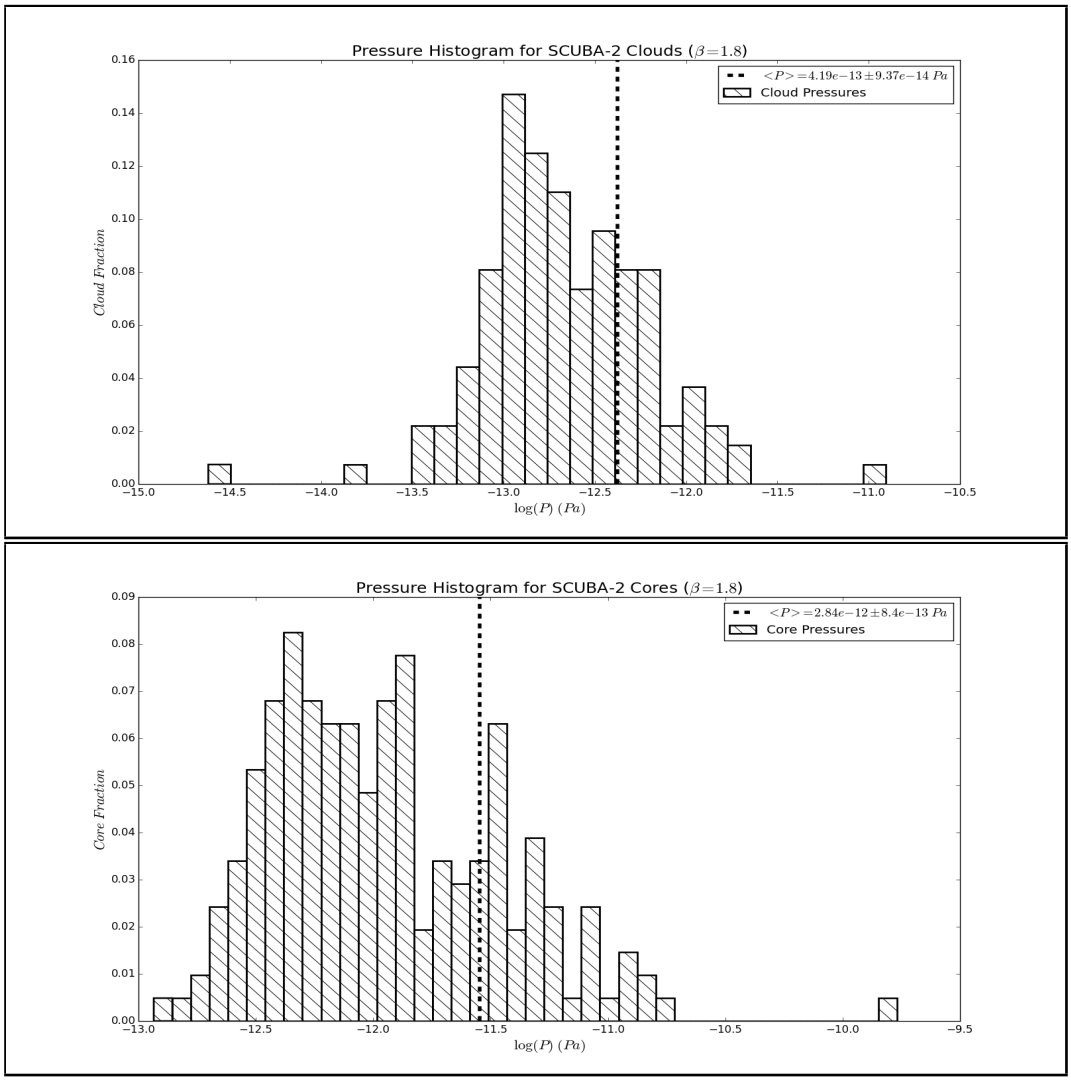

Figure 3.10: Histogram of cloud (Top) and core (Bottom) average pressures. A logarithmic base-10 scale is used on the x-axis and the y-axis is normalized so that the sum of the bins equals unity. The mean is indicated using a black, dashed line.

3.4 Associating Cores to HII Regions

In this section I will discuss the process through which cores are associated to HII regions. First, the HII region center coordinates and angular radii in physical units (J2000, arcseconds) have been presumably obtained through the methodology discussed in the beginning

of section 2.3. The SCUBA-2 source center coordinates and angular radii in both physical (J2000, arcseconds) and image (pixels) units are also presumably obtained by the methodology described in the later portion of the same section.

Before perfoming the association, it is necessary to obtain the HII region coordinates in image units on their respective SCUBA-2 images. To do this, the SCUBA-2 image is initialized using *SAOImageDS9*. A circular aperture is then created where the central coordinates and angular radius of the HII region are inputted in physical units. The resulting aperture is then saved and its image coordinates are separately stored as they will be used when producing the images presented in appendix .4.

Once this task is completed, the association begins with the use of a scripted routine. This routine considers each core's central coordinates in physical units and compares them to those of each HII region in the sample for the purpose of calculating the separation distance between the two. This 2-D angular separation distance is calculated in arcminutes using:

$$x_1 = sin\big(DEC_{CORE}\big)sin\big(DEC_{HII}\big) \tag{3.28}$$

$$x_2 = cos\big(DEC_{CORE}\big)cos\big(DEC_{HII}\big)cos\big(RA_{CORE} - RA_{HII}\big) \tag{3.29}$$

$$\theta_{SEP} = \frac{10800}{\pi}\cos^{-1}(x_1 + x_2) \tag{3.30}$$

Where θ_{SEP} indicates the separation distance between a core and an HII region in arcminutes, RA_{CORE} and DEC_{CORE} the right ascension and declination of the core under consideration and finally RA_{HII} and DEC_{HII} the right ascension and declination of the HII region that the separation distance is measured with respect to.

It would be reasonable at this point to deem the HII region with the smallest seperation distance as the one being associated with a particular core. However, HII regions vary significantly in size, and comparing center-to-center distances can be misleading. To picture why this is the case, let's use an example where a core lies 1' away from the center of a 0.5' diameter HII region and 2' from a 3' diameter HII region. Clearly, the core is closer to the center of the first HII region, but is actually inside the second. If the shortest separation distance is used, one will obtain the misleading result that the first HII region is the associated one. Clearly, a modification is needed. For this reason, a scaled separation distance is used instead, where the scaling is done by the HII region's angular radius. Formally, this reads:

$$\theta_{SCALED} = \frac{\theta_{SEP}}{R_{HII}} \tag{3.31}$$

Where R_{HII} indicates the HII region's angular radius in arcminutes. An HII region then is associated to a particular core if the two share the smallest scaled separation distance. A complication naturally arises and concerns cores which lie extremely far away from their associated HII region for the association to be justified. For this reason, separation distance thresholds are developed and enforced in section 3.7.1 in order to segregate cores that are not likely associated with their matched HII region from those that are. The results of the association process after the segregation of section 3.7.1 is performed can be viewed in table 3.

3.5 Associating OB Stars to HII Regions

In this section, I discuss the process through which massive, OB stars are associated to HII regions. Although distance plays an important factor to this process, spectroscopy is also necessary for the classification of a particular star. Fortunately, the spectroscopy aspect has been tended to by other academic work. Most massive stars have a precise temperature (T-Class) and luminosity (L-Class) classification. In addition, a large number of HII regions already have some information regarding potentially associated, massive OB stars.

The OB star to HII region association will then be a two-fold process. For the sample of HII regions that already has such information available, a literature review is conducted and the findings are used here. For the sample that doesn't have such information available, a manual catalogue survey is performed instead.

Beginning with the literature aspect then, the most helpful resource is a very detailed catalogue from *T. Foster* et al [54] which covers a large portion of the HII regions considered in this thesis. An additional such resource is a catalogue from *D. Russeil* et al [14] which provides information on a smaller portion of HII regions not included in *T.Foster's* work.

When no information is available in literature, the manual aspect takes place. Manual association is performed using *Reed's* massive, OB star catalogue. The central coordinates of the HII region of interest are inputted in the online version of this catalogue and a search for massive, OB stars up to a radial distance of 40' is performed. For the time being, all resulting OB stars are kept as associated with the inputted HII region. However, the results clearly include stars that were extremely far from some HII regions to justify

Table 3.1: Classification convention for OB stars with partial classifications

Partial Classification	**Full Classification**
'O' or 'B' without L-Class	O_V or B_V
'O' or 'B' without T-Class	O9_or B0_
Between 2 L-Classes	Average of the 2 L-Classes
Between 2 T-Classes	Average of the 2 T-Classes
'O or 'B' without both L and T Classes	O9V or B0V
'OB'	O9V

their association. To relieve this issue, another sophisticated threshold scheme is devised in section 3.7.2 to segregate highly unlikely associated stars obtained both from literature as well as manually.

Attention must be placed on an additional complication, which is the occasional lack of a precise classification for a given OB star. In order to treat such cases, educated assumptions are made based on the most likely derivative star type given the partial classification available. This assumption scheme is presented in table 3.1. Once the complete spectral classification of an OB star is determined, its luminosity and mass can be inferred through a conversion table. The masses and luminosities of each class in this table are averages from several studied stars with similar spectroscopies. The more cases investigated for a particular class, the more representative these average values will be for that class. However, OB stars are rather rare and define a wide parameter space, especially when it comes to luminosity ($10 - 10^7\ L_{SUN}$). This makes the determination of average properties very challenging, and considerable disagreements exist between works that become magnified when climbing the classification ladder toward the hotter and rarer "O" stars.

I will avoid jumping into the uncertainty particulars, as it is not clear to what degree of precision the current mean properties are established. Instead, I advise the reader to remain cautious when interpreting luminosities and masses presented in table 6 as they are approximations of moderate accuracy to the true values.

The conversion table used to infer the luminosities and masses for fully classified OB stars is a table created by *C.L Noll* [2] whose construction is based on an older table by *Spacegear*. Ionizing radiation rates are obtained from studies by *Sternberg* [5] and *Panagia* [48]. The same two studies are used to check the validity of the luminosities and masses presented in *C.L Noll's* table.

Finally, it is worthy to mention that an attempt to provide the full *SIMBAD* IDs for all associated OB stars is made. This is done through coordinate queries on the *SIMBAD* search engine. An ID is only provided when a star is very close ($< 20''$) to the inputted coordinates and its classification is no less vague than "O" or "B". In the few cases where the matching is ambiguous, or a match is not found, no SIMBAD ID is attached to the OB star. The overall results after the segregation of section 3.7.2 is performed, are presented in table 6.

3.6 Quality Thresholds

In this section, I discuss the implementation of cutoffs for the purpose of segregating reliable from unreliable data. So far any quantity with a symmetric uncertainty over 100%, or an asymmetric uncertainty greater than 100% on both sides has been automatically excluded from results.

However, this is not sufficient because it allows measurements with very noisy photometry to be excluded only from those derivative property calculations that yield an uncertainty of over 100%. I would like to completely prevent highly noisy photometric measurements from entering the derivative property stage. For this purpose, I place tighter constraints with two additional, robust cutoffs.

The first cutoff is concerned strictly with the quality of the photometry while the second cutoff deals with the existence of sources that are not well described by the assumptions made earlier in this chapter (particularly about opacity). The result of the additional segregation is a reliable dataset consisting of a homogeneous sample that can be further analyzed in a meaningful manner.

3.6.1 Reliability Threshold

To exclude derivative properties that stem from unreliable measurements, a cutoff must be placed near the beginning of the calculation stage. Since the temperature model is extremely sensitive to flux ratio uncertainty, I choose to enforce the reliability cutoff at the F_{450}/F_{850} calculation stage. I specifically prevent the use of a flux ratio with an SNR below a certain value from being used in the calculation of average temperature, and other temperature dependent properties.

To decide at what level this cutoff will be set, it is necessary to consider the distribution of the flux ratio SNRs, displayed in figure 3.11. In order to narrow down this value, let's begin by considering what is the minimum value this SNR can be. Clearly, an SNR cannot be negative as is the case for some sources whose 450μm image is extremely noisy and ambiguous. In addition it can't be lower than 1, as that would mean having an uncertainty of more than 100%.

On the other side of the spectrum, inspecting figure 3.11 reveals that the maximum SNR cannot be higher than 3.5, as clearly no source has an SNR greater than this value after all the uncertainties have been carried over. At a first glance then, the appropriate range for this cutoff seems to be anywhere between 1 and 3.5.

In order to continue narrowing down this range to a single value, an assessment of the goals of this reliability threshold needs to be made. Specifically, the following questions need to be addressed:

1. Is a larger sample size or higher precision level preferred?
2. What is the effect of the flux ratio SNRs to average temperature estimates?
3. What portion of the sample is rejected?

To answer the first question, the goal is a reasonable precision level that allows most of the sample to be considered in the results. Ideally, the majority of accepted SCUBA-2 sources will have both upper and lower temperature uncertainties less than 100%.

To answer the second question, it is evident from figure 3.12 that a moderate flux ratio of 5 can have an upper temperature uncertainty of over 100% if the SNR of that flux ratio is 1.5, while the negative uncertainty is much smaller. Considering that the majority of SCUBA-2 sources have a flux ratio greater than this value, an SNR of 1.5 would accept many sources with diverging upper temperature uncertainties.

To answer the third question, I consider an SNR of 2.0 and 2.5 and examine figure 3.11 once again. At an SNR of 2.5, $\approx$ 92% of cloud objects and $\approx$ 62% of core objects are accepted, while at an SNR of 2.0 $\approx$ 98% of cloud objects and $\approx$ 78% of core objects are accepted.

Since the goal is to include as many SCUBA-2 sources as possible with a preference for

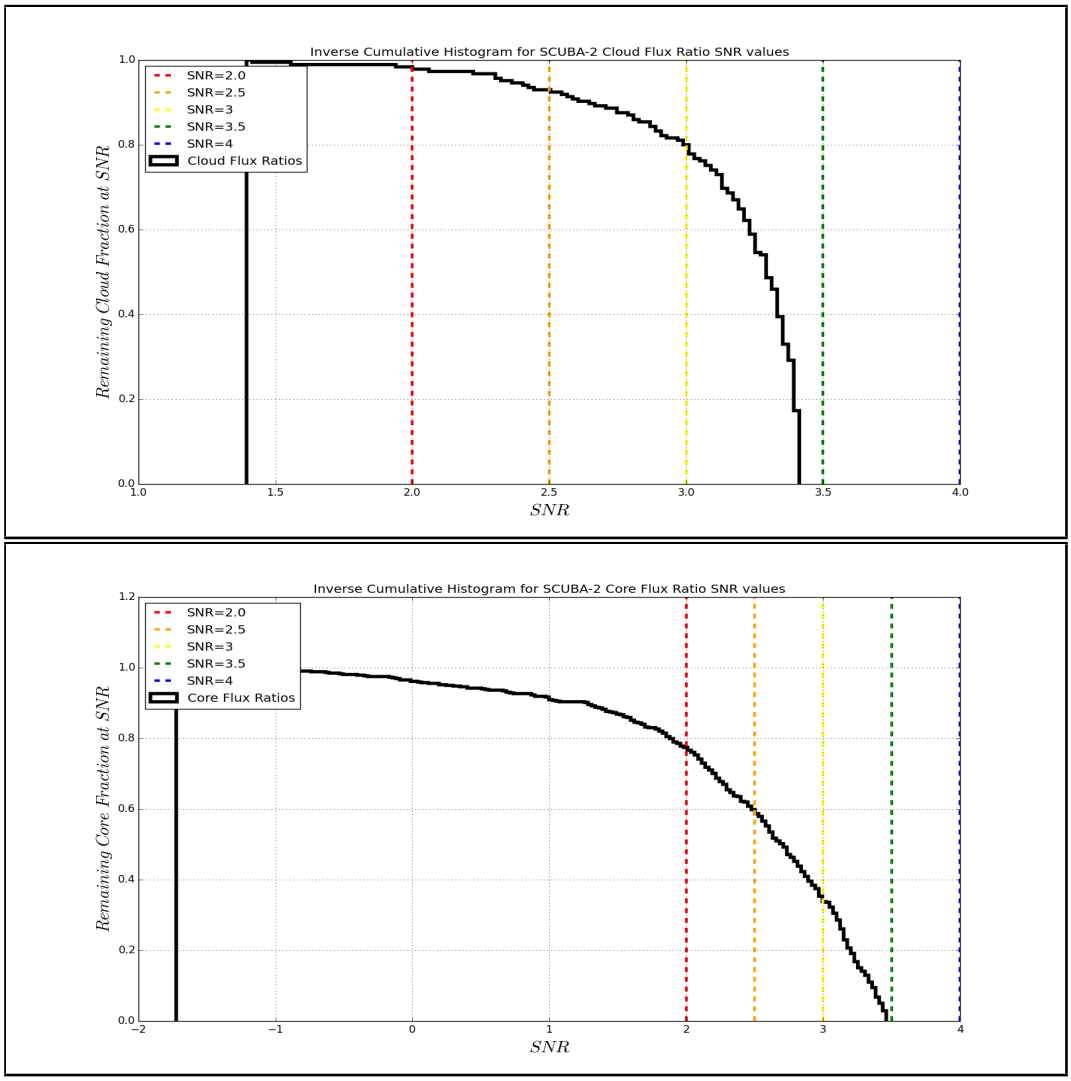

Figure 3.11: An inverse, cumulative histogram of cloud (Top) and core (Bottom) flux ratio SNRs. The y-axis is normalized to 1. Note the small fraction of core objects with an $SNR < 1.0$ due to the poor quality of their 450μm images.

the majority of accepted sources to have an upper and lower temperature uncertainty less than 100%, the cutoff is set at $SNR = 2$. Better 450μm photometry in the future can potentially allow this number to be set much higher instead.

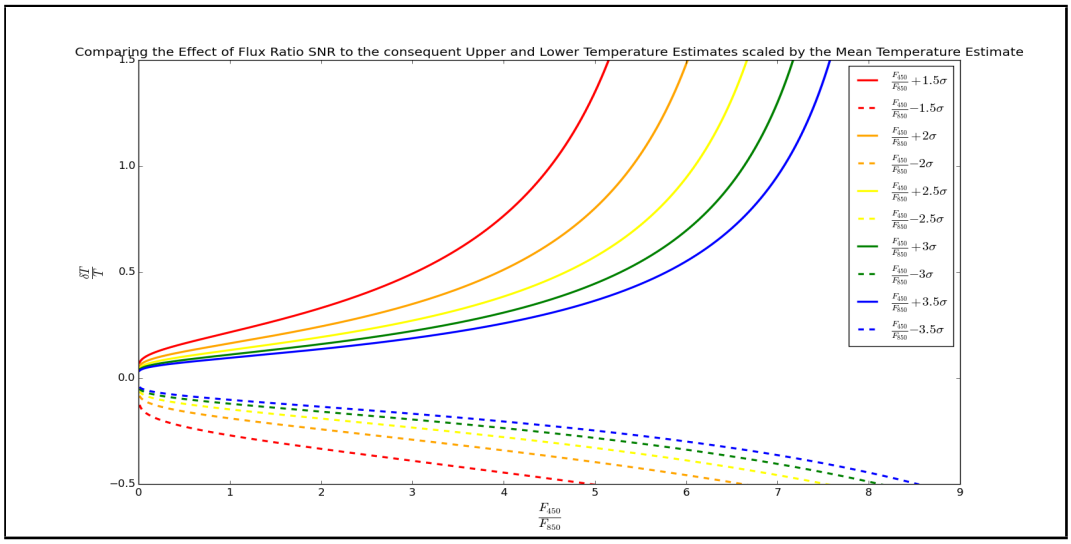

Figure 3.12: The effect of the flux ratio SNR on average temperature estimates. The solid curves represent the $+n\sigma$ cases while the dashed curves the $-n\sigma$ cases. Clearly, the resulting uncertainty is of asymmetric nature, at the plus curves climb much faster than the minus ones.

3.6.2 Exotic Source Threshold

At this point, the sources have passed the quality control filter and are ready to move into subsequent calculations. However, as mentioned earlier, some of these sources are bound to not be well characterized by one or more of the assumptions made in the calculation recipes of the previous sections. Some of these assumptions include, but are not limited to:

- Treating CO(3-2) as a uniform background
- Setting β to 1.8
- Assuming an optically thin regime
- Setting the mean molecular weight to 2.86
- Assuming the dust is well mixed with the gas

Such "exotic" sources will yield highly unphysical results if the previous recipes are used to calculate their properties. For this reason, a second cutoff is employed in order to prevent

unphysical derivative properties of these sources from contaminating those from the source majority that is well described by the above assumptions. This cutoff is employed at the temperature calculation stage and essentially prohibits sources with incoming flux ratios outside the range $0.49110 < R < 10.966918$ to be included in the results. This flux ratio range translates to a temperature range of $4K < T < 300K$ (using $\beta = 1.8$).

The logic behind the choice of the minimum acceptable temperature involves consideration of interstellar heating mechanisms. The first is radiation from the CMB, which automatically requires the source average temperature to be $T > T_{CMB}$ $2.7K$. In addition, sources experience constant bombardment from cosmic rays. Also, since the sources considered in this thesis are always located near one (or more) mature HII regions, it is more than likely that they are heated from both runaway, free-free emission from the HII regions themselves, as well as radiation from their associated OB star(s). The cumulative effect of the above mechanisms is expected to raise source average temperatures to at least $4K$.

The logic surrounding the choice of the maximum acceptable temperature on the other hand involves consideration of hot dust temperatures. This upper limit depends on the composition of dust, as more volatile compounds such as water tend to sublime at relatively low temperatures (90K), while some of the least volatile dust compounds may need temperatures up to 2000K. However, this is a wide range, and in order to choose a good maximum, I consider hot dust temperatures determined in *G. Sreenilayam* and *M. Fich's* work [17]. In table 2 of this paper, the largest peak dust temperature is $300 \pm 100K$. This is the value taken to be the maximum threshold for average temperatures in this thesis.

3.7 Separation Distance Thresholds

In this section, I will discuss the development of distance cutoff thresholds aimed to avoid the association of HII regions to objects that are separated by a distance too great to justify that association. First, I will take a look at how to employ such a cutoff in the "Core - HII region" association process and will continue by doing the same for the "OB star - HII region" association process.

3.7.1 Core - HII Region Separation Threshold

Previously, each core was matched with the Sharpless HII region with which it shared the smallest, scaled, angular separation. However, as already mentioned, there exist a number of cores residing too far from their matched Sharpless HII regions to justify their association. These distant cores may be associated with a non-Sharpless HII region, or may have formed from a different physical process altogether.

It is then of high importance to segregate the cores that are highly unlikely to be associated with their previously assigned HII region. After all, in this thesis the interest lies solely in the identification of cores that have formed in the vicinity of HII regions. In order to perform this segregation, I dictate two requirements that the cores must satisfy.

The first requirement rejects cores that exist at an angular, scaled, separation distance equal or greater to 15 times the radius of their previously matched HII region. Supplementing this, a second requirement rejects cores that have a center-to-center distance greater than 20 arcminutes to their previously matched HII region.

Following the core segregation, the clouds are segregated as well through a different requirement. Each cloud is required to have at least one core that meets the above distance criteria, otherwise the entire cloud segment is rejected from further analysis.

It is worth noting that the segregating conditionals above are intentionally biased to include cores that are probably associated with their Sharpless HII region but not definitely so. This decision is based on the fact that the radius of each HII region is determined using its VLA 10% flux contour. It's more likely then that the HII region radii are underestimated rather than overestimated and to account for this the scaled size conditional is relaxed.

The results of the segregation can be visualized in figure 3.13 where the two cutoffs are displayed in red. Before the segregation, I begin with 333 cores and 185 cloud segments. After filtering through using the aforementioned conditionals, I end up with 315 cores and 176 cloud segments that remain in the sample considered in this thesis.

3.7.2 OB Star - HII Region Separation Threshold

Previously, each OB star was associated to an HII region by consideration of information found in literature as well as manual searches in online catalogues. However, similarly to

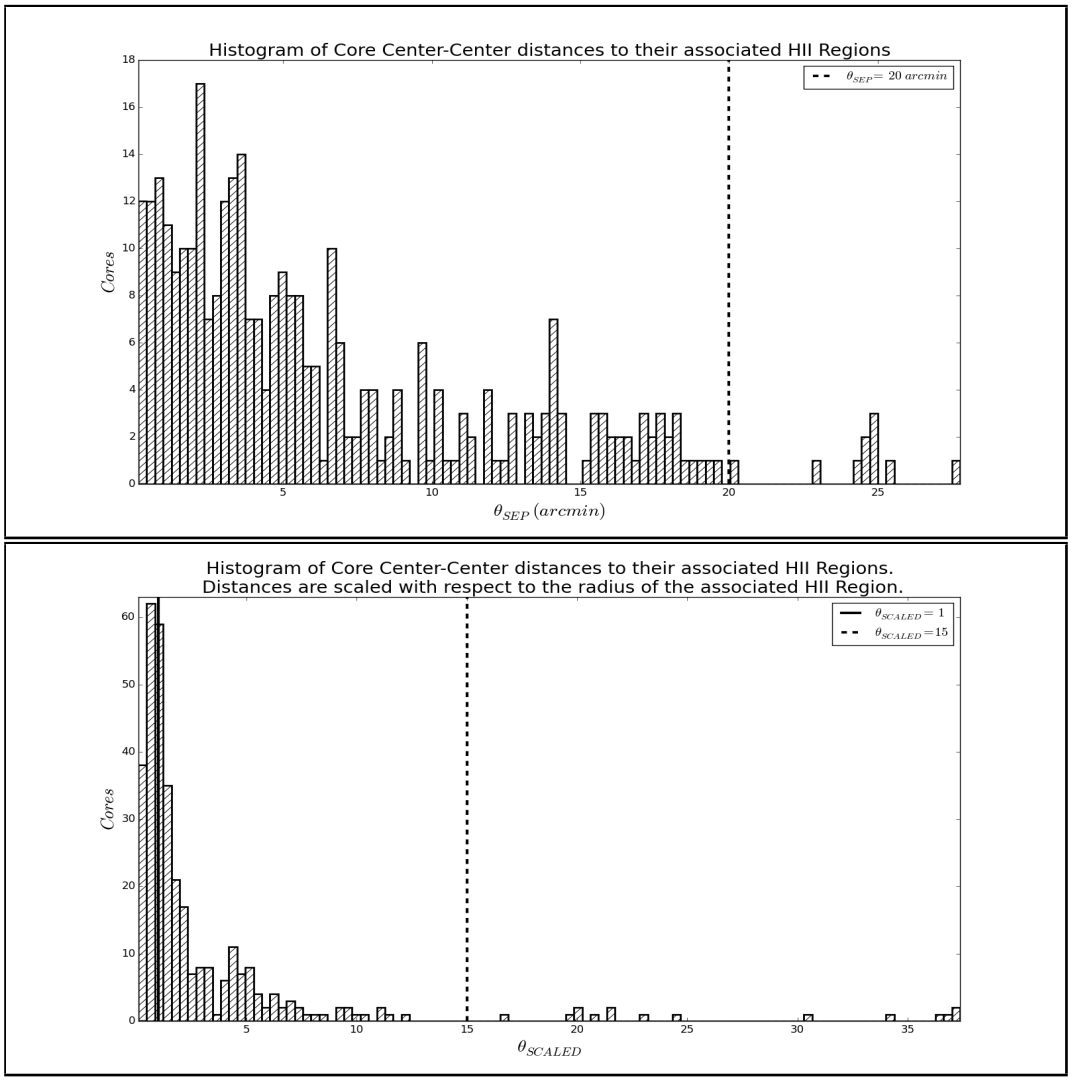

Figure 3.13: Histogram of each core's center-to-center distance to its matched HII region (Top). The same histogram is presented again after the center-to-center distances have been scaled by the angular radius of the matched HII region (Bottom). Note that the largest HII region angular radius is 9' (Sh-2 99), while the largest images have a radius of $\approx$ 70'.

cores, some associated OB stars lie extremely far away from their associated HII region to justify their association. This is particularly true for OB stars that were associated manually, as well as OB stars in literature that were not the first choices of the author as

the "most likely" to be associated.

To circumvent this problem, a similar threshold to that used for core segregation is constructed. However, in order to understand where the threshold should be placed, one needs to investigate the distribution of scaled angular separations of OB stars that are highly likely to be associated with their assigned HII region. The first "most likely" choices presented in Foster's [54] catalogue comprise a great such sample. However, all choices of that catalogue have been stored in our database.

This is great, as a histogram of the scaled angular separations for this combined sample allows us to view the point where the "highly likely" and "not likely" sample split apart. The cut won't be perfectly precise, but rather will form a range that will be very noticeable in the form of a "gap" in this histogram. This is exactly what is seen in figure 3.14 where the range between $4.5 < \theta_{SCALED} < 8.5$ is not populated at all. The choice for the cutoff is then made at a θ_{SCALED} of 7, as this value is near the middle of the unpopulated range. Any values within this range however would be reasonable for use.

This cutoff is then applied to the entire associated star sample, rejecting stars that lie further than a scaled angular separation of 7. The result of the filtration is a list of massive OB stars that are "highly likely" to be associated with their assigned HII region. The distribution of OB star - HII region scaled angular separations after the cutoff is applied is presented in figure 3.15.

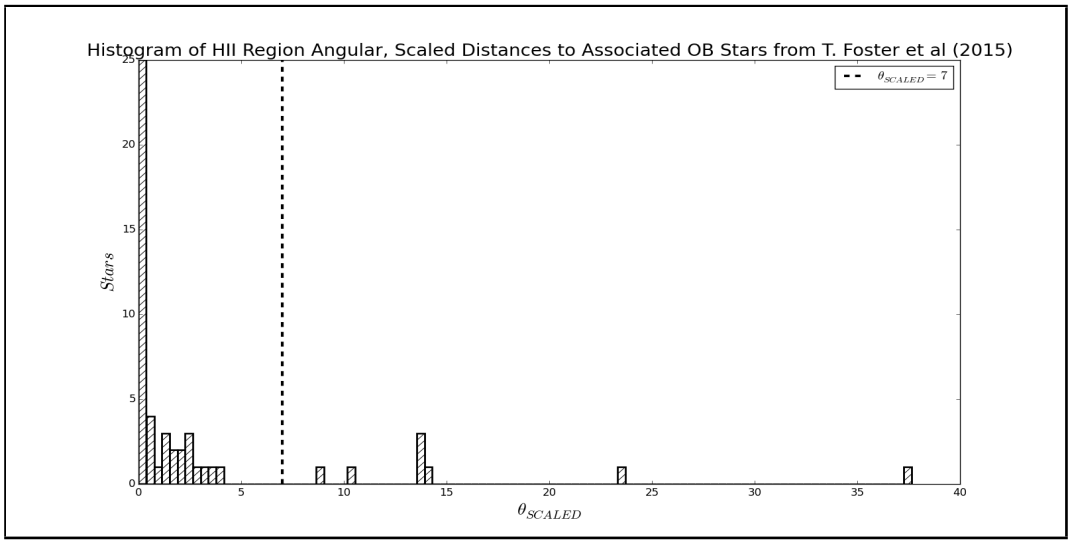

Figure 3.14: Histogram of the angular scaled separation distances of all massive, OB stars from *T. Foster's* association catalogue [54] to their assigned HII region. Note the gap between $4.5 < \theta_{SCALED} < 8.5$ and the choice to set the threshold at a value of 7.

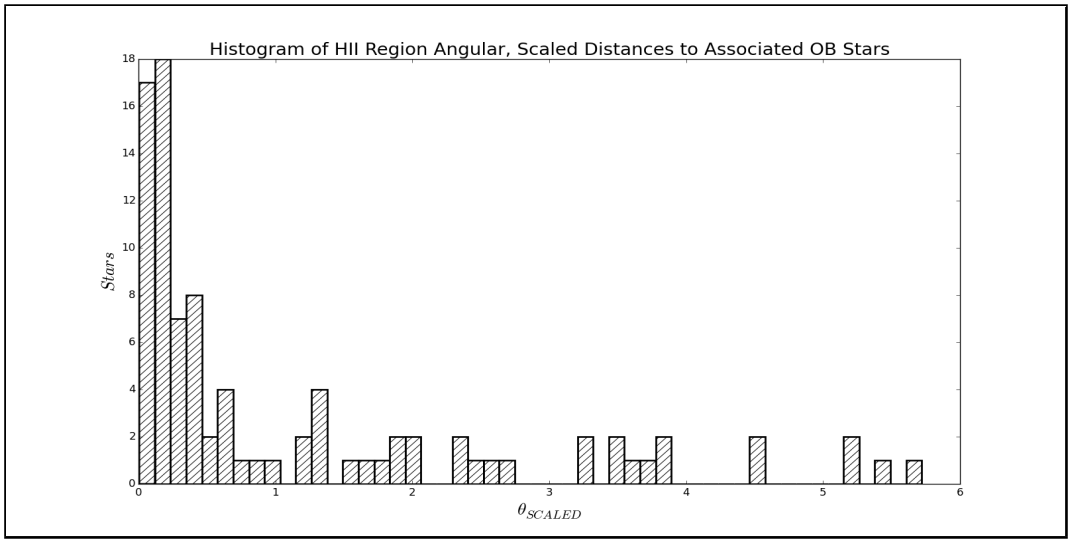

Figure 3.15: Histogram of the angular scaled separation distances of massive, OB stars to their associated HII region after the cutoff of $\theta_{SCALED} = 7$ has been set in place.

Chapter 4

Noise and Uncertainty

In this chapter, I will begin by carrying out an in-depth investigation of every potentially significant uncertainty contributor to SCUBA-2 photometric measurements. This will be followed by a thorough discussion about how uncertainty is attached to subsequent SCUBA-2 derived properties, where I will display how the effect from the non-linearity of the temperature model is tamed using Monte-Carlo simulations.

Before beginning, it is important to note that the uncertainty contributors discussed here are not expected to constitute a complete list, however, I believe that they contribute the vast majority of uncertainty in SCUBA-2 measurements and calculations.

In addition, the stochastic determination of temperature dependent uncertainties is one, but not the only, or best approach to this complicated statistical problem. A different approach incorporates the determination and use of the complete likelyhood functions for each temperature dependent variable. However, the gain in accuracy from this approach is questionable at best, and considering the large complexity that would be introduced to a calculation that is already complicated, it is not adopted here.

4.1 Measurement Uncertainties

In the following subsections I discuss every significant uncertainty contributor to photometric measurements. These generally include integrated flux and mean flux per pixel measurements in the two SCUBA-2 bands. The overall uncertainty for each photometric measurement is simply composed from merging the contributions from the contributors

discussed in this section.

In general, the types of noise taking place in SCUBA-2 photometry can be split into three distinct categories:

1. Systematic Noise
2. Random, Non-Spatially-Structured Noise
3. Random, Spatially-Structured Noise

The systematic noise category includes the following contributors:

- Measuring Routine Choice
- Aperture Properties
  - Placement
  - Size
  - Type
- Data Reduction Parameter Settings
  - Masking SNR
  - Fourier Filter Sensitivity
- FCF Uncertainty

The choice of measuring routine pertains to the choice in the software used for identifying and measuring SCUBA-2 sources. Aperture properties pertain to every single aperture parameter that an experimenter can control when identifying and measuring SCUBA-2 sources. Data reduction parameter settings pertain to the flexibility of tweakable parameters in the SCUBA-2 data reduction pipeline. Finally, FCF uncertainty pertains to the uncertainty surrounding the FCF set used for converting between flux units in SCUBA-2 images.

The random, non-spatially-structured noise category includes the following contributors:

- Atmospheric Emission

- Signal Extinction
- Image Background Artifacts

Atmospheric emission pertains to the combined uncertainty introduced from the atmosphere's emission due to the presence of water vapor and other submillimeter-emitting molecules. Signal extinction pertains to both the atmospheric kind caused from elevated water vapor levels as well as the galactic kind caused from the absorption or scattering of SCUBA-2 signals from objects lying along the line of sight between the SCUBA-2 camera and the targeted source. Background artifacts include image irregularities that are potentially introduced from the data reduction pipeline.

Finally, the random, spatially-structured noise category includes the following contributors:

- Telescope Integration Time
- CO Background Uncertainty
- Negative Bowl Uncertainty

Telescope integration time pertains to the time that each image pixel has been sampled by the telescope beam. CO background uncertainty pertains to the standard error of the mean CO background flux per pixel estimate. Similarly, negative bowl uncertainty pertains to the standard error of the mean negative bowl flux per pixel estimate.

For some of the uncertainty contributors introduced above, although presented individually, it is not possible to isolate their individual uncertainty contribution as it is tied with that of one or more other contributors in a very intricate way. For example there is no known way of measuring separately the noise introduced from atmospheric emission and then from background artifacts. For such sources of uncertainty, the combined contribution is what will be calculated and used in SCUBA-2 measurements. Having said this, we are finally in a position to address each category and its members individually.

4.1.1 Systematic Noise

In this subsection I elaborate on the major systematic uncertainty contributors to SCUBA-2 photometric measurements. It is worth remembering that systematic uncertainties arise from each and every controlled aspect in the measurement technique.

Measuring Routine

In this section, I will compare measurements made using an automatic routine developed in *Python* to the same measurements made using a highly reliable software package, namely, *SAOImageDS9*. This is done in order to establish the uncertainty introduced from preferring to use the tools within *Python's astropy* module, rather than performing the measurements manually in the alternative option of *SAOImageDS9*.

If the effect on measurements is determined to be a consistent overestimation or underestimation of the measured value, a scaling factor will be used to upscale or downscale measurements accordingly. However, if the effect is random, an uncertainty will be calculated and attached instead.

To determine this effect, the raw, 450μm and 850μm integrated fluxes of all G182 sources are measured using both routines. Then, the relative difference between each pair of flux measurements is calculated and plotted against the mean of the two measurements. This is done individually for each band, and the results are plotted in figure 4.1. The mean relative difference between measurements and its uncertainty are calculated and presented in each band using a red, dotted line.

An inspection of the two figures reveals that the mean relative difference of the 450μm measurements is $\mathbf{-1.12 \pm 0.68}$ % and for the 850μm measurements is $\mathbf{-2.41 \pm 0.96}$ %. Evidently, the effect is not as great as initially thought to be, making this one of the lower systematic uncertainty contributors.

A closer look at the two figures indicates that the 450μm and 850μm relative differences are spread randomly. Hence, rather than a scaling factor, an uncertainty of $\mathbf{1.12}$% and $\mathbf{2.41}$% is attached to each 450μm and 850μm integrated flux measurement respectively for choosing the automatic against the manual measurement approach.

Speculation on the cause of these relative differences involves mainly the manner in which pixels near the boundary of an aperture are treated in the two methods. In *Python*, a pixel is included in the count only if it has its center coordinates lie within the aperture boundary. In *SAOImageDS9* however, a pixel is included only if a certain fraction of a pixel's area lies within the aperture boundary. This leads to some boundary pixels being included in *Python* while simultaneously excluded in *SAOImageDS9* and vise versa.

The relative differences appear to be greater in the 850μm band due to the fact that

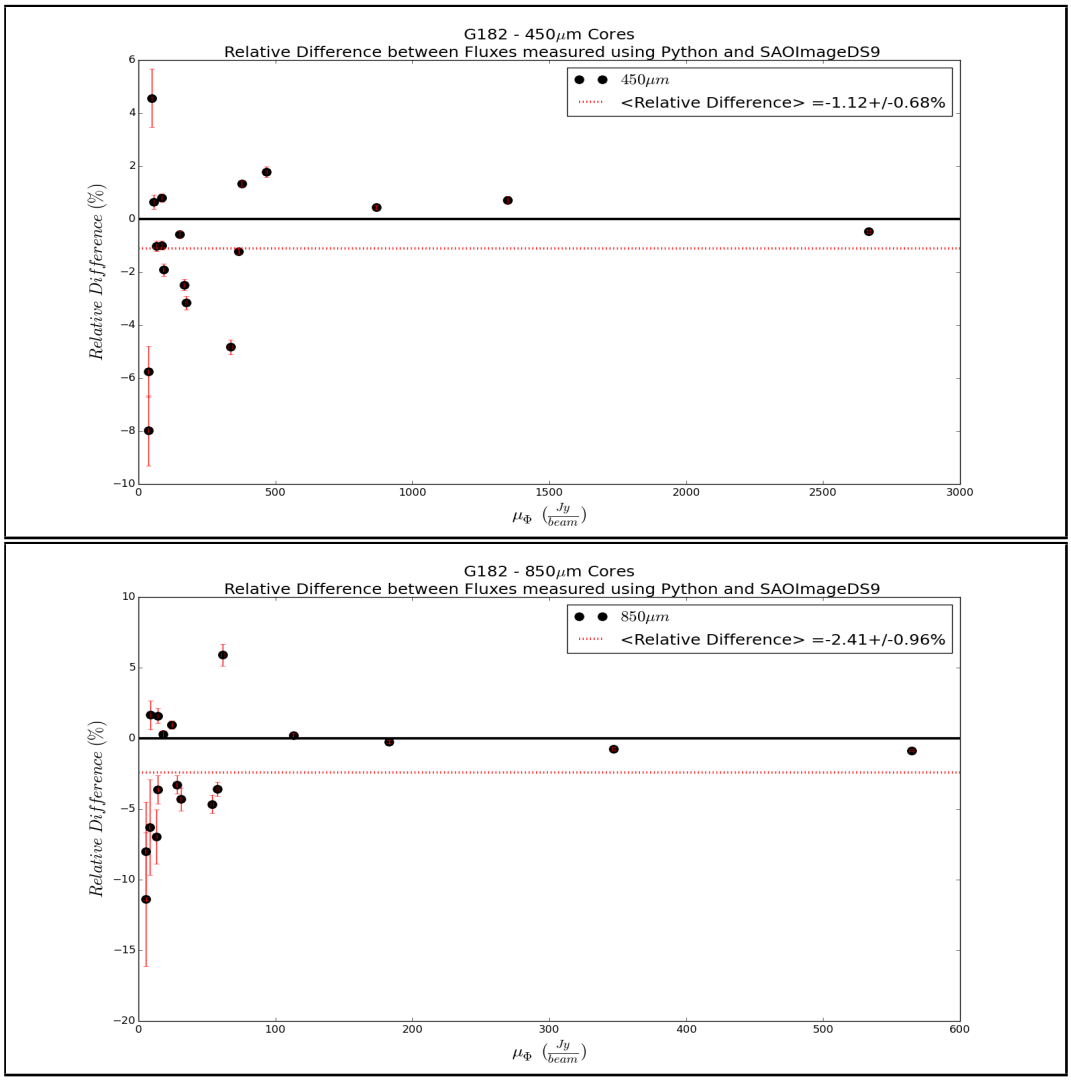

Figure 4.1: Plot of the 450μm (Top) and 850μm (Bottom) relative difference between *Python* and *SAOImageDS9* raw integrated flux measurements against the mean integrated flux. The objects being compared involve the cores, clouds and overall clump composites of image G182.

each aperture contains a smaller total number of pixels in this band. This means that if the two methods disagree on the inclusion of a particular pixel, the mitigated effect on the flux is much greater in the 850μm measurement.

Finally, there exists a minor trend, where the dimmer the source, the greater the measurement relative difference between the two methods. This is expected, as the effect on the flux from any inconsistency in the pixels considered between the two methods is magnified when the aperture has a small integrated flux to begin with.

Aperture Placement

One of the most obvious properties of an aperture controlled by the experimenter is its actual placement on the image. While other works attempt to do this by centering the aperture about the brightest pixel in the source, or using a weighed brightness, in this thesis, the intention is to place the aperture as close to the true geometrical center of the source as possible. However, the actual placement may be slightly off from this intended location.

To determine the uncertainty introduced from the placement's ambiguity, the aperture's center coordinates are varied in a certain manner. Specifically, the aperture is moved in a single-pixel, square pattern around its original placement. This manipulation is displayed in figure 4.2.

The raw integrated flux is then calculated for each of these new placement positions. The standard deviation of these measurements leads to an approximation of the uncertainty introduced from the aperture's original placement.

Aperture Size

Another property of apertures that is controlled by the experimenter is their size. Choosing a proper aperture size translates into a balancing act between incorporating as many of the pixels belonging to the source as possible while minimizing the number of background pixels incorporated in the process. An aperture too small will leave some source pixels unaccounted for, while an aperture too large will encompass more background pixels or even pixels belonging to neighboring sources. It is this compromise that introduces additional systematic uncertainty.

To determine the introduced uncertainty, the size of the aperture used for measuring the photometry of a source is varied. Due to the fact that circular apertures are used for SCUBA-2 sources, the radius of these apertures is simply upscaled and downscaled. Specifically, the radius is increased/decreased in single pixel increments, up to a maximum

of 1 pixel larger/smaller than the original aperture used. This manipulation can also be seen in figure 4.2.

The integrated flux is then calculated for each of these new aperture sizes. In a similar fashion to the previous section, the standard deviation of these measurements leads to a good estimate of the uncertainty introduced from the aperture sizing by the experimenter.

Aperture Type

The last aperture property that is controlled by the experimenter is its actual shape. The best fitting shape will always be a multi-segment polygon. A very close second will be an elliptical shape, with circles being a reliable third choice. In this thesis, circular apertures are preferred due to their ability to be easily manipulated in scripted routines. Using circular apertures however comes with the caveat of making slightly less precise measurements. This loss of precision is a systematic uncertainty contributor itself. It is therefore necessary to establish what is the extent of this introduced uncertainty to SCUBA-2 photometric measurements.

In order to do this, measurements of a specific source sample will be made using both circular apertures and more sophisticated elliptical apertures of identical size. If the effect on measurements is determined to be a consistent overestimation or underestimation of the measured value, a scaling factor will be used to upscale or downscale all future measurements accordingly. However, if the effect is random, an uncertainty will be calculated and attached instead.

The measurements are made using all sources of image G115. The 450μm and 850μm integrated flux of these sources is measured using both aperture types. The circle-to-elliptical aperture relative flux difference is then calculated and plotted against the mean of the two aperture measurements. This is performed for both bands and the result is displayed in figure 4.3. The mean circle-to-elliptical aperture relative flux difference and its uncertainty are calculated and displayed for each band using a red dotted line.

A first glance at figure 4.3 reveals that the mean circle-to-elliptical aperture relative flux difference in the 450μm band is $\mathbf{-5.27 \pm 1.18}\%$ while in the 850μm band it is $\mathbf{-5.09 \pm 1.04}\%$. Evidently, the effect is not large, but certainly larger than the effect introduced from the choice of measuring routine.

A closer inspection of this figure reveals that the 450μm and 850μm relative differences are not spread randomly, as the circular apertures consistently underestimate the integrated flux with very few exceptions. Thus, the effect introduced from choosing a circular aperture shape will be treated using a scale factor. From this point onward, an upscaling of **5.27** % and **5.09** % is performed on every 450μm and 850μm integrated flux measurement, while carrying forward an uncertainty of **1.18**% and **1.04**% for the 450μm and 850μm upscaling respectively.

Speculation on what causes the consistent underestimation of integrated flux involves primarily the kinds of pixels incorporated in each type of aperture. Since SCUBA-2 sources have slightly elongated shapes, elliptical apertures are a better fit to their pixels. In addition, being the better fit, elliptical apertures are expected to encompass more of the "warm" boundary pixels of a source, without incorporating many "cold" background pixels, contrary to their circular counterparts.

The relative differences appear to be of similar scale in the 450μm and 850μm bands. Finally, a small trend is visible where dimmer sources tend to have greater relative differences. This is expected, as the relative effect on the integrated flux from a difference between incorporated pixels is magnified when the source is dim to begin with, just like in the case of the two measuring routines earlier.

Reduction Parameters

There exist several tweakable parameters in the SCUBA-2 data reduction pipeline, of which some have more subtle, while others have more pronounced effects on the quantitative nature of a finalized image. Although the detailed photometric effects are of complex nature (i.e the specific effect on the negative bowl depth, the noise etc.), the overall photometric effect in SCUBA-2 measurements is very simple: Tweaking any parameter will lead to either an increase or decrease in the final integrated flux measurement of a SCUBA-2 source.

The range of values that can be used for these parameters is finite. This range can become constrained based on knowledge regarding the nature of SCUBA-2 sources at hand. For example, a dim, diffuse source is best treated by a different parameter range than a bright, compact one. It is common practice to initially reduce a SCUBA-2 image with default parameter values, then inspect the sources in the final image and re-run the reduction process after appropriately tweaking the parameters.

However, inspection of sources provides only a rough guideline to the appropriate range for a particular parameter. It comes down to the experimenter to choose the most representative value out of this appropriate range and use it in the final run of the data reduction pipeline. However, the experimenter needs to be aware of the trade-offs they are making in their setup choice. For example, some setups may better bring forward the true flux of a source at the cost of resolution, and vice versa. This ambiguity in the appropriate range of values clearly introduces systematic uncertainty to SCUBA-2 measurements.

Now, since every single tweakable parameter either upscales or downscales both peak and integrated flux measurements, it is most meaningful to investigate the effect from the most dominant parameter only. The uncertainty introduced from the single, most influential parameter will be used as an upper limit to the uncertainty introduced from the ambiguity surrounding the setting of all tweakable parameters in the SCUBA-2 data reduction pipeline.

There exist two such parameters that are far more influential than any other parameter in the SCUBA-2 data reduction pipeline. The first is a parameter controlling the signal-to-noise ratio of the mask provided to the reduction pipeline, while the second controls the sensitivity of the applied Fourier filter. The main purpose of these two parameters is to minimize the negative bowl effect around sources. Both of these parameters and their effects will be investigated in the following subsections.

Masking Signal-to-Noise Ratio

In this subsection I will be discussing the effects introduced from manipulating the signal-to-noise ratio (SNR) cutoff of the masking enforced to the data reduction pipeline, as well as the uncertainty introduced from the freedom of choice in setting this parameter. A mask is used in order to exclude pixels that likely belong to a source from the estimation of the noise (NOI) model in the data reduction pipeline. This model is used in order to weigh the bolometers in the final map estimate. It is therefore directly linked to the flux value that is attached to each pixel of the final image.

The masking level SNR cutoff is set by default to a value of 5. However, the construction of the ideal mask requires knowledge of source locations and the level of noise across the entire image. Both of these pieces of information are not available before data reduction takes place. Thus, all first runs are performed without a mask being supplied to the data reduction pipeline. However, such unmasked runs introduce the risk of missing out dim

sources due to the fact that the pipeline will by default attempt to blend them with the noisy background, a risk that becomes increasingly elevated with overall image noise.

In addition, having a properly tweaked mask is important for making flux measurements of high precision. Increasing the masking level SNR cutoff leads to the association of a smaller number of pixels to a particular source and vice versa. Ideally, one wants to account for every pixel that belongs to a particular source, however, this presents a practical impossibility. Fortunately, the pixels far from the center of a source are typically much "colder" and contribute much less to flux measurements than pixels closer to the center. Therefore, the boundary of a source doesn't need to be perfectly masked down to the pixel level for a reliable flux measurement to be made.

The default masking level cutoff SNR setting is an excellent fit to the SCUBA-2 image sample encountered in this thesis. However, tweaking this SNR about this default value leads to slight, but obvious differences in the final flux measurements of each source, while qualitatively the mask continues to be a good fit to those same sources. It is the magnitude of these differences that contributes systematic uncertainty.

In order to determine the contribution of this uncertainty, the 450μm and 850μm raw data of object G115 are reduced multiple times with a masking level SNR cutoff being supplied each time while all other parameters remain constant at their default values. The prescribed SNR values are varied symmetrically about the default value of 5, starting from an SNR of 1 and ending at an SNR of 10 in increments of 1. The unmasked case is also considered, and can be conceptually thought of as setting the masking SNR to infinity. The photometric properties of all G115 sources are then measured for all masking instances provided.

Integrated flux is one of these properties. Evidently, a lower masking level SNR cutoff will lead to slightly higher flux measurements for all cores, clouds and overall clump composites. The only exception is the unmasked case, which closely traces the result from using a mask with the default SNR cutoff of 5. This is no accident, as the pipeline will construct and provide its own mask after 5 iterations of the reduction algorithm using the default SNR cutoff of 5. To display this effect, the integrated flux measurements of all G115 cores are plotted against the choice of masking SNR in figure 4.5.

Changing the masking level SNR cutoff has a very noticeable effect on the depth of the negative bowl around clumps. Generally, a larger SNR will yield deeper negative bowls in both bands. This is no coincidence, as a higher SNR cutoff will mask less of the pixels

belonging to a source, leading to the value of the background being inflated, which in turn when subtracted from the data will yield even more negative "no-signal" pixels. There appear to be two exceptions to this trend. The first is the regime of really low SNRs, where changing the SNR cutoff has a quite variable effect on the negative bowl. The unmasked case is the other regime, where the effect on the negative bowl will be very similar to that of using the default SNR cutoff of 5 for the reason discussed above. To display these effects, the negative bowl estimates for all G115 clumps are plotted against the choice of masking SNR cutoff in figure 4.6.

To conclude, the uncertainty contribution from tweaking the masking SNR cutoff is estimated for each source by comparing the mean flux from all masking iterations against the uncertainty of this mean. This error-to-mean ratio is plotted against the mean itself for each G115 core. This is done for both bands and the result is displayed in figure 4.7. Inspection of this plot reveals that dim cores are affected more strongly from changes in the masking SNR cutoff than bright ones. Finally, the introduced uncertainty is taken to be the average error-to-mean ratio in each band. This ratio is $\mathbf{3.5 \pm 0.4}\%$ and $\mathbf{5.0 \pm 0.6}\%$ for each 450μm and 850μm band respectively.

Filtering Sensitivity

In this subsection I will be discussing the effects introduced from adjusting the sensitivity of the Fourier filter through the parameter *flt.filt_edge_largescale*, which is a convenient alternative of *flt.filt_edgehigh*. Both parameters control the sensitivity of the Fourier filter by specifying the largest physical scale to preserve when reducing data. The former parameter does this by allowing the direct selection of the size in arcseconds, while the latter through selection of the frequency cutoff above which all sampled frequencies will not be included in the construction of the Fourier (FLT) model.

Due to its strong association to the reduction pipeline's FLT model, the *flt.filt_edge_largescale* parameter will be simply referred to as the "FLT" parameter from here onwards. This parameter can be specified in the *dimmconfig_bright_extended.lis* text file, or in the *reduce_scuba2-fcfbeam.sh* script under *filter450* and *filter850*. The former specification however will override the latter.

Fine-tuning the FLT parameter is important for bringing forward certain features of a source. Increasing the FLT parameter leads to progressively less of the high frequencies being ignored from the pipeline, allowing more of the faint structure to be seen and con-

sequently providing a boost to background flux values at the cost of resolving power.

The default value for the FLT parameter is 480 arcseconds. Fortunately, this value accommodates well the sources encountered in this thesis. However, in a similar fashion to the masking SNR, variation of this parameter about the default value leads to final flux measurements that are quantitatively different. Once again, it is the magnitude of these differences that contributes systematic uncertainty.

In order to determine the contribution of this uncertainty, the 450μm and 850μm raw data of image G115 are reduced multiple times with a different FLT value being supplied each time while maintaining every other parameter constant at its default value. The prescribed FLT values range from 200 to 1200 in increments of 100. The photometric properties of all G115 sources are then measured for all FLT parameter values used.

Considering the integrated flux first, it is evident that the larger the FLT value provided, the larger the integrated flux measured for all cores, clouds and overall clump composites. To display this, a plot of the integrated flux measurements for all G115 cores against the choice of FLT value is presented in figure 4.8.

The choice of FLT value also affects the depth of negative bowls around clumps. From experiments using G115 sources, the effect appears to be significant but fairly unpredictable. This is largely because of the unknown amount of flux introduced or removed in the vicinity of a source as the FLT value is varied. In the G115 clump sample considered, the 450μm negative bowls became deeper with increasing FLT value, while the opposite happened for the equivalent 850μm cases. To display this, the negative bowl estimates are plotted against the choice of FLT value in figure 4.9.

Finally, the uncertainty contribution from tweaking the value of the FLT parameter is estimated for each source in an identical manner to the masking SNR case, namely, by comparing the mean flux from measurements using all FLT values against the uncertainty of this mean. The corresponding error-to-mean ratio is then plotted against the mean for each source. This is done for both bands individually and the results are presented in figure 4.10. Inspection of the plots reveals that once again dimmer sources are more sensitive to changes in the FLT parameter than bright ones. The uncertainty contribution to each band is taken to be the average error-to-mean ratio in that band. This ratio is $\mathbf{6.1 \pm 0.8}\%$ and $\mathbf{8.8 \pm 1.1}\%$ for the 450μm and 850μm band respectively.

Evidently, manipulation of the FLT parameter value is found to have a stronger over-

all effect on flux measurements. Therefore, from this point onward, an uncertainty of **6.1**% and **8.8**% is attached to every 450μm and 850μm integrated flux measurement respectively due to the flexibility of tweakable parameters in the SCUBA-2 data reduction pipeline.

FCF Uncertainty

In this subsection I will be discussing the uncertainty arising in the empirical determination of the SCUBA-2 Flux Conversion Factors (FCFs). It is important to remember that the values of the FCFs are continuously variable and depend on the performance of the telescope at any given time. However, telescope performance changes slowly, and thus a single set of FCF values is sufficient to treat data that is taken $\approx$ 1-2 years apart.

Recall that FCFs are calculated by comparing the received signal against the standard expectation for sources of well-known flux. I present a summary regarding the uncertainties involved in these comparisons. All information discussed is contained within the SCUBA-2 calibration article [25], where a more in-depth discussion of the uncertainties concerning the determination of the FCFs can be found.

Beginning with the systematics first, uncertainty is introduced through setting the aperture size to be 60" when making calibration measurements, a value that balances well the noise gain against the flux measurement precision. When using this aperture size, the integrated flux uncertainty in the 450μm and 850μm calibration measurements is optimized to a level of 4% and 8% for each band respectively. A second systematic uncertainty arises from the gradual deterioration of the focus during the timespan of measurements as these can potentially be taken several days apart.

Random errors are mainly introduced through unwanted changes in control variables, of which the most influential are temperature variations in the telescope optics chamber. Another random uncertainty arises from unfavorable atmospheric conditions as well as changes to these conditions during the time span of the calibration tests. Finally, calibration tests are sample-limited, as a larger number of calibrators would yield more reliable FCF averages.

Now, the data used for constructing the images considered in this thesis was obtained between 2012 and 2015. The FCF values from the 2012-2013 calibration tests appear unchanged over the overall time span that these tests took place, indicating that the performance of the SCUBA-2 bolometer array did not change over this timespan. Therefore,

it is deemed sufficient to use the 2012-2013 FCF set for the treatment of all SCUBA-2 images in this thesis.

The distribution of the determined FCF values from all 2012-2013 calibration tests is presented in a histogram fashion within figure 4.11. The uncertainty for each FCF parameter is established by considering the 1σ deviation from the mean value of its respective distribution. Examination of the two FCF_{arcsec} value distributions in this figure leads to an uncertainty of $\mathbf{10.62}\%$ and $\mathbf{3.42}\%$ for the 450μm and 850μm FCF_{arcsec} factors respectively. Examination of the two FCF_{peak} value distributions on the other hand leads to an uncertainty of $\mathbf{13.65}\%$ and $\mathbf{4.84}\%$ for the 450μm and 850μm FCF_{peak} factors respectively.

4.1.2 Random, Non-Spatially Structured Noise

In this subsection, I elaborate on the major random uncertainty contributors to SCUBA-2 photometric measurements that cannot be treated consistently using some predetermined recipe or method. The extent to which each of these contributors affects a SCUBA-2 image is unique to that image.

Background Artifacts

Each SCUBA-2 image appears to have an inherent "patchy" nature, with embedded lows and highs. The patches with a flux lower than the ambient background are referred to as *underbright* while those with a higher flux than the ambient background as *overbright*. The underbright patches are usually artifacts from the negative bowl of a nearby source. The overbright patches can either be real, low-SNR, large-scale features or artifacts from the data reduction process. It is particularly difficult to distinguish which overbright features are real and which are artifacts from the spatial filtering scale used during data reduction.

A solution comes by directly comparing the SCUBA-2 image to an equivalent image from a different submillimeter survey. If an overbright SCUBA-2 feature can be found in the equivalent image from the neighboring band, it can be deemed real with high confidence. However overlapping images in neighboring submillimeter bands are not typically available, and when they are, if the pixel scale used is different, overlapping will not be perfect and might lead to misinterpretations.

Comparisons such as the one presented in figure 4.12 have been performed for few SCUBA-2 images for which SPIRE 250μm equivalents were available. Some, like the case of Sh-2

104, revealed that the majority of the overbright features are indeed shared. However, a larger sample is necessary for a concrete take on the subject. For the purpose of this thesis, due to the inconclusive evidence at hand, all underbright and overbright regions are considered as random noise contributors to SCUBA-2 photometry.

In order to estimate the contribution of this uncertainty, several overbright and underbright regions are selected for photometric analysis on each SCUBA-2 image. A number of apertures of identical size are placed somewhere inside these regions as depicted in figure 4.13. The mean flux per pixel and associated standard deviation for each of these apertures is then determined. The contributed uncertainty is taken to be the standard deviation of the aforementioned standard deviations.

It is important to note that the previous method incorporates not only the uncertainty from the potential background artifacts, but in fact, the cumulative contribution from every single non-spatially structured noise contributor as their noise is inseparable.

Atmospheric Emission

The most dominant contributor to SCUBA-2 photometric uncertainty is emission from the Earth's atmosphere. This is because Earth's atmosphere is very bright at the two SCUBA-2 wavelengths. Atmospheric absorption also adds to this problem, but will be discussed separately in its own subsection.

Atmospheric emission is strongly dependent on water vapor content, as well as the presence of other molecular compounds that can emit in the submillimeter regime to a lesser extent. The contribution from water alone is most dominant. In fact, when the term "weather" is used in ground-based astronomy, it more often than not refers solely to the level of water vapor present in the atmosphere. If this is high, both atmospheric emission and absorption activity will be high as a consequence. To keep track of water vapor levels, the opacity of the atmosphere at 225 GHz (τ_{225}) is continuously monitored.

The 450μm band is much more susceptible to water vapor content. As a rough guide, 450μm atmospheric transmission at $\tau_{225} = 0.05$ is already low at $\approx 28\%$, while 850μm atmospheric transmission does not drop to this level even when $\tau_{225} = 0.2$, where it is still a relatively reliable $\approx 45\%$. This is the sole reason that 450μm images are always more noisy than their 850μm counterparts. Due to the enhanced sensitivity of the 450μm band, observations at the JCMT do not take place when $\tau_{225} > 0.2$.

In figure 4.14, the effect of τ_{225} on noise levels is displayed separately for each observing band. The measured noise naturally increases in both bands with increasing τ_{225}. However, the noise increases much more dramatically in the 450μm band as expected. The color coding shows how the integration time plays a secondary, yet consistent role in the overall noise of an image. The uncertainty contribution from atmospheric emission to photometric measurements is already incorporated in the cumulative measurement presented in section 4.1.2.

Signal Extinction

SCUBA-2 incoming flux can experience two kinds of extinction. One is galactic extinction and is caused from absorption and/or scattering of the incoming SCUBA-2 radiation from objects that intersect the line-of-sight between the SCUBA-2 camera and its target source. The other is atmospheric extinction from the presence of water vapor in Earth's atmosphere which acts to increase its respective opacity in the two SCUBA-2 bands.

It is assumed that no significant extinction occurs through interstellar space, as the diffuse dust along the line of sight will not cause any significant extinction in the submillimeter regime. However, once the signal from a SCUBA-2 source reaches the Earth's atmosphere, it may encounter vastly variable opacities based on the water vapor content at the time of observation.

In the previous section I mentioned that the atmosphere acts both as an emitter, but also as an absorber of incoming SCUBA-2 radiation. Similarly to the emission case, the 450μm band suffers much more than its 850μm counterpart from atmospheric opacity due the presence of water vapor.

However, this type of extinction can be corrected in both bands. This is done by sampling each piece of sky from a variety of different directions during an observation and keeping track of accurate water vapor readings throughout the scanning process. This information is used during data reduction in order to produce what is known as an extinction model (EXT). In essence this is a scaling factor that acts to remove the extinction caused by Earth's atmosphere.

Thus, due to the fact that atmospheric extinction is actively corrected in the SCUBA-2 data reduction pipeline and no significant extinction occurs from extraterrestrial factors,

it is assumed that this uncertainty contributor adds little to no random uncertainty in SCUBA-2 photometric measurements.

4.1.3 Random, Spatially Structured Noise

In this subsection, I elaborate on the major random uncertainty contributors to SCUBA-2 photometric measurements which have a predictable contribution that can be accounted in a consistent manner through the use of models and recipes.

Integration Time

Like all others, SCUBA-2 images inherent a spatially dependent type of noise from the amount of time the telescope spends at particular patches of sky. More specifically, the smaller the amount of time the telescope spends at a specific portion of an image, the greater the flux uncertainty in the pixels of that portion.

Integration times are a derivative of the telescope scanning pattern itself. Since all SCUBA-2 images are obtained through use of a *PONG* or *DAISY* scan pattern, the spatial profile of noise from integration time is well known. In fact, the data regarding the noise from integration time is stored in a separate array within each SCUBA-2 image's *.sdf* structure, called *STD_ARRAY*. I display the typical integration time noise profiles for a *PONG* and *DAISY* scan pattern in figure 4.15.

To determine the uncertainty introduced from this type of noise, it suffices to extract the information stored in the aforementioned *STD_ARRAY*. This array associates a specific noise value to each pixel based solely on the time that the telescope beam spent sampling it. When measuring the total flux of a source, the noise values of all pixels associated with that source are added in quadrature for a total uncertainty due to integration time to be established.

The impact of integration time noise on SCUBA-2 photometry varies. Inspection of figure 4.15 clearly displays that the effect is different between the two scan patterns. In a *PONG* scan, sources within some radius from the center are well sampled and don't suffer much from integration time noise. However, the telescope spends very little time at the edges, where the noise from integration time rises drastically to become the most dominant of all uncertainty contributors at that region. At the same time, in a *DAISY* scan, the noise

from integration time is small near the center, but becomes increasingly larger as one travels away from the center, however in a much smoother fashion than a *PONG* scan.

Finally, recall from figure 4.14 that when multiple images have been obtained under similar τ_{225} values, the one with less integration time will have a noticeably higher noise estimate. A high τ_{225} combined with a low integration time are enough to deem an image completely unreliable for measurements.

CO Background Uncertainty

In this subsection I discuss the uncertainty in the estimate of the CO (3-2) emission that pollutes SCUBA-2 850μm flux measurements. As previously discussed in section 2.3.2, most SCUBA-2 images do not possess CO (3-2) emission maps, and even for those that do, coverage may be incomplete.

Another prominent issue is that the available CO maps have an inferior resolution to those of either SCUBA-2 band. This further motivates the treatment of the CO emission as a background, rather as an effect that can be removed on a pixel-to-pixel basis.

The extent of the CO contamination is a topic of current research. It is so far known that all SCUBA-2 850μm images suffer from at least some CO (3-2) emission, the intensity of which varies from object to object. The preliminary estimate presented in section 2.3.2 for the mean CO flux per 850μm SCUBA-2 pixel is based on a handful of images that had CO maps of complete or partial coverage.

For those images, the CO(3-2) emission from areas overlapping with the position of SCUBA-2 sources was measured. Based on the small number of such sources that have been investigated so far, the standard error associated with the CO(3-2) mean flux per pixel value is on the order of **2.0**%.

Negative Bowl Background

The estimation of the Negative Bowl Background (NBB) suffers from a couple of random errors as well as a systematic error which cannot be fully unraveled. The two random errors in the estimation of the NBB pertain to the number of apertures used in each aperture set, where a maximum of 8 apertures can be used, and also the radial size of these apertures which includes options of 4, 8, 12, 16 and 20 pixels.

The systematic error arises from the fact that the method used estimates the NBB adjacent to a particular source and not inside it. There is no way of isolating the measurement inside the boundary of a source due to the fact that source pixels are coupled to those of the NBB in an irreversible way. Consequently, an estimate regarding the contribution from this systematic error cannot be made.

On the other hand, the uncertainty contribution from the aperture size options is much smaller than the one from the limited number of apertures employed in the estimate of the NBB. For this reason, unnecessary complexity is avoided by only considering the uncertainty introduced from the number of apertures used in the best estimate of the negative bowl background. Essentially, this is nothing fancier than a calculation of the standard error in the determined mean NBB flux per pixel, and is performed individually for each SCUBA-2 clump.

4.1.4 Summary

In this section I summarize the overall effect of all aforementioned uncertainty contributors. A neat summary is presented in table 4.1 where each contributor is presented along with an estimate of its contribution or an explanation of how that is obtained if it is not a generalized value.

Some uncertainty contributors, such as the choice of measurement routine, the uncertainty of the CO background mean flux per pixel and the uncertainty surrounding the determination of the FCF values do not change in significance from source to source. However, the contribution from the rest of the discussed uncertainty contributors can change significantly based on the image and individual source at hand. For example,

Aperture properties such as type, position and size are much more important for small and dim sources. In small sources, the number of included pixels is also small. Changing the aperture properties can lead to changing some of the included pixels. If a pixel with drastically different flux is introduced, it can significantly skew the original flux measurement.

Masking SNR becomes very important in two cases. The first is when dealing with sources that are not ordinary. These include either extremely bright or extremely dim sources. The experimenter needs to manually identify these and adjust the masking SNR until what is

Table 4.1: Summarized results to be used for the construction of the photometric uncertainty model

Error Description	**Contribution**
Systematic	
Measuring Routine	$\epsilon_{450} = 1.12 \times 10^{-2} F_{450}$, $\epsilon_{850} = 2.8 \times 10^{-3} F_{850}$
Parameter Freedom	$\epsilon_{450} = 6.1 \times 10^{-2} F_{450}$, $\epsilon_{850} = 8.8 \times 10^{-2} F_{850}$
Aperture Type	$\epsilon_{450} = 1.18 \times 10^{-2} F_{450}$, $\epsilon_{850} = 1.04 \times 10^{-2} F_{850}$
Aperture Position/Size	ϵ = source-by-source analysis
Random	
Integration Time	ϵ = pixel-by-pixel analysis (STD array)
Background Artifacts	ϵ = image-by-image analysis
Atmospheric Emission	ϵ = image-by-image analysis
Extinction	$\epsilon = 0$
Negative Bowl Estimate	ϵ = bowl-set-by-bowl-set analysis
CO Background Estimate	$\epsilon_{850} = 0.02 F_{850}$
FCF_{arc}	$\epsilon_{450} = 0.106 FCF_{arc}^{450}$, $\epsilon_{850} = 0.034 FCF_{arc}^{850}$
FCF_{peak}	$\epsilon_{450} = 0.136 FCF_{peak}^{450}$, $\epsilon_{850} = 0.048 FCF_{peak}^{850}$

thought of constituting real structure is completely masked. The second and more common case is when the noise level of a image is relatively high, as is the case when weather conditions are bad or pixel integration times are low. The high noise level means the masking SNR needs to be carefully tweaked downwards in order to not miss any dim sources from the final image.

The filtering sensitivity becomes important in the case where sources are either very diffuse or very compact. In the first case, *flt.filt_edge_largescale* needs to be increased and in the second decreased accordingly in order to properly accommodate the emission profile of these two extremes.

The uncertainty in the negative bowl background estimate rises when a clump is located among several other clumps or completely surrounded by a warm background. This can lead several of the apertures involved in the calculation of the mean flux per pixel to be dropped off as they fail the cutoff criterion discussed in chapter 2.3.1.

Extinction along the line of sight can become dominant when atmospheric water vapor levels are high. In addition, if an observed source is located deep down the length of a galactic arm, or, opposite of the galactic center, additional galactic extinction may take place.

Finally, atmospheric emission is by far the most dominant SCUBA-2 uncertainty contributor. It becomes increasingly important as water vapor levels rise and can single-handedly destroy the reliability of an image.

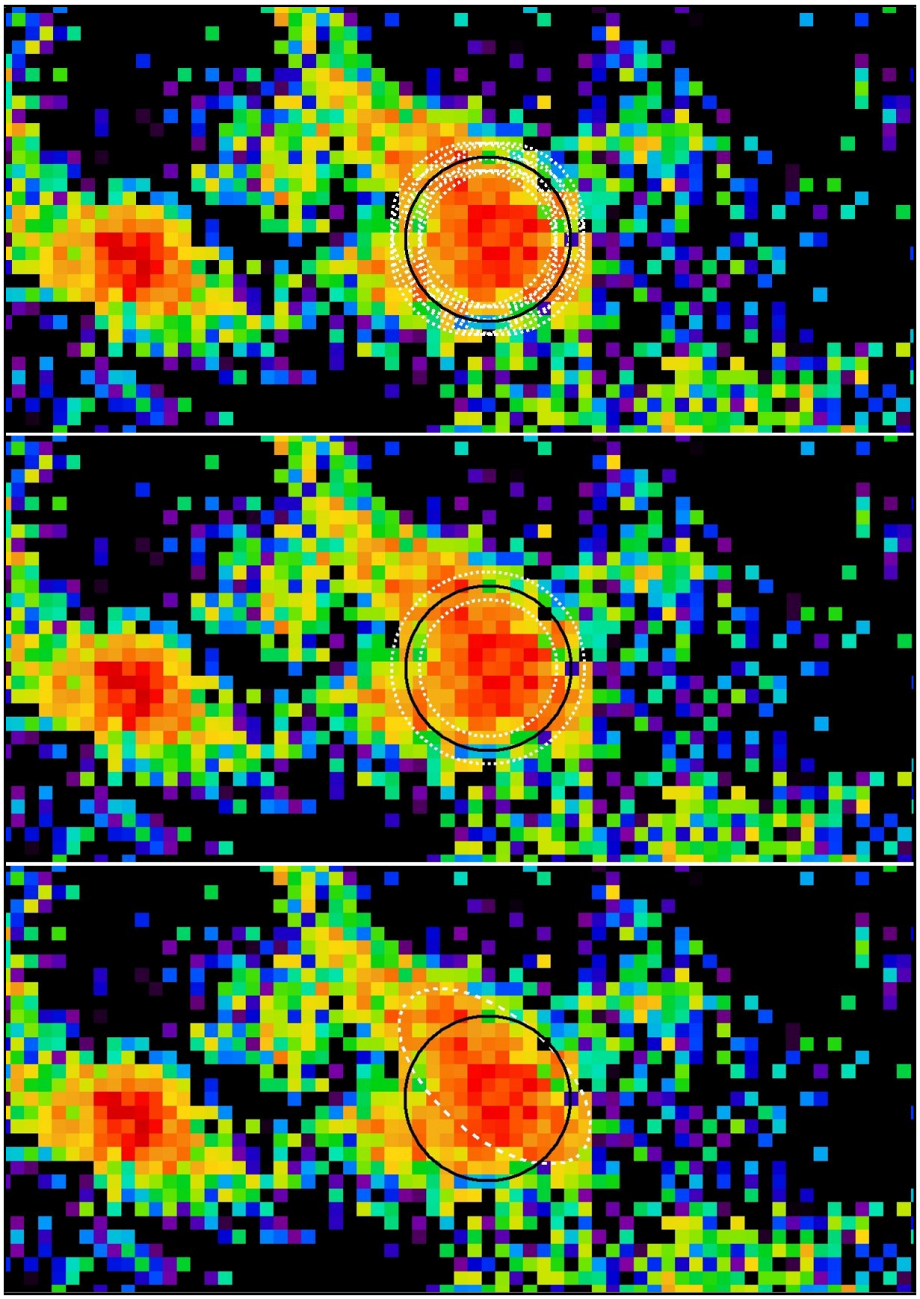

Figure 4.2: The original aperture (Black) for core G115-8-1 and variations (White) performed for the determination of uncertainty. The center of the original aperture is varied in a single-pixel square pattern (Top), then the size of the original aperture is varied by single-pixel increments up to 1 pixel larger/smaller (Middle) and finally an elliptical aperture is best-fitted (Bottom).

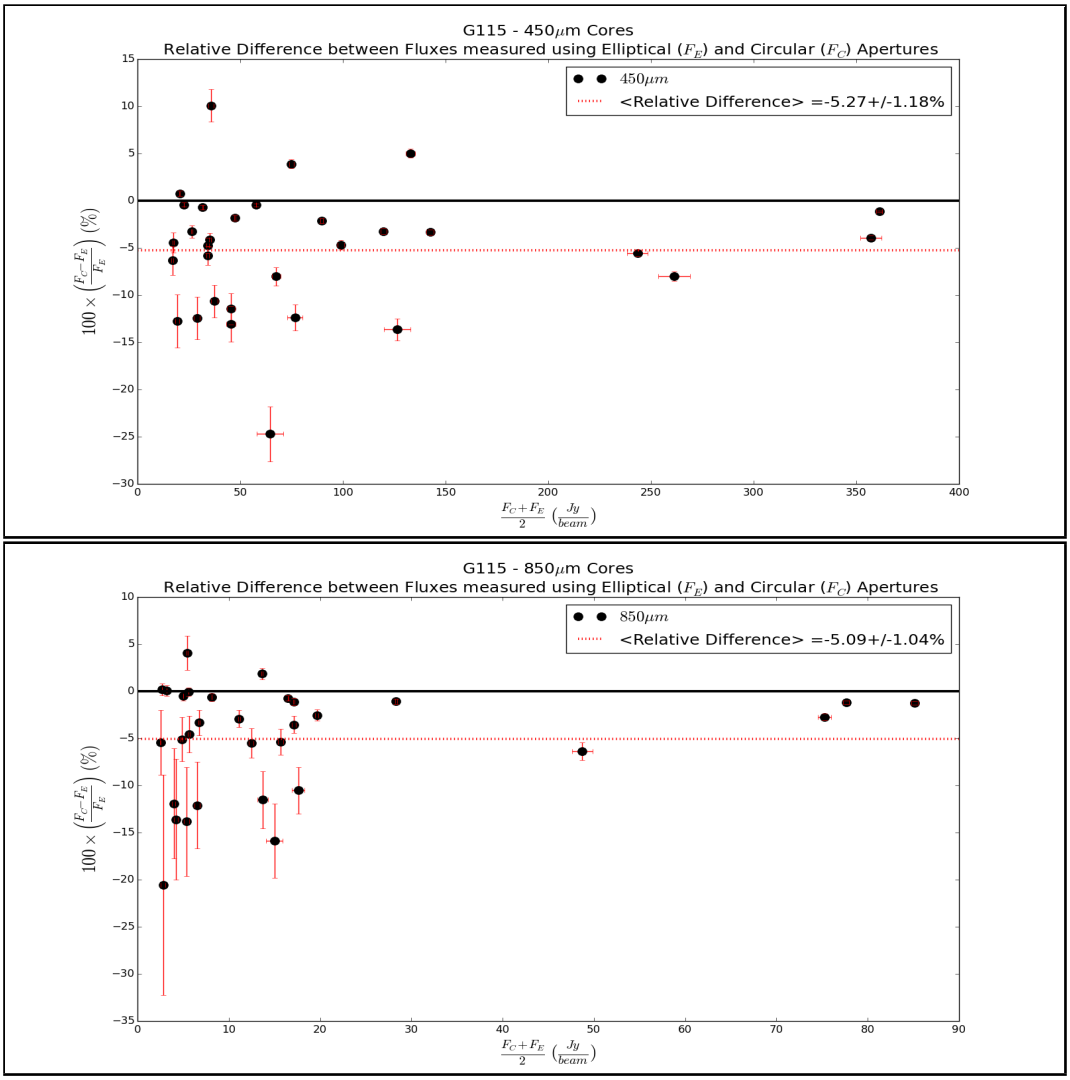

Figure 4.3: Plot of the 450μm (Top) and 850μm (Bottom) relative difference between raw, integrated flux measurements made using circular and elliptical apertures, against the mean integrated flux. The objects being compared involve the cores, clouds and overall clump composites of image G115.

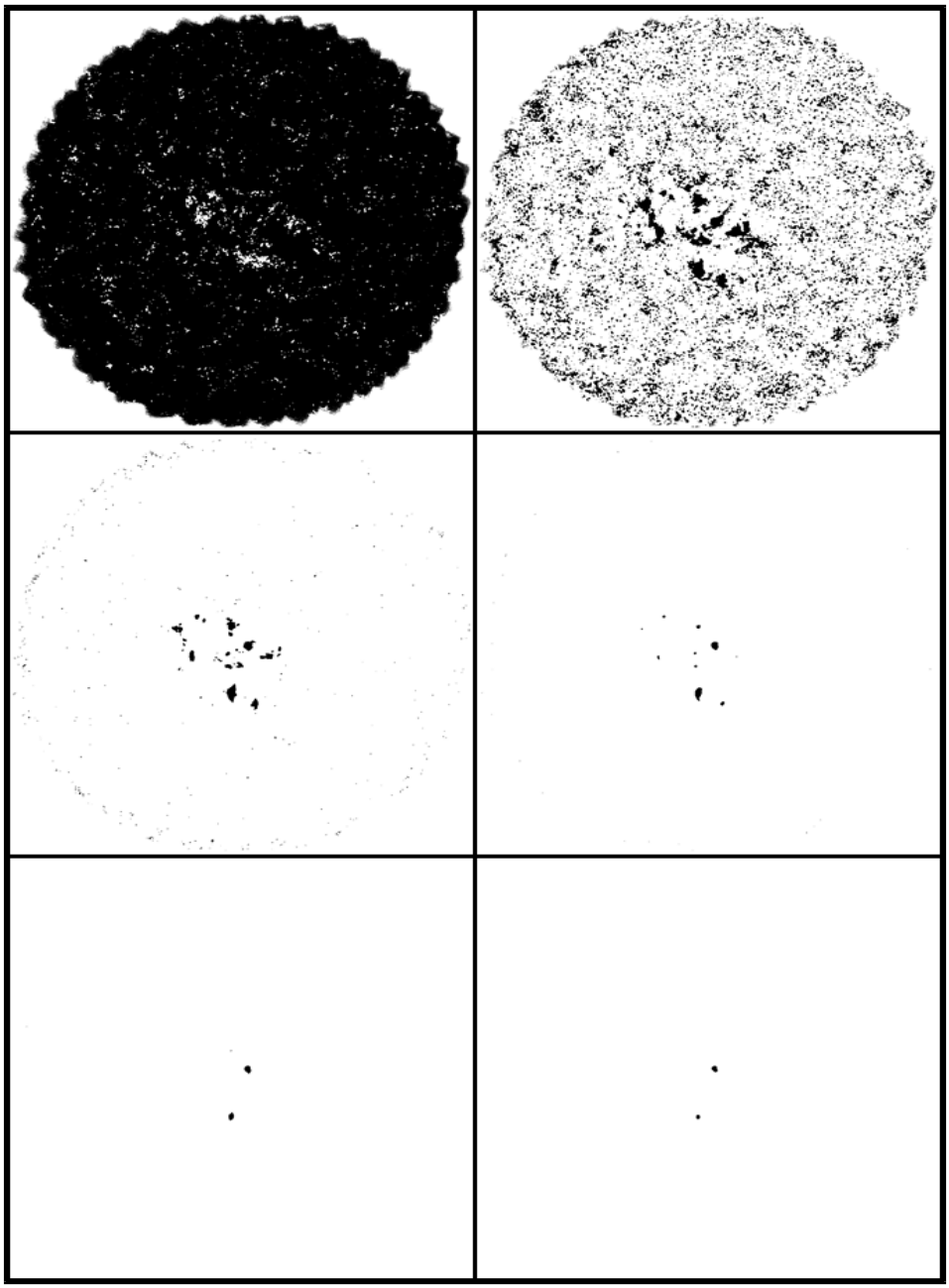

Figure 4.4: A compilation of mask instances for the 450μm image of image G115. The presented cases have an SNR of 1 (Top-Left), 2 (Top-Right), 3 (Middle-Left), 5 (Middle-Right), 7 (Bottom-Left) and 10 (Bottom-Right). The areas colored black are being masked and excluded from the construction of the noise model in the data reduction pipeline.

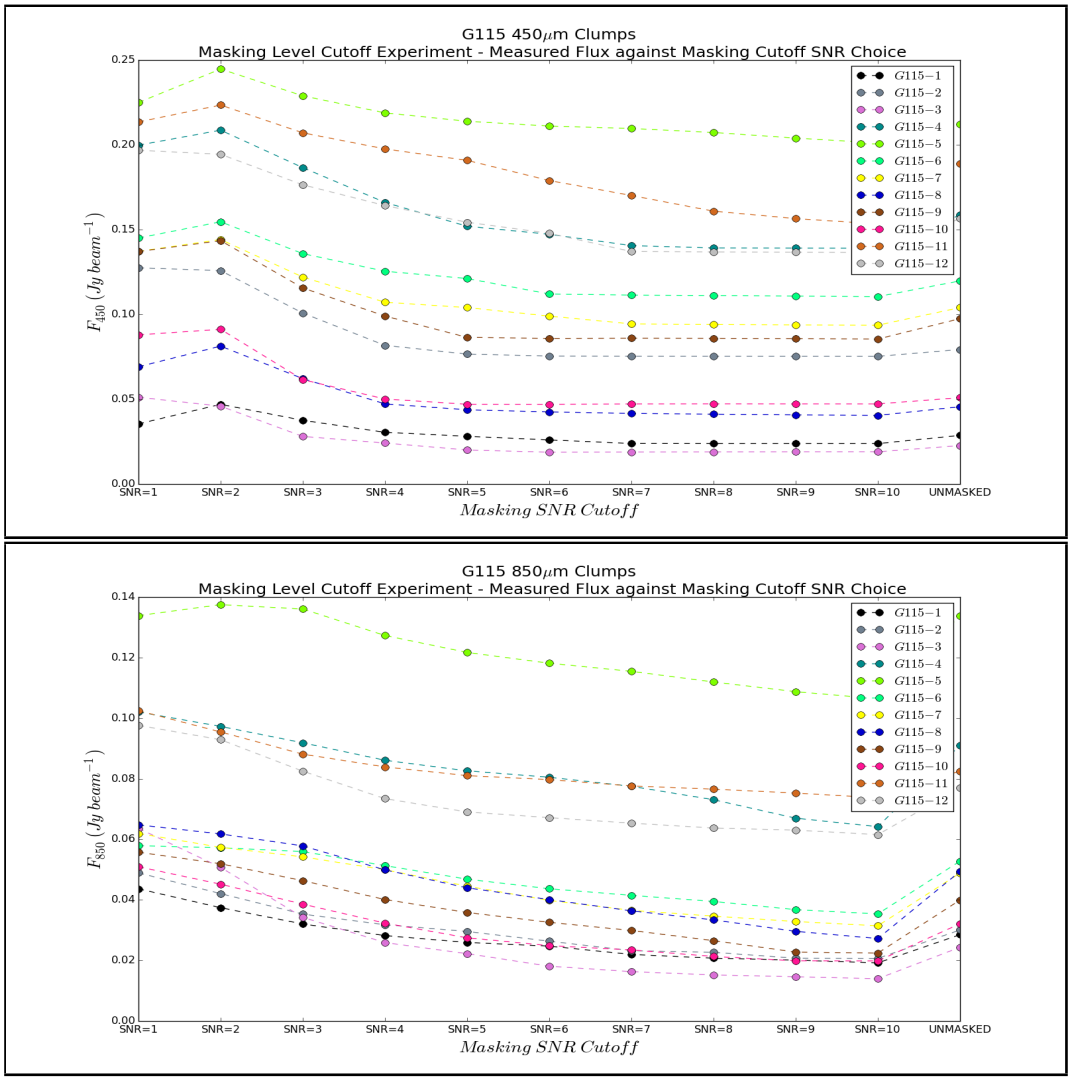

Figure 4.5: Plot comparing 450μm (Top) and 850μm (Bottom) clump flux measurements against different choices of the masking level SNR cutoff. The objects being compared are the cores of image G115.

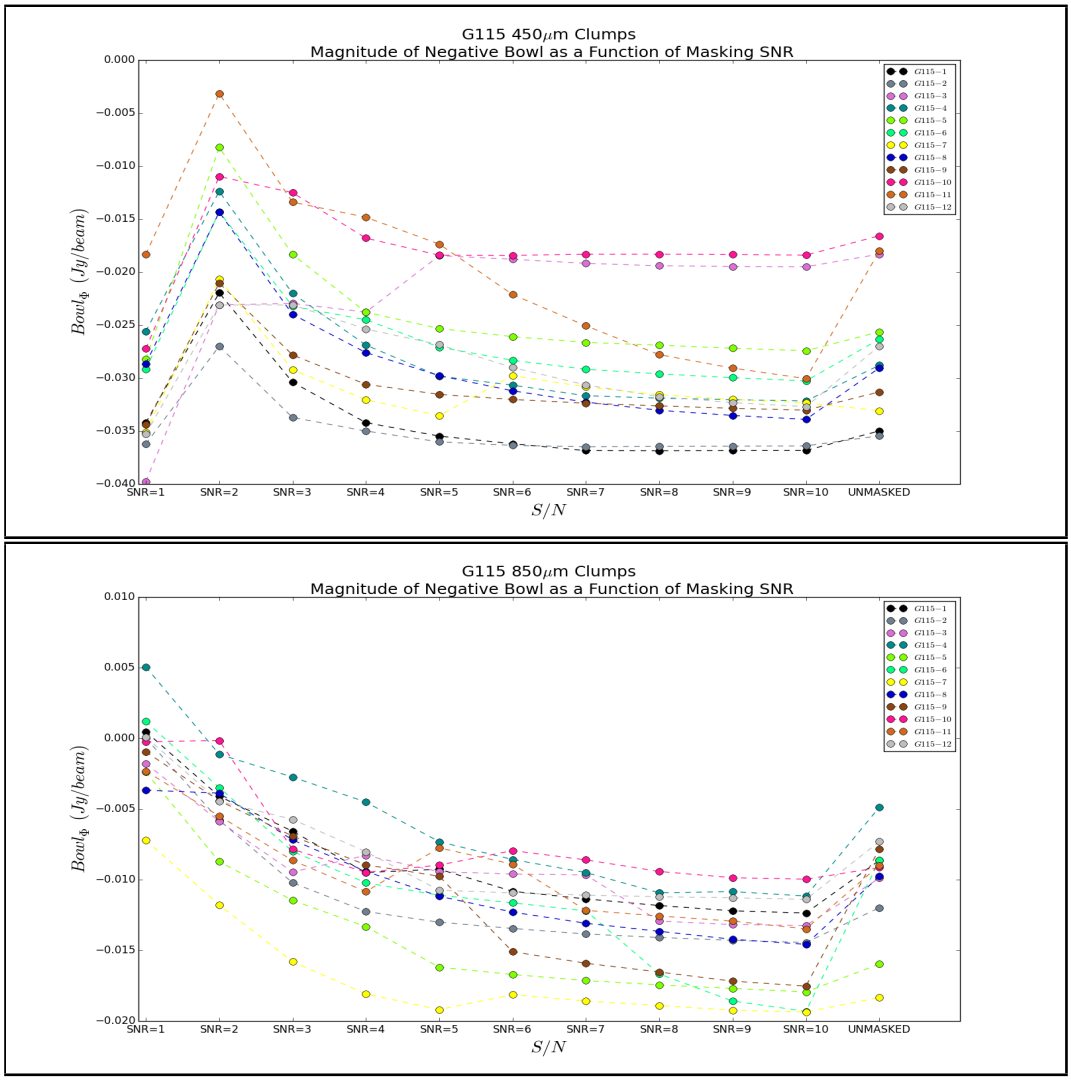

Figure 4.6: Plot of the 450μm (Top) and 850μm (Bottom) negative bowl measurements against different choices of masking level SNR cutoff. The objects being compared are the cores of image G115.

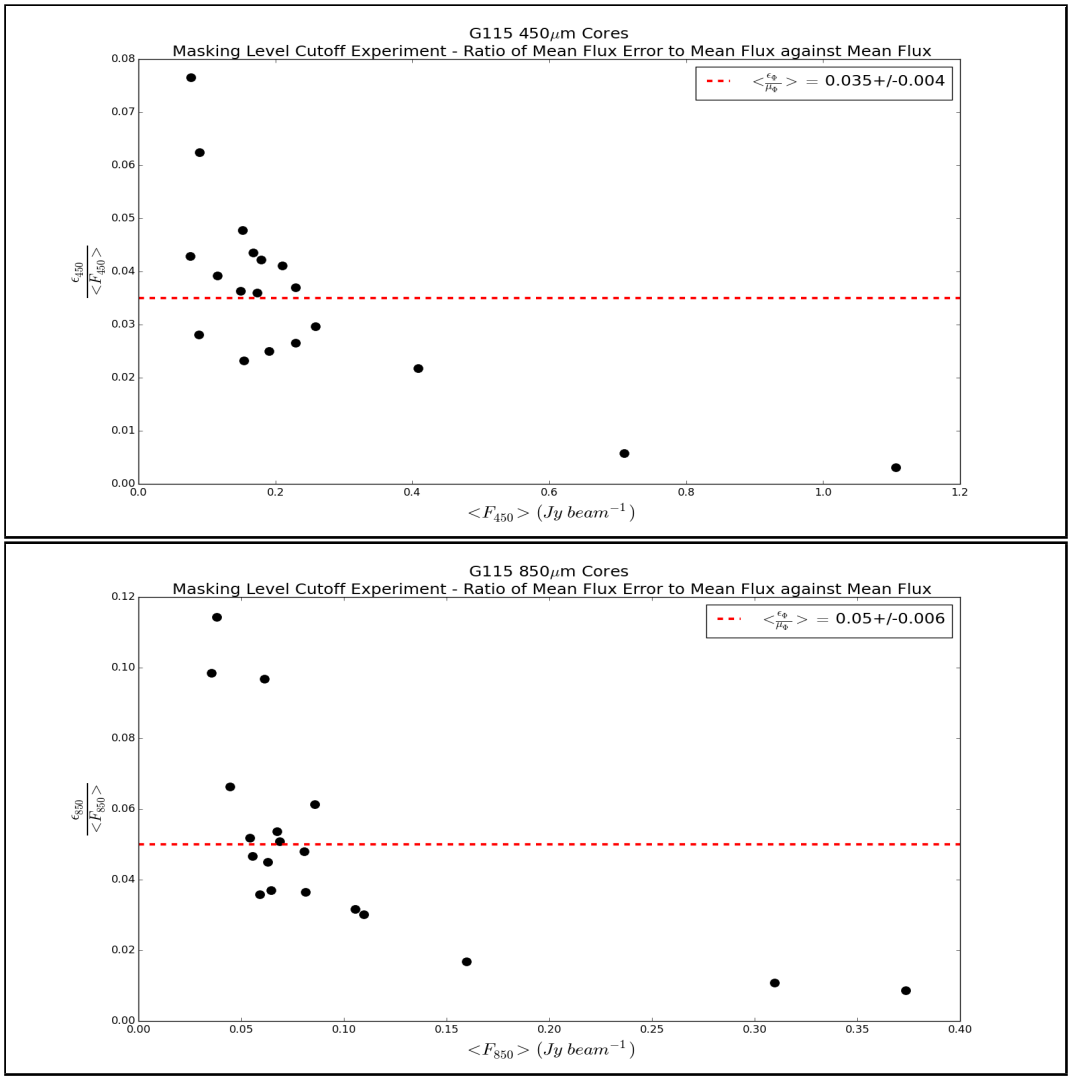

Figure 4.7: Plot of the 450μm (Top) and 850μm (Bottom) ratios of mean integrated flux uncertainty over mean integrated flux, against mean integrated flux. The mean incorporates measurements made using all masking instances. The objects being compared are the cores of image G115.

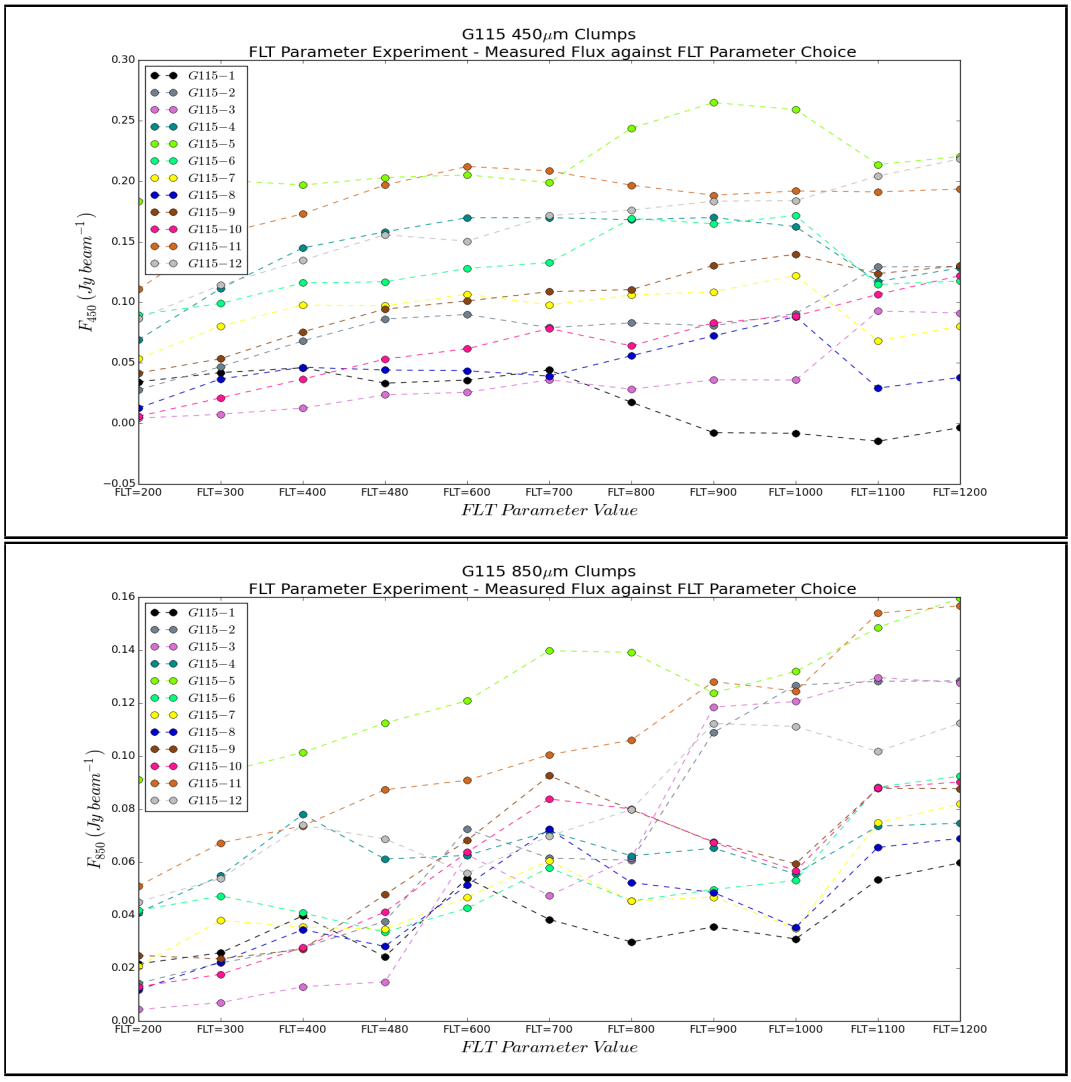

Figure 4.8: Plot comparing 450μm (Top) and 850μm (Bottom) clump flux measurements against different choices of the *flt.filt_edge_largescale* parameter. The objects compared are the cores of image G115.

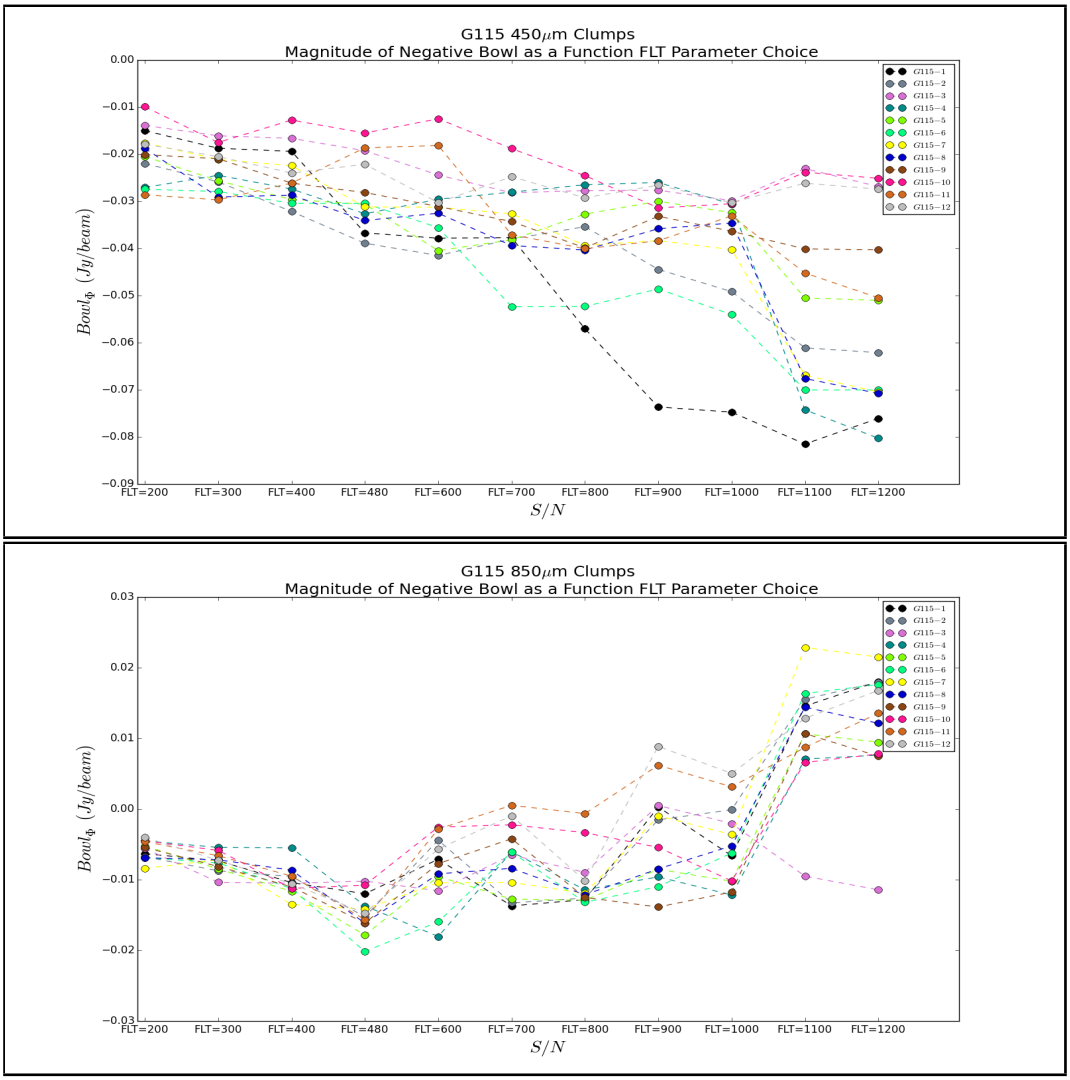

Figure 4.9: The negative bowl around each G115 clump composite in the 450μm (Top) and 850μm (Bottom) band against different FLT parameter choices. The effect introduced in the two bands appears to be different.

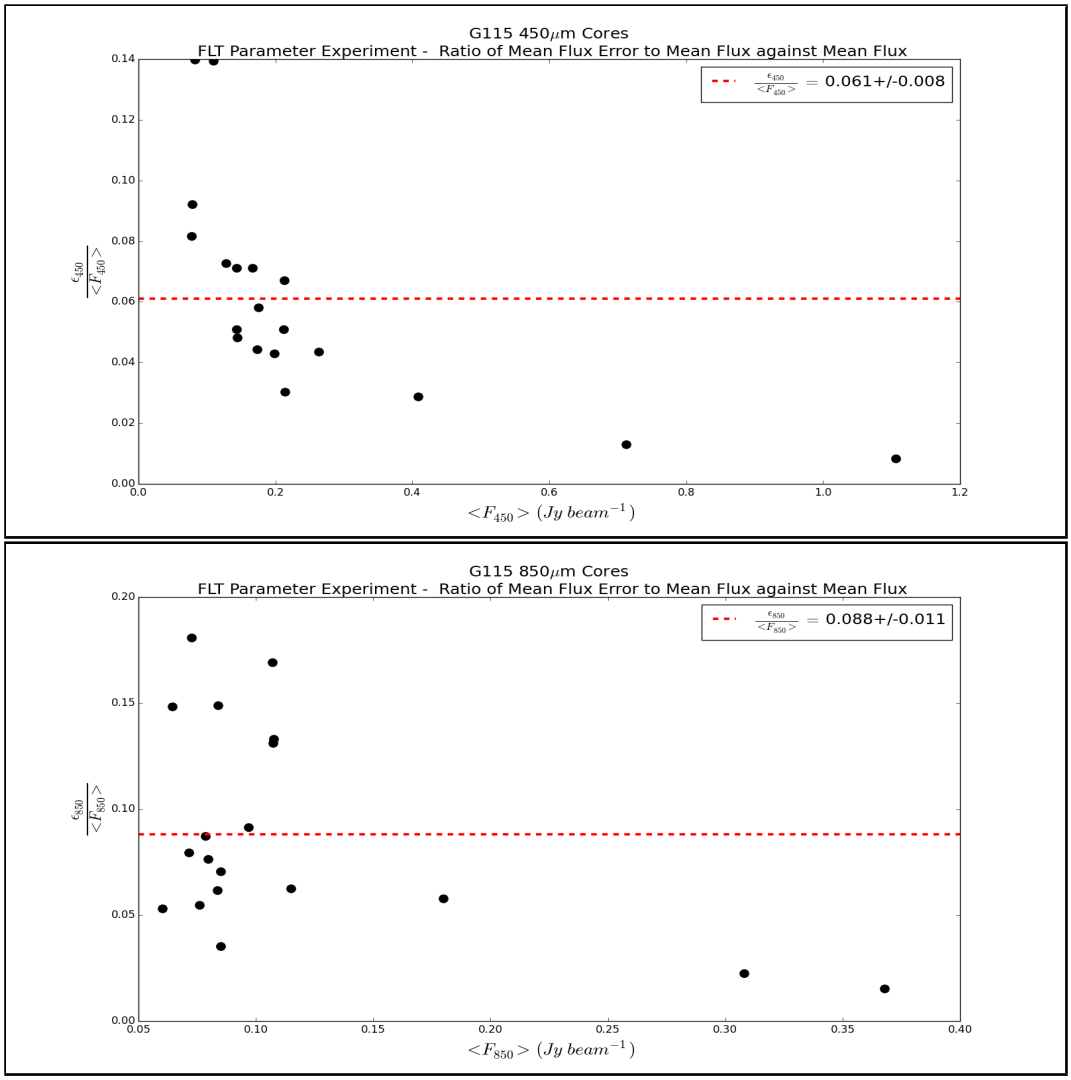

Figure 4.10: Plot of the 450μm (Top) and 850μm (Bottom) ratios of mean integrated flux uncertainty over mean integrated flux, against mean integrated flux. The mean incorporates measurements made using all *flt.filt_edge_largescale* choices. The objects being compared are the cores of image G115.

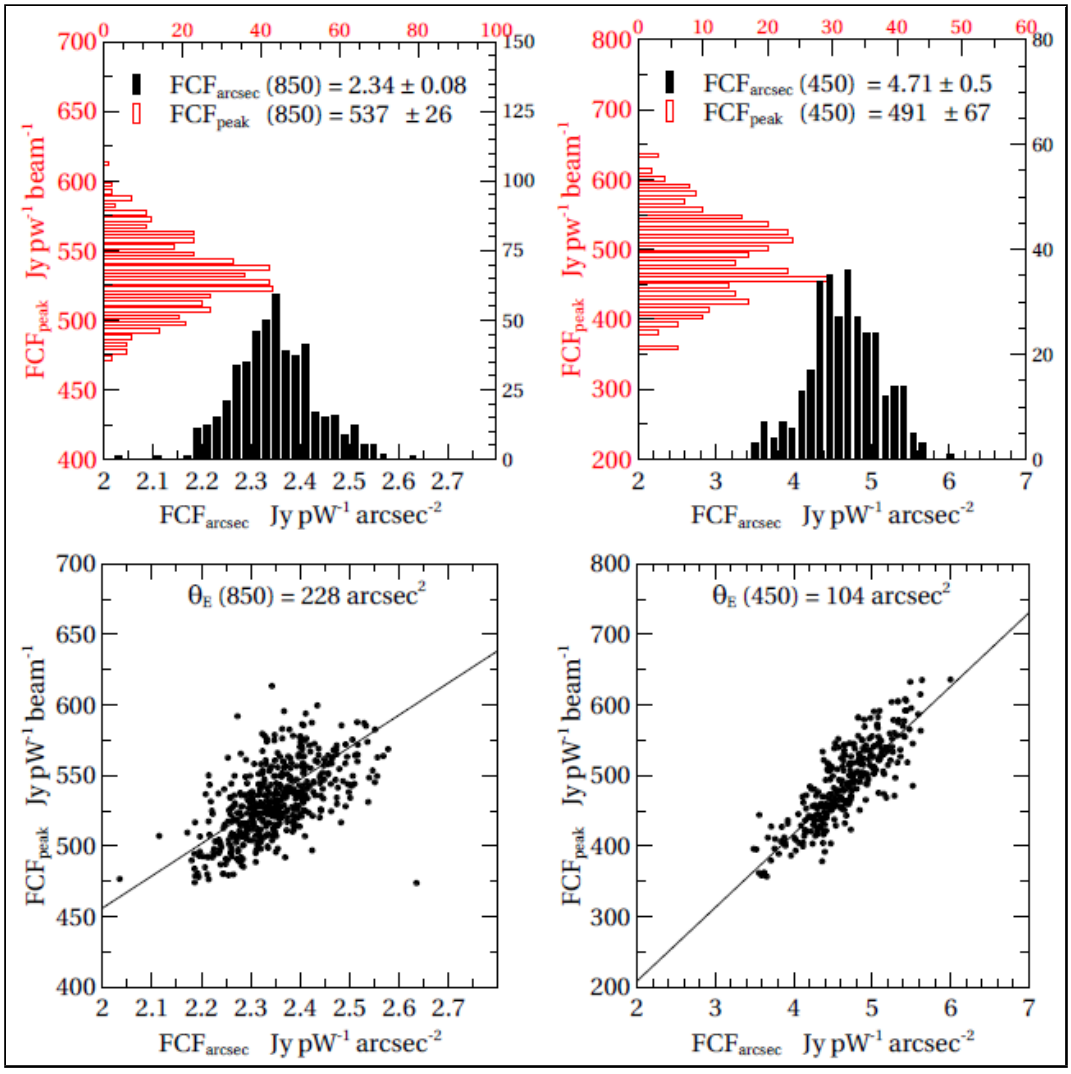

Figure 4.11: Plot of the 2012 SCUBA-2 calibration test results. First, The histogram distribution of the FCF_{arcsec} and FCF_{beam} values is presented for the 850μm band (Top-Left) and 450μm band (Top-Right). A scatter-plot for the FCF_{arcsec} against FCF_{peak} values is displayed for both the 850μm (Bottom-Left) and 450μm (Bottom-Right) band. [25]

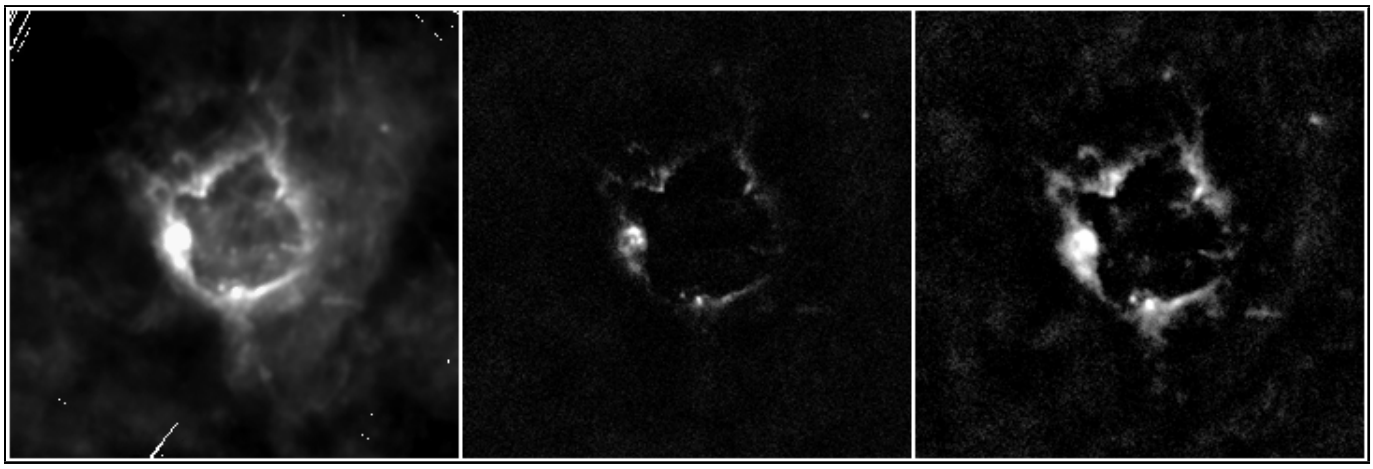

Figure 4.12: HERSCHEL SPIRE 250μm (Left), SCUBA-2 450μm (Middle) and 850μm (Right) image of HII region Sh-2 104. The majority of large scale structure is shared between the three images.

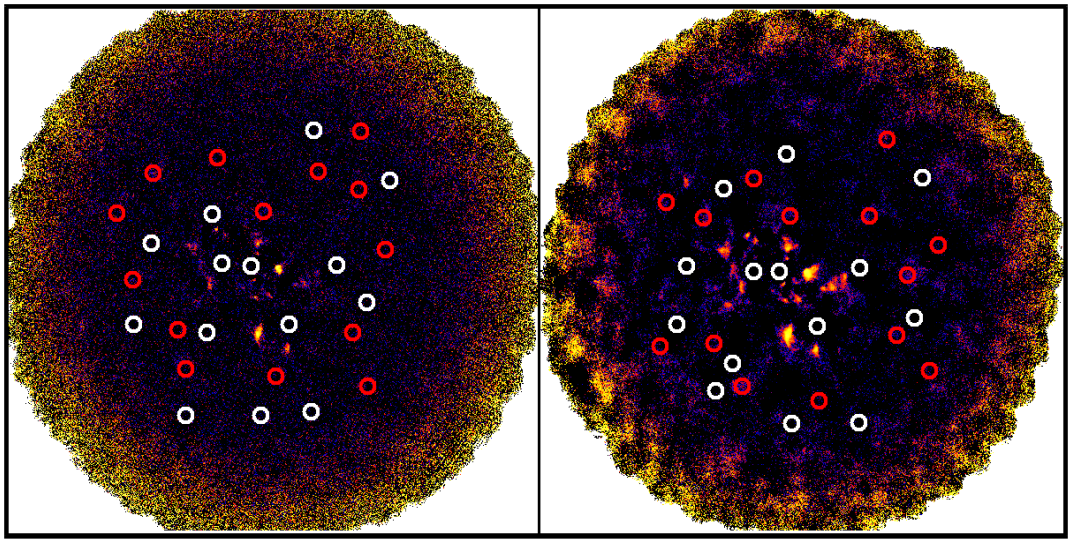

Figure 4.13: Underbright (White) and overbright (Red) apertures used in the 450μm (Left) and 850μm (Right) images of object G115 to determine the total random, non-spatially structured noise.

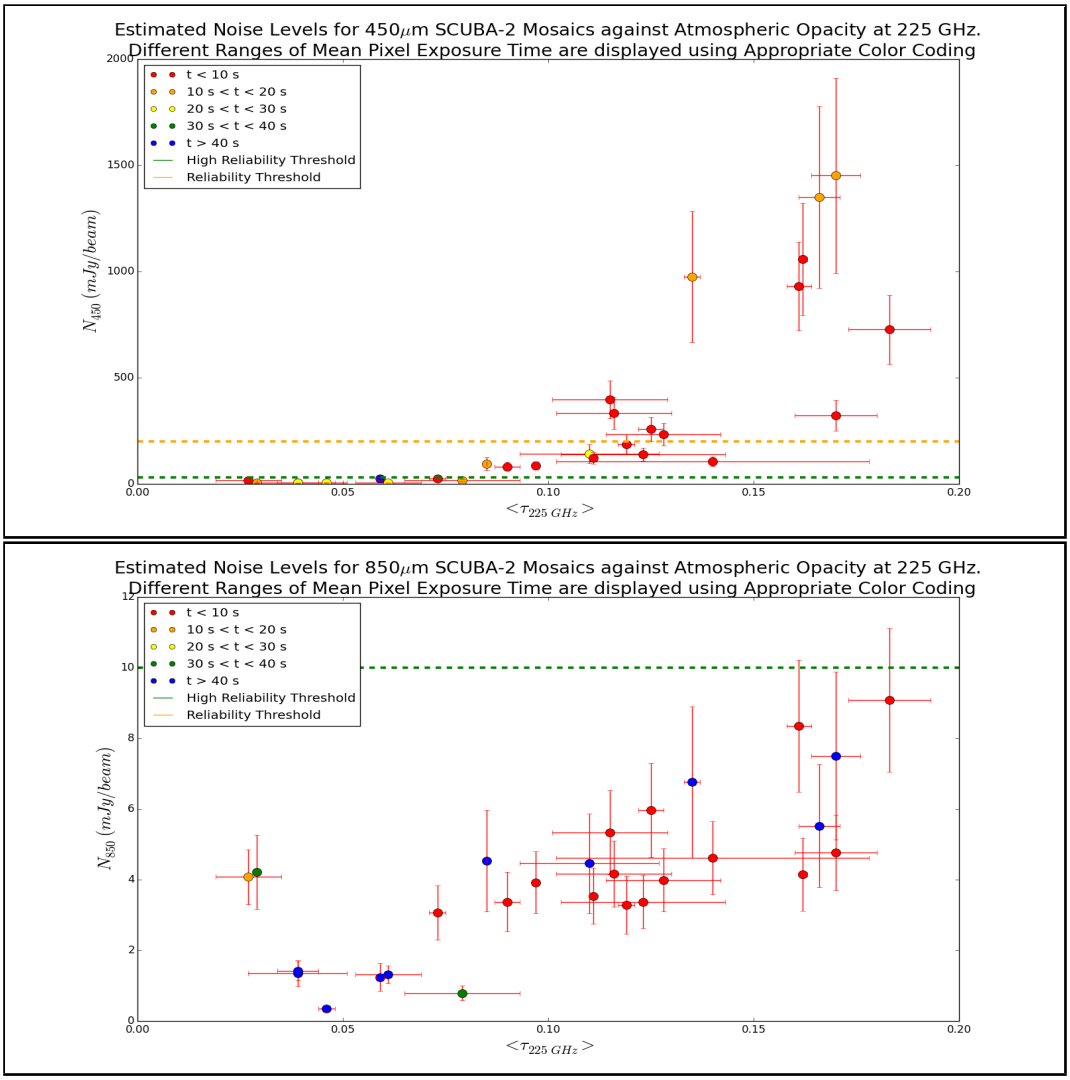

Figure 4.14: Plot of the estimated noise level for all SCUBA-2, 450μm (Top) and 850μm (Bottom) images against atmospheric opacity in the 225 GHz band. Different color coding is used to indicate different integration time ranges. Colored horizontal lines are used to indicate different reliability ranges.

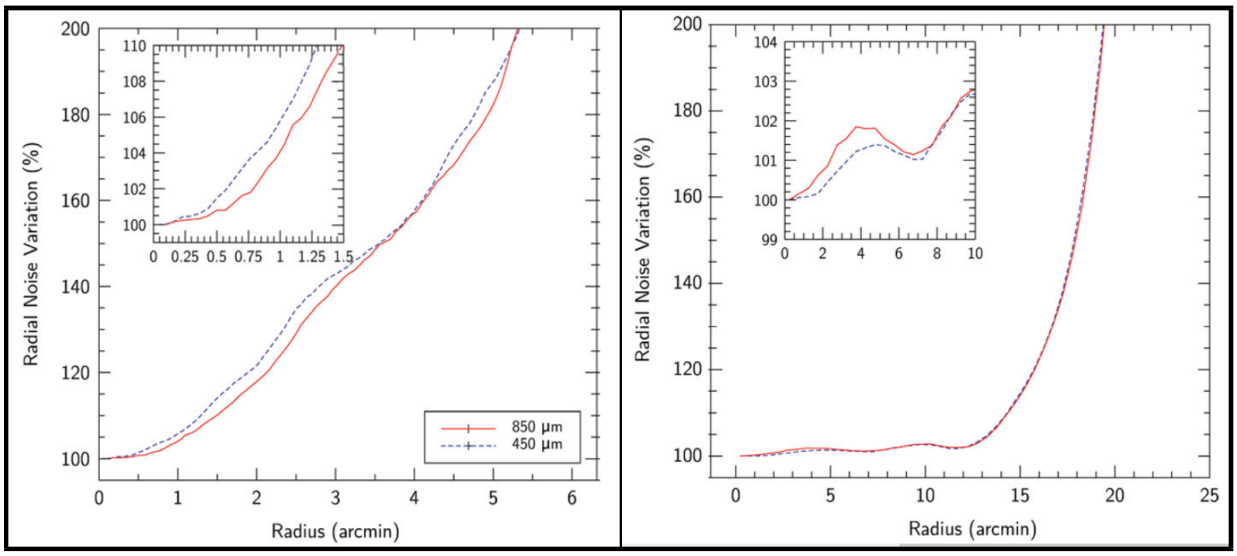

Figure 4.15: Plot of a *DAISY* (Left) and *PONG* (Right) typical integration time noise profile. Note that the *DAISY* pattern becomes increasingly unreliable with radius, while the *PONG* pattern remains very reliable up to a certain radius.

4.2 Calculation Uncertainties

In this section I discuss the manner in which uncertainties of all derivative properties presented in chapter 3 are calculated. As mentioned in that chapter, there is a need to separate the temperature and non-temperature dependent properties as the former require a much more robust treatment.

I begin this chapter with a discussion of the simpler, non-temperature dependent properties which are Gaussian variables and consequently have symmetric uncertainties attached. I then consider temperature dependent properties which are best described as skewed-Gaussian variables and have asymmetric uncertainties attached as a consequence. Finally, I describe the uncertainties attached to some other sources used as inputs in either of the two kinds of derivative properties.

4.2.1 Uncertainty of Non-Temperature Dependent Quantities

Non-Temperature dependent derivative properties include the following quantities:

- Spectral Indices
- 450μm and 850μm Luminosities
- 450μm and 850μm Surface Brightnesses
- Flux Ratios

The calculation of the uncertainty in these quantities is simple and uses the rules of standard error propagation. I present below the final recipe build for the uncertainty of each of the aforementioned quantities.

Spectral Index

The uncertainty of the spectral indices is calculated using:

$$\delta\alpha = \frac{\sqrt{\left(\frac{\delta F_{450}}{F_{450}}\right)^2 + \left(\frac{\delta F_{850}}{F_{850}}\right)^2}}{\ln\left(850\right) - \ln\left(450\right)} \tag{4.1}$$

Where $\delta\alpha$ indicates the symmetric uncertainty of the spectral index and F_{450} with F_{850} indicate the pure, integrated 450μm and 850μm flux respectively.

Luminosity

The uncertainty of the 450μm luminosities is calculated using:

$$\delta L_{450} = \left|L_{450}\right| \sqrt{\left(\frac{\delta F_{450}}{F_{450}}\right)^2 + 2\left(\frac{\delta d}{d}\right)^2} \tag{4.2}$$

Where L_{450} and δL_{450} indicate the luminosity in the 450μm band and its symmetric uncertainty, F_{450} and δF_{450} the pure, integrated, 450μm flux and its symmetric uncertainty and d with δd the radial distance and its symmetric uncertainty.

The uncertainty of the 850μm luminosities is calculated in a similar fashion using:

$$\delta L_{850} = \left|L_{850}\right| \sqrt{\left(\frac{\delta F_{850}}{F_{850}}\right)^2 + 2\left(\frac{\delta d}{d}\right)^2} \tag{4.3}$$

Where L_{850} and δL_{850} indicate the luminosity in the 850μm band and its symmetric uncertainty, F_{850} and δF_{850} the pure, integrated, 850μm flux and its symmetric uncertainty and d with δd the radial distance and its symmetric uncertainty.

Surface Brightness

The uncertainty of the 450μm average surface brightnesses is calculated using:

$$\delta S_{450} = \left|S_{450}\right| \left(\frac{\delta F_{450}}{F_{450}}\right) \tag{4.4}$$

Where S_{450} and δS_{450} indicate the 450μm surface brightness and its symmetric uncertainty, and F_{450} with δF_{450} the pure, integrated 450μm flux and its symmetric uncertainty.

The uncertainty of the 850μm average surface brightnesses is calculated using:

$$\delta S_{850} = \left|S_{850}\right| \left(\frac{\delta F_{850}}{F_{850}}\right) \tag{4.5}$$

Where S_{850} and δS_{850} indicate the 850μm surface brightness and its symmetric uncertainty, and F_{850} with δF_{850} the pure, integrated 850μm flux and its symmetric uncertainty.

Flux Ratio

The uncertainty of the 450μm to 850μm integrated flux ratios is calculated using:

$$\delta R = |R| \sqrt{\left(\frac{\delta F_{450}}{F_{450}}\right)^2 + \left(\frac{\delta F_{850}}{F_{850}}\right)^2} \tag{4.6}$$

Where R and δR indicate the flux ratio and its symmetric uncertainty, F_{450} and δF_{450} the pure, integrated 450μm flux and its symmetric uncertainty and δF_{850} with F_{850} the pure, integrated 850μm flux and its symmetric uncertainty.

4.2.2 Uncertainty of Temperature Dependent Quantities

Temperature dependent derivative properties include the following quantities:

- Average Temperatures
- Cumulative Masses
- Average H_2 Column Densities
- Average H_2 Number Densities
- Average Pressures

The calculation of uncertainty is done simultaneously for all the aforementioned quantities through Monte-Carlo simulations performed within a scripted *Python* routine. I will discuss the precise manner in which this routine operates.

To begin, each SCUBA-2 source already has a complete photometric description by this point. This photometry data, combined with information obtained from literature gives rise to some intermediate quantities that will be used as inputs in the calculation of derivative properties. These inputs can be separated into two distinct categories.

The first kind involves inputs that do not have an assigned uncertainty. These include:

- Physical Constants
- Angular Radii

- Opacities
- Mean Molecular Weights

Physical constants and angular radii do not have an assigned uncertainty due to the fact that the magnitude of the uncertainty is much smaller than the magnitude of the quantity itself. At the same time opacities and mean molecular weights do not have an assigned uncertainty due to the fact that the values used for them pertain to a particular assumed model. Overall then, these inputs will be treated as constants during the performance of Monte-Carlo simulations.

The second kind of inputs involves those that do have an attached symmetric uncertainty. These include:

- Pure 450μm Integrated Fluxes
- Pure 850μm Integrated Fluxes
- Flux Ratios
- Radial Distances

The uncertainties attached to the 450μm and 850μm pure, integrated fluxes arise from the cumulative effect of all uncertainties discussed in chapter 4.1. The flux ratio uncertainty is previously calculated in section 4.2.1. Radial distance uncertainties are obtained from literature. Unlike the previous set of inputs, these are not treated as constants, but rather as Gaussian-distributed variables.

More specifically, each member of this set of inputs is assigned a Gaussian representation with a standard deviation equal to the value of the quantity's symmetric uncertainty. This Gaussian is truncated, meaning that the probability of having the value of an input exist outside some specific range is set to zero. The truncation is performed for each variable through consideration of their individual ranges. The ranges used are the following:

- $0\ Jy\ <\ F_{450}\ <\ 500\ Jy$
- $0\ Jy\ <\ F_{850}\ <\ 50\ Jy$
- $0.491100\ <\ \frac{F_{450}}{F_{850}}\ <\ 10.966918$

- $1\ kpc\ <\ d\ <\ 30\ kpc$

The F_{450} and F_{850} ranges are determined from consideration of all SCUBA-2 photometry measurements and the extremes encountered within those. For the minimum, it is obvious that no SCUBA-2 source can have an integrated flux equal or less than 0 Jy. Thus, the minimum for both 450μm and 850μm bands is set to 0 Jy. At the same time, the maximum is determined by considering the maximum integrated flux encountered in each band and slightly relaxing this value in order to allow for the existence of even brighter sources that could potentially exist inside a different SCUBA-2 source sample. This leads to setting the maximum values of the 450μm and 850μm band to 500 Jy and 50 Jy respectively.

The flux ratio range is already determined through the exotic source cutoff made in subsection 3.6.2. The lower limit corresponds to a temperature of $4K$ and the upper limit to a temperature of $300K$. The logic behind these choices is discussed in detail within the subsection itself.

Finally, the minimum of the radial distance range is set by considering the smallest radial distance encountered in the HII region sample covered by this thesis (1.15 kpc) and relaxing this value slightly to 1 kpc in order to account for uncertainty. The maximum of the radial distance range is set to be the conservative estimate of the Milky-Way's diameter ($\approx$ 30 kpc), as none of the HII regions considered in this thesis are extragalactic.

After these ranges are established, each input variable can finally obtain a complete, truncated, Gaussian representation. At this point, the routine is in a position to begin randomly sampling these variable ranges using the supplied Gaussian representation for each.

The sampling begins with the generation of a random number between 0 and 1, representing a random probability draw. This probability corresponds to a specific value for each input variable. These values are determined by reversing the truncated Gaussian function for each input and are finally provided to the temperature dependent property recipes.

A total of 10000 such probability draws are made for each SCUBA-2 source. This results in 10000 different sets of [F_{450}, F_{850}, R, d] being provided to the temperature dependent property recipes. As an example, the generated distribution of these inputs for object G90-1-1 is displayed in figure 4.16. These input sets are provided to the temperature dependent property recipes in order to finally yield 10000 different estimates for each temperature dependent property.

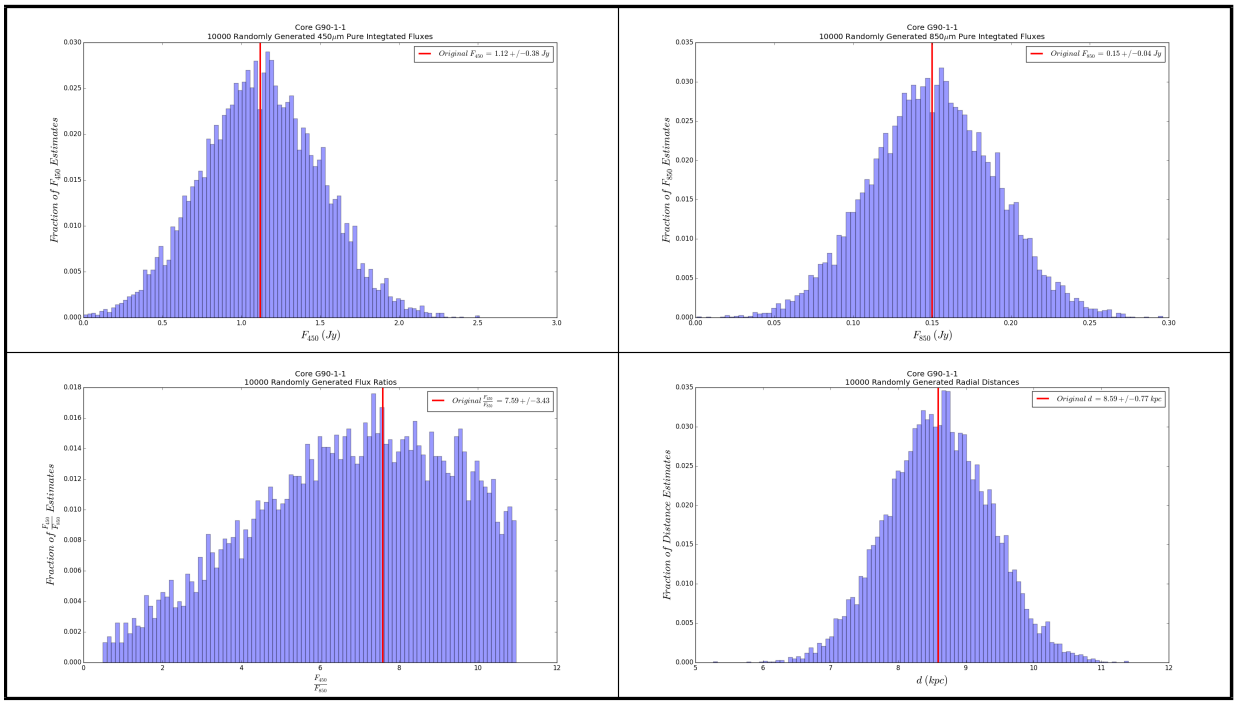

Figure 4.16: Plot of 10000 randomly generated values for F_{450} (Top-Left), F_{850} (Top-Right), $\frac{F_{450}}{F_{850}}$ (Bottom-Left) and radial distance (Bottom-Right) for object G90-1-1.

The next step involves turning these 10000 estimates for each temperature dependent property into an uncertainty. This begins by organizing them into a normalized, cumulative histogram. The normalization is such that 1 corresponds to 100% of the estimate sample. The uncertainty boundaries are determined by establishing the position of the 1σ levels in this histogram. The $+1\sigma$ level is taken to be the value at which 84.1% of the estimates lie below, while the other 15.9% lie above it. The -1σ level on the other hand is taken to be the value at which 15.9% of the estimates lie below, while the other 84.1% lie above it.

To convert these values into an upper and lower uncertainty it is a simple matter of comparing them to the mean estimate of the quantity as follows:

$$\epsilon_+ = \left|\mu - \sigma_+\right| \tag{4.7}$$

$$\epsilon_- = \left|\mu - \sigma_-\right| \tag{4.8}$$

Where ϵ_+ and ϵ_- indicate the upper and lower uncertainty of a particular temperature

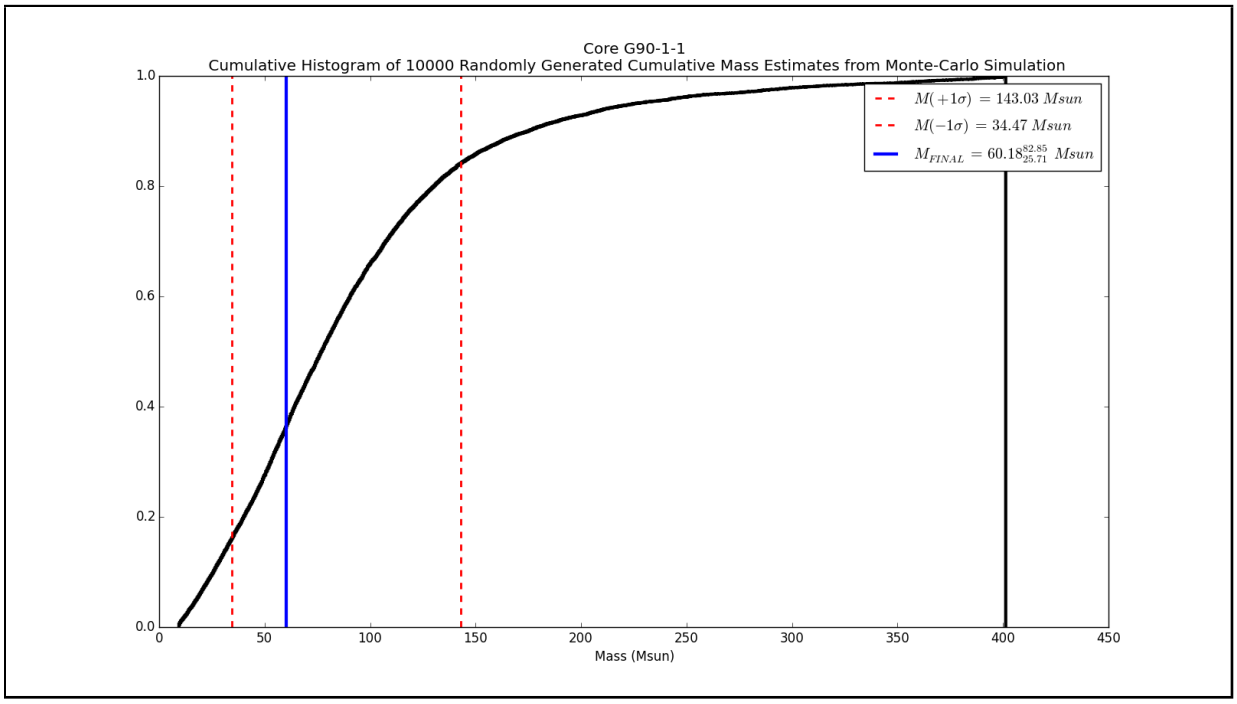

Figure 4.17: Plot of the cumulative histogram for 10000 randomly generated cumulative mass estimates for object G90-1-1 from a Monte-Carlo simulation. The $+1\sigma$ and -1σ levels are indicated using red, dashed lines, while the best estimate of the mass obtained by the mass recipe of section 3.3.2 is indicated using a blue, solid line.

dependent quantity, μ the quantity's mean estimate and σ_+ with σ_- the quantity's value at the $+1\sigma$ and -1σ level respectively. An example of this process being performed in order to determine the uncertainty bounds for the mass of core G90-1-1 is displayed in figure 4.17.

4.2.3 Other Uncertainties

To conclude the discussion of uncertainty in the calculation of derivative properties, it is important to note the source of uncertainty for some intermediate values that are used as inputs to these calculations.

To begin, some of these intermediate quantities are obtained directly from literature. Such quantities include HII region radial distances and flux conversion factors. For these, the

uncertainty found in the literature reference is used.

A number of other intermediate quantities pertain to an assumed model. Such quantities include the value of β and the consequent value of the 450μm and 850μm opacities. Due to the fact that they are part of an assumption, no uncertainty is attached to these quantities. This does not mean that they do not contribute uncertainty to the calculations, but instead that their uncertainty contribution is zero if the assumed model is absolutely correct.

Finally, some intermediate quantities have extremely small uncertainties compared to their established mean. Such quantities include physical constants, angular radii and angular areas. No uncertainty is attached to these quantities, however, a note needs to be made regarding the latter two. Even though angular radii and areas may be well measured, their measurements are made using circular apertures. It is this systematic choice regarding aperture shape that contributes some uncertainty to these values. However the contribution is expected to be less than 5% and for this reason the original choice of not assigning uncertainty is maintained.

Chapter 5

Analysis

In this chapter I will be analyzing the results from the photometry obtained in chapter 2 and subsequent derived properties obtained in chapter 3 in pursuit of obtaining important insights about the nature of HII region systems considered in this thesis. The leading hypothesis pertaining to stimulated star formation by the action of HII regions will also be investigated in this chapter. However, the analysis will explore several other features of the HII region systems as well.

To begin, the properties of the image sample analyzed will be determined and presented for the purpose of informing the reader regarding the expected quality of measurements from each. From there, the HII regions of the sample will be investigated in depth, where properties such as their number densities and masses will be determined. With this information available, an in-depth look at how HII regions interact with molecular clumps will be made. An investigation for evidence regarding clump compression and heating from HII regions will be performed. A clump census in search for evidence of extended clump formation along HII region boundaries will also be made.

After the effects from HII regions are addressed, an attempt will be made to identify potential interaction between the outer (clouds) and inner (cores) clump components. This will lead to the identification of potentially star forming cores.

Following this, an investigation pertaining to the heating effect of nearby, massive OB stars on associated clumps will be performed. The result will be compared against that for the associated HII regions.

Finally, once all the necessary information has been obtained by the end of this chapter, I will be in a position to provide an estimate for the star formation efficiency of each HII region system considered in this thesis.

5.1 The SCUBA-2 Images

In this section, I introduce the SCUBA-2 image sample used in the construction of this thesis alongside with some fundamental properties. These properties include the center coordinates, size, noise levels and contained HII regions. Note that in the determination of all aforementioned properties, only the usable area (i.e the area inside the noisy outer rim) of SCUBA-2 images is used.

The central coordinates of a SCUBA-2 image can be found in its header file. However, the center of the usable area of a SCUBA-2 image typically differs from that of the entire image, something that is especially true for mosaic composites. I approximate the center of the usable area for each SCUBA-2 image using an aperture whose center traces the center of the image's usable area to the best possible extent. This aperture has its size adjusted until it encompasses the entire usable area of the image, meaning that the area belonging to the highly noisy outer rim of either *PONG* and *DAISY* images is excluded. Once this is done, the radius and central coordinates of this aperture are then taken to be the best approximations to the angular radius and central coordinates of the SCUBA-2 image's usable area. The noise level estimates in each 450μm and 850μm band are obtained individually using the technique described in section 4.1.2.

The identification of HII regions in the vicinity of SCUBA-2 sources is a little trickier to tackle. Recall that the original images use data that target the position of a known "Sh-2" or "BFS" HII region. However, there is a chance that more than one HII region from these catalogues exists near the original target. To make sure that all "Sh-2" and "BFS" HII regions are accounted for, I perform queries on SIMBAD using an image's center coordinates and searching out to the outer radius of the image at hand. Sometimes, HII regions from other catalogues can also be found near SCUBA-2 targets, some of which are unconfirmed or potentially extragalactic. I choose to maintain a homogeneous galactic sample and for this purpose do not consider any of these in my sample.

The images and their compiled properties are presented in table 5.1. A few additional images did not end up being used in this thesis. This was due to the fact that they either

did not contain any "Sh-2" or "BFS" HII regions within their boundary, or, were completely lacking of any SCUBA-2 molecular clumps. A list of these excluded images along with some of their basic properties is presented in table 5.2.

In both tables, special attention should be placed on the noise level columns as the information contained in those can be used to judge the reliability level of a particular image, with reliability here pertaining to how dependable the results arising from measurements on it are expected to be. As a rule of thumb, the typical SCUBA-2 emission of a 450μm and 850μm cloud background pixel lies in the vicinity of 10-200 mJy/beam and 5-50 mJy/beam respectively. Thus, the closer the noise estimates reach to these values, the more unreliable the image at hand. In order to simplify this judgment for the reader, I provide a summary of criteria in table 5.3. Note that all 850μm images fall within the "reliable" threshold.

Table 5.1: The HII region systems that are considered in this thesis. Properties in order of appearance include system ID, galactic longitude and latitude in degrees, radial size in degrees, 450μm and 850μm noise levels in mJy/beam, contained HII regions and the number of identified molecular cores.

Image ID	**LONG (GAL)**	**LAT (GAL)**	**Radius (degrees)**	N_{450} $(\frac{mJy}{beam})$	N_{850} $(\frac{mJy}{beam})$	**HII Regions**	**Number of Cores**
G70	70.291462	1.5942207	0.337463	5.0 ± 1.3	1.3 ± 0.4	S99, S100	49
G74	74.792501	0.57342642	0.337255	5.7 ± 1.5	0.3 ± 0.1	S104	43
G90	90.388196	2.3798378	0.628223	24.8 ± 6.2	3.1 ± 0.8	S120	1
G97	97.518978	3.1717887	0.337309	5.8 ± 1.1	1.3 ± 0.2	S128	11
G105	105.88944	0.86477045	0.632921	1058.4 ± 264.6	4.1 ± 1.0	S138	1
G108	108.78650	-0.95365459	0.614033	81.2 ± 20.3	3.4 ± 0.8	S152	12
G115	115.79191	-1.5879669	0.330972	4.7 ± 0.9	1.4 ± 0.3	S168	19
G120	120.2519	2.1597373	0.0950988	25.55 ± 8.0	1.2 ± 0.4	S175	7
G125	125.17745	-0.021618887	1.1583	333.7 ± 74.6	4.2 ± 0.9	S186	1
G136	136.54361	1.783045	1.14885	233.3 ± 52.2	4.0 ± 0.9	S192-4	1
G138	138.49746	1.6377456	0.319483	17.1 ± 3.2	4.1 ± 0.8	S201	4
G142	142.75328	-1.7997364	1.2143	257.3 ± 57.5	6.0 ± 1.3	BFS31	1
G151	151.29133	1.9701098	0.0947661	1451.7 ± 459.1	7.5 ± 2.4	S208	4
G151B	151.62120	-0.25763003	0.0952703	1350.7 ± 427.1	5.5 ± 1.7	S209	7

Continued on next page

Table 5.1 – *Continued from previous page*

Image ID	**LONG (GAL)**	**LAT (GAL)**	**Radius (degrees)**	N_{450} $(\frac{mJy}{beam})$	N_{850} $(\frac{mJy}{beam})$	**HII Regions**	**Core Number**
G173	173.49994	2.5951217	0.609291	137.9 ± 30.8	3.4 ± 0.8	S231-3, S235	35
G173B	173.74318	0.0006436	0.630678	186.9 ± 46.7	3.3 ± 0.8	S234, S237	4
G182	182.41662	0.25673071	0.339916	8.1 ± 1.5	1.7 ± 0.3	S242	10
G188	188.83911	1.0708469	0.63666	16.5 ± 4.4	0.8 ± 0.2	S247	28
G192	192.59192	-0.05164492	0.301135	11.4 ± 3.0	3.0 ± 0.8	S254-8, S255B	38
G192B	192.59192	-0.05164492	0.301135	11.4 ± 3.0	3.0 ± 0.8	S259	1
G195	195.42183	-0.0087938456	1.1461	930.3 ± 208.0	8.4 ± 1.9	S266	1
G196	196.46068	-1.8035705	1.14506	727.0 ± 162.6	9.1 ± 2.0	S269	2
G210	210.78545	-2.5391619	0.0941503	95.5 ± 30.2	4.5 ± 1.4	S283	2
G217	217.12626	-1.8104132	1.16531	86.7 ± 19.4	3.9 ± 0.9	S286	2
G219	219.18548	1.7746899	1.16897	105.6 ± 23.6	4.6 ± 1.0	S288	2
G221	221.84028	-2.0347645	0.102702	140.6 ± 44.5	4.5 ± 1.4	BFS64	7
G223	223.31922	1.7663545	1.1397	323.4 ± 72.3	4.8 ± 1.1	S294	1
G225	225.47695	-2.5706539	0.0947553	975.6 ± 308.5	6.8 ± 2.1	S297	4
G231	231.58494	1.7632144	1.14915	121.5 ± 27.2	3.5 ± 0.8	S299, S300	2
G233	233.76044	-0.20929678	0.322234	5.4 ± 1.4	4.2 ± 1.1	S305	31
G234	234.70584	-0.013921393	1.15075	398.2 ± 89.0	5.3 ± 1.2	S307	2

Table 5.2: HII region systems that are not considered in this thesis. Properties in order of appearance include system ID, galactic longitude and latitude in degrees, radius in degrees, contained HII regions and a note depicting the existence or absence of molecular cores.

Image ID	**LONG (GAL)**	**LAT (GAL)**	**Radius (degrees)**	**HII Regions**	**Cores?**
G95	95.550987	0.85726364	0.645311	BFS6	None
G96	96.070611	1.724812	0.670024	AAJ2015 G096.433+01.322	Several
G198	198.51938	-1.8159872	1.12575	S271, S272	None
G210B	210.92743	-1.7876716	1.16933	BFS53, S283	None
G211	211.94935	-0.022441707	1.16275	BFS54, IRAS 06446+0029, IRAS 06501+0143	Several
G214	214.01394	-0.044066561	1.14398	S285	None

Continued on next page

Table 5.2 – *Continued from previous page*

Image ID	LONG (GAL)	LAT (GAL)	Radius (degrees)	HII Regions	Cores?
G218	218.15585	-0.030509338	1.14527	BFS58, UHP2009 VLA G217.3774-00.0832, AAJ2015 G217.377-00.084, RAFGL 5216, IRAS 06571-0441, S287-c, GLMP 169	Several

Table 5.3: Image Reliability Criteria

Reliability	N_{450} $(\frac{mJy}{beam})$	N_{850} $(\frac{mJy}{beam})$
Very Reliable	< 10	< 5
Reliable	$10 < N_{450} < 200$	$5 < N_{850} < 50$
Unreliable	> 200	> 50

5.2 HII Region Properties

In this section, I discuss updated properties obtained for the HII region sample used in this thesis. These include electron and hydrogen number density, mass density and cumulative mass. However, only the first and last of these properties are tabulated in the results as they are of utmost importance. Finally, the calculation recipes presented in this section can be used to treat other galactic HII regions as well.

5.2.1 HII Region Number Densities

In this subsection I present the manner in which HII region electron and hydrogen number densities can be obtained. What follows is an in-depth derivation of the recipes for calculating these two quantities. A good starting for this derivation is the general radiative transfer equation which reads as follows:

$$\frac{dI_\nu}{d\tau_\nu} = -I_\nu + S_\nu \tag{5.1}$$

Where I_ν indicates specific intensity and $S_\nu = \epsilon_\nu/\kappa_\nu$ spectral flux density. Solving this differential equation yields the following integral:

$$I_\nu = -I_\nu(0)e^{-\tau_\nu} + \int_0^{\tau_\nu} \frac{\epsilon_\nu}{\kappa_\nu} e^{-(\tau_\nu - \tau_\nu^{'})} d\tau_\nu^{'} \tag{5.2}$$

Assuming the spectral flux density is independent of opacity, ϵ_ν/κ_ν can be pulled out of the integral. At the same time, since we are concerned with emission in the radio spectrum, the limit $kT >> h\nu$ holds well. This means that the spectral flux density S_ν is well approximated by the Rayleigh-Jeans limit for blackbodies. Putting this information together, the specific intensity expression becomes:

$$I_\nu = -I_\nu(0)e^{-\tau_\nu} + B_\nu \int_0^{\tau_\nu} e^{-(\tau_\nu - \tau_\nu^{'})} d\tau_\nu^{'} \tag{5.3}$$

with:

$$B_\nu = \frac{\epsilon_\nu}{\kappa_\nu} = \frac{2k_B T\nu^2}{c^2} \tag{5.4}$$

Considering no source emission is coming from any other source behind the HII region, $I_\nu(0) \approx 0$ and the simplified specific intensity expression reads:

$$I_\nu \approx B_\nu \int_0^{\tau_\nu} e^{-(\tau_\nu - \tau_\nu^{'})} d\tau_\nu^{'} \tag{5.5}$$

$$I_\nu \approx B_\nu \big(1 - e^{-\tau_\nu}\big) \tag{5.6}$$

The VLA observes HII regions at optically thin wavelengths, where $\tau << 1$. This allows further simplification of the spectral intensity function as $(1 - e^{-\tau_\nu}) \rightarrow \tau_\nu$. The further simplified spectral intensity expression reads:

$$I_\nu \approx B_\nu \tau_\nu \tag{5.7}$$

One can obtain an expression for flux density from the above by integrating through the emission's solid angle $d\Omega$. Using a cylindrical approximation to the HII region's shape, where the cylindrical radius is equal to the length. allows the write-up of this integral and its analytic solution as follows:

$$F_\nu = I_\nu \int d\Omega \tag{5.8}$$

$$F_\nu = \pi \left(\frac{R_s}{d}\right)^2 I_\nu \tag{5.9}$$

$$F_\nu \approx \pi \left(\frac{R_s}{d}\right)^2 B_\nu \tau_\nu \tag{5.10}$$

Where d indicates the physical distance between the telescope and the targeted source while R_s the radius of the cylindrical shape approximation. It is now a matter of constructing a proper expression for the free-free optical depth τ_ν. Fortunately, this is something that has already been performed in the early 1960's by *P.Z. Mezger* and *A.P Henderson* [49]. Their exact expression for the free-free optical depth reads:

$$\tau_\nu = 3.014{\times}10^{-2}\left(\frac{T}{K}\right)^{-1.5}\left(\frac{\nu}{GHz}\right)^{-2.0}\left[\ln\left[4.955{\times}10^{-2}\left(\frac{\nu}{GHz}\right)^{-1.0}\right]+1.5\ln\left(\frac{T}{K}\right)\right]\left(\frac{EM}{pc\ cm^{-6}}\right) \tag{5.11}$$

Where T indicates the average electron temperature in Kelvin, ν the observing frequency in GHz and EM the emission measure usually expressed as $EM = \int_0^{L=R_s} n_e^2 dS$ where n_e indicates the electron number density within a line of sight segment dS and L indicates the length along the system's radial dimension, which in this case is simply equal to the radius R_s of the assumed cylindrical shape.

The above equation can be significantly simplified for use in HII regions which are primarily composed from ionized Hydrogen (Z=1) and have a roughly constant electron number density profile. Most HII regions are well fitted by these two assumptions, and, for these, the emission measure integral can be simplified to $EM \approx n_e^2 R_s$. The new expression for optical depth then reads:

$$\tau_\nu \approx 8.240 \times 10^{-2}\alpha\left(\frac{T}{K}\right)^{-1.35}\left(\frac{\nu}{GHz}\right)^{-2.1}\left(\frac{n_e}{cm^{-3}}\right)^{2.0}\left(\frac{R_s}{pc}\right) \quad [49] \tag{5.12}$$

Where α is a correction factor that accounts for the loss of precision in this approximate expression as compared to its exact counterpart presented earlier. Using table 6 in *P.Z Mezger* and *A.P. Henderson's* work [49], while considering the average electron temperature of the HII regions in this thesis to be $T \approx 8 \times 10^3 K$ and the two VLA observing bands $\nu = 1460, 4890$ MHz, a value of $\alpha \approx 0.9939$ is adopted here.

The above optical depth expression is converted for convenience to SI units. The converted expression reads:

$$\tau_\nu = 2.121 \times 10^{-11}\alpha \left(\frac{T}{K}\right)^{-1.35} \left(\frac{\nu}{Hz}\right)^{-2.1} \left(\frac{n_e}{m^{-3}}\right)^{2.0} \left(\frac{R_s}{m}\right) \tag{5.13}$$

We are now in a position to combine this expression for τ_ν with the S_ν and B_ν expressions presented earlier. The result of the merger reads:

$$F_\nu \approx \left(\frac{4.242\times10^{-11}\ \alpha\pi k_B}{c^2}\right)\left(\frac{T}{K}\right)^{-0.35}\left(\frac{\nu}{Hz}\right)^{-0.1}\left(\frac{n_e}{m^{-3}}\right)^{2.0}\left(\frac{R_s}{m}\right)^{3.0}\left(\frac{d}{m}\right)^{-2.0} \tag{5.14}$$

Re-arranging this expression and incorporating the value of all constants involved yields the following expression for electron number density:

$$\left(\frac{n_e}{m^{-3}}\right) \approx 6.991\times10^{24}\alpha\left(\frac{T}{K}\right)^{0.175}\left(\frac{\nu}{Hz}\right)^{0.05}\left(\frac{F_\nu}{W\ m^{-2}\ Hz^{-1}}\right)^{0.5}\left(\frac{R_s}{m}\right)^{-1.5}\left(\frac{d}{m}\right)^{1.0} \tag{5.15}$$

So far, HII regions have been simply described using an elongated cylindrical shape in order to simplify the integrals presented earlier on. However, this approximation is rather rough, and a spherical shape is more appropriate. A spherical cavity of radius R_s has a larger volume than a cylindrical cavity of radius and length R_s. This means that if we opt for the better, spherical approximation, the emitters contained in the HII region will be re-distributed inside a larger volume of space. Thus, the switch to a spherical approximation is expected to lower the number density by some arbitrary amount.

This indeed what is revealed in table 4 of *P.Z Mezger* and *A.P. Henderson's* work [49]. Specifically, a comparison of the numerical prefactors for the spherical and cylindrical models indicate that the electron number densities using the spherical model will be roughly smaller by $\approx 9.6\%$ than the ones using the cylindrical model. Therefore, a correction factor of $\beta \approx 0.904$ is applied to the above electron number density expression. Combining the two correction factors for the opacity model ($\alpha \approx 0.9939$) and the HII region shape ($\beta \approx 0.904$), yields the final expression for electron number density which reads:

$$\left(\frac{n_e}{m^{-3}}\right) \approx 6.281\times10^{24}\left(\frac{T}{K}\right)^{0.175}\left(\frac{\nu}{Hz}\right)^{0.05}\left(\frac{F_\nu}{W\ m^{-2}\ Hz^{-1}}\right)^{0.5}\left(\frac{R_s}{m}\right)^{-1.5}\left(\frac{d}{m}\right)^{1.0} \tag{5.16}$$

All uncertainties surrounding the aforementioned expression are of symmetric Gaussian nature. The biggest uncertainty contributor is distance, for which uncertainty values start at 5% and can reach as high as 40%. This uncertainty contribution is combined with that of the derived HII region radius due to its dependency on distance ($R_s = d\tan\theta$). A smaller contribution arises from the temperature uncertainty. Since the average temperature of the entire sample is used in calculations, the attached uncertainty is taken to be the standard error of this average. A considerably smaller contribution arises from the flux uncertainty, which is set to 1% based on *M. Fich's* 0.2 mJy estimate of the background noise levels in his VLA paper [16]. All aforementioned uncertainty contributors are combined in the

following unified expression:

$$\delta n_e = |n_e| \sqrt{1.5 \left(\frac{\delta d}{d} \right)^2 + \left(\frac{\delta T}{T} \right)^2 + 1.0 \times 10^{-4}} \tag{5.17}$$

The electron number densities and their uncertainties have been calculated for all HII regions considered in this thesis using equations 5.16 and 5.17 accordingly. The results can be viewed individually for each HII region in appendix table 5, or in a histogram fashion in figure 5.1.

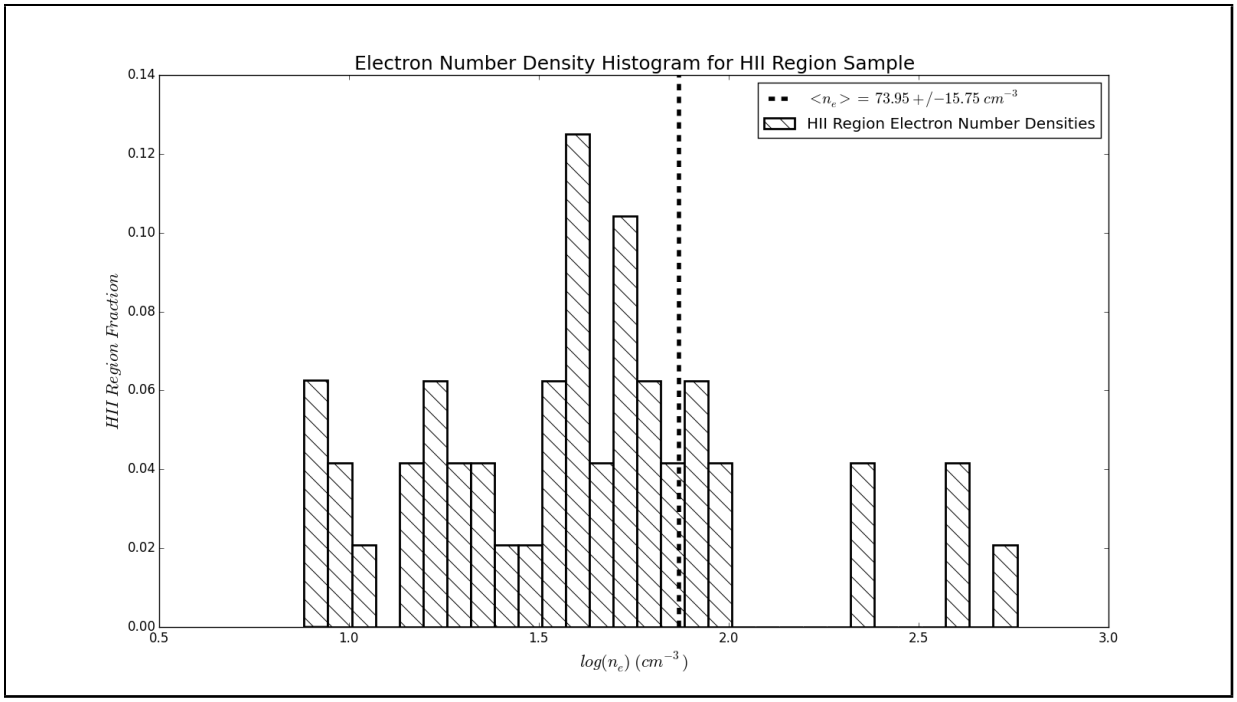

Figure 5.1: Histogram of the electron number densities for the HII regions considered in this thesis. A logarithmic base-10 scale is used on the x-axis and the y-axis is normalized so that the sum of the bins equals unity.

Furthermore, it is of interest to compare the radial size of each HII region to its obtained electron number density. This is exactly what is performed in figure 5.2, where the physical radial size of each HII region is compared to its electron number density estimate. Evidently, larger HII regions display progressively lower electron number densities.

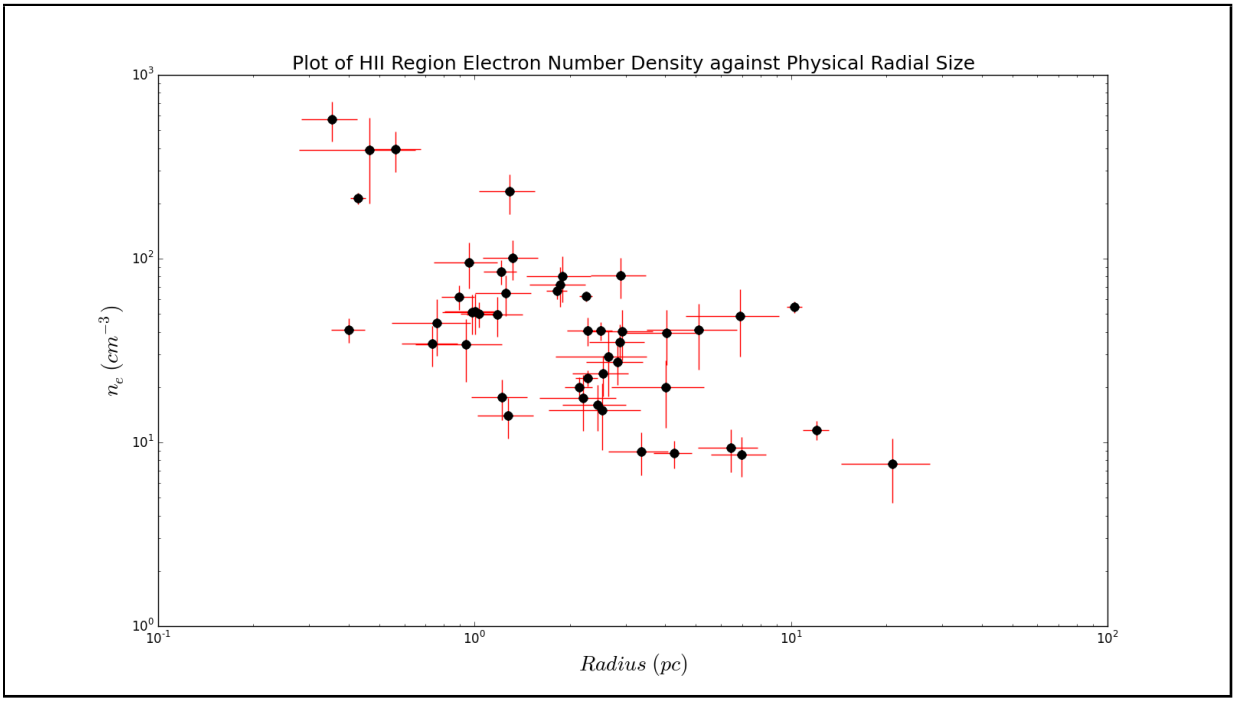

Figure 5.2: Plot of HII region electron number densities against physical radial size. A decrease in electron number density with radial size is observed.

Electron number densities can be subsequently converted into hydrogen number densities by subtracting the electrons contributed from other ionized elements present in the HII region nebula. In order of importance then, these contributors are ions of Helium, Oxygen, Nitrogen, Sulfur and to a much lesser extent, other heavier metals. However, the contribution from Helium surpasses by far the contribution from all heavier ions combined. This can be seen when comparing the abundance of each ion with respect to ionized hydrogen, where He^+ is roughly 100 times more abundant than any ionized version of any heavier metal. This permits approximating the hydrogen number density using the following expression:

$$n_H \approx n_e\left(1.0 - \frac{He^+}{H^+} - \frac{He^{++}}{H^+}\right) \tag{5.18}$$

Regarding the contribution of Helium to free electrons in a typical HII region, I consider works from *M. Fich* [8] and *L. Deharveng* [35] which suggest that Helium can be entirely singly-ionized (He^+) within an HII region if the host star is hotter than 39500K (class

"O6.5V" and higher). Doubly-ionized Helium He^{++} is very rare and requires even hotter stars.

A quick look at table 6 reveals that with the exception of 3 stars the entire associated star sample is cooler than 39500K. For this reason, I assume $He^{++}/H^{+} \approx 0$ for the HII regions considered in this thesis. Regarding He^{+} on the other hand, it is known to have an abundance with respect to ionized hydrogen than can range between 0 and 0.1. (G.R Bell [8]) The former value is approached the lower into the "B" class a host star is classified. The latter value is approached the closer a star is to class O6.5V. Beyond this value, all Helium is presumably singly-ionized, and the abundance fraction remains near 0.1 for all hotter classes. Once again, a quick look at table 6 reveals that the majority of our associated stars occupy classes between "O7V" and "B3V". It is then reasonable to use an abundance value somewhere between the two extremes. I use a value of 0.06 as was done for the sample of HII regions considered in the work by *G.R Bell* et al [8].

Putting everything together, yields the following hydrogen number density expression:

$$n_H \approx (1.0 - 0.06 - 0)n_e \tag{5.19}$$

$$n_H \approx 0.94 n_e \tag{5.20}$$

If one substitutes the electron number density equation from earlier on, the complete hydrogen number density equation can be written as:

$$\left(\frac{n_H}{m^{-3}}\right) \approx 5.9042\times10^{24}\left(\frac{T}{K}\right)^{0.175}\left(\frac{v}{Hz}\right)^{0.05}\left(\frac{F_\nu}{W\ m^{-2}\ Hz^{-1}}\right)^{0.5}\left(\frac{R_s}{m}\right)^{-1.5}\left(\frac{d}{m}\right)^{1.0} \tag{5.21}$$

The uncertainty contributors are the same as those present in the electron number density calculation, with the addition of an $\approx 5\%$ uncertainty from the Helium abundance value used. Thus, if required, the uncertainty in the hydrogen number density can be calculated as follows:

$$\delta n_H = \left|n_H\right|\sqrt{1.5\left(\frac{\delta d}{d}\right)^2 + \left(\frac{\delta T}{T}\right)^2 + 6.0\times10^{-4}} \tag{5.22}$$

Equipped then with knowledge regarding the Temperature "T", radius "R_s", distance "d" and integrated flux "F_v" in some radio frequency "ν" of a particular HII region, one is in a position to deduce its electron and hydrogen number density. This naturally leads into the development of a cumulative mass expression, a topic that will be tackled in the following subsection. For a closer look at the results of this section, see section 6.1.2.

5.2.2 HII Region Masses

In this subsection, I develop the recipe used for calculating the gas mass density and cumulative gas mass of HII regions. To begin, one needs to consider which atomic species contribute the most to the mass of an HII region by virtue of their abundance. In order of decreasing abundance, these atomic species are Hydrogen, Helium, Oxygen, Nitrogen and Sulfur. The expression for mass density can then initially be expressed as follows:

$$\rho = n_H m_H + n_{He} m_{He} + n_O m_O + n_N m_N + n_S m_S \tag{5.23}$$

Where n_H and m_H indicate the number density and mass of Hydrogen ions, n_{He} and m_{He} the number density and mass of Helium atoms, n_O and m_O the number density and mass of Oxygen atoms, n_N and m_N the number density and mass of Nitrogen atoms and finally n_S with m_S the number density and mass of Sulfur atoms.

This expression can be re-written in terms of the abundances of each element with respect to hydrogen as follows:

$$\rho = n_H \left[m_H + \left(\frac{He}{H}\right) m_{He} + \left(\frac{O}{H}\right) m_O + \left(\frac{N}{H}\right) m_N + \left(\frac{S}{H}\right) m_S \right] \tag{5.24}$$

Note that the abundance of each element in this equation incorporates the sum of its neutral and all ionized iterations. The next step is to obtain the necessary information regarding the mean atomic mass and abundance of each element involved.

For the atomic masses, the mass of the most abundant isotope is used for each element. All masses are expressed in terms of the mass of atomic hydrogen. The values used can be found in any astronomical reference and are the following:

$$m_H = 1.00794\ amu \tag{5.25}$$
$$m_{He} = 4.002602\ amu = 3.97107\ m_H \tag{5.26}$$
$$m_O = 15.999\ amu = 15.8730\ m_H \tag{5.27}$$
$$m_N = 14.0067\ amu = 13.8964\ m_H \tag{5.28}$$
$$m_S = 32.0650\ amu = 31.8124\ m_H \tag{5.29}$$
$$\tag{5.30}$$

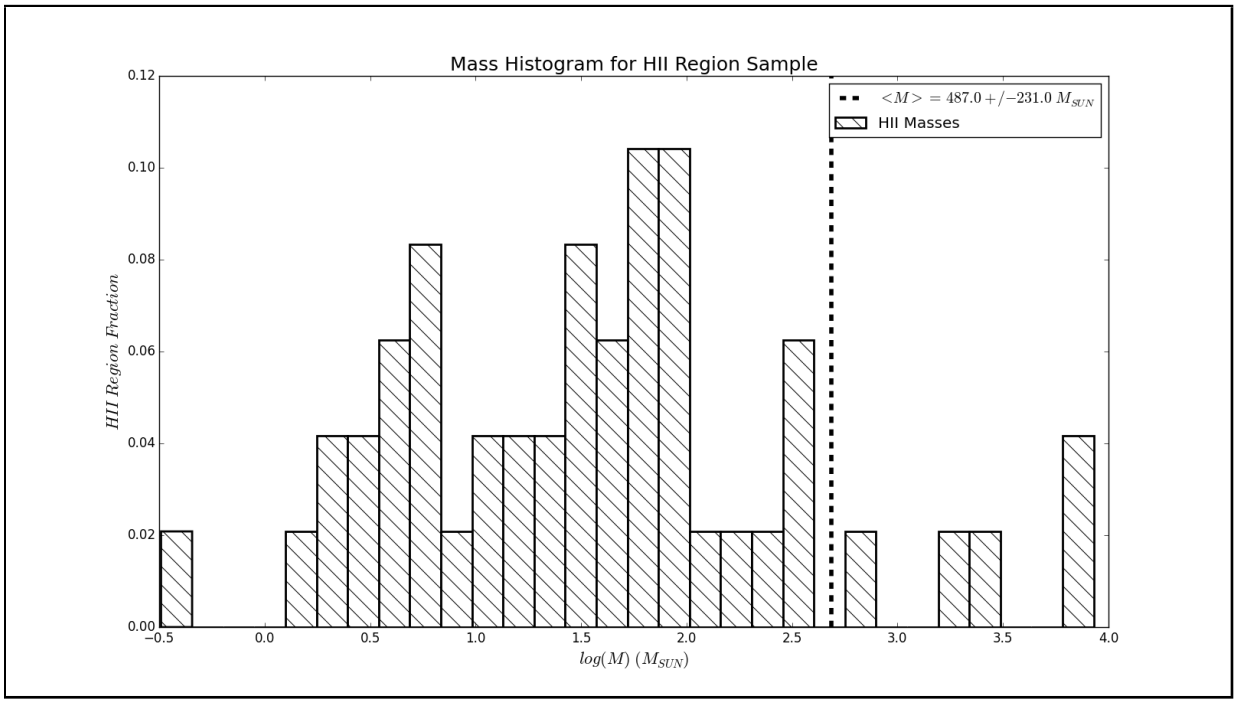

Figure 5.3: Histogram of the gas masses for the HII regions considered in this thesis. A logarithmic base-10 scale is used on the x-axis and the y-axis is normalized so that the sum of the bins equals unity.

For the atomic abundances, all elements are compared against hydrogen. The values used are taken from *M. Fich's* work [8] and are the following:

$$\left(\frac{He}{H}\right) \approx 0.06 \tag{5.31}$$

$$\left(\frac{O}{H}\right) \approx 10^{-3.35} \tag{5.32}$$

$$\left(\frac{N}{H}\right) \approx 10^{-4.24} \tag{5.33}$$

$$\left(\frac{S}{H}\right) \approx 10^{-4.83} \tag{5.34}$$

$$\tag{5.35}$$

Substituting the above values into the mass density expression, one obtains:

$$\rho \approx 1.24696\ n_H m_H \quad kg\ m^3 \tag{5.36}$$

$$\rho \approx 1.17210\ n_e m_H \quad kg\ m^3 \tag{5.37}$$

$$\rho \approx 1.96184 \times 10^{-27}\ n_e \quad kg\ m^3 \tag{5.38}$$

$$\tag{5.39}$$

Substituting the expression for electron number density developed in the previous subsection, the final expression for gas mass density reads:

$$\left(\frac{\rho}{kg\ m^{-3}}\right) \approx 1.2323 \times 10^{-2}\left(\frac{T}{K}\right)^{0.175}\left(\frac{v}{Hz}\right)^{0.05}\left(\frac{F_\nu}{W\ m^{-2}\ Hz^{-1}}\right)^{0.5}\left(\frac{R_s}{m}\right)^{-1.5}\left(\frac{d}{m}\right)^{1.0} \tag{5.40}$$

Regarding uncertainty, the contributors are the same as those present in the hydrogen number density calculation from the previous subsection. Thus, if required, the uncertainty of an HII region's gas mass density can be estimated as follows:

$$\delta\rho = \left|\rho\right|\sqrt{1.5\left(\frac{\delta d}{d}\right)^2 + \left(\frac{\delta T}{T}\right)^2 + 6.0 \times 10^{-4}} \tag{5.41}$$

At this point, it is simple to obtain the total gas mass through multiplication of the density with the HII region's equivalent volume. Using a spherical shape approximation, the total gas mass can be obtained as follows:

$$M = \rho V \tag{5.42}$$

$$M \approx \frac{4\pi R_s^3 \rho}{3} \tag{5.43}$$

Substituting the previous expression for gas mass density, the final equation for cumulative gas mass can be expressed as follows:

$$\left(\frac{M}{kg}\right) \approx 5.1616 \times 10^{-2}\left(\frac{T}{K}\right)^{0.175}\left(\frac{v}{Hz}\right)^{0.05}\left(\frac{F_\nu}{W\ m^{-2}\ Hz^{-1}}\right)^{0.5}\left(\frac{R_s}{m}\right)^{1.5}\left(\frac{d}{m}\right)^{1.0} \tag{5.44}$$

Regarding the uncertainty, the contributors are the same as those considered in the gas mass density calculation. Note that even though the exponent of R_s changes in this calculation, its magnitude is still the same. The gas mass uncertainty can then be estimated using:

$$\delta M = \left|M\right|\sqrt{1.5\left(\frac{\delta d}{d}\right)^2 + \left(\frac{\delta T}{T}\right)^2 + 6.0 \times 10^{-4}} \tag{5.45}$$

The total gas masses and their uncertainties have been calculated for all HII regions considered in this thesis using equations 5.44 and 5.45 accordingly. The results can be viewed individually for each HII region in appendix table 5, or in a histogram fashion in figure 5.3.

Furthermore, it is of interest to investigate the effect of HII region radial size to obtained total mass. This is what is performed in figure 5.4, where the physical radial size of each HII region is compared to its total mass estimate. Evidently, larger HII regions display larger total mass values. This roughly linear, log-log behavior is expected, as the particle number densities of this HII region sample define a narrow range of values and are quite similar. For a closer look at the results of this and the previous section, see section 6.1.2.

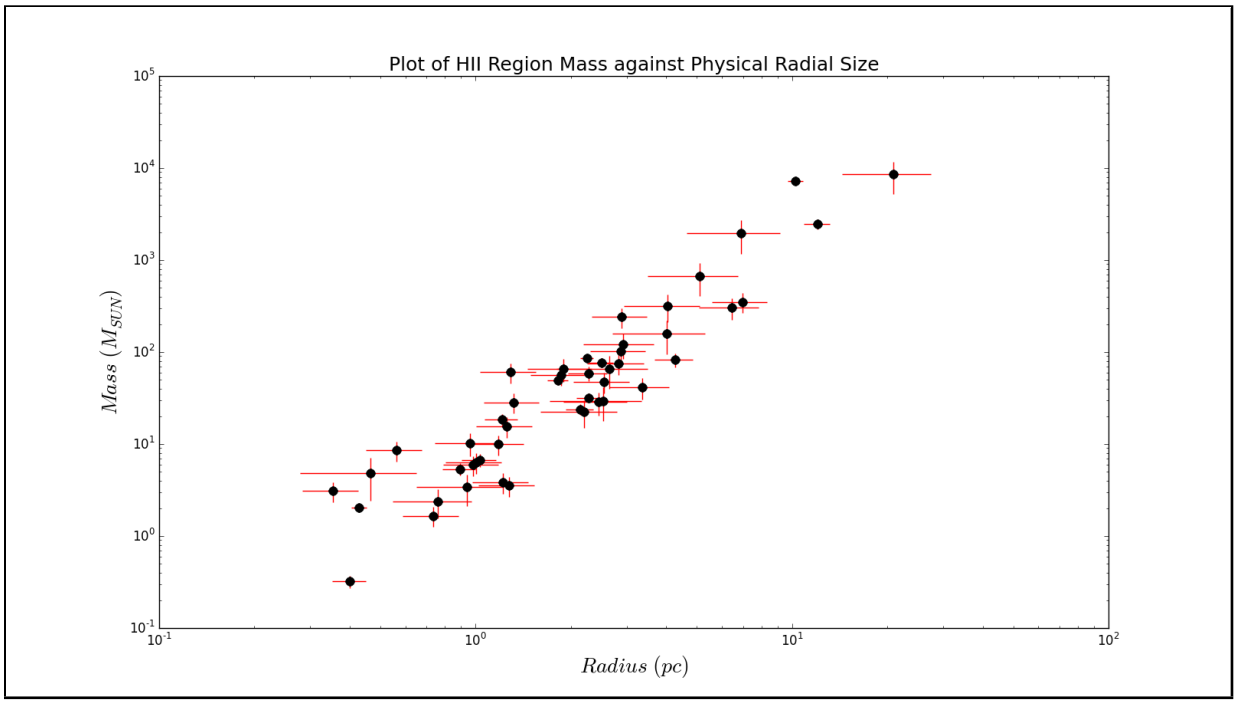

Figure 5.4: Plot of HII region total mass against physical radial size. An increase in total mass with radial size is observed.

5.3 Effect of HII regions on Molecular Clumps

In this section, I present some important effects induced on molecular clumps due to the nearby presence of HII regions. To begin, evidence pointing to enhanced molecular clump formation at the boundaries of HII regions will be presented and discussed. Then, the dynamic interaction between the molecular and ionized gas will be investigated. Finally, the section will close with an in-depth investigation of a potential heating effect induced by the HII regions themselves onto their associated molecular clumps.

5.3.1 Clump Formation

In this subsection I analyze the location of SCUBA-2 molecular clumps with the goal of addressing the original hypothesis of this thesis, which states that increased molecular clump condensation is expected in the vicinity of HII region boundaries due to the collect-collapse process taking place, with "boundary" here referring to the outer edge of the HII region's ionized gas.

A second expectation is that progressively fewer clumps should be identified while moving radially inward toward the center of an HII region due to the progressively increasing amount of ionizing radiation from the exciting, massive star(s). Within a certain range, this radiation can actually lead pre-existing clumps into collapse through the RDI process (Bisbas,2011 [55]). However, once the level of ionizing radiation exceeds this range, clumps are lead into complete evaporation.

In order to investigate the first expectation, I use center-to-center separation distance measurements between cores and associated HII regions. This was previously performed in section 3.7.1 for the purpose of segregating cores that may not be associated with their originally assigned HII region. Having done this segregation and considering a strictly homogeneous "Sh-2" and "BFS" HII region sample, the final core-to-HII-Region scaled distance can be viewed in figure 5.5.

Inspection of this histogram shows an obvious spike in the vicinity of $\theta_{SCALED} = 1$. This translates to HII region boundaries providing a favorable location for molecular clump formation, in alignment with the original hypothesis. A progressive decrease in clumps at decreasing values of θ_{SCALED} below this value also supports the second claim made earlier in this section.

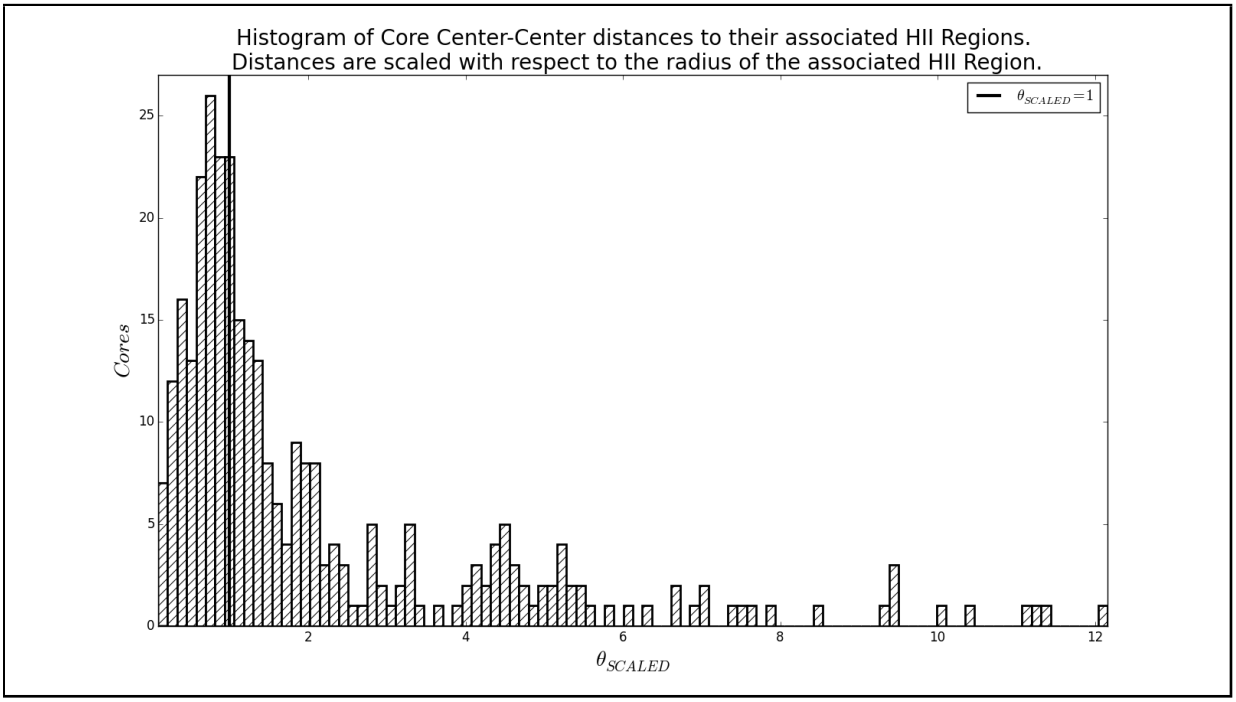

Figure 5.5: Histogram of each SCUBA-2 core's center-to-center distance to its associated HII region. Only the cores that passed the cutoff criterion in section 3.7.1 are presented here. The distances are scaled by the radial size of the associated HII region. A noticeable excess exists in the vicinity of $\theta_{SCALED} = 1$

However, due to the fact that the data analyzed for the production of this result come from pre-existing projects and do not all cover the nearby exterior area of their identified HII regions, a complex bias is in place. For a more detailed discussion, see section 6.1.6.

5.3.2 Gas Dynamics

In this section I investigate the hypothesis that molecular clumps in the vicinity of HII regions experience a compression effect from the expansion of the latter structure. This compression effect is suspected to take place both for accumulating molecular material that is being carried forward in the ionization-shock front cradle, as well as full-fledged clumps that have been left behind by the two fronts inside the HII region.

In order to assert this hypothesis, I compare the average pressure of all HII regions to

their associated clumps. Specifically, the average pressure of a clump's cloud component is of interest as it is suspected to be approximately isothermal and in direct contact with the material of the HII region, as opposed to the cores which are also suspected to be isothermal but are embedded deep within the clump structure. Evidence supporting the compression hypothesis will come from observing cloud average pressures being generally lower than those of their associated HII regions.

To obtain the average pressure of an HII region, the ideal gas law is implemented in order to give the following equation of state:

$$P = nk_BT_{HII} = (n_i + n_e)k_BT \tag{5.46}$$

Where n indicates the HII region's total particle number density, T its average temperature, n_i its ion number density and n_e its free electron number density.

Working under the reasonable assumption that every atomic element inside the HII region is at most singly-ionized, the ionic and electron number densities will be roughly equal. This is a reasonable assumption as subsequent ionizations after the first require extremely hot star temperatures and are rather rare. The average HII region pressure is then simply expressed as:

$$P \approx 2n_ek_BT \tag{5.47}$$

The electron number densities are already obtained in subsection 5.2.1. As for the electron temperatures, investigation of the HII region electron temperatures in the work of *A.L Rudolph et al* [8] reveals that these span a range from 4800K (Sh2-48) to 11200K (Sh2-138) and there is evidence for a galactic scale temperature gradient, where HII regions closer to the galactic center tend to be cooler than those toward the galactic outskirts.

However, the galactocentric distances of the HII regions in this thesis are quite large, spanning a range of $\approx$ 6-16 kpc. This means that the electron temperature of these is expected to lie on the higher end of the aforementioned temperature range. In addition, the entire temperature range is less than an order of magnitude wide, meaning that an average value is well representative of the temperature of the individual HII regions.

Since a lot of HII regions in this thesis do not have individual electron temperature estimates in the paper by *A.L Rudolph et al* [8], and due to the reasons mentioned above, I decide to calculate the average electron temperature of all Sharpless HII regions found in this paper and use it as an approximation to the electron temperature of each HII region in this thesis. This average temperature is determined to be $< T > \approx 8725K \pm 207K$.

In regards of the molecular clumps, the calculation recipe for the average pressure of cores, clouds and overall clump composites has been presented and discussed in subsection 3.3.5. Keep in mind that the clouds and cores are considered to be approximately isothermal.

Once the average pressure for each HII region as well as the average pressure of each associated cloud is obtained, a comparison is carried on a cloud-to-HII Region basis. The result of this comparison is displayed in figure 5.6. Note the distinct horizontal arrangement of points. This is due to the fact that most HII regions have multiple clump composites associated with them. The clouds of these clump composites are all individually compared to the associated HII region itself.

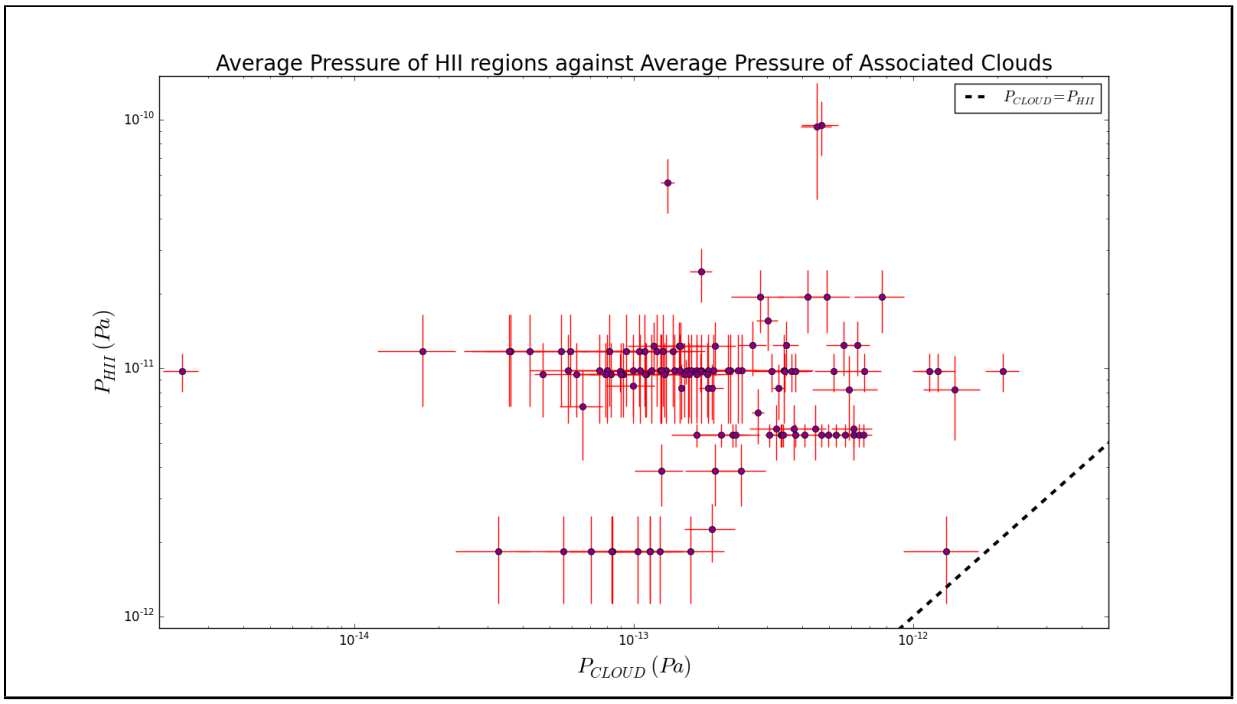

Figure 5.6: Log-Log plot of each cloud's average pressure against the average pressure of its most likely associated HII Region. The dashed line indicates HII Region and cloud average pressure equivalence. Evidently, the HII regions exhibit much larger average pressures than their associated clouds, with few exceptions.

It is evident that all points lie above the pressure equivalence line, meaning that all SCUBA-

2 cloud segments in the comparison have a lower average pressure than their associated HII region. This strongly favors a compression effect from the presence of HII regions in the vicinity of molecular clumps. Such a compression effect acts in alignment with gravity, putting HII regions in the list of mechanisms acting in favor of molecular clump collapse. Finally, the HII region pressures are commonly seen to be 2-3 orders of magnitude greater than those of the outer layers of their associated clumps. For a further discussion of these results, see section 6.1.7.

5.3.3 HII Region Heating

In this section, I attempt to identify any heating effect from the presence of HII regions in the vicinity of molecular clumps. To accomplish this, I compare the position of each HII region's center to that of its associated clump components (cores and cloud segments), all while keeping track of the average temperature of these components. Two different comparison methods are used in pursuit of detecting evidence for a heating effect, namely, a comparison of:

1. Scaled Angular Distance vs Average Temperature
2. Physical Distance vs Average Temperature

The first approach involves obtaining the center-center angular separation of each HII region to each of its associated cores and cloud segments, then scaling that separation by the radial size of the associated HII region, a process identical to that used in section 5.3.1. The expectation is that clump components existing near the boundary of their associated HII region ($\theta_{SCALED} \approx 1$) will display higher average temperature estimates. The result of the comparison is displayed in figure 5.7. It appears that there is no strong indication of a temperature dependency on the core/cloud-to-HII region scaled angular separation.

The second method involves converting the center-to-center angular separation distance into a physical distance. It should be noted that this physical distance is a 2-dimensional, lower limit to the true distance due to the lack of information regarding the radial distance component. The expectation is that clump components at smaller physical distances will display a higher average temperature estimate. The result of the comparison is displayed in figure 5.8. Evidently, both clump components appear to become progressively warmer at physical separation distances $\lessapprox 10$ *pc*.

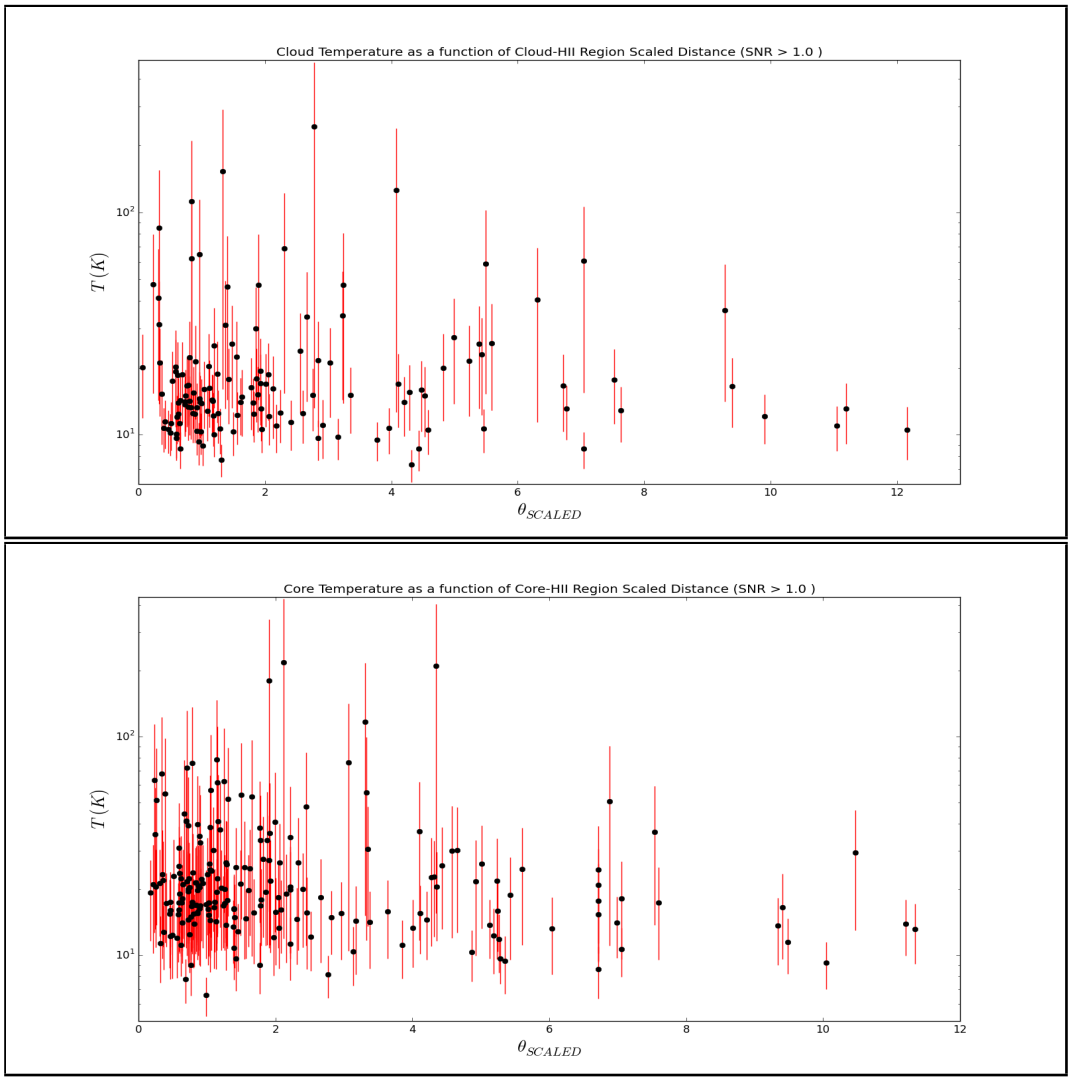

Figure 5.7: Plot of the HII region to cloud (Top) and core (Bottom) center-to-center, **scaled angular distances** against average temperature.

In conclusion, while the scaled, angular, center-to-center distance approach provides an inconclusive result, the physical center-to-center distance approach displays a decreasing temperature trend with increasing physical separation distance. The effect can be modeled, however its significance is a very complicated statistical problem due to the asymmetric uncertainties in the clump component temperatures. Further discussion of this result is held in section 6.1.4.

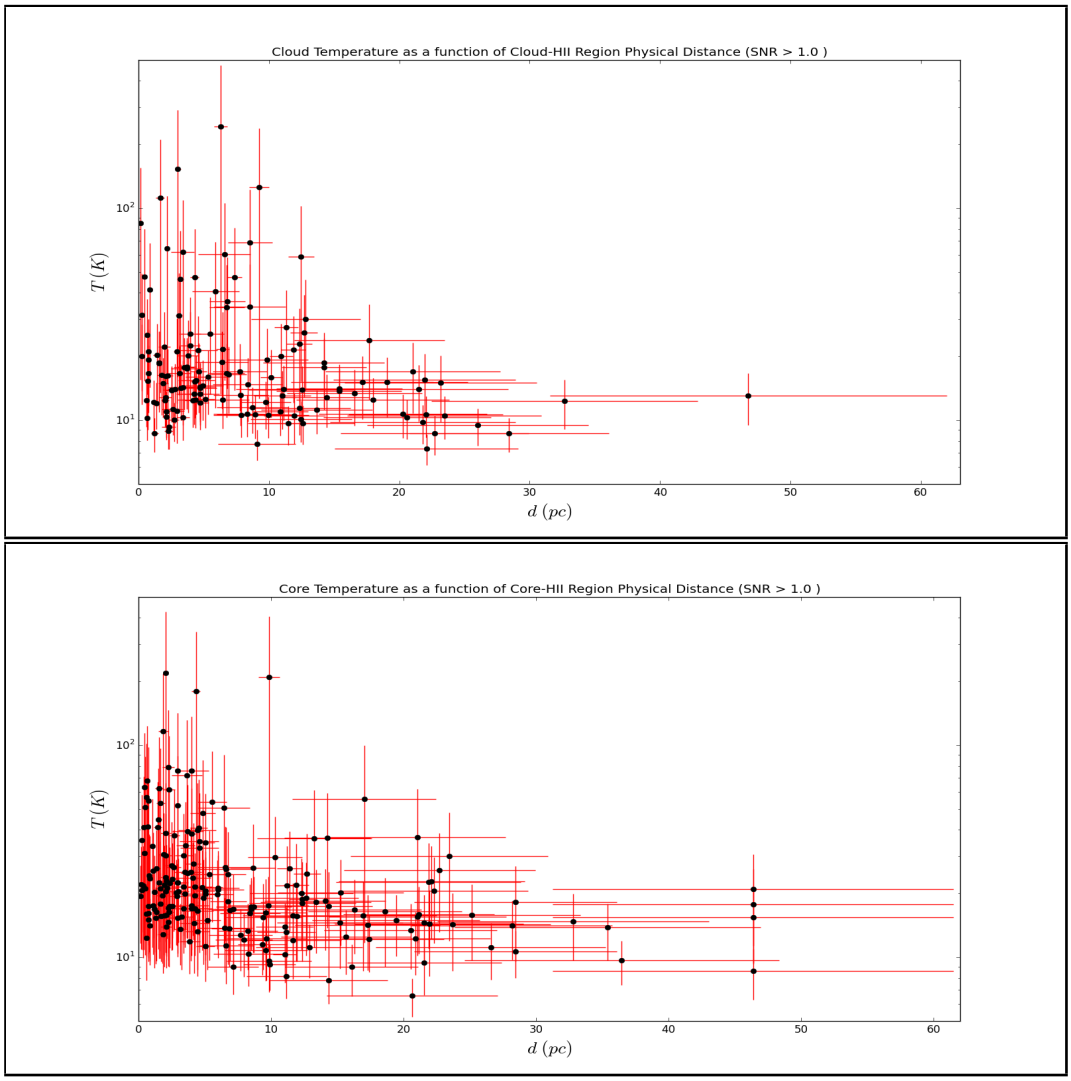

Figure 5.8: Plot of the HII region to cloud (Top) and core (Bottom) center-to-center, **physical distances** against average temperature.

5.4 OB Star Heating

In this section, I try to identify any potential heating effect from the presence of massive, OB stars in the vicinity of molecular clumps. This is accomplished by comparing the central position of each clump component (cores and cloud segments) to that of their associated OB star, against the average temperature of these components. In addition,

the total incident flux from the nearest OB stars to each associated clump's components is calculated and also compared against the average temperature of these components. In synopsis then, the two different approaches involve a comparison of:

1. Physical Distance vs Average Temperature
2. Incident Flux vs Average Temperature

In the first method, the central positions of all identified OB stars are compared to those of each clump component for the purpose of establishing their angular separation distance. The OB star with the smallest angular separation distance is labeled as "associated" with a particular clump component. The angular distance is then converted to a physical distance in the same manner as was done previously for the HII regions. Once again, these physical distances are 2-dimensional, lower limits to the true distance due to the lack of the radial component from the measurement.

The expectation is that lower center-to-center physical separation distances will exhibit larger temperatures. The result from the comparison is presented in figure 5.9. Evidently, both clump components appear to become progressively warmer at physical separation distances $\lessapprox 10\ pc$.

The second and most meaningful method of searching for a heating effect comes from comparing the incident flux from the nearest OB stars to a particular clump component.

To calculate the total incident OB star flux onto a particular clump component, the fluxes from all identified OB stars within a radius of 1 degree need to be calculated. The angular distance of each of these stars is converted to a physical distance using right-angle triangle geometry. Remember that this physical distance is a lower limit to the true distance due to the lack of the radial component, meaning, all incident fluxes calculated here are upper limits to the true incident flux. The luminosity of each of these stars is obtained from matching its classification to a luminosity-mass table. The incident flux contribution is then easily obtainable for each of the stars, and the total incident flux comes simply from summing these individual fluxes together. The total incident flux onto a clump component is then compared against its average temperature.

The expectation is that an increasing total incident flux yields progressively higher average temperatures. Also, the outer part of a clump (i.e cloud) is expected to be much more susceptible to this heating effect than the inner parts (i.e cores). The result of the

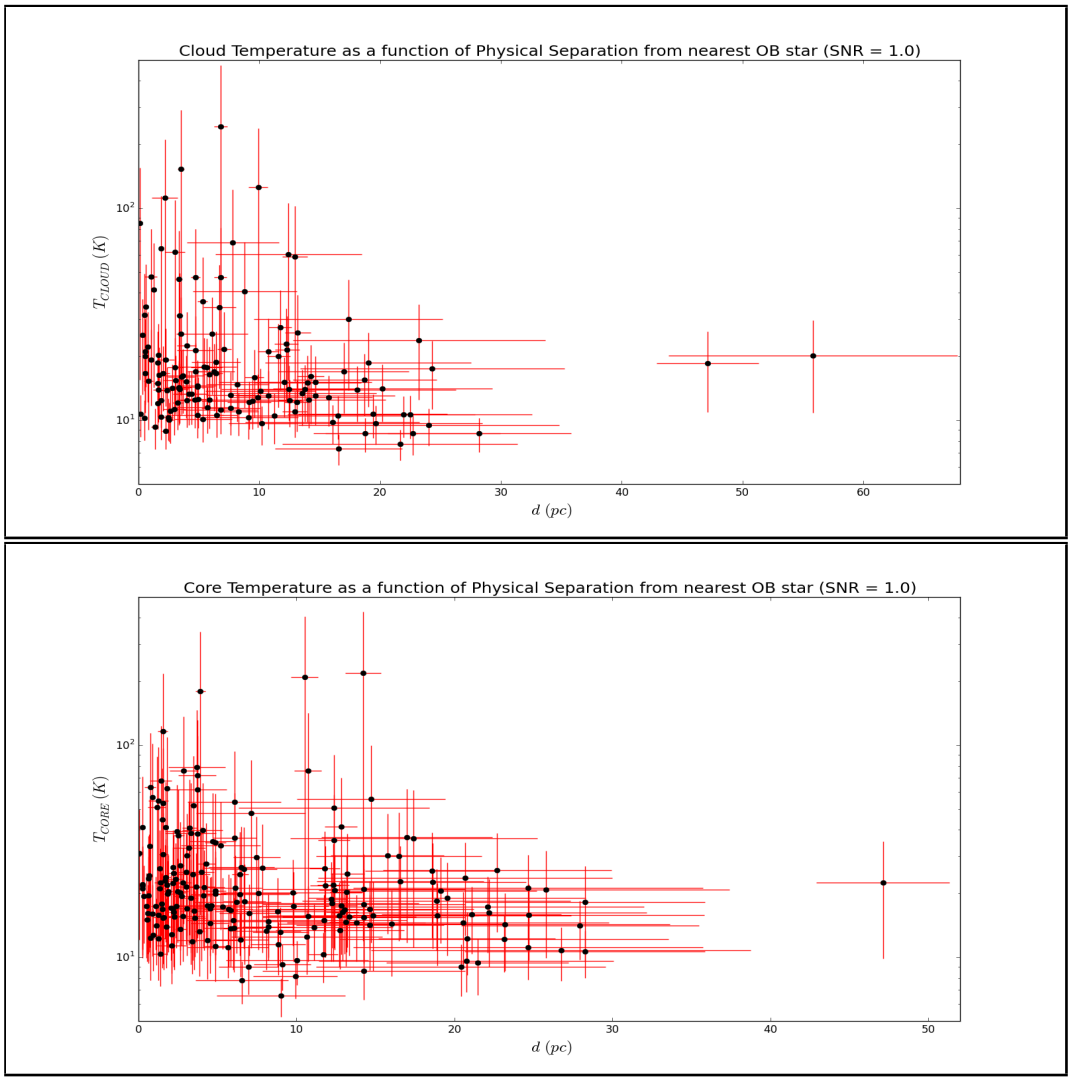

Figure 5.9: Plot of the OB star to cloud (Top) and core (Bottom) center-to-center, **physical distances** against average temperature.

comparison is presented in figure 5.10. Evidently, no significant evidence for a heating effect is obtained from this approach.

In conclusion, the incident flux approach is inconclusive. However, similarly to the HII region case, the center-to-center physical separation distance approach displays a decreasing temperature trend with increasing physical separation distance. Once again, the effect

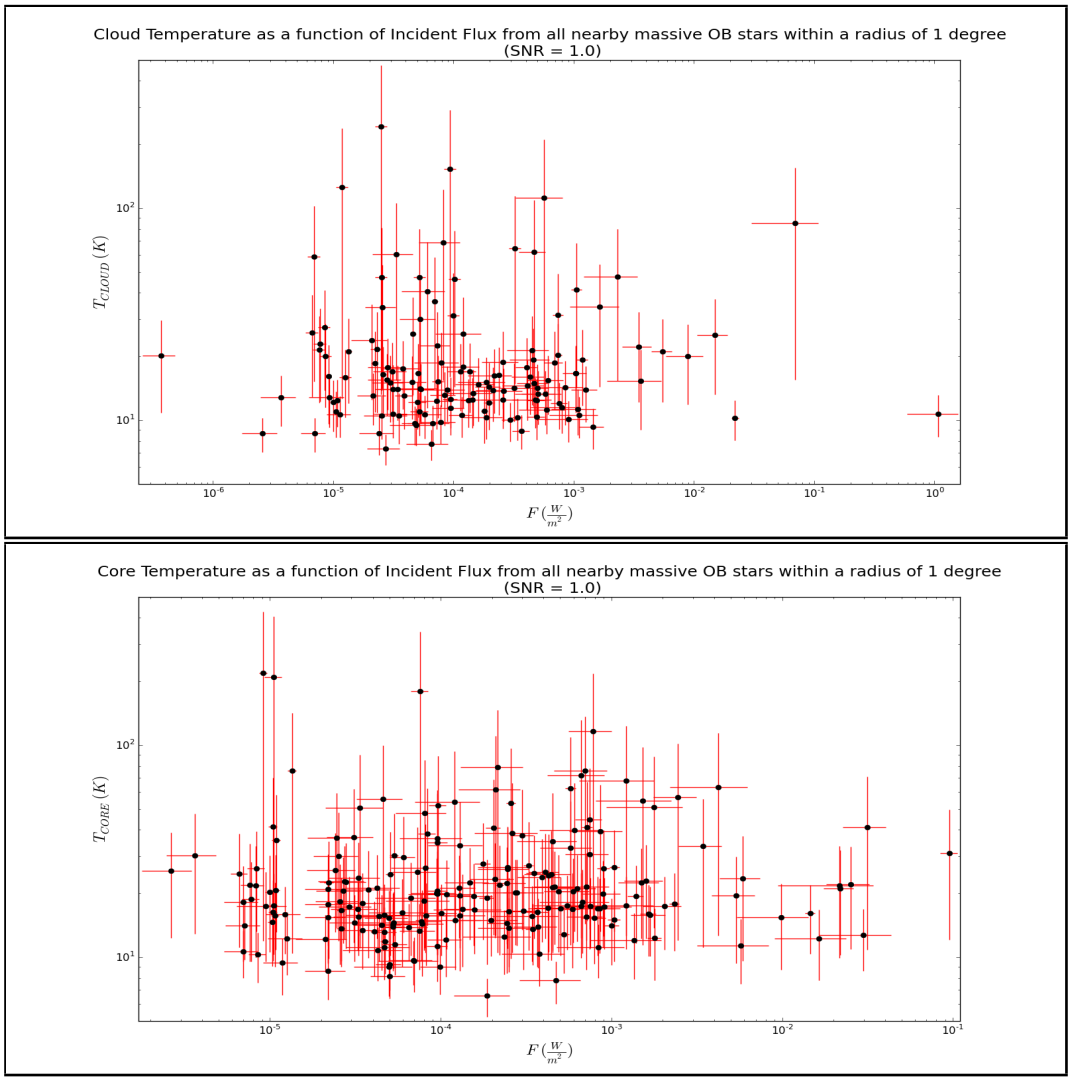

Figure 5.10: Plot of the **total incident flux** from nearby OB stars to cloud (Top) and core (Bottom) objects against average temperature.

can be modeled, however its significance is a very complicated statistical problem due to the asymmetric uncertainties in the clump component temperatures. For a further discussion, see section 6.1.4.

5.5 Cloud & Core Analysis

In the following sections I will perform an in-depth investigation of the cloud-core systems. It is of great interest to investigate how the number and column densities of these structures affect their average temperatures as this will reveal how important external and internal heating mechanisms really are.

A comparison between core and cloud temperatures is also of great interest since such comparison can indicate what fraction of cores from the sample is potentially star-forming. Supplementing this, a comparison between the temperature of clouds and the mass of their embedded cores can reveal any correlation between the heat supplied by clouds and the coagulation of mass in their embedded cores.

5.5.1 External and Internal Heating

One of the goals of this thesis is to determine the significance of internal and external heating mechanisms in molecular clump systems. Identifying which type of heating mechanism plays a more important role in molecular clump systems leads to a better, richer understanding of the early stages of star formation.

A comparison between average temperature and average H_2 column density can reveal if external heating is significant or not for the molecular clump sample of this thesis. An observed decrease in temperature with increasing column density would align with the expectation that denser structures extinguish a larger fraction of incoming radiation, and their interiors are independent from a heating effect induced by this radiation. This would suggest that such structures are indeed not significantly affected by external heating mechanisms and any observed heating effect should be part of an internal process.

The result of this comparison is presented in figure 5.11. Evidently, cloud temperatures decrease with increasing column density. The same happens to core structures, however to a lesser extent, with the result also suffering from higher amounts of noise for those. This points to clouds and cores not being particularly affected by external heating mechanisms, a result that is in direct alignment with the previous HII region and OB star heating effect investigation.

Supplementing this comparison, a comparison between average temperature and average H_2 number density can clarify if gravitational contraction is taking place in core struc-

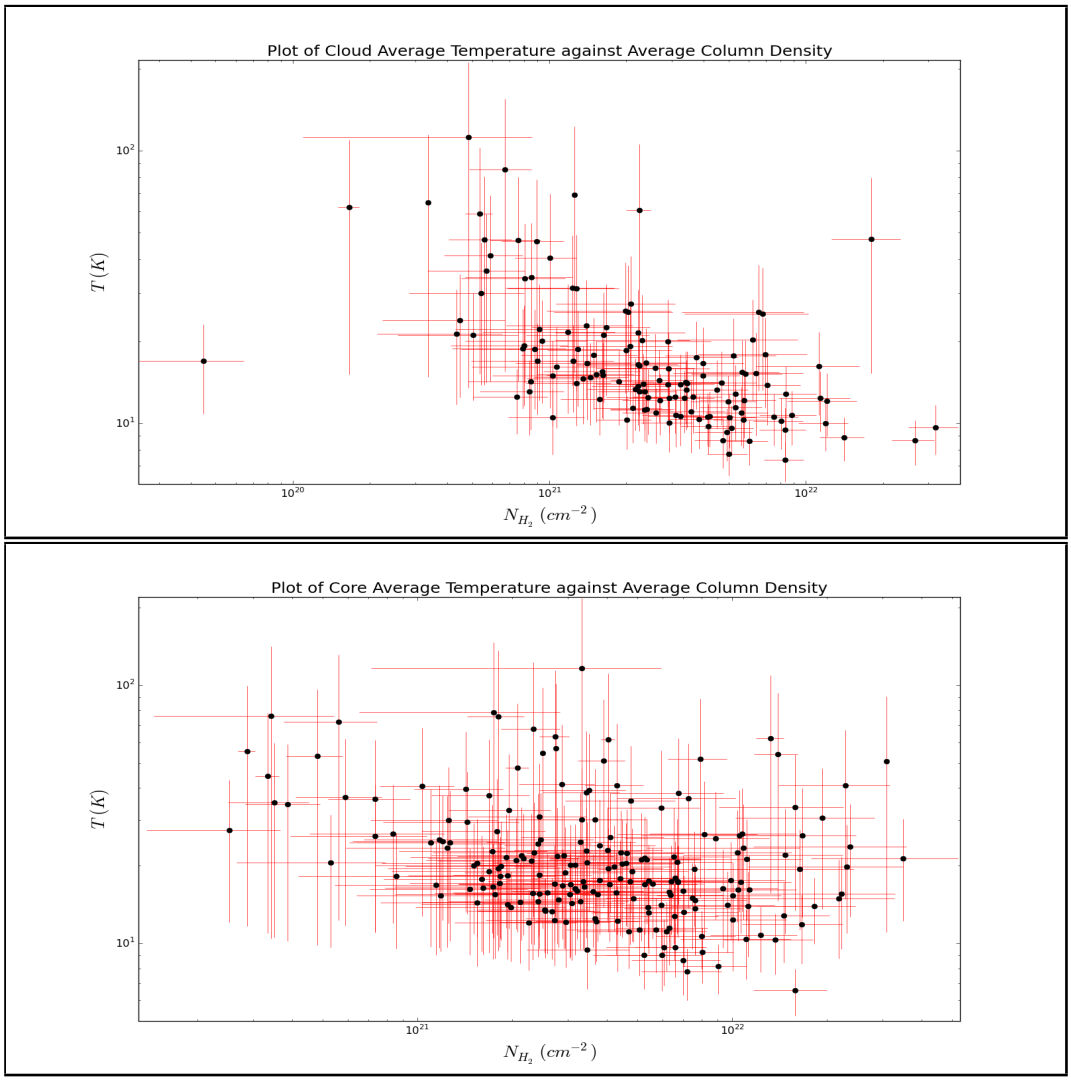

Figure 5.11: Plot of the cloud (Top) and core (Bottom) average temperature against average column density.

tures. Cores and clouds with higher number densities suggest they are contracting, as they all originate from a uniform GMC with a nearly constant H_2 number density. Based on the previous result that internal heating mechanisms are dominant, an observation of denser cores being hotter would provide evidence for gravitational contraction taking place.

The result of this comparison is presented in figure 5.12. Evidently, cloud temperatures

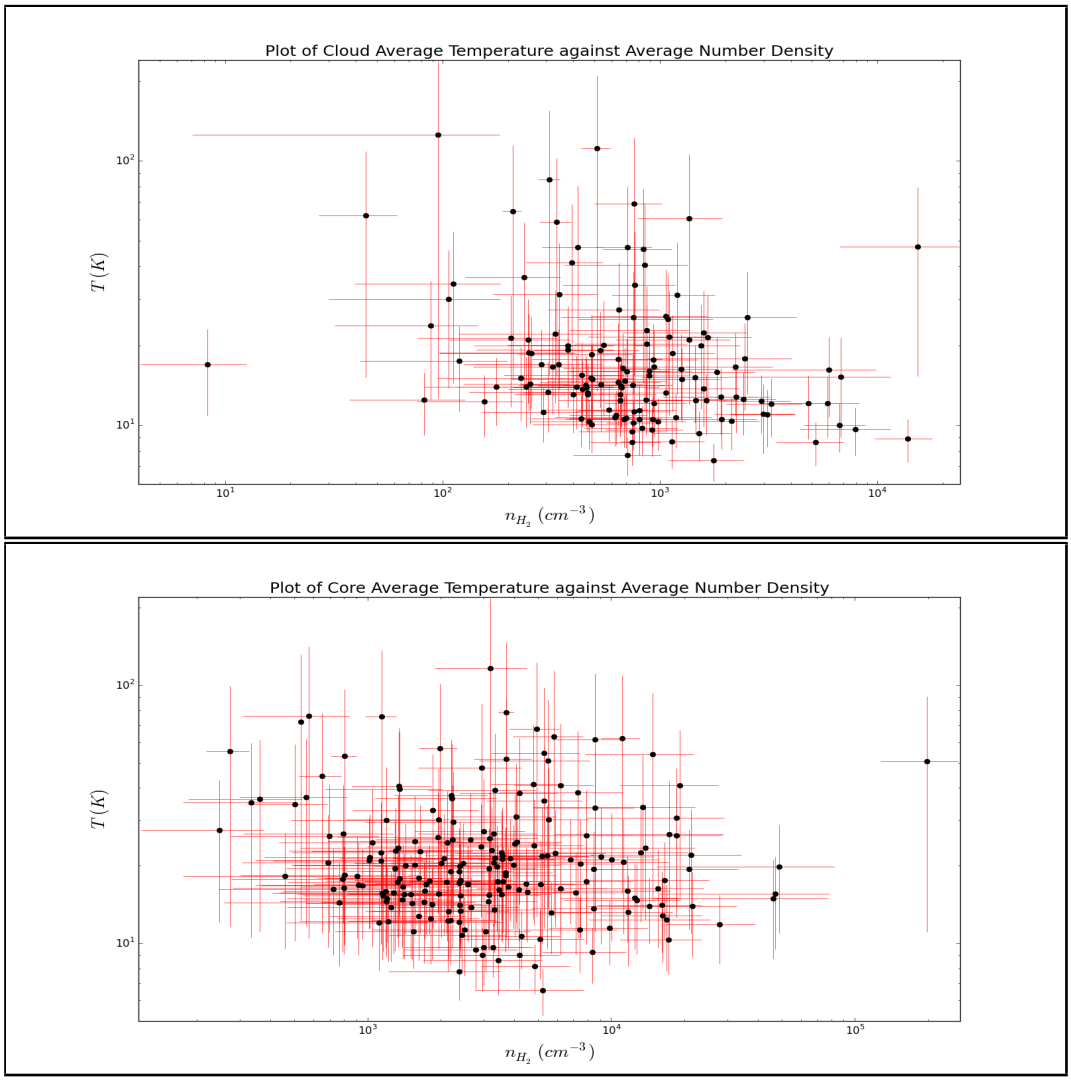

Figure 5.12: Plot of the cloud (Top) and core (Bottom) average temperature against average number density.

decrease with increasing number density, an observation in alignment with various cooling models suggesting a strong negative power dependence of cloud temperature to density. No significant change is observed for the cores, but the noise is very high for a conclusive judgment to me made. This is interesting, as we're seeing clouds becoming colder as they get denser, but cores remaining relatively unaffected from changes in density. This is likely due to the fact that outer clump layers (clouds) cool much more efficiently with increas-

ing density and the fact that a large fraction of inner clump layers (cores) are actually contracting, producing heat, but also cool in a convective manner to their surrounding clouds, dissipating heat in the process. For further discussion of the results in this and the previous two sections, see section 6.1.4.

5.5.2 Star Forming Cores

In this subsection, I investigate the fraction of SCUBA-2 cores that exhibit evidence for collapse and star-formation taking place. It is suspected that a considerable portion of the SCUBA-2 cores are in the process of collapse and traversing the early stages of star formation.

In order to differentiate which cores are potentially star-forming and which are not, a temperature analysis is performed. Specifically, the temperature of SCUBA-2 clouds is directly compared to that of their embedded cores. Cores that are contracting are heated by virtue of their collapse and are expected to naturally exhibit higher average temperatures than their surrounding cloud medium. Finally, such contracting cores rapidly reach a quasistatic protostar stage whose emission is dominated from the accretion of surrounding core and potentially cloud material.

The result of the temperature comparison is displayed in figure 5.13. It is evident that the majority of points lie above the core-cloud temperature equivalence line. This is in line with the initial hypothesis that a large portion of SCUBA-2 cores are undergoing star-formation.

In order to provide a more detailed look, the same temperature comparison is done in a histogram fashion, where the temperature of each core is compared to that of its surrounding cloud and the resulting fraction is histogrammed. The different temperature fraction bins are distinguished using color coding in order to indicate how likely the cores belonging to these are to be collapsing and consequently star-forming purely on the basis of their temperature. The result is displayed in figure 5.14.

One needs to keep in mind that the uncertainties in cloud and core average temperatures are quite large, and consequently the result of the established temperature ratio will be even larger. This means that ratios near the edge of a likelihood group may be part of the adjacent one and vice versa. Again, due to the asymmetric uncertainties attached to the temperature values, it is not possible at the time to provide a precise uncertainty value

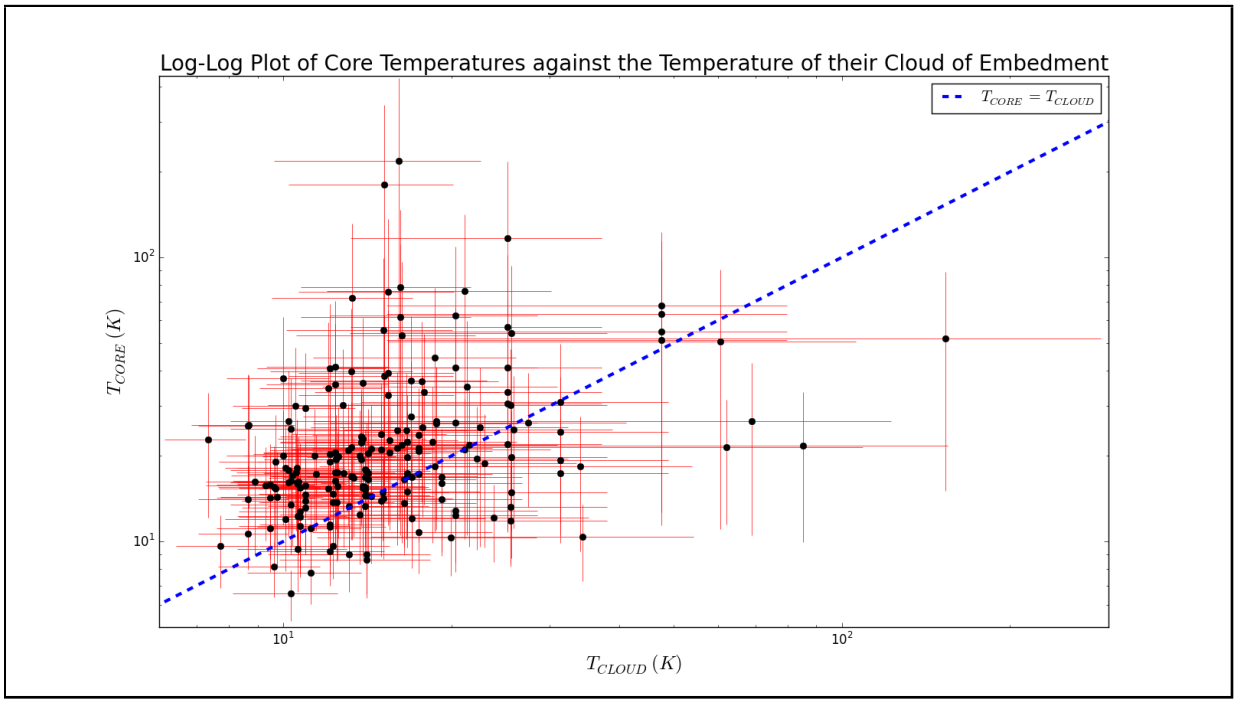

Figure 5.13: Log-log plot of cloud temperatures against the temperature of each of their embedded cores. The core-cloud temperature equivalence line is indicated using a dashed line.

for the temperature ratios. For this reason, the reader is advised to use this histogram as a rough guideline only.

In addition, the observation of cores that are hotter than their surrounding cloud medium is a single line of evidence out of many that need to be taken to conclude that star formation is taking place, For this purpose I avoid making conclusive statements and do not label the cores lying above the core-cloud temperature equivalence line as "star-forming" in appendix tables 3 and 4. Instead, I invite further attention to be placed on this core sample in the future for the purpose of researching the early stages of star formation. For further discussion of the results here, see section 6.1.5.

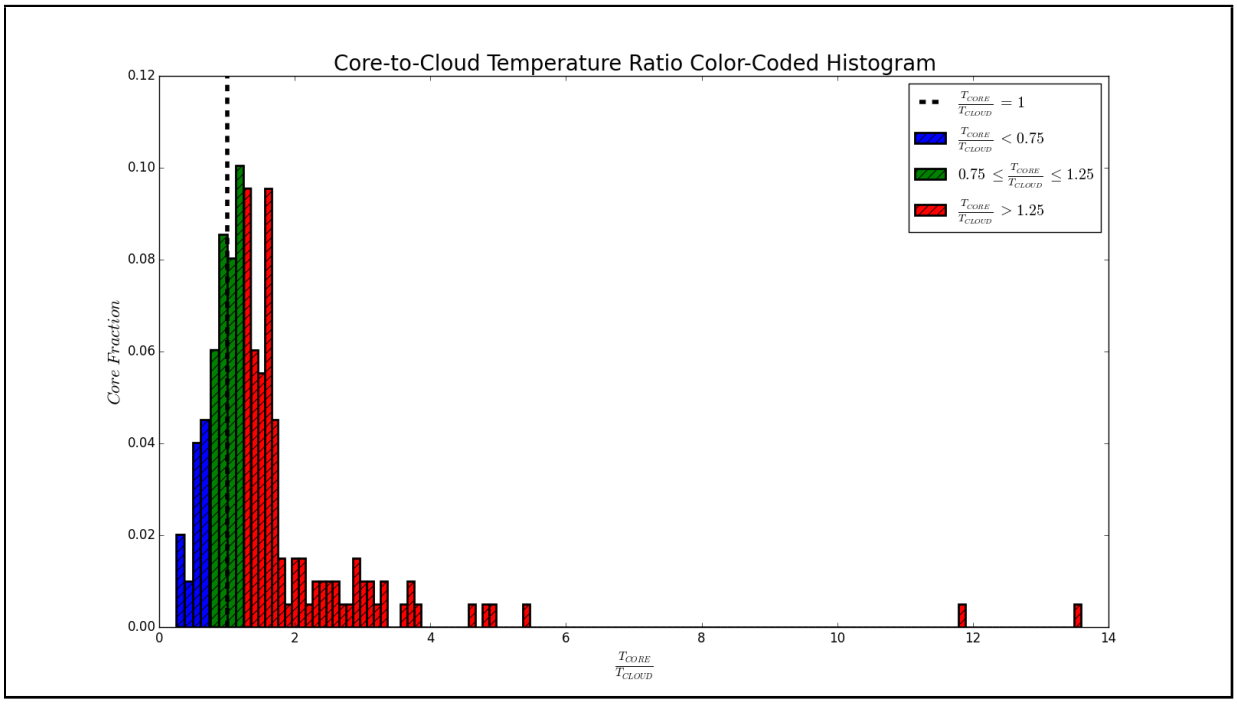

Figure 5.14: Histogram of core-to-cloud average temperature ratios. The three different color codes indicate the likelihood of the cores being star forming, with blue being "highly unlikely", green "somewhat likely" and red "very likely". Note however that a "cold" core could also be in the very early and brief stages of star-formation as well.

5.5.3 Core Mass Accumulation

In this section I investigate the hypothesis that the heat supplied from the warm cloud background has an effect on the coagulation of molecular material in its embedded cores. It is suspected that warmer cloud backgrounds provide stronger support against core collapse and consequently allow for more massive cores to form inside them.

In order to assert this hypothesis, a comparison between the temperature of surrounding cloud filaments is made to the mass of the cores formed inside of these. If a trend favoring the formation of more massive cores inside warmer clouds is observed, the hypothesis is supported and vice versa.

The result of this comparison is displayed in figure 5.15. At first glance, the noise level is extremely high and no trend is observed on a cloud-to-core basis. In an attempt to overcome

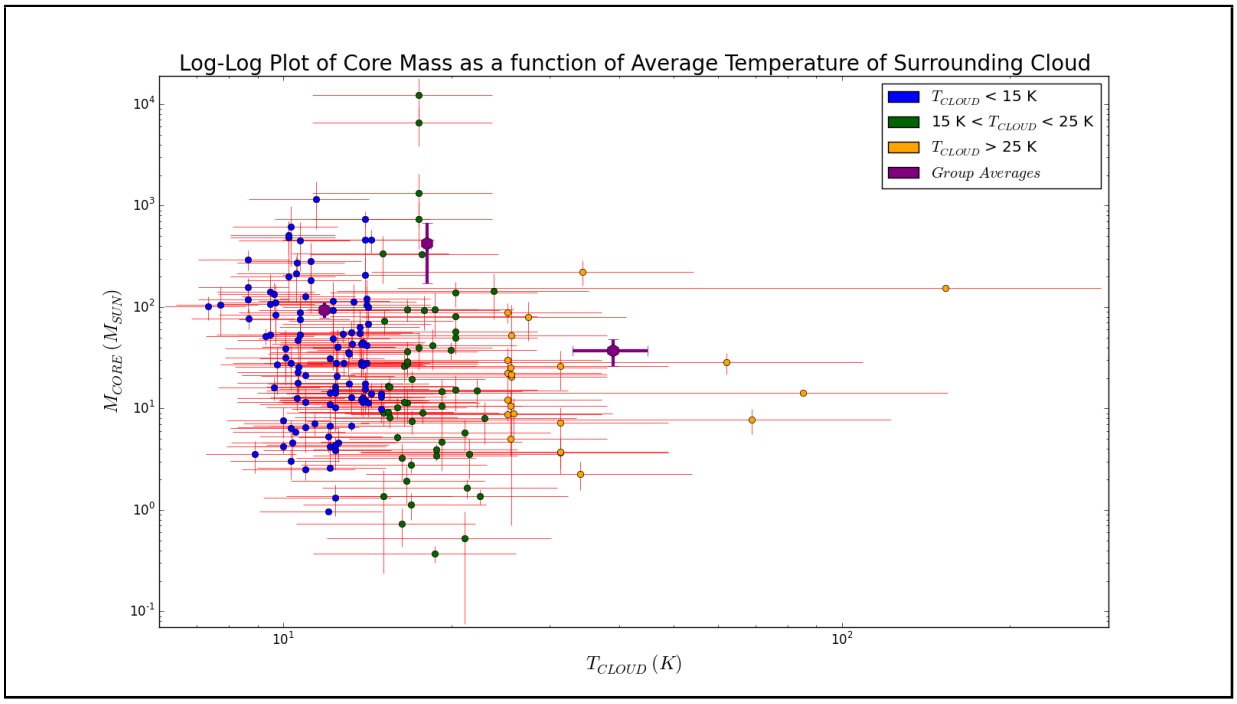

Figure 5.15: Log-log plot of cloud average temperature against the mass of each embedded core. Different cloud temperature classifications are indicated using color coding. Averages for each class are displayed using purple hexagonal markers.

the difficulties introduced from this high noise level, I separate the clouds into three temperature range groups, namely, "cold" ($T_{CLOUD} < 15K$), "warm" ($15K < T_{CLOUD} < 25K$) and "hot" ($T_{CLOUD} > 25K$) indicated by the color coding used. Keep in mind that cloud temperature uncertainties are quite large and clouds near the end of a temperature group could be part of the adjacent one and vice versa. The average core mass for each of these cloud temperature groups is then determined and presented using purple hexagonal points.

Considering the position of these three points, it is tempting to argue in support of a temperature dependency, however I deem the evidence here inconclusive and I further elaborate on the reasoning behind this in section 6.1.3.

In conclusion, this comparison neither supports nor disproves the initial hypothesis. Although, considering just the "cold" and "warm" cloud groups, the average core mass is larger for the "warm" group as expected. The average core mass in the warm group

however is certainly "dragged" upwards from the two very massive core outliers near the 10^4 $M_\odot$ mark. In addition, it seems that the "warm" group allows for the formation of cores with much wider mass ranges, some of which are very massive ($\approx 10^4$ $M_\odot$). For further discussion, see section 6.1.3.

5.6 Star Formation Efficiency

In this section I will be calculating the star formation efficiency (SFE) in the vicinity of the HII region systems considered in this thesis. I will first describe the implemented methodology and then proceed to discuss the obtained results.

To calculate the star formation efficiency of an astronomical system, one needs to directly compare the stellar-to-gas mass components of that system. Essentially, this can be done as follows:

$$\epsilon = \frac{M_*}{M_* + M_{GAS}} \tag{5.48}$$

Where ϵ indicates a system's SFE, M_* its total stellar mass and M_{GAS} its total gaseous mass. The value of ϵ is typically stated as a percentage. Determining what value will go into each of the two components is fairly complicated.

To begin, let's consider the stellar component. It will be useful to distinguish low and high-mass stars, as high-mass stars can typically be observed, while low-mass stars rarely so. This means that the mass in high-mass stars can be directly determined, while that in low-mass stars needs to be inferred based on some reliable model.

So far the massive, OB stars associated with each HII region have been identified in appendix table 6. There are a couple of important concerns regarding the mass in high-mass stars. First of all, the list of associated OB stars could potentially be incomplete, as massive stars lying radially behind an HII region could have their radiation sufficiently extinguished, rendering them unobservable from Earth. In addition, the mass assigned to the stars listed in this table arise from what often is a rough provided classification, and the mass assigned to each class is itself a rough characteristic average for stars within a particular temperature range. Nonetheless, the rough total mass in high-mass stars can be obtained by summing the masses denoted in appendix table 6 for each HII region system.

For the low-mass stars on the other hand, an initial mass function (IMF) needs to be

used to infer how many of them exist within a particular HII region system. The IMF derived by *Kroupa* [31] is adopted here. This IMF is valid in the stellar mass range $0.01 < M \leq 120\ M_{\odot}$ and can be expressed as follows:

$$\xi(M)dM \approx M^{-\alpha}dM \tag{5.49}$$

Where ξ indicates the number of stars in the mass interval $[M,\ M+dM]$ and α indicates the power law index of the IMF. This index changes between stellar mass ranges and assumes the following values:

$$\alpha = \begin{cases} 0.3 \pm 0.7 & \text{if } 0.01\ M_{\odot} \leq M < 0.08\ M_{\odot} \\ 1.3 \pm 0.5 & \text{if } 0.08\ M_{\odot} \leq M < 0.01\ M_{\odot} \\ 2.3 \pm 0.3 & \text{if } 0.01\ M_{\odot} \leq M < 1\ M_{\odot} \\ 2.3 \pm 0.7 & \text{if } M \geq 1\ M_{\odot} \end{cases}$$

In order to convert $\xi(M)$ into a function describing the total mass found in stars between the mass interval $[M,\ M+dM]$, we multiply it by a factor of M. The resulting cumulative mass version of the IMF can be expressed as follows:

$$\phi(M) = \begin{cases} M_0 M^{1.3} dM & \text{if } 0.01\ M_{\odot} \leq M < 0.08\ M_{\odot} \\ M_0 M^{-0.3} dM & \text{if } 0.08\ M_{\odot} \leq M < 0.01\ M_{\odot} \\ M_0 M^{-1.3} dM & \text{if } M \geq 0.01\ M_{\odot} \end{cases}$$

Where M_0 is a normalization constant that is obtainable by integrating through the applicable mass range of this IMF, namely $0.01 < M \leq 120\ M_{\odot}$, and setting the result equal to one. Doing so, yields a value of $M_0 \approx 0.25288$.

To obtain the total mass contributed by low and intermediate-mass stars then is a simple manner of integrating ϕ_M between appropriate mass bounds. The lower limit of integration will always be 0. As for the upper limit, it is set to the mass of the least massive OB star associated with a particular HII region system. The underlying assumption regarding this choice is that all stars above this upper mass limit have been identified in table 6, while all stars below this limit have not and require the IMF to account for their mass contribution.

In regards of the gas component now, it is best to split it into an HII and an H_2 component. The HII component pertains to the summed mass of all HII regions present in a particular system. More often than not, only a single HII region is present, however there are cases where multiple HII regions belong to the same system (i.e Sh-2 254 - Sh-2 258 complex).

Fortunately, the masses of all HII regions have been previously calculated using the recipe developed through sections 5.2.1 and 5.2.2.

As for the H_2 component, it pertains to the summed mass of all SCUBA-2 clumps within a particular HII region system. Typically a system will contain multiple such molecular clumps. The masses of these clumps have already been calculated using the recipe developed in section 3.3.2.

Complications typically arise from some SCUBA-2 molecular clumps having a very uncertain mass estimate, which leads them to being ignored from the gaseous component. Much less frequently, the mass of the HII region may be undetermined due to VLA radio photometry not being available. In some other rare cases, no massive OB star has been associated with a particular HII region. Lack of mass information regarding SCUBA-2 clumps, HII regions, OB stars or a combination thereof may lead to an estimate of the SFE that is an upper/lower limit, or in the worst case scenario, no estimate at all. A more detailed discussion regarding the complications in this calculation will be held in chapter 6.

The systems for which an estimate of the SFE can be made with the data available in this thesis are presented in table 5.4. The constituents of these systems as well as what components were missing and the quality of the SFE estimate are denoted in the "Comments" column. The largest reliable SFE estimate is 26.17% while the lowest is 0.216%. The highest recorded SFE is an upper limit and has a value of 38.72%. Finally, the mean value of the reliable SFE estimates is 4.82%. For a closer look at the systems analyzed and a further discussion of the results, see section 6.1.8.

Table 5.4: Star formation efficiencies of SCUBA-2 systems. The quantities presented in order of appearance include the image ID, the star formation efficiency percentage and comments pertaining to the nature of the system at hand.

System ID	**SFE %**	**Comments**
G70	0.216	2 HII Regions, 23 molecular clump composites, 7 associated OB stars. SFE value is highly reliable.
G74	1.43	1 HII Region, 25 molecular clump composites, 4 associated OB stars. SFE value is highly reliable.
G97	0.254	1 HII region, 3 molecular clump composites, 1 associated OB star. SFE value is highly reliable.

Continued on next page

Table 5.4 – *Continued from previous page*

System ID	SFE %	Comments
G108	1.23	1 HII region, 1 molecular clump composite, 1 associated OB star. SFE value is highly reliable.
G115	8.04	1 HII region, 12 molecular clump composites, 1 associated OB star. SFE value is highly reliable.
G120	4.22	1 HII region, 4 molecular clump composites, 1 associated OB star. SFE value is highly reliable.
G173	$\leq$6.87	1 HII region, 9 molecular clump composites, 4 associated OB stars. No mass for clumps G173-1,2,7,9,10,12,13,14,17. SFE value is an upper limit.
G173B	$\leq$38.72	1 HII region, 1 molecular clump composite, 15 associated OB stars. No mass for HII region S234 and clumps G173B-1,2,3. SFE value is an upper limit.
G182	1.56	1 HII region, 4 molecular clump composites, 1 associated OB star. SFE value is highly reliable.
G188	$\leq$1.37	1 HII region, 16 molecular clump composites, 1 associated OB star. No mass for clumps G188-1,2,4,8,20. SFE value is an upper limit.
G192	2.03	5 HII regions, 17 molecular clump composites, 5 associated OB stars. No mass for HII region S255B. SFE value is highly reliable.
G192B	0.634	1 HII region, 1 molecular clump composite, 1 associated OB star. SFE value is highly reliable.
G210	11.50	1 HII region, 1 molecular clump composite, 3 associated OB stars. SFE value is highly reliable.
G219	26.17	1 HII region, 1 molecular clump composite, 1 associated OB star. SFE value is highly reliable.
G221	$\leq$10.16	1 HII region, 3 molecular clump composites, 3 associated OB stars. No mass for clump G221-1. SFE value is an upper limit.
G233	0.517	1 HII region, 13 molecular clump composites, 3 associated OB stars. SFE value is highly reliable.

Chapter 6

Discussion

In this chapter I will be taking a closer look to some of the results obtained from the previous sections of this thesis. To begin, I will present the greatest outliers encountered in the obtained data. Immediately after I will discuss the meaning of the obtained results from the previous chapter as well as emphasize the problems and shortcomings of the available data and/or methodology used.

Later on, comparisons of the obtained results will be held with those from studies of similar nature for the purpose of establishing their validity as well as to understand better where this thesis fits in with respect to other submillimeter studies.

Further in this chapter, I will discuss some difficulties, problems and residual concerns regarding the quality of the data and further processing that could be done in the future for achieving results of higher accuracy. Some of the topics that will be covered will be the progressive loss of precision with increasing data processing steps, the stability of the stochastic Monte-Carlo technique, the potential existence of background clumps in the sample as well as some additional processing of the photometry that could be applied in the future.

6.1 Result Interpretation

In this section, I elaborate on the results obtained from the previous chapter. I begin with a presentation of data outliers and continue with the discussion of important results. These results include the updated electron number densities and masses for the HII region

sample, star formation efficiency calculations, effects from clouds on embedded cores as well as effects from HII regions and OB stars on cloud-core systems as a whole.

Furthermore evidence supporting important claims such as enhanced clump condensation along the outer rims of HII regions, compression of clumps from nearby HII regions and star formation taking place in the core sample will be presented and discussed.

6.1.1 Data Outliers

In this section, I present the extreme values obtained from the photometry and derivative property calculations. For each property, the maximum, minimum and mean values are presented. This is done separately for the cloud segments and their embedded cores. These extreme values are displayed in table 6.1 for the cloud segments and table 6.2 for the cores. The name of the objects associated with a particular minimum or maximum value is included within brackets.

It is important to note that all photometric quantities presented are pure. This means that they've had all the backgrounds discussed in chapter 2 removed. In a subsequent section, I will take a closer look at the temperature extremes as they reflect an important issue that hinders the measurements of a large fraction of objects from the total sample.

6.1.2 HII Region Electron Number Densities and Masses

The determined range of HII region electron number densities is 7.62 $cm^{-3} < n_e <$ 574.2 cm^{-3}, with a mean of 73.9 cm^{-3}. It is important to keep in mind that the radius used for the HII regions is the outer ionized layer boundary of the gas, which was identified using the VLA 1.46/4.89 GHz data. For this boundary to be established, the 10% flux contour was used, which roughly corresponds to the use of an SNR = 2.0. This atypically higher cutoff is expected to yield a consistent underestimation of the true HII region boundary, however, the measurement itself is much more reliable in return.

In addition, the assumption of a constant electron number density may be inflating the value of the determined average electron number density for some systems in which a weak radial dependence exists. Furthermore, the use of an average electron temperature can also sway the determined electron number densities in either the upper or lower direction.

Table 6.1: Table of outlier cloud segment properties. The quantities listed in order of appearance are the overall maximum and minimum for each property as well as the overall mean of all obtained values for that property. The ID of each cloud pertaining to the maximum and minimum of a particular quantity is displayed in brackets.

Property	**Maximum Value Recorded**	**Minimum Value Recorded**	**Mean of Recorded Values**
Radius (pc)	7.62 (G70-4)	0.167 (G225-2)	0.91±0.06
F_{450} (Jy)	422.98 (G105-1)	0.314 (G120-1)	24.59±4.4
F_{850} (Jy)	48.98 (G192-2)	0.059 (G74-18)	2.70±0.46
S_{450} $(Jy/arcsec^2)$	7.67×10^{-2} (G105-1)	2.68×10^{-5} (G115-7)	$3.40 \times 10^{-3} \pm 5.27 \times 10^{-4}$
S_{850} $(Jy/arcsec^2)$	1.23×10^{-3} (G196-1)	4.11×10^{-6} (G115-7)	$2.76 \times 10^{-4} \pm 1.67 \times 10^{-5}$
f_{450}^{bowl} (mJy)	-0.53 (G74-24)	-238.4 (G97-1)	-12.46±1.90
f_{850}^{bowl} (mJy)	-0.134 (G74-4)	-3.05 (G173-3)	-0.853±0.04
f_{450} (mJy)	377.4 (G105-1)	0.96 (G120-1)	17.34±2.6
f_{850} (mJy)	13.95 (G196-1)	0.50 (G120-1)	3.08±0.18
$v_{450}L_{450}$ (L_{SUN})	3874 (G70-4)	0.467 (G120-1)	96.1 ± 24.3
$v_{850}L_{850}$ (L_{SUN})	308 (G70-4)	0.048 (G115-6)	6.17 ± 1.82
T (K)	242.8 (G173-7)	7.35 (G74-3)	23.42±2.4
Mass $(M_\odot)$	15660 (G70-4)	2.21 (G115-5)	585±145
n_H (cm^{-3})	15284 (G138-3)	8.31 (G115-6)	1345±184
N_H (cm^{-2})	3.22×10^{22} (G70-16)	4.47×10^{19} (G115-6)	$3.75 \times 10^{21} \pm 3.80 \times 10^{20}$
Pressure (Pa)	1.24×10^{-11} (G138-3)	2.41×10^{-15} (G115-6)	$4.19 \times 10^{-13} \pm 9.37 \times 10^{-14}$

On the other hand, the determined range of HII region total gas masses is $0.32\ M_\odot < M < 8500 M_\odot$, with a mean of 487.0 $M_\odot$. The calculation of the mass is prone to the same problems that the electron number density is, but also the additional problem of assuming that the fraction of Helium is approximately equal to that of He^+. Clearly, in the presence of a much hotter star, some of the Helium will be doubly ionized (He^{++}). Under this assumption then, the total Helium fraction will be underestimated for these HII region systems, leading to a lower gas mass density and consequently a lower total gas mass estimate than the true value.

Comparison between HII region radial size and determined electron number densities revealed a rapid decrease in electron number density between angular sizes of 0 and 50

Table 6.2: Table of outlier core properties. The quantities listed in order of appearance are the overall maximum and minimum for each property as well as the overall mean of all obtained values for that property. The ID of each core pertaining to the maximum and minimum of a particular quantity is displayed in brackets.

Property	**Maximum Value Recorded**	**Minimum Value Recorded**	**Mean of Recorded Values**
R (pc)	2.21 (G70-4-7)	0.038 (G173-18-2)	0.319±0.01
F_{450} (Jy)	306.62 (G70-4-6)	0.084 (G115-12-1)	9.11±1.9
F_{850} (Jy)	41.42 (G70-4-6)	0.022 (G233-9-1)	1.00± 0.2
S_{450} $(Jy/arcsec^2)$	6.65×10^{-2} (G188-2-3)	1.99×10^{-4} (G115-12-1)	$5.46 \times 10^{-3} \pm 5.34 \times 10^{-4}$
S_{850} $(Jy/arcsec^2)$	7.06×10^{-3} (G192-1-1)	4.81×10^{-5} (G115-6-1)	$6.48 \times 10^{-4} \pm 5.15 \times 10^{-5}$
$v_{450}L_{450}$ (L_{SUN})	4560 (G70-4-6)	0.125 (G115-12-1)	46.2 ± 20.0
$v_{850}L_{850}$ (L_{SUN})	326 (G70-4-6)	0.022 (G115-12-1)	2.92 ± 1.23
T (K)	218.8 (G173-15-2)	6.58 (G70-19-1)	26.4±1.8
Mass $(M_{\odot})$	12325 (G70-4-5)	0.37 (G74-25-1)	178±73
n_H (cm^-3)	1.97×10^5 (G120-3-2)	247 (G97-1-3)	6250±1070
N_H (cm^-2)	3.50×10^{22} (G70-4-5)	2.53×10^{20} (G97-1-3)	$5.60 \times 10^{21} \pm 3.86 \times 10^{20}$
Pressure (Pa)	1.71×10^{-10} (G120-3-2)	1.16×10^{-13} (G97-1-3)	$2.84 \times 10^{-12} \pm 8.40 \times 10^{-13}$

arcseconds and physical sizes of 0 to 1 pc. The decrease continues beyond these values in a progressively smoother manner.

Finally, comparison between HII region radial size and determined total gas mass revealed a consistent, rapid increase in mass with both increasing angular and physical size. The physical size approach depicted this increase much more clearly than the angular size approach which displayed a larger scatter.

6.1.3 Evidence for Clouds affecting Core Mass Accumulation

Earlier I presented a comparison between cloud temperatures and mass of embedded cores. The individual core-to-cloud comparisons did not indicate any particular effect. Consideration of the average properties in the "cold", "warm" and "hot" cloud temperature bins was also inconclusive. Although, consideration of only the "cold" and "warm" bins does display a rise in accumulated mass with increasing cloud temperature, there is strong reason against adopting this interpretation of the displayed result.

First, note that the number of clouds in each temperature bin is quite different, with cold clouds being by far the most common. This makes the average properties of the "cold" bin much more well determined than those of the other two bins.

In addition, note the range of masses in each temperature bin. The "warm" bin spans more than 4 orders of magnitude, while the "cold" bin spans 3 and the "hot" bin 2. Such wide ranges in the mass parameter space make the determined averages considerably uncharacteristic of the sample they are trying to represent.

Finally, the uncertainties tend to be greater for larger parameter values, meaning that large core masses and large cloud temperatures tend to be quite uncertain. Hence the "hot" temperature bin is not only under-populated for a reliable average to be obtained, but its members tend to suffer from much higher individual uncertainties as well.

One can then see the danger in acknowledging such a mild increasing trend while the aforementioned problems are lurking in the result. It is therefore better to deem this experiment as inconclusive.

6.1.4 Evidence for Molecular Clump Heating

Investigation of H_2 average column and number densities against average temperature lead to some interesting results. Cloud temperatures appeared to decrease with increasing column density, as well as increasing number density. The cores showed a noisier and milder temperature decrease with increasing column density and appeared to become mildly warmer with increasing number density.

The decreasing column density trend that is apparent for both clouds and cores suggests that clouds, and to a greater extent, cores, are much more prone to heating effects from internal, rather than external mechanisms. More specifically, the denser and more opaque clouds with high column density essentially shield the internal structure from incoming radiation, preventing its heating from external mechanisms such as OB star radiation. One should keep in mind that a column density of $\approx 1.8 \times 10^{21}\ cm^{-2}$ corresponds to an optical extinction of 1 magnitude and the majority of clouds as well as embedded cores have a column density greater than this value.

On the other hand, the decreasing number density trend observed for clouds suggests that denser kinds of outer clump layers are cooler as they dissipate the heat from the inner

layers more efficiently. The absence of a number density trend for cores on the other hand, suggests that heating from potential gravitational contraction and cooling from convective heat dissipation toward outer clump layers are of similar magnitude. The findings are in direct agreement with the mild heating effect observed from HII regions and OB stars.

More specifically, examination of HII region positions with respect to each associated cloud and embedded core revealed a mild heating effect taking place. However, the scatter in combination with the noise made it very hard to speculate the average scale of this heating effect in terms of a temperature increase. Center-to-center physical separation distances picked out the small dependency of the average core and cloud temperature on the location of the HII region. The induced heating effect appears to increase dramatically for center-to-center physical separation distances less than ≈ 10 *pc*.

In addition, examination of OB star positions with respect to each associated cloud and embedded core also revealed a mild heating effect taking place. Like in the HII region case however, the large scatter and noise made it difficult to judge the magnitude of this heating effect in terms of temperature. The center-to-center physical separation distance approach managed to reveal the mild heating effect from OB stars. This heating effect was found to increase dramatically below a center-to-center physical separation distance of roughly ≈ 10 *pc*. In addition, the incident flux approach was inconclusive. This is not in alignment with expectation, as a much larger dependency of average temperatures to incident OB star flux was expected.

It is suspected that the reason behind the null result in the incident flux approach is tied to the tiny incident flux values at hand. Total incident fluxes span the range $10^{-6}\ W/m^2 < F < 10^{-1}\ W/m^2$ and $10^{-6}\ W/m^2 < F < 10^{0}\ W/m^2$ for the cores and cloud segments respectively. The largest incident flux recorded in this approach is on the order of 1 W/m^2. For comparison, this is approximately equal to the incident flux that Pluto receives from our own Sun. To make matters worse, recall that all incident fluxes are upper limits to the true flux due to the distances lacking a radial component. Therefore, at such small incident flux values, the incurred increase in temperature is so small with increasing flux that it can easily be drowned by the temperature noise levels. It is highly likely that the effect would be more dramatic if the stars happened to lie closer to the molecular clumps than they do in this sample. However, evidence from this analysis suggest that the heating effect from OB stars on this sample of clumps is small, regardless of the approach taken.

6.1.5 Evidence for Star-Formation

Evidently, a large portion of molecular cores identified in this thesis depict average temperatures that are greater than their surrounding cloud medium. This alone suggests that the hotter cores are highly likely to be star-forming. However, caution should be exercized in the interpretation of this result.

To begin, a comparison between core and surrounding cloud medium average temperatures could be misleading in the presence of external heating mechanisms, such as nearby, massive OB stars, or HII ionization fronts that are gradually eroding the outer clump layers through the RDI process. Such a clump can host a collapsing core whose temperature could be lower than that of the surrounding cloud medium. Fortunately, as displayed in section 5.4, the incident fluxes from associated OB stars are extremely small to justify a large effect on the surrounding cloud temperature. However, potential effects from the RDI process could still have a considerable effect on average cloud temperatures.

In addition, this is a single line of evidence that can be used in support of star formation taking place. In order to confirm this to a higher degree of certainty, other approaches must be taken as well. For example, observations of a dusty content that is significantly lower than the mean would further support the presence of a YSO that is clearing its surrounding dust envelope. In addition, some cores may present good candidates for spectral line observations for the determination of infall velocities. Furthermore, the spectral index of a core in the mid-infrared can indicate the particular stage of star formation that a core is undergoing at the time of observation. Since such information has not been obtained here, it cannot be said with complete certainty that every single core that lies above the core-cloud temperature equivalence line is star-forming, but only that it is probably so.

Nonetheless, an additional line of evidence comes from the modest rise in core temperatures with increasing number density, which suggests heating is taking place from gravitational contraction. This further supports the initial claim made here.

6.1.6 Evidence for "Collect-Collapse" Taking Place

Evidently, an increased molecular clump presence can be seen near the boundary of almost every single HII region comprising the sample of this thesis. However, evidence pertaining to this result only compromises a 2-dimensional interpretation of each system, and the consequences of the missing radial component must be acknowledged.

First, let's begin by stating that there is a very high likelihood for clumps with scaled distances less than one to also lie on or near the boundary of their associated HII region. This is because they are suspected to be positioned directly in front or behind their associated HII region, rather than on the side. However, this claim can only be confirmed with knowledge regarding the radial component of clumps.

In addition, a portion of the clumps lying between a scaled distance of one and two-to-three are also suspected to be forming near the boundary of their associated HII region. This is because the shape of the contour flux for a minority of HII regions is quite asymmetric, yet their boundary has been approximated using a circular aperture. Furthermore, a conservative approximation to the HII region boundaries has been made using their 10% VLA flux contour. This means that the size of a few diffuse HII regions may be underestimated, leading to higher core-to-HII-Region scaled distances as a consequence.

Overall though, the large number of clumps appearing near the $\theta_{SCALED} = 1$ bin in the 2-dimensional scaled separation distance histogram, in combination with a suspicion that a portion of clumps in the nearby bins could also be forming at the boundary of their associated HII region due to the reasons discussed above, the original hypothesis that increased molecular clump condensation occurs near the boundary of HII regions is strongly supported. Due to the lack of the radial component however, not much can be said about the occurrence of RDI in this HII region sample.

Finally, as mentioned in Chapter 2, the data is obtained from already-existing data archives. Because of this, the sample consists of two roughly equally-sized types of images, one group that covers a substantial area outside the HII region in question, and one group that marginally covers the HII region's extent. This introduces an unwanted bias of complex nature, where the population of cores at areas outside the HII region is accounted for, but not completely so.

However, even with the extra cores that could potentially exist near but not at the HII region boundaries, the expected overall effect is a small increase in the population at scaled separations larger than ≈ 2. At worst, if the images that did not cover the nearby exterior of the identified HII region depict the same core distribution as those that did, the population at bins larger than ≈ 2 should be roughly double. Clearly, that would still not change the overall observation of enhanced condensation near $\theta_{SCALED} = 1$.

6.1.7 Evidence for Molecular Clump Compression

Evidently, all HII regions in this thesis exhibit higher average gas pressures than the outer layers of their associated clumps. This translates to the HII regions exerting a compressing force on these and possibly acting to assist their collapse. This result should be interpreted with caution due to potentially unaccounted variables, however, I will argue why it is highly supportive, if not conclusively so, to the compression claim made here.

Even though the term "associated" is used loosely throughout this section, the lack of a 3-dimensional interpretation of the clump-HII region systems prevents the definitive use of this term. Some clumps may be part of the distant radial background, but 2-dimensionally appear to exist inside the HII region boundary. The probability however of such background clumps polluting our sample is very small as is determined in subsection 6.4.

On the other hand, the use of an average temperature for all HII regions, even though an accurate approximation for most, may not be that great for exotic members of our sample. According to *A.L Rudolph et al* [8] ionized nebulae were found to have temperatures as low as 4800 K, a temperature which can drop the average pressure estimate by almost an entire order of magnitude. Inspection of figure 5.6 however clearly shows that even if the pressures of all HII regions were scaled down by an entire order of magnitude, they would still lie above the pressure equivalence line, with the exception of the single outlier near the middle of the plot. Furthermore, most HII regions are expected to have electron temperatures toward the higher end of the temperature range encountered in that paper due to their relatively large galactocentric distances.

Hence, even in the worst case scenario, average HII region pressures would still be higher than those of the outer layers of their associated clumps, something that further supports the initial claim of HII regions exerting a compression force on their associated clumps.

It should be noted that the expected compression effect will only take place if the HII region is in direct contact with a particular clump. This means that for clumps that are considerably far from the HII region boundary ($\theta_{SCALED} \gtrapprox 2$) this compression effect does not take place at all.

Finally, the pressures of HII regions are seen to be 2-3 orders of magnitude greater than those of the outer layers of their associated clumps. To understand why this is expected, it should be noted that clouds are comprised mostly of neutral Hydrogen (H_2) and atomic Hydrogen (H), while HII regions are composed primarily of ionized Hydrogen (HII). The

number density of HII is 4 times greater than H_2 and 2 times greater than H. In addition, the temperature of HII ($\approx 10000K$) is roughly 100 to 1000 times greater than both the temperature of H and H_2 ($\approx 10 - 100K$) as these two cloud components are expected to be in thermal equilibrium. Therefore, the HII region's pressure is expected to be anywhere between 200 and 4000 times greater than that of the outer clump layers, which is what is observed. Outliers are likely either clumps that constitute a single, collapsing core (higher cloud pressure than predicted) or clumps that are quite far from their HII region's boundary (lower cloud pressure than predicted).

6.1.8 A Closer Look at Star Formation Efficiency

Evidently, the mean star formation efficiency (SFE) of the HII region systems for which a complete account for the gas and stellar mass was available is roughly 4.82% with a maximum of 38.72% and a minimum of 0.216%.

I will now discuss particular caveats embedded in the SFE calculation and then proceed to analyze HII region systems whose determined SFE value is far from the established mean (4.82%) in order to speculate on the potential reasons behind this.

In regards of the stellar mass component, it is important to keep in mind that all cores are counted on the molecular gas portion, even though they could be hosts to newly-forming stars. In fact, as discussed in section 5.5.2, a majority of SCUBA-2 cores is expected to be star-forming indeed. However, a simple cloud-to-core temperature comparison is not sufficient to guarantee star formation taking place in a particular core. Consequently, it is unwise to use the result from that comparison to assert with complete certainty which cores are star-forming and which are not. The consequence of having the core masses contribute solely to the gaseous component is an intrinsic bias toward slightly lower SFE values.

In addition, the residual problem of not having identified all associated OB stars to a particular HII region system remains. Stars lying behind the HII region gas could have their emission significantly obscured, to the point of rendering them invisible. The non-detection of such stars would lead to a lower stellar mass component which consequently would lead to slightly lower SFE values.

In addition, the rough classification of some of the identified OB stars introduces uncertainty into the mass that they are speculated to contribute to the stellar mass component. The extent of this uncertainty is a topic that has not been covered in this thesis due to

its complex nature. Another uncertainty contributor comes from the IMF being used to account for the mass from low and intermediate-mass stars. The IMF itself is expected to be relatively accurate, however, the upper bounds used for its integration could prove to be unreliable due to both potentially unidentified OB stars and poor classification of the ones already identified.

In regards of the gas mass component, the masses of the HII regions at hand are expected to be well determined, however the same cannot be said for the masses of all molecular clumps. Some molecular clumps fall victim of the problem discussed in section 6.3. Typically, really high clump masses are a result of unphysical flux ratios, which can be traced back to poor 450μm photometry. Such overestimated clump masses would lead to lower SFE values.

Finally, sometimes an HII region system may lack information regarding the mass of a particular molecular clump due to high uncertainty in its value. In fact, most of the SFE outliers suffer from this problem. Molecular clumps contribute a considerable amount of mass to the gas mass component. Therefore, when a system lacks mass information regarding a portion of its molecular clumps, its SFE value is taken as an upper limit.

Let's switch the attention now to the outliers of the SFE calculation, beginning with the greatest one, namely, G173B, which has an unlikely high SFE at a value of 38.72%. An image of G173B can be seen in figure 17. This system hosts 2 HII regions (Sh-2 234 and Sh-2 237), 3 molecular clumps and an entire group of 15 unique, associated OB stars. The only molecular clump out of the four that has a mass estimate available is G173B-4, a clump that has been segregated out of the associated clump list, as it lies too far from the HII regions in the area of image G173B. The large number of massive OB stars in combination with the lack of mass information for the majority of the molecular gas component works together to yield an unreliable, very high SFE value.

The next greatest outlier is G219 with an SFE value of 26.17%. An image of G219 can be seen in figure 26. This system is home to a single HII region (Sh-2 288), a single, unique associated star and a single molecular clump. However, the 450μm image of the molecular clump is suffering from high levels of noise, and as a consequence its temperature is expected to be overestimated while its mass underestimated. However, such an underestimation cannot account for a difference greater than 10-15% in the clump's mass. Therefore, the SFE value for G219 is indeed expected to be high, but not as high as the provided estimate, maybe a few percent less. It is worthy of revisiting this system in the future for further analysis.

On the opposite side of the spectrum, G70 has the smallest SFE, at a mere value of 0.216%. An image of G70 can be seen in figure 1. This system hosts 2 HII regions (Sh-2 99 and Sh-2 100), 24 molecular clumps and 7 unique associated OB stars. It presents some of the lowest noise levels for both the 450μm and 850μm photometry and as such, is expected to provide the grounds for a complete clump identification and highly reliable mass estimates for these clumps. The only reason why this SFE may be found to be slightly higher in the future is if some of the many cores of the identified clumps are confirmed to be star forming. For this reason, this system's SFE is expected to be very reliable and highly representative of the system at hand.

Finally, the last outlier is G74, which has the second smallest SFE, at a value of 0.254%. An image of G74 can be seen in figure 2. This system is home to a single HII region (Sh-2 104), 25 molecular clumps and 4 unique associated OB stars. Like G70, G74 is home to some of the most reliable photometry in this thesis. The molecular clump identification is expected to be complete and the masses of these clumps are expected to be highly reliable. Once again, the only reason why the SFE of this system could be slightly higher is if some of the identified cores are found to be conclusively star forming in the future. Other than that, this system's SFE is very reliable and highly representative.

In conclusion, it appears that the lower outliers are actually the better determined SFE values from the total sample. Most of the higher SFE values, especially the really high ones, appear to suffer from underlying problems, of which the most common is poor SCUBA-2 photometry leading to bad molecular clump mass estimates. Overall then, high SFE values should be interpreted with caution, as they can either be the product of a poorly determined mass budget, or, in the well determined cases, a product of some type of time dependency.

6.2 Comparisons to Previous Work

In this section I attempt to compare findings from this thesis to those from other compatible works. These comparisons involve properties of the HII region sample as well as the molecular clump sample. The ultimate goal is to gain a better understanding of how the results of this thesis fit in the general field of star formation. Throughout this section one should keep in mind that deviations do exist, and there is no cookie-cutter method of deeming an approach "the better one", as all approaches provide their own unique bits of

information into this newly developing branch of star formation research.

6.2.1 HII Region Properties - KAO

In this subsection, I am examining HII region electron number densities obtained from using the Kuiper Airborne Observatory (KAO) to those obtained in this thesis. The most recent and thorough treatment for a good portion of galactic HII regions can be found in the work by *A.L Rudolph et al* [8] which I discuss below.

A.L. Rudolph et al (2006)

In this subsection, the HII region electron number densities obtained in chapter 5.2.1 are compared against the values obtained in the work by *A.L. Rudolph et al* [8] for the sample portion shared between the two. The result of the comparisons is presented in table 6.3 but also graphically in figure 6.1.

Although similar, the estimates disagree and sometimes considerably so. In addition, all new estimates obtained in this thesis, excluding that of Sh-2 288, are lower than the previous. To understand why this is so, the systematic and theoretical differences between the two approaches are discussed below.

Starting with a quick glance at the equation for electron number density, the proportionality $n_e \propto R_s^{-1.5}$ is evident. However, the size estimates for HII regions in this thesis are derivatives from a different methodology than the one used in *M. Fich's* VLA work [16], which is the supplier of the radial sizes for *A.L. Rudolph et al.* Specifically, I use the HII region's 10% flux contour, to which I best-fit a circular aperture of some radius R. In *M. Fich's* paper however, the 2 mJy flux contour line is used instead. Which of these two conditionals will yield a larger size and consequently a smaller electron number density is quite random. However, this is certainly a contributor to the discrepancy between the compared electron number density values.

Another look at the electron number density equation reveals the proportionality $n_e \propto d$. However, for a large number of HII regions, the distances used differ between the two works. In the work by *A.L Rudolph et al*, the distances are supplied by *G. Chan* and *M. Fich's* IRAS work [12]. In this thesis however, the newer and more refined distances from *T. Foster* and *C.M Brunt's* work [54] are used when available, and the IRAS ones in the few cases when they are not. More often than not the newer distance estimates are

smaller than the older ones and are expected to yield smaller electron number densities as a consequence.

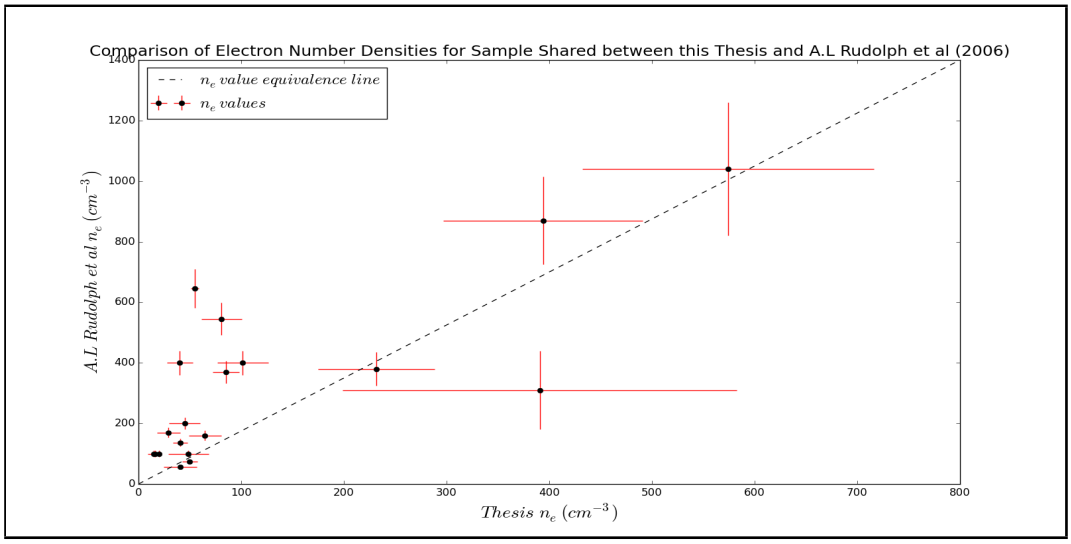

Figure 6.1: Plot of the electron number densities calculated in this thesis against the values found in *A.L Rudolph et al* [8]. Value equivalence is indicated by a black, dashed-line.

Finally, a smaller deviation should arise due to the updated theoretical model used in this thesis, which is inclusive of correction factors that were not part of the earlier iteration. These include a correction factor to account for the deviation from the complete free-free opacity model, as well as a correction to account for the use of a cylindrical rather than a spherical geometry in the optical depth integral. Both of these correction factors lower the electron number density measurement by roughly 10%. In conclusion, the newer electron number density measurements are expected to be more reliable as they use an updated and corrected version of the base-model in combination with newer and more reliable measurements for input variables such as radial size and most importantly, distance.

6.2.2 Molecular Clumps - PMO

Considering the molecular clumps now, I begin by comparing my obtained SCUBA-2 properties for the clumps found along the boundary of HII region Sh-2 104 against the properties

Table 6.3: Comparison between HII region electron number densities obtained in this thesis against *"Abundance Gradients in the Galaxy"* by *A.L Rudolph et al* [8].

HII Region	n_e (cm^{-3}) **This Thesis**	n_e (cm^{-3}) **A.L Rudolph et al**
BFS31	44.85±15.4	200±20
BFS54	14.97±5.9	100±10
BFS64	16.04±4.5	100±10
Sh2-104	40.81 ± 16.0	56±5
Sh2-100	48.7±19.5	100±10
Sh2-127	80.9±19.9	545±54
Sh2-128	231.6±57.0	380±55
Sh2-138	574.2±141.9	1040±220
Sh2-152	394.0±97.0	870±145
Sh2-168	40.54±7.0	137±13
Sh2-208	49.96±7.7	74±7
Sh2-209	54.64±3.9	645±64
Sh2-255	101.4±24.8	400±40
Sh2-257	64.8±15.9	160±16
Sh2-266	40.27±12.5	400±40
Sh2-271	85.24±12.8	370±37
Sh2-283	29.20±11.4	170±17
Sh2-285	20.03±2.5	100±10
Sh2-288	390.7±192	310±130

obtained in the work by *J.L Xu et al.*

J.L. Xu (2017)

In this paper, a multi-wavelength study of HII region Sh-2 104 is performed to further test the hypothesis that increased molecular condensation occurs at the boundary of HII region structures. The study uses the Purple Mountain Observatory (PMO) to observe line emission from the ^{13}CO J(1-0), ^{12}CO J(1-0) and $C^{18}O$ J(1-0) transitions. This emission traces well the distribution of molecular gas in the system.

Clump identification is performed manually in this thesis, while in the study, a clump identification algorithm part of the "GILDAS" software package is employed instead. The result of the manual identification in this thesis is 25 clumps that host a total of 43 cores, while in the *J.L Xu* study, a total of 21 clumps are identified, most of which can be matched up to a core of this thesis. The *J.L Xu* study seems to be concerned more with filamentary structure rather than concentrated core matter, as suggested by the larger aperture sizes used. To avoid confusion however, I compare each source identified in that study to its SCUBA-2 equivalent core in this thesis.

The study also uses 20 cm data from NVSS to trace ionized gas, leading to an estimate of 2.5 arcminutes for the radial size of Sh-2 104, while consideration of the VLA 1.46 GHz data in this thesis gives a larger estimate of 4 arcminutes.

Analysis of the molecular CO line emission data in the study is performed in order to obtain estimates for the mass, column density and number density of the clump condensations along the rim of Sh-2 104. The study forwards an estimate of 22000 $M_{\odot}$ for the total molecular mass inside the HII region structure, while summation of the masses of the individual clumps identified in this thesis provides a lower estimate of 6639 $M_{\odot}$. Part of the disagreement has to do with the study incorporating all warm filaments found in the ring, regardless if they host a distinguishable core or not, while this thesis considers only filaments containing distinguishable cores inside.

Comparison of the radial size, total mass, average column density and number density is carried forward for the clump sample that was able to be matched up between the two works. The result of the comparisons can be viewed in table 6.4. To begin, it should be noted that the radial sizes are in relatively good agreement, even though the apertures used are different and the distances come from a different source. More often than not however the matching is not precise and more than one core can correspond to a particular clump from the study. For these cases, I indicate all potential matches in the table.

In regards of the total mass, all estimates from the *J.L. Xu* study are greater and sometimes greatly so as compared to the ones provided in this thesis. This is certainly due to the fact that the study identifies cores together with their accompanying cloud filaments as opposed to this thesis identifying cores on their own. Since most of the mass of a clump is found in the colder cloud filament, the *Xu* study is expected to present consistently higher mass values. This is suspected to be the reason behind the higher column densities as well.

Table 6.4: Comparison between the values obtained in the work by [] to those obtained in this thesis. The comparison includes

Core ID J.L Xu / This Thesis	**R (pc) J.L Xu / This Thesis**	**M ($M_\odot$) J.L Xu / This Thesis**	N_{H_2} (10^{22} cm^{-2}) **J.L Xu / This Thesis**	n_{H_2} (cm^{-3}) **J.L Xu / This Thesis**
1 / G74-17-1	0.30 / 0.38 ± 0.12	251.1 / -	2.8 / $0.181^{1.00}_{0.04}$	5225 / 1144^{9788}_{164}
2 / G74-21-3	0.27 / 0.38 ± 0.12	82.6 / -	1.1 / $0.528^{0.474}_{0.265}$	1912.2 / 3344^{5924}_{2074}
3 / G74-17-3	0.58 / 0.26 ± 0.08	330.0 / $9.2^{6.4}_{0.6}$	1.0 / $0.196^{0.458}_{0.070}$	1097.1 / 1856^{7166}_{990}
4 / G74-17-2	0.19 / 0.26 ± 0.08	29.8 / $16.6^{12.5}_{2.1}$	0.8 / $0.351^{0.846}_{0.107}$	2317.7 / 3336^{13004}_{1568}
5 / G74-21-2	0.45 / 0.26 ± 0.08	151.4 / $6.7^{5.1}_{0.7}$	0.7 / $0.142^{0.350}_{0.045}$	1270.6 / 1352^{5479}_{684}
6 / G74-9-1 G74-9-2	0.49 / 0.38 ± 0.12 0.26 ± 0.08	156.8 / $43.2^{1.4}_{12.1}$ -	0.7 / $0.407^{0.298}_{0.189}$ $0.056^{0.361}_{0.018}$	843.6 / 2576^{3899}_{1543} 532^{5240}_{0}
7 / G74-12-1	0.46 / 0.38 ± 0.12	127.4 / $40.3^{1.3}_{11.8}$	0.6 / $0.380^{0.263}_{0.188}$	737.6 / 2404^{3424}_{1518}
9 / G74-21-1	0.39 / 0.26 ± 0.08	67.3 / $12.9^{0.4}_{3.7}$	0.4 / $0.273^{0.194}_{0.138}$	766.9 / 2588^{3719}_{1655}
10 / G74-17-4	0.49 / 0.26 ± 0.08	111.2 / -	0.5 / -	413.4 / -
11 / G74-8-1 G74-8-2	0.27 / 0.26 ± 0.08 0.26 ± 0.08	42.8 / $5.2^{2.2}_{0.6}$ $10.3^{1.6}_{2.3}$	0.6 / $0.110^{0.200}_{0.049}$ $0.217^{0.244}_{0.109}$	1328.1 / 1045^{3281}_{611} 2063^{4233}_{1297}
13 / G74-12-2	0.77 / 0.26 ± 0.08	218.1 / -	0.4 / -	263.1 / -
16 / G74-19-1	0.44 / 0.26 ± 0.08	51.1 / -	0.3 / -	312.3 / -
20 / G74-15-1	0.64 / 0.26 ± 0.08	121.3 / $1.7^{1.7}_{0.4}$	0.3 / $0.035^{0.113}_{0.010}$	328.5 / 332^{1707}_{157}
21 / G74-18-1	0.28 / 0.26 ± 0.08	19.2 / -	0.2 / -	439.3 / -

In regards of the number densities, the opposite occurs, as the study provides consistently lower estimates to the ones provided in this thesis. The most likely reason for the consistent discrepancy is that the clumps are approximated using spheroids in the study and the number density is obtained by directly comparing the mass to the volume of these spheroids and the mean molecular weight of its constituents. On the contrary, in this thesis the number density is obtained from a different route that uses the obtained 850μm photometry and the derived temperature. It seems that in the study the much larger volume of the spheroids outweighs the effect of the larger mass estimates to give an overall lower number density estimate than the one provided in this thesis.

6.2.3 Molecular Clumps - SCUBA

SCUBA is the former camera used in the JCMT telescope between 1995 and 2005. It had multiple wavelength windows of operation that included the 450μm and 850μm wavelengths of the current SCUBA-2 instrument. However, SCUBA had significantly less pixels than its SCUBA-2 successor, with only 91 in the 450μm band and 37 in the 850μm band as opposed to a total of 5120 in each band of SCUBA-2. These pixels were also distributed differently, as SCUBA organized them in two arrays as opposed to SCUBA-2 which organizes them in eight arrays.

SCUBA was used extensively in the past for the same scientific goals SCUBA-2 is used for today, namely, the identification and photometry of dusty molecular clumps in star forming regions. Regarding the SCUBA instrument, the work of *M. Reid* and *C.D. Wilson* on high mass star formation is of particular interest. This work spans three separate paper submissions, with the first two discussing the results of the observations. In addition, work done by *G. Sreenilayam et al* regarding cold dust in the vicinity of hot, HII regions is also relevant to the scope of this thesis.

M. Reed & C. Wilson (2005 & 2006)

To begin, I will be investigating two papers from a trilogy published by *M. Reed* and *C. Wilson* [41], [42] for the purpose of comparing their work to that done in this thesis. Specifically, I will discuss their methodology, as well as their noteworthy results, with emphasis on the temperature, mass and size of the identified sources.

To begin, the recipes used in the two papers for the temperature and mass of the identified molecular clumps are the same as the ones used in this thesis. In regards of the opacity,

in the first paper, it is discovered that the identified sources can span a β value between 1.2 and 2 and consequently, a value of 1.5 is adopted for β in both works. In this thesis however, a value of 1.8 is used instead. In addition, the first paper quickly acknowledges the fact that individual temperature and opacity estimates cannot be obtained for each source and proposes the solution of using a prescribed opacity model. Both papers use an opacity of $\kappa_\lambda = 0.1(250\ \mu m/\lambda)^\beta$ while in this thesis $\kappa_\lambda = 0.01(\nu/1.0 \times 10^{12})^\beta$ is used instead. The two models yield similar, but not identical values.

Regarding the methodology, both papers use an automated technique called "clfind2d" for the identification of sources, contrary to this thesis where sources are identified manually. In addition, a clump's size is considered to be the radius of a circle of equal area to the clump, contrary to this thesis where a best-fit aperture is used instead.

When it comes to processing the obtained photometry, both papers acknowledge the presence of negative bowls and use masking as well as a technique called "flattening" to suppress them. "Flattening" is a predecessor technique to the one used in the current data reduction algorithm. Both techniques do not completely eliminate the negative bowl problem and the residual negative fluxes, while treated in this thesis on a clump-by-clump basis, are not treated in the two *M. Reed* and *C. Wilson* papers.

In addition, both papers do not apply a correction for the 850μm contamination by the CO(3-2) transition, as the corrections are deemed small and quite variable from clump to clump. In this thesis, a 10% correction is applied to all 850μm photometry.

Furthermore, both papers account for the radio continuum contamination, while this thesis does not. The presence of such contamination depends on the position of the molecular clumps with respect to a nearby radio continuum source, such as an HII region. In the two papers, it is found that no significant contamination occurs in the 450μm band, however, corrections ranging from 0 to 30% are applied to the 850μm fluxes.

Finally, the two papers provide corrections to the SCUBA-2 error beam, while this thesis does not. These corrections are sometimes required as the error beam tends to vary over the span of observations. Corrections ranging from 3% to 18% are applied to 450μm photometry while corrections ranging from 3% to 14% are applied to the 850μm photometry instead.

Regarding the results, both papers depict clump cases that are easily resolvable in the 850μm band while poorly resolved or completely absent in the 450μm band. These cases provided a challenge when it comes to estimating their temperature. While such sources

are simply not considered when it comes to a temperature estimate, they are dropped off using strict cutoff criteria in this thesis.

In addition, both papers do not attach uncertainty to their produced temperature estimates while this thesis does. In fact, the temperature uncertainty is never considered in further calculations such as that of mass. It is highly likely that stochastic techniques used in this thesis were not popular at the time of these papers and the asymmetry of the temperature uncertainties was an unresolved problem.

Finally, for the sake of comparison, I present obtained properties that are comparable across the two papers and this thesis in table 6.5. A reminder that a β value of 1.5 is used in the two papers while a value of 1.8 is used in this thesis. Finally, the masses defining the mass ranges are all determined using 850μm photometry in both the *M. Reid* and *C.D Wilson* study and this thesis.

Table 6.5: Comparison between the values obtained in the two works by *M. Reid* and *C.D Wilson* to those obtained in this thesis. The comparison includes max and min noise levels in each band as well as the range of obtained temperatures, masses and equivalent radii.

Property	**Reid & Wilson (2005)**	**Reid & Wilson (2006)**	**This Thesis**
450μm Noise (mJy/beam)	180.0	320.0	$4.7 < N_{450} < 1452$
850μm Noise (mJy/beam)	21.0	27.3	$3.0 < N_{850} < 9.1$
Temperature (K)	$8 < T < 325$	$6 < T < 235$	$6.6 < T < 219$
Mass ($M_{\odot}$)	$1.2 < M < 2700$	$0.3 < M < 200$	$0.37 < M < 12325$
Radius (pc)	$0.03 < R < 0.67$	$0.01 < R < 0.21$	$0.038 < R < 2.21$

G. Sreenilayam et al (2011)

Although several papers have been published by *G. Sreenilayam et al* regarding dusty systems, I choose to focus on a particular paper specifically pertaining to dust found in HII region systems [17]. The mass in hot ($\geq 100K$) and cool ($20K < T < 40K$) dust in this paper is obtained using the IRAS instrument, while the mass in cold ($\leq 20K$) dust is obtained using the original SCUBA instrument.

An important result arising from this particular paper is the fraction of molecular mass associated with the dust of each of these three different temperature regimes. More specifically, the mass accounted by the cool dust is observed to be on the order of $10^4 - 10^5$ times larger than that accounted by the hot dust. In addition, the mass accounted by the cold dust appears to be even greater, typically $10 - 100$ times larger than that accounted by the cool dust itself. This is very important, as the masses calculated from the SCUBA-2 450μm and 850μm photometry pertains to the cold dust component, and, according to the findings of this study, the mass obtained from the cold dust is a great approximation to the total mass of a clump's molecular content.

To begin, it is important to mention a commonality between this paper and this thesis. This is none other than the occasionally troubling flux ratio values which can make the determination of an average temperature impossible. The issue is one of the derivative problems from a prescribed rather than determined opacity value. The issue most commonly occurs with high flux ratios, which require unphysical dust temperatures (upwards of 500K) to fit the inflated flux ratios. In both the paper and this thesis, this typically occurs from sub-par 450μm photometry. To circumvent this problem partly, the study assumes a cold dust temperature of 10K for clumps where this problem is encountered in order to be able to give an estimate of their mass. In this thesis however such clumps are entirely discarded from temperature dependent property calculations.

Comparing the results from the *G. Sreenilayam* study to those from this thesis is a little tricky, as the *G. Sreenilayam* study analyzes clump complexes and sometimes large, individual clumps, while in this thesis individual cores inside clumps are distinguished. In order to compare integrated fluxes in each band, I sum the SCUBA-2 fluxes in a particular clump complex. Then, in order to compare average temperature estimates, I average the SCUBA-2 temperatures obtained for all clumps within a particular complex. Finally, in order to compare the cumulative masses, I sum the SCUBA-2 masses of all clumps within a particular complex. The result of the comparisons is presented in table 6.6.

The 450μm and 850μm integrated fluxes, though similar, can be found to differ substantially as can be seen in the cases of S 233C and S 247C. The greatest reason behind these deviations are the clumps considered in each of the two works. Inspection of the images for S 233C and S 247C in figures 16 and 19 respectively reveals that the two systems are very open in nature. While it may be the case that all clumps identified in these two images are considered for the integrated flux totals from this thesis, this is not true for the study, as it focuses on the first one or two closest clumps to a particular HII region. This leads

Table 6.6: Comparison between the values obtained in the work by *G. Sreenilayam et al* to those obtained in this thesis. The comparison includes integrated clump complex 450μm and 850μm fluxes, average clump complex temperatures and total dust and gas masses.

System ID G. Sreenilayam / This Thesis	F_{450} **(Jy) G. Sreenilayam / This Thesis**	F_{850} **(Jy) G. Sreenilayam / This Thesis**	**T (K) G. Sreenilayam / This Thesis**	**M** ($M_{\odot}$) **G. Sreenilayam / This Thesis**
S 104 / G74	- / 255.1±16.4	115.0±0.2 / 43.0±3.2	10 / 13.8±0.76	497 / 6339
S 138C / G105	346.0±7 / 472.2±166.2	27.3±0.3 / 8.94±2.0	- / -	- / -
S 201C / G138	327±7 / 318.2±37.4	43.6±0.2 / 50.6±7.0	17±1 / 15.74±2.2	107±6 / 5551
S 233C / G173	506±8.2 / 1184±103	73.2±0.5 / 131.7±11.5	12.6±3 / 34.5±5.2	77.4±6.2 / 1260
S 242C / G182	278±4 / 198.0±27.2	24.2±0.5 / 32.2±5.5	- / 21.0±3.0	- / 1056
S 247C / G188	328±2 / 1152±103	32±1 / 125.5±13.6	- / 35.0±4.4	- / 1224
S 254-8C / G192	1170±10 / 968.4±122.3	100±1 / 130.5±19.3	- / 26.0±5.5	- / 3599
S 266C / G195	75±1 / 20.02±19.7	13.4±0.2 / 1.33±0.30	9.2±0.4 / -	810±60 / -
S 269 / G196	242±1 / 353.8±116.4	28.5±0.2 / 13.42±3.02	21±1 / -	47±1 / -

to higher integrated flux totals coming from this thesis, as it considers clumps that are further away from a particular HII region.

In cases where the opposite is observed it is more than likely a result of the study incorporating the flux from all the filamentary structure into its integrated flux totals, while this thesis only includes the integrated flux of the dense clump formations in the system.

In regards of the temperatures and total masses, only three clump complexes are directly comparable. The average temperatures of these do not deviate substantially. The masses are different, because the study provides estimates of the total dust mass, as opposed to this thesis which is concerned with total gas and dust mass. Nonetheless it is interesting to compare the two in order to check the validity of the commonly used 1:100 dust-to-gas mass ratio. For the three comparable systems, the dust-to-gas mass ratio is found to be slightly higher than the standard assumption at 8.5:100, 2.0:100 and 6.5:100 for S 104, S 201C and S 233C respectively.

6.2.4 Molecular Clumps - SCUBA-2

Following from the previous section, I now take a look at previous studies using the newer SCUBA-2 instrument. The continuation of the work concerning cold dust near hot HII regions by *G. Sreenilayam et al* appears greatly relevant to this thesis. Hence, I focus on a particular paper from *G. Sreenilayam et al* [18] which considers dusty systems near some familiar HII regions that are also considered in this thesis.

G. Sreenilayam et al (2014)

In this paper, *G. Sreenilayam et al* uses data from the SCUBA-2 instrument to map the dusty component near a variety of galactic HII regions. From the sample covered in that study Sh-2 305 and the Sh-2 254 - Sh-2 258 complex are also part of the sample of this thesis.

Before venturing into direct comparisons between the two studies, it is important to discuss some of their major systematic differences. First and most importantly, the *Sreenilayam* study creates individual pixel-to-pixel maps for temperature, number density, mass and other relevant properties. The temperature for the sources in this study is determined by comparing the fluxes of the brightest 450μm and 850μm pixel within the boundary of the source. This is very different from the approach used in this thesis, where the integrated flux in the 450μm and 850μm bands is compared instead.

The *Sreenilayam* study also uses a value of 2.0 for β contrary to this thesis where a value of 1.8 is used instead. Also, an opacity of 0.01 $cm^2\ g^{-1}$ is adopted for the 850μm band in the study, while in this thesis a value of $\approx 0.0153\ cm^2\ g^{-1}$ is used for this band instead. The study also acknowledges the problem of negative bowl backgrounds and CO line contamination but does not attempt to treat either of them, contrary to this thesis. Finally, objects that are described using the term "clump" in this thesis are described using the term "cloud" in the study. This is more than likely due to the fact that the study is concerned with entire clump composites where cloud subtraction does not take place, and so there is no need for the extra jargon to be introduced.

With the systematics out of the way, it is time to compare the properties of the matching clumps between the two works. These properties include their radial size, average temperature, cumulative mass and column density. The result of the comparisons can be found in table 6.7.

Table 6.7: Comparison between the values obtained in the work by *G. Sreenilayam et al* [18] to those obtained in this thesis. The comparison includes radial size, average temperature, cumulative mass and H_2 column density.

System ID **G. Sreenilayam / This Thesis**	**R (pc)** **G. Sreenilayam / This Thesis**	**T (K)** **G. Sreenilayam / This Thesis**	**M** ($M_\odot$) **G. Sreenilayam / This Thesis**	N_{H_2} (10^{22} cm^{-2}) **G. Sreenilayam / This Thesis**
S254N / G192-2-1	0.38 / 0.29 ± 0.02	24.6 / $62.5^{18.6}_{46.8}$	130 ± 40 / $80.7^{244.1}_{6.0}$	37 / $1.32^{4.9}_{0.1}$
S254S1 / G192-2-2	0.45 / 0.29 ± 0.02	23.4 / $40.9^{33.7}_{26.06}$	110 ± 30 / $139.6^{235.3}_{39.0}$	43 / $2.29^{5.0}_{0.9}$
S254S2 / G192-2-3	0.25 / 0.22 ± 0.02	28.6 / $26.2^{26.8}_{13.6}$	19 ± 7 / $57.2^{51.2}_{23.0}$	8.0 / $1.67^{2.1}_{0.8}$
S305N / G233-1-1	0.81 / 0.61 ± 0.16	13.7 / $16.1^{10.3}_{5.9}$	890 ± 400 / $275.0^{2.3}_{66.7}$	12 / $1.04^{0.7}_{0.4}$
S305W1 / G233-7-2	- / 0.30 ± 0.08	13.8 / $23.0^{23.4}_{10.8}$	170 ± 60 / $26.5^{3.7}_{5.9}$	- / $0.40^{0.41}_{0.20}$
S305W2 / G233-3-3	- / 0.30 ± 0.08	14.7 / $17.0^{13.5}_{6.6}$	200 ± 90 / $36.8^{0.57}_{8.7}$	- / $0.56^{0.37}_{0.26}$
S305W3 / G233-3-4	- / 0.45 ± 0.12	14.1 / $17.4^{13.8}_{6.5}$	260 ± 110 / $95.0^{1.2}_{23.0}$	- / $0.64^{0.44}_{0.29}$
S305W4 / G233-9-1	- / 0.45 ± 0.12	12.9 / $21.5^{22.2}_{10.1}$	70 ± 20 / $28.4^{3.4}_{6.6}$	- / $0.19^{0.19}_{0.1}$
S305W5 / G233-3-1,2	- / 0.30 ± 0.08 0.30 ± 0.08	13.8 / $19.9^{21.1}_{8.7}$ $22.4^{23.5}_{10.2}$	240 ± 60 / $27.8^{2.0}_{7.3}$ $29.2^{3.8}_{6.8}$	- / $0.42^{0.36}_{0.22}$ $0.44^{0.43}_{0.22}$
S305E1 / G233-5-2,3	- / 0.45 ± 0.12 0.45 ± 0.12	14.3 / $20.5^{20.5}_{8.8}$ $17.3^{13.9}_{6.3}$	730 ± 230 / $68.3^{4.7}_{17.3}$ $99.6^{1.3}_{23.3}$	- / $0.46^{0.38}_{0.23}$ $0.67^{0.43}_{0.31}$
S305S / G233-10-4	1.15 / 0.76 ± 0.20	16.7 / $21.2^{20.6}_{8.9}$	560 ± 210 / $457.4^{28.8}_{116.1}$	14 / $1.11^{0.89}_{0.55}$
S305E2 / G233-10-1	- / 0.30 ± 0.08	14.5 / $14.4^{14.6}_{6.1}$	15 ± 2 / $14.0^{0.1}_{3.8}$	- / $0.212^{0.15}_{0.11}$

Evidently, the radial sizes are in good agreement, although the fitting method is very different between the study and this thesis. In the study, a radius for a circle with equal area to the area of the source under consideration is used while in this thesis a best-fit circular aperture is used instead, whose radial size is only varied in 2 pixel increments in order to ease the translation between the 450μm and 850μm images.

The temperatures on the other hand appear to be consistently higher in this thesis with few exceptions. This is probably due to accounting for potential CO contamination in this thesis, contrary to the study. Accounting for the CO contaminations alone makes the 850μm fluxes in this thesis 10% smaller, leading to larger 450μm to 850μm flux ratios and consequently higher temperatures. The negative bowl is treated in both bands in this thesis and is therefore not expected to significantly alter flux ratios and consequently temperature estimates.

On the other hand, some of the mass estimates are in good agreement while others are not.

There are three major reasons for discrepancy here, and all of them pertain to the treatment of different backgrounds. The correction for the CO background in this thesis, drops the 850μm flux and consequently the mass estimate. The correction of the negative bowl on the other hand, boosts the 850μm flux, and consequently the mass estimate. Finally, the separation of the cloud background from the clump composite and its cores lowers the 850μm flux, and consequently the mass estimate. The discrepancies then observed in the mass column come from an interplay of the aforementioned reasons. Most of the time, this thesis is expected to underestimate the mass as 2 out of the 3 aforementioned systematic differences have a decreasing effect on the mass. However, in the case of a really bright, compact core, the negative bowl correction could overthrow the lowering effect of the other 2 corrections and produce a larger mass estimate.

Finally, in regards of the column density, all values in the study are larger than the values of this thesis. This is expected because of the inclusion of the cloud background in the study, which clearly increases the amount of material that is present along any particular line of sight through the source.

6.3 The Consequences of Noisy 450μm Data

It is of interest to tend to the extreme temperature cases of the previous section, as they pertain to an issue that has been brought up throughout the course of this thesis. This issue is none other than the reliability of the 450μm images which a lot of the time is not ideal.

As discussed earlier in chapter 4, the common denominator between the most unreliable 450μm images is bad weather, specifically, a high atmospheric water content. Water molecules not only like to absorb incoming SCUBA-2 radiation, but also provide their own emission in the same wavelength range. The emission is treated through various filtering stages during data reduction, however it results in an image of higher noise. Therefore, in the presence of considerable water vapor, SCUBA-2 emission from dusty clumps will be noisier and consequently less reliable.

The higher noise levels in the image leads directly to the existence of deeper negative bowls. When trying to treat these deeper bowls, a much larger flux needs to be re-introduced to the sources being measured. It is because of this that all noisy 450μm photometry is expected to be overestimated, sometimes grossly so.

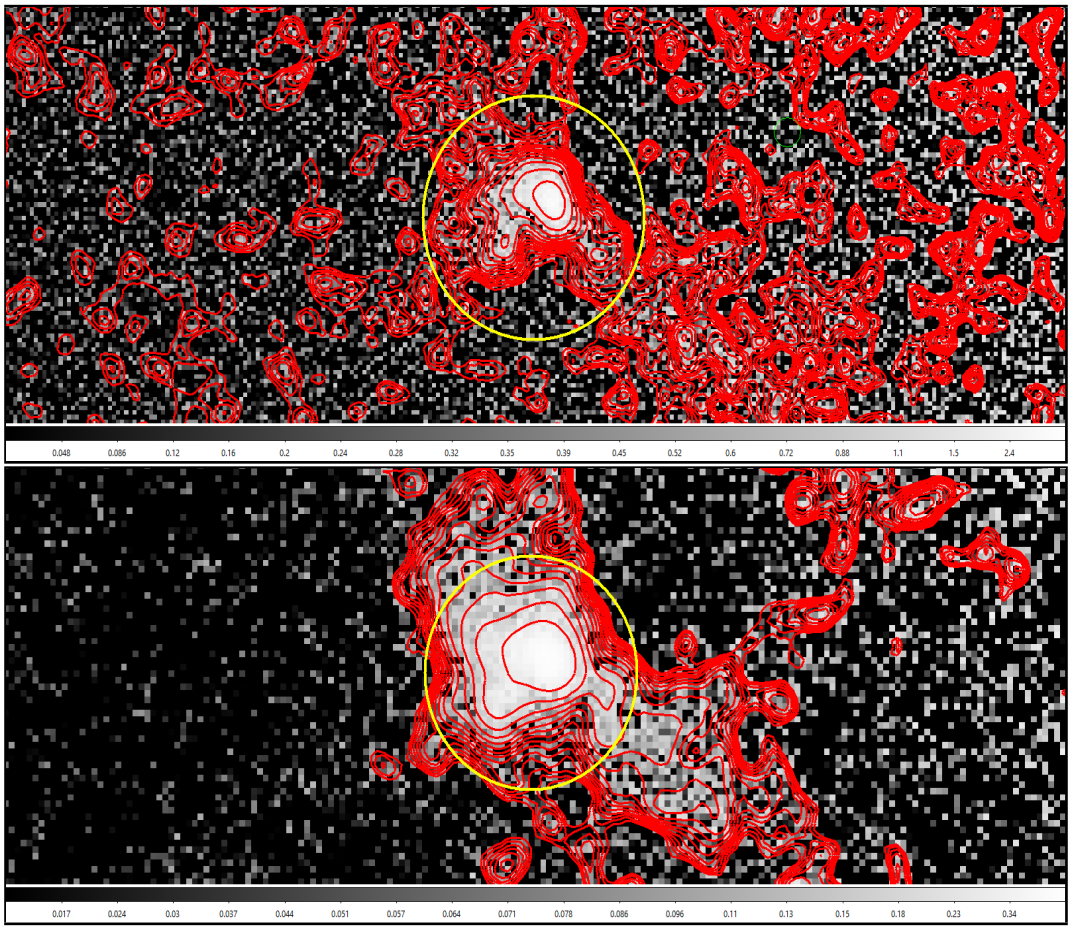

Figure 6.2: Image of the 450μm (Top) and 850μm (Bottom) contour plot of **G74-3**, the cloud with the lowest recorded average temperature. Both images are produced in *SAOImageDS9*. A total of 15 contour levels are used spanning 0.01 to 25 Jy/beam for the 450μm image and 0.01 to 5 Jy/beam for the 850μm image. The smoothness level is set to 5.

This wouldn't be much of an issue if the previously described effect was similar between the two wavelengths. However, it is this asymmetry that introduces the problem of unreasonably high flux ratios. Specifically, the 450μm band is much more sensitive to both the absorption and the emission effect introduced from the presence of water vapor. This means that 450μm fluxes will always be more overestimated than their 850μm counterparts, provided the observations in the two bands were made at the same time.

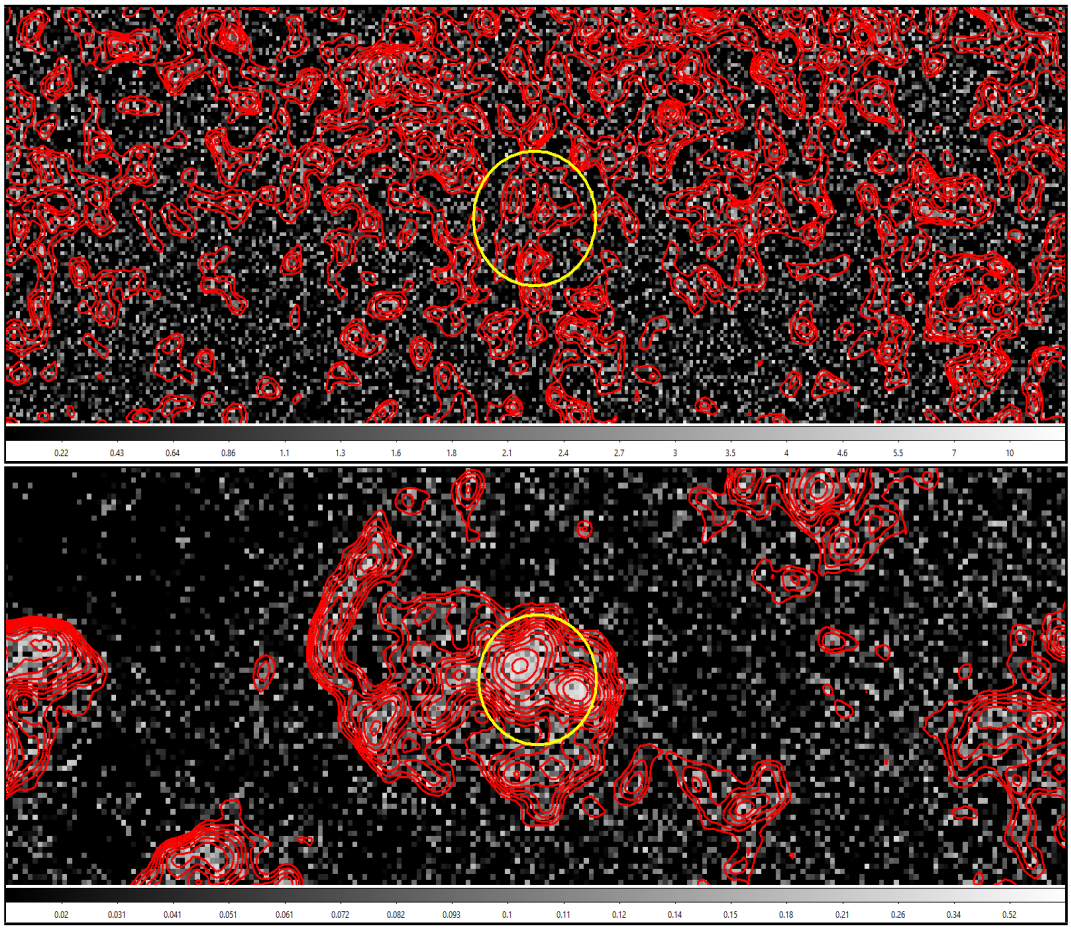

Figure 6.3: Image of the 450μm (Top) and 850μm (Bottom) contour plot of **G173-7**, the cloud with the highest recorded average temperature. Both images are produced in *SAOImageDS9*. A total of 15 contour levels are used spanning 0.01 to 25 Jy/beam for the 450μm image and 0.01 to 5 Jy/beam for the 850μm image. The smoothness level is set to 5.

The consequence of this asymmetry is an overestimation of the 450μm to 850μm flux ratio, which inevitably leads to higher average temperature estimates. Fortunately, this issue is captured well in the uncertainties produced from the stochastic Monte-Carlo technique implemented for dealing with the uncertainty of temperature-dependent quantities.

In addition, it is known that the two SCUBA-2 bands are mostly sensitive to cold ($\leq$ 20K) dust. When combining this with the above known issue, it becomes evident that the

most extreme average temperature estimates will be some of the most unreliable and their unreliability should be traceable to their noisy 450μm mosaics.

In support of the above claim, I investigate the 450μm and 850μm images of the hottest and coldest core and cloud segment objects from the entire sample in this thesis. The temperature values for these cores and clouds can be found in tables 6.1 and 6.2 respectively.

Starting with the cloud segments, the coldest cloud is found to be **G74-3** (displayed in figure 6.2), while the hottest cloud is found to be **G173-7** (displayed in figure 6.3). The structure is highly resolved in the 850μm band for both objects. However, the same cannot be said for the 450μm band where G74-3 is highly resolved but G173-7 is unresolvable. Essentially if the location of G173-7 wasn't found using the 850μm position coordinates, it would've never been found in the 450μm image.

Continuing on with the cores, the coldest core is found to be **G70-19-1** (displayed in figure 6.4) while the hottest core is found to be **G173-15-2** (displayed in figure 6.5). Inspection of G70-19-1 shows that it is very well resolved in both 450μm and 850μm bands. On the contrary, core G173-15-2 is well resolved in the 850μm but not well resolved at all in the 450μm band as the image is suffering from a very high noise level. Note that G173-15-1 and G173-15-2 are neighboring cores that are barely distinguishable and could potentially constitute a single core composite.

Evidently, both temperature extremes presented here are associated with a terrible 450μm image. It is expected that all extremely high temperatures are a consequence of such unreliable 450μm data, however, one should not discard the possibility of few really hot temperatures actually being physical.

Finally, the consequences of the temperature overestimation propagate to other temperature-dependent quantities as well, leading to underestimated total masses, number and column densities, as well as average pressures.

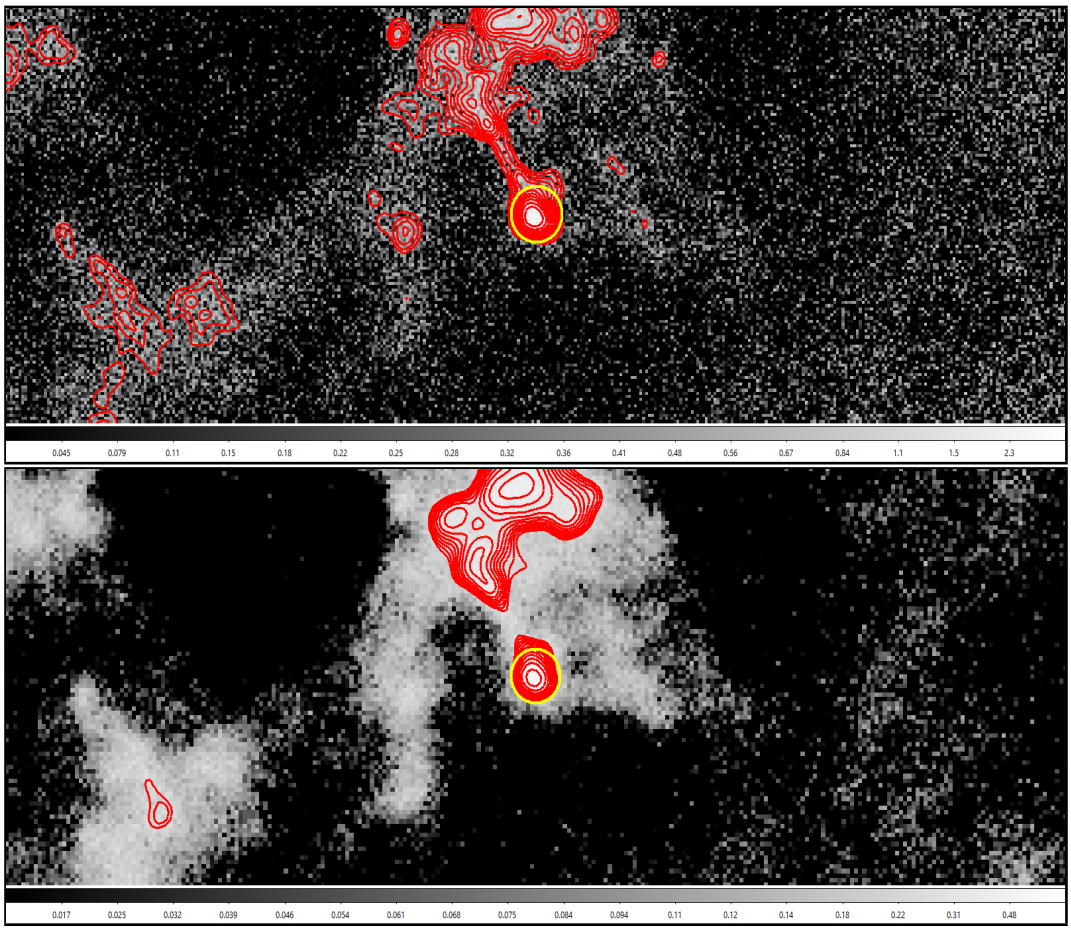

Figure 6.4: Image of the 450μm (Top) and 850μm (Bottom) contour plot of **G70-19-1**, the core with the lowest recorded average temperature. Both images are produced in *SAOImageDS9*. A total of 15 contour levels are used spanning 0.1 to 50 Jy/beam for the 450μm image and 0.1 to 10 Jy/beam for the 850μm image. The smoothness level is set to 5.

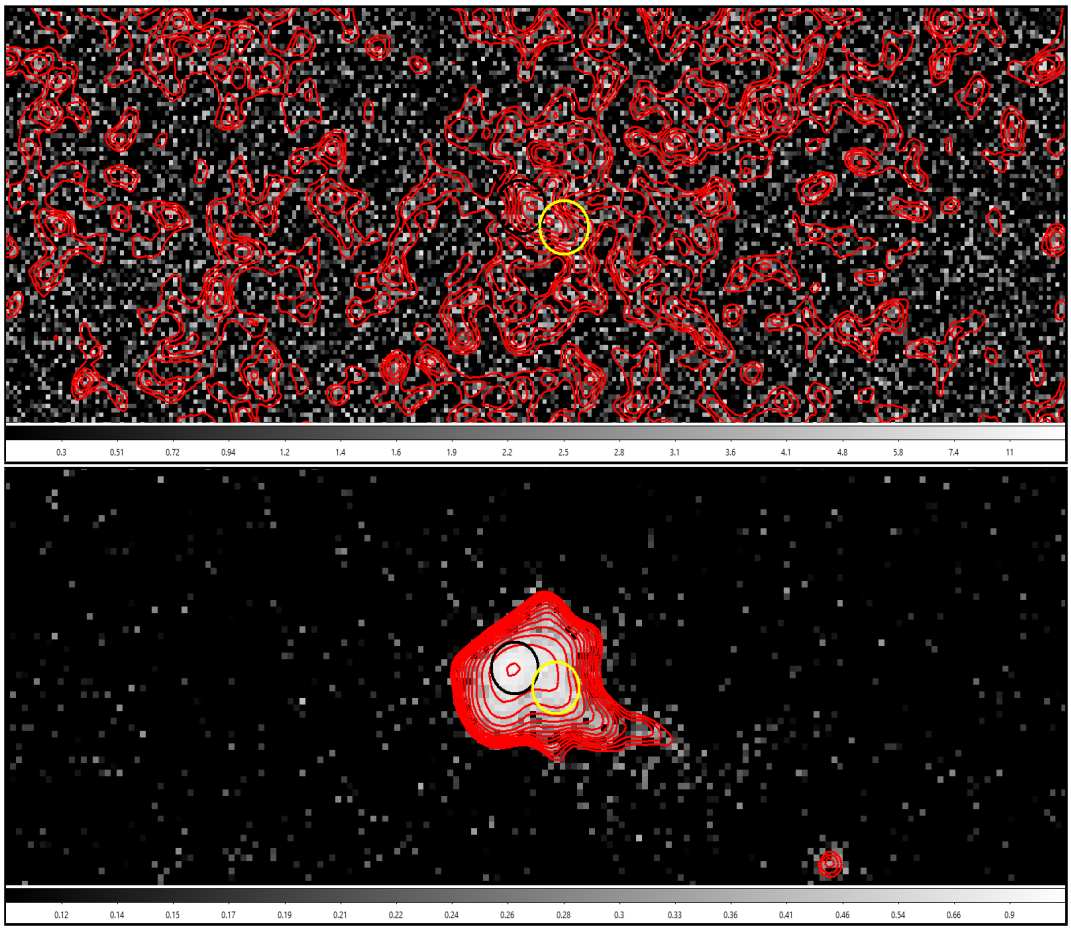

Figure 6.5: Image of the 450μm (Top) and 850μm (Bottom) contour plot of **G173-15-2** (in yellow) which may comprise a single core along with G173-15-1 (in black). G173-15-2 is the core with the highest recorded average temperature. Both images are produced in *SAOImageDS9*. A total of 15 contour levels are used spanning 0.1 to 50 Jy/beam for the 450μm image and 0.1 to 10 Jy/beam for the 850μm image. The smoothness level is set to 5.

6.4 Background Clumps

In this section I will be investigating the issue of falsely identifying clumps that are not part of a particular system, but rather part of the distant background or a different system. I will do this by determining the rough probability of such a misidentification taking place. This will also answer some questions that naturally arise, such as "How many of the clumps present should one expect to be part of the background?" and "What is the probability of encountering a background clump within a certain distance from the associated HII Region?".

To start, I consider the bottom plot of figure 3.13 to which I fit a simple toy model that portrays what clump formation would look like in an HII-Region-Free ISM. Stripped of HII regions and any other feedback mechanisms, such hypothetical molecular cloud of infinite size would form cores randomly throughout, the number density of which would be best described by a constant.

In my toy model, I allow one free parameter, namely n_0, which is the number density of cores in the undisturbed, background ISM. The equation for this toy model can then be expressed as follows:

$$dN = n_0 dA \tag{6.1}$$

$$N = n_0 \int dA \tag{6.2}$$

$$N = n_0 2\pi \int r dr \tag{6.3}$$

$$N = n_0 \pi r^2 \tag{6.4}$$

$$\tag{6.5}$$

Where n_0 is the core number density in the undisturbed, background ISM and r represents the 2-dimensional distance from the center of an associated HII region. This distance can be in either angular or physical units without loss of generality. In order to determine the value of n_0 it is necessary to consider a portion of cores from our sample that are highly unlikely to be associated with their assigned HII region. The most reliable way of obtaining these is through a careful inspection of the top plot in figure 3.13 coupled with a visual inspection of the SCUBA-2 images at hand.

It appears that there exists a dip in the number of cores lying between 20-25 arcminutes from their matched HII region. This occurs because cores existing beyond such radii

are very unlikely to be associated with their assigned HII region. Therefore, it is reasonable to assume that cores existing at or beyond this radius range represent well the core number density in a supposedly empty ISM.

Before venturing into an estimation of n_0, a small discussion on the effect of an incurred bias needs to take place. The largest images considered in this thesis are PONG7200s, with a usable area of radius $\approx$ 70 arcminutes (see table 5.1). Ideally, these large images provide the perfect ground for an estimation of n_0 as there is plenty of room around the Sharpless HII regions for non-associated cores to exist.

However, with larger PONG patterns comes a faster scanning velocity, reducing the sensitivity of the scan. Only the brightest cores are visible in those legacy scans, and as expected, the brightest cores tend to be the ones associated with an HII region and not the other way around.

Not all hope is lost though, as mid-size PONG images provide a good trade between resolving ability and the likelihood that identified cores are not associated with the nearby HII region. A great example is G108 (see figure 6), where it is visually clear which cores are associated with Sh-2 152 and which are not. Non-associated cores, such as those of image G108 populate the distance bins close to 25 arcminutes in the bottom plot of figure 3.13. Due to the insensitivity of larger PONG scans, the distance bins beyond 25 arcminutes become increasingly vacant of identified objects. Therefore, it is possible to approximate the value of n_0 by best fitting equation 6.1 to the bins near the 25 arcminute separation distance mark. I produce a conservative and a non-conservative fit to the objects of these bins, displayed using a solid and dashed-line respectively in figure 6.6

Using the fitted models, I produce a conservative and non-conservative estimate for the probability of finding a core that is actually part of the background within a certain separation distance. I also estimate the number of cores from the sample that I expect to be part of the background. My results are summarized in table 6.8. It is evident that the probability of an identified core being part of the background is very small.

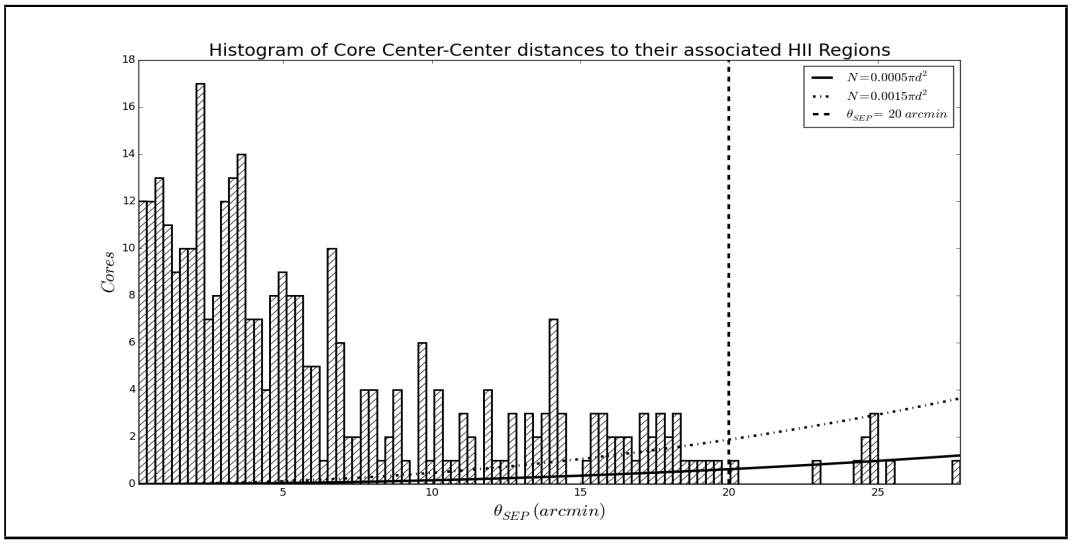

Figure 6.6: Histogram of each core's center-to-center distance to its matched Sharpless HII region. Two fits attempting to model core formation at the absence of HII regions are presented. The solid line represents the conservative fit and the dashed line the non-conservative fit.

Table 6.8: Table of fitted n_0 values and resulting probabilities of finding a core belonging to the background within 10 and 20 arcminutes, as well as the expectation of background cores within the entire core sample.

Fit	$\boldsymbol{n_0}$ $\boldsymbol{(arcmin^{-2})}$	$\boldsymbol{P(<10arcmin)}$	$\boldsymbol{P(<20arcmin)}$	**Background Cores**
Conservative	0.0005	0.065 %	0.196 %	2
Non-Conservative	0.0015	0.196 %	0.589 %	6

6.5 The Stability of the Monte-Carlo Simulations

In this section I will investigate the reliability of the Monte-Carlo simulations used for the calculation of upper and lower uncertainties in temperature-dependent quantities. Any instability in the results could be caused due to the high sensitivity to a particular heuristic used. Heuristics here pertain to the definition of acceptable ranges for random sampling, as well as controlling the number of iterations that the simulation takes place.

Overall, the experimenter has control of 4 acceptable ranges which include those for the 450μm, 850μm, distance and flux ratio sampling space. In addition, the experimenter has

control of the number of draws performed for the determination of the uncertainty in each temperature-dependent quantity. It is then of interest to investigate how the routine behaves when these 5 inputs are changed and to check if the output is particularly sensitive to these changes, something that would require reconsideration of the heuristics used and potentially the entire algorithm itself.

In order to do this, I investigate the calculation of the upper and lower uncertainties for all temperature-dependent quantities of core G97-1-2. I vary individually each of the 5 aforementioned control variables and note how the upper and lower uncertainty estimates change as a consequence. The results are presented in plots where the uncertainty-to-mean ratio is compared against the values of the varied input variable.

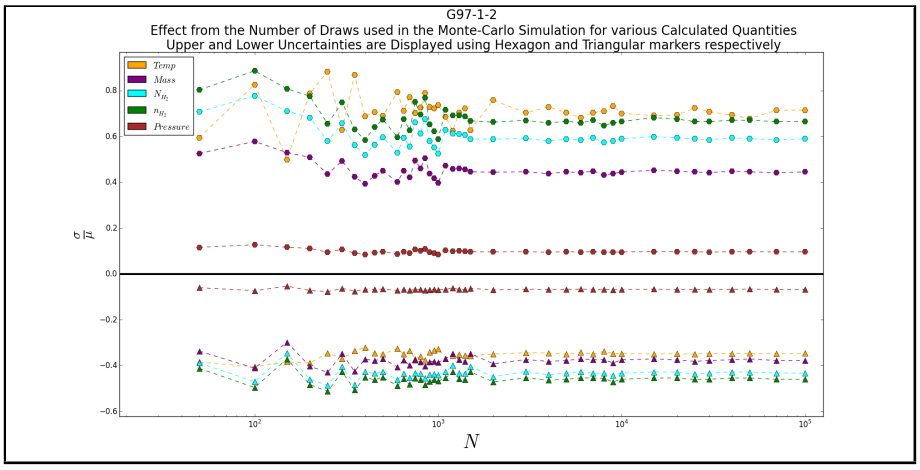

Figure 6.7: A plot comparing simultaneously the upper (Top-Part) and lower (Bottom-Part) uncertainties for all temperature-dependent quantities using a varying number of random draws. The y-axis compares the corresponding upper or lower uncertainty to the best estimate of the respective quantity. The x-axis displays the different number of draws used.

To begin, it is of great importance to check that the Monte-Carlo simulations are stable at the number of draws used in this thesis (5000). To do this, the number of draws is varied from 50 all the way to 100000. The result is plotted in figure 6.7. It is evident that both upper and lower uncertainty estimates vary significantly less when more than 1000 random draws are used. Therefore, it seems that 5000 draws in an excellent choice for reliable uncertainty estimates to be made.

Next, I investigate the effect of varying the acceptable distance range. The minimum for this acceptable range is not varied, as the closest HII regions to Earth are known to be on the order of 1 kpc away. However, the maximum is indeed varied, as galactic HII regions can be found all the way out to the outskirts of the Milky-Way galaxy. Therefore, the max of the distance range is varied from the largest distance recorded in our HII region sample ($\approx$ 12 kpc) all the way out to a non-conservative estimate of the Milky-Way's diameter ($\approx$ 65 kpc). The result is displayed in figure 6.8. Evidently, uncertainty estimates do not vary significantly with changes in the max of the acceptable distance range.

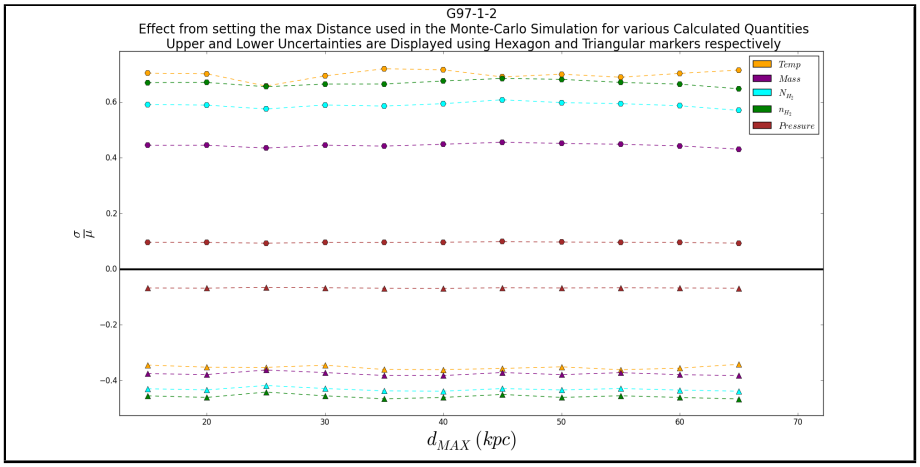

Figure 6.8: A plot comparing simultaneously the upper (Top-Part) and lower (Bottom-Part) uncertainties for all temperature-dependent quantities using a varying upper limit to the acceptable distance range. The y-axis compares the corresponding upper or lower uncertainty to the best estimate of the respective quantity. The x-axis displays the different upper distance limits used

Continuing on, I investigate the effect of varying the acceptable range of 450μm and 850μm integrated fluxes. The minimum is not varied, as a source will always have an integrated flux greater than 0 Jy. However, the maximum is varied for both bands up to the ridiculously large value of 1000 Jy. The results for the 450μm and 850μm bands are presented in figures 6.9 and 6.10 respectively. Evidently, no significant variation in the uncertainty estimates occurs when changing the max of the acceptable integrated flux ranges. I do not investigate the effect of varying the acceptable flux ratio range, as the range used in the Monte-Carlo simulation is the same as the hard physical cutoff applied in section

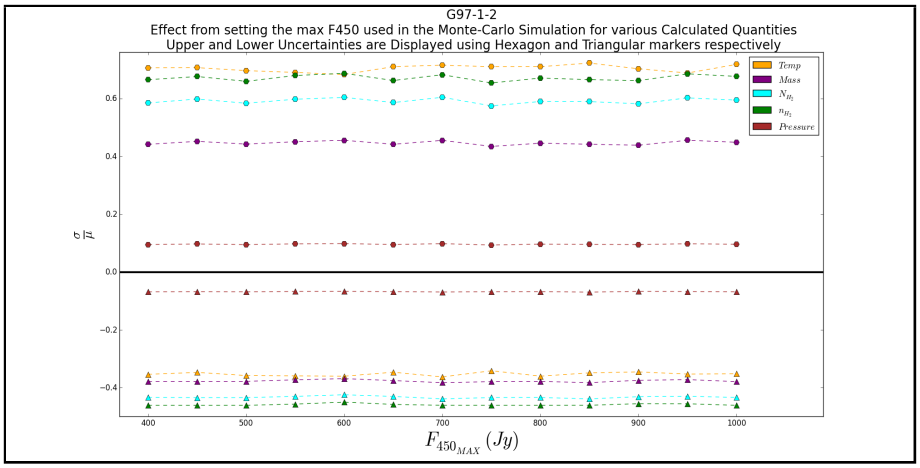

Figure 6.9: A plot comparing simultaneously the upper (Top-Part) and lower (Bottom-Part) uncertainties for all temperature-dependent quantities using a varying upper limit to the acceptable 450μm integrated flux. The y-axis compares the corresponding upper or lower uncertainty to the best estimate of the respective quantity. The x-axis displays the different upper 450μm integrated flux limits used

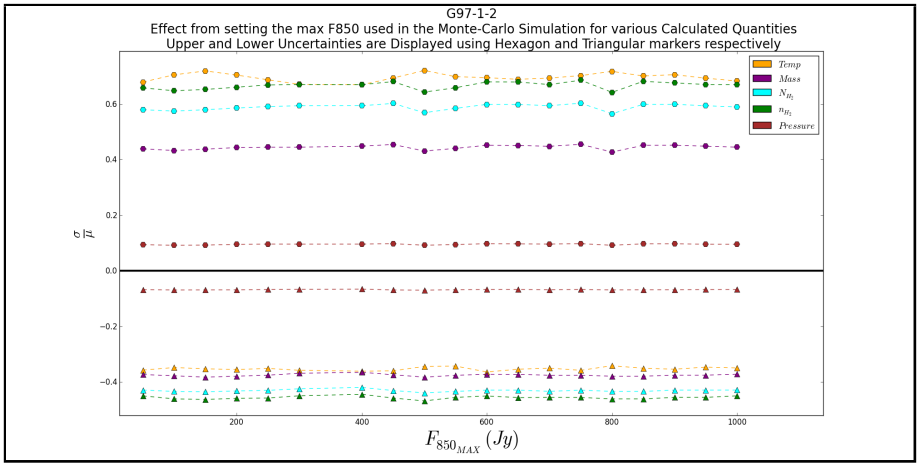

Figure 6.10: A plot comparing simultaneously the upper (Top-Part) and lower (Bottom-Part) uncertainties for all temperature-dependent quantities using a varying upper limit to the acceptable 850μm integrated flux. The y-axis compares the corresponding upper or lower uncertainty to the best estimate of the respective quantity. The x-axis displays the different upper 850μm integrated flux limits used

3.6.2. In conclusion then, the 5000 draw Monte-Carlo routine produces stable and reliable uncertainty estimates which are not strongly dependent on the heuristics used.

6.6 The Progressive Loss of Precision

Observing the noise pollution of the analysis plots in chapter 5, or the high uncertainties for derivative properties in the appendix tables of this thesis, it is easy to assume that the original SCUBA-2 photometry is at fault. While this is sometimes true for few images taken during unfavorable weather conditions, particularly in the 450μm band, most of the time the images used are of good quality.

It is then natural to question how the dramatic loss of precision occurs. The simplest answer to this is that it occurs gradually from the introduction of various levels of uncertainty during the progression through each of the many processing stages involved. The biggest offenders for this are the non-linearity of the temperature model combined with a single "best-guess" estimate for β, as well as the typically large uncertainties involved in distance estimates. However, every little bit counts, and I will attempt to display how this progressive loss of precision occurs for a single SCUBA-2 core.

The chosen core for this purpose is G115-1-2, whose image is displayed in figure 6.11 This core is well resolved, with raw photometry of high SNR and a true β value which, based on the temperature estimates, does not differ much from the assumed β of 1.8 in this thesis. This core is chosen in order to display what happens to an object with good photometry as it traverses the data reduction stages.

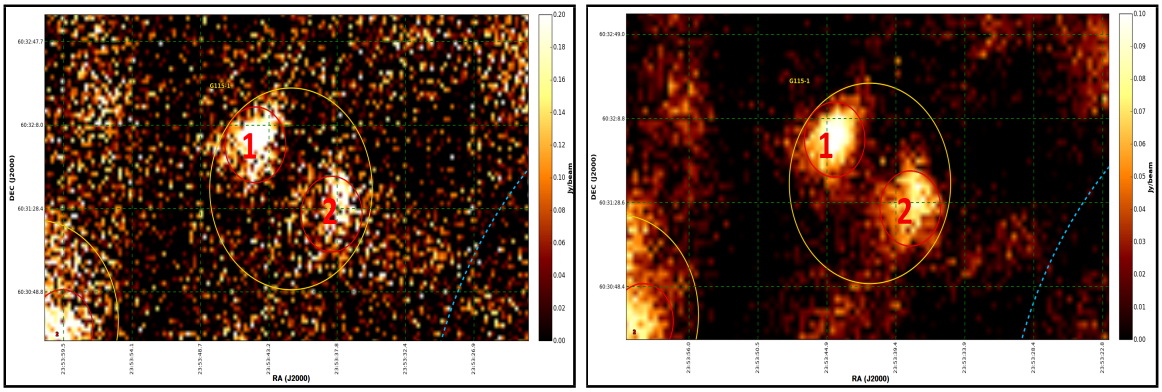

Figure 6.11: 450μm (Left) and 850μm (Right) image of core G115-1-2 and its parent clump composite

Beginning then with raw measurements, the raw 450μm and 850μm integrated flux for

this core is 23.47±2.07 Jy/beam and 6.06±0.61 Jy/beam respectively. This means the raw 450μm and 850μm SNR values are **11.3** and **9.9** respectively. Evidently, both band measurements are of excellent precision.

Treatment of the negative bowl, cloud and CO(3-2) backgrounds as well as propagation of the uncertainty introduced from every contributor discussed in chapter 4, the final, pure 450μm and 850μm flux for the same object is now 23.39±2.9 Jy/beam and 4.15±1.1 Jy/beam respectively. Evidently the 450μm and 850μm SNR values have now dropped to **8.1** and **3.8** respectively.

Conversion from units of Jy/beam to mJy introduces another small amount of uncertainty, where now the pure, integrated, 450μm and 850μm fluxes will be 897.5±191 mJy and 162.7±44 mJy respectively. This is the final stage of photometry, and evidently the core has made it through with a final 450μm and 850μm SNR of **4.7** and **3.7** respectively. This is a staggering drop of 58.4% and 62.6% in precision for each the 450μm and 850μm flux measurement respectively.

Beginning the calculation stage, the first quantity that is needed is the ratio of the integrated flux in the two bands. Comparing then the final 450μm and 850μm integrated fluxes to get their ratio, one obtains 5.51±1.9, with a mere SNR of **2.9**.

Providing the values of 5.51 and 1.9 as the values of μ and σ in the temperature Monte-Carlo simulation, we arrive at the final temperature estimate of $13.52^{7.8}_{4.3}$ K. For the sake of comparison, calculating the average symmetric uncertainty allows to re-write the above roughly as 13.52±6.1, which has a mean SNR of **2.2**.

This temperature will have to be used in the calculation of subsequent temperature-dependent quantities, such as mass, pressure, number and column density, where additional uncertainties will have to be integrated into the calculation and the SNR is expected to drop even further.

However, this is prevented via a clever work-around, where instead of calculating each temperature-dependent quantity on its own, they are all calculated simultaneously with each of their variable ingredients provided through random-draws that are confined within reasonable physical ranges. This means that the really low SNR of the temperature calculation will not affect the uncertainty of temperature-dependent quantities, rather, the uncertainty of the constituents of the temperature (i.e F_{450} and F_{850}) will, which are of much higher certainty than the temperature itself.

To see this in effect, the temperature-dependent quantities for G115-1-2 are presented below in decreasing order of certainty. The mass is found to be $6.38^{0.8}_{1.3}$ $M_{\odot}$ with a mean SNR of **6.2**. The pressure is found to be $7.65 \times 10^{-13}{}^{1.6\times10^{-13}}_{1.1\times10^{-13}}$ Pa, with a mean SNR of **5.6**. The H_2 column density is found to be $2.54 \times 10^{21}{}^{1.3\times10^{21}}_{9.8\times10^{20}}$ cm^{-2}, with a mean SNR of **2.2**. Finally, the only quantity with a lower SNR than the temperature is the H_2 number density which is found to be 3307^{2502}_{1542} cm^{-3}, with a mean SNR of **1.6**.

Evidently, a large amount of uncertainty is introduced during the data reduction stages from a large number of sources. The above results should be interpreted with caution however, as the use of an SNR to represent precision can be misleading. This is because it is a fractional comparison, meaning that the propagation of an identical sized error to a high SNR value will drop its value much more than it would to an already low SNR value, something that can be seen in action during the unit conversion portion earlier in this section.

Chapter 7

Conclusion

In this thesis, 450μm and 850μm SCUBA-2 and 1.46/4.89 GHz VLA observations of dusty HII region systems were used in asserting the hypothesis of increased clump condensation occurring along the boundary of HII regions through the "collect-collapse" process.

In total, 38 images were considered. Of these, 31 contained one or more HII regions from the "Sh-2" or "BFS" catalogue as well as one or more molecular clumps. In total, 185 such molecular clump composites were identified, hosting a total of 333 cores. After data segregation took place, 176 of these clumps along with 315 embedded cores continued into analysis.

All clump composites were split into a cloud and core component. For the cores, the cloud component was removed, along with the effect from the negative bowl background and the CO(3-2) line emission. Similarly, for the clouds both the negative bowl and CO(3-2) line emission were removed as well.

Several properties were obtained for the cores, clouds and clump composites. These included physical properties such as central coordinates, distance, angular and physical size; photometric properties such as 450μm and 850μm integrated flux, mean flux per pixel, surface brightness and in-band luminosity; and finally derived properties such as spectral index, average temperature, total mass, average pressure, average column density and average number density.

Furthermore, several properties for the HII regions present in the images were also obtained. These included physical properties such as central coordinates, distance, angular

and physical size; photometric properties such as integrated flux in either the 1.46 GHz or 4.89 GHz band; and finally derived properties such as electron number density and total mass.

Analysis of the aforementioned properties lead to some interesting discoveries. The most prominent was strong evidence in support of the increased molecular condensation claim made in the beginning of this thesis through observation of an enhanced number of cores existing in the neighborhood of a core-to-HII region scaled separation distance of 1. In addition, evidence for HII regions compressing their associated clumps came from observing much larger average pressures for the HII regions as compared to the outer layers of their associated clumps.

Regarding HII region heating effects, the scaled center-to-center angular distance displayed little-to-no evidence of heating taking place. However, the center-to-center physical distance did display increasing temperatures, particularly below $\approx 10\ pc$

Regarding OB star heating effects, the center-to-center physical distance did display increasing temperatures, particularly below $\approx 10\ pc$. Furthermore, the total incident flux from neighboring OB stars to associated clumps displayed no clear evidence for a correlation with average clump component temperatures, contrary to what was expected. This was mostly attributed to the extremely small incident flux values encountered ($\leq 1\ W/m^2$) and the large noise levels at hand.

Cloud structures depicted a decreasing temperature with increasing column and number density, something that suggested they are not being significantly heated by external mechanisms and that they are more efficient at cooling at a denser state. Furthermore, core structures also depicted a decreasing temperature with increasing column density and no change in temperature with increasing number density, suggesting that their heating comes mostly from internal processes of which the most likely is gravitational contraction and that the convective cooling taking place is on the same order as the heating from gravitational contraction energy being released.

The temperature of the surrounding cloud medium was found to have no significant effect on the coagulation of core mass inside. Furthermore, a significant portion of cores from the sample was found to be hotter than their surrounding cloud, suggesting collapse and potential star formation taking place.

The star formation efficiency (SFE) for some of the HII region systems that had a com-

plete, or nearly complete description of their stellar and gaseous mass components was calculated. These systems suggested a mean SFE value of 4.82%, with a maximum of 38.72% and a minimum of 0.216%. However, most of the analyzed systems depicted an SFE value $\leq 1\%$. Also, lower SFE values tended to be better determined.

Finally, some significant work was done in bringing forward the greatest uncertainty contributors to SCUBA-2 data. The large noise levels introduced from unfavorable weather conditions, especially in the 450μm band were deemed the dominant contributor to SCUBA-2 noise. For the first time in this subject area, asymmetric uncertainties were attached to temperature-dependent quantities using a stochastic Monte-Carlo approach, shedding light to the magnitude of uncertainty introduced from a prescribed opacity model and a highly non-linear temperature model for dust.

7.1 Future Work

The first future goal that should be noted is a better understanding of asymmetric uncertainties and how these can be propagated through different operations. This will allow the results presented in Chapter 5 to be properly fitted with models whose significance can actually be calculated. It will also allow the determination of uncertainty in calculations such as star formation efficiency, core-to-cloud temperature ratio and others.

Continuing with SCUBA-2 observations, additional telescope time should be requested in order to observe distant HII region systems for which only noisy legacy surveys were available. In addition to those, re-observing targets whose current 450μm image is polluted by high levels of noise due to poor atmospheric conditions would lead to a dramatic uncertainty decrease in the results, but also allow a larger portion of the sample to have a full property description.

In addition, further treatment of the obtained photometry would improve the accuracy of the results. One such treatment is accounting for the variation of the SCUBA-2 error beam during observations. Another improvement would come from accounting for additional contamination sources. One of these is radio-continuum radiation, for which HII regions are the biggest offenders. Another is molecular line emission from molecules other than CO, such as CH_3OH and SO_2.

The biggest improvement however would come from a consideration of a larger variety

of submillimeter and far-infrared observations in neighboring wavelengths to those of the SCUBA-2 instrument. The reasons why these would be handy are many.

For starters, dust emission from hot dust typically peaks around 100μm while that of cool dust around 250μm. SCUBA-2 observations in the 450μm and 850μm wavelengths are obtaining mostly flux from the cold dust component. Even though almost all of the mass of the dust is expected to be traced by the cold dust component, it leaves the particular composition of a dusty system unknown. For example, a particular core could have a much larger hot and cool dust component than expected as it is being heated from a nearby OB star or HII region front. Without additional submillimeter observations, this means that a large portion of its mass could end up being unaccounted for. In addition, it makes it impossible to identify the different dust temperature components of the system in order to investigate how such heating sources affect individual clump components.

Another issue of not having these observations available is the restriction of using a static β value rather than one determined on a source-by-source basis. This can seriously underestimate (and much more rarely, overestimate) a clump's dust opacity. If observations in multiple submillimeter wavelengths are available, a better estimate for each source's β value can be made by fitting over all its integrated flux measurements.

Furthermore, sometimes the SCUBA-2 bands may not receive significant emission from a particular source. This could be due to a variety of reasons, such as a case of enhanced extinction, or a particularly hot system. Having these extra submillimeter observations allows one to use the band pair of highest received flux for temperature estimates, instead of being stuck with having to use a bad 450μm (or in very rare cases 850μm) measurement.

Overall then, extra submillimeter and far-infrared observations would allow for a fuller, richer understanding of dusty molecular clumps. A great place to start would be 24μm, 70μm and 160μm data from the "Multiband Imaging Photometer for Spitzer" (MIPS) as well as 250μm, 360μm and 520μm data from the "Spectral and Photometric Imaging Receiver" (SPIRE) for Herschel.

References

[1] Free free radio emission from an hii region. https://www.cv.nrao.edu/course/astr534/PDFnewfiles/FreeFreeEmission.pdf. Published: 2010-10-25, Accessed: 2018-06-18.

[2] Landon curt noll. stellar classification table - sorted by hr class. http://www.isthe.com/chongo/tech/astro/HR-temp-mass-table-byhrclass.html. Accessed: 2018-06-23.

[3] R. pogge, iii ionized hydrogen (hii) regions. http://www.astronomy.ohio-state.edu/~pogge/Ast871/Notes/Ionized.pdf. Accessed: 2018-06-18.

[4] Very large array. national radio astronomy observatory. https://public.nrao.edu/telescopes/vla/. Accessed: 2018-06-18.

[5] A.W.A Pauldrach A. Sternberg, T.L Hoffman. Ionizing Photon Emission Rates from O- and Early B-Type Stars and Clusters. *The Astrophysical Journal*, 599:1333–1343, 2003.

[6] J. Brand F. Massi J. Caplan F. Comeron B. Lefloch A. Zavagno, L. Deharveng. Triggered Massive-Star Formation on the Borders of Galactic HII Regions. *IAU*, 227:346–351, 2005.

[7] L. Dehareng T. Hosokawa D. Russeil J. Caplan A. Zavagno, M. Pomares. Triggered Star Formation on the Borders of the Galactic HII Region RCW 120. *Astronomy and Astrophysics*, 472:835–846, 2007.

[8] G.R Bell T. Norsen J.P Simpson M.R. Haas E.F Erickson A.L. Rudolph, M. Fich. Abundance Gradients In The Galaxy. *The Astronomical Journal Supplement Series*, 162:346–374, 2006.

[9] J.S Mathis B.D. Savage. Observed Properties of Interstellar Dust. *Astron Astrophysics*, 17:73–111, 1979.

[10] S.F. Beaulieu. Technical Notes: JCMT SCUBA-2 Data Reduction at University of Waterloo. *SFB-UWaterloo-JCMT-SCUBA-2*, 1:1–23, 2016.

[11] C.J. Lada B.G. Elmegreen. Sequential Formation of Subgroups in OB Associations. *The Astrophysical Journal*, 214:725–741, 1977.

[12] Fich M. Chan, G. An IRAS Survey of HII Regions. *The Astronomical Journal*, 109, 1995.

[13] Lada C.J. Star Formation: From OB Associations to Protostars. *IAU*, 1987.

[14] Y.M. Georgelin D. Russeil, C. Adami. Revised Distances of Northern HII Regions. *Astronomy and Astrophysicsl*, 470:161–171, 2007.

[15] M. Fich. A Complete VLA Survey In The Outer Galaxy. *The Astronomical Journal*, 92:787–804, 1986.

[16] M. Fich. A VLA Survey of Optically Visible Galactic HII Regions. *The Astrophysical Journal Supplement Series*, 86, 1993.

[17] M. Fich G. Sreenilayam. Hot and Cold Dust Near HII Regions. *The Astronomical Journal*, 142, 2011.

[18] P. Ade D. Bintley E. Chapin A. Chrysostomou J.S. Dunlop A. Gibb J.S. Greaves M. Halpern W.S. Holland R. Ivison T. Jenness-I. Robson D. Scott G. Sreenilayam, M. Fich. Cold Dust in Hot Regions. *The Astronomical Journal*, 147, 2014.

[19] E.W Greisen. Non-linear Coordinate Systems in AIPS. Reissue of November 1983 version. *AIPS Memo*, 27:1–13, 1993.

[20] E.T. Vishniac W.D Cochran H, Noh. Gravitational Instabilities in a Protoplanetary Disk. *The Astrophysical Journal*, 383:372–379, 1991.

[21] T. Henning. Interstellar Dust Grains - An Overview. *IAU*, 383:343–356, 1996.

[22] M.J Currie H.S Thomas. The SCUBA-2 Data Reduction Cookbook. *Joint Astronomy Center, Starlink Project*, 21, 2014.

[23] M. Tapia J. Bohigas. Sh 2-128: An HII and Star-Forming Region in the Galactic Outback. *The Astronomical Journal*, 126, 2003.

[24] A. Zavagno L. Deharveng B. Lefloch J. Brand, F. Massi. Triggered Star Formation at the Borders of the HII Region Sh2-217. *Astronomy and Astrophysics*, 527:1–23, 2011.

[25] T. Jenness R. P. J. Tilanus H. S. Thomas W. S. Holland D. Bintley D. S. Berry E. L. Chapin A. Chrysostomou G.R. Davis A. G. Gibb H. Parsons E. I. Robson J. T. Dempsey, P. Friberg. SCUBA-2: on-sky calibration using submillimetre standard sources. *MNRAS*, 430:2534–2544, 2013.

[26] J. Greaves J. S. Richer B.C. Matthews D. Johnstone H. Kirk S. F. Beaulieu D. S. Berry H. Broekhoven-Fiene M. J. Currie M. Fich J. Hatchell T. Jenness J. C. Mottram D. Nutter K. Pattle J. E. Pineda C. Salji S. Tisi J. Di Francesco M. R. Hogerheijde D. Ward-Thompson P. Bastien H. Butner M. Chen A. Chrysostomou S. Coude C. J. Davis A. Duarte-Cabral P. Friberg R. Friesen G. A. Fuller S. Graves J. Gregson W. Holland G. Joncas J. M. Kirk L. B. G. Knee S. Mairs K. Marsh G. Moriarty-Schieven J. Rawlings E. Rosolowsky D. Rumble S. Sadavoy H. Thomas N. Tothill S. Viti G. J. White C. D. Wilson J. Wouterloot J. Yates M. Zhu J. V. Buckle, E. Drabek-Maunder. The JCMT Gould Belt Survey: SCUBA-2 observations of circumstellar discs in L 1495. *MNRAS*, 449:2472–2488, 2015.

[27] N. Yu C.P Zhang X.L Liu J.J Wang C.C Ning B.G Ju G.Y. Zhang J.L Xu, Y. Xu. Two-Dimensional Molecular Gas and Ongoing Star Formation around HII Region Sh2-104. *The Astronomical Journal*, 849:1–19, 2017.

[28] Oliveira J.M. Star Formation in the Eagle Nebula. *Handbook of Star Forming Regions*, 5:599, 2008.

[29] H. Shang K. Motoyama, T. Umemoto. A Radiation Driven Implosion Model for the Enhanced Luminosity of Protostars near HII Regions. *Astronomy and Astrophysics*, 467:657–664, 2007.

[30] J. M. Kirk J. Di Francesco H. Kirk J. C. Mottram J. Keown J. Buckle S. F. Beaulieu D. S. Berry H. Broekhoven-Fiene M. J. Currie M. Fich J. Hatchell T. Jenness D. Johnstone D. Nutter J. E. Pineda C. Quinn C. Salji S. Tisi S. Walker-Smith M. R. Hogerheijde P. Bastien D. Bresnahan H. Butner M. Chen A. Chrysostomou S. Coud C. J. Davis E. Drabek-Maunder A. Duarte-Cabral J. Fiege P. Friberg R. Friesen G. A. Fuller S. Graves J. Greaves J. Gregson W. Holland G. Joncas L. B. G. Knee S. Mairs K. Marsh B. C. Matthews G. Moriarty-Schieven C. Mowat J. Rawlings J. Richer D. Robertson E. Rosolowsky D. Rumble S. Sadavoy H. Thomas N. Tothill S. Viti G. J. White J. Wouterloot J. Yates M. Zhu K. Pattle, D. Ward-Thompson. The JCMT

Gould Belt Survey: First results from SCUBA-2 observations of the Cepheus Flare Region. *MNRAS*, 464, 2017.

[31] P. Kroupa. On the Variation of the Initial Mass Function. *MNRAS*, 322:231–246, 2001.

[32] A.A. Stark L. Blitz, M. Fich. Catalog of CO Radial Velocities Toward Galactic HII Regions. *The Astrophysical Journal Supplement Series*, 49:183–206, 1982.

[33] A. Zavagno J. Caplan A.P. Whitworth D. Nadeau S. Martin L. Deharveng, B. Lefloch. Triggered Massive-Star Formation at the Border of the HII Region Sh 104. *Astronomy and Astrophysics*, 408:L25–L28, 2003.

[34] F. Massi J. Brand S. Kurtz A. Zavagno J. Caplan L. Deharveng, B. Lefloch. Triggered Massive-Star Formation on the Borders of Galactic HII Regions III: Star Formation at the Periphery of Sh2-219. *Astronomy and Astrophysics*, 458:191–201, 2006.

[35] J. Caplan R. Costero L. Deharveng, M. Pena. Oxygen and Helium Abundances in Galactic HII Regions - II. Abundance Gradients. *MNRAS*, 311:329–345, 2000.

[36] S. Kurtz D. Nadeau M. Pomares J. Caplan A. Zavagno L. Deharveng, B. Lefloch. Triggered Massive-Star Formation on the Borders of Galactic HII Regions IV: Star Formation at the Periphery of Sh2-212. *Astronomy and Astrophysics*, 482:585–596, 2008.

[37] A. Luna B. G. Anandarao J. P. Ninan K. K. Mallick L. K. Dewangan, D. K. Ojha and Y. D. Mayya. A Multi-Wavelength Study of Star Formation Activity in the S235 Complex. *The Astrophysical Journal*, 819, 2016.

[38] J.L Hora C.M Brunt G.G Fazio L.A. Chavarria, L.E Allen. SPITZER Observations of the Massive Star-Forming Complex S254-S258: Structure and Evolution. *The Astrophysical Journal*, 682:445–462, 2008.

[39] D.K Ojha P. Janardhan R. Devaraj A. Luna L.K Dewangan, T. Baug. The Molecular Cloud S242: Physical Environment and Star Formation Activities. *The Astrophysical Journal*, 845:1–19, 2017.

[40] R. Cesaroni M. Felli, R.M Hjellming. S201: an HII region produced by an ionization front eroding a molecular cloud. *Astron. Astrophys.*, 182:313–323, 1987.

[41] C.D. Wilson M. Reid. High-Mass Star Formation. I. - The Mass Distribution of Submillimeter Clumps in NGC 7538. *The Astrophysical Journal*, 625:891–905, 2005.

[42] C.D. Wilson M. Reid. High-Mass Star Formation. II. - The Mass Function of Submillimeter Clumps in M17. *The Astrophysical Journal*, 644, 2006.

[43] L. Deharveng S. Molinari D.K Ojha D. Paradis J. Tige A.K Pandey D. Russeil M.R Samal, A. Zavagno. The Molecular Complex Associated with the Galactic HII Region Sh2-90: A Possible Site of Triggered Star Formation. *Astronomy and Astrophysics*, 566:1–22, 2014.

[44] F. Renaud N. Guillard, E. Emsellem. Impact of Radiation Feedback on the Assembly of Star Clusters in Galactic Context. *MNRAS*, 477:5001–5010, 2018.

[45] L. Bronfman J. Borissova M. Gromadzki N.U. Duronea, C.E Cappa. Triggered Massive Star Formation Associated with the Bubble HII Region Sh2-39 (N5). *Astronomy and Astrophysics*, 606:1–14, 2017.

[46] K. Ogura. Triggered Star Formation Associated with HII Regions. *ASI Conference Series*, 1:19–26, 2010.

[47] D.Ward-Thompson M. Barsony P, Andre. Submillimeter Continuum Observations of ρ Ophiuchi A: The Candidate Protostar VLA 1623 and Prestellar Clumps. *The Astrophysical Journal*, 406:122–141, 1993.

[48] N. Panagia. Some Physical Parameters of Early-Type Stars. *The Astronomical Journal*, 78, 1973.

[49] A.P. Henderson P.Z. Mezger. Galactic HII Regions I. Observations of their Continuum Radiation at the Frequency 5 GHz. *The Astrophysical Journal*, 147:471–489, 1967.

[50] J. Jose A. Zavango S. Takahashi B. Neichel J.S Kim N. Chauhan A.K Pandey I. Zinchenko M. Tamura S.K Ghosh R. Samal, D.K Ojha. Star Formation in the Filament of S254-S258 OB Complex: A Cluster in the Process of being Created. *Astronomy and Astrophysics*, 581, 2015.

[51] B.C Reed. Catalog of Galactic OB Stars. *The Astrophysical Journal*, 125:2531–2533, 2003.

[52] J. Ritzerveld. The diffuse nature of Stromgren Spheres. *Astronomy and Astrophysics*, 439:L23–L26, 2005.

[53] S. Sharpless. A Catalogue of HII Regions. *American Astronomical Society*, 4:257–279, 1959.

[54] C.M. Brunt T. Foster. A CGPS look at the Spiral Structure of the Outer Milky Way. I. Distances and Velocities to Star-Forming Regions. *The Astronomical Journal*, 150:0–13, 2015.

[55] A.P. Whitworth D.A Hubber S. Walch T. G. Bisbas, R. Wunch. Radiation Driven Implosion and Triggered Star Formation. *ASI Conference Series*, 736:1–36, 2011.

[56] S.Httemeister T. Wilson. *Tools of Radio Astronomy*. Springer, 2000.

[57] A.Men'shchikov P. Palmeirim D.Arzoumanian N. Schneider A. Roy P. Didelon A. Maury Y. Shimajiri J. Di Francesco S. Bontemps N. Peretto M.Benedettini J-Ph. Bernard D. Elia M.J Griffin T. Hill J. Kirk B. Ladjelate K. Marsh P.G. Martin F. Motte Q.N. Luong S. Pezzuto H. Roussel K.L.J. Rygl S.I Sadavoy E. Schisano L. Spinoglio D. Ward-Thompson G.J. White V. Konyves, Ph. Andre. A Census of Dense Cores in the Aquila Cloud Complex: SPIRE/PACS Observations from the Herschel Gould Belt Survey. *Astronomy and Astrophysics*, 584, 2015.

[58] T. Henning V. Ossenkopf. Dust opacities for protostellar cores. *Astron. Astrophys.*, 291, 1994.

[59] M.S Kirsanova M.S Y.N Pavlyuchenkov D.S Wiebe V.V, Akimkin. Dust dynamics and evolution in expanding HII regions. I. Radiative drift of neutral and charged grains. *MNRAS*, 449:440–450, 2015.

[60] M.S Kirsanova M.S Y.N Pavlyuchenkov D.S Wiebe V.V, Akimkin. Dust dynamics and evolution in expanding HII regions. II. Effects of dynamical coupling between dust and gas. *MNRAS*, 469:630–638, 2017.

[61] E. L. Chapin A. Chrysostomou G. R. Davis J. T. Dempsey W. D.Duncan M. Fich P. Friberg M. Halpern K. D. Irwin T. Jenness B. D. Kelly M. J. MacIntosh E. I. Robson D. Scott P. A. R. Ade E. Atad-Ettedgui D. S. Berry S. C. Craig X. Gao A. G. Gibb G. C. Hilton M. I. Hollister J. B. Kycia D. W. Lunney H. McGregor D. Montgomery W. Parkes R. P. J. Tilanus J. N. Ullom C. A. Walther A. J. Walton A. L. Woodcraft M. Amiri D. Atkinson B. Burger T. Chuter I. M. Coulson W. B. Doriese C. Dunare F. Economou M. D. Niemack H. A. L. Parsons C. D. Reintsema B. Sibthorpe I. Smail R. Sudiwala W. S. Holland, D. Bintley and H. S. Thomas. SCUBA-2: the 10 000 pixel bolometer camera on the James Clerk Maxwell Telescope. *MNRAS*, 430:2513–2533, 2013.

[62] B.A. Wilking. The Formation of Low-Mass Stars. *Publications of the Astronomical Society of the Pacific*, 101:229–243, 1989.

[63] V.G. Zubko. Modern Models of Interstellar Dust. *ISBN*, 3, 1999.

APPENDICES

.1 Cloud Data Tables

Table 1: Cloud Measured Properties. In order of appearance, cloud name, central coordinates, distance, angular radius, angular area, 450μm negative bowl estimate, 450μm mean flux per pixel, 450μm integrated flux, 850μm negative bowl estimate, 850μm mean flux per pixel and 850μm integrated flux are presented.

Cloud ID	**RA (J2000)**	**DEC (J2000)**	**d (kpc)**	**Radius (arcsec)**	**Area** ($arcsec^2$)	$< f_{450} >_{NBB}$ (mJy/pix)	$< f_{450} >$ (mJy/pix)	F_{450} (Jy)	$< f_{850} >_{NBB}$ (mJy/pix)	$< f_{850} >$ (mJy/pix)	F_{850} (Jy)
G70-1	20:02:00.858	+33:39:12.94	8.45 ± 3.8	30	2799	-1.51 ± 0.59	3.3 ± 0.64	1.5 ± 0.29	-0.37 ± 0.12	0.95 ± 0.22	0.19 ± 0.05
G70-2	20:01:10.887	+33:38:30.71	8.45 ± 3.8	66	13635	-1.44 ± 0.36	4.61 ± 0.85	13.5 ± 2.49	-0.46 ± 0.18	2.76 ± 0.63	3.59 ± 0.82
G70-3	20:01:06.594	+33:34:15.63	8.45 ± 3.8	42	5499	-1.18 ± 0.33	3.62 ± 0.68	4.05 ± 0.75	-0.41 ± 0.11	1.49 ± 0.34	0.74 ± 0.17
G70-4	20:01:47.400	+33:34:01.00	8.45 ± 3.8	186	108531	-3.48 ± 0.76	12.23 ± 2.25	260.52 ± 47.95	-0.93 ± 0.15	4.14 ± 0.94	39.17 ± 8.93
G70-5	20:01:24.599	+33:33:48.90	8.45 ± 3.8	30	2799	-3.43 ± 0.68	5.94 ± 1.12	2.7 ± 0.51	-1.04 ± 0.19	1.93 ± 0.45	0.39 ± 0.09
G70-6	20:01:08.048	+33:32:18.66	8.45 ± 3.8	30	2799	-2.9 ± 0.65	4.68 ± 0.88	2.25 ± 0.42	-0.43 ± 0.16	1.86 ± 0.43	0.4 ± 0.09
G70-7	20:02:10.673	+33:31:57.83	8.45 ± 3.8	78	19035	-3.67 ± 1.12	4.13 ± 0.76	16.89 ± 3.12	-0.83 ± 0.29	1.64 ± 0.38	2.98 ± 0.68
G70-8	20:00:54.617	+33:31:42.36	8.45 ± 3.8	54	9063	-1.93 ± 0.53	6.75 ± 1.25	10.66 ± 1.97	-0.41 ± 0.14	3.28 ± 0.75	2.26 ± 0.52
G70-9	20:01:15.732	+33:31:21.78	8.45 ± 3.8	42	5499	-2.83 ± 0.56	4.4 ± 0.82	4.09 ± 0.76	-0.57 ± 0.13	1.64 ± 0.38	0.68 ± 0.16
G70-10	20:01:35.644	+33:31:03.98	8.45 ± 3.8	42	5499	-1.12 ± 0.83	1.32 ± 0.26	1.51 ± 0.3	-	1.07 ± 0.25	0.55 ± 0.13
G70-11	20:01:28.688	+33:31:00.93	8.45 ± 3.8	42	5499	-2.96 ± 0.68	5.87 ± 1.09	6.72 ± 1.25	-0.85 ± 0.28	2.32 ± 0.53	1.19 ± 0.27
G70-12	20:01:03.264	+33:30:27.56	8.45 ± 3.8	36	3951	-3.01 ± 0.6	2.24 ± 0.43	1.75 ± 0.34	-0.59 ± 0.2	1.26 ± 0.29	0.43 ± 0.1
G70-13	20:01:39.963	+33:30:03.99	8.45 ± 3.8	36	3951	-3.33 ± 0.69	3.36 ± 0.63	3.0 ± 0.56	-0.88 ± 0.22	1.77 ± 0.41	0.69 ± 0.16
G70-14	20:00:53.920	+33:29:24.35	8.45 ± 3.8	84	22059	-2.87 ± 0.68	7.38 ± 1.36	34.99 ± 6.45	-0.68 ± 0.13	3.79 ± 0.86	7.98 ± 1.82
G70-15	20:01:21.739	+33:29:12.86	8.45 ± 3.8	54	9063	-1.83 ± 0.52	5.9 ± 1.15	1.92 ± 0.38	-0.74 ± 0.26	2.56 ± 0.6	0.37 ± 0.09
G70-16	20:00:12.923	+33:28:46.87	8.45 ± 3.8	24	1755	-2.2 ± 0.94	6.48 ± 1.22	7.42 ± 1.4	-1.11 ± 0.6	3.75 ± 0.86	1.92 ± 0.44
G70-17	20:00:06.929	+33:28:46.59	8.45 ± 3.8	42	5499	-2.36 ± 0.51	5.46 ± 1.01	10.03 ± 1.86	-0.81 ± 0.28	2.17 ± 0.5	1.76 ± 0.4
G70-18	20:01:44.041	+33:27:58.00	8.45 ± 3.8	30	2799	-3.15 ± 0.7	4.5 ± 0.85	2.68 ± 0.5	-0.79 ± 0.15	1.19 ± 0.28	0.32 ± 0.07
G70-19	20:00:52.021	+33:27:27.30	8.45 ± 3.8	36	3951	-1.77 ± 0.41	3.82 ± 0.72	2.88 ± 0.54	-0.42 ± 0.24	2.05 ± 0.47	0.67 ± 0.15
G70-20	20:00:59.698	+33:26:51.49	8.45 ± 3.8	48	7155	-2.04 ± 0.52	2.71 ± 0.51	3.49 ± 0.66	-0.5 ± 0.16	1.33 ± 0.31	0.76 ± 0.17
G70-21	20:01:14.324	+33:26:03.76	8.45 ± 3.8	72	16119	-1.76 ± 0.46	4.27 ± 0.79	14.67 ± 2.71	-0.57 ± 0.11	2.31 ± 0.53	3.51 ± 0.8
G70-22	20:01:30.862	+33:25:21.95	8.45 ± 3.8	30	2799	-1.35 ± 0.47	2.61 ± 0.5	1.55 ± 0.3	-0.34 ± 0.1	1.49 ± 0.35	0.4 ± 0.09
G70-23	20:01:21.302	+33:19:48.86	8.45 ± 3.8	60	11259	-1.06 ± 0.31	1.92 ± 0.36	4.76 ± 0.89	-0.35 ± 0.14	0.85 ± 0.19	0.94 ± 0.22
G70-24	20:01:56.239	+33:14:42.98	8.45 ± 3.8	30	2799	-0.81 ± 0.32	3.56 ± 0.68	2.11 ± 0.41	-0.46 ± 0.12	1.48 ± 0.34	0.39 ± 0.09
G74-1	20:18:00.561	+37:03:38.69	4.4 ± 1.4	30	2799	-0.83 ± 0.37	4.04 ± 0.79	2.4 ± 0.47	-0.56 ± 0.08	2.11 ± 0.48	0.56 ± 0.13
G74-2	20:17:46.027	+37:02:29.66	4.4 ± 1.4	60	11259	-1.23 ± 0.36	2.31 ± 0.44	5.48 ± 1.05	-0.35 ± 0.06	0.91 ± 0.21	0.96 ± 0.22
G74-3	20:16:28.500	+36:54:51.68	4.4 ± 1.4	54	9063	-1.0 ± 0.51	2.12 ± 0.46	3.34 ± 0.73	-0.38 ± 0.17	1.93 ± 0.44	1.33 ± 0.31
G74-4	20:17:37.795	+36:53:23.61	4.4 ± 1.4	24	1755	-0.9 ± 0.26	3.49 ± 0.7	1.14 ± 0.23	-0.24 ± 0.07	1.11 ± 0.26	0.16 ± 0.04
G74-5	20:17:02.311	+36:51:16.94	4.4 ± 1.4	30	2799	-	2.16 ± 0.44	1.28 ± 0.26	-0.13 ± 0.05	1.03 ± 0.24	0.27 ± 0.06

Continued on next page

Table 1 – *Continued from previous page*

Cloud ID	**RA (J2000)**	**DEC (J2000)**	**d (kpc)**	**Radius (arcsec)**	**Area** ($arcsec^2$)	$< f_{450} >_{NB}$ (mJy/pix)	$< f_{450} >$ (mJy/pix)	F_{450} (Jy)	$< f_{850} >_{NB}$ (mJy/pix)	$< f_{850} >$ (mJy/pix)	F_{850} (Jy)
G74-6	20:18:56.532	+36:50:52.75	4.4 ± 1.4	30	2799	-0.95 ± 0.37	2.65 ± 0.53	1.57 ± 0.31	-0.4 ± 0.04	1.35 ± 0.31	0.36 ± 0.08
G74-7	20:17:57.050	+36:49:38.70	4.4 ± 1.4	36	3951	-2.04 ± 0.46	3.05 ± 0.59	2.4 ± 0.46	-0.3 ± 0.09	1.01 ± 0.23	0.35 ± 0.08
G74-8	20:17:31.565	+36:49:20.54	4.4 ± 1.4	42	5499	-2.84 ± 0.76	6.59 ± 1.23	7.54 ± 1.4	-0.36 ± 0.22	2.34 ± 0.54	1.2 ± 0.28
G74-9	20:17:51.804	+36:48:20.69	4.4 ± 1.4	48	7155	-2.63 ± 0.6	7.57 ± 1.4	10.79 ± 2.0	-0.41 ± 0.19	3.14 ± 0.72	1.99 ± 0.45
G74-10	20:18:03.544	+36:48:11.69	4.4 ± 1.4	42	5499	-1.64 ± 0.43	3.71 ± 0.7	3.73 ± 0.71	-0.21 ± 0.16	1.62 ± 0.37	0.73 ± 0.17
G74-12	20:17:27.828	+36:47:44.49	4.4 ± 1.4	48	7155	-2.09 ± 0.49	5.62 ± 1.05	7.4 ± 1.38	-0.55 ± 0.1	2.46 ± 0.57	1.44 ± 0.33
G74-13	20:17:34.075	+36:47:05.57	4.4 ± 1.4	36	3951	-2.37 ± 0.58	2.58 ± 0.51	2.02 ± 0.4	-0.53 ± 0.08	1.28 ± 0.3	0.44 ± 0.1
G74-15	20:17:23.843	+36:46:08.42	4.4 ± 1.4	24	1755	-1.09 ± 0.53	2.33 ± 0.51	0.76 ± 0.17	-0.33 ± 0.08	0.7 ± 0.17	0.1 ± 0.02
G74-16	20:18:48.547	+36:45:16.44	4.4 ± 1.4	36	4077	-1.37 ± 0.26	3.63 ± 0.7	2.84 ± 0.54	-0.36 ± 0.05	1.38 ± 0.32	0.47 ± 0.11
G74-17	20:17:58.546	+36:44:56.70	4.4 ± 1.4	72	16119	-1.93 ± 0.34	12.75 ± 2.35	44.14 ± 8.13	-0.4 ± 0.08	4.71 ± 1.07	7.22 ± 1.65
G74-18	20:17:29.093	+36:44:53.51	4.4 ± 1.4	18	999	-1.4 ± 0.37	2.48 ± 0.62	0.34 ± 0.08	-0.6 ± 0.15	0.96 ± 0.24	0.06 ± 0.01
G74-19	20:17:22.853	+36:44:53.41	4.4 ± 1.4	24	1755	-1.38 ± 0.81	3.15 ± 0.64	1.03 ± 0.21	-0.57 ± 0.1	1.2 ± 0.28	0.18 ± 0.04
G74-20	20:16:13.745	+36:43:29.95	4.4 ± 1.4	48	7155	-1.46 ± 0.9	2.19 ± 0.53	2.96 ± 0.71	-0.66 ± 0.19	1.5 ± 0.35	0.89 ± 0.21
G74-21	20:17:40.834	+36:42:02.64	4.4 ± 1.4	84	22059	-1.89 ± 0.42	4.95 ± 0.91	24.99 ± 4.61	-0.4 ± 0.07	2.06 ± 0.47	4.61 ± 1.05
G74-22	20:17:14.642	+36:42:02.25	4.4 ± 1.4	24	1755	-1.3 ± 0.33	3.48 ± 0.7	1.13 ± 0.23	-0.4 ± 0.06	1.31 ± 0.31	0.19 ± 0.05
G74-23	20:18:46.092	+36:33:02.06	4.4 ± 1.4	24	1755	-0.79 ± 0.52	2.56 ± 0.57	0.83 ± 0.19	-0.27 ± 0.06	0.96 ± 0.23	0.14 ± 0.03
G74-24	20:17:01.059	+36:30:37.91	4.4 ± 1.4	42	5499	-1.42 ± 0.68	3.79 ± 0.73	4.34 ± 0.84	-0.43 ± 0.15	1.38 ± 0.32	0.71 ± 0.16
G74-25	20:17:09.769	+36:30:35.14	4.4 ± 1.4	30	2799	-0.53 ± 0.38	2.56 ± 0.54	1.52 ± 0.32	-	0.88 ± 0.21	0.23 ± 0.05
G90-1	21:03:41.397	+49:51:46.97	8.59 ± 0.77	24	1755	-5.65 ± 1.45	8.01 ± 1.97	2.61 ± 0.64	-0.91 ± 0.18	2.6 ± 0.62	0.38 ± 0.09
G97-1	21:32:09.843	+55:52:55.80	6.82 ± 0.32	78	19035	-1.64 ± 0.44	6.87 ± 1.27	23.46 ± 4.33	-0.32 ± 0.13	3.71 ± 0.85	5.67 ± 1.29
G105-1	22:32:45.376	+58:28:09.89	3.04 ± 0.61	42	5499	-238.4 ± 104.24	377.44 ± 84.95	421.98 ± 94.97	-1.54 ± 0.5	10.46 ± 2.4	5.21 ± 1.2
G108-1	22:58:44.099	+58:46:24.20	2.9 ± 0.58	108	36459	-30.46 ± 8.99	41.42 ± 7.68	325.46 ± 60.38	-1.87 ± 0.29	11.73 ± 2.68	40.86 ± 9.32
G115-1	23:53:41.662	+60:31:37.50	2.14 ± 0.3	48	7155	-1.79 ± 0.41	1.8 ± 0.34	2.3 ± 0.44	-0.56 ± 0.15	0.97 ± 0.22	0.55 ± 0.13
G115-2	23:53:11.578	+60:31:01.87	2.14 ± 0.3	36	3951	-1.43 ± 0.42	3.94 ± 0.73	5.13 ± 0.96	-0.82 ± 0.12	1.82 ± 0.42	1.04 ± 0.24
G115-3	23:54:01.954	+60:30:34.01	2.14 ± 0.3	48	7155	-1.45 ± 0.42	2.03 ± 0.38	22.59 ± 4.17	-0.54 ± 0.3	0.92 ± 0.21	4.53 ± 1.03
G115-4	23:52:54.925	+60:28:16.89	2.14 ± 0.3	48	7155	-1.89 ± 0.5	6.16 ± 1.16	3.44 ± 0.65	-0.37 ± 0.13	1.93 ± 0.45	0.47 ± 0.11
G115-5	23:52:28.153	+60:27:37.66	2.14 ± 0.3	42	5499	-1.75 ± 0.37	6.09 ± 1.12	9.51 ± 1.76	-0.32 ± 0.13	3.38 ± 0.77	2.36 ± 0.54
G115-6	23:53:16.019	+60:27:22.84	2.14 ± 0.3	18	999	-1.87 ± 0.4	4.68 ± 0.92	0.66 ± 0.13	-0.79 ± 0.18	1.51 ± 0.36	0.1 ± 0.02
G115-7	23:53:59.004	+60:27:04.09	2.14 ± 0.3	126	49707	-1.43 ± 0.32	3.88 ± 0.74	1.33 ± 0.26	-0.59 ± 0.09	1.4 ± 0.33	0.2 ± 0.05
G115-8	23:52:40.329	+60:27:01.81	2.14 ± 0.3	42	5499	-2.01 ± 0.46	3.04 ± 0.57	3.41 ± 0.64	-0.92 ± 0.28	1.63 ± 0.37	0.81 ± 0.19
G115-9	23:53:03.848	+60:25:55.90	2.14 ± 0.3	42	5499	-1.89 ± 0.48	4.41 ± 0.82	4.47 ± 0.83	-0.65 ± 0.17	1.95 ± 0.45	0.88 ± 0.2
G115-10	23:53:14.385	+60:25:49.85	2.14 ± 0.3	24	1755	-1.47 ± 0.38	2.79 ± 0.53	2.42 ± 0.46	-0.62 ± 0.22	1.82 ± 0.42	0.7 ± 0.16

Continued on next page

Table 1 – *Continued from previous page*

Cloud ID	**RA (J2000)**	**DEC (J2000)**	**d (kpc)**	**Radius (arcsec)**	**Area** ($arcsec^2$)	$< f_{450} >_{NB}$ (mJy/pix)	$< f_{450} >$ (mJy/pix)	F_{450} (Jy)	$< f_{850} >_{NB}$ (mJy/pix)	$< f_{850} >$ (mJy/pix)	F_{850} (Jy)
G115-11	23:53:13.957	+60:22:40.86	2.14 ± 0.3	54	9063	-1.41 ± 0.3	5.39 ± 1.0	8.54 ± 1.58	-0.51 ± 0.07	2.42 ± 0.56	1.67 ± 0.38
G115-12	23:52:50.901	+60:21:04.88	2.14 ± 0.3	30	2799	-1.37 ± 0.32	5.49 ± 1.04	2.48 ± 0.47	-0.58 ± 0.17	2.38 ± 0.55	0.48 ± 0.11
G120-1	0:26:37.849	+64:57:01.99	2.67 ± 0.53	24	1755	-0.74 ± 0.22	0.96 ± 0.28	0.31 ± 0.09	-0.22 ± 0.08	0.5 ± 0.12	0.07 ± 0.02
G120-2	0:26:43.491	+64:55:55.91	2.67 ± 0.53	24	1755	-1.18 ± 0.33	1.47 ± 0.35	0.48 ± 0.11	-0.34 ± 0.1	0.62 ± 0.15	0.09 ± 0.02
G120-3	0:26:09.501	+64:54:14.20	2.67 ± 0.53	78	19035	-1.05 ± 0.34	2.4 ± 0.44	9.51 ± 1.76	-0.2 ± 0.05	1.21 ± 0.27	2.12 ± 0.48
G120-4	0:26:36.374	+64:53:59.01	2.67 ± 0.53	54	9063	-2.23 ± 0.62	3.33 ± 0.62	6.41 ± 1.19	-0.39 ± 0.09	1.52 ± 0.35	1.28 ± 0.29
G125-1	1:08:51.513	+63:07:33.62	2.76 ± 0.15	30	2799	-23.54 ± 8.18	28.66 ± 10.47	13.01 ± 4.75	-1.21 ± 0.45	4.36 ± 1.04	0.88 ± 0.21
G136-1	2:47:26.816	+61:56:39.43	3.54 ± 1.3	30	2799	-39.13 ± 11.59	60.05 ± 14.02	35.67 ± 8.33	-1.14 ± 0.22	3.98 ± 0.94	1.06 ± 0.25
G138-1	3:01:34.333	+60:29:43.15	3.9 ± 0.89	72	16119	-7.58 ± 1.39	20.94 ± 3.87	56.08 ± 10.37	-1.62 ± 0.41	7.1 ± 1.63	8.37 ± 1.92
G138-2	3:03:01.250	+60:28:21.63	3.9 ± 0.89	48	7155	-3.64 ± 1.76	13.48 ± 2.5	18.2 ± 3.38	-1.3 ± 0.29	5.79 ± 1.33	3.46 ± 0.79
G138-3	3:03:23.163	+60:27:51.70	3.9 ± 0.89	65	13635	-3.96 ± 0.93	13.01 ± 2.41	31.2 ± 5.77	-1.63 ± 0.45	8.8 ± 2.01	9.45 ± 2.16
G138-4	3:01:32.518	+60:25:46.06	3.9 ± 0.89	36	3951	-6.26 ± 1.37	8.67 ± 1.65	6.54 ± 1.25	-1.73 ± 0.4	3.81 ± 0.88	1.24 ± 0.29
G142-1	3:24:51.383	+54:57:34.68	3.26 ± 0.91	42	5499	-38.65 ± 10.91	53.47 ± 11.6	59.78 ± 12.96	-1.46 ± 0.51	3.6 ± 0.84	1.79 ± 0.42
G151-1	4:19:31.168	+52:59:28.00	4.44 ± 0.55	24	1755	-45.55 ± 19.69	64.81 ± 17.34	21.13 ± 5.65	-0.58 ± 0.19	2.14 ± 0.51	0.31 ± 0.07
G151-2	4:19:31.226	+52:58:15.88	4.44 ± 0.55	42	5499	-33.65 ± 15.4	52.3 ± 11.69	53.98 ± 12.06	-0.56 ± 0.09	3.07 ± 0.7	1.42 ± 0.33
G151B-1	4:11:04.310	+51:10:22.24	10.58 ± 0.57	30	2799	-49.51 ± 23.6	33.09 ± 11.83	19.66 ± 7.03	-1.23 ± 0.33	5.23 ± 1.2	1.39 ± 0.32
G151B-2	4:11:08.993	+51:08:39.83	10.58 ± 0.57	30	2799	-40.93 ± 15.69	30.71 ± 11.16	14.77 ± 5.37	-1.44 ± 0.33	3.58 ± 0.83	0.78 ± 0.18
G151B-3	4:11:02.971	+51:09:20.23	10.58 ± 0.57	24	1755	-41.18 ± 16.73	42.04 ± 14.4	13.7 ± 4.69	-2.6 ± 0.64	3.95 ± 0.92	0.58 ± 0.13
G151B-4	4:11:03.317	+51:07:51.19	10.58 ± 0.57	24	1755	-59.37 ± 24.93	92.96 ± 20.8	30.3 ± 6.78	-2.51 ± 0.6	3.24 ± 0.75	0.47 ± 0.11
G151B-5	4:10:54.275	+51:07:56.55	10.58 ± 0.57	24	1755	-61.34 ± 21.06	38.47 ± 14.84	12.54 ± 4.84	-1.79 ± 0.55	2.9 ± 0.68	0.42 ± 0.1
G151B-6	4:10:58.795	+51:06:56.56	10.58 ± 0.57	24	1755	-32.62 ± 14.98	50.47 ± 15.76	16.45 ± 5.14	-1.56 ± 0.52	2.16 ± 0.51	0.31 ± 0.07
G173-1	5:41:22.524	+36:10:02.60	1.97 ± 0.96	48	7155	-20.55 ± 6.33	17.43 ± 4.21	23.53 ± 5.68	-0.92 ± 0.24	2.41 ± 0.56	1.44 ± 0.33
G173-2	5:41:24.472	+35:52:31.23	1.97 ± 0.96	54	9063	-24.22 ± 5.88	32.76 ± 6.42	60.12 ± 11.78	-1.43 ± 0.48	5.8 ± 1.33	4.71 ± 1.08
G173-3	5:41:30.355	+35:49:33.20	1.97 ± 0.96	48	7155	-14.92 ± 8.88	30.3 ± 6.07	44.0 ± 8.82	-1.77 ± 0.47	10.73 ± 2.46	6.95 ± 1.59
G173-4	5:41:15.100	+35:52:09.99	1.97 ± 0.96	24	1755	-21.45 ± 5.35	8.79 ± 5.32	2.87 ± 1.73	-2.09 ± 0.48	3.5 ± 0.84	0.51 ± 0.12
G173-5	5:41:05.996	+35:52:11.91	1.97 ± 0.96	24	1755	-19.47 ± 6.36	35.54 ± 8.43	11.59 ± 2.75	-3.04 ± 0.57	6.37 ± 1.49	0.93 ± 0.22
G173-6	5:41:05.357	+35:49:28.16	1.97 ± 0.96	30	25335	-22.98 ± 5.94	31.94 ± 6.0	176.97 ± 33.26	-2.94 ± 0.36	7.59 ± 1.73	18.68 ± 4.26
G173-7	5:40:42.817	+35:55:06.50	1.97 ± 0.96	36	3951	-23.73 ± 6.7	23.16 ± 5.42	18.09 ± 4.24	-1.14 ± 0.34	3.25 ± 0.76	1.11 ± 0.26
G173-8	5:40:54.588	+35:49:45.67	1.97 ± 0.96	24	1755	-20.42 ± 7.04	16.72 ± 5.65	5.45 ± 1.84	-2.37 ± 0.52	6.14 ± 1.44	0.9 ± 0.21
G173-9	5:40:45.657	+35:48:13.36	1.97 ± 0.96	24	1755	-18.69 ± 5.19	27.07 ± 7.04	8.83 ± 2.29	-2.38 ± 0.39	5.76 ± 1.36	0.84 ± 0.2
G173-10	5:40:42.868	+35:46:06.22	1.97 ± 0.96	24	1755	-19.18 ± 5.9	31.83 ± 7.71	10.38 ± 2.51	-1.99 ± 0.46	5.54 ± 1.31	0.81 ± 0.19
G173-11	5:40:53.684	+35:41:20.71	1.97 ± 0.96	72	16119	-19.03 ± 12.76	24.64 ± 4.82	76.11 ± 14.89	-1.32 ± 0.23	8.3 ± 1.9	11.29 ± 2.58

Continued on next page

Table 1 – *Continued from previous page*

Cloud ID	**RA (J2000)**	**DEC (J2000)**	**d (kpc)**	**Radius (arcsec)**	**Area** ($arcsec^2$)	$< f_{450} >_{NB}$ (mJy/pix)	$< f_{450} >$ (mJy/pix)	F_{450} (Jy)	$< f_{850} >_{NB}$ (mJy/pix)	$< f_{850} >$ (mJy/pix)	F_{850} (Jy)
G173-12	5:40:53.912	+35:38:25.81	1.97 ± 0.96	36	3951	-16.28 ± 5.42	37.44 ± 7.65	28.23 ± 5.77	-0.66 ± 0.12	4.64 ± 1.07	1.51 ± 0.35
G173-13	5:39:33.639	+35:48:56.95	1.97 ± 0.96	30	2799	-16.93 ± 7.56	14.68 ± 4.61	8.72 ± 2.74	-0.76 ± 0.25	2.17 ± 0.51	0.58 ± 0.14
G173-14	5:38:35.849	+35:59:57.67	1.97 ± 0.96	30	2799	-17.1 ± 8.69	13.25 ± 4.34	7.87 ± 2.58	-0.77 ± 0.13	3.23 ± 0.75	0.86 ± 0.2
G173-15	5:39:27.656	+35:40:48.73	1.97 ± 0.96	42	5499	-16.56 ± 8.69	34.27 ± 6.9	39.24 ± 7.9	-1.04 ± 0.24	7.63 ± 1.75	3.92 ± 0.9
G173-16	5:39:11.003	+35:46:00.65	1.97 ± 0.96	66	13635	-22.92 ± 6.1	44.0 ± 8.28	120.56 ± 22.69	-0.87 ± 0.33	12.33 ± 2.82	15.04 ± 3.43
G173-17	5:38:03.804	+36:00:57.37	1.97 ± 0.96	36	3951	-19.95 ± 7.99	18.83 ± 4.69	14.71 ± 3.66	-0.8 ± 0.27	1.77 ± 0.42	0.6 ± 0.14
G173-18	5:38:01.189	+35:58:36.66	1.97 ± 0.96	42	5499	-33.36 ± 10.33	52.15 ± 10.01	59.71 ± 11.46	-1.0 ± 0.21	11.81 ± 2.71	6.06 ± 1.39
G173B-1	5:29:13.873	+34:22:44.04	2.97 ± 0.3	24	1755	-46.77 ± 13.07	51.31 ± 14.06	16.73 ± 4.58	-1.41 ± 0.35	4.07 ± 0.98	0.59 ± 0.14
G173B-2	5:28:48.137	+34:23:35.37	2.97 ± 0.3	36	3951	-61.1 ± 27.79	77.1 ± 15.91	58.13 ± 12.0	-1.03 ± 0.31	3.49 ± 0.82	1.14 ± 0.27
G173B-3	5:28:39.333	+34:23:52.96	2.97 ± 0.3	24	1755	-28.49 ± 12.37	26.49 ± 11.27	8.64 ± 3.67	-1.15 ± 0.45	3.83 ± 0.92	0.56 ± 0.14
G182-1	5:51:38.248	+27:11:46.71	2.19 ± 0.44	24	1755	-2.55 ± 0.65	9.52 ± 1.82	3.1 ± 0.59	-0.52 ± 0.12	2.42 ± 0.57	0.35 ± 0.08
G182-2	5:52:04.792	+27:03:16.98	2.19 ± 0.44	72	16119	-2.89 ± 0.65	8.81 ± 1.63	28.91 ± 5.34	-0.48 ± 0.14	3.33 ± 0.76	4.83 ± 1.1
G182-3	5:52:10.633	+27:00:35.00	2.19 ± 0.44	102	32571	-4.17 ± 0.92	12.24 ± 2.26	84.45 ± 15.56	-0.81 ± 0.13	4.92 ± 1.12	15.05 ± 3.43
G182-4	5:52:06.148	+26:56:10.99	2.19 ± 0.44	24	1755	-3.58 ± 0.9	9.8 ± 1.86	3.19 ± 0.61	-0.71 ± 0.19	2.88 ± 0.67	0.42 ± 0.1
G188-1	6:09:07.848	+21:52:46.64	2.23 ± 0.18	30	2799	-6.18 ± 1.92	11.68 ± 2.41	6.94 ± 1.43	-0.62 ± 0.15	1.73 ± 0.4	0.46 ± 0.11
G188-2	6:09:09.133	+21:51:01.63	2.23 ± 0.18	72	16119	-8.01 ± 3.14	24.42 ± 4.53	73.34 ± 13.6	-0.69 ± 0.13	4.56 ± 1.04	6.05 ± 1.38
G188-3	6:09:19.043	+21:50:49.45	2.23 ± 0.18	42	5499	-10.05 ± 2.06	13.48 ± 2.63	13.55 ± 2.64	-1.0 ± 0.16	4.21 ± 0.97	1.89 ± 0.43
G188-4	6:09:17.086	+21:47:46.50	2.23 ± 0.18	24	1755	-10.46 ± 2.19	6.5 ± 1.93	2.12 ± 0.63	-0.96 ± 0.19	1.37 ± 0.33	0.2 ± 0.05
G188-5	6:08:49.083	+21:46:49.89	2.23 ± 0.18	24	1755	-5.04 ± 1.93	6.44 ± 1.84	2.1 ± 0.6	-0.56 ± 0.09	1.93 ± 0.46	0.28 ± 0.07
G188-6	6:09:56.017	+21:42:21.50	2.23 ± 0.18	42	5499	-5.65 ± 2.06	13.46 ± 2.6	15.05 ± 2.91	-1.27 ± 0.24	3.76 ± 0.86	1.87 ± 0.43
G188-7	6:09:55.788	+21:41:03.51	2.23 ± 0.18	36	3951	-6.84 ± 2.53	13.38 ± 2.66	10.09 ± 2.0	-0.83 ± 0.23	3.15 ± 0.73	1.03 ± 0.24
G188-8	6:08:51.435	+21:40:40.88	2.23 ± 0.18	30	2799	-8.98 ± 2.48	9.21 ± 2.07	4.43 ± 1.0	-0.65 ± 0.16	1.67 ± 0.39	0.36 ± 0.09
G188-9	6:09:14.890	+21:40:01.56	2.23 ± 0.18	24	1755	-5.35 ± 1.58	7.65 ± 2.03	2.49 ± 0.66	-0.76 ± 0.19	1.57 ± 0.38	0.23 ± 0.05
G188-10	6:09:52.549	+21:39:54.62	2.23 ± 0.18	30	2799	-4.28 ± 2.44	10.3 ± 2.18	6.12 ± 1.29	-0.72 ± 0.13	3.09 ± 0.71	0.82 ± 0.19
G188-11	6:08:54.011	+21:38:31.86	2.23 ± 0.18	90	25335	-10.91 ± 3.04	20.53 ± 3.8	93.76 ± 17.36	-0.62 ± 0.13	4.33 ± 0.99	8.77 ± 2.0
G188-12	6:09:49.521	+21:38:18.72	2.23 ± 0.18	72	16119	-9.51 ± 2.67	15.33 ± 2.86	51.23 ± 9.56	-1.17 ± 0.15	4.23 ± 0.96	6.23 ± 1.42
G188-13	6:09:03.044	+21:37:37.75	2.23 ± 0.18	24	1755	-5.35 ± 2.09	14.43 ± 3.08	4.7 ± 1.01	-0.78 ± 0.34	3.41 ± 0.8	0.5 ± 0.12
G188-14	6:08:20.016	+21:37:25.99	2.23 ± 0.18	36	3951	-5.52 ± 1.89	9.47 ± 1.98	7.14 ± 1.49	-0.44 ± 0.1	2.2 ± 0.51	0.72 ± 0.17
G188-15	6:08:54.650	+21:36:22.85	2.23 ± 0.18	24	1755	-4.86 ± 2.9	13.24 ± 2.91	4.31 ± 0.95	-1.12 ± 0.6	3.45 ± 0.81	0.5 ± 0.12
G188-16	6:08:53.786	+21:35:25.86	2.23 ± 0.18	24	1755	-7.39 ± 1.45	16.73 ± 3.49	5.45 ± 1.14	-1.22 ± 0.26	3.96 ± 0.93	0.58 ± 0.14
G188-17	6:08:43.884	+21:31:13.95	2.23 ± 0.18	90	25335	-8.84 ± 2.57	17.25 ± 3.21	68.62 ± 12.78	-1.02 ± 0.27	6.43 ± 1.47	11.35 ± 2.59
G188-18	6:08:26.900	+21:26:17.00	2.23 ± 0.18	30	2799	-4.57 ± 2.1	9.17 ± 2.07	5.45 ± 1.23	-0.81 ± 0.21	2.16 ± 0.5	0.58 ± 0.13

Continued on next page

Table 1 – *Continued from previous page*

Cloud ID	**RA (J2000)**	**DEC (J2000)**	**d (kpc)**	**Radius (arcsec)**	**Area** ($arcsec^2$)	$< f_{450} >_{NB}$ (mJy/pix)	$< f_{450} >$ (mJy/pix)	F_{450} (Jy)	$< f_{850} >_{NB}$ (mJy/pix)	$< f_{850} >$ (mJy/pix)	F_{850} (Jy)
G188-19	6:09:30.911	+21:23:43.24	2.23 ± 0.18	36	3951	-4.55 ± 1.45	8.27 ± 1.84	6.24 ± 1.39	-0.78 ± 0.18	2.5 ± 0.58	0.81 ± 0.19
G188-20	6:09:21.457	+21:23:19.45	2.23 ± 0.18	24	1755	-5.12 ± 1.55	11.5 ± 2.69	3.75 ± 0.88	-0.69 ± 0.3	1.54 ± 0.37	0.23 ± 0.05
G188-21	6:08:20.887	+21:22:07.99	2.23 ± 0.18	36	3951	-5.15 ± 1.56	7.86 ± 1.76	6.14 ± 1.37	-0.62 ± 0.09	2.88 ± 0.67	0.98 ± 0.23
G192-1	6:12:25.243	+17:59:21.88	2.5 ± 0.2	30	2817	-3.68 ± 1.39	8.02 ± 1.62	4.77 ± 0.97	-0.54 ± 0.07	1.94 ± 0.46	0.52 ± 0.12
G192-2	6:12:53.631	+17:58:58.00	2.5 ± 0.2	144	65178	-5.04 ± 1.25	24.23 ± 4.46	354.36 ± 65.25	-1.18 ± 0.39	7.54 ± 1.72	48.98 ± 11.17
G192-3	6:13:10.032	+17:58:57.95	2.5 ± 0.2	78	19116	-6.72 ± 1.87	7.13 ± 1.34	30.81 ± 5.78	-1.21 ± 0.34	2.28 ± 0.52	4.38 ± 1.0
G192-4	6:12:33.886	+17:56:30.40	2.5 ± 0.2	36	4068	-3.22 ± 1.36	10.43 ± 2.0	9.33 ± 1.79	-0.89 ± 0.25	3.71 ± 0.85	1.45 ± 0.33
G192-5	6:12:53.841	+17:55:55.00	2.5 ± 0.2	24	1791	-10.35 ± 2.2	11.6 ± 2.34	3.78 ± 0.76	-0.73 ± 0.34	2.27 ± 0.55	0.33 ± 0.08
G192-6	6:13:29.243	+17:55:53.47	2.5 ± 0.2	72	16290	-4.45 ± 1.12	11.3 ± 2.1	37.82 ± 7.03	-0.47 ± 0.09	2.97 ± 0.68	4.41 ± 1.01
G192-7	6:12:23.166	+17:55:11.21	2.5 ± 0.2	24	1755	-2.4 ± 0.8	3.9 ± 1.14	1.27 ± 0.37	-0.95 ± 0.35	1.92 ± 0.46	0.28 ± 0.07
G192-8	6:13:47.649	+17:54:51.52	2.5 ± 0.2	54	9144	-5.99 ± 2.07	12.79 ± 2.39	24.91 ± 4.65	-1.06 ± 0.22	3.62 ± 0.83	3.11 ± 0.71
G192-9	6:12:34.134	+17:54:39.45	2.5 ± 0.2	36	4077	-	6.44 ± 1.32	5.03 ± 1.03	-0.45 ± 0.27	2.32 ± 0.54	0.79 ± 0.18
G192-10	6:13:58.690	+17:52:12.72	2.5 ± 0.2	66	13716	-3.83 ± 1.4	5.87 ± 1.12	17.02 ± 3.25	-0.64 ± 0.18	2.06 ± 0.47	2.66 ± 0.61
G192-11	6:13:05.816	+17:50:12.98	2.5 ± 0.2	48	7245	-2.34 ± 0.93	6.33 ± 1.23	9.73 ± 1.89	-0.47 ± 0.11	1.6 ± 0.37	1.09 ± 0.25
G192-12	6:12:20.888	+17:48:51.67	2.5 ± 0.2	30	2844	-1.2 ± 0.82	3.82 ± 0.96	2.27 ± 0.57	-0.64 ± 0.12	1.32 ± 0.32	0.35 ± 0.08
G192-13	6:14:30.711	+17:45:20.45	2.5 ± 0.2	24	1755	-5.01 ± 1.53	8.27 ± 1.76	2.7 ± 0.57	-0.66 ± 0.24	3.7 ± 0.87	0.54 ± 0.13
G192-14	6:14:23.356	+17:44:23.58	2.5 ± 0.2	78	19035	-4.84 ± 1.09	14.65 ± 2.71	59.66 ± 11.03	-0.8 ± 0.22	6.47 ± 1.48	11.7 ± 2.67
G192-15	6:14:07.816	+17:44:05.79	2.5 ± 0.2	24	1755	-1.01 ± 0.54	8.53 ± 1.83	2.78 ± 0.6	-0.89 ± 0.18	2.58 ± 0.61	0.38 ± 0.09
G192-16	6:14:31.090	+17:42:54.68	2.5 ± 0.2	24	1809	-5.91 ± 1.18	3.15 ± 1.05	1.03 ± 0.34	-0.78 ± 0.07	1.12 ± 0.28	0.16 ± 0.04
G192-17	6:14:19.358	+17:42:32.64	2.5 ± 0.2	36	3951	-1.79 ± 1.14	5.6 ± 1.18	4.37 ± 0.92	-	2.86 ± 0.66	0.97 ± 0.23
G192B-1	6:11:24.248	+17:26:21.49	8.71 ± 1.74	48	7155	-4.22 ± 1.67	7.02 ± 1.48	9.48 ± 1.99	-1.07 ± 0.27	2.79 ± 0.64	1.67 ± 0.39
G195-1	6:18:53.901	+15:17:54.80	12.55 ± 3.16	24	1755	-115.12 ± 42.22	41.98 ± 28.41	13.68 ± 9.26	-1.14 ± 0.2	5.85 ± 1.39	0.85 ± 0.2
G196-1	6:14:35.362	+13:49:12.17	4.27 ± 0.85	48	7155	-137.8 ± 58.61	211.62 ± 41.85	301.56 ± 59.64	-2.06 ± 0.36	13.95 ± 3.19	8.83 ± 2.02
G210-1	6:38:28.182	+0:44:43.19	9.1 ± 2.9	42	5499	-2.79 ± 1.1	8.94 ± 1.71	10.24 ± 1.96	-0.46 ± 0.14	2.27 ± 0.52	1.16 ± 0.27
G217-1	6:54:34.717	-4:32:01.51	5.79 ± 1.24	36	3951	-18.55 ± 3.98	12.55 ± 3.5	8.06 ± 2.25	-1.26 ± 0.35	4.02 ± 0.95	1.12 ± 0.26
G219-1	7:08:38.732	-4:19:13.70	3.0 ± 1.2	36	3951	-23.48 ± 5.52	25.54 ± 5.11	19.95 ± 3.99	-1.67 ± 0.31	5.7 ± 1.32	1.95 ± 0.45
G221-1	7:00:37.437	-8:50:38.66	3.88 ± 0.88	48	7155	-4.41 ± 1.59	4.44 ± 0.9	6.45 ± 1.31	-0.64 ± 0.13	0.67 ± 0.16	0.43 ± 0.1
G221-2	7:00:25.730	-8:49:56.15	3.88 ± 0.88	30	2799	-2.92 ± 0.97	4.7 ± 1.0	2.79 ± 0.59	-0.54 ± 0.16	1.56 ± 0.36	0.42 ± 0.1
G221-3	7:00:27.600	-8:51:23.08	3.88 ± 0.88	42	5499	-3.32 ± 1.49	3.03 ± 0.71	3.04 ± 0.71	-0.74 ± 0.24	1.85 ± 0.42	0.83 ± 0.19
G221-4	7:00:30.745	-8:53:00.55	3.88 ± 0.88	36	3951	-3.2 ± 1.36	5.15 ± 1.14	3.88 ± 0.86	-0.53 ± 0.11	1.58 ± 0.36	0.51 ± 0.12
G223-1	7:16:38.639	-9:25:46.23	4.6 ± 1.5	24	1755	-23.44 ± 7.17	31.34 ± 11.47	10.22 ± 3.74	-1.75 ± 0.25	6.26 ± 1.48	0.91 ± 0.22
G225-1	7:05:20.010	-12:20:26.26	1.15 ± 0.14	36	3951	-20.07 ± 10.61	12.84 ± 5.92	8.23 ± 3.8	-0.46 ± 0.12	2.82 ± 0.66	0.78 ± 0.18

Continued on next page

Table 1 – *Continued from previous page*

Cloud ID	**RA (J2000)**	**DEC (J2000)**	**d (kpc)**	**Radius (arcsec)**	**Area** ($arcsec^2$)	$< f_{450} >_{NB}$ (mJy/pix)	$< f_{450} >$ (mJy/pix)	F_{450} (Jy)	$< f_{850} >_{NB}$ (mJy/pix)	$< f_{850} >$ (mJy/pix)	F_{850} (Jy)
G225-2	7:05:10.699	-12:19:04.62	1.15 ± 0.14	30	2799	-40.94 ± 14.76	47.15 ± 12.08	21.4 ± 5.48	-0.62 ± 0.16	3.14 ± 0.73	0.64 ± 0.15
G225-3	7:05:03.538	-12:16:39.56	1.15 ± 0.14	30	2799	-53.34 ± 31.11	38.05 ± 16.67	17.28 ± 7.57	-0.96 ± 0.25	1.7 ± 0.42	0.34 ± 0.08
G231-1	7:30:45.960	-15:17:31.05	2.78 ± 0.62	24	1755	-9.95 ± 3.68	19.51 ± 5.03	6.36 ± 1.64	-0.99 ± 0.34	2.6 ± 0.63	0.38 ± 0.09
G231-2	7:30:37.760	-15:18:29.19	2.78 ± 0.62	24	1755	-8.68 ± 5.23	15.71 ± 4.58	5.12 ± 1.49	-0.74 ± 0.16	1.75 ± 0.45	0.26 ± 0.07
G233-1	7:29:57.518	-18:28:09.00	5.2 ± 1.4	78	19035	-1.46 ± 0.32	5.81 ± 1.07	24.52 ± 4.52	-0.57 ± 0.13	3.04 ± 0.69	5.69 ± 1.3
G233-2	7:30:13.334	-18:30:26.98	5.2 ± 1.4	24	1755	-1.32 ± 0.64	4.1 ± 0.79	1.34 ± 0.26	-0.27 ± 0.07	1.59 ± 0.38	0.23 ± 0.05
G233-3	7:30:01.524	-18:31:09.00	5.2 ± 1.4	72	16119	-2.99 ± 0.84	6.47 ± 1.19	22.42 ± 4.13	-0.6 ± 0.15	2.27 ± 0.52	3.47 ± 0.79
G233-4	7:29:44.649	-18:31:50.94	5.2 ± 1.4	42	5499	-1.86 ± 0.45	3.61 ± 0.67	4.13 ± 0.77	-0.66 ± 0.19	1.23 ± 0.28	0.63 ± 0.15
G233-5	7:30:13.969	-18:32:08.98	5.2 ± 1.4	72	16119	-2.32 ± 0.45	6.32 ± 1.16	21.68 ± 4.0	-0.73 ± 0.17	2.49 ± 0.57	3.78 ± 0.86
G233-6	7:30:06.164	-18:33:06.00	5.2 ± 1.4	24	1755	-3.06 ± 0.61	4.43 ± 0.84	1.44 ± 0.28	-0.84 ± 0.2	1.37 ± 0.32	0.2 ± 0.05
G233-7	7:29:58.781	-18:33:21.00	5.2 ± 1.4	42	5499	-2.28 ± 0.56	5.2 ± 0.97	5.95 ± 1.11	-0.64 ± 0.23	2.06 ± 0.47	1.06 ± 0.24
G233-8	7:29:34.096	-18:33:56.86	5.2 ± 1.4	54	9063	-0.97 ± 0.22	3.08 ± 0.57	5.92 ± 1.1	-0.35 ± 0.09	1.82 ± 0.42	1.54 ± 0.35
G233-9	7:30:00.468	-18:34:51.00	5.2 ± 1.4	36	3951	-2.04 ± 0.66	4.43 ± 0.83	3.34 ± 0.62	-0.39 ± 0.15	1.04 ± 0.24	0.34 ± 0.08
G233-10	7:30:15.027	-18:35:08.98	5.2 ± 1.4	102	32571	-1.86 ± 0.57	4.99 ± 0.92	35.57 ± 6.56	-0.45 ± 0.27	1.94 ± 0.44	6.13 ± 1.4
G233-11	7:30:04.055	-18:38:09.00	5.2 ± 1.4	54	9063	-1.72 ± 0.45	3.37 ± 0.63	6.57 ± 1.22	-0.53 ± 0.09	1.42 ± 0.33	1.22 ± 0.28
G233-12	7:30:14.619	-18:47:23.97	5.2 ± 1.4	72	16119	-1.46 ± 0.39	2.65 ± 0.49	9.18 ± 1.7	-0.54 ± 0.05	1.38 ± 0.32	2.12 ± 0.48
G233-13	7:29:53.490	-18:51:32.97	5.2 ± 1.4	78	19035	-0.93 ± 0.45	2.4 ± 0.45	9.78 ± 1.83	-0.92 ± 0.28	1.64 ± 0.38	2.97 ± 0.68
G234-1	7:35:32.439	-18:45:32.65	2.2 ± 0.5	24	1755	-39.8 ± 14.46	57.82 ± 13.85	18.85 ± 4.52	-1.17 ± 0.3	2.04 ± 0.55	0.3 ± 0.08
G234-2	7:35:38.733	-18:48:50.08	2.2 ± 0.5	24	1755	-28.91 ± 11.6	49.17 ± 12.33	16.03 ± 4.02	-1.39 ± 0.28	4.48 ± 1.07	0.65 ± 0.16

Table 2: Cloud Calculated Properties. In order of appearance, cloud name, 450μm and 850μm surface brightness, 450μm and 850μm in-band luminosity, 450μm to 850μm flux ratio, average temperature, total mass, average H_2 column density, average H_2 number density, average gas pressure and spectral index are presented.

Cloud ID	S_{450} $10^{-4} \times (Jy/arcsec^2)$	S_{850} $10^{-4} \times (Jy/arcsec^2)$	L_{450} $10^{-12} \times (L_{SUN})$	L_{850} $10^{-12} \times (L_{SUN})$	F_{450}/F_{850}	T (K)	M $(M_\odot)$	N_{H_2} $10^{20} \times (cm^{-2})$	n_{H_2} (cm^{-3})	P $10^{-13} \times (Pa)$	α
G70-1	5.35 ± 1.03	0.69 ± 0.16	22.28 ± 14.81	1.51 ± 1.03	7.79 ± 2.37	$23.85^{24.18}_{11.37}$	$48.7^{5.6}_{21.1}$	$4.48^{4.63}_{2.24}$	88^{224}_{56}	$0.36^{0.33}_{0.1}$	3.23 ± 0.48
G70-2	9.9 ± 1.83	2.64 ± 0.6	200.77 ± 132.96	28.29 ± 19.12	3.76 ± 1.1	$9.48^{2.26}_{1.89}$	$4368.8^{2268.0}_{2475.1}$	$83.0^{23.98}_{17.06}$	746^{907}_{324}	$1.21^{0.94}_{0.35}$	2.08 ± 0.46
G70-3	7.36 ± 1.37	1.35 ± 0.31	60.16 ± 39.87	5.83 ± 3.94	5.46 ± 1.62	$13.37^{6.31}_{3.95}$	$462.2^{122.9}_{243.1}$	$21.68^{9.58}_{7.54}$	306^{461}_{174}	$0.7^{0.57}_{0.22}$	2.67 ± 0.47
G70-4	24.0 ± 4.42	3.61 ± 0.82	3874.3 ± 2565.1	308.4 ± 208.35	6.65 ± 1.95	$17.49^{13.22}_{6.2}$	$15659.8^{1554.3}_{7801.6}$	$37.46^{22.75}_{17.02}$	119^{214}_{77}	$0.36^{0.29}_{0.11}$	2.98 ± 0.46
G70-5	9.64 ± 1.81	1.39 ± 0.32	40.11 ± 26.6	3.07 ± 2.08	6.92 ± 2.06	$18.7^{15.64}_{7.11}$	$140.6^{11.0}_{68.2}$	$12.93^{8.81}_{6.09}$	255^{481}_{159}	$0.82^{0.68}_{0.25}$	3.04 ± 0.47
G70-6	8.04 ± 1.51	1.44 ± 0.33	33.48 ± 22.2	3.18 ± 2.15	5.57 ± 1.66	$13.69^{6.55}_{3.83}$	$241.7^{58.3}_{123.0}$	$22.22^{9.92}_{7.63}$	439^{642}_{238}	$1.03^{0.8}_{0.32}$	2.7 ± 0.47
G70-7	8.87 ± 1.64	1.56 ± 0.36	251.17 ± 166.35	23.43 ± 15.83	5.68 ± 1.67	$14.0^{6.75}_{4.03}$	$1713.6^{390.6}_{850.4}$	$23.31^{10.08}_{8.13}$	177^{242}_{95}	$0.42^{0.31}_{0.13}$	2.73 ± 0.46
G70-8	11.76 ± 2.18	2.5 ± 0.57	158.52 ± 105.0	17.81 ± 12.04	4.71 ± 1.39	$11.47^{3.95}_{2.79}$	$1871.2^{750.4}_{1035.3}$	$53.1^{19.61}_{14.53}$	583^{801}_{289}	$1.14^{0.93}_{0.35}$	2.44 ± 0.46
G70-9	7.44 ± 1.39	1.24 ± 0.28	60.84 ± 40.32	5.36 ± 3.62	6.01 ± 1.78	$15.08^{9.03}_{4.71}$	$345.5^{58.8}_{175.4}$	$16.21^{8.15}_{6.44}$	228^{361}_{134}	$0.59^{0.47}_{0.19}$	2.82 ± 0.47
G70-10	2.74 ± 0.55	1.0 ± 0.23	22.42 ± 14.95	4.32 ± 2.92	2.75 ± 0.84	$7.73^{1.5}_{1.29}$	$1068.7^{677.4}_{619.9}$	$50.13^{12.48}_{9.04}$	708^{814}_{307}	$0.94^{0.74}_{0.29}$	1.59 ± 0.48
G70-11	12.22 ± 2.27	2.17 ± 0.5	99.95 ± 66.21	9.38 ± 6.34	5.64 ± 1.66	$13.9^{6.93}_{4.02}$	$694.4^{158.8}_{360.6}$	$32.57^{14.87}_{11.54}$	460^{686}_{250}	$1.09^{0.88}_{0.34}$	2.72 ± 0.46
G70-12	4.44 ± 0.85	1.09 ± 0.25	26.07 ± 17.32	3.39 ± 2.3	4.07 ± 1.22	$10.08^{2.68}_{2.22}$	$460.2^{214.1}_{260.1}$	$29.38^{9.72}_{6.69}$	484^{639}_{224}	$0.84^{0.68}_{0.24}$	2.21 ± 0.47
G70-13	7.6 ± 1.42	1.75 ± 0.4	44.63 ± 29.59	5.45 ± 3.68	4.34 ± 1.29	$10.64^{3.07}_{2.44}$	$662.8^{294.9}_{371.2}$	$42.32^{14.45}_{10.17}$	697^{919}_{315}	$1.27^{1.03}_{0.38}$	2.31 ± 0.47
G70-14	15.86 ± 2.92	3.62 ± 0.83	520.32 ± 344.53	62.85 ± 42.46	4.38 ± 1.29	$10.73^{3.27}_{2.41}$	$7510.4^{3467.6}_{4130.4}$	$88.08^{28.87}_{22.03}$	622^{783}_{293}	$1.14^{0.88}_{0.34}$	2.32 ± 0.46
G70-15	2.12 ± 0.41	0.41 ± 0.1	28.59 ± 19.02	2.95 ± 2.0	5.14 ± 1.57	$12.5^{5.32}_{3.34}$	$263.3^{79.4}_{137.1}$	$7.47^{3.13}_{2.41}$	82^{117}_{44}	$0.18^{0.14}_{0.05}$	2.57 ± 0.48
G70-16	42.29 ± 7.97	10.96 ± 2.51	110.38 ± 73.21	15.14 ± 10.24	3.86 ± 1.15	$9.68^{2.47}_{2.0}$	$2237.8^{1137.7}_{1272.3}$	$321.5^{98.58}_{70.63}$	7946^{10087}_{3514}	$13.16^{10.48}_{3.96}$	2.12 ± 0.47
G70-17	18.23 ± 3.38	3.19 ± 0.73	149.1 ± 98.77	13.83 ± 9.35	5.71 ± 1.68	$14.1^{7.46}_{4.24}$	$999.4^{223.6}_{510.4}$	$46.89^{21.31}_{17.46}$	662^{983}_{387}	$1.6^{1.25}_{0.5}$	2.74 ± 0.46
G70-18	9.56 ± 1.8	1.13 ± 0.26	39.78 ± 26.39	2.49 ± 1.68	8.47 ± 2.53	$29.96^{29.41}_{16.12}$	$58.8^{14.2}_{19.2}$	$5.4^{7.37}_{2.58}$	106^{325}_{76}	$0.55^{0.5}_{0.14}$	3.36 ± 0.47
G70-19	7.29 ± 1.37	1.69 ± 0.39	42.81 ± 28.39	5.27 ± 3.56	4.3 ± 1.28	$10.56^{3.18}_{2.31}$	$649.8^{300.2}_{353.3}$	$41.49^{13.43}_{10.36}$	683^{839}_{317}	$1.24^{0.93}_{0.38}$	2.29 ± 0.47
G70-20	4.88 ± 0.92	1.06 ± 0.24	51.95 ± 34.45	5.97 ± 4.04	4.6 ± 1.37	$11.22^{3.58}_{2.6}$	$654.8^{269.4}_{350.8}$	$23.52^{8.2}_{6.27}$	290^{369}_{139}	$0.56^{0.42}_{0.17}$	2.4 ± 0.47
G70-21	9.1 ± 1.68	2.18 ± 0.5	218.09 ± 144.44	27.62 ± 18.67	4.18 ± 1.23	$10.31^{2.88}_{2.19}$	$3580.0^{1704.8}_{1972.5}$	$57.15^{17.76}_{13.41}$	470^{581}_{221}	$0.83^{0.63}_{0.25}$	2.25 ± 0.46
G70-22	5.55 ± 1.07	1.42 ± 0.33	23.09 ± 15.34	3.13 ± 2.12	3.9 ± 1.18	$9.76^{2.56}_{2.04}$	$454.3^{225.5}_{252.4}$	$41.77^{12.9}_{9.38}$	826^{1027}_{379}	$1.38^{1.06}_{0.42}$	2.14 ± 0.47
G70-23	4.23 ± 0.79	0.84 ± 0.19	70.79 ± 46.94	7.42 ± 5.01	5.05 ± 1.5	$12.28^{4.58}_{3.23}$	$684.9^{227.7}_{373.2}$	$15.74^{6.43}_{4.66}$	155^{229}_{79}	$0.33^{0.27}_{0.1}$	2.55 ± 0.47
G70-24	7.55 ± 1.45	1.41 ± 0.33	31.42 ± 20.88	3.11 ± 2.1	5.35 ± 1.61	$13.07^{5.5}_{3.59}$	$256.6^{68.9}_{130.4}$	$23.59^{9.94}_{7.67}$	466^{660}_{252}	$1.04^{0.8}_{0.32}$	2.64 ± 0.47
G74-1	8.57 ± 1.67	2.0 ± 0.46	9.67 ± 4.74	1.2 ± 0.6	4.28 ± 1.29	$10.52^{3.32}_{2.41}$	$148.7^{47.1}_{52.7}$	$50.41^{17.19}_{13.19}$	1914^{1771}_{863}	$3.45^{1.72}_{0.94}$	2.29 ± 0.47
G74-2	4.87 ± 0.93	0.86 ± 0.2	22.1 ± 10.81	2.06 ± 1.04	5.68 ± 1.7	$14.01^{7.06}_{4.18}$	$150.5^{16.2}_{46.9}$	$12.76^{6.11}_{4.63}$	242^{277}_{126}	$0.58^{0.3}_{0.16}$	2.73 ± 0.47

Continued on next page

Table 2 – *Continued from previous page*

Cloud ID	S_{450} $10^{-4} \times (Jy/arcsec^2)$	S_{850} $10^{-4} \times (Jy/arcsec^2)$	L_{450} $10^{-12} \times (L_{SUN})$	L_{850} $10^{-12} \times (L_{SUN})$	F_{450}/F_{850}	T (K)	M $(M_\odot)$	N_{H_2} $10^{20} \times (cm^{-2})$	n_{H_2} (cm^{-3})	P $10^{-13} \times (Pa)$	α
G74-3	3.69 ± 0.8	1.47 ± 0.34	13.47 ± 6.73	2.84 ± 1.44	2.51 ± 0.79	$7.35^{1.31}_{1.22}$	$796.8^{344.9}_{319.0}$	$83.4^{21.97}_{14.64}$	1759^{1463}_{663}	$2.21^{1.17}_{0.59}$	1.45 ± 0.5
G74-4	6.49 ± 1.3	0.92 ± 0.22	4.59 ± 2.26	0.35 ± 0.18	7.05 ± 2.18	$19.33^{16.85}_{7.72}$	$15.0^{0.6}_{4.4}$	$7.96^{6.01}_{3.85}$	378^{578}_{234}	$1.25^{0.68}_{0.32}$	3.07 ± 0.49
G74-5	4.58 ± 0.94	0.98 ± 0.23	5.17 ± 2.55	0.59 ± 0.3	4.67 ± 1.44	$11.38^{4.22}_{2.87}$	$62.5^{15.5}_{21.0}$	$21.18^{8.44}_{6.26}$	804^{827}_{381}	$1.57^{0.82}_{0.43}$	2.42 ± 0.49
G74-6	5.61 ± 1.12	1.28 ± 0.3	6.34 ± 3.12	0.77 ± 0.39	4.37 ± 1.33	$10.71^{3.43}_{2.5}$	$92.0^{27.1}_{32.2}$	$31.2^{11.12}_{8.22}$	1185^{1136}_{540}	$2.17^{1.11}_{0.58}$	2.32 ± 0.48
G74-7	6.07 ± 1.17	0.87 ± 0.2	9.66 ± 4.73	0.74 ± 0.37	6.94 ± 2.09	$18.8^{15.58}_{7.48}$	$33.5^{1.1}_{10.1}$	$7.89^{5.76}_{3.71}$	249^{383}_{153}	$0.8^{0.46}_{0.21}$	3.05 ± 0.47
G74-8	13.72 ± 2.55	2.19 ± 0.5	30.42 ± 14.81	2.57 ± 1.3	6.28 ± 1.85	$16.01^{10.19}_{5.34}$	$150.0^{7.8}_{44.5}$	$25.96^{14.23}_{10.76}$	704^{873}_{396}	$1.93^{0.99}_{0.52}$	2.89 ± 0.46
G74-9	15.08 ± 2.79	2.77 ± 0.64	43.5 ± 21.17	4.24 ± 2.14	5.43 ± 1.6	$13.29^{5.85}_{3.74}$	$339.3^{51.9}_{108.6}$	$44.94^{19.69}_{14.78}$	1066^{1155}_{536}	$2.43^{1.23}_{0.65}$	2.66 ± 0.46
G74-10	6.78 ± 1.28	1.32 ± 0.31	15.04 ± 7.34	1.55 ± 0.79	5.12 ± 1.53	$12.46^{5.05}_{3.34}$	$139.9^{27.9}_{45.7}$	$24.2^{9.81}_{7.54}$	656^{679}_{317}	$1.4^{0.7}_{0.37}$	2.57 ± 0.47
G74-12	10.34 ± 1.93	2.01 ± 0.46	29.82 ± 14.52	3.07 ± 1.55	5.14 ± 1.52	$12.51^{4.67}_{3.33}$	$274.2^{53.8}_{91.0}$	$36.33^{14.84}_{10.77}$	862^{894}_{409}	$1.85^{0.94}_{0.47}$	2.57 ± 0.47
G74-13	5.12 ± 1.01	1.11 ± 0.26	8.15 ± 4.01	0.93 ± 0.47	4.62 ± 1.41	$11.25^{3.77}_{2.75}$	$101.7^{26.3}_{34.0}$	$23.96^{8.82}_{6.62}$	758^{731}_{350}	$1.46^{0.72}_{0.39}$	2.41 ± 0.48
G74-15	4.32 ± 0.94	0.58 ± 0.14	3.06 ± 1.53	0.22 ± 0.11	7.42 ± 2.41	$21.36^{21.31}_{9.6}$	$8.2^{0.7}_{2.1}$	$4.35^{4.11}_{2.22}$	206^{367}_{129}	$0.75^{0.44}_{0.19}$	3.15 ± 0.51
G74-16	6.97 ± 1.33	1.16 ± 0.27	11.45 ± 5.6	1.01 ± 0.51	6.02 ± 1.81	$15.11^{9.29}_{4.98}$	$64.7^{4.3}_{19.3}$	$15.23^{7.99}_{6.22}$	482^{577}_{276}	$1.25^{0.65}_{0.35}$	2.82 ± 0.47
G74-17	27.38 ± 5.04	4.48 ± 1.02	177.98 ± 86.54	15.41 ± 7.78	6.11 ± 1.79	$15.42^{9.23}_{4.77}$	$958.3^{64.7}_{279.9}$	$56.42^{27.93}_{22.41}$	892^{1002}_{497}	$2.36^{1.14}_{0.63}$	2.85 ± 0.46
G74-18	3.42 ± 0.85	0.59 ± 0.15	1.38 ± 0.71	0.13 ± 0.06	5.76 ± 2.01	$14.27^{9.26}_{4.79}$	$9.0^{0.3}_{2.3}$	$8.44^{5.07}_{3.62}$	534^{683}_{303}	$1.3^{0.71}_{0.37}$	2.75 ± 0.55
G74-19	5.85 ± 1.19	1.0 ± 0.24	4.14 ± 2.05	0.37 ± 0.19	5.86 ± 1.82	$14.58^{8.54}_{4.6}$	$25.5^{1.8}_{7.3}$	$13.54^{7.09}_{5.39}$	642^{769}_{361}	$1.6^{0.83}_{0.44}$	2.78 ± 0.49
G74-20	4.13 ± 1.0	1.25 ± 0.29	11.93 ± 6.09	1.91 ± 0.97	3.31 ± 1.1	$8.67^{2.1}_{1.81}$	$359.6^{121.8}_{130.3}$	$47.64^{17.01}_{10.82}$	1130^{1112}_{474}	$1.68^{0.96}_{0.45}$	1.88 ± 0.53
G74-21	11.33 ± 2.09	2.09 ± 0.48	100.75 ± 49.0	9.84 ± 4.96	5.42 ± 1.59	$13.26^{5.88}_{3.8}$	$791.0^{122.3}_{254.4}$	$34.21^{14.9}_{11.21}$	464^{496}_{230}	$1.05^{0.54}_{0.28}$	2.66 ± 0.46
G74-22	6.47 ± 1.3	1.09 ± 0.26	4.58 ± 2.25	0.41 ± 0.21	5.92 ± 1.83	$14.76^{8.57}_{4.9}$	$27.4^{1.8}_{8.1}$	$14.5^{7.84}_{5.75}$	688^{844}_{385}	$1.74^{0.92}_{0.47}$	2.8 ± 0.49
G74-23	4.76 ± 1.06	0.79 ± 0.19	3.37 ± 1.69	0.3 ± 0.15	5.99 ± 1.96	$14.98^{9.28}_{5.22}$	$19.4^{0.8}_{5.4}$	$10.29^{6.35}_{4.29}$	488^{664}_{280}	$1.25^{0.72}_{0.34}$	2.81 ± 0.52
G74-24	7.9 ± 1.52	1.29 ± 0.3	17.51 ± 8.57	1.51 ± 0.76	6.14 ± 1.84	$15.51^{9.65}_{5.03}$	$92.9^{5.2}_{27.8}$	$16.07^{8.86}_{6.58}$	436^{539}_{245}	$1.16^{0.61}_{0.31}$	2.85 ± 0.47
G74-25	5.44 ± 1.14	0.83 ± 0.2	6.14 ± 3.05	0.5 ± 0.25	6.52 ± 2.05	$16.96^{12.78}_{6.2}$	$26.5^{0.7}_{7.7}$	$9.0^{6.08}_{4.04}$	341^{490}_{201}	$0.99^{0.56}_{0.27}$	2.95 ± 0.49
G90-1	14.88 ± 3.65	2.16 ± 0.52	40.13 ± 11.09	3.09 ± 0.84	6.88 ± 2.36	$18.52^{17.39}_{7.64}$	$143.6^{78.8}_{58.7}$	$19.96^{17.16}_{10.14}$	485^{504}_{264}	$1.54^{0.33}_{0.17}$	3.03 ± 0.54
G97-1	12.33 ± 2.28	2.98 ± 0.68	227.26 ± 44.59	29.09 ± 6.91	4.14 ± 1.21	$10.22^{2.59}_{2.19}$	$3836.4^{742.3}_{562.0}$	$80.11^{24.9}_{17.51}$	754^{282}_{188}	$1.32^{0.11}_{0.08}$	2.23 ± 0.46
G105-1	767.38 ± 172.71	9.47 ± 2.17	812.23 ± 294.18	5.31 ± 1.94	81.01 ± 26.05	-	-	-	-	-	6.91 ± 0.51
G108-1	89.27 ± 16.56	11.21 ± 2.56	570.07 ± 192.83	37.89 ± 13.77	7.97 ± 2.34	$25.2^{26.68}_{12.0}$	$1128.6^{342.9}_{319.2}$	$67.98^{70.81}_{34.36}$	1088^{1685}_{665}	$4.69^{1.68}_{0.71}$	3.26 ± 0.46
G115-1	3.22 ± 0.62	0.77 ± 0.18	2.2 ± 0.61	0.28 ± 0.08	4.19 ± 1.25	$10.32^{2.97}_{2.28}$	$35.9^{0.0}_{0.5}$	$20.11^{6.65}_{4.82}$	981^{532}_{331}	$1.73^{0.36}_{0.24}$	2.25 ± 0.47
G115-2	12.99 ± 2.42	2.62 ± 0.6	4.89 ± 1.33	0.52 ± 0.16	4.95 ± 1.46	$12.03^{4.45}_{2.97}$	$50.2^{1.3}_{3.8}$	$49.98^{18.76}_{14.43}$	3252^{1907}_{1236}	$6.7^{1.34}_{0.96}$	2.52 ± 0.46
G115-3	31.57 ± 5.83	6.33 ± 1.45	21.54 ± 5.84	2.29 ± 0.69	4.99 ± 1.46	$12.12^{4.68}_{3.13}$	$216.5^{5.8}_{17.5}$	$121.26^{47.39}_{36.5}$	5917^{3654}_{2312}	$12.27^{2.58}_{1.81}$	2.53 ± 0.46
G115-4	4.81 ± 0.91	0.65 ± 0.15	3.28 ± 0.9	0.24 ± 0.07	7.37 ± 2.22	$21.1^{19.71}_{8.97}$	$9.0^{3.2}_{3.0}$	$5.06^{4.26}_{2.5}$	246^{282}_{138}	$0.89^{0.22}_{0.11}$	3.14 ± 0.47
G115-5	17.29 ± 3.19	4.29 ± 0.98	9.07 ± 2.46	1.19 ± 0.36	4.03 ± 1.18	$10.01^{2.54}_{2.09}$	$163.9^{1.2}_{4.9}$	$119.86^{36.26}_{26.32}$	6684^{3414}_{2091}	$11.45^{2.27}_{1.54}$	2.19 ± 0.46

Continued on next page

Table 2 – *Continued from previous page*

Cloud ID	S_{450} $10^{-4} \times (Jy/arcsec^2)$	S_{850} $10^{-4} \times (Jy/arcsec^2)$	L_{450} $10^{-12} \times (L_{SUN})$	L_{850} $10^{-12} \times (L_{SUN})$	F_{450}/F_{850}	T (K)	M $(M_\odot)$	N_{H_2} $10^{20} \times (cm^{-2})$	n_{H_2} (cm^{-3})	P $10^{-13} \times (Pa)$	α
G115-6	6.61 ± 1.3	0.96 ± 0.23	0.63 ± 0.18	0.05 ± 0.01	6.92 ± 2.14	$18.71^{16.45}_{7.41}$	$2.2^{0.6}_{0.7}$	$8.79^{6.58}_{4.27}$	1143^{1192}_{631}	$3.66^{0.9}_{0.53}$	3.04 ± 0.49
G115-7	0.27 ± 0.05	0.04 ± 0.01	1.27 ± 0.35	0.1 ± 0.03	6.52 ± 1.98	$16.96^{12.03}_{6.11}$	$5.5^{1.1}_{1.5}$	$0.45^{0.28}_{0.2}$	8^{7}_{4}	$0.02^{0.01}_{0.0}$	2.95 ± 0.48
G115-8	6.21 ± 1.17	1.47 ± 0.34	3.26 ± 0.89	0.41 ± 0.12	4.21 ± 1.25	$10.37^{3.05}_{2.3}$	$52.4^{0.0}_{1.0}$	$38.33^{12.73}_{9.31}$	2137^{1169}_{720}	$3.79^{0.78}_{0.54}$	2.26 ± 0.47
G115-9	8.12 ± 1.52	1.59 ± 0.37	4.26 ± 1.16	0.44 ± 0.13	5.1 ± 1.51	$12.41^{4.81}_{3.2}$	$40.1^{1.5}_{3.6}$	$29.3^{11.52}_{8.82}$	1633^{1009}_{630}	$3.47^{0.71}_{0.5}$	2.56 ± 0.47
G115-10	13.81 ± 2.64	4.01 ± 0.93	2.31 ± 0.64	0.36 ± 0.11	3.44 ± 1.03	$8.91^{1.97}_{1.64}$	$63.0^{2.5}_{3.1}$	$141.15^{37.38}_{27.67}$	13776^{6322}_{4054}	$20.99^{4.05}_{2.85}$	1.94 ± 0.47
G115-11	9.42 ± 1.75	1.84 ± 0.42	8.14 ± 2.21	0.84 ± 0.26	5.11 ± 1.51	$12.43^{4.83}_{3.17}$	$76.2^{2.8}_{6.9}$	$33.73^{12.9}_{10.16}$	1463^{874}_{563}	$3.11^{0.62}_{0.45}$	2.56 ± 0.46
G115-12	8.87 ± 1.67	1.72 ± 0.4	2.37 ± 0.65	0.24 ± 0.07	5.15 ± 1.54	$12.54^{5.2}_{3.36}$	$21.6^{1.0}_{2.3}$	$30.98^{12.53}_{9.85}$	2419^{1505}_{983}	$5.19^{1.06}_{0.77}$	2.58 ± 0.47
G120-1	1.79 ± 0.52	0.42 ± 0.1	0.47 ± 0.19	0.06 ± 0.02	4.29 ± 1.61	$10.53^{4.03}_{2.82}$	$7.2^{0.1}_{0.3}$	$10.3^{5.32}_{3.38}$	805^{713}_{354}	$1.45^{0.56}_{0.32}$	2.29 ± 0.59
G120-2	2.74 ± 0.64	0.51 ± 0.12	0.71 ± 0.26	0.07 ± 0.03	5.35 ± 1.78	$13.06^{6.29}_{4.0}$	$5.8^{0.0}_{0.5}$	$8.39^{4.58}_{3.03}$	656^{609}_{305}	$1.47^{0.51}_{0.29}$	2.64 ± 0.52
G120-3	5.0 ± 0.92	1.11 ± 0.25	14.12 ± 4.75	1.67 ± 0.6	4.48 ± 1.32	$10.95^{3.57}_{2.51}$	$191.5^{12.8}_{25.6}$	$26.08^{8.93}_{6.87}$	627^{419}_{245}	$1.18^{0.34}_{0.22}$	2.36 ± 0.46
G120-4	7.07 ± 1.31	1.42 ± 0.32	9.51 ± 3.2	1.01 ± 0.36	4.99 ± 1.47	$12.13^{4.47}_{3.06}$	$95.2^{2.0}_{10.7}$	$27.07^{10.43}_{7.84}$	941^{684}_{384}	$1.95^{0.57}_{0.36}$	2.53 ± 0.46
G125-1	46.49 ± 16.99	3.15 ± 0.75	20.65 ± 7.71	0.74 ± 0.19	14.76 ± 6.44	-	-	-	-	-	4.23 ± 0.69
G136-1	127.43 ± 29.75	3.78 ± 0.89	93.09 ± 53.01	1.46 ± 0.83	33.69 ± 11.16	-	-	-	-	-	5.53 ± 0.52
G138-1	34.79 ± 6.43	5.19 ± 1.19	177.65 ± 66.08	14.03 ± 5.55	6.7 ± 1.97	$17.71^{13.71}_{6.54}$	$698.6^{11.5}_{140.2}$	$52.36^{33.75}_{24.11}$	934^{1054}_{541}	$2.83^{1.06}_{0.6}$	2.99 ± 0.46
G138-2	25.44 ± 4.72	4.84 ± 1.11	57.66 ± 21.47	5.81 ± 2.3	5.26 ± 1.55	$12.81^{5.29}_{3.42}$	$496.8^{17.6}_{81.9}$	$83.76^{34.73}_{26.37}$	2243^{1870}_{987}	$4.92^{1.69}_{1.02}$	2.61 ± 0.46
G138-3	22.88 ± 4.23	6.93 ± 1.59	98.83 ± 36.76	15.86 ± 6.27	3.3 ± 0.97	$8.66^{1.86}_{1.61}$	$2994.4^{684.6}_{741.4}$	$267.05^{71.08}_{50.87}$	5200^{3340}_{1779}	$7.7^{2.61}_{1.56}$	1.88 ± 0.46
G138-4	16.55 ± 3.15	3.14 ± 0.73	20.71 ± 7.76	2.08 ± 0.83	5.26 ± 1.58	$12.83^{5.43}_{3.59}$	$177.7^{5.4}_{27.8}$	$53.28^{22.11}_{17.45}$	1902^{1553}_{874}	$4.18^{1.41}_{0.89}$	2.61 ± 0.47
G142-1	108.7 ± 23.58	3.26 ± 0.76	132.31 ± 59.59	2.1 ± 0.96	33.34 ± 10.64	-	-	-	-	-	5.51 ± 0.5
G151-1	120.39 ± 32.22	1.78 ± 0.43	86.75 ± 27.75	0.68 ± 0.2	67.58 ± 24.24	-	-	-	-	-	6.62 ± 0.56
G151-2	98.16 ± 21.93	2.59 ± 0.59	221.63 ± 62.93	3.1 ± 0.89	37.88 ± 12.13	-	-	-	-	-	5.71 ± 0.5
G151B-1	70.23 ± 25.11	4.97 ± 1.14	458.26 ± 167.52	17.18 ± 4.16	14.13 ± 6.01	-	-	-	-	-	4.16 ± 0.67
G151B-2	52.77 ± 19.17	2.78 ± 0.64	344.34 ± 127.84	9.6 ± 2.34	18.99 ± 8.18	-	-	-	-	-	4.63 ± 0.68
G151B-3	78.09 ± 26.75	3.29 ± 0.77	319.5 ± 112.11	7.12 ± 1.75	23.76 ± 9.85	-	-	-	-	-	4.98 ± 0.65
G151B-4	172.67 ± 38.63	2.69 ± 0.63	706.49 ± 166.98	5.84 ± 1.43	64.08 ± 20.69	-	-	-	-	-	6.54 ± 0.51
G151B-5	71.47 ± 27.56	2.41 ± 0.57	292.41 ± 114.94	5.22 ± 1.29	29.66 ± 13.4	-	-	-	-	-	5.33 ± 0.71
G151B-6	93.74 ± 29.27	1.79 ± 0.42	383.55 ± 123.28	3.88 ± 0.97	52.29 ± 20.5	-	-	-	-	-	6.22 ± 0.62
G173-1	32.89 ± 7.94	2.01 ± 0.47	19.02 ± 13.89	0.62 ± 0.45	16.36 ± 5.48	-	-	-	-	-	4.39 ± 0.53
G173-2	66.34 ± 13.0	5.19 ± 1.19	48.59 ± 34.82	2.01 ± 1.46	12.77 ± 3.85	-	-	-	-	-	4.01 ± 0.47
G173-3	61.5 ± 12.32	9.72 ± 2.23	35.57 ± 25.53	2.98 ± 2.16	6.33 ± 1.93	$16.19^{11.1}_{5.44}$	$170.8^{58.9}_{24.4}$	$112.86^{63.61}_{48.81}$	5983^{6615}_{3846}	$16.58^{7.07}_{6.25}$	2.9 ± 0.48
G173-4	16.34 ± 9.87	2.91 ± 0.7	2.32 ± 2.12	0.22 ± 0.16	-	-	-	-	-	-	2.71 ± 1.02
G173-5	66.02 ± 15.65	5.3 ± 1.24	9.37 ± 6.83	0.4 ± 0.29	12.46 ± 4.15	-	-	-	-	-	3.97 ± 0.52

Continued on next page

Table 2 – *Continued from previous page*

Cloud ID	S_{450} $10^{-4} \times (Jy/arcsec^2)$	S_{850} $10^{-4} \times (Jy/arcsec^2)$	L_{450} $10^{-12} \times (L_{SUN})$	L_{850} $10^{-12} \times (L_{SUN})$	F_{450}/F_{850}	T (K)	M $(M_\odot)$	N_{H_2} $10^{20} \times (cm^{-2})$	n_{H_2} (cm^{-3})	P $10^{-13} \times (Pa)$	α
G173-6	69.85 ± 13.13	7.37 ± 1.68	143.05 ± 102.18	7.99 ± 5.8	9.48 ± 2.8	$47.47^{27.82}_{32.16}$	$106.5^{125.5}_{76.2}$	$180.19^{473.66}_{54.11}$	15284^{60102}_{8569}	$124.16^{74.79}_{31.96}$	3.54 ± 0.46
G173-7	45.78 ± 10.72	2.81 ± 0.65	14.62 ± 10.64	0.47 ± 0.35	16.31 ± 5.39	-	-	-	-	-	4.39 ± 0.52
G173-8	31.05 ± 10.49	5.11 ± 1.2	4.41 ± 3.38	0.38 ± 0.28	6.08 ± 2.5	$15.29^{13.78}_{6.26}$	$24.2^{5.7}_{1.1}$	$63.96^{63.42}_{33.54}$	6781^{11751}_{4705}	$17.74^{11.51}_{7.29}$	2.84 ± 0.65
G173-9	50.29 ± 13.07	4.79 ± 1.13	7.13 ± 5.25	0.36 ± 0.26	10.49 ± 3.68	$111.9^{33.36}_{98.43}$	-	$4.83^{51.0}_{3.74}$	512^{7646}_{78}	$9.81^{9.12}_{1.71}$	3.7 ± 0.55
G173-10	59.12 ± 14.33	4.61 ± 1.09	8.39 ± 6.13	0.35 ± 0.25	12.83 ± 4.34	-	-	-	-	-	4.01 ± 0.53
G173-11	47.22 ± 9.24	7.0 ± 1.6	61.52 ± 44.07	4.83 ± 3.51	6.74 ± 2.03	$17.89^{13.46}_{6.51}$	$237.0^{72.5}_{29.6}$	$69.6^{45.18}_{31.59}$	2459^{3041}_{1583}	$7.53^{3.33}_{2.75}$	3.0 ± 0.47
G173-12	71.44 ± 14.61	3.83 ± 0.89	22.81 ± 16.4	0.65 ± 0.47	18.66 ± 5.76	-	-	-	-	-	4.6 ± 0.49
G173-13	31.15 ± 9.79	2.06 ± 0.49	7.05 ± 5.34	0.25 ± 0.18	15.1 ± 5.94	-	-	-	-	-	4.27 ± 0.62
G173-14	28.12 ± 9.21	3.07 ± 0.71	6.36 ± 4.85	0.37 ± 0.27	9.17 ± 3.69	$40.42^{21.99}_{29.04}$	$5.9^{9.4}_{4.4}$	$10.05^{38.78}_{2.71}$	852^{4855}_{488}	$5.9^{5.41}_{1.55}$	3.48 ± 0.63
G173-15	71.36 ± 14.36	7.12 ± 1.63	31.72 ± 22.77	1.68 ± 1.22	10.02 ± 3.06	$68.86^{11.15}_{53.48}$	-	$12.54^{56.09}_{0.17}$	759^{4874}_{259}	$8.95^{6.1}_{1.95}$	3.62 ± 0.48
G173-16	88.42 ± 16.64	11.03 ± 2.52	97.45 ± 69.61	6.44 ± 4.67	8.02 ± 2.37	$25.61^{26.04}_{12.43}$	$187.6^{71.2}_{8.4}$	$65.56^{72.34}_{32.74}$	2527^{4791}_{1706}	$11.08^{5.66}_{3.7}$	3.27 ± 0.47
G173-17	37.23 ± 9.27	1.53 ± 0.37	11.89 ± 8.71	0.26 ± 0.19	24.31 ± 8.39	-	-	-	-	-	5.02 ± 0.54
G173-18	108.59 ± 20.84	11.02 ± 2.52	48.27 ± 34.53	2.59 ± 1.88	9.86 ± 2.95	$60.64^{18.11}_{45.23}$	-	$22.41^{83.16}_{2.49}$	1357^{7391}_{571}	$14.09^{9.25}_{3.25}$	3.6 ± 0.47
G173B-1	95.31 ± 26.11	3.39 ± 0.81	30.73 ± 9.49	0.58 ± 0.16	28.15 ± 10.25	-	-	-	-	-	5.25 ± 0.57
G173B-2	147.14 ± 30.37	2.88 ± 0.68	106.8 ± 26.81	1.11 ± 0.3	51.12 ± 15.99	-	-	-	-	-	6.19 ± 0.49
G173B-3	49.2 ± 20.93	3.19 ± 0.77	15.86 ± 7.12	0.54 ± 0.15	15.43 ± 7.55	-	-	-	-	-	4.3 ± 0.77
G182-1	17.69 ± 3.38	2.01 ± 0.47	3.1 ± 1.06	0.19 ± 0.07	8.79 ± 2.66	$33.99^{29.89}_{19.91}$	$3.8^{2.8}_{0.6}$	$8.03^{13.63}_{3.49}$	765^{1816}_{410}	$4.45^{1.83}_{0.41}$	3.42 ± 0.48
G182-2	17.93 ± 3.31	3.0 ± 0.68	28.88 ± 9.79	2.56 ± 0.93	5.98 ± 1.76	$14.97^{8.55}_{4.63}$	$166.9^{0.2}_{20.2}$	$39.67^{20.17}_{15.32}$	1261^{1115}_{626}	$3.23^{1.0}_{0.63}$	2.81 ± 0.46
G182-3	25.93 ± 4.78	4.62 ± 1.05	84.36 ± 28.57	7.96 ± 2.9	5.61 ± 1.65	$13.81^{6.48}_{3.94}$	$596.4^{0.4}_{70.5}$	$70.62^{31.35}_{24.49}$	1584^{1257}_{728}	$3.74^{1.1}_{0.72}$	2.71 ± 0.46
G182-4	18.19 ± 3.46	2.4 ± 0.56	3.19 ± 1.09	0.22 ± 0.08	7.59 ± 2.29	$22.47^{21.59}_{9.82}$	$7.8^{1.8}_{2.1}$	$16.64^{15.04}_{8.14}$	1586^{2186}_{922}	$6.1^{2.1}_{1.0}$	3.19 ± 0.47
G188-1	24.79 ± 5.12	1.65 ± 0.38	7.19 ± 1.7	0.25 ± 0.07	15.06 ± 4.68	-	-	-	-	-	4.26 ± 0.49
G188-2	45.5 ± 8.43	3.76 ± 0.86	75.96 ± 16.54	3.32 ± 0.85	12.12 ± 3.57	-	-	-	-	-	3.92 ± 0.46
G188-3	24.64 ± 4.81	3.43 ± 0.79	14.03 ± 3.17	1.04 ± 0.27	7.17 ± 2.16	$19.98^{16.91}_{8.48}$	$42.9^{22.6}_{16.7}$	$28.93^{23.81}_{13.79}$	1548^{1532}_{794}	$5.29^{0.93}_{0.47}$	3.1 ± 0.47
G188-4	12.07 ± 3.59	1.14 ± 0.28	2.19 ± 0.7	0.11 ± 0.03	10.58 ± 4.06	$125.68^{50.09}_{113.06}$	-	-	95^{1421}_{88}	$2.05^{1.26}_{0.43}$	3.71 ± 0.6
G188-5	11.96 ± 3.42	1.6 ± 0.38	2.17 ± 0.67	0.15 ± 0.04	7.46 ± 2.77	$21.6^{24.14}_{10.73}$	$5.7^{5.5}_{2.6}$	$11.78^{15.68}_{6.29}$	1103^{1699}_{638}	$4.08^{1.21}_{0.35}$	3.16 ± 0.58
G188-6	27.37 ± 5.29	3.4 ± 0.78	15.59 ± 3.5	1.03 ± 0.26	8.05 ± 2.42	$25.86^{26.91}_{12.98}$	$29.5^{24.4}_{12.2}$	$19.86^{23.23}_{10.1}$	1063^{1454}_{580}	$4.71^{0.95}_{0.22}$	3.28 ± 0.47
G188-7	25.53 ± 5.07	2.6 ± 0.6	10.45 ± 2.39	0.56 ± 0.15	9.82 ± 3.0	$58.87^{18.37}_{43.64}$	$5.8^{17.3}_{0.2}$	$5.35^{19.54}_{0.66}$	334^{1351}_{55}	$3.37^{1.08}_{0.35}$	3.59 ± 0.48
G188-8	15.83 ± 3.57	1.3 ± 0.31	4.59 ± 1.16	0.2 ± 0.05	12.2 ± 3.98	-	-	-	-	-	3.93 ± 0.51
G188-9	14.21 ± 3.77	1.3 ± 0.31	2.58 ± 0.75	0.13 ± 0.03	10.9 ± 3.9	$242.8^{169.0}_{229.61}$	-	-	-	$2.26^{1.35}_{0.55}$	3.76 ± 0.56
G188-10	21.85 ± 4.62	2.94 ± 0.68	6.34 ± 1.52	0.45 ± 0.12	7.44 ± 2.33	$21.51^{23.08}_{9.43}$	$16.8^{10.5}_{7.4}$	$22.17^{20.41}_{11.61}$	1661^{1813}_{948}	$6.11^{1.15}_{0.52}$	3.16 ± 0.49
G188-11	37.01 ± 6.85	3.46 ± 0.79	97.11 ± 21.13	4.81 ± 1.23	10.7 ± 3.14	$153.12^{66.08}_{137.13}$	-	-	-	$1.68^{0.66}_{0.32}$	3.73 ± 0.46

Continued on next page

Table 2 – *Continued from previous page*

Cloud ID	S_{450} $10^{-4} \times (Jy/arcsec^2)$	S_{850} $10^{-4} \times (Jy/arcsec^2)$	L_{450} $10^{-12} \times (L_{SUN})$	L_{850} $10^{-12} \times (L_{SUN})$	F_{450}/F_{850}	T (K)	M ($M_\odot$)	N_{H_2} $10^{20} \times (cm^{-2})$	n_{H_2} (cm^{-3})	P $10^{-13} \times (Pa)$	α
G188-12	31.78 ± 5.93	3.87 ± 0.88	53.06 ± 11.61	3.42 ± 0.87	8.22 ± 2.42	$27.43^{28.32}_{13.65}$	$90.7^{75.1}_{36.7}$	$20.79^{23.77}_{10.19}$	649^{862}_{343}	$3.05^{0.58}_{0.11}$	3.31 ± 0.46
G188-13	26.81 ± 5.73	2.83 ± 0.67	4.87 ± 1.18	0.27 ± 0.07	9.46 ± 3.01	$47.08^{20.95}_{32.74}$	$3.7^{8.6}_{0.3}$	$7.57^{22.24}_{1.69}$	709^{2342}_{207}	$5.71^{1.82}_{0.43}$	3.53 ± 0.5
G188-14	18.07 ± 3.78	1.82 ± 0.42	7.39 ± 1.76	0.39 ± 0.1	9.94 ± 3.1	$64.61^{11.6}_{49.76}$	$3.7^{13.0}_{0.6}$	$3.36^{14.67}_{0.01}$	209^{1010}_{21}	$2.32^{0.83}_{0.27}$	3.61 ± 0.49
G188-15	24.59 ± 5.41	2.87 ± 0.67	4.47 ± 1.11	0.28 ± 0.07	8.57 ± 2.75	$31.17^{29.05}_{18.05}$	$6.2^{7.9}_{2.2}$	$12.77^{21.51}_{5.89}$	1196^{2291}_{598}	$6.38^{1.65}_{0.04}$	3.38 ± 0.5
G188-16	31.07 ± 6.48	3.29 ± 0.77	5.65 ± 1.34	0.32 ± 0.08	9.44 ± 2.96	$46.43^{26.5}_{32.04}$	$4.3^{9.8}_{0.7}$	$8.95^{25.42}_{2.44}$	837^{2666}_{295}	$6.66^{2.06}_{0.48}$	3.53 ± 0.49
G188-17	27.08 ± 5.04	4.48 ± 1.02	71.07 ± 15.53	6.22 ± 1.59	6.05 ± 1.78	$15.19^{8.79}_{4.96}$	$396.3^{113.9}_{112.8}$	$58.14^{30.54}_{22.49}$	1452^{962}_{629}	$3.77^{0.53}_{0.39}$	2.83 ± 0.46
G188-18	19.46 ± 4.4	2.06 ± 0.48	5.64 ± 1.43	0.32 ± 0.08	9.46 ± 3.07	$47.17^{26.13}_{33.36}$	$4.2^{10.5}_{0.6}$	$5.6^{17.54}_{1.54}$	419^{1456}_{132}	$3.38^{1.16}_{0.25}$	3.53 ± 0.51
G188-19	15.79 ± 3.52	2.06 ± 0.48	6.46 ± 1.62	0.45 ± 0.12	7.66 ± 2.46	$22.9^{24.11}_{10.64}$	$15.2^{11.4}_{6.6}$	$13.94^{14.78}_{7.16}$	870^{1076}_{489}	$3.41^{0.72}_{0.25}$	3.2 ± 0.51
G188-20	21.36 ± 5.0	1.28 ± 0.31	3.88 ± 1.01	0.12 ± 0.03	16.66 ± 5.59	-	-	-	-	-	4.42 ± 0.53
G188-21	15.54 ± 3.47	2.49 ± 0.57	6.36 ± 1.59	0.54 ± 0.14	6.25 ± 2.01	$15.9^{11.33}_{5.58}$	$31.8^{12.3}_{11.1}$	$29.2^{18.55}_{13.08}$	1823^{1413}_{896}	$4.96^{0.85}_{0.57}$	2.88 ± 0.51
G192-1	16.92 ± 3.43	1.84 ± 0.43	6.2 ± 1.44	0.36 ± 0.09	9.22 ± 2.86	$41.35^{28.17}_{27.07}$	$5.6^{10.3}_{1.3}$	$5.89^{13.74}_{2.01}$	393^{1028}_{153}	$2.79^{0.77}_{0.14}$	3.49 ± 0.49
G192-2	54.37 ± 10.01	7.52 ± 1.71	461.28 ± 99.69	33.76 ± 8.59	7.23 ± 2.12	$20.32^{18.9}_{8.18}$	$1365.7^{652.2}_{554.7}$	$62.27^{46.23}_{30.76}$	867^{772}_{464}	$3.01^{0.46}_{0.27}$	3.11 ± 0.46
G192-3	16.11 ± 3.02	2.29 ± 0.52	40.1 ± 8.78	3.02 ± 0.77	7.03 ± 2.08	$19.22^{15.88}_{7.55}$	$132.8^{59.3}_{50.1}$	$20.63^{14.55}_{9.67}$	530^{453}_{269}	$1.74^{0.27}_{0.16}$	3.07 ± 0.47
G192-4	22.93 ± 4.39	3.56 ± 0.82	12.14 ± 2.7	1.0 ± 0.26	6.45 ± 1.93	$16.66^{11.87}_{5.81}$	$54.7^{19.5}_{18.8}$	$39.87^{24.18}_{17.62}$	2220^{1662}_{1078}	$6.33^{0.95}_{0.66}$	2.93 ± 0.47
G192-5	21.11 ± 4.26	1.85 ± 0.45	4.92 ± 1.14	0.23 ± 0.06	11.4 ± 3.59	-	-	-	-	-	3.83 ± 0.49
G192-6	23.22 ± 4.32	2.7 ± 0.62	49.23 ± 10.72	3.04 ± 0.77	8.59 ± 2.53	$31.34^{29.0}_{17.56}$	$67.7^{74.7}_{24.5}$	$12.34^{18.51}_{5.57}$	343^{593}_{172}	$1.84^{0.4}_{0.02}$	3.38 ± 0.46
G192-7	7.24 ± 2.12	1.6 ± 0.39	1.65 ± 0.52	0.19 ± 0.05	4.54 ± 1.72	$11.06^{4.7}_{3.27}$	$21.7^{7.0}_{5.4}$	$35.67^{19.92}_{12.67}$	2980^{2077}_{1208}	$5.64^{1.22}_{0.77}$	2.38 ± 0.6
G192-8	27.24 ± 5.09	3.4 ± 0.78	32.42 ± 7.08	2.14 ± 0.55	8.01 ± 2.37	$25.56^{25.05}_{12.42}$	$62.6^{47.9}_{25.2}$	$20.3^{22.19}_{9.86}$	753^{966}_{401}	$3.3^{0.62}_{0.16}$	3.27 ± 0.46
G192-9	12.33 ± 2.53	1.94 ± 0.45	6.54 ± 1.53	0.54 ± 0.14	6.36 ± 1.97	$16.32^{11.0}_{5.77}$	$30.9^{11.6}_{10.4}$	$22.51^{14.15}_{9.78}$	1253^{972}_{589}	$3.5^{0.56}_{0.37}$	2.91 ± 0.49
G192-10	12.41 ± 2.37	1.94 ± 0.44	22.16 ± 4.92	1.83 ± 0.47	6.4 ± 1.91	$16.47^{11.11}_{5.71}$	$102.4^{34.9}_{33.4}$	$22.21^{12.98}_{9.45}$	674^{485}_{316}	$1.9^{0.28}_{0.2}$	2.92 ± 0.47
G192-11	13.43 ± 2.61	1.5 ± 0.35	12.67 ± 2.85	0.75 ± 0.19	8.94 ± 2.7	$36.3^{31.23}_{22.22}$	$13.9^{20.2}_{4.4}$	$5.69^{10.88}_{2.34}$	237^{512}_{110}	$1.48^{0.37}_{0.03}$	3.44 ± 0.47
G192-12	7.98 ± 2.0	1.24 ± 0.3	2.95 ± 0.81	0.24 ± 0.06	6.44 ± 2.23	$16.63^{13.5}_{6.3}$	$13.3^{6.5}_{5.2}$	$14.02^{10.39}_{6.65}$	937^{834}_{486}	$2.67^{0.52}_{0.31}$	2.93 ± 0.55
G192-13	15.37 ± 3.26	3.08 ± 0.72	3.51 ± 0.84	0.37 ± 0.1	5.0 ± 1.58	$12.14^{5.3}_{3.29}$	$35.1^{7.9}_{7.4}$	$57.6^{25.85}_{18.97}$	4812^{2761}_{1851}	$10.0^{1.51}_{1.09}$	2.53 ± 0.5
G192-14	31.34 ± 5.79	6.15 ± 1.4	77.66 ± 16.83	8.07 ± 2.05	5.1 ± 1.5	$12.4^{5.05}_{3.07}$	$732.2^{126.8}_{139.9}$	$113.78^{42.43}_{35.37}$	2924^{1415}_{1061}	$6.2^{0.75}_{0.62}$	2.56 ± 0.46
G192-15	15.84 ± 3.4	2.15 ± 0.51	3.62 ± 0.88	0.26 ± 0.07	7.37 ± 2.36	$21.1^{20.44}_{9.11}$	$10.0^{6.2}_{4.2}$	$16.33^{14.84}_{8.2}$	1364^{1472}_{737}	$4.93^{0.92}_{0.39}$	3.14 ± 0.5
G192-16	5.68 ± 1.89	0.9 ± 0.23	1.34 ± 0.47	0.11 ± 0.03	6.3 ± 2.63	$16.1^{15.82}_{6.48}$	$6.5^{4.3}_{3.0}$	$10.68^{10.05}_{5.68}$	892^{978}_{509}	$2.46^{0.65}_{0.34}$	2.89 ± 0.66
G192-17	11.06 ± 2.34	2.46 ± 0.57	5.69 ± 1.36	0.67 ± 0.17	4.49 ± 1.41	$10.96^{3.62}_{2.69}$	$76.9^{13.6}_{11.9}$	$56.1^{21.75}_{15.28}$	3124^{1593}_{1019}	$5.86^{0.85}_{0.59}$	2.36 ± 0.49
G192B-1	13.25 ± 2.79	2.33 ± 0.54	149.84 ± 52.77	13.96 ± 5.1	5.68 ± 1.78	$14.02^{7.37}_{4.37}$	$1019.0^{0.1}_{111.7}$	$34.45^{18.01}_{12.97}$	413^{375}_{199}	$0.99^{0.33}_{0.2}$	2.73 ± 0.49
G195-1	77.97 ± 52.76	4.87 ± 1.15	448.89 ± 343.26	14.83 ± 6.34	-	-	-	-	-	-	4.36 ± 1.13
G196-1	421.47 ± 83.35	12.34 ± 2.83	1145.2 ± 393.98	17.75 ± 6.44	34.15 ± 10.33	-	-	-	-	-	5.55 ± 0.48

Continued on next page

Table 2 – *Continued from previous page*

Cloud ID	S_{450} $10^{-4} \times (Jy/arcsec^2)$	S_{850} $10^{-4} \times (Jy/arcsec^2)$	L_{450} $10^{-12} \times (L_{SUN})$	L_{850} $10^{-12} \times (L_{SUN})$	F_{450}/F_{850}	T (K)	M ($M_{\odot}$)	N_{H_2} $10^{20} \times (cm^{-2})$	n_{H_2} (cm^{-3})	P $10^{-13} \times (Pa)$	α
G210-1	18.62 ± 3.56	2.11 ± 0.48	176.6 ± 86.45	10.61 ± 5.37	8.81 ± 2.63	$34.31^{31.67}_{19.91}$	$210.6^{81.1}_{31.6}$	$8.52^{14.37}_{3.83}$	111^{325}_{72}	$0.66^{0.43}_{0.12}$	3.42 ± 0.47
G217-1	20.39 ± 5.69	2.83 ± 0.67	56.25 ± 23.17	4.13 ± 1.59	7.21 ± 2.64	$20.18^{21.92}_{9.36}$	$168.9^{54.4}_{52.4}$	$22.97^{26.13}_{12.42}$	552^{952}_{352}	$1.91^{0.91}_{0.39}$	3.11 ± 0.57
G219-1	50.49 ± 10.1	4.92 ± 1.14	37.39 ± 22.44	1.93 ± 1.18	10.26 ± 3.13	$85.08^{3.6}_{69.6}$	-	$6.7^{39.29}_{1.82}$	310^{2906}_{35}	$4.52^{4.04}_{0.58}$	3.66 ± 0.48
G221-1	9.02 ± 1.83	0.61 ± 0.14	20.23 ± 7.68	0.72 ± 0.29	14.83 ± 4.58	-	-	-	-	-	4.24 ± 0.49
G221-2	9.97 ± 2.12	1.48 ± 0.34	8.75 ± 3.37	0.69 ± 0.27	6.72 ± 2.1	$17.79^{14.83}_{6.58}$	$34.1^{1.4}_{7.1}$	$14.88^{10.52}_{7.13}$	640^{766}_{383}	$1.95^{0.76}_{0.42}$	3.0 ± 0.49
G221-3	5.53 ± 1.3	1.51 ± 0.35	9.54 ± 3.79	1.38 ± 0.54	3.67 ± 1.2	$9.31^{2.64}_{2.03}$	$221.2^{31.9}_{40.2}$	$49.21^{18.0}_{12.49}$	1513^{1158}_{600}	$2.41^{0.93}_{0.55}$	2.04 ± 0.52
G221-4	9.82 ± 2.17	1.3 ± 0.3	12.16 ± 4.74	0.85 ± 0.34	7.55 ± 2.41	$22.22^{24.56}_{10.09}$	$30.3^{6.0}_{8.5}$	$9.17^{9.0}_{4.88}$	329^{506}_{211}	$1.25^{0.52}_{0.25}$	3.18 ± 0.5
G223-1	58.21 ± 21.3	5.21 ± 1.23	45.02 ± 26.51	2.13 ± 1.1	11.18 ± 4.87	-	-	-	-	-	3.8 ± 0.68
G225-1	20.84 ± 9.61	1.98 ± 0.46	2.27 ± 1.12	0.11 ± 0.03	-	-	-	-	-	-	3.7 ± 0.81
G225-2	76.47 ± 19.59	2.27 ± 0.53	5.9 ± 1.82	0.09 ± 0.03	33.69 ± 11.64	-	-	-	-	-	5.53 ± 0.54
G225-3	61.72 ± 27.03	1.23 ± 0.3	4.76 ± 2.24	0.05 ± 0.01	-	-	-	-	-	-	6.16 ± 0.79
G231-1	36.25 ± 9.34	2.16 ± 0.53	10.24 ± 4.17	0.32 ± 0.13	16.77 ± 5.95	-	-	-	-	-	4.43 ± 0.56
G231-2	29.17 ± 8.51	1.46 ± 0.38	8.24 ± 3.54	0.22 ± 0.09	20.05 ± 7.8	-	-	-	-	-	4.71 ± 0.61
G233-1	12.88 ± 2.37	2.99 ± 0.68	138.08 ± 58.41	16.97 ± 7.53	4.31 ± 1.26	$10.57^{3.16}_{2.29}$	$2090.0^{465.8}_{584.1}$	$75.07^{23.86}_{18.57}$	927^{724}_{383}	$1.68^{0.67}_{0.39}$	2.3 ± 0.46
G233-2	7.61 ± 1.47	1.32 ± 0.31	7.52 ± 3.21	0.69 ± 0.31	5.75 ± 1.75	$14.22^{7.4}_{4.36}$	$49.4^{1.6}_{10.8}$	$18.73^{9.12}_{6.82}$	752^{770}_{387}	$1.83^{0.77}_{0.43}$	2.75 ± 0.48
G233-3	13.91 ± 2.56	2.16 ± 0.49	126.27 ± 53.42	10.36 ± 4.6	6.45 ± 1.89	$16.68^{11.07}_{5.64}$	$566.8^{4.8}_{132.2}$	$23.89^{13.77}_{10.15}$	319^{371}_{181}	$0.91^{0.4}_{0.22}$	2.93 ± 0.46
G233-4	7.51 ± 1.4	1.15 ± 0.26	23.26 ± 9.87	1.89 ± 0.84	6.53 ± 1.93	$17.0^{12.0}_{5.98}$	$100.1^{0.8}_{23.6}$	$12.41^{7.31}_{5.37}$	284^{327}_{159}	$0.83^{0.35}_{0.2}$	2.95 ± 0.47
G233-5	13.45 ± 2.48	2.35 ± 0.54	122.11 ± 51.66	11.27 ± 5.0	5.73 ± 1.68	$14.18^{7.44}_{4.2}$	$806.8^{35.1}_{180.9}$	$34.01^{15.67}_{12.54}$	455^{440}_{232}	$1.1^{0.46}_{0.27}$	2.75 ± 0.46
G233-6	8.22 ± 1.57	1.14 ± 0.27	8.12 ± 3.46	0.6 ± 0.27	7.19 ± 2.17	$20.06^{18.78}_{8.2}$	$24.7^{1.1}_{6.2}$	$9.36^{7.25}_{4.66}$	376^{529}_{236}	$1.29^{0.59}_{0.3}$	3.1 ± 0.48
G233-7	10.83 ± 2.01	1.92 ± 0.44	33.53 ± 14.21	3.15 ± 1.4	5.64 ± 1.67	$13.89^{6.72}_{4.09}$	$233.5^{11.9}_{54.9}$	$28.92^{13.31}_{10.21}$	663^{659}_{328}	$1.58^{0.67}_{0.37}$	2.72 ± 0.46
G233-8	6.53 ± 1.21	1.7 ± 0.39	33.31 ± 14.12	4.59 ± 2.04	3.84 ± 1.13	$9.64^{2.43}_{1.99}$	$685.4^{180.2}_{209.6}$	$51.36^{15.48}_{11.06}$	916^{713}_{355}	$1.51^{0.63}_{0.35}$	2.11 ± 0.46
G233-9	8.46 ± 1.58	0.86 ± 0.2	18.83 ± 7.99	1.01 ± 0.45	9.89 ± 2.94	$62.12^{17.85}_{46.97}$	$9.8^{15.4}_{4.7}$	$1.66^{6.4}_{0.16}$	44^{253}_{17}	$0.47^{0.31}_{0.03}$	3.6 ± 0.47
G233-10	10.92 ± 2.01	1.88 ± 0.43	200.33 ± 84.74	18.29 ± 8.12	5.8 ± 1.7	$14.38^{7.08}_{4.25}$	$1277.4^{51.2}_{301.7}$	$26.83^{12.87}_{9.58}$	253^{257}_{129}	$0.62^{0.26}_{0.15}$	2.76 ± 0.46
G233-11	7.24 ± 1.35	1.35 ± 0.31	36.97 ± 15.66	3.65 ± 1.62	5.37 ± 1.58	$13.11^{5.4}_{3.72}$	$299.1^{23.8}_{71.9}$	$22.41^{9.62}_{7.1}$	400^{379}_{182}	$0.9^{0.38}_{0.21}$	2.64 ± 0.46
G233-12	5.69 ± 1.06	1.31 ± 0.3	51.68 ± 21.89	6.32 ± 2.8	4.33 ± 1.28	$10.63^{3.2}_{2.36}$	$769.9^{168.1}_{216.7}$	$32.45^{10.72}_{8.15}$	434^{349}_{179}	$0.79^{0.32}_{0.18}$	2.31 ± 0.46
G233-13	5.14 ± 0.96	1.56 ± 0.36	55.1 ± 23.37	8.86 ± 3.93	3.29 ± 0.97	$8.65^{1.76}_{1.59}$	$1677.6^{497.9}_{536.8}$	$60.25^{15.97}_{11.05}$	744^{537}_{264}	$1.1^{0.45}_{0.24}$	1.87 ± 0.46
G234-1	107.41 ± 25.73	1.7 ± 0.46	19.0 ± 7.62	0.16 ± 0.07	63.25 ± 22.83	-	-	-	-	-	6.52 ± 0.57
G234-2	91.34 ± 22.9	3.72 ± 0.89	16.16 ± 6.59	0.35 ± 0.14	24.52 ± 8.5	-	-	-	-	-	5.03 ± 0.54

.2 Core Data Tables

Table 3: Core Measured Properties. In order of appearance, core name, central coordinates, distance, angular radius, angular area, associated HII region, core-to-HII-region angular distance and scaled distance and 450μm and 850μm integrated flux are presented.

Core ID	RA (J2000)	DEC (J2000)	d (kpc)	Radius (arcsec)	Area ($arcsec^2$)	HII Region	Core-HII Distance (arcmin)	Core-HII Scaled Distance	F_{450} (Jy)	F_{850} (Jy)
G70-1-1	20:02:00.617	+33:39:06.94	8.45 ± 3.8	18	999	S100	6.72	2.52	0.98 ± 0.25	0.2 ± 0.05
G70-2-1	20:01:10.644	+33:38:48.70	8.45 ± 3.8	12	423	S100	10.27	3.85	0.56 ± 0.13	0.12 ± 0.04
G70-2-2	20:01:13.288	+33:38:36.75	8.45 ± 3.8	18	999	S100	9.71	3.64	1.89 ± 0.39	0.3 ± 0.09
G70-2-3	20:01:08.966	+33:38:18.67	8.45 ± 3.8	12	423	S99	10.19	1.13	0.56 ± 0.13	0.1 ± 0.03
G70-3-1	20:01:06.596	+33:34:00.63	8.45 ± 3.8	18	999	S99	6.99	0.78	1.72 ± 0.35	0.27 ± 0.07
G70-4-1	20:01:54.125	+33:36:00.98	8.45 ± 3.8	30	2799	S100	3.37	1.26	11.81 ± 2.44	1.79 ± 0.48
G70-4-2	20:01:37.797	+33:35:21.99	8.45 ± 3.8	30	2799	S100	3.72	1.39	6.33 ± 1.5	1.44 ± 0.4
G70-4-3	20:01:46.921	+33:34:55.00	8.45 ± 3.8	12	423	S100	2.3	0.86	0.62 ± 0.19	0.1 ± 0.04
G70-4-4	20:01:45.000	+33:34:46.00	8.45 ± 3.8	12	423	S100	2.32	0.87	0.96 ± 0.24	0.13 ± 0.05
G70-4-5	20:01:54.601	+33:34:03.98	8.45 ± 3.8	48	7155	S100	1.59	0.6	200.56 ± 37.32	25.82 ± 6.0
G70-4-6	20:01:38.759	+33:34:00.99	8.45 ± 3.8	12	423	S100	2.74	1.03	-	-
G70-4-7	20:01:46.440	+33:32:37.00	8.45 ± 3.8	54	9063	S100	0.84	0.31	306.62 ± 56.94	41.42 ± 9.58
G70-5-1	20:01:24.702	+33:33:40.60	8.45 ± 3.8	18	1035	S100	5.44	2.04	1.78 ± 0.38	0.26 ± 0.07
G70-6-1	20:01:08.286	+33:32:33.66	8.45 ± 3.8	12	423	S99	6.72	0.75	0.46 ± 0.12	0.09 ± 0.03
G70-6-2	20:01:08.050	+33:32:06.66	8.45 ± 3.8	12	423	S99	6.55	0.73	1.23 ± 0.25	0.17 ± 0.05
G70-7-1	20:02:06.116	+33:32:21.89	8.45 ± 3.8	18	999	S100	3.29	1.23	3.18 ± 0.64	0.49 ± 0.12
G70-7-2	20:02:12.108	+33:31:12.82	8.45 ± 3.8	24	1755	S100	4.77	1.79	8.06 ± 1.55	1.19 ± 0.29
G70-8-1	20:00:54.379	+33:31:33.36	8.45 ± 3.8	30	2799	S99	3.66	0.41	18.87 ± 3.59	2.86 ± 0.7
G70-9-1	20:01:15.012	+33:31:21.77	8.45 ± 3.8	24	1755	S100	7.51	2.81	3.89 ± 0.76	0.65 ± 0.16
G70-10-1	20:01:33.725	+33:31:12.97	8.45 ± 3.8	12	423	S100	3.8	1.42	0.34 ± 0.12	0.09 ± 0.03
G70-10-2	20:01:37.084	+33:31:03.98	8.45 ± 3.8	12	423	S100	3.24	1.22	0.3 ± 0.11	0.06 ± 0.02
G70-11-1	20:01:29.793	+33:31:24.20	8.45 ± 3.8	12	441	S100	4.5	1.69	0.59 ± 0.14	0.09 ± 0.03
G70-11-2	20:01:27.295	+33:31:00.22	8.45 ± 3.8	12	459	S100	5.12	1.92	0.78 ± 0.17	0.09 ± 0.03
G70-12-1	20:01:05.183	+33:30:27.60	8.45 ± 3.8	12	423	S99	5.75	0.64	0.58 ± 0.12	0.08 ± 0.03
G70-12-2	20:01:01.587	+33:30:15.53	8.45 ± 3.8	12	423	S99	5.01	0.56	0.26 ± 0.07	0.05 ± 0.02
G70-13-1	20:01:39.484	+33:29:48.99	8.45 ± 3.8	12	423	S100	3.71	1.39	0.36 ± 0.09	0.06 ± 0.02
G70-14-1	20:00:52.958	+33:29:39.32	8.45 ± 3.8	24	1755	S99	3.31	0.37	3.51 ± 0.77	0.67 ± 0.2
G70-14-2	20:00:50.083	+33:29:21.24	8.45 ± 3.8	12	423	S99	2.85	0.32	0.48 ± 0.14	0.1 ± 0.04
G70-14-3	20:00:56.559	+33:29:15.41	8.45 ± 3.8	12	423	S99	4.15	0.46	0.52 ± 0.14	0.1 ± 0.04

Continued on next page

Table 3 – *Continued from previous page*

Core ID	RA (J2000)	DEC (J2000)	d (kpc)	Radius (arcsec)	Area ($arcsec^2$)	HII Region	Core-HII Distance (arcmin)	Core-HII Scaled Distance	F_{450} (Jy)	F_{850} (Jy)
G70-14-4	20:00:55.125	+33:28:45.38	8.45 ± 3.8	12	423	S99	4.05	0.45	0.67 ± 0.17	0.11 ± 0.04
G70-15-1	20:01:23.177	+33:29:27.88	8.45 ± 3.8	12	423	S100	6.55	2.46	0.53 ± 0.15	0.08 ± 0.03
G70-16-1	20:00:12.924	+33:28:43.87	8.45 ± 3.8	12	423	S99	5.43	0.6	1.67 ± 0.36	0.24 ± 0.07
G70-16-2	20:01:56.479	+33:14:51.98	8.45 ± 3.8	12	423	S99	5.43	0.6	1.38 ± 0.31	0.23 ± 0.07
G70-17-1	20:00:07.166	+33:28:55.60	8.45 ± 3.8	12	423	S99	6.53	0.73	0.46 ± 0.12	0.08 ± 0.03
G70-17-2	20:00:05.490	+33:28:46.52	8.45 ± 3.8	12	423	S99	6.91	0.77	0.27 ± 0.09	0.08 ± 0.03
G70-17-3	20:01:56.479	+33:14:51.98	8.45 ± 3.8	12	423	S99	6.91	0.77	0.26 ± 0.09	0.08 ± 0.03
G70-17-4	20:01:56.479	+33:14:51.98	8.45 ± 3.8	12	423	S99	6.91	0.77	0.48 ± 0.12	0.07 ± 0.03
G70-18-1	20:01:44.041	+33:27:58.00	8.45 ± 3.8	12	423	S100	4.95	1.86	0.11 ± 0.08	0.03 ± 0.01
G70-19-1	20:00:52.020	+33:27:33.30	8.45 ± 3.8	18	999	S99	4.21	0.47	3.53 ± 0.68	0.53 ± 0.14
G70-20-1	20:00:59.454	+33:27:21.48	8.45 ± 3.8	18	999	S99	5.54	0.62	0.96 ± 0.22	0.21 ± 0.06
G70-20-2	20:00:59.462	+33:26:21.48	8.45 ± 3.8	18	999	S99	6.16	0.68	0.41 ± 0.15	0.15 ± 0.04
G70-21-1	20:01:10.965	+33:26:33.71	8.45 ± 3.8	12	423	S99	8.0	0.89	0.4 ± 0.11	0.06 ± 0.02
G70-21-2	20:01:14.324	+33:26:00.76	8.45 ± 3.8	18	999	S99	8.88	0.99	0.42 ± 0.16	0.21 ± 0.07
G70-21-3	20:01:16.005	+33:25:18.79	8.45 ± 3.8	18	999	S99	9.54	1.06	0.38 ± 0.16	0.16 ± 0.06
G70-22-1	20:01:30.862	+33:25:18.95	8.45 ± 3.8	12	423	S100	8.47	3.18	0.28 ± 0.09	0.05 ± 0.02
G70-23-1	20:01:24.652	+33:20:09.90	8.45 ± 3.8	12	423	S100	13.67	5.13	0.89 ± 0.17	0.16 ± 0.04
G70-23-2	20:01:22.499	+33:19:54.88	8.45 ± 3.8	12	423	S100	14.08	5.28	0.38 ± 0.09	0.1 ± 0.03
G70-23-3	20:01:18.433	+33:19:15.83	8.45 ± 3.8	12	423	S99	14.1	1.57	0.55 ± 0.12	0.09 ± 0.02
G70-24-1	20:01:56.479	+33:14:51.98	8.45 ± 3.8	12	423	S100	17.92	6.72	0.87 ± 0.18	0.12 ± 0.03
G74-1-1	20:18:00.561	+37:03:38.69	4.4 ± 1.4	12	423	S104	18.32	4.58	1.0 ± 0.22	0.12 ± 0.04
G74-2-1	20:17:46.276	+37:03:17.66	4.4 ± 1.4	12	423	S104	17.6	4.4	0.75 ± 0.16	0.04 ± 0.01
G74-2-2	20:17:45.526	+37:02:32.66	4.4 ± 1.4	12	423	S104	16.84	4.21	0.62 ± 0.14	0.11 ± 0.03
G74-2-3	20:17:46.028	+37:02:08.66	4.4 ± 1.4	12	423	S104	16.45	4.11	0.83 ± 0.17	0.13 ± 0.03
G74-2-4	20:17:44.776	+37:01:44.66	4.4 ± 1.4	12	423	S104	16.04	4.01	0.39 ± 0.1	0.07 ± 0.02
G74-3-1	20:16:28.499	+36:54:54.68	4.4 ± 1.4	30	2799	S104	17.28	4.32	10.6 ± 2.03	1.39 ± 0.35
G74-4-1	20:17:37.545	+36:53:20.61	4.4 ± 1.4	12	423	S104	7.67	1.92	0.26 ± 0.09	0.04 ± 0.01
G74-5-1	20:17:02.368	+36:51:14.71	4.4 ± 1.4	12	468	S104	9.61	2.4	0.58 ± 0.14	0.08 ± 0.02
G74-6-1	20:18:56.532	+36:50:52.75	4.4 ± 1.4	12	423	S104	15.85	3.96	0.23 ± 0.09	0.05 ± 0.02
G74-7-1	20:17:57.050	+36:49:50.70	4.4 ± 1.4	12	423	S104	5.15	1.29	0.46 ± 0.11	0.06 ± 0.02
G74-7-2	20:17:58.299	+36:49:35.70	4.4 ± 1.4	12	423	S104	5.11	1.28	0.54 ± 0.12	0.07 ± 0.02
G74-8-1	20:17:32.314	+36:49:26.55	4.4 ± 1.4	12	423	S104	4.17	1.04	0.62 ± 0.16	0.08 ± 0.03

Continued on next page

Table 3 – *Continued from previous page*

Core ID	RA (J2000)	DEC (J2000)	d (kpc)	Radius (arcsec)	Area ($arcsec^2$)	HII Region	Core-HII Distance (arcmin)	Core-HII Scaled Distance	F_{450} (Jy)	F_{850} (Jy)
G74-8-2	20:17:31.568	+36:48:53.54	4.4 ± 1.4	12	423	S104	3.76	0.94	0.94 ± 0.22	0.13 ± 0.04
G74-9-1	20:17:50.305	+36:48:32.69	4.4 ± 1.4	18	999	S104	3.32	0.83	2.48 ± 0.53	0.38 ± 0.11
G74-9-2	20:17:51.055	+36:47:50.69	4.4 ± 1.4	12	423	S104	2.84	0.71	1.52 ± 0.32	0.15 ± 0.05
G74-10-1	20:18:03.294	+36:48:23.69	4.4 ± 1.4	18	999	S104	5.1	1.27	0.73 ± 0.2	0.13 ± 0.05
G74-10-2	20:18:04.792	+36:47:53.68	4.4 ± 1.4	12	423	S104	5.12	1.28	0.28 ± 0.09	0.04 ± 0.02
G74-12-1	20:17:30.075	+36:47:50.52	4.4 ± 1.4	18	999	S104	3.14	0.79	2.49 ± 0.51	0.37 ± 0.1
G74-12-2	20:17:28.080	+36:47:23.49	4.4 ± 1.4	12	423	S104	3.19	0.8	0.54 ± 0.14	0.05 ± 0.02
G74-12-3	20:17:25.833	+36:47:17.46	4.4 ± 1.4	12	423	S104	3.54	0.88	0.36 ± 0.11	0.06 ± 0.02
G74-13-1	20:17:35.073	+36:47:08.58	4.4 ± 1.4	12	423	S104	1.94	0.48	0.1 ± 0.07	0.04 ± 0.01
G74-13-2	20:17:33.076	+36:47:05.56	4.4 ± 1.4	12	423	S104	2.2	0.55	0.21 ± 0.08	0.04 ± 0.01
G74-15-1	20:17:23.844	+36:46:02.42	4.4 ± 1.4	12	423	S104	3.58	0.89	0.36 ± 0.11	0.04 ± 0.01
G74-16-1	20:18:48.116	+36:45:29.95	4.4 ± 1.4	12	459	S104	13.32	3.33	0.56 ± 0.13	0.06 ± 0.02
G74-16-2	20:18:48.976	+36:45:08.90	4.4 ± 1.4	12	441	S104	13.5	3.37	0.34 ± 0.1	0.06 ± 0.02
G74-17-1	20:17:57.299	+36:45:44.70	4.4 ± 1.4	18	999	S104	3.14	0.78	11.66 ± 2.25	1.15 ± 0.29
G74-17-2	20:17:56.050	+36:45:20.70	4.4 ± 1.4	12	423	S104	2.91	0.73	4.2 ± 0.84	0.46 ± 0.13
G74-17-3	20:17:59.046	+36:44:50.70	4.4 ± 1.4	12	423	S104	3.59	0.9	1.79 ± 0.4	0.21 ± 0.07
G74-17-4	20:17:57.298	+36:44:02.70	4.4 ± 1.4	12	423	S104	3.55	0.89	0.92 ± 0.25	0.12 ± 0.05
G74-18-1	20:17:29.142	+36:44:55.17	4.4 ± 1.4	12	450	S104	2.63	0.66	0.27 ± 0.09	0.03 ± 0.01
G74-19-1	20:17:22.853	+36:44:53.41	4.4 ± 1.4	12	423	S104	3.85	0.96	0.35 ± 0.13	0.03 ± 0.01
G74-20-1	20:16:13.745	+36:43:29.95	4.4 ± 1.4	24	1755	S104	17.75	4.44	10.11 ± 1.93	1.26 ± 0.3
G74-21-1	20:17:45.822	+36:42:41.67	4.4 ± 1.4	12	423	S104	3.14	0.78	0.74 ± 0.16	0.11 ± 0.03
G74-21-2	20:17:35.344	+36:42:29.59	4.4 ± 1.4	12	423	S104	3.46	0.87	1.73 ± 0.35	0.19 ± 0.05
G74-21-3	20:17:41.831	+36:42:23.65	4.4 ± 1.4	18	999	S104	3.32	0.83	5.24 ± 1.0	0.7 ± 0.17
G74-22-1	20:17:14.642	+36:42:02.25	4.4 ± 1.4	12	423	S104	6.54	1.64	0.21 ± 0.08	0.04 ± 0.02
G74-23-1	20:18:46.092	+36:33:02.06	4.4 ± 1.4	12	423	S104	18.11	4.53	0.14 ± 0.1	0.04 ± 0.01
G74-24-1	20:17:01.557	+36:30:37.92	4.4 ± 1.4	12	423	S104	17.09	4.27	0.85 ± 0.2	0.11 ± 0.03
G74-24-2	20:16:59.818	+36:30:25.87	4.4 ± 1.4	12	423	S104	17.44	4.36	1.41 ± 0.29	0.19 ± 0.05
G74-25-1	20:17:09.769	+36:30:35.14	4.4 ± 1.4	12	423	S104	16.43	4.11	0.65 ± 0.15	0.07 ± 0.02
G90-1-1	21:03:41.397	+49:51:46.97	8.59 ± 0.77	12	423	S120	0.62	0.62	1.12 ± 0.38	0.15 ± 0.04
G97-1-1	21:32:11.627	+55:53:46.80	6.82 ± 0.32	24	1755	S128	1.13	2.06	27.79 ± 5.19	3.42 ± 0.82
G97-1-2	21:32:10.913	+55:52:58.80	6.82 ± 0.32	24	1755	S128	0.33	0.59	10.96 ± 2.11	1.74 ± 0.44
G97-1-3	21:32:06.635	+55:52:10.80	6.82 ± 0.32	24	1755	S128	0.71	1.3	5.33 ± 1.08	0.79 ± 0.23

Continued on next page

Table 3 – *Continued from previous page*

Core ID	RA (J2000)	DEC (J2000)	d (kpc)	Radius (arcsec)	Area ($arcsec^2$)	HII Region	Core-HII Distance (arcmin)	Core-HII Scaled Distance	F_{450} (Jy)	F_{850} (Jy)
G105-1-1	22:32:45.376	+58:28:09.89	3.04 ± 0.61	18	999	S138	0.15	0.39	-	2.57 ± 0.65
G108-1-1	22:58:43.033	+58:47:46.33	2.9 ± 0.58	24	1755	S152	0.7	1.05	22.04 ± 5.67	2.26 ± 0.67
G108-1-2	22:58:43.041	+58:47:03.37	2.9 ± 0.58	12	423	S152	0.24	0.36	6.81 ± 1.78	0.91 ± 0.25
G108-1-3	22:58:40.189	+58:46:39.87	2.9 ± 0.58	12	423	S152	0.47	0.7	5.52 ± 1.63	0.6 ± 0.19
G108-1-4	22:58:44.508	+58:45:55.92	2.9 ± 0.58	12	423	S152	1.25	1.88	5.65 ± 1.61	0.65 ± 0.2
G108-1-5	22:58:51.086	+58:45:16.80	2.9 ± 0.58	18	999	S152	2.23	3.35	35.72 ± 7.11	4.19 ± 1.02
G108-1-6	22:58:46.887	+58:45:01.68	2.9 ± 0.58	18	999	S152	2.21	3.31	35.83 ± 7.13	3.4 ± 0.85
G115-1-1	23:53:44.516	+60:31:58.44	2.14 ± 0.3	18	999	S168	5.98	1.63	1.57 ± 0.3	0.2 ± 0.05
G115-1-2	23:53:38.407	+60:31:25.56	2.14 ± 0.3	18	999	S168	5.06	1.38	0.9 ± 0.19	0.16 ± 0.04
G115-2-1	23:53:11.984	+60:30:52.87	2.14 ± 0.3	24	1755	S168	2.13	0.58	1.02 ± 0.24	0.17 ± 0.05
G115-2-2	23:52:50.092	+60:21:10.88	2.14 ± 0.3	18	999	S168	2.13	0.58	0.87 ± 0.22	0.1 ± 0.04
G115-3-1	23:54:04.797	+60:30:33.92	2.14 ± 0.3	18	999	S168	7.91	2.16	1.31 ± 0.31	0.19 ± 0.07
G115-3-2	23:53:59.921	+60:30:31.07	2.14 ± 0.3	18	999	S168	7.31	1.99	2.94 ± 0.58	0.32 ± 0.1
G115-3-3	23:52:50.092	+60:21:10.88	2.14 ± 0.3	18	999	S168	7.31	1.99	1.22 ± 0.29	0.26 ± 0.09
G115-4-1	23:52:57.359	+60:28:34.90	2.14 ± 0.3	12	423	S168	0.79	0.22	2.19 ± 0.54	0.3 ± 0.1
G115-5-1	23:52:27.335	+60:28:01.65	2.14 ± 0.3	18	999	S168	4.37	1.19	4.27 ± 0.82	0.47 ± 0.12
G115-5-2	23:52:27.754	+60:27:13.65	2.14 ± 0.3	18	999	S168	4.6	1.25	2.67 ± 0.52	0.37 ± 0.1
G115-6-1	23:53:15.208	+60:27:25.85	2.14 ± 0.3	12	423	S168	2.43	0.66	0.48 ± 0.12	0.05 ± 0.02
G115-7-1	23:53:55.399	+60:28:40.19	2.14 ± 0.3	24	1755	S168	6.65	1.81	0.7 ± 0.15	0.08 ± 0.02
G115-8-1	23:52:37.489	+60:27:04.78	2.14 ± 0.3	18	999	S168	3.64	0.99	1.13 ± 0.24	0.17 ± 0.06
G115-9-1	23:53:03.848	+60:25:55.90	2.14 ± 0.3	18	999	S168	3.27	0.89	1.39 ± 0.31	0.19 ± 0.06
G115-9-2	23:52:50.092	+60:21:10.88	2.14 ± 0.3	18	999	S168	3.27	0.89	0.48 ± 0.12	0.07 ± 0.02
G115-10-1	23:53:14.385	+60:25:49.85	2.14 ± 0.3	12	423	S168	3.71	1.01	0.78 ± 0.18	0.12 ± 0.05
G115-10-2	23:52:50.092	+60:21:10.88	2.14 ± 0.3	18	999	S168	3.71	1.01	0.42 ± 0.14	0.05 ± 0.04
G115-11-1	23:53:12.743	+60:22:31.86	2.14 ± 0.3	30	2799	S168	6.8	1.85	9.19 ± 1.79	1.3 ± 0.33
G115-12-1	23:52:50.092	+60:21:10.88	2.14 ± 0.3	18	999	S168	8.13	2.22	1.58 ± 0.35	0.22 ± 0.07
G120-1-1	0:26:37.849	+64:57:01.99	2.67 ± 0.53	12	423	S175	15.4	12.16	0.13 ± 0.06	0.03 ± 0.01
G120-2-1	0:26:43.962	+64:55:52.90	2.67 ± 0.53	12	423	S175	14.12	11.15	0.08 ± 0.06	0.03 ± 0.01
G120-3-1	0:26:15.164	+64:54:59.18	2.67 ± 0.53	18	999	S175	14.36	11.34	1.79 ± 0.35	0.33 ± 0.08
G120-3-2	0:26:06.672	+64:54:17.20	2.67 ± 0.53	24	1755	S175	14.2	11.21	12.41 ± 2.31	2.19 ± 0.51
G120-3-3	0:26:07.614	+64:53:14.20	2.67 ± 0.53	12	423	S175	13.26	10.47	1.11 ± 0.22	0.13 ± 0.03
G120-4-1	0:26:34.019	+64:54:05.04	2.67 ± 0.53	18	999	S175	12.72	10.05	0.89 ± 0.23	0.24 ± 0.07

Continued on next page

Table 3 – *Continued from previous page*

Core ID	RA (J2000)	DEC (J2000)	d (kpc)	Radius (arcsec)	Area ($arcsec^2$)	HII Region	Core-HII Distance (arcmin)	Core-HII Scaled Distance	F_{450} (Jy)	F_{850} (Jy)
G120-4-2	0:26:36.835	+64:53:26.00	2.67 ± 0.53	12	423	S175	12.01	9.48	0.62 ± 0.14	0.13 ± 0.04
G125-1-1	1:08:51.865	+63:07:24.44	2.76 ± 0.15	18	999	S186	0.13	0.25	-	0.22 ± 0.11
G136-1-1	2:47:26.032	+61:56:48.72	3.54 ± 1.3	12	423	S194	1.2	1.39	-	0.19 ± 0.06
G138-1-1	3:01:33.545	+60:29:16.11	3.9 ± 0.89	42	5499	S201	12.57	7.54	96.19 ± 18.27	10.74 ± 2.64
G138-2-1	3:03:01.250	+60:28:21.63	3.9 ± 0.89	24	1755	S201	1.82	1.09	11.72 ± 2.44	1.38 ± 0.38
G138-3-1	3:03:21.946	+60:27:57.70	3.9 ± 0.89	36	3951	S201	0.98	0.59	48.12 ± 9.15	6.01 ± 1.57
G138-4-1	3:01:32.918	+60:25:52.08	3.9 ± 0.89	18	999	S201	12.65	7.59	2.15 ± 0.52	0.32 ± 0.11
G142-1-1	3:24:51.383	+54:57:34.68	3.26 ± 0.91	18	999	BFS31	0.55	0.68	-	0.47 ± 0.14
G151-1-1	4:19:31.408	+52:59:21.65	4.44 ± 0.55	12	423	S208	0.84	1.05	3.93 ± 3.46	0.12 ± 0.04
G151-2-1	4:19:31.449	+52:58:30.74	4.44 ± 0.55	12	423	S208	0.22	0.27	-	0.27 ± 0.07
G151-2-2	4:19:33.108	+52:58:11.76	4.44 ± 0.55	12	423	S208	0.35	0.44	4.68 ± 2.95	0.34 ± 0.09
G151-2-3	4:19:29.361	+52:57:58.78	4.44 ± 0.55	12	423	S208	0.77	0.97	-	0.11 ± 0.04
G151B-1-1	4:11:04.527	+51:10:24.44	10.58 ± 0.57	12	423	S209	1.14	0.34	5.84 ± 3.87	0.48 ± 0.13
G151B-2-1	4:11:09.845	+51:08:52.86	10.58 ± 0.57	12	423	S209	0.6	0.18	-	0.33 ± 0.09
G151B-2-2	4:11:07.391	+51:08:45.65	10.58 ± 0.57	12	423	S209	0.68	0.2	-	0.23 ± 0.07
G151B-3-1	4:11:03.856	+51:09:24.78	10.58 ± 0.57	12	423	S209	0.68	0.2	3.78 ± 3.22	0.07 ± 0.04
G151B-4-1	4:11:03.083	+51:07:53.23	10.58 ± 0.57	12	423	S209	1.74	0.52	-	0.22 ± 0.06
G151B-5-1	4:10:54.726	+51:07:56.71	10.58 ± 0.57	12	423	S209	2.58	0.77	-	0.08 ± 0.04
G151B-6-1	4:10:58.778	+51:07:00.80	10.58 ± 0.57	12	423	S209	2.83	0.85	-	0.15 ± 0.05
G173-1-1	5:41:22.103	+36:09:59.43	1.97 ± 0.96	24	1755	S232	13.37	1.34	-	0.78 ± 0.21
G173-2-1	5:41:26.410	+35:52:38.77	1.97 ± 0.96	12	423	S235	5.21	1.04	4.01 ± 1.37	0.44 ± 0.12
G173-2-2	5:41:24.979	+35:53:06.82	1.97 ± 0.96	12	423	S235	5.16	1.03	1.21 ± 1.17	0.27 ± 0.09
G173-2-3	5:41:24.501	+35:52:42.04	1.97 ± 0.96	12	423	S235	4.88	0.98	3.38 ± 1.32	0.28 ± 0.09
G173-2-4	5:41:22.764	+35:52:07.77	1.97 ± 0.96	12	423	S235	4.32	0.86	4.95 ± 1.46	0.8 ± 0.2
G173-3-1	5:41:30.993	+35:50:06.24	1.97 ± 0.96	12	423	S235	5.69	1.14	5.25 ± 1.72	0.52 ± 0.16
G173-3-2	5:41:31.034	+35:49:31.26	1.97 ± 0.96	12	423	S235	5.77	1.15	8.99 ± 2.22	0.91 ± 0.25
G173-3-3	5:41:29.717	+35:49:00.16	1.97 ± 0.96	12	423	S235	5.62	1.12	1.53 ± 1.41	0.39 ± 0.14
G173-4-1	5:41:14.970	+35:52:12.54	1.97 ± 0.96	12	423	S235	2.97	0.59	2.92 ± 1.31	0.24 ± 0.07
G173-5-1	5:41:05.787	+35:52:10.33	1.97 ± 0.96	12	423	S235	1.76	0.35	-	0.33 ± 0.1
G173-6-1	5:41:10.987	+35:50:00.08	1.97 ± 0.96	12	423	S235	1.69	0.34	5.86 ± 1.59	0.59 ± 0.16
G173-6-2	5:41:06.202	+35:50:02.80	1.97 ± 0.96	12	423	S235	0.79	0.16	2.71 ± 1.22	0.51 ± 0.14
G173-6-3	5:41:07.424	+35:49:33.18	1.97 ± 0.96	18	999	S235	1.3	0.26	15.21 ± 3.45	1.58 ± 0.4

Continued on next page

Table 3 – *Continued from previous page*

Core ID	RA (J2000)	DEC (J2000)	d (kpc)	Radius (arcsec)	Area ($arcsec^2$)	HII Region	Core-HII Distance (arcmin)	Core-HII Scaled Distance	F_{450} (Jy)	F_{850} (Jy)
G173-6-4	5:41:03.846	+35:49:52.06	1.97 ± 0.96	12	423	S235	0.66	0.13	1.71 ± 1.15	0.35 ± 0.1
G173-6-5	5:41:00.364	+35:49:29.28	1.97 ± 0.96	12	423	S235	1.14	0.23	6.3 ± 1.62	0.64 ± 0.17
G173-6-6	5:41:00.771	+35:48:35.84	1.97 ± 0.96	12	423	S235	1.96	0.39	4.76 ± 1.43	0.49 ± 0.14
G173-7-1	5:40:44.099	+35:54:58.52	1.97 ± 0.96	12	423	S235	5.89	1.18	-	0.14 ± 0.05
G173-7-2	5:40:41.484	+35:55:21.16	1.97 ± 0.96	12	423	S235	6.52	1.3	-	0.11 ± 0.04
G173-8-1	5:40:54.588	+35:49:45.67	1.97 ± 0.96	12	423	S235	1.86	0.37	2.76 ± 1.34	0.21 ± 0.07
G173-9-1	5:40:45.657	+35:48:13.36	1.97 ± 0.96	12	423	S235	4.19	0.84	2.08 ± 1.24	0.14 ± 0.06
G173-10-1	5:40:42.738	+35:46:08.77	1.97 ± 0.96	12	423	S235	5.99	1.2	-	0.13 ± 0.06
G173-11-1	5:40:53.480	+35:41:47.43	1.97 ± 0.96	30	2799	S235	8.92	1.78	94.5 ± 19.76	10.78 ± 2.57
G173-11-2	5:40:53.492	+35:40:33.33	1.97 ± 0.96	18	999	S235	10.13	2.03	6.33 ± 3.63	0.71 ± 0.23
G173-12-1	5:40:53.364	+35:38:25.19	1.97 ± 0.96	18	999	S235	12.24	2.45	7.46 ± 2.62	0.79 ± 0.21
G173-13-1	5:39:33.352	+35:48:51.22	1.97 ± 0.96	12	423	S231	6.22	1.04	-	0.12 ± 0.04
G173-14-1	5:38:35.508	+35:59:58.61	1.97 ± 0.96	12	423	S233	8.84	6.32	2.34 ± 1.42	0.27 ± 0.07
G173-15-1	5:39:28.596	+35:40:41.75	1.97 ± 0.96	12	423	S231	13.99	2.33	5.25 ± 1.74	0.65 ± 0.18
G173-15-2	5:39:27.055	+35:40:54.76	1.97 ± 0.96	12	423	S231	13.75	2.29	4.17 ± 1.64	0.33 ± 0.11
G173-16-1	5:39:12.207	+35:45:48.60	1.97 ± 0.96	24	1755	S231	9.03	1.5	104.63 ± 19.79	10.8 ± 2.59
G173-16-2	5:39:08.357	+35:46:40.65	1.97 ± 0.96	12	423	S231	8.4	1.4	4.37 ± 1.42	0.73 ± 0.22
G173-16-3	5:39:10.828	+35:45:13.26	1.97 ± 0.96	12	423	S231	9.66	1.61	8.68 ± 2.06	1.22 ± 0.33
G173-17-1	5:38:03.506	+36:01:19.93	1.97 ± 0.96	12	423	S233	11.81	8.43	1.95 ± 1.3	0.13 ± 0.04
G173-17-2	5:38:04.519	+36:00:38.02	1.97 ± 0.96	12	423	S233	11.1	7.93	-	0.18 ± 0.05
G173-18-1	5:38:00.419	+35:59:02.69	1.97 ± 0.96	12	423	S233	10.29	7.35	3.61 ± 1.61	0.65 ± 0.2
G173-18-2	5:38:01.223	+35:58:19.17	1.97 ± 0.96	4	423	S233	9.63	6.88	5.92 ± 1.85	0.62 ± 0.19
G173B-1-1	5:29:13.873	+34:22:44.04	2.97 ± 0.3	12	423	S234	14.06	2.34	-	0.26 ± 0.08
G173B-2-1	5:28:48.137	+34:23:35.37	2.97 ± 0.3	18	999	S234	8.68	1.45	-	0.78 ± 0.2
G173B-3-1	5:28:39.333	+34:23:52.96	2.97 ± 0.3	12	423	S234	6.85	1.14	-	0.17 ± 0.06
G182-1-1	5:51:38.248	+27:11:46.71	2.19 ± 0.44	12	423	S242	10.63	2.66	0.62 ± 0.19	0.09 ± 0.03
G182-2-1	5:52:04.343	+27:03:46.98	2.19 ± 0.44	18	999	S242	3.18	0.8	4.59 ± 0.92	0.59 ± 0.16
G182-2-2	5:52:02.097	+27:03:28.97	2.19 ± 0.44	18	999	S242	2.61	0.65	5.12 ± 1.02	0.69 ± 0.18
G182-2-3	5:52:06.589	+27:03:10.99	2.19 ± 0.44	12	423	S242	3.26	0.82	1.9 ± 0.45	0.34 ± 0.1
G182-3-1	5:52:10.183	+27:01:53.00	2.19 ± 0.44	12	423	S242	3.71	0.93	0.55 ± 0.33	-
G182-3-2	5:52:10.857	+27:00:35.00	2.19 ± 0.44	18	999	S242	4.02	1.0	12.68 ± 2.43	1.64 ± 0.41
G182-3-3	5:52:08.613	+27:00:13.99	2.19 ± 0.44	18	999	S242	3.67	0.92	4.92 ± 1.02	0.65 ± 0.18

Continued on next page

Table 3 – *Continued from previous page*

Core ID	RA (J2000)	DEC (J2000)	d (kpc)	Radius (arcsec)	Area ($arcsec^2$)	HII Region	Core-HII Distance (arcmin)	Core-HII Scaled Distance	F_{450} (Jy)	F_{850} (Jy)
G182-3-4	5:52:12.878	+27:00:11.00	2.19 ± 0.44	18	999	S242	4.57	1.14	13.32 ± 2.55	1.89 ± 0.46
G182-3-5	5:52:11.980	+26:59:35.00	2.19 ± 0.44	18	999	S242	4.63	1.16	11.21 ± 2.16	1.48 ± 0.37
G182-4-1	5:52:06.148	+26:56:10.99	2.19 ± 0.44	12	423	S242	6.2	1.55	0.7 ± 0.21	0.09 ± 0.03
G188-1-1	6:09:08.495	+21:52:49.63	2.23 ± 0.18	12	423	S247	17.25	4.93	1.25 ± 0.44	0.17 ± 0.04
G188-2-1	6:09:13.227	+21:51:10.56	2.23 ± 0.18	12	423	S247	16.38	4.68	-	0.12 ± 0.05
G188-2-2	6:09:11.503	+21:51:07.59	2.23 ± 0.18	12	423	S247	16.12	4.61	-	0.13 ± 0.05
G188-2-3	6:09:11.717	+21:50:43.59	2.23 ± 0.18	12	423	S247	15.81	4.52	0.86 ± 0.51	0.13 ± 0.05
G188-2-4	6:09:06.976	+21:50:40.66	2.23 ± 0.18	30	2799	S247	15.19	4.34	62.5 ± 12.05	5.76 ± 1.38
G188-3-1	6:09:20.120	+21:50:49.43	2.23 ± 0.18	18	999	S247	17.03	4.87	2.2 ± 0.54	0.53 ± 0.15
G188-3-2	6:09:17.750	+21:50:49.48	2.23 ± 0.18	12	423	S247	16.7	4.77	3.66 ± 0.92	0.22 ± 0.07
G188-4-1	6:09:17.086	+21:47:46.50	2.23 ± 0.18	12	423	S247	14.27	4.08	1.37 ± 0.43	0.08 ± 0.02
G188-5-1	6:08:49.083	+21:46:46.89	2.23 ± 0.18	12	423	S247	9.89	2.83	0.84 ± 0.4	0.1 ± 0.03
G188-6-1	6:09:56.232	+21:42:24.49	2.23 ± 0.18	18	999	S247	19.61	5.6	4.22 ± 1.09	0.53 ± 0.15
G188-7-1	6:09:56.217	+21:40:54.50	2.23 ± 0.18	18	999	S247	19.29	5.51	2.43 ± 0.93	0.25 ± 0.09
G188-8-1	6:08:51.651	+21:40:52.88	2.23 ± 0.18	12	423	S247	5.23	1.49	0.79 ± 0.4	0.08 ± 0.03
G188-8-2	6:08:51.219	+21:40:28.88	2.23 ± 0.18	12	423	S247	4.9	1.4	0.89 ± 0.41	0.1 ± 0.03
G188-9-1	6:09:14.890	+21:40:01.56	2.23 ± 0.18	12	423	S247	9.72	2.78	0.52 ± 0.37	0.07 ± 0.02
G188-10-1	6:09:52.763	+21:39:51.61	2.23 ± 0.18	12	423	S247	18.34	5.24	1.33 ± 0.48	0.18 ± 0.05
G188-11-1	6:08:53.795	+21:38:25.86	2.23 ± 0.18	48	7155	S247	4.58	1.31	225.43 ± 42.19	23.42 ± 5.47
G188-12-1	6:09:49.951	+21:38:15.70	2.23 ± 0.18	30	2799	S247	17.55	5.01	41.71 ± 7.99	5.16 ± 1.23
G188-13-1	6:09:02.829	+21:37:40.75	2.23 ± 0.18	12	423	S247	6.58	1.88	-	0.09 ± 0.04
G188-14-1	6:08:20.231	+21:37:25.99	2.23 ± 0.18	18	999	S247	3.32	0.95	1.13 ± 0.69	0.16 ± 0.06
G188-15-1	6:08:54.434	+21:36:22.85	2.23 ± 0.18	12	423	S247	4.76	1.36	0.51 ± 0.49	0.16 ± 0.05
G188-16-1	6:08:53.571	+21:35:28.86	2.23 ± 0.18	12	423	S247	4.86	1.39	1.12 ± 0.45	0.12 ± 0.05
G188-17-1	6:08:45.820	+21:31:52.93	2.23 ± 0.18	36	3951	S247	6.19	1.77	70.29 ± 13.4	7.76 ± 1.9
G188-17-2	6:08:40.874	+21:30:58.96	2.23 ± 0.18	42	5499	S247	6.67	1.91	194.83 ± 36.29	18.08 ± 4.28
G188-18-1	6:08:26.685	+21:26:14.00	2.23 ± 0.18	12	423	S247	11.4	3.26	-	0.05 ± 0.02
G188-19-1	6:09:30.911	+21:23:43.24	2.23 ± 0.18	18	999	S247	19.01	5.43	2.25 ± 0.76	0.32 ± 0.09
G188-20-1	6:09:21.458	+21:23:22.45	2.23 ± 0.18	12	423	S247	17.84	5.1	0.75 ± 0.42	0.11 ± 0.03
G188-21-1	6:08:19.813	+21:22:16.99	2.23 ± 0.18	12	423	S247	15.58	4.45	0.62 ± 0.36	0.08 ± 0.03
G188-21-2	6:08:21.746	+21:21:53.00	2.23 ± 0.18	12	423	S247	15.88	4.54	1.23 ± 0.42	0.11 ± 0.04
G192-1-1	6:12:25.263	+17:59:22.08	2.5 ± 0.2	12	459	S254	1.26	0.31	0.8 ± 0.29	0.07 ± 0.03

Continued on next page

Table 3 – *Continued from previous page*

Core ID	RA (J2000)	DEC (J2000)	d (kpc)	Radius (arcsec)	Area ($arcsec^2$)	HII Region	Core-HII Distance (arcmin)	Core-HII Scaled Distance	F_{450} (Jy)	F_{850} (Jy)
G192-2-1	6:12:53.455	+18:00:22.67	2.5 ± 0.2	24	1800	S257	2.49	1.24	119.62 ± 22.33	12.09 ± 2.83
G192-2-2	6:12:54.045	+17:59:21.52	2.5 ± 0.2	24	1800	S257	2.33	1.16	116.94 ± 21.84	12.71 ± 2.98
G192-2-3	6:12:56.574	+17:58:31.00	2.5 ± 0.2	18	1017	S255	2.08	1.04	23.73 ± 4.62	2.94 ± 0.72
G192-2-4	6:12:46.902	+17:58:24.99	2.5 ± 0.2	12	459	S257	0.98	0.49	1.24 ± 0.41	0.24 ± 0.09
G192-2-5	6:12:45.010	+17:58:09.99	2.5 ± 0.2	12	459	S257	1.03	0.51	-	-
G192-2-6	6:12:53.624	+17:57:18.03	2.5 ± 0.2	18	1026	S257	2.91	1.45	4.46 ± 1.13	0.85 ± 0.25
G192-3-1	6:13:07.088	+17:59:00.97	2.5 ± 0.2	12	450	S255	0.56	0.28	-	0.08 ± 0.03
G192-3-2	6:13:12.862	+17:58:41.63	2.5 ± 0.2	12	450	S255	1.8	0.9	0.82 ± 0.29	0.13 ± 0.04
G192-3-3	6:13:10.662	+17:58:33.95	2.5 ± 0.2	12	459	S255	1.28	0.64	1.68 ± 0.4	0.29 ± 0.08
G192-3-4	6:13:08.769	+17:58:12.96	2.5 ± 0.2	12	459	S255	0.93	0.47	1.66 ± 0.39	0.26 ± 0.07
G192-4-1	6:12:33.870	+17:56:30.94	2.5 ± 0.2	12	468	S256	1.02	0.77	1.53 ± 0.4	0.25 ± 0.07
G192-5-1	6:12:54.136	+17:55:55.58	2.5 ± 0.2	12	459	S255	3.81	1.9	1.2 ± 0.34	0.15 ± 0.04
G192-6-1	6:13:26.403	+17:56:14.79	2.5 ± 0.2	12	441	S258	0.89	1.06	1.34 ± 0.35	0.17 ± 0.05
G192-6-2	6:13:33.021	+17:56:03.91	2.5 ± 0.2	12	450	S258	1.04	1.25	0.66 ± 0.27	0.12 ± 0.04
G192-6-3	6:13:25.640	+17:55:53.79	2.5 ± 0.2	12	441	S258	0.86	1.03	1.35 ± 0.36	0.2 ± 0.06
G192-6-4	6:13:29.462	+17:55:30.96	2.5 ± 0.2	18	1044	S258	0.14	0.17	6.12 ± 1.25	0.87 ± 0.22
G192-6-5	6:13:27.366	+17:55:20.69	2.5 ± 0.2	12	459	S258	0.49	0.59	2.04 ± 0.46	0.24 ± 0.07
G192-7-1	6:12:22.914	+17:55:11.89	2.5 ± 0.2	12	468	S256	3.94	2.95	0.26 ± 0.22	0.06 ± 0.03
G192-8-1	6:13:45.209	+17:55:06.57	2.5 ± 0.2	12	459	S258	3.88	4.65	2.66 ± 0.59	0.31 ± 0.08
G192-8-2	6:13:47.257	+17:54:53.32	2.5 ± 0.2	12	441	S258	4.39	5.27	1.82 ± 0.46	0.37 ± 0.1
G192-8-3	6:13:49.705	+17:54:31.06	2.5 ± 0.2	12	459	S258	5.03	6.04	1.04 ± 0.37	0.19 ± 0.06
G192-9-1	6:12:34.573	+17:54:47.71	2.5 ± 0.2	12	441	S256	2.21	1.65	0.88 ± 0.28	0.09 ± 0.03
G192-9-2	6:12:33.046	+17:54:33.63	2.5 ± 0.2	12	459	S256	2.57	1.93	0.98 ± 0.3	0.13 ± 0.04
G192-10-1	6:13:59.386	+17:52:41.89	2.5 ± 0.2	18	990	S258	7.79	9.34	2.74 ± 0.66	0.49 ± 0.13
G192-10-2	6:13:57.412	+17:51:37.81	2.5 ± 0.2	18	1044	S258	7.84	9.41	1.97 ± 0.56	0.31 ± 0.09
G192-11-1	6:13:05.322	+17:50:08.92	2.5 ± 0.2	18	990	S258	7.87	9.44	0.78 ± 0.39	0.17 ± 0.05
G192-12-1	6:12:20.896	+17:48:52.24	2.5 ± 0.2	12	450	S256	8.95	6.71	0.72 ± 0.25	0.09 ± 0.03
G192-13-1	6:14:30.879	+17:45:19.19	2.5 ± 0.2	12	441	S255B	1.62	1.21	1.77 ± 0.42	0.24 ± 0.07
G192-14-1	6:14:25.460	+17:45:17.54	2.5 ± 0.2	12	423	S255B	0.33	0.25	2.73 ± 0.59	0.37 ± 0.11
G192-14-2	6:14:23.988	+17:44:53.57	2.5 ± 0.2	18	999	S255B	0.32	0.24	11.18 ± 2.19	1.26 ± 0.33
G192-14-3	6:14:25.456	+17:44:20.54	2.5 ± 0.2	12	423	S255B	0.93	0.7	3.71 ± 0.76	0.4 ± 0.12
G192-14-4	6:14:23.353	+17:43:44.58	2.5 ± 0.2	12	423	S255B	1.48	1.11	2.88 ± 0.62	0.43 ± 0.13

Continued on next page

Table 3 – *Continued from previous page*

Core ID	RA (J2000)	DEC (J2000)	d (kpc)	Radius (arcsec)	Area ($arcsec^2$)	HII Region	Core-HII Distance (arcmin)	Core-HII Scaled Distance	F_{450} (Jy)	F_{850} (Jy)
G192-14-5	6:14:22.721	+17:43:23.59	2.5 ± 0.2	12	423	S255B	1.85	1.39	2.31 ± 0.53	0.36 ± 0.11
G192-15-1	6:14:07.613	+17:44:05.12	2.5 ± 0.2	12	441	S255B	4.09	3.06	0.99 ± 0.31	0.1 ± 0.03
G192-16-1	6:14:30.941	+17:42:54.61	2.5 ± 0.2	12	450	S255B	2.82	2.12	0.92 ± 0.26	0.08 ± 0.02
G192-17-1	6:14:18.939	+17:42:50.65	2.5 ± 0.2	12	423	S255B	2.67	2.0	0.98 ± 0.3	0.16 ± 0.05
G192-17-2	6:14:20.069	+17:42:16.95	2.5 ± 0.2	12	441	S255B	3.09	2.32	1.47 ± 0.36	0.25 ± 0.07
G192B-1-1	6:11:24.038	+17:26:21.49	8.71 ± 1.74	24	1755	S259	1.16	1.02	8.58 ± 1.86	1.41 ± 0.35
G195-1-1	6:18:53.901	+15:17:54.80	12.55 ± 3.16	12	423	S266	2.24	2.79	-	0.19 ± 0.08
G196-1-1	6:14:36.696	+13:49:32.95	4.27 ± 0.85	18	999	S269	0.57	0.38	-	1.9 ± 0.53
G196-1-2	6:14:33.272	+13:48:59.06	4.27 ± 0.85	12	423	S269	1.5	1.0	-	0.49 ± 0.17
G210-1-1	6:38:29.346	+0:44:42.04	9.1 ± 2.9	12	423	S283	3.13	3.13	0.81 ± 0.27	0.19 ± 0.05
G210-1-2	6:38:26.398	+0:44:36.19	9.1 ± 2.9	12	423	S283	3.27	3.27	0.58 ± 0.25	0.08 ± 0.03
G217-1-1	6:54:35.444	-4:32:16.17	5.79 ± 1.24	18	999	S286	2.49	0.65	3.55 ± 1.51	0.81 ± 0.21
G217-1-2	6:54:33.541	-4:31:46.92	5.79 ± 1.24	12	423	S286	1.92	0.5	-	0.08 ± 0.04
G219-1-1	7:08:39.187	-4:19:20.31	3.0 ± 1.2	12	423	S288	0.23	0.43	1.62 ± 0.8	0.25 ± 0.08
G219-1-2	7:08:37.736	-4:19:04.52	3.0 ± 1.2	12	423	S288	0.38	0.71	2.93 ± 0.92	0.39 ± 0.11
G221-1-1	7:00:37.141	-8:50:03.82	3.88 ± 0.88	12	423	BFS64	1.75	0.81	0.41 ± 0.23	0.05 ± 0.01
G221-1-2	7:00:38.162	-8:50:39.89	3.88 ± 0.88	12	423	BFS64	1.27	0.58	-	0.04 ± 0.01
G221-1-3	7:00:37.640	-8:51:10.83	3.88 ± 0.88	12	423	BFS64	0.76	0.35	0.65 ± 0.26	0.08 ± 0.02
G221-2-1	7:00:25.730	-8:49:56.15	3.88 ± 0.88	12	423	BFS64	3.09	1.43	1.46 ± 0.32	0.18 ± 0.05
G221-3-1	7:00:28.413	-8:51:20.28	3.88 ± 0.88	18	999	BFS64	1.87	0.86	3.26 ± 0.74	0.52 ± 0.13
G221-3-2	7:00:26.981	-8:51:44.64	3.88 ± 0.88	12	423	BFS64	2.17	1.0	0.46 ± 0.24	0.13 ± 0.04
G221-4-1	7:00:31.100	-8:52:51.11	3.88 ± 0.88	18	999	BFS64	1.57	0.73	1.49 ± 0.54	0.21 ± 0.06
G223-1-1	7:16:38.639	-9:25:46.23	4.6 ± 1.5	12	423	S294	1.38	0.46	5.97 ± 2.54	0.35 ± 0.1
G225-1-1	7:05:21.295	-12:20:30.07	1.15 ± 0.14	12	423	S297	1.02	0.38	-	0.2 ± 0.06
G225-1-2	7:05:19.001	-12:20:23.74	1.15 ± 0.14	18	999	S297	0.78	0.29	-	0.54 ± 0.14
G225-2-1	7:05:10.699	-12:19:04.62	1.15 ± 0.14	18	999	S297	2.15	0.81	8.58 ± 5.06	1.16 ± 0.28
G225-3-1	7:05:03.538	-12:16:39.56	1.15 ± 0.14	18	999	S297	4.84	1.82	14.14 ± 10.07	0.6 ± 0.15
G231-1-1	7:30:45.960	-15:17:31.05	2.78 ± 0.62	12	423	S299	1.76	1.47	-	0.16 ± 0.05
G231-2-1	7:30:37.760	-15:18:29.19	2.78 ± 0.62	12	423	S299	0.55	0.46	-	0.1 ± 0.03
G233-1-1	7:29:56.253	-18:27:53.99	5.2 ± 1.4	24	1755	S305	5.56	2.09	10.04 ± 1.91	1.59 ± 0.39
G233-1-2	7:29:57.505	-18:51:41.98	5.2 ± 1.4	18	999	S305	5.56	2.09	0.61 ± 0.15	0.09 ± 0.03
G233-2-1	7:30:13.335	-18:30:29.98	5.2 ± 1.4	12	423	S305	3.09	1.16	0.17 ± 0.1	0.05 ± 0.02

Continued on next page

Table 3 – *Continued from previous page*

Core ID	RA (J2000)	DEC (J2000)	d (kpc)	Radius (arcsec)	Area ($arcsec^2$)	HII Region	Core-HII Distance (arcmin)	Core-HII Scaled Distance	F_{450} (Jy)	F_{850} (Jy)
G233-3-1	7:30:04.687	-18:30:42.00	5.2 ± 1.4	12	423	S305	2.3	0.86	1.59 ± 0.33	0.22 ± 0.06
G233-3-2	7:30:04.687	-18:31:03.00	5.2 ± 1.4	12	423	S305	1.95	0.73	2.12 ± 0.42	0.28 ± 0.07
G233-3-3	7:30:00.258	-18:31:09.00	5.2 ± 1.4	12	423	S305	2.24	0.84	1.51 ± 0.31	0.23 ± 0.06
G233-3-4	7:30:00.258	-18:31:54.00	5.2 ± 1.4	18	999	S305	1.69	0.63	4.1 ± 0.82	0.62 ± 0.16
G233-4-1	7:29:44.015	-18:31:59.94	5.2 ± 1.4	12	423	S305	5.25	1.97	0.34 ± 0.09	0.07 ± 0.02
G233-4-2	7:29:46.125	-18:32:05.95	5.2 ± 1.4	12	423	S305	4.74	1.78	0.3 ± 0.09	0.05 ± 0.02
G233-5-1	7:30:15.866	-18:31:20.97	5.2 ± 1.4	12	423	S305	2.94	1.1	0.44 ± 0.12	0.07 ± 0.03
G233-5-2	7:30:13.125	-18:32:05.98	5.2 ± 1.4	18	999	S305	1.99	0.75	4.16 ± 0.82	0.57 ± 0.15
G233-5-3	7:30:12.071	-18:32:38.99	5.2 ± 1.4	18	999	S305	1.57	0.59	4.3 ± 0.84	0.65 ± 0.16
G233-6-1	7:30:06.586	-18:33:06.00	5.2 ± 1.4	12	423	S305	0.25	0.09	0.1 ± 0.07	0.04 ± 0.02
G233-7-1	7:29:56.882	-18:33:26.99	5.2 ± 1.4	12	423	S305	2.14	0.8	0.39 ± 0.11	0.06 ± 0.02
G233-7-2	7:30:00.468	-18:33:36.00	5.2 ± 1.4	12	423	S305	1.38	0.52	2.01 ± 0.39	0.26 ± 0.07
G233-8-1	7:29:34.940	-18:33:56.87	5.2 ± 1.4	18	999	S305	7.39	2.77	0.62 ± 0.16	0.21 ± 0.06
G233-8-2	7:29:33.040	-18:34:23.85	5.2 ± 1.4	12	423	S305	7.9	2.96	0.54 ± 0.12	0.09 ± 0.03
G233-9-1	7:30:00.468	-18:34:51.00	5.2 ± 1.4	18	999	S305	2.23	0.84	1.91 ± 0.41	0.26 ± 0.07
G233-10-1	7:30:16.714	-18:33:53.97	5.2 ± 1.4	12	423	S305	2.79	1.05	0.39 ± 0.11	0.07 ± 0.03
G233-10-2	7:30:13.339	-18:34:38.98	5.2 ± 1.4	12	423	S305	2.47	0.93	0.21 ± 0.09	0.05 ± 0.02
G233-10-3	7:30:18.403	-18:35:02.96	5.2 ± 1.4	12	423	S305	3.67	1.38	0.15 ± 0.09	0.02 ± 0.02
G233-10-4	7:30:16.716	-18:35:56.97	5.2 ± 1.4	30	2799	S305	3.97	1.49	29.9 ± 5.59	4.04 ± 0.95
G233-11-1	7:30:05.533	-18:37:42.00	5.2 ± 1.4	12	423	S305	4.71	1.77	0.24 ± 0.08	0.07 ± 0.02
G233-11-2	7:30:05.744	-18:38:27.00	5.2 ± 1.4	12	423	S305	5.46	2.05	0.4 ± 0.1	0.07 ± 0.02
G233-11-3	7:30:04.055	-18:38:48.00	5.2 ± 1.4	12	423	S305	5.82	2.18	0.17 ± 0.07	0.03 ± 0.01
G233-12-1	7:30:16.308	-18:46:44.97	5.2 ± 1.4	18	999	S305	13.99	5.25	1.7 ± 0.34	0.27 ± 0.07
G233-12-2	7:30:11.450	-18:46:44.98	5.2 ± 1.4	12	423	S305	13.83	5.19	0.33 ± 0.09	0.07 ± 0.02
G233-12-3	7:30:12.718	-18:47:08.98	5.2 ± 1.4	12	423	S305	14.26	5.35	0.18 ± 0.07	0.05 ± 0.02
G233-12-4	7:30:15.465	-18:48:20.97	5.2 ± 1.4	12	423	S305	15.54	5.83	-	0.04 ± 0.01
G233-13-1	7:29:50.108	-18:51:14.96	5.2 ± 1.4	24	1755	S305	18.63	6.99	4.17 ± 0.81	0.73 ± 0.18
G233-13-2	7:29:57.505	-18:51:41.98	5.2 ± 1.4	18	999	S305	18.81	7.05	1.42 ± 0.3	0.33 ± 0.09
G234-1-1	7:35:32.439	-18:45:32.65	2.2 ± 0.5	12	423	S307	0.59	0.39	-	0.21 ± 0.06
G234-2-1	7:35:38.733	-18:48:50.08	2.2 ± 0.5	12	423	S307	3.14	2.09	-	0.22 ± 0.07

Table 4: Core Calculated Properties. In order of appearance, core name, 450μm and 850μm surface brightness, 450μm and 850μm in-band luminosity, 450μm to 850μm flux ratio, average temperature, total mass, average H_2 column density, average H_2 number density, average gas pressure and spectral index are presented.

Core ID	S_{450} $10^{-4} \times (Jy/arcsec^2)$	S_{850} $10^{-4} \times (Jy/arcsec^2)$	L_{450} $10^{-12} \times (L_{SUN})$	L_{850} $10^{-12} \times (L_{SUN})$	F_{450}/F_{850}	T (K)	M $(M_\odot)$	N_{H_2} $10^{20} \times (cm^{-2})$	n_{H_2} (cm^{-3})	P $10^{-13} \times (Pa)$	α
G70-1-1	9.82 ± 2.52	1.96 ± 0.51	14.58 ± 10.0	1.54 ± 1.06	5.01 ± 1.83	$12.17^{6.12}_{3.68}$	$144.7^{28.5}_{68.4}$	$36.96^{19.03}_{13.51}$	1218^{1892}_{696}	$2.54^{2.05}_{0.82}$	2.5 ± 0.6
G70-2-1	13.28 ± 3.13	2.91 ± 0.94	8.36 ± 5.67	0.97 ± 0.69	4.57 ± 1.83	$11.14^{5.3}_{3.33}$	$107.5^{26.8}_{54.9}$	$61.79^{26.58}_{21.14}$	3054^{4403}_{1626}	$5.82^{4.26}_{1.74}$	2.4 ± 0.6
G70-2-2	18.89 ± 3.94	3.03 ± 0.91	28.06 ± 18.78	2.38 ± 1.68	6.24 ± 2.28	$15.86^{12.2}_{6.22}$	$141.3^{10.7}_{69.4}$	$36.1^{23.98}_{16.23}$	1189^{2238}_{738}	$3.23^{2.58}_{0.92}$	2.9 ± 0.6
G70-2-3	13.22 ± 3.11	2.29 ± 0.82	8.32 ± 5.64	0.76 ± 0.56	5.78 ± 2.47	$14.31^{12.86}_{5.69}$	$53.7^{3.6}_{27.2}$	$30.88^{20.23}_{14.84}$	1526^{2913}_{971}	$3.74^{2.94}_{1.11}$	2.8 ± 0.7
G70-3-1	17.19 ± 3.53	2.65 ± 0.7	25.54 ± 17.07	2.09 ± 1.44	6.48 ± 2.17	$16.78^{12.91}_{6.4}$	$113.1^{9.0}_{54.3}$	$28.89^{18.96}_{13.05}$	952^{1754}_{587}	$2.73^{2.18}_{0.81}$	2.9 ± 0.5
G70-4-1	42.18 ± 8.72	6.4 ± 1.71	175.57 ± 117.41	14.1 ± 9.72	6.59 ± 2.23	$17.25^{14.24}_{6.72}$	$731.7^{55.4}_{356.1}$	$67.28^{48.67}_{31.45}$	1330^{2699}_{859}	$3.93^{3.37}_{1.17}$	3.0 ± 0.5
G70-4-2	22.61 ± 5.36	5.13 ± 1.43	94.1 ± 63.86	11.31 ± 7.85	4.4 ± 1.61	$10.78^{4.23}_{3.06}$	$1340.0^{426.0}_{715.7}$	$123.21^{55.21}_{37.86}$	2436^{3742}_{1221}	$4.49^{3.83}_{1.37}$	2.3 ± 0.6
G70-4-3	14.61 ± 4.58	2.39 ± 0.97	9.19 ± 6.51	0.79 ± 0.6	-	-	-	-	-	-	2.8 ± 0.8
G70-4-4	22.61 ± 5.64	3.09 ± 1.09	14.23 ± 9.72	1.03 ± 0.75	7.33 ± 3.16	$20.84^{23.02}_{10.9}$	$40.1^{6.8}_{16.0}$	$23.03^{29.83}_{11.46}$	1138^{3465}_{729}	$4.06^{3.8}_{0.96}$	3.1 ± 0.7
G70-4-5	280.31 ± 52.16	36.09 ± 8.38	2982.6 ± 1976.4	203.31 ± 137.65	7.77 ± 2.31	$23.68^{24.16}_{11.0}$	$6604.1^{708.3}_{2790.5}$	$237.2^{230.29}_{120.22}$	2931^{6966}_{1937}	$11.88^{10.4}_{3.29}$	3.2 ± 0.5
G70-4-6	-	-	-	-	-	-	-	-	-	-	-
G70-4-7	338.32 ± 62.82	45.7 ± 10.57	4559.9 ± 3021.1	326.09 ± 220.68	7.4 ± 2.2	$21.29^{20.11}_{9.07}$	$12324.6^{967.5}_{5811.1}$	$349.76^{288.65}_{172.03}$	3842^{8389}_{2649}	$14.0^{12.06}_{4.06}$	3.1 ± 0.5
G70-5-1	17.19 ± 3.64	2.51 ± 0.68	26.46 ± 17.74	2.04 ± 1.41	6.86 ± 2.37	$18.43^{15.82}_{7.66}$	$95.6^{6.6}_{44.6}$	$24.42^{19.7}_{11.44}$	804^{1741}_{505}	$2.54^{2.17}_{0.72}$	3.0 ± 0.5
G70-6-1	10.91 ± 2.76	2.13 ± 0.68	6.86 ± 4.7	0.71 ± 0.5	5.12 ± 2.08	$12.46^{7.51}_{4.17}$	$63.8^{9.2}_{31.8}$	$36.66^{19.97}_{14.63}$	1812^{3030}_{1058}	$3.86^{3.1}_{1.17}$	2.6 ± 0.6
G70-6-2	28.98 ± 5.88	4.03 ± 1.1	18.23 ± 12.17	1.34 ± 0.93	7.2 ± 2.46	$20.11^{20.61}_{8.76}$	$55.1^{4.6}_{24.7}$	$31.67^{27.93}_{16.08}$	1565^{3527}_{1076}	$5.39^{4.57}_{1.55}$	3.1 ± 0.5
G70-7-1	31.84 ± 6.42	4.89 ± 1.22	47.31 ± 31.56	3.85 ± 2.63	6.51 ± 2.08	$16.89^{13.62}_{6.09}$	$206.5^{17.6}_{101.9}$	$52.73^{34.24}_{24.67}$	1737^{3184}_{1133}	$5.02^{4.16}_{1.55}$	2.9 ± 0.5
G70-7-2	45.94 ± 8.85	6.8 ± 1.64	119.9 ± 79.68	9.4 ± 6.39	6.75 ± 2.08	$17.95^{14.14}_{6.89}$	$458.6^{36.8}_{234.0}$	$65.89^{46.57}_{30.38}$	1628^{3335}_{1010}	$5.0^{4.47}_{1.53}$	3.0 ± 0.5
G70-8-1	67.41 ± 12.81	10.2 ± 2.5	280.6 ± 186.25	22.48 ± 15.32	6.61 ± 2.05	$17.31^{12.76}_{6.39}$	$1160.1^{104.4}_{569.8}$	$106.67^{68.7}_{47.44}$	2109^{3928}_{1272}	$6.25^{5.15}_{1.84}$	3.0 ± 0.5
G70-9-1	22.17 ± 4.33	3.72 ± 0.94	57.88 ± 38.5	5.14 ± 3.51	5.96 ± 1.9	$14.91^{9.67}_{4.81}$	$337.9^{50.2}_{167.5}$	$48.54^{25.43}_{20.07}$	1199^{1929}_{732}	$3.06^{2.38}_{0.98}$	2.8 ± 0.5
G70-10-1	8.13 ± 2.77	2.12 ± 0.7	5.11 ± 3.69	0.71 ± 0.51	3.83 ± 1.82	$9.63^{4.19}_{2.77}$	$105.6^{24.0}_{52.9}$	$60.68^{29.26}_{20.91}$	2999^{4680}_{1583}	$4.94^{4.13}_{1.58}$	2.1 ± 0.7
G70-10-2	7.15 ± 2.67	1.38 ± 0.57	4.5 ± 3.32	0.46 ± 0.35	-	-	-	-	-	-	2.6 ± 0.9
G70-11-1	13.31 ± 3.21	2.15 ± 0.72	8.73 ± 5.94	0.75 ± 0.54	6.19 ± 2.55	$15.7^{15.22}_{6.59}$	$45.0^{2.6}_{21.3}$	$25.87^{19.22}_{12.96}$	1278^{2609}_{844}	$3.44^{2.79}_{1.02}$	2.9 ± 0.6
G70-11-2	17.02 ± 3.78	1.91 ± 0.66	11.62 ± 7.83	0.69 ± 0.5	8.94 ± 3.67	$36.22^{25.45}_{25.12}$	$12.8^{10.3}_{0.4}$	$7.33^{20.71}_{2.14}$	362^{2050}_{178}	$2.25^{2.42}_{0.29}$	3.4 ± 0.6
G70-12-1	13.67 ± 2.8	2.01 ± 0.59	8.6 ± 5.74	0.67 ± 0.47	6.81 ± 2.45	$18.19^{17.96}_{7.73}$	$31.9^{2.3}_{15.1}$	$18.36^{14.43}_{9.17}$	907^{1871}_{602}	$2.82^{2.28}_{0.8}$	3.0 ± 0.6
G70-12-2	6.04 ± 1.64	1.22 ± 0.42	3.8 ± 2.63	0.41 ± 0.3	4.94 ± 2.18	$12.01^{7.9}_{4.15}$	$39.2^{5.0}_{20.2}$	$22.53^{12.6}_{9.41}$	1114^{1993}_{650}	$2.29^{1.91}_{0.71}$	2.5 ± 0.7
G70-13-1	8.47 ± 2.14	1.34 ± 0.5	5.33 ± 3.65	0.45 ± 0.33	6.33 ± 2.84	$16.2^{17.82}_{7.18}$	$25.6^{1.4}_{12.3}$	$14.69^{12.27}_{7.63}$	726^{1613}_{480}	$2.01^{1.64}_{0.56}$	2.9 ± 0.7

Continued on next page

Table 4 – *Continued from previous page*

Core ID	S_{450} $10^{-4} \times (Jy/arcsec^2)$	S_{850} $10^{-4} \times (Jy/arcsec^2)$	L_{450} $10^{-12} \times (L_{SUN})$	L_{850} $10^{-12} \times (L_{SUN})$	F_{450}/F_{850}	T (K)	M ($M_{\odot}$)	N_{H_2} $10^{20} \times (cm^{-2})$	n_{H_2} (cm^{-3})	P $10^{-13} \times (Pa)$	α
G70-14-1	20.02 ± 4.41	3.83 ± 1.16	52.26 ± 35.17	5.29 ± 3.73	5.23 ± 1.96	$12.74^{7.07}_{4.14}$	$456.5^{81.4}_{232.2}$	$65.59^{33.03}_{24.76}$	1621^{2586}_{919}	$3.54^{2.76}_{1.06}$	2.6 ± 0.6
G70-14-2	11.39 ± 3.27	2.45 ± 0.96	7.17 ± 5.0	0.82 ± 0.61	4.64 ± 2.26	$11.31^{7.43}_{3.82}$	$88.2^{10.8}_{44.8}$	$50.68^{23.51}_{20.96}$	2505^{3788}_{1457}	$4.85^{3.37}_{1.46}$	2.4 ± 0.8
G70-14-3	12.19 ± 3.4	2.42 ± 0.96	7.67 ± 5.33	0.81 ± 0.6	5.03 ± 2.44	$12.23^{9.33}_{4.47}$	$75.1^{5.8}_{38.5}$	$43.16^{23.28}_{19.3}$	2133^{3651}_{1303}	$4.47^{3.28}_{1.33}$	2.5 ± 0.8
G70-14-4	15.77 ± 4.01	2.57 ± 1.01	9.92 ± 6.79	0.86 ± 0.64	6.13 ± 2.85	$15.46^{16.3}_{6.72}$	$53.1^{2.7}_{25.5}$	$30.49^{23.83}_{15.57}$	1507^{3197}_{989}	$3.99^{3.13}_{1.11}$	2.8 ± 0.7
G70-15-1	12.41 ± 3.62	2.01 ± 0.75	7.81 ± 5.46	0.67 ± 0.49	6.18 ± 2.93	$15.67^{16.03}_{7.05}$	$40.5^{1.8}_{19.5}$	$23.26^{20.67}_{11.9}$	1149^{2704}_{743}	$3.08^{2.66}_{0.86}$	2.9 ± 0.7
G70-16-1	39.38 ± 8.46	5.63 ± 1.72	24.77 ± 16.63	1.88 ± 1.32	6.99 ± 2.6	$19.04^{19.74}_{8.87}$	$83.6^{6.8}_{39.5}$	$48.07^{45.53}_{24.27}$	2376^{5924}_{1561}	$7.74^{7.01}_{2.15}$	3.1 ± 0.6
G70-16-2	32.51 ± 7.37	5.33 ± 1.67	20.45 ± 13.81	1.78 ± 1.26	6.1 ± 2.35	$15.37^{13.1}_{5.95}$	$110.9^{8.1}_{53.8}$	$63.75^{41.87}_{30.33}$	3151^{5771}_{1976}	$8.29^{6.41}_{2.5}$	2.8 ± 0.6
G70-17-1	10.85 ± 2.77	1.85 ± 0.67	6.82 ± 4.68	0.62 ± 0.45	5.86 ± 2.58	$14.57^{13.23}_{5.72}$	$42.2^{2.3}_{19.7}$	$24.22^{16.4}_{11.75}$	1197^{2254}_{761}	$2.98^{2.27}_{0.87}$	2.8 ± 0.7
G70-17-2	6.34 ± 2.15	1.81 ± 0.66	3.99 ± 2.87	0.6 ± 0.44	3.5 ± 1.73	$9.0^{3.95}_{2.46}$	$104.4^{29.4}_{54.6}$	$59.98^{23.19}_{20.32}$	2965^{4136}_{1571}	$4.57^{3.44}_{1.47}$	2.0 ± 0.8
G70-17-3	6.25 ± 2.11	1.91 ± 0.68	3.93 ± 2.83	0.64 ± 0.46	3.27 ± 1.6	$8.61^{3.31}_{2.3}$	$121.5^{38.5}_{66.7}$	$69.8^{27.38}_{21.84}$	3450^{5128}_{1766}	$5.08^{4.2}_{1.6}$	1.9 ± 0.8
G70-17-4	11.25 ± 2.87	1.68 ± 0.64	7.07 ± 4.85	0.56 ± 0.41	6.7 ± 3.06	$17.7^{19.98}_{8.42}$	$27.9^{2.5}_{12.2}$	$16.02^{15.53}_{8.22}$	791^{1921}_{517}	$2.4^{1.95}_{0.61}$	3.0 ± 0.7
G70-18-1	2.66 ± 1.81	0.81 ± 0.31	1.68 ± 1.56	0.27 ± 0.2	-	-	-	-	-	-	1.9 ± 1.2
G70-19-1	35.36 ± 6.77	5.32 ± 1.35	52.53 ± 34.89	4.19 ± 2.87	6.64 ± 2.12	$17.46^{14.63}_{6.56}$	$213.0^{17.5}_{102.8}$	$54.41^{35.53}_{25.74}$	1793^{3251}_{1120}	$5.36^{4.27}_{1.64}$	3.0 ± 0.5
G70-20-1	9.61 ± 2.2	2.1 ± 0.58	14.28 ± 9.65	1.66 ± 1.15	4.57 ± 1.63	$11.14^{4.6}_{3.14}$	$184.0^{56.8}_{96.5}$	$47.0^{20.66}_{14.89}$	1549^{2330}_{817}	$2.95^{2.42}_{0.92}$	2.4 ± 0.6
G70-20-2	4.12 ± 1.46	1.48 ± 0.45	6.12 ± 4.46	1.16 ± 0.82	2.78 ± 1.3	$7.79^{2.36}_{1.77}$	$282.3^{107.9}_{149.5}$	$72.11^{28.47}_{20.56}$	2376^{3375}_{1159}	$3.17^{2.77}_{1.05}$	1.6 ± 0.7
G70-21-1	9.57 ± 2.53	1.5 ± 0.58	6.02 ± 4.15	0.5 ± 0.37	6.38 ± 3.0	$16.38^{17.66}_{7.35}$	$28.2^{1.7}_{12.9}$	$16.18^{13.68}_{8.29}$	799^{1732}_{520}	$2.24^{1.72}_{0.59}$	2.9 ± 0.7
G70-21-2	4.24 ± 1.64	2.1 ± 0.66	6.3 ± 4.69	1.65 ± 1.17	2.02 ± 1.01	$6.58^{1.64}_{1.34}$	$620.8^{256.4}_{370.0}$	$158.55^{49.23}_{41.7}$	5225^{7400}_{2475}	$5.89^{5.43}_{1.99}$	1.1 ± 0.8
G70-21-3	3.79 ± 1.58	1.63 ± 0.57	5.63 ± 4.29	1.28 ± 0.93	-	-	-	-	-	-	1.3 ± 0.9
G70-22-1	6.72 ± 2.04	1.16 ± 0.42	4.23 ± 2.98	0.39 ± 0.28	5.8 ± 2.75	$14.39^{13.88}_{6.25}$	$26.9^{0.8}_{13.1}$	$15.46^{12.2}_{7.85}$	764^{1676}_{506}	$1.88^{1.64}_{0.57}$	2.8 ± 0.7
G70-23-1	21.01 ± 4.11	3.75 ± 0.93	13.21 ± 8.79	1.25 ± 0.85	5.6 ± 1.77	$13.78^{7.38}_{4.13}$	$93.8^{18.9}_{48.0}$	$53.93^{26.04}_{19.84}$	2666^{4116}_{1502}	$6.29^{4.99}_{1.95}$	2.7 ± 0.5
G70-23-2	8.96 ± 2.08	2.33 ± 0.61	5.64 ± 3.81	0.77 ± 0.53	3.85 ± 1.35	$9.66^{2.89}_{2.28}$	$115.0^{48.5}_{62.4}$	$66.07^{24.7}_{16.76}$	3266^{4474}_{1524}	$5.4^{4.41}_{1.64}$	2.1 ± 0.6
G70-23-3	12.96 ± 2.74	2.19 ± 0.58	8.15 ± 5.46	0.73 ± 0.5	5.91 ± 2.01	$14.74^{9.78}_{5.1}$	$48.9^{5.9}_{24.8}$	$28.09^{16.95}_{11.75}$	1388^{2577}_{837}	$3.5^{3.04}_{1.07}$	2.8 ± 0.5
G70-24-1	20.47 ± 4.34	2.79 ± 0.77	12.88 ± 8.63	0.93 ± 0.64	7.35 ± 2.55	$20.98^{19.74}_{9.63}$	$35.8^{3.5}_{15.3}$	$20.57^{20.11}_{9.93}$	1016^{2453}_{671}	$3.65^{3.15}_{0.97}$	3.1 ± 0.5
G74-1-1	23.57 ± 5.17	2.78 ± 0.83	4.02 ± 2.01	0.25 ± 0.14	8.47 ± 3.13	$30.01^{29.47}_{18.05}$	$5.9^{2.8}_{0.3}$	$12.55^{22.8}_{5.45}$	1191^{3594}_{707}	$6.12^{3.91}_{0.94}$	3.4 ± 0.6
G74-2-1	17.82 ± 3.89	1.0 ± 0.32	3.04 ± 1.52	0.09 ± 0.05	17.79 ± 6.88	-	-	-	-	-	4.5 ± 0.6
G74-2-2	14.72 ± 3.35	2.51 ± 0.66	2.51 ± 1.27	0.23 ± 0.12	5.86 ± 2.03	$14.56^{9.75}_{5.04}$	$15.5^{0.6}_{4.3}$	$32.91^{20.38}_{14.14}$	3124^{4291}_{1830}	$7.78^{4.36}_{2.15}$	2.8 ± 0.5
G74-2-3	19.54 ± 4.11	3.18 ± 0.8	3.33 ± 1.65	0.29 ± 0.15	6.14 ± 2.02	$15.52^{11.23}_{5.36}$	$17.7^{0.6}_{5.2}$	$37.44^{22.95}_{16.5}$	3554^{4782}_{2082}	$9.44^{5.06}_{2.57}$	2.9 ± 0.5
G74-2-4	9.12 ± 2.46	1.67 ± 0.46	1.56 ± 0.82	0.15 ± 0.08	5.45 ± 2.1	$13.35^{8.92}_{4.56}$	$12.0^{0.4}_{3.2}$	$25.45^{15.8}_{10.98}$	2416^{3213}_{1378}	$5.52^{3.06}_{1.57}$	2.7 ± 0.6
G74-3-1	37.89 ± 7.24	4.96 ± 1.24	42.76 ± 20.9	2.96 ± 1.53	7.64 ± 2.41	$22.8^{22.8}_{10.64}$	$101.4^{10.8}_{26.9}$	$34.4^{34.63}_{17.08}$	1306^{2520}_{829}	$5.1^{2.98}_{1.16}$	3.2 ± 0.5
G74-4-1	6.1 ± 2.16	0.91 ± 0.33	1.04 ± 0.6	0.08 ± 0.05	-	-	-	-	-	-	3.0 ± 0.8

Continued on next page

Table 4 – *Continued from previous page*

Core ID	S_{450} $10^{-4} \times (Jy/arcsec^2)$	S_{850} $10^{-4} \times (Jy/arcsec^2)$	L_{450} $10^{-12} \times (L_{SUN})$	L_{850} $10^{-12} \times (L_{SUN})$	F_{450}/F_{850}	T (K)	M $(M_{\odot})$	N_{H_2} $10^{20} \times (cm^{-2})$	n_{H_2} (cm^{-3})	P $10^{-13} \times (Pa)$	α
G74-5-1	12.42 ± 2.94	1.73 ± 0.49	2.34 ± 1.19	0.17 ± 0.09	7.18 ± 2.66	$20.04^{21.4}_{9.18}$	$7.1^{0.7}_{1.8}$	$15.12^{15.34}_{7.79}$	1435^{2734}_{937}	$4.92^{2.87}_{1.17}$	3.1 ± 0.6
G74-6-1	5.51 ± 2.03	1.14 ± 0.39	0.94 ± 0.55	0.1 ± 0.06	-	-	-	-	-	-	2.5 ± 0.8
G74-7-1	10.83 ± 2.63	1.34 ± 0.41	1.85 ± 0.94	0.12 ± 0.07	8.06 ± 3.15	$26.02^{26.31}_{15.03}$	$3.5^{1.2}_{0.4}$	$7.33^{12.14}_{3.39}$	695^{1976}_{421}	$3.1^{2.06}_{0.53}$	3.3 ± 0.6
G74-7-2	12.8 ± 2.92	1.58 ± 0.45	2.18 ± 1.1	0.14 ± 0.08	8.13 ± 2.97	$26.55^{25.79}_{14.59}$	$3.9^{1.3}_{0.5}$	$8.37^{12.62}_{3.83}$	794^{2050}_{485}	$3.61^{2.26}_{0.65}$	3.3 ± 0.6
G74-8-1	14.76 ± 3.87	1.87 ± 0.7	2.52 ± 1.31	0.17 ± 0.1	7.89 ± 3.62	$24.61^{25.99}_{14.93}$	$5.2^{2.2}_{0.6}$	$11.01^{19.99}_{4.94}$	1045^{3281}_{611}	$4.4^{2.91}_{0.61}$	3.2 ± 0.7
G74-8-2	22.3 ± 5.09	3.01 ± 0.95	3.8 ± 1.92	0.27 ± 0.15	7.41 ± 2.88	$21.31^{23.1}_{10.55}$	$10.3^{1.6}_{2.3}$	$21.74^{24.41}_{10.92}$	2063^{4233}_{1297}	$7.53^{4.24}_{1.56}$	3.1 ± 0.6
G74-9-1	24.79 ± 5.3	3.8 ± 1.12	9.99 ± 4.98	0.81 ± 0.44	6.52 ± 2.37	$16.96^{14.19}_{6.8}$	$43.2^{1.4}_{12.1}$	$40.71^{29.79}_{18.87}$	2576^{3899}_{1543}	$7.48^{3.85}_{1.82}$	2.9 ± 0.6
G74-9-2	35.84 ± 7.47	3.56 ± 1.13	6.11 ± 3.03	0.32 ± 0.18	10.08 ± 3.83	$72.01^{1.16}_{59.7}$	-	$5.61^{36.09}_{1.85}$	532^{5240}_{0}	$6.57^{5.7}_{0.0}$	3.6 ± 0.6
G74-10-1	7.33 ± 2.05	1.31 ± 0.47	2.95 ± 1.56	0.28 ± 0.16	5.6 ± 2.56	$13.77^{12.81}_{5.25}$	$21.0^{0.1}_{6.2}$	$19.77^{13.0}_{9.89}$	1251^{1741}_{784}	$2.95^{1.44}_{0.8}$	2.7 ± 0.7
G74-10-2	6.52 ± 2.2	0.98 ± 0.45	1.11 ± 0.62	0.09 ± 0.06	-	-	-	-	-	-	3.0 ± 0.9
G74-12-1	24.9 ± 5.08	3.74 ± 1.01	10.03 ± 4.96	0.8 ± 0.42	6.66 ± 2.26	$17.53^{16.36}_{6.72}$	$40.3^{1.3}_{11.8}$	$37.99^{26.33}_{18.77}$	2404^{3424}_{1518}	$7.21^{3.6}_{1.9}$	3.0 ± 0.5
G74-12-2	12.87 ± 3.29	1.22 ± 0.55	2.19 ± 1.14	0.11 ± 0.07	-	-	-	-	-	-	3.7 ± 0.8
G74-12-3	8.43 ± 2.67	1.38 ± 0.59	1.44 ± 0.79	0.12 ± 0.08	-	-	-	-	-	-	2.8 ± 0.8
G74-13-1	2.44 ± 1.76	0.88 ± 0.33	0.42 ± 0.35	0.08 ± 0.05	-	-	-	-	-	-	1.6 ± 1.3
G74-13-2	4.93 ± 1.94	0.86 ± 0.32	0.84 ± 0.5	0.08 ± 0.05	-	-	-	-	-	-	2.8 ± 0.9
G74-15-1	8.41 ± 2.56	0.95 ± 0.29	1.43 ± 0.78	0.09 ± 0.05	8.86 ± 3.82	$35.06^{22.15}_{24.54}$	$1.7^{1.7}_{0.4}$	$3.51^{11.28}_{1.01}$	332^{1707}_{157}	$2.0^{1.79}_{0.22}$	3.4 ± 0.7
G74-16-1	12.15 ± 2.82	1.25 ± 0.41	2.25 ± 1.14	0.12 ± 0.07	9.73 ± 3.91	$55.59^{10.95}_{43.91}$	$1.4^{2.7}_{1.1}$	$2.87^{14.44}_{0.18}$	272^{2114}_{54}	$2.59^{2.22}_{0.06}$	3.6 ± 0.6
G74-16-2	7.73 ± 2.15	1.35 ± 0.43	1.38 ± 0.73	0.13 ± 0.07	5.73 ± 2.42	$14.15^{11.41}_{5.48}$	$9.1^{0.1}_{2.4}$	$19.34^{13.21}_{9.05}$	1836^{2595}_{1103}	$4.45^{2.33}_{1.2}$	2.7 ± 0.7
G74-17-1	116.7 ± 22.57	11.52 ± 2.94	47.01 ± 23.02	2.46 ± 1.27	10.13 ± 3.25	$75.55^{1.44}_{61.14}$	-	$18.08^{99.95}_{3.72}$	1144^{9788}_{164}	$14.79^{12.38}_{0.76}$	3.6 ± 0.5
G74-17-2	99.33 ± 19.95	10.91 ± 2.97	16.94 ± 8.35	0.99 ± 0.52	9.1 ± 3.08	$39.15^{24.97}_{25.93}$	$16.6^{12.5}_{2.1}$	$35.14^{84.62}_{10.75}$	3336^{13004}_{1568}	$22.35^{15.4}_{2.64}$	3.5 ± 0.5
G74-17-3	42.28 ± 9.41	4.86 ± 1.6	7.21 ± 3.62	0.44 ± 0.24	8.7 ± 3.45	$32.79^{26.4}_{21.41}$	$9.2^{6.4}_{0.6}$	$19.55^{45.84}_{7.0}$	1856^{7166}_{990}	$10.42^{7.3}_{1.16}$	3.4 ± 0.6
G74-17-4	21.67 ± 5.95	2.77 ± 1.18	3.7 ± 1.95	0.25 ± 0.15	-	-	-	-	-	-	3.2 ± 0.8
G74-18-1	5.98 ± 2.06	0.58 ± 0.26	1.09 ± 0.62	0.06 ± 0.04	-	-	-	-	-	-	3.7 ± 0.9
G74-19-1	8.38 ± 3.05	0.74 ± 0.3	1.43 ± 0.83	0.07 ± 0.04	-	-	-	-	-	-	3.8 ± 0.9
G74-20-1	57.59 ± 10.99	7.17 ± 1.7	40.75 ± 19.92	2.68 ± 1.36	8.04 ± 2.44	$25.79^{25.09}_{12.65}$	$77.5^{12.8}_{17.5}$	$41.06^{46.46}_{19.78}$	1949^{4055}_{1196}	$8.6^{5.0}_{1.87}$	3.3 ± 0.5
G74-21-1	17.57 ± 3.86	2.69 ± 0.79	3.0 ± 1.5	0.24 ± 0.13	6.54 ± 2.4	$17.02^{16.68}_{6.87}$	$12.9^{0.4}_{3.7}$	$27.26^{19.43}_{13.77}$	2588^{3719}_{1655}	$7.54^{3.7}_{1.97}$	3.0 ± 0.6
G74-21-2	41.0 ± 8.16	4.49 ± 1.2	6.99 ± 3.44	0.41 ± 0.21	9.13 ± 3.05	$39.63^{27.01}_{26.42}$	$6.7^{5.1}_{0.7}$	$14.24^{35.05}_{4.48}$	1352^{5479}_{684}	$9.17^{6.49}_{1.14}$	3.5 ± 0.5
G74-21-3	52.46 ± 10.03	7.05 ± 1.73	21.13 ± 10.33	1.5 ± 0.77	7.44 ± 2.31	$21.49^{21.16}_{9.52}$	$56.1^{4.1}_{15.7}$	$52.84^{47.45}_{26.47}$	3344^{5924}_{2074}	$12.3^{6.99}_{3.01}$	3.2 ± 0.5
G74-22-1	5.01 ± 1.99	0.99 ± 0.36	0.85 ± 0.51	0.09 ± 0.05	-	-	-	-	-	-	2.6 ± 0.8
G74-23-1	3.33 ± 2.31	0.91 ± 0.32	0.57 ± 0.47	0.08 ± 0.05	-	-	-	-	-	-	2.0 ± 1.2
G74-24-1	19.99 ± 4.72	2.62 ± 0.74	3.41 ± 1.73	0.24 ± 0.13	7.62 ± 2.8	$22.68^{23.8}_{11.72}$	$8.2^{1.5}_{1.7}$	$17.32^{21.76}_{8.59}$	1644^{3750}_{1054}	$6.38^{4.0}_{1.37}$	3.2 ± 0.6

Continued on next page

Table 4 – *Continued from previous page*

Core ID	S_{450} $10^{-4} \times (Jy/arcsec^2)$	S_{850} $10^{-4} \times (Jy/arcsec^2)$	L_{450} $10^{-12} \times (L_{SUN})$	L_{850} $10^{-12} \times (L_{SUN})$	F_{450}/F_{850}	T (K)	M ($M_\odot$)	N_{H_2} $10^{20} \times (cm^{-2})$	n_{H_2} (cm^{-3})	P $10^{-13} \times (Pa)$	α
G74-24-2	33.23 ± 6.88	4.56 ± 1.17	5.67 ± 2.81	0.41 ± 0.21	7.29 ± 2.4	$20.61^{20.22}_{8.96}$	$16.3^{1.2}_{4.4}$	$34.59^{31.11}_{17.19}$	3283^{5679}_{2032}	$11.58^{6.49}_{2.81}$	3.1 ± 0.5
G74-25-1	15.31 ± 3.63	1.71 ± 0.52	2.61 ± 1.33	0.15 ± 0.08	8.98 ± 3.46	$36.89^{24.8}_{25.16}$	$2.8^{2.4}_{0.5}$	$5.91^{16.59}_{1.8}$	561^{2570}_{264}	$3.54^{2.75}_{0.38}$	3.5 ± 0.6
G90-1-1	26.58 ± 8.93	3.5 ± 1.06	17.28 ± 6.2	1.21 ± 0.4	7.59 ± 3.43	$22.47^{26.21}_{12.59}$	$42.1^{53.9}_{18.0}$	$23.43^{40.96}_{12.23}$	1139^{2297}_{646}	$4.38^{1.51}_{0.15}$	3.2 ± 0.7
G97-1-1	158.34 ± 29.55	19.49 ± 4.65	269.2 ± 53.31	17.54 ± 4.35	8.12 ± 2.46	$26.54^{27.14}_{13.29}$	$486.9^{471.4}_{214.8}$	$107.38^{125.34}_{52.8}$	3288^{4156}_{1686}	$14.94^{2.2}_{0.02}$	3.3 ± 0.5
G97-1-2	62.48 ± 11.99	9.89 ± 2.49	106.22 ± 21.58	8.91 ± 2.32	6.31 ± 2.0	$16.15^{10.64}_{5.78}$	$513.4^{234.8}_{184.8}$	$113.24^{68.94}_{46.85}$	3468^{2392}_{1529}	$9.58^{0.95}_{0.62}$	2.9 ± 0.5
G97-1-3	30.37 ± 6.18	4.51 ± 1.3	51.63 ± 11.05	4.06 ± 1.2	6.73 ± 2.38	$17.84^{16.21}_{7.13}$	$200.0^{116.1}_{86.5}$	$44.11^{32.5}_{21.2}$	1350^{1102}_{684}	$4.12^{0.4}_{0.19}$	3.0 ± 0.6
G105-1-1	-	25.75 ± 6.55	-	2.62 ± 1.0	-	-	-	-	-	-	-
G108-1-1	125.57 ± 32.32	12.86 ± 3.82	38.6 ± 14.76	2.09 ± 0.86	9.77 ± 3.84	$56.9^{14.89}_{44.86}$	$22.6^{66.8}_{10.5}$	$27.51^{141.41}_{0.14}$	1981^{13093}_{358}	$19.29^{12.28}_{0.92}$	3.6 ± 0.6
G108-1-2	161.02 ± 42.1	21.41 ± 6.01	11.93 ± 4.6	0.84 ± 0.33	7.52 ± 2.88	$22.02^{25.44}_{11.11}$	$30.2^{14.1}_{9.3}$	$147.49^{190.71}_{77.59}$	21245^{39537}_{13051}	$80.05^{34.1}_{11.91}$	3.2 ± 0.6
G108-1-3	130.48 ± 38.47	14.18 ± 4.43	9.67 ± 3.95	0.56 ± 0.23	9.2 ± 3.95	$41.02^{22.02}_{30.21}$	$8.8^{18.7}_{1.3}$	$43.13^{167.16}_{9.08}$	6213^{31530}_{2251}	$43.61^{27.93}_{0.62}$	3.5 ± 0.7
G108-1-4	133.52 ± 37.98	15.25 ± 4.66	9.89 ± 3.97	0.6 ± 0.25	8.75 ± 3.66	$33.51^{23.61}_{22.4}$	$12.2^{17.3}_{0.4}$	$59.68^{164.35}_{19.29}$	8597^{31667}_{3818}	$49.3^{27.84}_{1.43}$	3.4 ± 0.7
G108-1-5	357.53 ± 71.14	41.93 ± 10.26	62.56 ± 21.64	3.88 ± 1.45	8.53 ± 2.69	$30.65^{30.12}_{17.07}$	$89.1^{56.8}_{19.5}$	$193.15^{295.36}_{90.68}$	18549^{39662}_{10596}	$97.29^{39.05}_{10.46}$	3.4 ± 0.5
G108-1-6	358.64 ± 71.33	34.08 ± 8.54	62.76 ± 21.7	3.16 ± 1.19	10.52 ± 3.37	$116.47^{33.71}_{101.32}$	-	$33.32^{295.8}_{26.18}$	3199^{35840}_{1309}	$63.76^{38.24}_{4.64}$	3.7 ± 0.5
G115-1-1	15.67 ± 3.03	1.98 ± 0.51	1.49 ± 0.41	0.1 ± 0.03	7.93 ± 2.57	$24.88^{25.27}_{12.62}$	$3.0^{1.8}_{1.0}$	$12.05^{14.35}_{5.84}$	1567^{2450}_{877}	$6.67^{1.84}_{0.56}$	3.3 ± 0.5
G115-1-2	8.98 ± 1.91	1.63 ± 0.44	0.86 ± 0.25	0.08 ± 0.03	5.51 ± 1.9	$13.52^{7.83}_{4.33}$	$6.4^{0.8}_{1.3}$	$25.42^{13.12}_{9.85}$	3307^{2502}_{1541}	$7.65^{1.61}_{1.13}$	2.7 ± 0.5
G115-2-1	5.8 ± 1.37	0.95 ± 0.29	0.97 ± 0.3	0.08 ± 0.03	6.09 ± 2.34	$15.32^{12.45}_{6.03}$	$5.3^{1.3}_{1.6}$	$11.88^{8.43}_{5.48}$	1159^{1155}_{615}	$3.04^{0.7}_{0.43}$	2.8 ± 0.6
G115-2-2	8.67 ± 2.18	0.98 ± 0.38	0.83 ± 0.26	0.05 ± 0.02	8.83 ± 4.07	$34.65^{24.38}_{24.43}$	$1.0^{1.9}_{0.0}$	$3.86^{11.76}_{1.03}$	502^{1865}_{181}	$2.98^{1.2}_{0.31}$	3.4 ± 0.7
G115-3-1	13.16 ± 3.07	1.88 ± 0.73	1.25 ± 0.38	0.09 ± 0.04	6.99 ± 3.18	$19.05^{21.99}_{9.84}$	$4.2^{2.3}_{1.5}$	$16.85^{18.38}_{8.56}$	2192^{3155}_{1249}	$7.15^{1.56}_{0.45}$	3.1 ± 0.7
G115-3-2	29.46 ± 5.79	3.21 ± 0.96	2.81 ± 0.78	0.16 ± 0.06	9.19 ± 3.28	$40.71^{25.2}_{27.96}$	$2.6^{4.6}_{0.1}$	$10.33^{28.0}_{2.73}$	1344^{4426}_{479}	$9.37^{3.42}_{0.46}$	3.5 ± 0.6
G115-3-3	12.2 ± 2.92	2.63 ± 0.86	1.16 ± 0.36	0.13 ± 0.05	4.64 ± 1.87	$11.29^{5.34}_{3.6}$	$14.4^{1.1}_{2.2}$	$57.28^{26.42}_{19.38}$	7453^{5219}_{3124}	$14.4^{2.7}_{1.97}$	2.4 ± 0.6
G115-4-1	51.77 ± 12.77	7.03 ± 2.31	2.09 ± 0.66	0.15 ± 0.06	7.37 ± 3.03	$21.08^{22.25}_{10.86}$	$5.8^{3.7}_{2.0}$	$51.55^{64.28}_{25.34}$	10062^{16221}_{5570}	$36.3^{10.24}_{2.67}$	3.1 ± 0.6
G115-5-1	42.74 ± 8.18	4.74 ± 1.22	4.07 ± 1.12	0.24 ± 0.08	9.01 ± 2.9	$37.5^{26.57}_{24.06}$	$4.2^{5.6}_{0.6}$	$16.9^{36.38}_{5.81}$	2199^{5866}_{920}	$14.12^{4.85}_{0.05}$	3.5 ± 0.5
G115-5-2	26.7 ± 5.2	3.71 ± 0.98	2.54 ± 0.71	0.19 ± 0.06	7.2 ± 2.37	$20.11^{19.49}_{8.7}$	$7.7^{2.8}_{2.6}$	$30.61^{25.91}_{15.18}$	3983^{4586}_{2214}	$13.71^{3.24}_{1.64}$	3.1 ± 0.5
G115-6-1	11.31 ± 2.76	1.21 ± 0.43	0.46 ± 0.14	0.03 ± 0.01	9.36 ± 4.03	$44.42^{17.28}_{33.5}$	$0.4^{1.0}_{0.1}$	$3.34^{13.66}_{0.29}$	651^{3217}_{129}	$4.95^{2.31}_{0.64}$	3.5 ± 0.7
G115-7-1	3.96 ± 0.84	0.48 ± 0.14	0.66 ± 0.19	0.04 ± 0.01	8.23 ± 2.92	$27.51^{26.78}_{15.43}$	$1.1^{1.0}_{0.3}$	$2.53^{3.82}_{1.15}$	246^{472}_{128}	$1.16^{0.35}_{0.05}$	3.3 ± 0.6
G115-8-1	11.26 ± 2.41	1.72 ± 0.55	1.07 ± 0.31	0.09 ± 0.03	6.55 ± 2.53	$17.06^{15.94}_{7.4}$	$4.6^{1.4}_{1.5}$	$18.23^{14.3}_{8.81}$	2373^{2563}_{1301}	$6.93^{1.46}_{0.81}$	3.0 ± 0.6
G115-9-1	13.94 ± 3.08	1.92 ± 0.6	1.33 ± 0.39	0.1 ± 0.04	7.26 ± 2.77	$20.46^{21.41}_{9.92}$	$3.9^{2.0}_{1.4}$	$15.45^{16.19}_{7.75}$	2010^{2775}_{1129}	$7.04^{1.78}_{0.65}$	3.1 ± 0.6
G115-9-2	4.82 ± 1.18	0.66 ± 0.24	0.46 ± 0.14	0.03 ± 0.01	7.28 ± 3.14	$20.56^{22.53}_{10.89}$	$1.3^{0.9}_{0.5}$	$5.29^{6.63}_{2.62}$	688^{1126}_{383}	$2.42^{0.64}_{0.15}$	3.1 ± 0.7
G115-10-1	18.51 ± 4.37	2.91 ± 1.12	0.75 ± 0.23	0.06 ± 0.03	6.35 ± 2.87	$16.28^{16.22}_{7.27}$	$3.5^{1.2}_{1.2}$	$31.74^{25.3}_{15.49}$	6195^{6759}_{3396}	$17.26^{3.12}_{1.73}$	2.9 ± 0.7
G115-10-2	4.16 ± 1.37	0.53 ± 0.38	0.4 ± 0.15	0.03 ± 0.02	-	-	-	-	-	-	3.2 ± 1.2

Continued on next page

Table 4 – *Continued from previous page*

Core ID	S_{450} $10^{-4} \times (Jy/arcsec^2)$	S_{850} $10^{-4} \times (Jy/arcsec^2)$	L_{450} $10^{-12} \times (L_{SUN})$	L_{850} $10^{-12} \times (L_{SUN})$	F_{450}/F_{850}	T (K)	M ($M_\odot$)	N_{H_2} $10^{20} \times (cm^{-2})$	n_{H_2} (cm^{-3})	P $10^{-13} \times (Pa)$	α
G115-11-1	32.82 ± 6.39	4.63 ± 1.19	8.76 ± 2.43	0.66 ± 0.21	7.08 ± 2.29	$19.5^{17.79}_{8.43}$	$28.2^{9.4}_{9.3}$	$40.37^{33.26}_{19.63}$	3152^{3576}_{1755}	$10.52^{2.55}_{1.35}$	3.1 ± 0.5
G115-12-1	15.84 ± 3.5	2.21 ± 0.71	1.51 ± 0.45	0.11 ± 0.04	7.17 ± 2.78	$19.95^{21.21}_{9.67}$	$4.6^{2.3}_{1.6}$	$18.45^{19.31}_{9.28}$	2400^{3346}_{1345}	$8.2^{2.04}_{0.76}$	3.1 ± 0.6
G120-1-1	3.19 ± 1.38	0.67 ± 0.21	0.2 ± 0.1	0.02 ± 0.01	-	-	-	-	-	-	2.5 ± 0.8
G120-2-1	1.99 ± 1.36	0.72 ± 0.23	0.13 ± 0.09	0.02 ± 0.01	-	-	-	-	-	-	1.6 ± 1.2
G120-3-1	17.93 ± 3.55	3.33 ± 0.83	2.66 ± 0.91	0.26 ± 0.1	5.39 ± 1.72	$13.17^{6.37}_{4.06}$	$21.3^{0.1}_{2.3}$	$54.4^{26.25}_{18.82}$	5674^{4905}_{2622}	$12.79^{3.96}_{2.41}$	2.6 ± 0.5
G120-3-2	70.71 ± 13.14	12.5 ± 2.91	18.43 ± 6.2	1.72 ± 0.63	5.66 ± 1.68	$13.94^{6.72}_{3.98}$	$127.1^{0.4}_{14.7}$	$182.87^{82.2}_{63.22}$	14305^{11398}_{6467}	$34.12^{9.75}_{6.3}$	2.7 ± 0.5
G120-3-3	26.3 ± 5.13	3.12 ± 0.82	1.65 ± 0.56	0.1 ± 0.04	8.43 ± 2.75	$29.55^{29.28}_{16.53}$	$2.5^{1.6}_{0.5}$	$14.37^{21.93}_{6.6}$	2247^{4850}_{1276}	$11.36^{4.49}_{1.1}$	3.4 ± 0.5
G120-4-1	8.86 ± 2.26	2.44 ± 0.66	1.31 ± 0.5	0.19 ± 0.07	3.62 ± 1.35	$9.24^{2.79}_{2.25}$	$31.4^{1.7}_{3.4}$	$80.25^{32.46}_{20.69}$	8371^{6377}_{3171}	$13.23^{4.45}_{2.54}$	2.0 ± 0.6
G120-4-2	14.74 ± 3.31	3.13 ± 0.84	0.93 ± 0.33	0.1 ± 0.04	4.71 ± 1.65	$11.45^{4.93}_{3.23}$	$11.0^{0.0}_{1.0}$	$63.09^{28.05}_{20.54}$	9871^{7890}_{4320}	$19.35^{5.92}_{3.72}$	2.4 ± 0.6
G125-1-1	-	2.2 ± 1.08	-	0.18 ± 0.09	-	-	-	-	-	-	-
G136-1-1	-	4.55 ± 1.47	-	0.27 ± 0.16	-	-	-	-	-	-	-
G138-1-1	174.93 ± 33.21	19.54 ± 4.8	304.73 ± 114.1	18.02 ± 7.31	8.95 ± 2.78	$36.53^{30.79}_{22.79}$	$330.3^{245.5}_{28.3}$	$72.74^{143.92}_{29.62}$	2226^{6373}_{1149}	$13.92^{6.79}_{1.34}$	3.4 ± 0.5
G138-2-1	66.78 ± 13.92	7.87 ± 2.19	37.12 ± 14.26	2.32 ± 0.99	8.48 ± 2.95	$30.16^{31.37}_{17.3}$	$54.3^{33.1}_{9.3}$	$36.59^{60.6}_{16.93}$	1959^{4662}_{1136}	$10.11^{4.53}_{1.11}$	3.4 ± 0.5
G138-3-1	121.79 ± 23.16	15.22 ± 3.99	152.44 ± 57.1	10.08 ± 4.19	8.0 ± 2.59	$25.5^{26.09}_{13.18}$	$295.6^{88.2}_{65.4}$	$88.62^{107.8}_{42.89}$	3164^{5949}_{1841}	$13.81^{5.81}_{2.02}$	3.3 ± 0.5
G138-4-1	21.52 ± 5.2	3.25 ± 1.06	6.81 ± 2.75	0.54 ± 0.25	6.62 ± 2.69	$17.36^{17.41}_{7.84}$	$28.0^{3.2}_{7.2}$	$33.57^{29.85}_{16.81}$	2396^{3485}_{1424}	$7.12^{2.72}_{1.29}$	3.0 ± 0.6
G142-1-1	-	4.66 ± 1.43	-	0.55 ± 0.27	-	-	-	-	-	-	-
G151-1-1	92.92 ± 81.91	2.93 ± 0.89	16.14 ± 14.5	0.27 ± 0.09	-	-	-	-	-	-	5.4 ± 1.5
G151-2-1	-	6.47 ± 1.77	-	0.6 ± 0.19	-	-	-	-	-	-	-
G151-2-2	110.69 ± 69.83	8.04 ± 2.1	19.23 ± 12.59	0.74 ± 0.23	-	-	-	-	-	-	4.1 ± 1.1
G151-2-3	-	2.53 ± 0.9	-	0.23 ± 0.09	-	-	-	-	-	-	-
G151B-1-1	138.08 ± 91.54	11.25 ± 3.03	136.17 ± 90.87	5.87 ± 1.64	-	-	-	-	-	-	3.9 ± 1.1
G151B-2-1	-	7.87 ± 2.09	-	4.11 ± 1.14	-	-	-	-	-	-	-
G151B-2-2	-	5.47 ± 1.56	-	2.85 ± 0.84	-	-	-	-	-	-	-
G151B-3-1	89.35 ± 76.1	1.71 ± 0.94	88.12 ± 75.34	0.89 ± 0.5	-	-	-	-	-	-	6.2 ± 1.6
G151B-4-1	-	5.16 ± 1.47	-	2.69 ± 0.79	-	-	-	-	-	-	-
G151B-5-1	-	1.92 ± 0.87	-	1.0 ± 0.46	-	-	-	-	-	-	5.8 ± 1.8
G151B-6-1	-	3.55 ± 1.08	-	1.85 ± 0.58	-	-	-	-	-	-	-
G173-1-1	-	4.47 ± 1.18	-	0.34 ± 0.25	-	-	-	-	-	-	-
G173-2-1	94.81 ± 32.43	10.46 ± 2.89	3.24 ± 2.49	0.19 ± 0.14	9.07 ± 3.99	$38.43^{22.25}_{27.94}$	$3.3^{5.4}_{2.5}$	$34.47^{140.35}_{9.5}$	7308^{44026}_{3847}	$48.06^{45.16}_{11.56}$	3.5 ± 0.7
G173-2-2	28.53 ± 27.6	6.29 ± 2.03	-	0.11 ± 0.09	-	-	-	-	-	-	2.4 ± 1.6
G173-2-3	79.97 ± 31.15	6.56 ± 2.1	2.73 ± 2.16	0.12 ± 0.09	-	-	-	-	-	-	3.9 ± 0.8

Continued on next page

Table 4 – *Continued from previous page*

Core ID	S_{450} $10^{-4} \times (Jy/arcsec^2)$	S_{850} $10^{-4} \times (Jy/arcsec^2)$	L_{450} $10^{-12} \times (L_{SUN})$	L_{850} $10^{-12} \times (L_{SUN})$	F_{450}/F_{850}	T (K)	M ($M_{\odot}$)	N_{H_2} $10^{20} \times (cm^{-2})$	n_{H_2} (cm^{-3})	P $10^{-13} \times (Pa)$	α
G173-2-4	117.01 ± 34.59	18.99 ± 4.79	4.0 ± 3.0	0.34 ± 0.25	6.16 ± 2.39	$15.58^{12.75}_{6.07}$	$21.0^{5.4}_{0.4}$	$222.07^{184.17}_{107.96}$	47089^{70493}_{31384}	$125.57^{67.87}_{48.29}$	2.9 ± 0.6
G173-3-1	124.13 ± 40.55	12.2 ± 3.82	4.24 ± 3.24	0.22 ± 0.17	10.17 ± 4.6	$78.52^{14.59}_{68.0}$	-	$17.48^{174.9}_{10.95}$	3706^{52324}_{258}	$49.79^{52.48}_{6.33}$	3.6 ± 0.7
G173-3-2	212.61 ± 52.54	21.52 ± 5.88	7.27 ± 5.32	0.39 ± 0.29	9.88 ± 3.64	$61.73^{10.63}_{49.1}$	-	$40.41^{216.04}_{2.1}$	8569^{66073}_{2829}	$90.52^{72.44}_{17.52}$	3.6 ± 0.6
G173-3-3	36.2 ± 33.31	9.32 ± 3.25	-	0.17 ± 0.13	-	-	-	-	-	-	2.1 ± 1.5
G173-4-1	69.11 ± 30.88	5.56 ± 1.59	2.36 ± 1.94	0.1 ± 0.08	-	-	-	-	-	-	4.0 ± 0.8
G173-5-1	-	7.9 ± 2.33	-	0.14 ± 0.11	-	-	-	-	-	-	-
G173-6-1	138.55 ± 37.56	13.85 ± 3.71	4.74 ± 3.51	0.25 ± 0.19	10.0 ± 3.81	$67.83^{1.92}_{55.17}$	-	$23.37^{144.91}_{4.99}$	4955^{42813}_{1153}	$57.52^{47.79}_{10.4}$	3.6 ± 0.6
G173-6-2	64.03 ± 28.81	12.15 ± 3.36	2.19 ± 1.8	0.22 ± 0.16	-	-	-	-	-	-	2.6 ± 0.8
G173-6-3	152.29 ± 34.52	15.87 ± 4.02	12.3 ± 8.92	0.68 ± 0.5	9.6 ± 3.26	$51.05^{20.76}_{37.28}$	-	$38.98^{140.11}_{6.71}$	5510^{28749}_{2648}	$48.14^{33.15}_{11.05}$	3.6 ± 0.5
G173-6-4	40.32 ± 27.26	8.19 ± 2.47	1.38 ± 1.33	0.15 ± 0.11	-	-	-	-	-	-	2.5 ± 1.2
G173-6-5	148.9 ± 38.32	15.02 ± 4.04	5.09 ± 3.75	0.27 ± 0.2	9.92 ± 3.69	$63.29^{6.64}_{50.64}$	-	$27.41^{154.23}_{2.96}$	5813^{46896}_{1856}	$62.96^{51.83}_{11.92}$	3.6 ± 0.6
G173-6-6	112.58 ± 33.71	11.59 ± 3.22	3.85 ± 2.89	0.21 ± 0.16	9.71 ± 3.97	$54.75^{12.83}_{43.35}$	-	$25.01^{139.27}_{0.28}$	5303^{42645}_{2115}	$49.69^{45.2}_{9.91}$	3.6 ± 0.6
G173-7-1	-	3.39 ± 1.14	-	0.06 ± 0.05	-	-	-	-	-	-	-
G173-7-2	-	2.49 ± 0.97	-	0.04 ± 0.04	-	-	-	-	-	-	-
G173-8-1	65.14 ± 31.57	4.87 ± 1.73	2.23 ± 1.88	0.09 ± 0.07	-	-	-	-	-	-	4.1 ± 0.9
G173-9-1	49.11 ± 29.39	3.21 ± 1.37	1.68 ± 1.53	0.06 ± 0.05	-	-	-	-	-	-	4.3 ± 1.2
G173-10-1	-	3.09 ± 1.36	-	0.06 ± 0.05	-	-	-	-	-	-	-
G173-11-1	337.62 ± 70.61	38.52 ± 9.19	76.38 ± 55.01	4.61 ± 3.36	8.76 ± 2.78	$33.67^{29.39}_{20.21}$	$93.8^{66.6}_{34.9}$	$158.6^{292.08}_{67.71}$	13452^{39200}_{8683}	$77.52^{45.5}_{22.54}$	3.4 ± 0.5
G173-11-2	63.4 ± 36.38	7.1 ± 2.3	5.12 ± 4.59	0.3 ± 0.23	-	-	-	-	-	-	3.4 ± 1.0
G173-12-1	74.68 ± 26.19	7.87 ± 2.12	6.03 ± 4.66	0.34 ± 0.25	9.49 ± 4.2	$47.91^{15.2}_{36.85}$	-	$20.84^{110.36}_{1.79}$	2946^{22013}_{1331}	$24.15^{23.37}_{5.14}$	3.5 ± 0.7
G173-13-1	-	2.85 ± 0.91	-	0.05 ± 0.04	-	-	-	-	-	-	-
G173-14-1	55.31 ± 33.55	6.39 ± 1.76	1.89 ± 1.74	0.12 ± 0.09	-	-	-	-	-	-	3.4 ± 1.0
G173-15-1	124.1 ± 41.05	15.3 ± 4.21	4.24 ± 3.24	0.28 ± 0.21	8.11 ± 3.49	$26.45^{26.26}_{15.92}$	$7.7^{5.7}_{2.1}$	$81.65^{179.88}_{38.48}$	17313^{58648}_{11499}	$78.36^{58.91}_{23.98}$	3.3 ± 0.7
G173-15-2	98.54 ± 38.85	7.78 ± 2.59	3.37 ± 2.67	0.14 ± 0.11	-	-	-	-	-	-	4.0 ± 0.8
G173-16-1	596.17 ± 112.78	61.52 ± 14.73	84.57 ± 60.44	4.62 ± 3.37	9.69 ± 2.96	$54.09^{21.5}_{39.46}$	$52.8^{80.4}_{52.1}$	$139.59^{466.75}_{22.14}$	14799^{73844}_{6975}	$137.0^{89.67}_{31.65}$	3.6 ± 0.5
G173-16-2	103.4 ± 33.53	17.34 ± 5.13	3.54 ± 2.69	0.31 ± 0.24	5.96 ± 2.62	$14.9^{13.25}_{6.16}$	$20.7^{5.0}_{0.1}$	$218.34^{187.55}_{109.21}$	46298^{70690}_{31447}	$118.07^{62.59}_{44.82}$	2.8 ± 0.7
G173-16-3	205.19 ± 48.69	28.73 ± 7.76	7.02 ± 5.11	0.52 ± 0.38	7.14 ± 2.57	$19.82^{20.6}_{8.89}$	$21.8^{6.8}_{0.4}$	$230.88^{225.39}_{118.44}$	48957^{83023}_{33603}	$166.02^{83.12}_{58.63}$	3.1 ± 0.6
G173-17-1	46.12 ± 30.76	2.98 ± 0.91	1.58 ± 1.51	0.05 ± 0.04	-	-	-	-	-	-	4.3 ± 1.2
G173-17-2	-	4.28 ± 1.17	-	0.08 ± 0.06	-	-	-	-	-	-	-
G173-18-1	85.31 ± 37.99	15.33 ± 4.66	2.92 ± 2.39	0.28 ± 0.21	-	-	-	-	-	-	2.7 ± 0.8
G173-18-2	139.85 ± 43.71	14.59 ± 4.47	4.78 ± 3.62	0.26 ± 0.2	9.59 ± 4.2	$50.69^{11.94}_{39.61}$	-	$309.9^{1620.5}_{0.91}$	$197143^{1463945}_{69652}$	$1710.0^{1486.0}_{308.61}$	3.6 ± 0.7

Continued on next page

Table 4 – *Continued from previous page*

Core ID	S_{450} $10^{-4} \times (Jy/arcsec^2)$	S_{850} $10^{-4} \times (Jy/arcsec^2)$	L_{450} $10^{-12} \times (L_{SUN})$	L_{850} $10^{-12} \times (L_{SUN})$	F_{450}/F_{850}	T (K)	M $(M_\odot)$	N_{H_2} $10^{20} \times (cm^{-2})$	n_{H_2} (cm^{-3})	P $10^{-13} \times (Pa)$	α
G173B-1-1	-	6.04 ± 1.82	-	0.25 ± 0.08	-	-	-	-	-	-	-
G173B-2-1	-	7.85 ± 2.04	-	0.76 ± 0.23	-	-	-	-	-	-	3.4 ± 1.8
G173B-3-1	-	3.91 ± 1.43	-	0.16 ± 0.06	-	-	-	-	-	-	4.2 ± 1.8
G182-1-1	14.69 ± 4.59	2.15 ± 0.74	0.62 ± 0.26	0.05 ± 0.02	6.84 ± 3.19	$18.35^{20.26}_{9.1}$	$2.3^{0.9}_{0.7}$	$19.38^{23.43}_{10.02}$	3695^{6571}_{2222}	$11.61^{4.69}_{1.71}$	3.0 ± 0.7
G182-2-1	45.94 ± 9.19	5.89 ± 1.58	4.58 ± 1.59	0.31 ± 0.12	7.8 ± 2.61	$23.88^{25.39}_{12.1}$	$10.0^{3.7}_{2.7}$	$37.99^{44.0}_{19.08}$	4830^{8206}_{2845}	$19.74^{7.24}_{2.66}$	3.2 ± 0.5
G182-2-2	51.27 ± 10.24	6.95 ± 1.82	5.12 ± 1.78	0.37 ± 0.14	7.37 ± 2.43	$21.11^{20.51}_{9.23}$	$14.1^{3.3}_{3.8}$	$53.44^{47.04}_{26.14}$	6795^{8996}_{3936}	$24.55^{7.96}_{3.87}$	3.1 ± 0.5
G182-2-3	44.87 ± 10.69	7.95 ± 2.45	1.9 ± 0.7	0.18 ± 0.07	5.64 ± 2.2	$13.91^{9.74}_{5.04}$	$13.2^{0.4}_{2.4}$	$112.59^{67.05}_{48.88}$	21476^{21095}_{11358}	$51.1^{15.11}_{9.71}$	2.7 ± 0.6
G182-3-1	12.93 ± 7.8	-	0.55 ± 0.36	-	-	-	-	-	-	-	3.7 ± 2.4
G182-3-2	126.9 ± 24.37	16.41 ± 4.08	12.66 ± 4.34	0.87 ± 0.33	7.73 ± 2.43	$23.42^{24.9}_{11.08}$	$28.6^{8.4}_{8.2}$	$108.76^{110.13}_{55.13}$	13830^{20713}_{8309}	$55.43^{19.25}_{8.52}$	3.2 ± 0.5
G182-3-3	49.28 ± 10.23	6.51 ± 1.85	4.92 ± 1.73	0.34 ± 0.14	7.57 ± 2.66	$22.31^{25.32}_{10.71}$	$12.2^{4.1}_{3.6}$	$46.23^{49.68}_{24.0}$	5879^{9313}_{3602}	$22.44^{7.8}_{3.19}$	3.2 ± 0.6
G182-3-4	133.37 ± 25.56	18.87 ± 4.63	13.31 ± 4.56	1.0 ± 0.37	7.07 ± 2.2	$19.43^{18.0}_{8.12}$	$43.1^{5.4}_{11.2}$	$163.86^{127.37}_{80.58}$	20838^{25615}_{12248}	$69.3^{23.01}_{12.46}$	3.1 ± 0.5
G182-3-5	112.23 ± 21.62	14.78 ± 3.69	11.2 ± 3.84	0.78 ± 0.3	7.59 ± 2.39	$22.47^{21.84}_{10.36}$	$27.3^{7.0}_{7.2}$	$103.82^{99.58}_{50.85}$	13203^{18953}_{7599}	$50.77^{17.4}_{7.82}$	3.2 ± 0.5
G182-4-1	16.44 ± 4.87	2.06 ± 0.79	0.69 ± 0.29	0.05 ± 0.02	7.97 ± 3.86	$25.27^{25.0}_{15.67}$	$1.4^{1.3}_{0.2}$	$11.71^{23.5}_{4.97}$	2234^{6128}_{1158}	$9.66^{4.38}_{0.37}$	3.3 ± 0.8
G188-1-1	29.59 ± 10.43	3.96 ± 1.06	1.3 ± 0.48	0.09 ± 0.03	7.48 ± 3.31	$21.73^{22.85}_{11.77}$	$3.4^{4.3}_{1.4}$	$27.79^{47.44}_{14.38}$	5205^{10107}_{2844}	$19.36^{7.08}_{1.15}$	3.2 ± 0.7
G188-2-1	-	2.76 ± 1.13	-	0.06 ± 0.03	-	-	-	-	-	-	-
G188-2-2	-	3.05 ± 1.19	-	0.07 ± 0.03	-	-	-	-	-	-	-
G188-2-3	20.4 ± 12.12	3.13 ± 1.21	0.89 ± 0.54	0.07 ± 0.03	-	-	-	-	-	-	2.9 ± 1.1
G188-2-4	223.29 ± 43.05	20.59 ± 4.92	64.73 ± 14.5	3.16 ± 0.84	10.85 ± 3.33	$210.09^{122.68}_{194.52}$	-	-	-	$29.33^{12.4}_{6.39}$	3.7 ± 0.5
G188-3-1	22.06 ± 5.41	5.28 ± 1.5	2.28 ± 0.62	0.29 ± 0.09	4.18 ± 1.57	$10.31^{4.2}_{2.72}$	$37.4^{7.2}_{7.2}$	$137.28^{55.22}_{43.18}$	17144^{8915}_{6331}	$30.26^{4.06}_{3.24}$	2.2 ± 0.6
G188-3-2	86.47 ± 21.84	5.21 ± 1.57	3.79 ± 1.05	0.12 ± 0.04	16.6 ± 6.52	-	-	-	-	-	4.4 ± 0.6
G188-4-1	32.37 ± 10.28	1.94 ± 0.58	1.42 ± 0.48	0.05 ± 0.01	16.66 ± 7.27	-	-	-	-	-	4.4 ± 0.7
G188-5-1	19.88 ± 9.35	2.38 ± 0.73	0.87 ± 0.42	0.06 ± 0.02	-	-	-	-	-	-	3.3 ± 0.9
G188-6-1	42.25 ± 10.89	5.35 ± 1.46	4.37 ± 1.23	0.29 ± 0.09	7.9 ± 2.97	$24.7^{26.05}_{13.59}$	$9.0^{10.1}_{3.7}$	$32.89^{50.2}_{16.3}$	4108^{7188}_{2169}	$17.36^{4.61}_{0.38}$	3.3 ± 0.6
G188-7-1	24.34 ± 9.26	2.51 ± 0.86	2.52 ± 1.0	0.14 ± 0.05	-	-	-	-	-	-	3.6 ± 0.8
G188-8-1	18.76 ± 9.57	1.91 ± 0.62	0.82 ± 0.43	0.04 ± 0.02	-	-	-	-	-	-	3.6 ± 0.9
G188-8-2	21.03 ± 9.76	2.25 ± 0.68	0.92 ± 0.44	0.05 ± 0.02	-	-	-	-	-	-	3.5 ± 0.9
G188-9-1	12.37 ± 8.66	1.56 ± 0.54	0.54 ± 0.38	0.04 ± 0.01	-	-	-	-	-	-	3.3 ± 1.2
G188-10-1	31.47 ± 11.41	4.2 ± 1.25	1.38 ± 0.52	0.1 ± 0.03	7.5 ± 3.52	$21.88^{23.26}_{12.31}$	$3.5^{4.9}_{1.5}$	$29.19^{53.83}_{14.66}$	5467^{11446}_{2936}	$20.47^{7.53}_{0.73}$	3.2 ± 0.7
G188-11-1	315.07 ± 58.97	32.73 ± 7.64	233.49 ± 51.19	12.84 ± 3.34	9.63 ± 2.88	$51.92^{23.28}_{36.88}$	$154.0^{373.9}_{10.7}$	$79.41^{242.82}_{16.94}$	3719^{12675}_{981}	$33.04^{9.69}_{2.84}$	3.6 ± 0.5
G188-12-1	149.01 ± 28.54	18.42 ± 4.39	43.2 ± 9.63	2.83 ± 0.75	8.09 ± 2.47	$26.22^{28.33}_{13.01}$	$79.8^{66.1}_{33.3}$	$105.37^{122.8}_{53.85}$	7895^{10690}_{4349}	$35.42^{6.86}_{1.39}$	3.3 ± 0.5
G188-13-1	-	2.15 ± 0.93	-	0.05 ± 0.02	-	-	-	-	-	-	-

Continued on next page

Table 4 – *Continued from previous page*

Core ID	S_{450} $10^{-4} \times (Jy/arcsec^2)$	S_{850} $10^{-4} \times (Jy/arcsec^2)$	L_{450} $10^{-12} \times (L_{SUN})$	L_{850} $10^{-12} \times (L_{SUN})$	F_{450}/F_{850}	T (K)	M ($M_\odot$)	N_{H_2} $10^{20} \times (cm^{-2})$	n_{H_2} (cm^{-3})	P $10^{-13} \times (Pa)$	α
G188-14-1	11.35 ± 6.89	1.62 ± 0.58	1.17 ± 0.73	0.09 ± 0.03	-	-	-	-	-	-	3.1 ± 1.1
G188-15-1	12.09 ± 11.57	3.73 ± 1.29	0.53 ± 0.51	0.09 ± 0.03	-	-	-	-	-	-	1.8 ± 1.6
G188-16-1	26.43 ± 10.59	2.92 ± 1.09	1.16 ± 0.48	0.07 ± 0.03	-	-	-	-	-	-	3.5 ± 0.9
G188-17-1	177.9 ± 33.93	19.64 ± 4.82	72.8 ± 16.18	4.26 ± 1.15	9.06 ± 2.81	$38.27^{30.9}_{24.14}$	$73.6^{118.6}_{20.1}$	$67.52^{140.27}_{26.33}$	4216^{9925}_{1831}	$27.61^{6.98}_{1.23}$	3.5 ± 0.5
G188-17-2	354.31 ± 66.0	32.87 ± 7.78	201.8 ± 44.09	9.91 ± 2.6	10.78 ± 3.25	$179.83^{92.36}_{164.01}$	-	-	-	$33.76^{13.67}_{6.97}$	3.7 ± 0.5
G188-18-1	-	1.27 ± 0.55	-	0.03 ± 0.01	-	-	-	-	-	-	-
G188-19-1	22.54 ± 7.58	3.24 ± 0.92	2.33 ± 0.83	0.18 ± 0.05	6.95 ± 3.06	$18.84^{19.8}_{9.28}$	$8.1^{7.6}_{3.6}$	$29.52^{38.39}_{15.42}$	3686^{5520}_{2063}	$11.89^{3.51}_{1.02}$	3.0 ± 0.7
G188-20-1	17.74 ± 9.89	2.57 ± 0.78	0.78 ± 0.44	0.06 ± 0.02	-	-	-	-	-	-	3.0 ± 1.0
G188-21-1	14.59 ± 8.55	1.85 ± 0.74	0.64 ± 0.38	0.04 ± 0.02	-	-	-	-	-	-	3.2 ± 1.1
G188-21-2	29.14 ± 9.82	2.49 ± 0.86	1.28 ± 0.45	0.06 ± 0.02	11.69 ± 5.65	-	-	-	-	-	3.9 ± 0.8
G192-1-1	17.52 ± 6.34	1.44 ± 0.55	1.05 ± 0.4	0.05 ± 0.02	-	-	-	-	-	-	3.9 ± 0.8
G192-2-1	664.55 ± 124.06	67.14 ± 15.73	155.71 ± 33.99	8.33 ± 2.17	9.9 ± 2.97	$62.45^{18.65}_{46.79}$	$80.7^{244.1}_{6.0}$	$132.4^{492.94}_{13.44}$	11061^{45265}_{1977}	$118.21^{35.87}_{13.42}$	3.6 ± 0.5
G192-2-2	649.64 ± 121.34	70.64 ± 16.54	152.22 ± 33.24	8.76 ± 2.28	9.2 ± 2.75	$40.94^{33.66}_{26.07}$	$139.6^{235.3}_{39.0}$	$229.09^{498.42}_{88.47}$	19140^{46646}_{8289}	$134.09^{34.05}_{6.44}$	3.5 ± 0.5
G192-2-3	233.36 ± 45.45	28.87 ± 7.08	30.89 ± 6.96	2.02 ± 0.55	8.08 ± 2.53	$26.19^{26.83}_{13.61}$	$57.2^{51.2}_{23.0}$	$166.84^{209.65}_{81.32}$	18585^{27121}_{9923}	$83.3^{16.98}_{2.73}$	3.3 ± 0.5
G192-2-4	27.01 ± 8.86	5.31 ± 1.88	1.61 ± 0.56	0.17 ± 0.06	5.08 ± 2.46	$12.36^{9.81}_{4.56}$	$15.3^{5.9}_{6.0}$	$100.74^{63.97}_{48.22}$	16832^{13039}_{8723}	$35.6^{5.1}_{4.38}$	2.6 ± 0.8
G192-2-5	-	-	-	-	-	-	-	-	-	-	-
G192-2-6	43.45 ± 11.04	8.27 ± 2.46	5.8 ± 1.61	0.58 ± 0.19	5.26 ± 2.05	$12.81^{7.4}_{4.4}$	$50.0^{16.2}_{15.0}$	$145.88^{81.89}_{57.88}$	16250^{11266}_{7199}	$35.62^{5.14}_{3.78}$	2.6 ± 0.6
G192-3-1	-	1.83 ± 0.68	-	0.06 ± 0.02	-	-	-	-	-	-	-
G192-3-2	18.32 ± 6.39	2.81 ± 0.88	1.07 ± 0.39	0.09 ± 0.03	6.51 ± 3.04	$16.9^{20.03}_{8.02}$	$4.7^{3.9}_{2.3}$	$30.7^{35.69}_{17.17}$	5130^{6912}_{3050}	$14.84^{3.93}_{1.47}$	2.9 ± 0.7
G192-3-3	36.54 ± 8.79	6.41 ± 1.68	2.18 ± 0.58	0.2 ± 0.06	5.7 ± 2.02	$14.07^{8.82}_{4.88}$	$14.7^{5.5}_{4.7}$	$96.61^{61.18}_{39.93}$	16143^{12551}_{7371}	$38.86^{6.73}_{4.36}$	2.7 ± 0.6
G192-3-4	36.06 ± 8.6	5.75 ± 1.49	2.15 ± 0.57	0.18 ± 0.05	6.28 ± 2.21	$16.0^{12.59}_{5.92}$	$10.6^{4.7}_{4.0}$	$69.82^{48.69}_{32.44}$	11667^{9809}_{5891}	$31.94^{5.4}_{3.47}$	2.9 ± 0.6
G192-4-1	32.6 ± 8.5	5.44 ± 1.55	1.99 ± 0.56	0.18 ± 0.05	5.99 ± 2.32	$15.0^{12.06}_{5.49}$	$11.4^{4.9}_{4.3}$	$74.94^{50.81}_{35.28}$	12521^{10261}_{6366}	$32.15^{5.26}_{3.51}$	2.8 ± 0.6
G192-5-1	26.16 ± 7.44	3.2 ± 0.98	1.56 ± 0.48	0.1 ± 0.03	8.19 ± 3.42	$27.11^{25.01}_{16.34}$	$2.7^{4.2}_{0.9}$	$17.91^{35.77}_{7.61}$	2992^{6754}_{1428}	$13.88^{4.27}_{0.43}$	3.3 ± 0.7
G192-6-1	30.3 ± 8.03	3.86 ± 1.18	1.74 ± 0.5	0.12 ± 0.04	7.85 ± 3.17	$24.3^{24.72}_{13.76}$	$3.7^{4.4}_{1.4}$	$24.13^{38.73}_{11.49}$	4031^{7396}_{2083}	$16.76^{4.37}_{0.02}$	3.2 ± 0.6
G192-6-2	14.71 ± 5.97	2.62 ± 0.89	0.86 ± 0.36	0.08 ± 0.03	-	-	-	-	-	-	2.7 ± 0.8
G192-6-3	30.73 ± 8.07	4.63 ± 1.35	1.76 ± 0.5	0.14 ± 0.04	6.63 ± 2.61	$17.4^{17.57}_{7.49}$	$7.2^{4.4}_{3.1}$	$47.34^{42.37}_{24.58}$	7911^{8343}_{4402}	$23.56^{4.44}_{2.13}$	3.0 ± 0.6
G192-6-4	58.62 ± 12.0	8.31 ± 2.07	7.97 ± 1.86	0.6 ± 0.16	7.05 ± 2.28	$19.36^{18.74}_{7.76}$	$26.0^{13.2}_{10.8}$	$75.88^{58.26}_{38.33}$	8453^{7733}_{4597}	$28.0^{4.41}_{2.45}$	3.1 ± 0.5
G192-6-5	44.34 ± 10.1	5.19 ± 1.45	2.65 ± 0.67	0.16 ± 0.05	8.55 ± 3.09	$30.9^{26.88}_{18.79}$	$3.7^{5.6}_{1.2}$	$24.44^{48.17}_{9.95}$	4084^{9129}_{1884}	$21.6^{5.86}_{0.79}$	3.4 ± 0.6
G192-7-1	5.49 ± 4.66	1.31 ± 0.58	0.33 ± 0.29	0.04 ± 0.02	-	-	-	-	-	-	2.3 ± 1.5
G192-8-1	57.88 ± 12.85	6.82 ± 1.83	3.46 ± 0.86	0.22 ± 0.06	8.48 ± 2.95	$30.13^{25.82}_{17.5}$	$5.1^{6.7}_{1.6}$	$33.23^{57.76}_{13.88}$	5552^{10923}_{2555}	$28.63^{7.18}_{0.58}$	3.4 ± 0.5
G192-8-2	41.25 ± 10.46	8.45 ± 2.23	2.37 ± 0.66	0.26 ± 0.07	4.88 ± 1.79	$11.86^{5.52}_{3.54}$	$25.3^{7.3}_{6.2}$	$166.3^{86.17}_{58.68}$	27787^{18118}_{11043}	$56.38^{9.42}_{6.36}$	2.5 ± 0.6

Continued on next page

Table 4 – *Continued from previous page*

Core ID	S_{450} $10^{-4} \times (Jy/arcsec^2)$	S_{850} $10^{-4} \times (Jy/arcsec^2)$	L_{450} $10^{-12} \times (L_{SUN})$	L_{850} $10^{-12} \times (L_{SUN})$	F_{450}/F_{850}	T (K)	M $(M_{\odot})$	N_{H_2} $10^{20} \times (cm^{-2})$	n_{H_2} (cm^{-3})	P $10^{-13} \times (Pa)$	α
G192-8-3	22.76 ± 7.95	4.2 ± 1.28	1.36 ± 0.5	0.13 ± 0.04	5.42 ± 2.51	$13.25^{10.46}_{5.11}$	$10.7^{5.6}_{4.3}$	$70.27^{56.33}_{34.03}$	11742^{11318}_{6118}	$26.62^{5.95}_{3.61}$	2.7 ± 0.7
G192-9-1	19.97 ± 6.37	2.07 ± 0.78	1.15 ± 0.39	0.06 ± 0.02	9.66 ± 4.79	$53.16^{5.38}_{43.29}$	$0.7^{3.8}_{0.3}$	$4.81^{30.77}_{0.98}$	803^{5666}_{99}	$7.31^{3.73}_{1.87}$	3.6 ± 0.8
G192-9-2	21.36 ± 6.43	2.84 ± 0.9	1.28 ± 0.41	0.09 ± 0.03	7.51 ± 3.28	$21.93^{22.05}_{11.68}$	$3.3^{3.6}_{1.3}$	$21.38^{31.42}_{10.32}$	3572^{5994}_{1856}	$13.41^{3.53}_{0.25}$	3.2 ± 0.7
G192-10-1	27.65 ± 6.72	4.99 ± 1.26	3.56 ± 0.95	0.34 ± 0.09	5.55 ± 1.95	$13.62^{8.0}_{4.61}$	$26.1^{9.1}_{7.9}$	$76.16^{45.24}_{30.82}$	8484^{6216}_{3793}	$19.77^{3.42}_{2.28}$	2.7 ± 0.6
G192-10-2	18.88 ± 5.35	2.94 ± 0.82	2.57 ± 0.78	0.21 ± 0.06	6.43 ± 2.56	$16.6^{15.64}_{7.01}$	$11.7^{7.0}_{5.0}$	$34.0^{30.37}_{17.36}$	3787^{4003}_{2077}	$10.76^{2.28}_{1.15}$	2.9 ± 0.6
G192-11-1	7.84 ± 3.98	1.72 ± 0.54	1.01 ± 0.53	0.12 ± 0.04	-	-	-	-	-	-	2.4 ± 0.9
G192-12-1	15.94 ± 5.5	2.02 ± 0.59	0.93 ± 0.34	0.06 ± 0.02	7.89 ± 3.58	$24.59^{26.55}_{14.39}$	$1.9^{2.9}_{0.8}$	$12.68^{24.65}_{6.27}$	2119^{4634}_{1116}	$8.92^{3.17}_{0.05}$	3.2 ± 0.7
G192-13-1	40.18 ± 9.5	5.55 ± 1.63	2.31 ± 0.6	0.17 ± 0.05	7.24 ± 2.72	$20.34^{22.0}_{9.79}$	$6.8^{5.1}_{2.9}$	$44.76^{47.22}_{22.99}$	7479^{9260}_{4107}	$26.03^{4.96}_{1.39}$	3.1 ± 0.6
G192-14-1	64.53 ± 13.92	8.85 ± 2.64	3.55 ± 0.87	0.26 ± 0.08	7.29 ± 2.68	$20.63^{21.23}_{9.77}$	$10.2^{7.1}_{4.2}$	$67.05^{66.25}_{33.49}$	11203^{12945}_{6041}	$39.54^{6.59}_{1.82}$	3.1 ± 0.6
G192-14-2	111.87 ± 21.94	12.57 ± 3.32	14.55 ± 3.29	0.87 ± 0.25	8.9 ± 2.93	$35.68^{28.18}_{22.51}$	$16.3^{25.8}_{4.4}$	$47.68^{97.58}_{18.19}$	5311^{12269}_{2240}	$32.43^{8.13}_{1.66}$	3.4 ± 0.5
G192-14-3	87.79 ± 18.08	9.53 ± 2.81	4.83 ± 1.14	0.28 ± 0.09	9.21 ± 3.31	$41.27^{25.31}_{28.88}$	$4.4^{10.0}_{0.6}$	$28.77^{83.27}_{7.74}$	4807^{15573}_{1589}	$33.95^{10.14}_{3.72}$	3.5 ± 0.6
G192-14-4	68.1 ± 14.62	10.22 ± 2.98	3.75 ± 0.91	0.3 ± 0.09	6.66 ± 2.41	$17.54^{16.01}_{7.23}$	$15.1^{7.3}_{6.0}$	$98.89^{73.74}_{47.9}$	16524^{14777}_{8634}	$49.6^{7.06}_{3.89}$	3.0 ± 0.6
G192-14-5	54.7 ± 12.44	8.6 ± 2.63	3.01 ± 0.77	0.25 ± 0.08	6.36 ± 2.42	$16.32^{15.45}_{6.74}$	$14.2^{7.0}_{5.8}$	$93.27^{72.03}_{46.28}$	15585^{14481}_{8301}	$43.53^{6.45}_{3.79}$	2.9 ± 0.6
G192-15-1	22.48 ± 6.95	2.22 ± 0.78	1.29 ± 0.42	0.07 ± 0.02	10.14 ± 4.75	$75.98^{10.11}_{65.52}$	$0.5^{4.1}_{0.4}$	$3.44^{32.04}_{1.99}$	574^{5861}_{266}	$7.46^{4.21}_{2.11}$	3.6 ± 0.7
G192-16-1	20.39 ± 5.81	1.88 ± 0.53	1.19 ± 0.37	0.06 ± 0.02	10.86 ± 4.38	$218.82^{148.9}_{206.89}$	-	-	-	$5.98^{3.81}_{1.76}$	3.8 ± 0.6
G192-17-1	23.11 ± 7.01	3.72 ± 1.23	1.27 ± 0.41	0.11 ± 0.04	6.21 ± 2.79	$15.75^{16.1}_{6.75}$	$6.5^{3.9}_{2.9}$	$42.78^{38.02}_{22.39}$	7148^{7526}_{3992}	$19.27^{3.53}_{1.82}$	2.9 ± 0.7
G192-17-2	33.3 ± 8.23	5.65 ± 1.63	1.91 ± 0.52	0.17 ± 0.05	5.89 ± 2.23	$14.66^{11.3}_{5.59}$	$11.6^{4.8}_{4.2}$	$76.25^{51.43}_{34.83}$	12741^{10457}_{6336}	$31.97^{5.11}_{3.41}$	2.8 ± 0.6
G192B-1-1	48.89 ± 10.61	8.04 ± 1.98	135.58 ± 48.3	11.8 ± 4.42	6.08 ± 2.0	$15.31^{10.15}_{5.27}$	$742.1^{22.6}_{130.9}$	$100.34^{62.02}_{42.87}$	2406^{2472}_{1253}	$6.3^{2.11}_{1.24}$	2.8 ± 0.5
G195-1-1	-	4.56 ± 1.78	-	3.35 ± 1.77	-	-	-	-	-	-	4.6 ± 3.2
G196-1-1	-	19.02 ± 5.31	-	3.82 ± 1.51	-	-	-	-	-	-	-
G196-1-2	-	11.48 ± 4.03	-	0.98 ± 0.44	-	-	-	-	-	-	-
G210-1-1	19.03 ± 6.46	4.52 ± 1.24	13.89 ± 7.83	1.75 ± 0.92	4.21 ± 1.84	$10.37^{4.98}_{3.1}$	$223.7^{10.2}_{62.2}$	$110.86^{66.87}_{42.29}$	5089^{6915}_{2686}	$9.03^{6.06}_{2.64}$	2.3 ± 0.7
G210-1-2	13.65 ± 5.91	1.86 ± 0.66	9.96 ± 6.22	0.72 ± 0.41	-	-	-	-	-	-	3.1 ± 0.9
G217-1-1	35.49 ± 15.12	8.07 ± 2.12	24.76 ± 12.94	2.98 ± 1.19	-	-	-	-	-	-	2.3 ± 0.8
G217-1-2	-	1.93 ± 1.03	-	0.3 ± 0.19	-	-	-	-	-	-	3.2 ± 2.2
G219-1-1	38.38 ± 18.92	5.87 ± 1.92	3.04 ± 2.28	0.25 ± 0.16	-	-	-	-	-	-	3.0 ± 0.9
G219-1-2	69.37 ± 21.8	9.28 ± 2.6	5.5 ± 3.56	0.39 ± 0.25	7.47 ± 3.14	$21.71^{23.23}_{11.77}$	$14.3^{3.7}_{0.7}$	$65.29^{102.5}_{33.35}$	9091^{26615}_{5932}	$33.77^{28.65}_{9.33}$	3.2 ± 0.7
G221-1-1	9.73 ± 5.36	1.24 ± 0.35	1.29 ± 0.82	0.09 ± 0.04	-	-	-	-	-	-	3.2 ± 1.0
G221-1-2	-	0.95 ± 0.3	-	0.07 ± 0.03	-	-	-	-	-	-	2.2 ± 2.1
G221-1-3	15.27 ± 6.04	1.97 ± 0.51	2.03 ± 1.03	0.14 ± 0.06	7.73 ± 3.64	$23.45^{25.42}_{13.83}$	$4.6^{4.3}_{1.2}$	$12.44^{28.93}_{6.51}$	1339^{4488}_{807}	$5.38^{4.21}_{0.92}$	3.2 ± 0.7
G221-2-1	34.59 ± 7.68	4.34 ± 1.12	4.59 ± 1.79	0.3 ± 0.13	7.97 ± 2.72	$25.27^{24.15}_{13.05}$	$9.0^{3.4}_{1.9}$	$24.64^{31.83}_{11.69}$	2652^{5091}_{1561}	$11.47^{5.07}_{1.64}$	3.3 ± 0.5

Continued on next page

Table 4 – *Continued from previous page*

Core ID	S_{450} $10^{-4} \times (Jy/arcsec^2)$	S_{850} $10^{-4} \times (Jy/arcsec^2)$	L_{450} $10^{-12} \times (L_{SUN})$	L_{850} $10^{-12} \times (L_{SUN})$	F_{450}/F_{850}	T (K)	M ($M_{\odot}$)	N_{H_2} $10^{20} \times (cm^{-2})$	n_{H_2} (cm^{-3})	P $10^{-13} \times (Pa)$	α
G221-3-1	32.62 ± 7.4	5.25 ± 1.31	10.22 ± 4.01	0.87 ± 0.35	6.22 ± 2.1	$15.79^{12.16}_{5.7}$	$52.0^{0.9}_{9.6}$	$62.97^{39.67}_{29.34}$	4520^{4912}_{2593}	$12.22^{4.51}_{2.73}$	2.9 ± 0.5
G221-3-2	10.98 ± 5.61	3.12 ± 0.88	1.46 ± 0.88	0.22 ± 0.09	-	-	-	-	-	-	2.0 ± 0.9
G221-4-1	14.88 ± 5.45	2.1 ± 0.58	4.66 ± 2.27	0.35 ± 0.15	7.09 ± 3.26	$19.56^{23.38}_{10.22}$	$14.9^{7.6}_{4.8}$	$18.06^{27.86}_{10.02}$	1296^{2968}_{832}	$4.34^{2.65}_{0.86}$	3.1 ± 0.7
G223-1-1	141.03 ± 60.03	8.19 ± 2.45	26.29 ± 16.5	0.81 ± 0.44	-	-	-	-	-	-	4.5 ± 0.8
G225-1-1	-	4.63 ± 1.34	-	0.03 ± 0.01	-	-	-	-	-	-	-
G225-1-2	-	5.37 ± 1.42	-	0.08 ± 0.02	-	-	-	-	-	-	-
G225-2-1	85.91 ± 50.7	11.65 ± 2.83	2.36 ± 1.45	0.17 ± 0.05	-	-	-	-	-	-	3.1 ± 1.0
G225-3-1	141.53 ± 100.81	6.05 ± 1.48	3.89 ± 2.85	0.09 ± 0.03	-	-	-	-	-	-	5.0 ± 1.2
G231-1-1	-	3.85 ± 1.19	-	0.14 ± 0.06	-	-	-	-	-	-	-
G231-2-1	-	2.44 ± 0.82	-	0.09 ± 0.04	-	-	-	-	-	-	-
G233-1-1	57.23 ± 10.91	9.08 ± 2.24	56.56 ± 24.09	4.75 ± 2.16	6.3 ± 1.97	$16.11^{10.35}_{5.9}$	$275.0^{2.3}_{66.7}$	$104.34^{65.58}_{42.54}$	4191^{5306}_{2283}	$11.55^{5.4}_{2.62}$	2.9 ± 0.5
G233-1-2	6.09 ± 1.46	0.89 ± 0.34	3.43 ± 1.54	0.27 ± 0.14	6.81 ± 3.04	$18.19^{20.54}_{8.62}$	$12.7^{1.6}_{3.2}$	$8.59^{8.12}_{4.41}$	459^{752}_{285}	$1.43^{0.58}_{0.25}$	3.0 ± 0.7
G233-2-1	4.1 ± 2.28	1.12 ± 0.44	0.98 ± 0.66	0.14 ± 0.08	-	-	-	-	-	-	2.0 ± 1.1
G233-3-1	37.65 ± 7.7	5.27 ± 1.41	8.97 ± 3.88	0.66 ± 0.31	7.15 ± 2.41	$19.85^{21.1}_{8.7}$	$27.8^{2.0}_{7.3}$	$42.21^{36.45}_{21.83}$	3390^{5221}_{2136}	$11.52^{5.27}_{2.55}$	3.1 ± 0.5
G233-3-2	50.01 ± 9.97	6.59 ± 1.71	11.91 ± 5.12	0.83 ± 0.38	7.59 ± 2.48	$22.43^{23.47}_{10.22}$	$29.2^{3.8}_{6.8}$	$44.24^{43.28}_{22.41}$	3554^{5979}_{2259}	$13.64^{6.33}_{2.71}$	3.2 ± 0.5
G233-3-3	35.78 ± 7.44	5.48 ± 1.46	8.52 ± 3.7	0.69 ± 0.32	6.53 ± 2.21	$16.98^{13.46}_{6.56}$	$36.8^{0.6}_{8.7}$	$55.8^{37.47}_{25.55}$	4482^{5669}_{2585}	$13.02^{5.53}_{2.92}$	2.9 ± 0.5
G233-3-4	41.08 ± 8.17	6.21 ± 1.55	23.11 ± 9.93	1.85 ± 0.84	6.62 ± 2.12	$17.36^{13.77}_{6.54}$	$95.0^{1.2}_{23.0}$	$64.05^{43.99}_{29.29}$	3430^{4512}_{1965}	$10.19^{4.63}_{2.33}$	3.0 ± 0.5
G233-4-1	8.06 ± 2.13	1.62 ± 0.5	1.92 ± 0.89	0.2 ± 0.1	4.97 ± 2.02	$12.07^{6.71}_{3.99}$	$19.5^{0.1}_{4.1}$	$29.61^{16.39}_{11.35}$	2378^{2671}_{1217}	$4.91^{2.18}_{1.17}$	2.5 ± 0.6
G233-4-2	7.18 ± 2.02	1.11 ± 0.39	1.71 ± 0.81	0.14 ± 0.07	6.49 ± 2.94	$16.82^{18.41}_{7.8}$	$7.5^{0.6}_{2.0}$	$11.44^{10.68}_{5.97}$	919^{1496}_{573}	$2.65^{1.21}_{0.55}$	2.9 ± 0.7
G233-5-1	10.5 ± 2.8	1.64 ± 0.63	2.5 ± 1.16	0.21 ± 0.11	6.42 ± 3.01	$16.54^{18.0}_{7.83}$	$11.4^{0.8}_{3.1}$	$17.37^{15.93}_{8.91}$	1395^{2283}_{866}	$3.95^{1.72}_{0.77}$	2.9 ± 0.7
G233-5-2	41.59 ± 8.17	5.73 ± 1.46	23.4 ± 10.03	1.71 ± 0.78	7.26 ± 2.34	$20.46^{20.49}_{8.78}$	$68.3^{4.7}_{17.3}$	$46.08^{38.23}_{23.29}$	2468^{3622}_{1515}	$8.64^{3.81}_{1.86}$	3.1 ± 0.5
G233-5-3	43.02 ± 8.4	6.5 ± 1.63	24.2 ± 10.36	1.94 ± 0.88	6.62 ± 2.1	$17.35^{13.95}_{6.33}$	$99.6^{1.3}_{23.3}$	$67.16^{42.87}_{31.08}$	3596^{4379}_{2093}	$10.68^{4.47}_{2.47}$	3.0 ± 0.5
G233-6-1	2.38 ± 1.59	1.01 ± 0.39	0.57 ± 0.44	0.13 ± 0.07	-	-	-	-	-	-	1.4 ± 1.2
G233-7-1	9.19 ± 2.59	1.5 ± 0.58	2.19 ± 1.04	0.19 ± 0.1	6.14 ± 2.95	$15.5^{16.46}_{6.79}$	$11.6^{0.5}_{3.3}$	$17.65^{14.5}_{9.16}$	1417^{2124}_{876}	$3.76^{1.56}_{0.78}$	2.9 ± 0.8
G233-7-2	47.59 ± 9.26	6.21 ± 1.59	11.34 ± 4.85	0.78 ± 0.36	7.67 ± 2.47	$22.98^{23.43}_{10.77}$	$26.5^{3.7}_{5.9}$	$40.23^{41.0}_{19.88}$	3231^{5649}_{2012}	$12.71^{6.08}_{2.5}$	3.2 ± 0.5
G233-8-1	6.2 ± 1.6	2.07 ± 0.61	3.49 ± 1.6	0.62 ± 0.3	3.0 ± 1.18	$8.14^{2.15}_{1.78}$	$134.1^{31.6}_{38.7}$	$90.42^{29.33}_{20.75}$	4842^{3941}_{1917}	$6.75^{2.84}_{1.55}$	1.7 ± 0.6
G233-8-2	12.87 ± 2.82	2.09 ± 0.65	3.07 ± 1.35	0.26 ± 0.13	6.16 ± 2.35	$15.6^{12.75}_{6.07}$	$16.1^{0.1}_{4.0}$	$24.37^{16.82}_{11.24}$	1957^{2582}_{1125}	$5.22^{2.23}_{1.16}$	2.9 ± 0.6
G233-9-1	19.08 ± 4.11	2.56 ± 0.66	10.73 ± 4.7	0.76 ± 0.35	7.45 ± 2.5	$21.54^{22.15}_{10.07}$	$28.4^{3.4}_{6.6}$	$19.12^{19.35}_{9.66}$	1024^{1785}_{646}	$3.78^{1.88}_{0.79}$	3.2 ± 0.5
G233-10-1	9.31 ± 2.67	1.6 ± 0.61	2.22 ± 1.06	0.2 ± 0.11	5.82 ± 2.78	$14.44^{14.62}_{6.07}$	$14.0^{0.1}_{3.8}$	$21.24^{15.45}_{10.88}$	1706^{2319}_{1059}	$4.22^{1.7}_{0.95}$	2.8 ± 0.8
G233-10-2	5.03 ± 2.15	1.23 ± 0.55	1.2 ± 0.69	0.15 ± 0.09	-	-	-	-	-	-	2.2 ± 1.0
G233-10-3	3.46 ± 2.04	0.53 ± 0.45	0.82 ± 0.58	0.07 ± 0.06	-	-	-	-	-	-	2.9 ± 1.6

Continued on next page

Table 4 – *Continued from previous page*

Core ID	S_{450} $10^{-4} \times (Jy/arcsec^2)$	S_{850} $10^{-4} \times (Jy/arcsec^2)$	L_{450} $10^{-12} \times (L_{SUN})$	L_{850} $10^{-12} \times (L_{SUN})$	F_{450}/F_{850}	T (K)	M ($M_{\odot}$)	N_{H_2} $10^{20} \times (cm^{-2})$	n_{H_2} (cm^{-3})	P $10^{-13} \times (Pa)$	α
G233-10-4	106.83 ± 19.96	14.45 ± 3.4	168.4 ± 71.42	12.06 ± 5.4	7.39 ± 2.22	$21.23^{20.58}_{8.92}$	$457.4^{28.8}_{116.1}$	$111.06^{89.2}_{55.18}$	3568^{5066}_{2251}	$12.97^{5.74}_{2.82}$	3.1 ± 0.5
G233-11-1	5.6 ± 1.83	1.59 ± 0.49	1.33 ± 0.67	0.2 ± 0.1	3.51 ± 1.58	$9.03^{3.33}_{2.38}$	$34.5^{3.5}_{7.5}$	$52.4^{23.64}_{16.27}$	4209^{4131}_{1910}	$6.5^{3.04}_{1.64}$	2.0 ± 0.7
G233-11-2	9.5 ± 2.36	1.75 ± 0.52	2.26 ± 1.03	0.22 ± 0.11	5.44 ± 2.11	$13.3^{8.7}_{4.6}$	$17.6^{0.0}_{3.6}$	$26.74^{15.56}_{11.17}$	2148^{2468}_{1168}	$4.89^{2.11}_{1.17}$	2.7 ± 0.6
G233-11-3	3.94 ± 1.65	0.67 ± 0.31	0.94 ± 0.53	0.08 ± 0.05	-	-	-	-	-	-	2.8 ± 1.0
G233-12-1	17.01 ± 3.42	2.72 ± 0.7	9.57 ± 4.12	0.81 ± 0.37	6.26 ± 2.04	$15.94^{10.58}_{5.55}$	$47.6^{0.3}_{10.7}$	$32.13^{19.54}_{13.59}$	1720^{2059}_{929}	$4.69^{2.02}_{1.07}$	2.9 ± 0.5
G233-12-2	7.77 ± 2.01	1.54 ± 0.46	1.85 ± 0.85	0.19 ± 0.09	5.05 ± 2.01	$12.27^{7.14}_{4.06}$	$17.9^{0.2}_{3.5}$	$27.23^{14.62}_{10.78}$	2187^{2369}_{1154}	$4.59^{1.96}_{1.12}$	2.5 ± 0.6
G233-12-3	4.32 ± 1.59	1.16 ± 0.39	1.03 ± 0.54	0.15 ± 0.07	3.73 ± 1.85	$9.43^{4.19}_{2.79}$	$22.8^{0.4}_{4.5}$	$34.66^{17.18}_{12.43}$	2784^{2902}_{1378}	$4.49^{2.08}_{1.17}$	2.1 ± 0.8
G233-12-4	-	0.85 ± 0.33	-	0.11 ± 0.06	-	-	-	-	-	-	-
G233-13-1	23.76 ± 4.64	4.16 ± 1.04	23.48 ± 10.05	2.18 ± 0.99	5.71 ± 1.82	$14.1^{8.01}_{4.39}$	$157.2^{4.2}_{35.1}$	$59.63^{29.19}_{23.08}$	2395^{2408}_{1275}	$5.78^{2.36}_{1.4}$	2.7 ± 0.5
G233-13-2	14.2 ± 3.05	3.27 ± 0.86	7.99 ± 3.49	0.97 ± 0.45	4.34 ± 1.47	$10.64^{3.8}_{2.69}$	$118.5^{18.4}_{29.6}$	$79.91^{30.57}_{22.55}$	4279^{3758}_{1902}	$7.79^{3.2}_{1.81}$	2.3 ± 0.5
G234-1-1	-	5.0 ± 1.44	-	0.11 ± 0.05	-	-	-	-	-	-	-
G234-2-1	-	5.14 ± 1.68	-	0.12 ± 0.05	-	-	-	-	-	-	-

.3 HII Region Data Tables

Table 5: A complete property list for all HII regions targeted in the SCUBA-2 observations. In order of appearance the HII region name, central coordinates, distance, integrated flux in either 1.46 GHz or 4.89 GHz band, electron number density and total gas mass are presented.

HII Region	RA (J200)	DEC (J200)	d (kpc)	R (pc)	F_ν (Jy, @GHz)	n_e (cm^{-3})	Mass ($M_\odot$)
BFS6	21:36:27.561	+52:28:09.50	8.85 ± 0.83 (1)	12.01±1.13	1200 @1.46 (3)	11.70±1.4	2463±295
BFS31	3:24:51.315	+54:57:01.97	3.26 ± 0.91 (1)	0.76±0.21	29 @4.89 (3)	44.85±15.4	2.38±0.8
BFS53	6:44:36.935	+1:07:47.73	4.54 ± 1.24 (1)	2.20±0.60	55 @4.89 (3)	17.41±5.8	22.5±7.6
BFS54	6:46:52.611	+1:18:52.03	8.70 ± 2.80 (1)	2.53±0.81	19 @1.46 (3)	14.97±5.9	29.5±11.7
BFS58	7:00:53.104	-3:50:57.81	5.78 ± 1.23 (1)	3.36±0.72	36 @1.46 (3)	8.94±2.3	41.3±10.9
BFS64	7:00:35.739	-8:51:46.79	3.88 ± 0.88 (1)	2.45±0.55	99 @1.46 (3)	16.04±4.5	28.5±8.0
S99	20:00:37.580	+33:30:29.70	8.0 ± 2.5 (1)	20.94±6.54	3300 @1.46 (3)	7.62±2.9	8500±3266
S100	20:01:50.417	+33:32:44.33	8.9 ± 2.9 (1)	6.90±2.25	3900 @1.46 (3)	48.7±19.5	1946±636
S104	20:17:41.643	+36:45:43.04	4.4 ± 1.4 (1)	5.12±1.63	4570 @1.46 (3)	40.81±16.0	665±260
S120	21:03:45.092	+49:51:57.46	8.59 ± 0.77 (1)	2.50±0.22	121 @4.89 (3)	40.39±4.6	76.5±8.8
S121	21:05:15.442	+49:39:50.02	6.82 ± 0.32 (2)	2.25±0.11	333 @4.89 (3)	62.32±3.9	86.0±5.8
S127	21:28:42.546	+54:37:01.26	9.97 ± 1.99 (2)	2.90±0.58	563 @4.89 (3)	80.9±19.9	240±59
S128	21:32:10.386	+55:52:39.69	8.06 ± 1.61 (2)	1.29±0.26	621 @4.89 (6)	231.6±57.0	60.3±14.9
S138	22:32:46.189	+58:28:16.61	3.04 ± 0.61 (2)	0.35±0.07	554 @4.89 (3)	574.2±141.9	3.09±0.77
S152	22:58:41.229	+58:47:06.70	2.9 ± 0.58 (2)	0.56±0.11	1300 @1.46 (3)	394.0±97.0	8.51±2.1
S168	23:53:01.543	+60:29:11.18	2.14 ± 0.30 (2)	2.28±0.32	1690 @1.46 (3)	40.54±7.0	58.5±10.3
S175	0:27:16.500	+64:42:11.43	2.67 ± 0.53 (2)	0.98±0.20	123 @4.89 (3)	51.23±12.5	5.92±1.5
S186	1:08:51.183	+63:07:30.97	2.76 ± 0.15 (2)	0.43±0.02	165 @4.89 (3)	213.6±15.3	2.04±0.15
S192	2:47:23.476	+61:54:51.95	3.49 ± 0.70 (2)	1.22±0.24	16 @4.89 (3)	17.53±4.3	3.85±0.95
S193	2:47:44.131	+61:58:34.84	2.44 ± 0.49 (2)	1.28±0.26	24 @4.89 (3)	13.97±3.5	3.54±0.89
S194	2:47:20.247	+61:57:48.11	4.68 ± 0.93 (1)	1.18±0.23	65 @4.89 (3)	49.71±12.2	9.91±2.4
S196	2:51:20.845	+62:12:10.39	5.52 ± 1.10 (2)	6.96±1.39	323 @1.46 (3)	8.59±2.1	351±86.6
S201	3:03:14.602	+60:27:34.43	3.90 ± 0.89 (2)	1.89±0.43	1140 @1.46 (3)	80.49±22.6	66.1±18.6
S208	4:19:32.871	+52:58:32.78	4.44 ± 0.55 (2)	1.03±0.13	49 @4.89 (3)	49.96±7.7	6.69±1.0
S209	4:11:08.212	+51:09:25.50	10.58 ± 0.57 (2)	10.26±0.55	11400 @1.46 (3)	54.64±3.9	7163±532
S231	5:39:21.85 (4)	+35:54:37.43 (4)	2.12 ± 0.42 (2)	3.70±0.73 (4)	-	-	-
S232	5:42:28.41 (4)	+36:11:23.91 (4)	2.09 ± 0.42 (2)	6.08±1.22 (4)	-	-	-
S233	5:38:32.998	+35:51:08.84	2.30 ± 0.70 (1)	0.94±0.29	63 @4.89 (3)	34.0±12.7	3.39±1.3
S234	5:28:06.000 (4)	+34:25:00.00 (4)	2.19 ± 0.10 (2)	3.82±0.17 (4)	-	-	-
S235	5:41:3.76 (4)	+35:50:30.03 (4)	1.36 ± 0.27 (2)	1.98±0.39 (4)	-	-	-
S237	5:31:27.116	+34:14:31.63	3.76 ± 0.28 (2)	1.82±0.14	751 @1.46 (3)	66.54±6.3	48.9±4.8
S242	5:51:53.526	+27:01:42.27	2.19 ± 0.44 (2)	2.55±0.51	763 @1.46 (3)	23.63±5.9	47.5±11.8
S247	6:08:34.523	+21:37:29.08	2.23 ± 0.18 (2)	2.27±0.18	468 @1.46 (3)	22.41±2.3	31.9±3.3
S254	6:12:23.278	+18:00:31.95	2.43 ± 0.49 (2)	2.83±0.57	1140 @1.46 (3)	27.43±6.8	75.3±18.8

Continued on next page

Table 5 – *Continued from previous page*

HII Region	RA (J200)	DEC (J200)	d (kpc)	R (pc)	F_v (Jy, @GHz)	n_e (cm^{-3})	Mass ($M_\odot$)
S255	6:13:05.299	+17:58:39.20	2.27 ± 0.45 (2)	1.32±0.26	1820 @1.46 (3)	101.4±24.8	28.4±7.0
S255B	6:14:24.100 (5)	+17:45:13.00 (5)	2.5 ± 0.20 (5)	0.97±0.08 (5)	-	-	-
S256	6:12:37.931	+17:56:51.05	2.59 ± 0.52 (2)	1.00±0.20	158 @1.46 (3)	51.39±12.7	6.33±1.6
S257	6:12:44.282	+17:59:10.64	2.16 ± 0.43 (2)	1.26±0.25	706 @1.46 (3)	64.8±15.9	15.6±3.8
S258	6:13:29.058	+17:55:37.39	3.03 ± 0.61 (2)	0.73±0.15	18 @4.89 (3)	34.48±8.6	1.66±0.4
S259	6:11:28.891	+17:26:24.18	8.71 ± 1.74 (2)	2.87±0.57	136 @4.89 (3)	35.24±8.7	101±25
S266	6:18:45.558	+15:16:56.33	12.55 ± 3.16 (1)	2.92±0.74	90 @4.89 (3)	40.27±12.5	122±38
S269	6:14:39.033	+13:49:32.19	4.27 ± 0.85 (2)	1.86±0.37	729 @1.46 (3)	72.05±17.7	56.6±13.9
S271	6:14:53.543	+12:21:21.07	3.90 ± 0.47 (2)	1.21±0.15	297 @4.89 (3)	85.24±12.8	18.3±2.8
S283	6:38:31.902	+0:41:37.90	9.1 ± 2.9 (1)	2.65±0.84	67 @4.89 (3)	29.20±11.4	65.8±25.8
S285	6:55:17.048	-0:31:41.94	6.9 ± 0.7 (1)	2.14±0.22	29 @4.89 (3)	20.03±2.5	23.9±3.1
S286	6:54:25.942	-4:31:30.47	5.79 ± 1.24 (1)	6.46±1.38	278 @1.46 (3)	9.35±2.5	306±81
S288	7:08:39.239	-4:19:06.50	3.0 ± 1.2 (1)	0.47±0.19	677 @1.46 (3)	390.7±192	4.78±2.4
S294	7:16:33.274	-9:25:23.58	4.6 ± 1.5 (1)	4.01±1.31	484 @1.46 (3)	20.00±8.0	157±63
S297	7:05:19.215	-12:19:36.84	1.15 ± 0.14 (1)	0.89±0.11	814 @1.46 (3)	61.89±9.4	5.33±0.8
S299	7:30:38.970	-15:18:01.49	1.15 ± 0.14 (1)	0.40±0.05	29 @4.89 (3)	41.11±6.2	0.32±0.05
S300	7:31:07.545	-15:25:13.42	4.4 ± 0.6 (1)	4.27±0.58	121 @1.46 (3)	8.73±1.5	82.3±14
S305	7:30:05.651	-18:32:59.37	5.2 ± 1.4 (1)	4.03±1.09	1490 @1.46 (3)	39.38±13.0	314±104
S307	7:35:34.532	-18:45:51.45	2.2 ± 0.5 (1)	0.96±0.22	661 @1.46 (3)	95.58±26.7	10.3±2.9

(1) IRAS [12]
(2) CGPS [54]
(3) VLA (1993) [16]
(4) POSS [32]
(5) WISE [50]
(6) VLA (1986) [15]

Table 6: Table of properties for the associated stars of the HII regions targeted for SCUBA-2 observations after a scaled distance cutoff of 7 is enforced. In order of appearance HII regions along with each of their associated stars are presented with each star having its SIMBAD name, coordinates, spectral type, luminosity and total mass presented individually.

HII Region	Star Name (SIMBAD)	RA (J2000)	DEC (J2000)	Spectral Type	L (L_{SUN})	M ($M_{\odot}$)	Φ_N (s^{-1})	Reference
BFS6	BD+51 3094	21 34 48.129	+52 19 25.25	B8V	211	3.8	-	(Reed;2003)
	HD 206259	21 39 17.525	+52 21 44.91	B3III	13500	16.8	1.995e+44	(Reed;2003)
BFS31	-	03 24 51.2	+54 57 05.0	B2V	9360	10.9	4.467e+44	(Russeil;2007)
BFS53	-	06 44 36.4	+01 07 54.6	B2V	9360	10.9	4.467e+44	(Russeil;2007)
BFS54	HD 289120	06 46 51.635	+01 18 56.94	B2V	9360	10.9	4.467e+44	(Reed;2003)
BFS58	-	-	-	-	-	-	-	-
BFS64	LS VI -08 2	07 00 30.711	-08 52 18.45	O9V	57600	20.0	2.951e+48	(Reed;2003)
	BD-08 1666	07 00 35.05	-08 51 38.7	B1V	19400	14.2	1.950e+45	(Reed;2003)
	LS 121	07 00 36.338	-08 51 37.74	O9V	57600	20.0	2.951e+48	(Reed;2003)
S99	LS II +33 13	20 00 17.102	+33 20 50.18	O9V	57600	20.0	2.951e+48	(Reed;2003)
	[CGG78] S099 Anon	20 00 54.2	+33 29 23	O5V	398000	60.0	3.090e+49	(Reed;2003)
	LS II +33 15	20 01 00.609	+33 23 42.85	B0V	36200	17.5	1.047e+48	(Reed;2003)
	LS II +33 16	20 01 02.995	+33 20 07.84	O9V	57600	20.0	2.951e+48	(Reed;2003)
S100	[CGG78] S099 Anon	20 00 54.2	+33 29 23	O5V	398000	60.0	3.090e+49	(Reed;2003)
	LS II +33 15	20 01 00.609	+33 23 42.85	B0V	36200	17.5	1.047e+48	(Reed;2003)
	LS II +33 17	20 01 55.983	+33 20 39.91	B1V	19400	14.2	1.950e+45	(Reed;2003)
	LS II +33 18	20 02 09.611	+33 23 20.43	B0V	36200	17.5	1.047e+48	(Reed;2003)
	LS II +33 20	20 02 34.571	+33 32 53.86	O9V	57600	20.0	2.951e+48	(Reed;2003)
S104	EM* MWC 337	20 17 31.738	+36 52 07.68	O9V	57600	20.0	2.951e+48	(Reed;2003)
	[CGG78] S104 Anon 3	20 17 41.8	+36 45 23	O6V	260000	37.0	1.950e+49	(Reed;2003)
	[CGG78] S104 Anon 1	20 17 46.6	+36 45 05	B0V	36200	17.5	1.047e+48	(Reed;2003)
	[NH52] 63	20 18 00.622	+36 39 03.05	O9V	57600	20.0	2.951e+48	(Reed;2003)
S120	-	-	-	-	-	-	-	-
S121	2MASS J21051145+4939168	21 05 11.46	+49 39 16.8	O4V	504000	90.0	4.786e+49	(Foster;2015)
	2MASS J21051346+4940107	21 05 13.47	+49 40 10.8	B0II	190000	33.8	2.922e+48	(Foster;2015)
	ALS 19699	21 05 14.5	+49 39 47	B2II	93600	25.5	8.457e+45	(Foster;2015)
S127	ALS 18695	21 28 40.7	+54 36 28	O8V	99100	23.0	5.623e+48	(Foster;2015)
S128	ALS 19702	21 32 10.3	+55 52 42	O7V	154000	30.0	1.148e+49	(Foster;2015)
S138	-	22 32 45.34	+58 28 21.96	O9.5V	46900	18.75	1.820e+48	(Foster;2015)
S152	[CGG78] S152 Anon	22 58 42.3	+58 46 45	O9V	57600	20.0	2.951e+48	(Foster;2015)
S168	EM* VES 971	23 52 41.099	+60 43 10.86	B1.5III	40850	22.55	4.596e+45	(Foster;2015)
	LS I +60 50	23 52 59.615	+60 28 53.98	O9.5V	46900	18.75	1.820e+48	(Foster;2015)
	LS I +60 52	23 53 08.275	+60 36 27.36	B0.5V	27800	15.85	5.129e+47	(Foster;2015)

Continued on next page

Table 6 – *Continued from previous page*

HII Region	Star Name (SIMBAD)	RA (J2000)	DEC (J2000)	Spectral Type	L (L_{SUN})	M ($M_{\odot}$)	Φ_N (s^{-1})	Reference
	LS I +60 53	23 53 22.811	+60 38 07.36	B1.5V	14380	12.55	1.198e+45	(Foster;2015)
	HD 240435	23 53 24.450	+60 40 49.22	B0.5V	27800	15.85	5.129e+47	(Foster;2015)
	LS I +60 55	23 53 48.457	+60 35 31.05	B1V	19400	14.2	1.950e+45	(Foster;2015)
S175	LS I +64 26	00 27 17.002	+64 42 19.65	B1III	53400	24.5	7.413e+45	(Foster;2015)
S186	-	-	-	-	-	-	-	-
S192	Anon	02 47 24.4	+61 54 48.0	B2.5V	7125	9.25	2.478e+44	(Russeil;2007)
S193	Anon	02 47 42.0	+61 58 28.1	B2.5V	7125	9.25	2.478e+44	(Russeil;2007)
	Anon	02 47 40.0	+61 58 32.7	B1.5V	14380	12.55	1.198e+45	(Russeil;2007)
S194	-	-	-	-	-	-	-	-
S196	Anon	02 51 32.0	+62 13 19.7	O9.5V	46900	18.75	1.820e+48	(Russeil;2007)
S201	-	-	-	-	-	-	-	-
S208	MFJ SH 2-208 3	04 19 32.8	+52 58 39	O9.5V	46900	18.75	1.820e+48	(Foster;2015)
S209	2MASS J04110586+5110016	04 11 05.86	+51 10 01.7	B1III	53400	24.5	7.413e+45	(Foster;2015)
	ALS 18697	04 11 06.8	+51 09 10	O9III	159000	37.3	7.244e+48	(Foster;2015)
S231	LS V +35 24	05 39 45.641	+35 53 56.35	O9V	57600	20.0	2.951e+48	(Foster;2015)
S232	HD 37737	05 42 31.158	+36 12 00.51	O9.5III	134000	32.85	4.677e+48	(Foster;2015)
	HD 37767	05 42 41.477	+36 08 59.44	B3V	4890	7.6	4.898e+43	(Foster;2015)
S233	-	-	-	-	-	-	-	-
S234	BD+34 1054	05 28 07.1536	+34 25 26.870	O9.5V	46900	18.75	1.820e+48	(Foster;2015)
	HD 35619	05 27 36.1446	+34 45 18.999	O7V	154000	30.0	1.148e+49	(Foster;2015)
	BD+34 1056	05 28 08.37	+34 23 45.2	B0V	36200	17.5	1.047e+48	(Foster;2015)
	HD 35633	05 27 43.2842	+34 31 56.674	B0.5IV	56350	21.14	8.305e+47	(Foster;2015)
	HD 281150	05 27 15.9345	+34 25 43.489	B0.5V	27800	15.85	5.129e+47	(Foster;2015)
	ALS8389	05 28 39.4073	+34 40 08.731	O8V	99100	23.0	5.623e+48	(Foster;2015)
	BD+34 1053	05 28 06.1170	+34 27 21.993	B1.5V	14380	12.55	1.198e+45	(Foster;2015)
	LS V +34 21	05 27 33.402	+34 27 01.80	B0IV	75700	22.9	1.751e+48	(Foster;2015)
	LS V +34 18	05 27 29.3188	+34 25 02.595	O8V	99100	23.0	5.623e+48	(Foster;2015)
	LS V +34 15	05 27 23.2948	+34 23 40.577	B0V	36200	17.5	1.047e+48	(Foster;2015)
	LS V +34 12	05 27 16.7820	+34 30 56.830	B2V	9360	10.9	4.467e+44	(Foster;2015)
	HD 281151	05 27 05.6585	+34 19 31.572	B0.5V	27800	15.85	5.129e+47	(Foster;2015)
	LS V +34 30	05 28 08.231	+34 25 14.45	B1V	19400	14.2	1.950e+45	(Foster;2015)
S235	BD+35 1201	05 40 59.441	+35 50 46.48	B0V	36200	17.5	1.047e+48	(Foster;2015)
S237	LS V +34 46	05 31 26.546	+34 14 44.91	B0V	36200	17.5	1.047e+48	(Foster;2015)
	LS V +34 47	05 31 27.074	+34 14 49.54	B0.5V	27800	15.85	5.129e+47	(Foster;2015)
S242	BD+26 980	05 51 55.409	+27 01 57.95	B0V	36200	17.5	1.047e+48	(Foster;2015)
S247	LS V +21 27	06 08 32.100	+21 36 39.26	B0V	36200	17.5	1.047e+48	(Foster;2015)
S254	HD 253247	06 12 22.112	+18 00 57.87	O9.5V	46900	18.75	1.820e+48	(Foster;2015)
S255	LS 19	06 13 04.210	+17 58 41.48	B0V	36200	17.5	1.047e+48	(Foster;2015)
S255B	-	-	-	-	-	-	-	-

Continued on next page

Table 6 – *Continued from previous page*

HII Region	Star Name (SIMBAD)	RA (J2000)	DEC (J2000)	Spectral Type	L (L_{SUN})	M ($M_{\odot}$)	Φ_N (s^{-1})	Reference
S256	2MASS J06123651+1756548	06 12 36.6	+17 56 53.4	B2.5V	7125	9.25	2.478e+44	(Russeil;2007)
S257	HD 253327	06 12 44.174	+17 59 14.22	B0.5V	27800	15.85	5.129e+47	(Foster;2015)
S258	CXOU J061327.6+175517	06 13 27.6	+17 55 20.9	B3V	4890	7.6	4.898e+43	(Russeil;2007)
S259	ALS 18669	06 11 29.9	+17 26 25	B1V	19400	14.2	1.950e+45	(Foster;2015)
S266	EM* MWC 137	06 18 45.519	+15 16 52.25	B0V	36200	17.5	1.047e+48	(Reed;2003)
S269	MFJ SH 2-269 2	06 14 38.3	+13 49 40	B0.5V	27800	15.85	5.129e+47	(Foster;2015)
S271	ALS 18672	06 14 53.0	+12 21 22	O9V	57600	20.0	2.951e+48	(Foster;2015)
S283	ALS 18674	06 38 27.3	+00 44 38.1	B1V	19400	14.2	1.950e+45	(Russeil;2007)
	ALS 18677	06 38 12.4	+00 44 00.9	B3V	4890	7.6	4.898e+43	(Russeil;2007)
	TYC 147-1026-1	06 38 13.6	+00 44 09.9	O7V	154000	30.0	1.148e+49	(Russeil;2007)
S285	2MASS J06551684-0031145	06 55 16.84	-00 31 14.6	B0V	36200	17.5	1.047e+48	(Reed;2003)
	BD-00 1491	06 55 17.369	-00 33 40.92	B0V	36200	17.5	1.047e+48	(Reed;2003)
S286	-	-	-	-	-	-	-	-
S288	GSC 04823-00146	07 08 38.796	-04 19 04.86	B0V	36200	17.5	1.047e+48	(Reed;2003)
S294	MFJ SH 2-294 4	07 16 33.2	-09 25 25.6	B1.5V	14380	12.55	1.198e+45	(Russeil;2007)
S297	HD 53623	07 05 16.748	-12 19 34.49	B1II-III	93700	27.1	2.062e+46	(Reed;2003)
S299	TYC 5979-1136-1	07 30 38.999	-15 17 49.89	B0V	36200	17.5	1.047e+48	(Reed;2003)
	MFJ SH 2-299 3	07 30 41.2	-15 17 46	O9V	57600	20.0	2.951e+48	(Reed;2003)
	2MASS J07304154-1517426	07 30 41.55	-15 17 42.7	O9V	57600	20.0	2.951e+48	(Reed;2003)
S300	UCAC4 373-032535	07 31 08.420	-15 24 51.61	B0V	36200	17.5	1.047e+48	(Reed;2003)
	TYC 5979-2383-1	07 31 11.741	-15 29 24.64	B0.5Ib	206000	37.0	3.981e+47	(Reed;2003)
S305	MFJ SH 2-305 2	07 30 01.8	-18 32 32	O9.5V	46900	18.75	1.820e+48	(Reed;2003)
	MFJ SH 2-305 4	07 30 04.6	-18 33 06	O8.5V	78350	21.5	4.074e+48	(Reed;2003)
	ALS 17536	07 30 06.3	-18 31 52	O9V	57600	20.0	2.951e+48	(Reed;2003)
S307	BD-18 1920	07 35 13.945	-18 47 57.16	O9V	57600	20.0	2.951e+48	(Reed;2003)
	LS 566	07 35 27.699	-18 49 08.68	B3III	13500	16.8	1.995e+44	(Reed;2003)
	ALS 17537	07 35 34.1	-18 45 38	B0V	36200	17.5	1.047e+48	(Reed;2003)

.4 Images

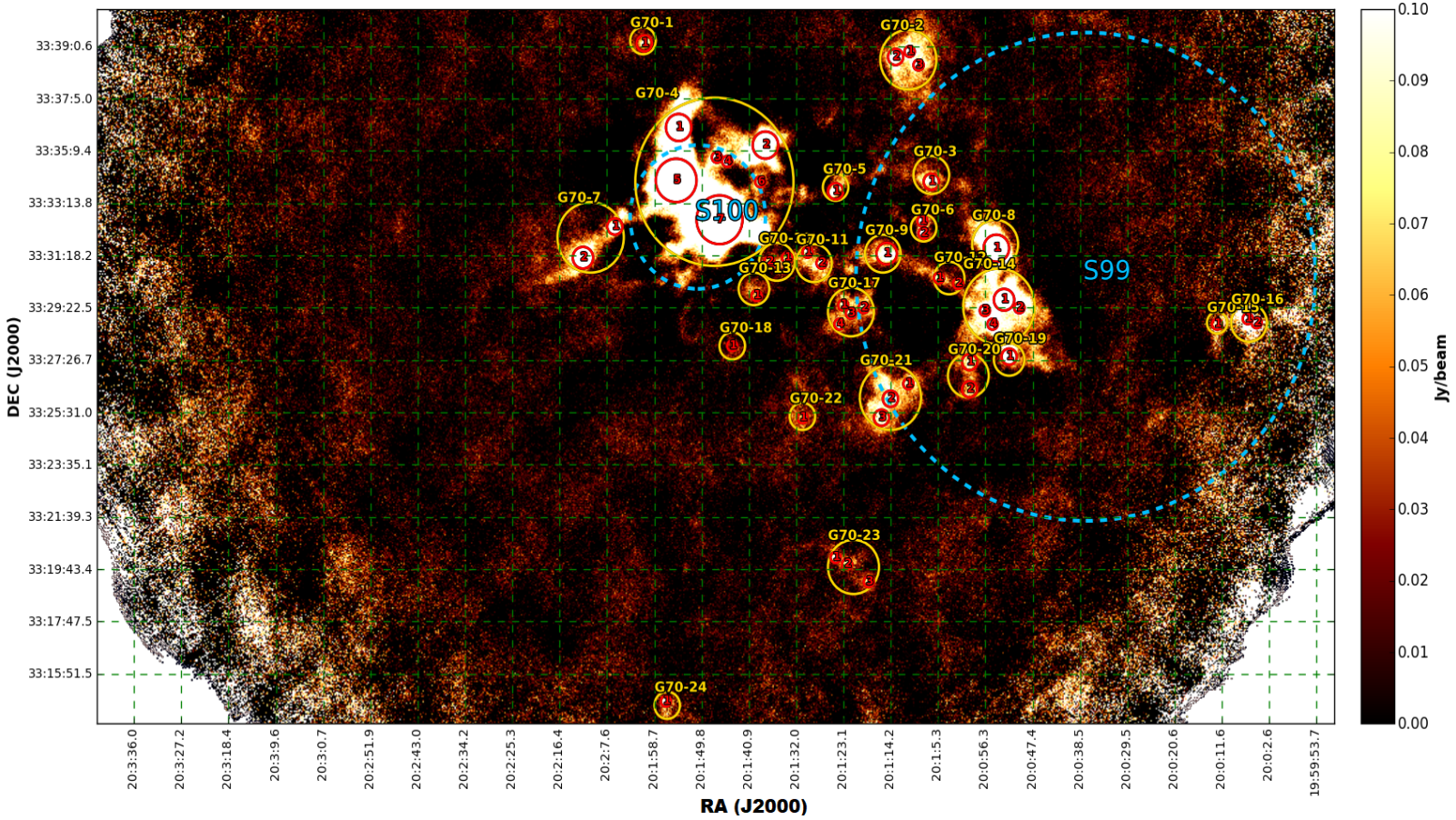

Figure 1: 850μm image of object G70. This object contains HII Regions "S99" and "S100" as well as 24 clump composites which host a grand total of 49 cores.

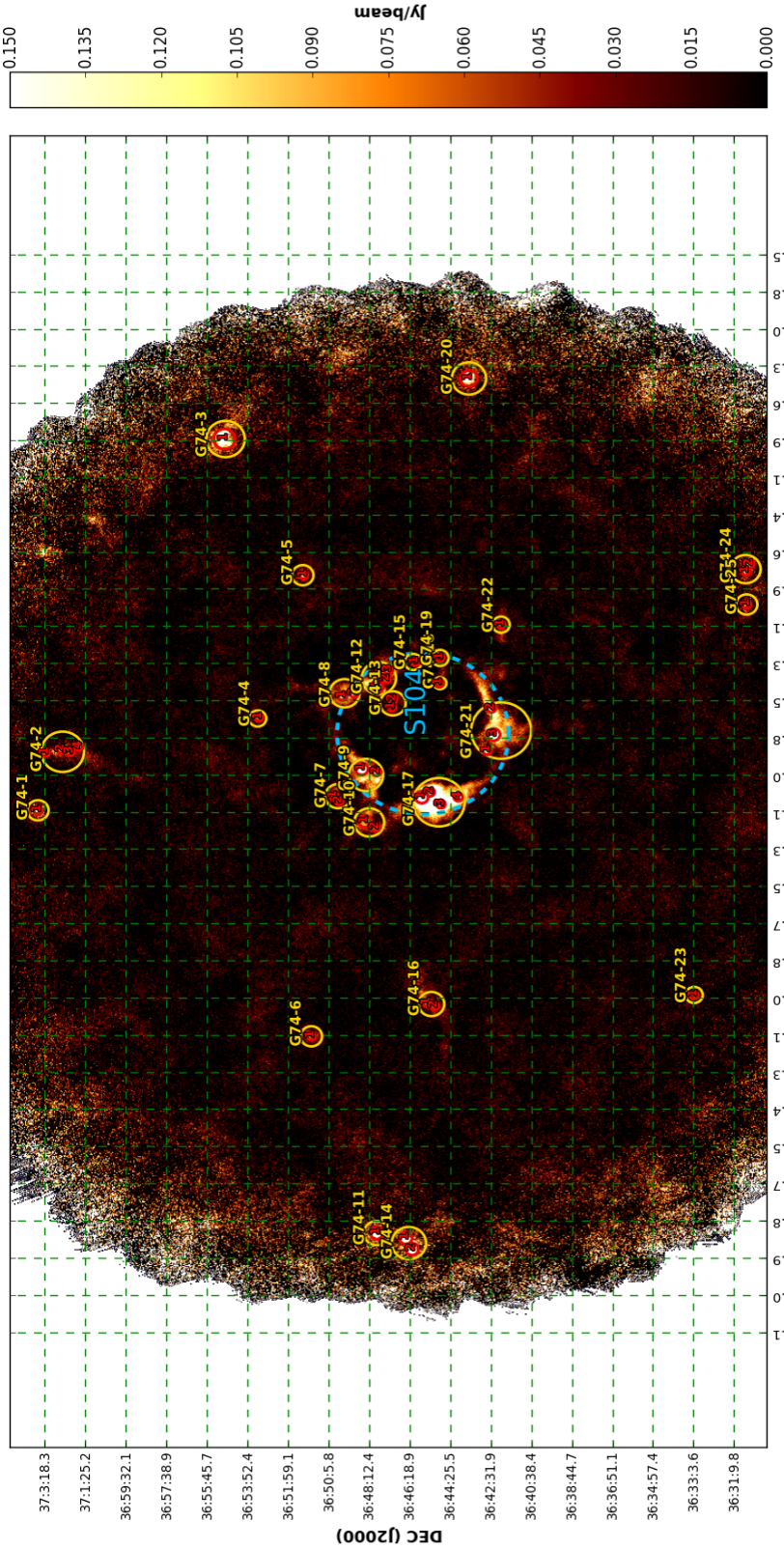

Figure 2: 850μm image of object G74. This object contains HII Region "S104" as well as 25 clump composites which host a grand total of 43 cores.

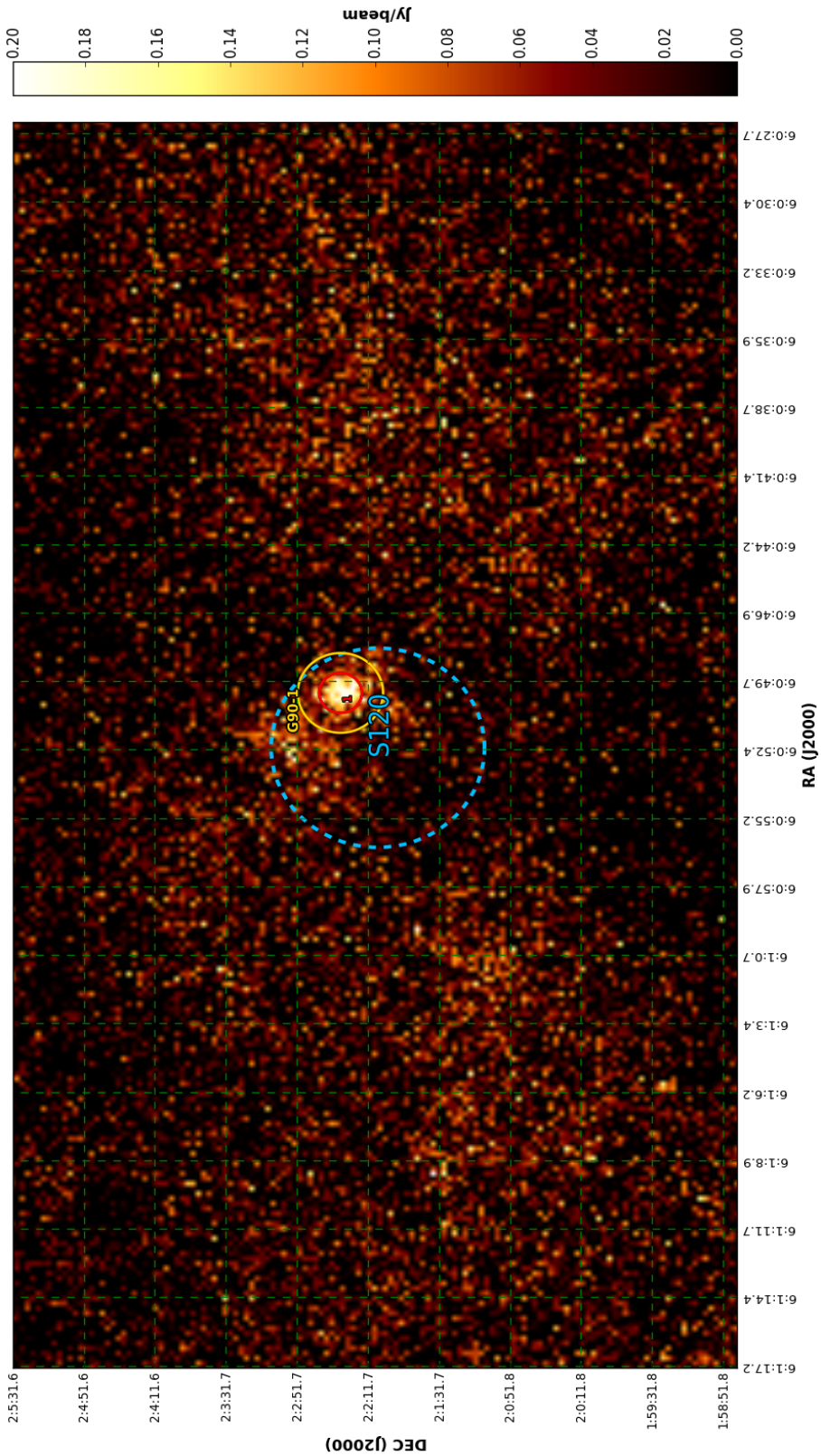

Figure 3: 850μm image of object G90. This object contains HII Region "S120" as well as 1 clump composite which hosts 1 core.

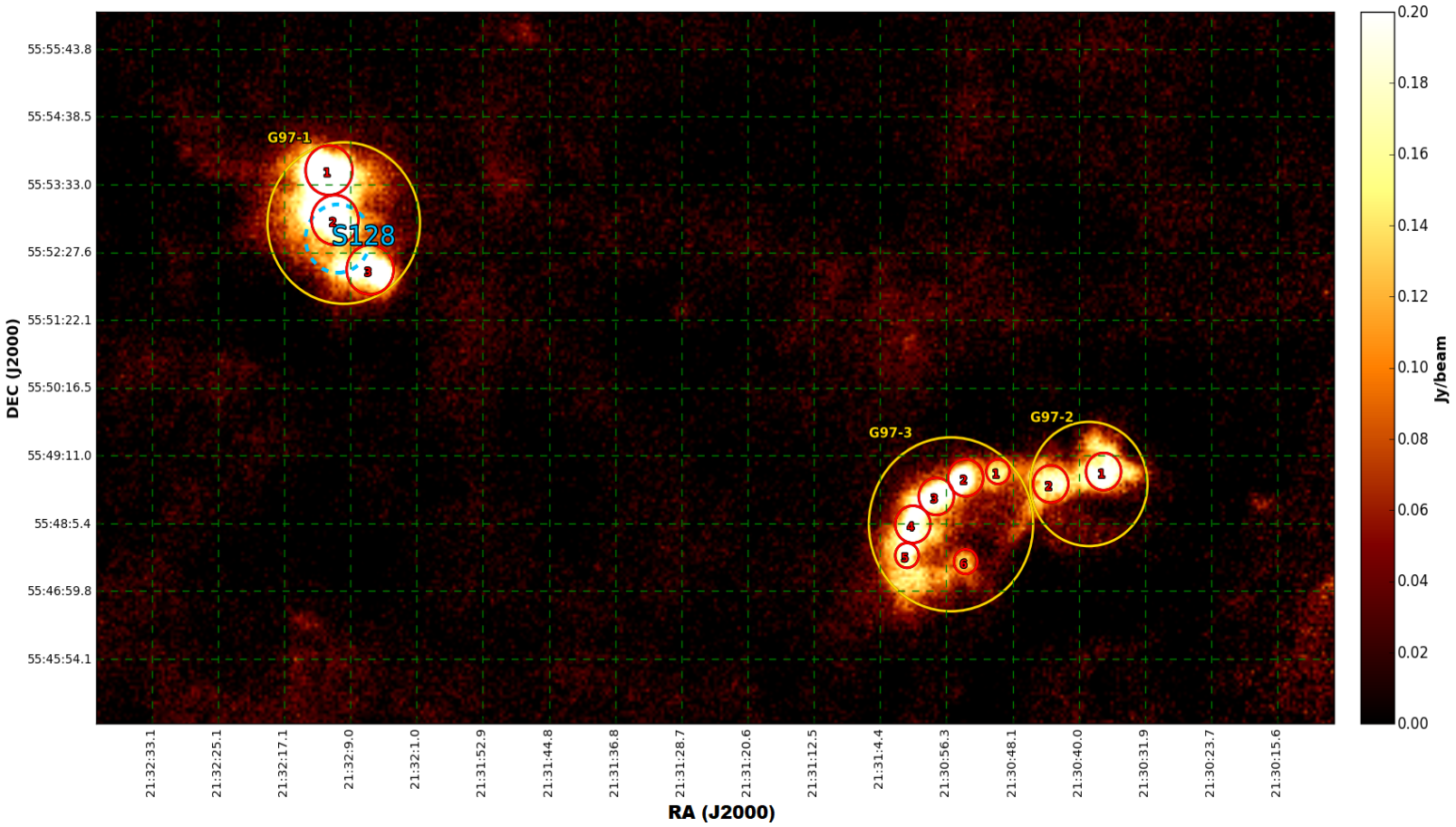

Figure 4: 850μm image of object G97. This object contains HII Region "S128" as well as 3 clump composites which host a total of 11 cores.

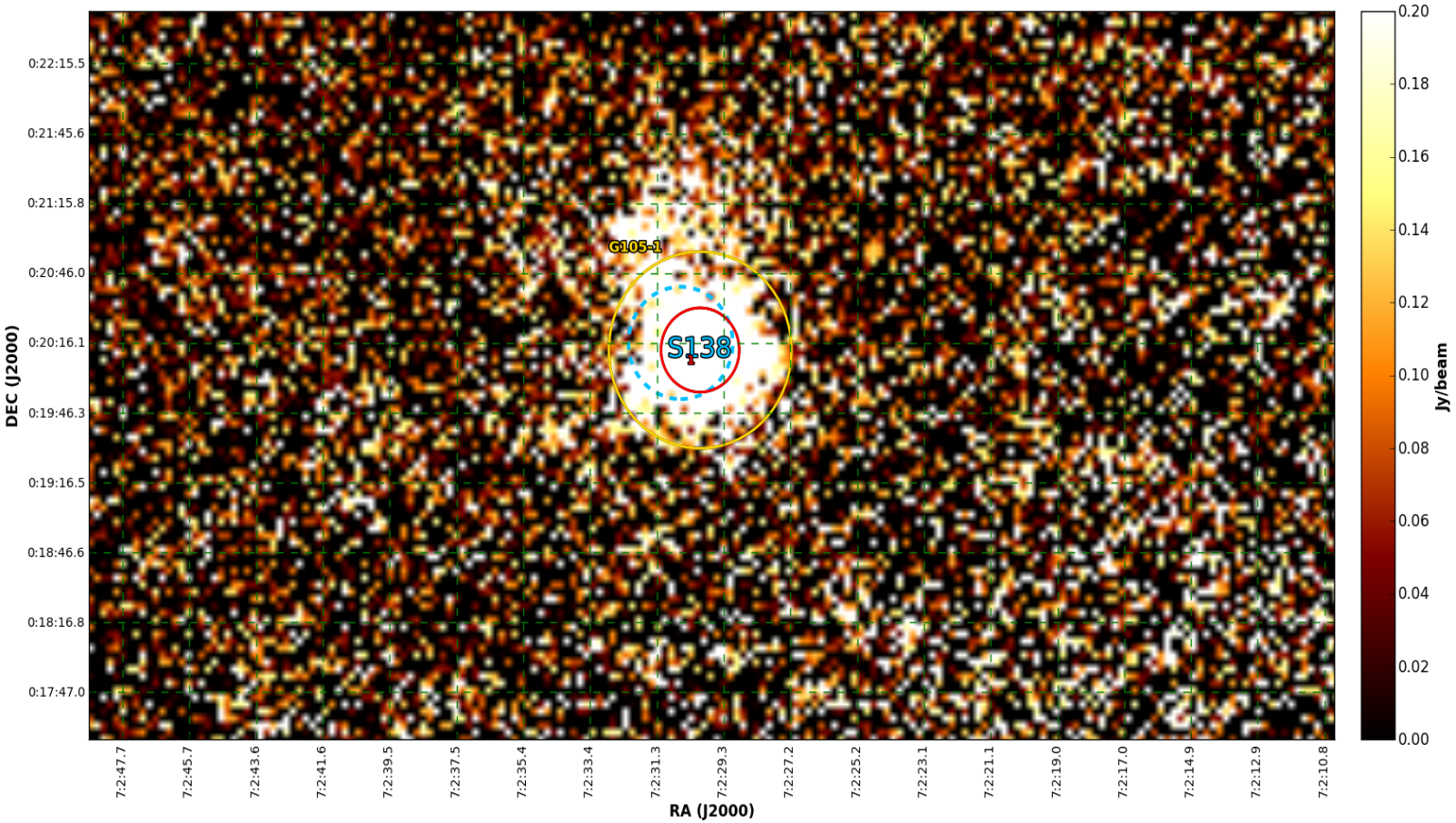

Figure 5: $850\mu m$ image of object G105. This object contains HII Region "S138" as well as 1 clump composite which hosts 1 core.

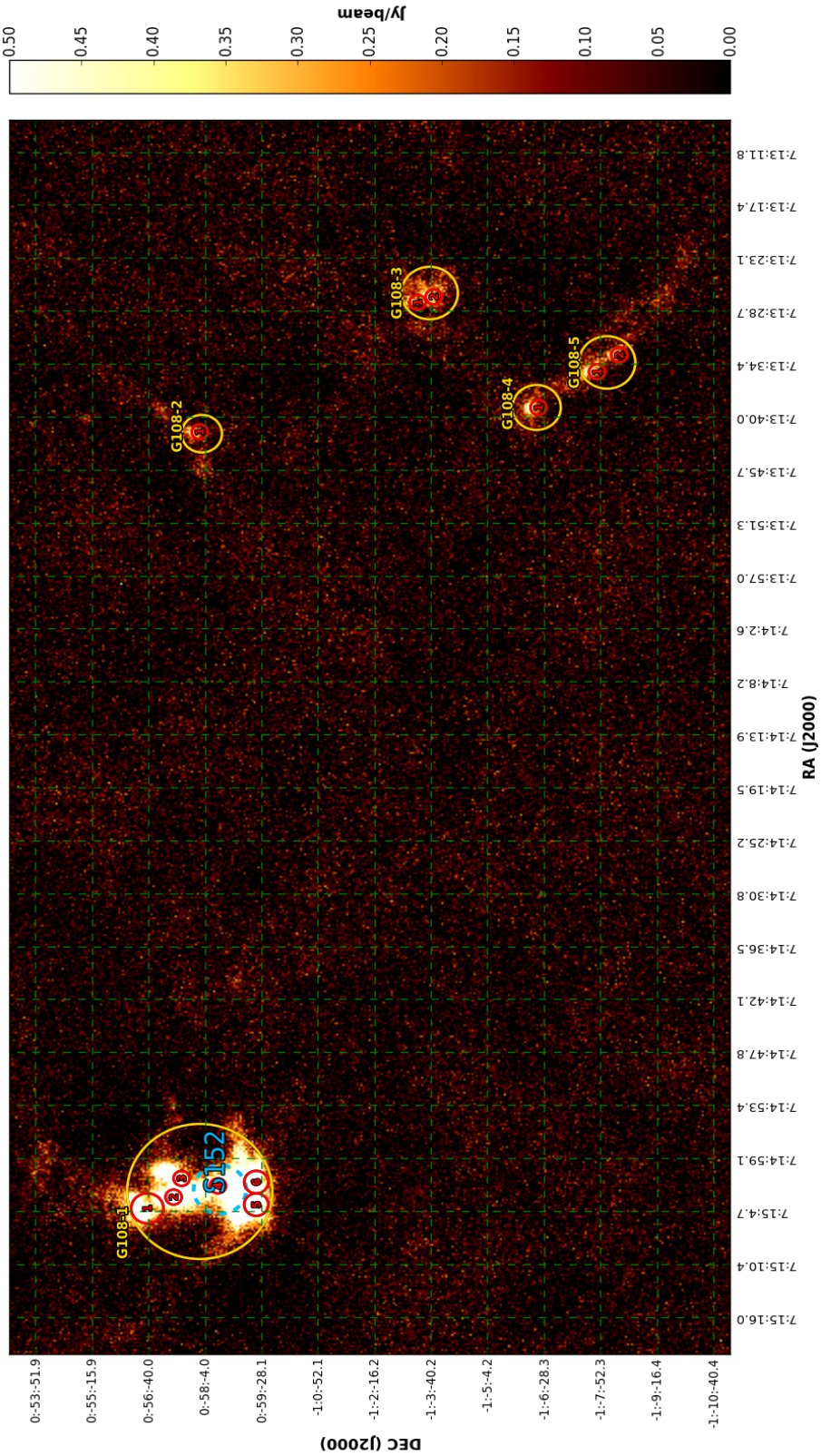

Figure 6: 850μm image of object G108. This object contains HII Region "S152" as well as 5 clump composites which host a total of 12 cores.

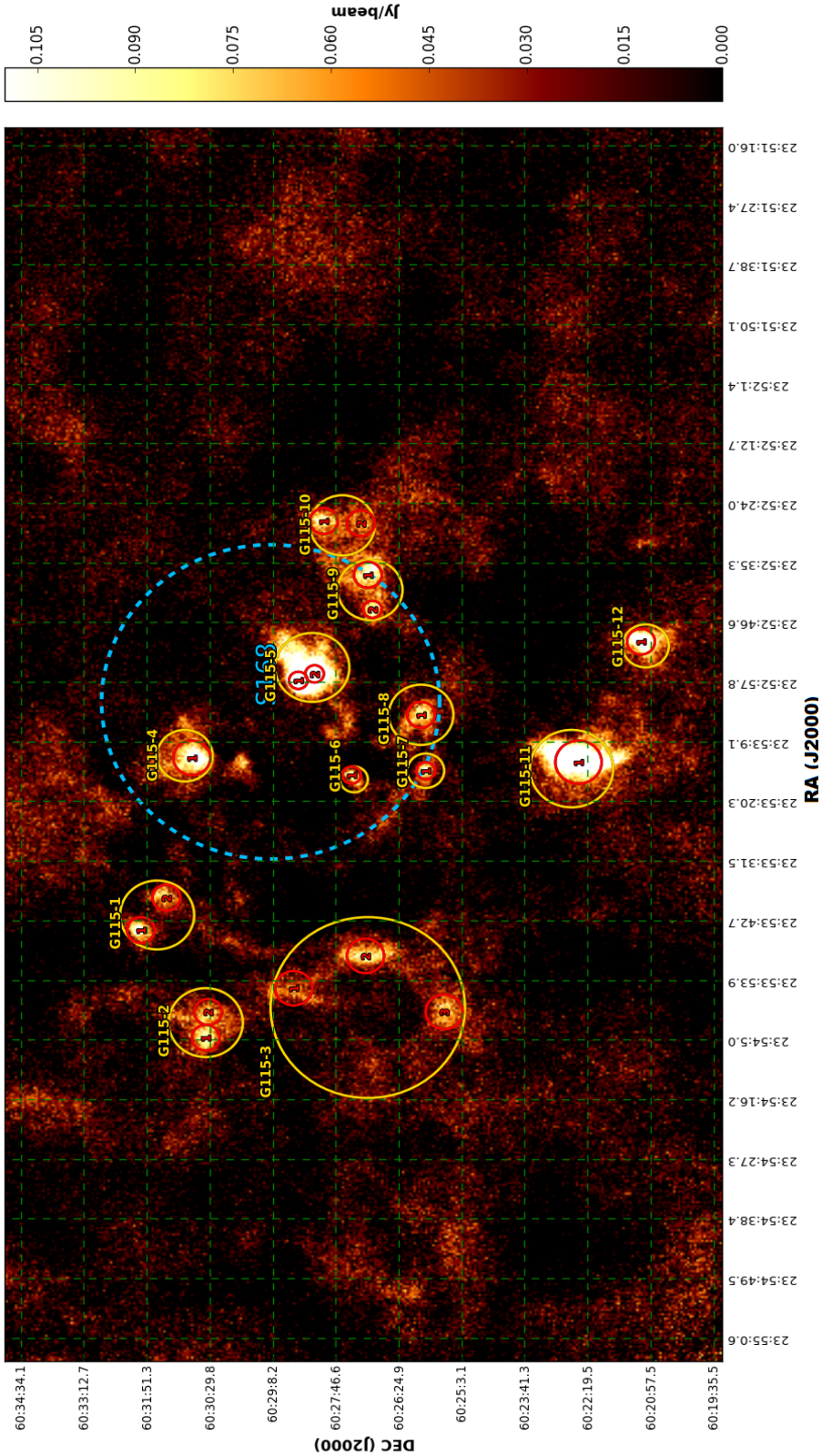

Figure 7: 850μm image of object G115. This object contains HII Region "S168" as well as 12 clump composites which host a total of 19 cores.

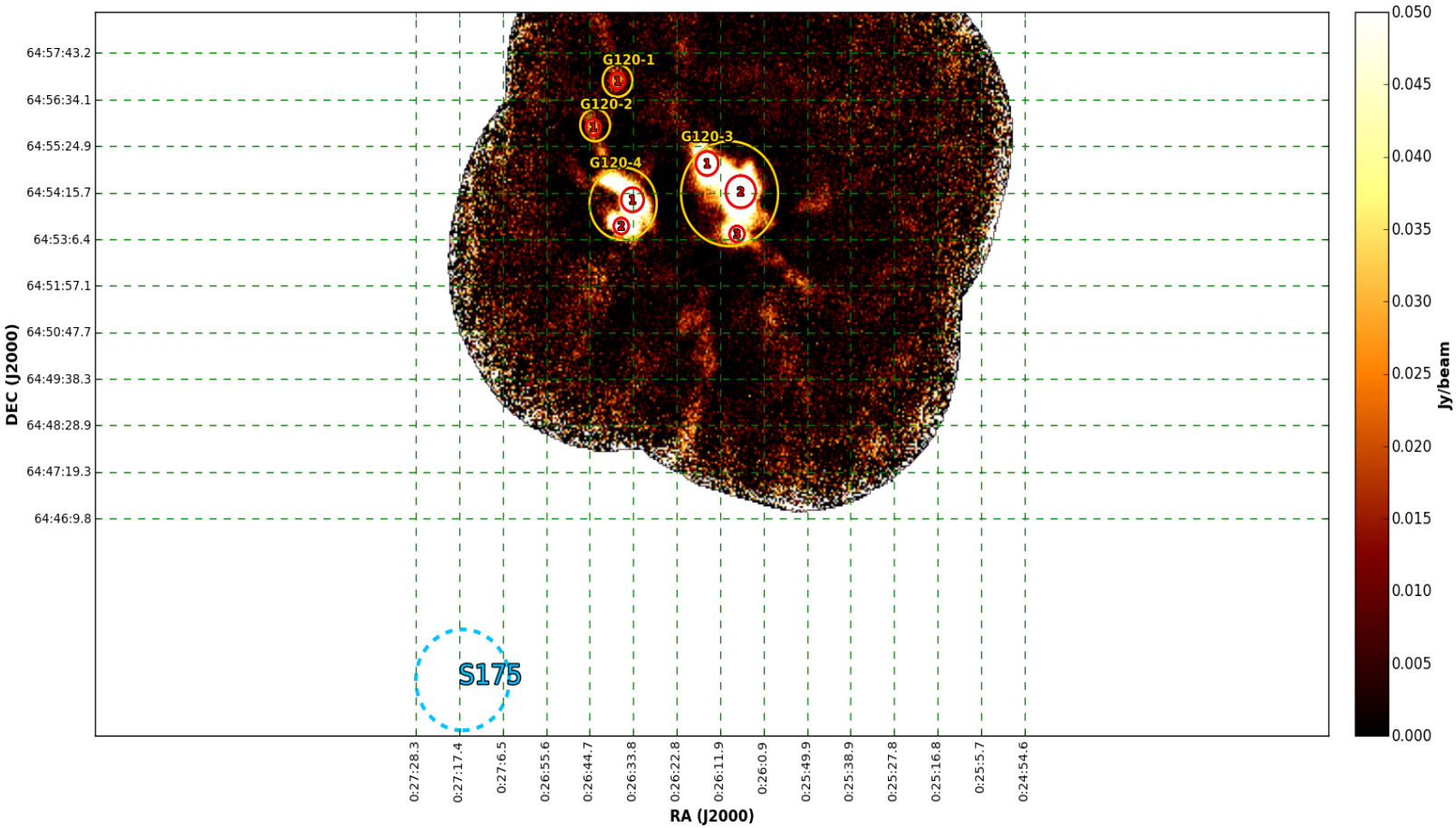

Figure 8: 850μm image of object G120. This object contains HII Region "S175" as well as 4 clump composites which host a total of 7 cores.

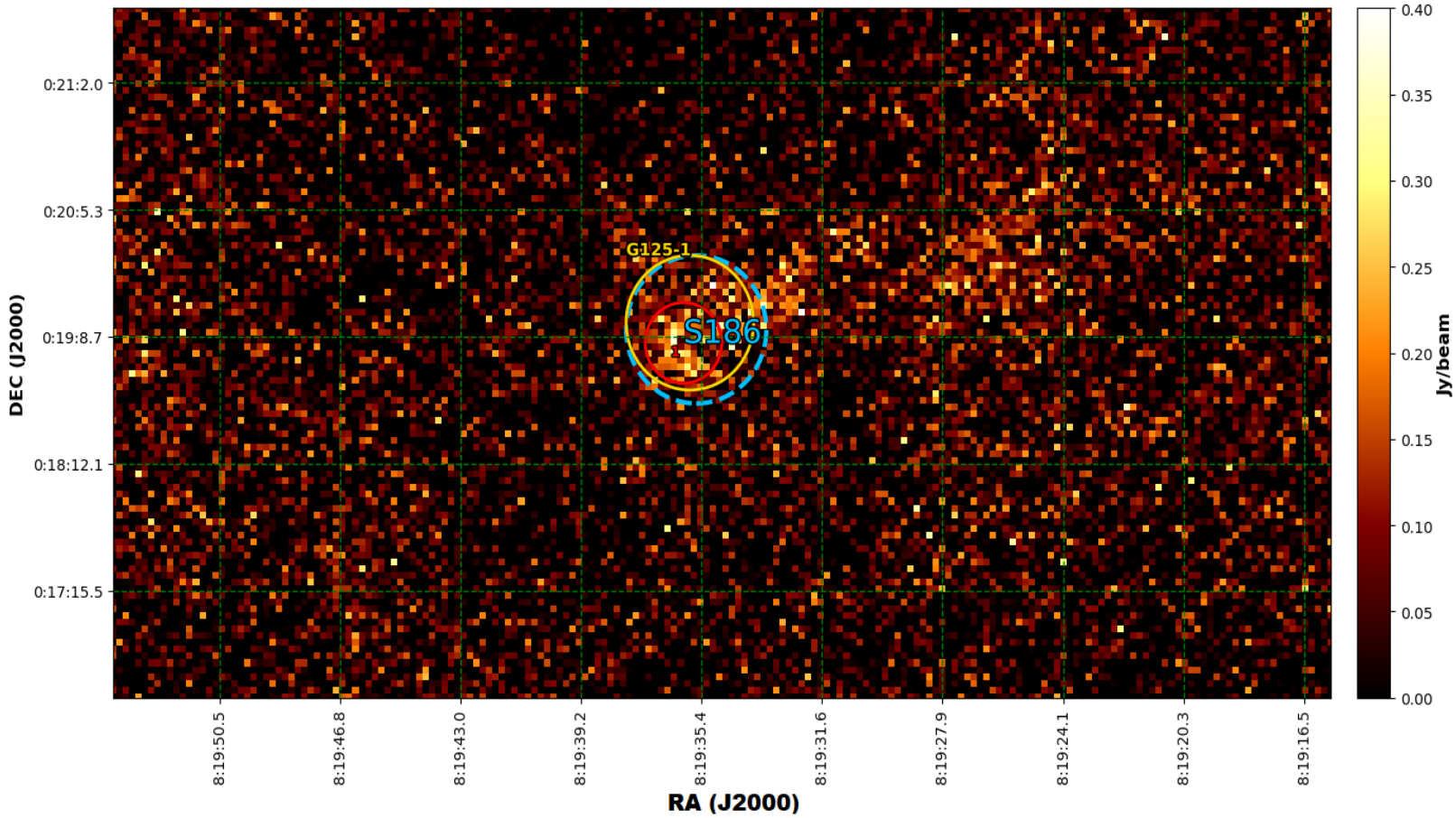

Figure 9: 850μm image of object G125. This object contains HII Region "S186" as well as 1 clump composite which hosts 1 core.

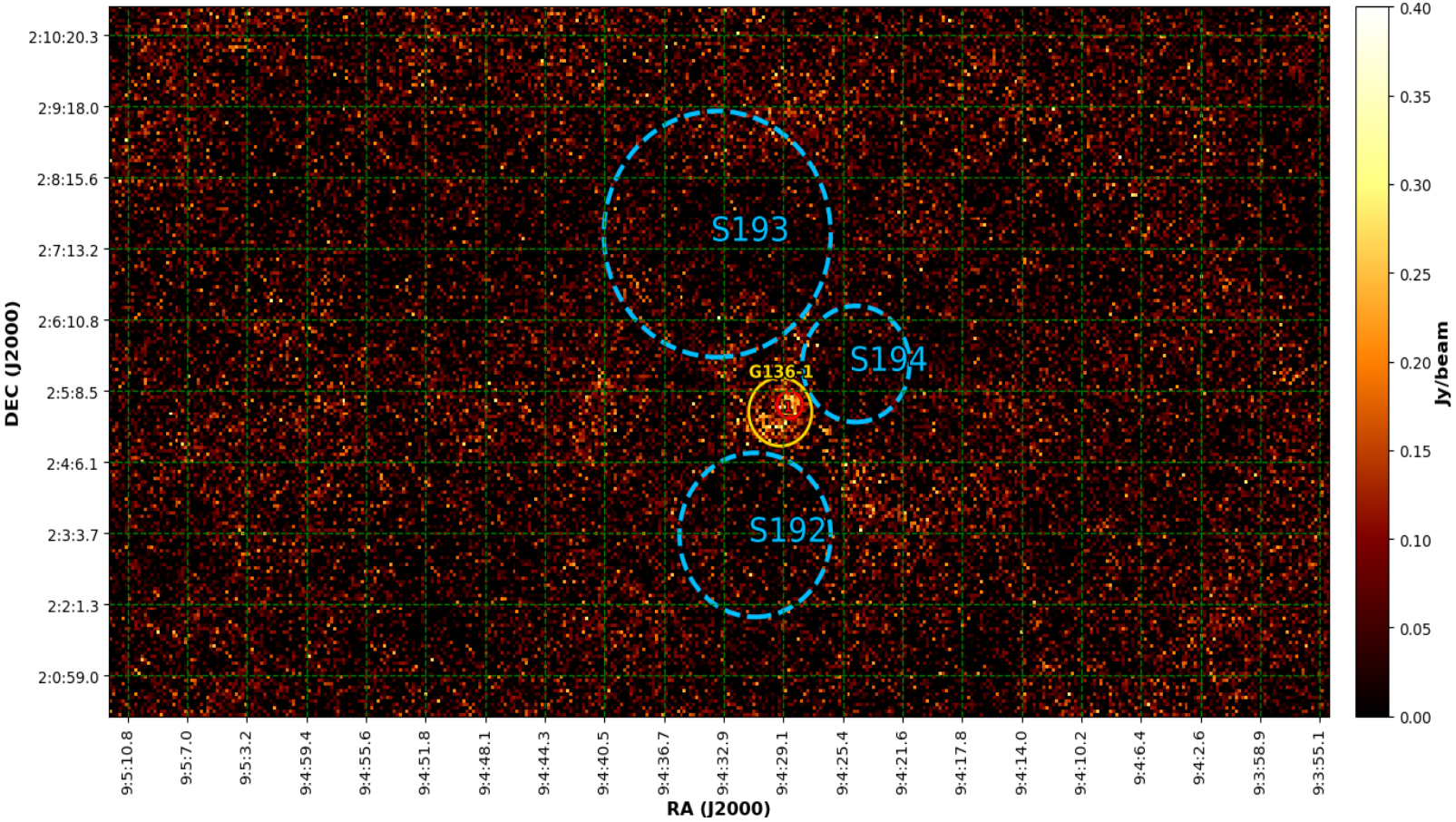

Figure 10: 850μm image of object G136. This object contains HII Regions "S192", "S193", "S194" as well as 1 clump composite which hosts 1 core.

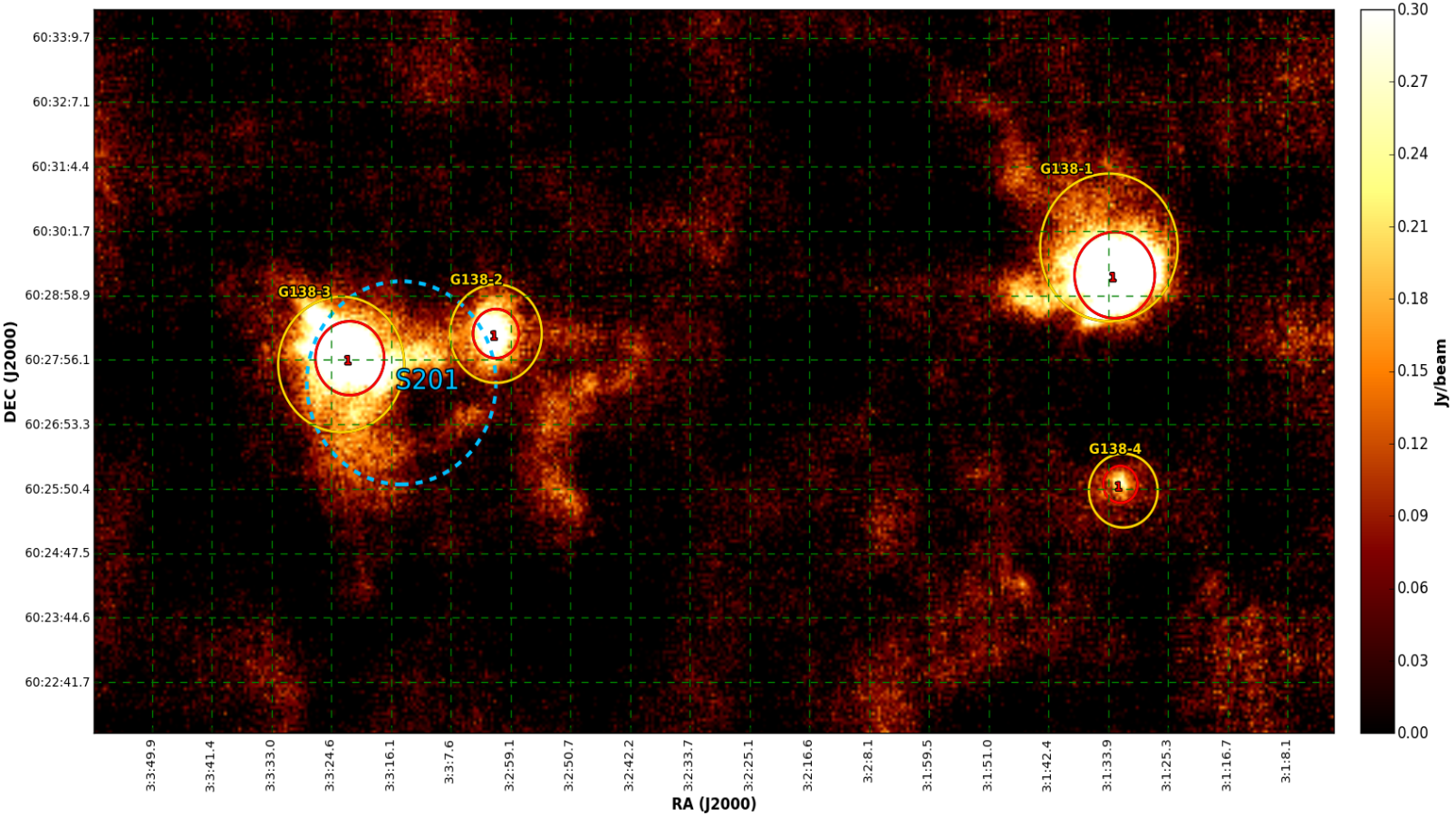

Figure 11: 850μm image of object G138. This object contains HII Region "S201" as well as 4 clump composites which host a total of 4 cores.

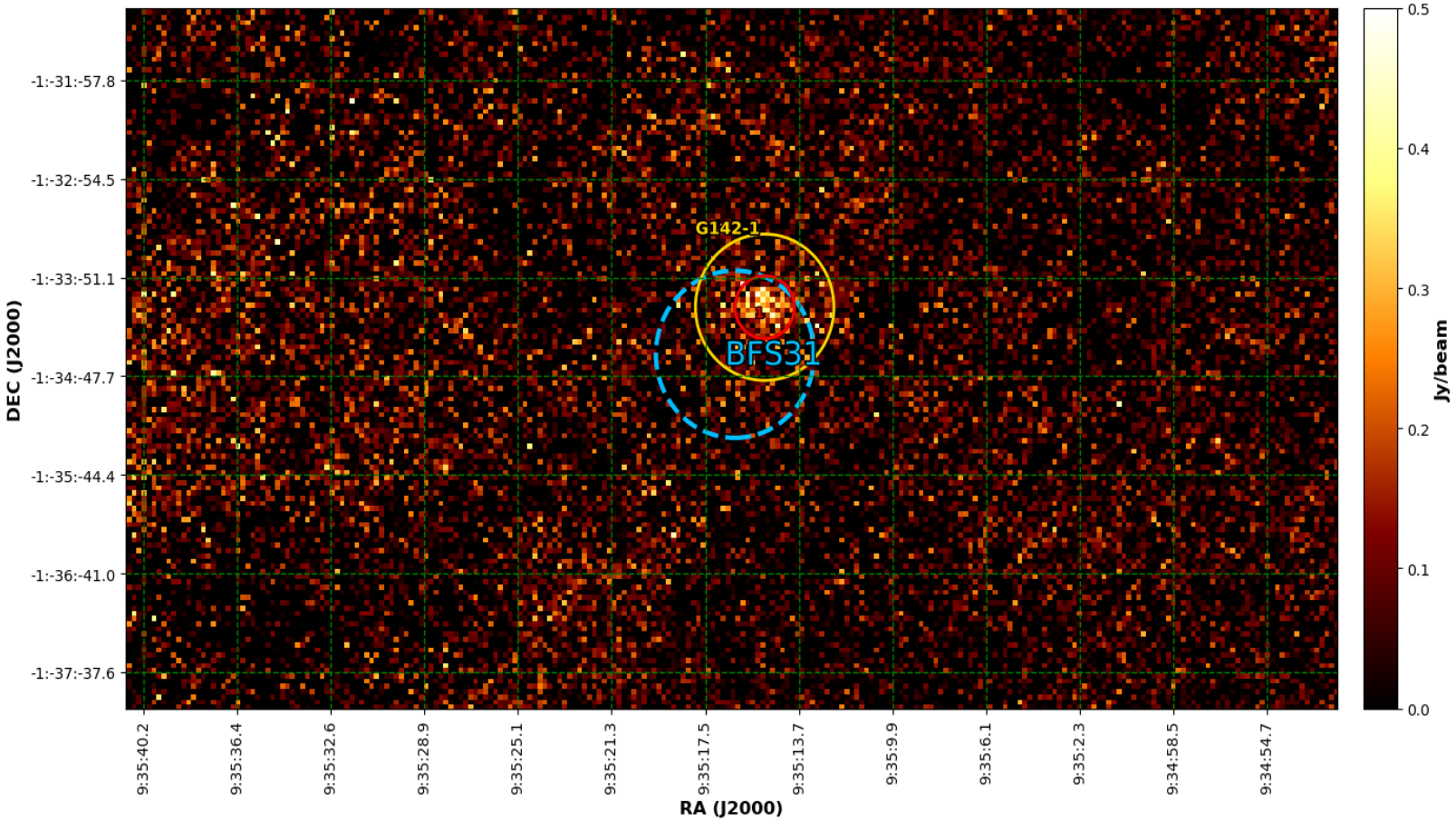

Figure 12: 850μm image of object G142. This object contains HII Region "BFS31" as well as 1 clump composite which hosts 1 core.

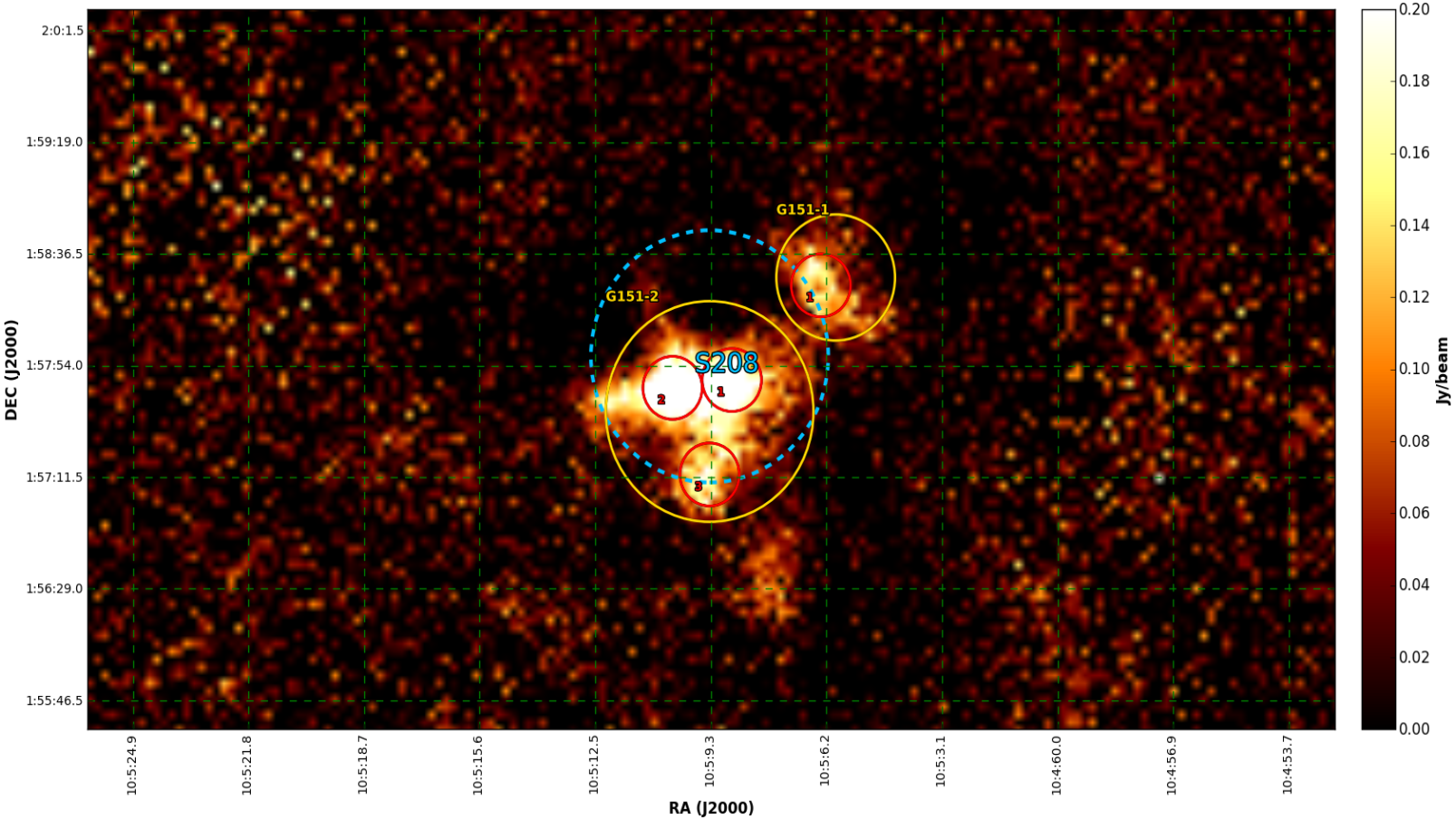

Figure 13: $850\mu m$ image of object G151. This object contains HII Region "S208" as well as 2 clump composites which host a total of 4 cores.

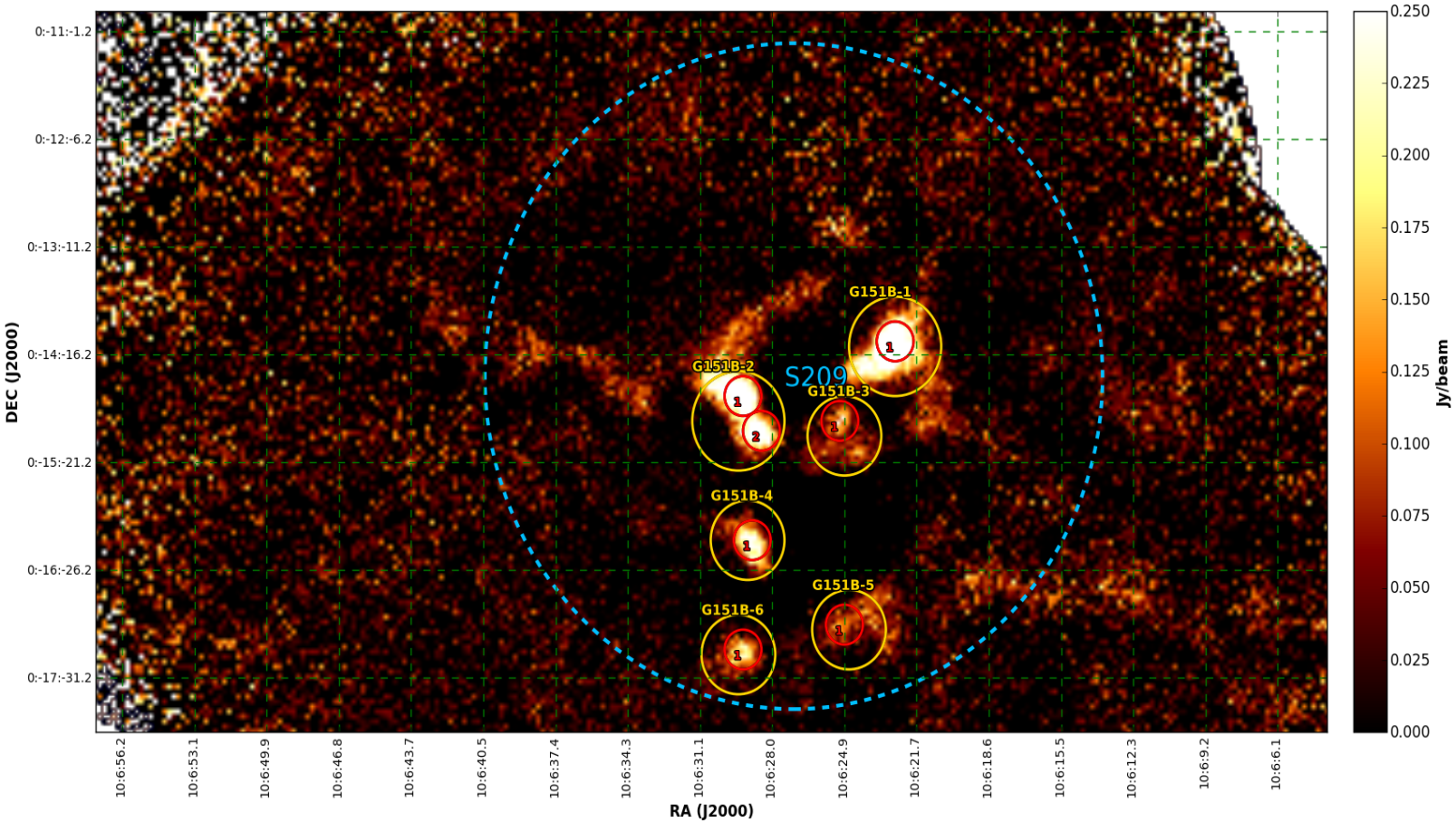

Figure 14: $850\mu m$ image of object G151B. This object contains HII Region "S209" as well as 6 clump composites which host a total of 7 cores.

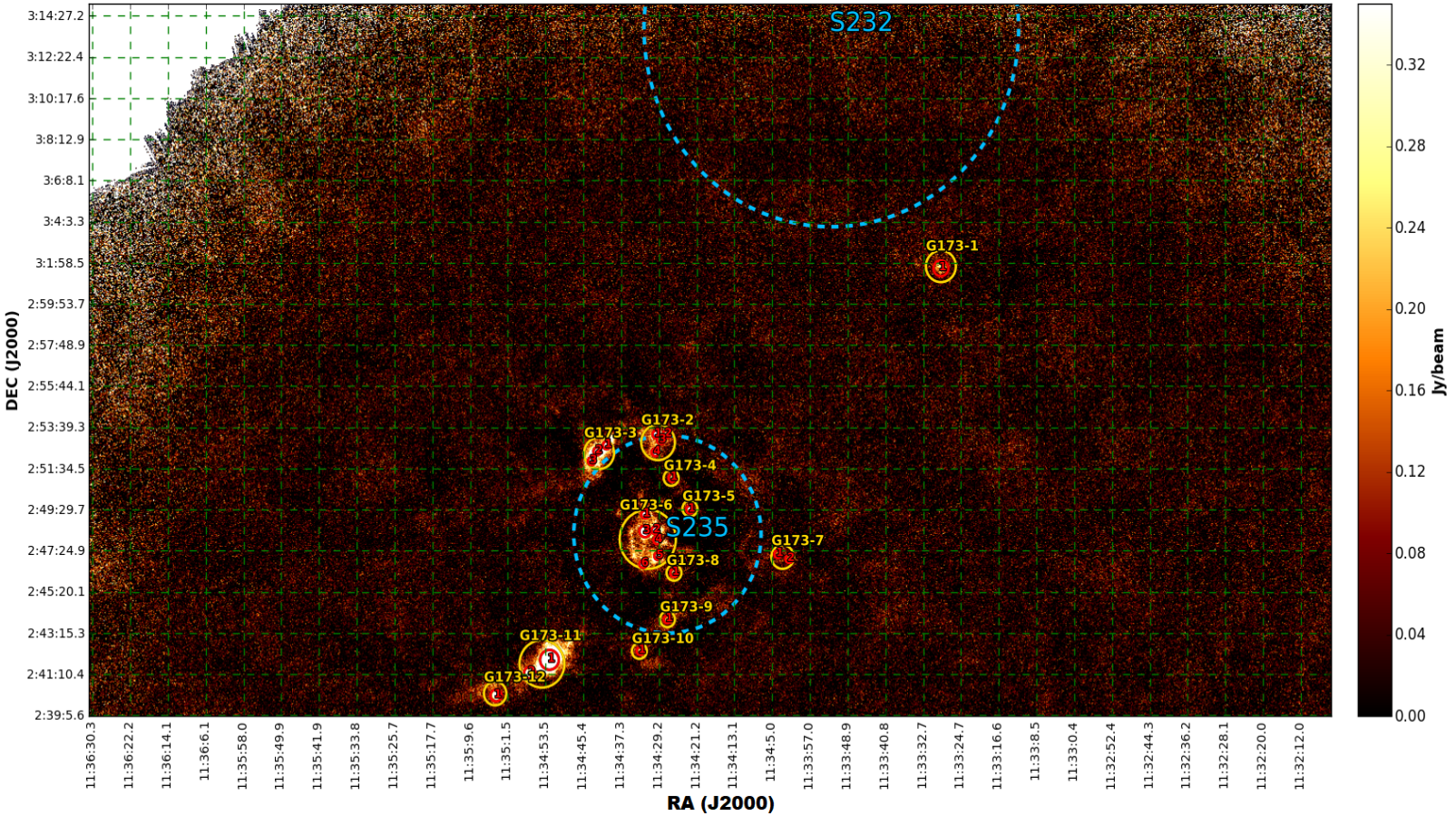

Figure 15: 850μm image of object G173 (top half). This region of G173 contains HII Regions "S232" and "S235" as well as 12 clump composites which host a total of 24 cores.

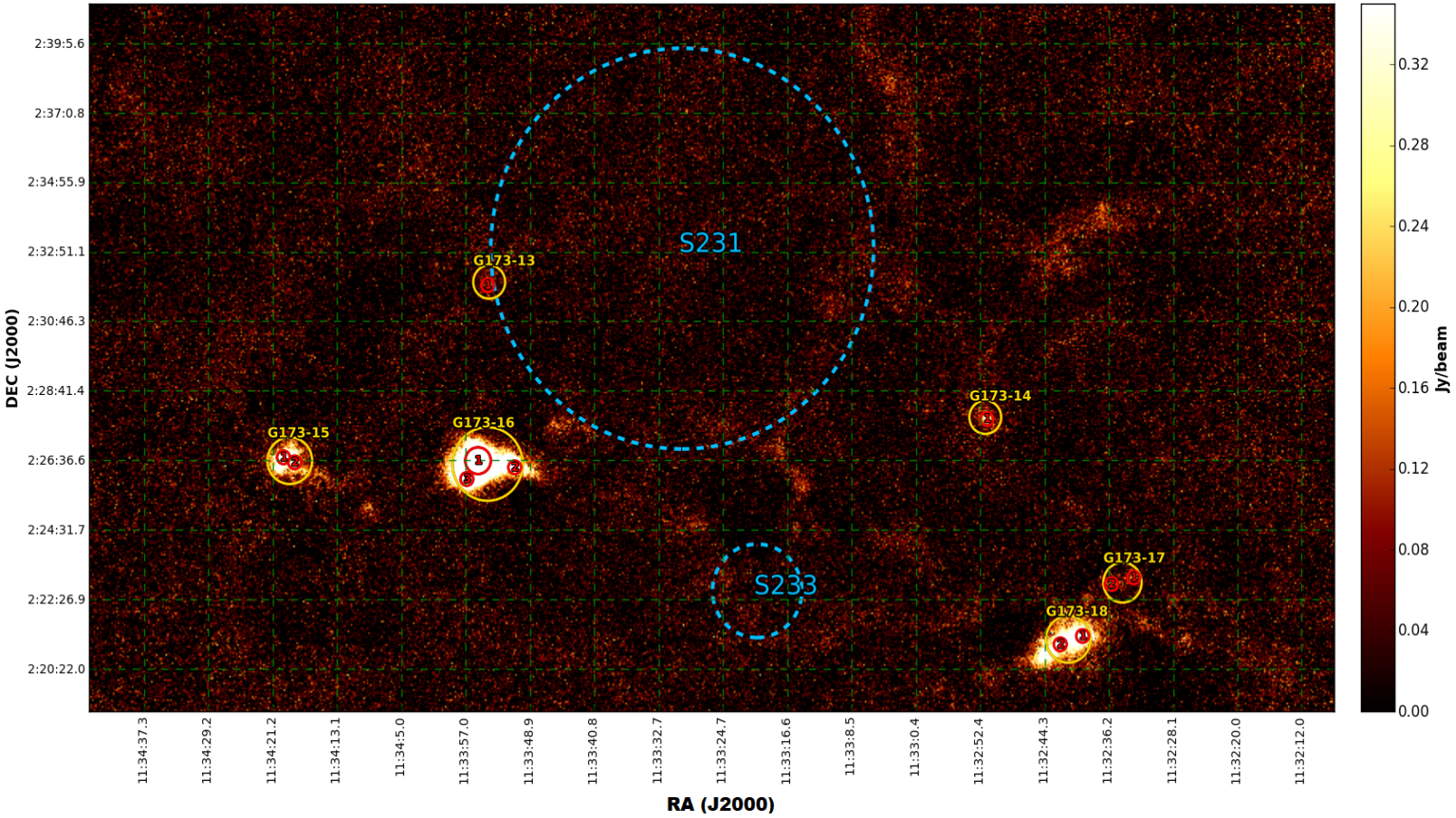

Figure 16: 850μm image of object G173 (bottom half). This region of G173 contains HII Regions "S231" and "S233" as well as 6 clump composites which host a total of 11 cores.

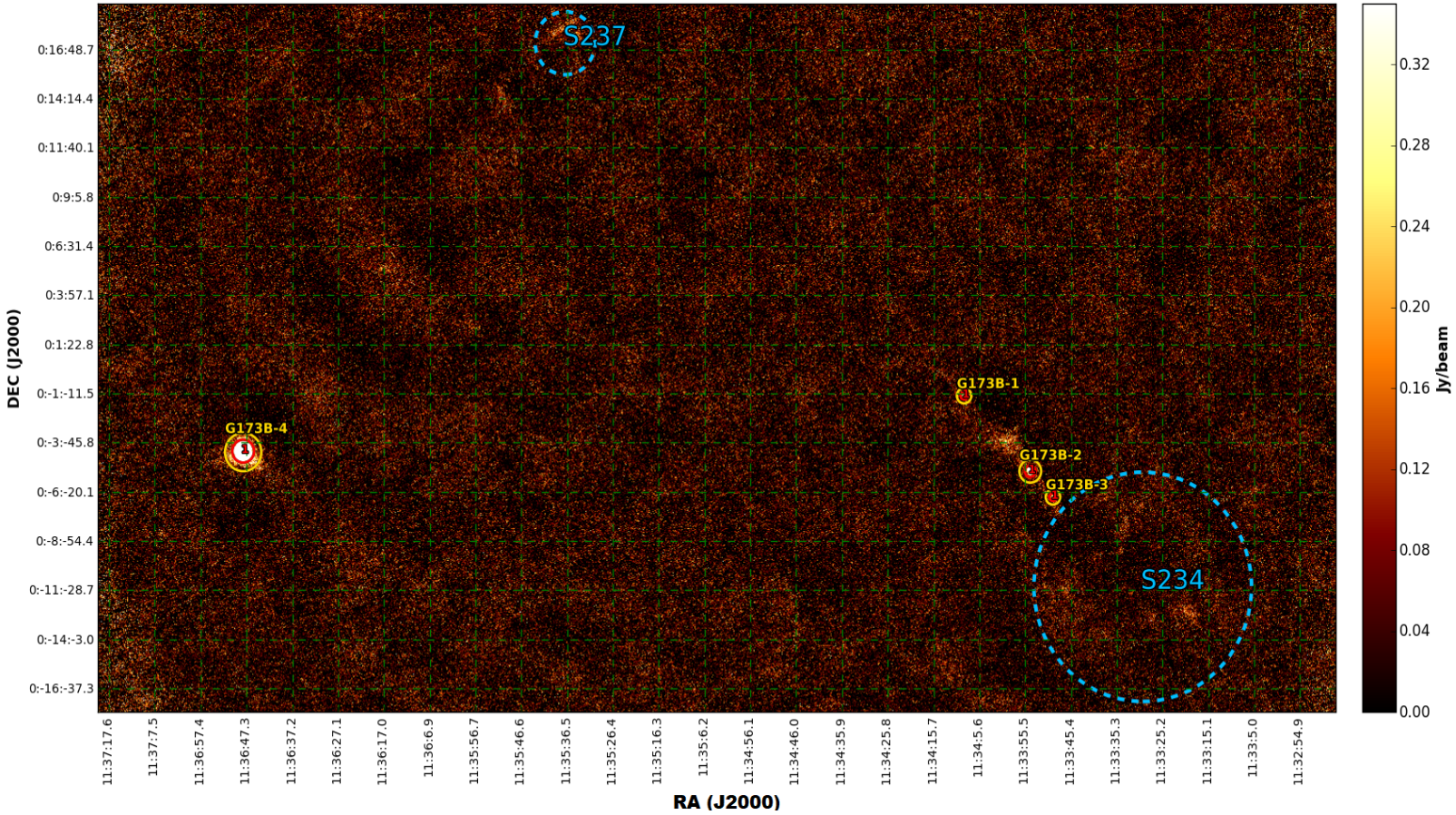

Figure 17: 850μm image of object G173B. This object contains HII Regions "S234" and "S237" as well as 4 clump composites which host a total of 4 cores.

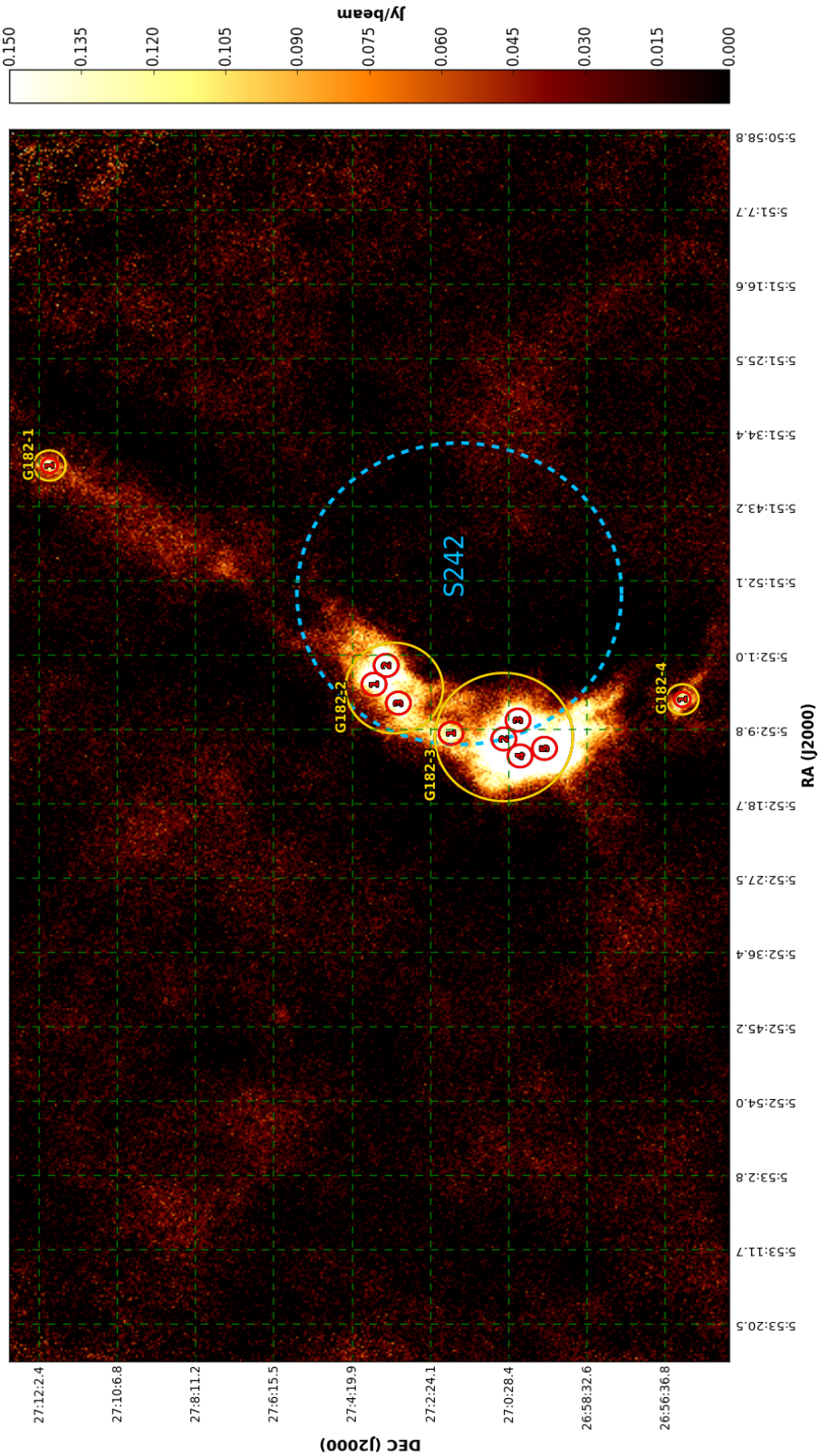

Figure 18: 850μm image of object G182. This object contains HII Region "S242" as well as 4 clump composites which host a total of 10 cores.

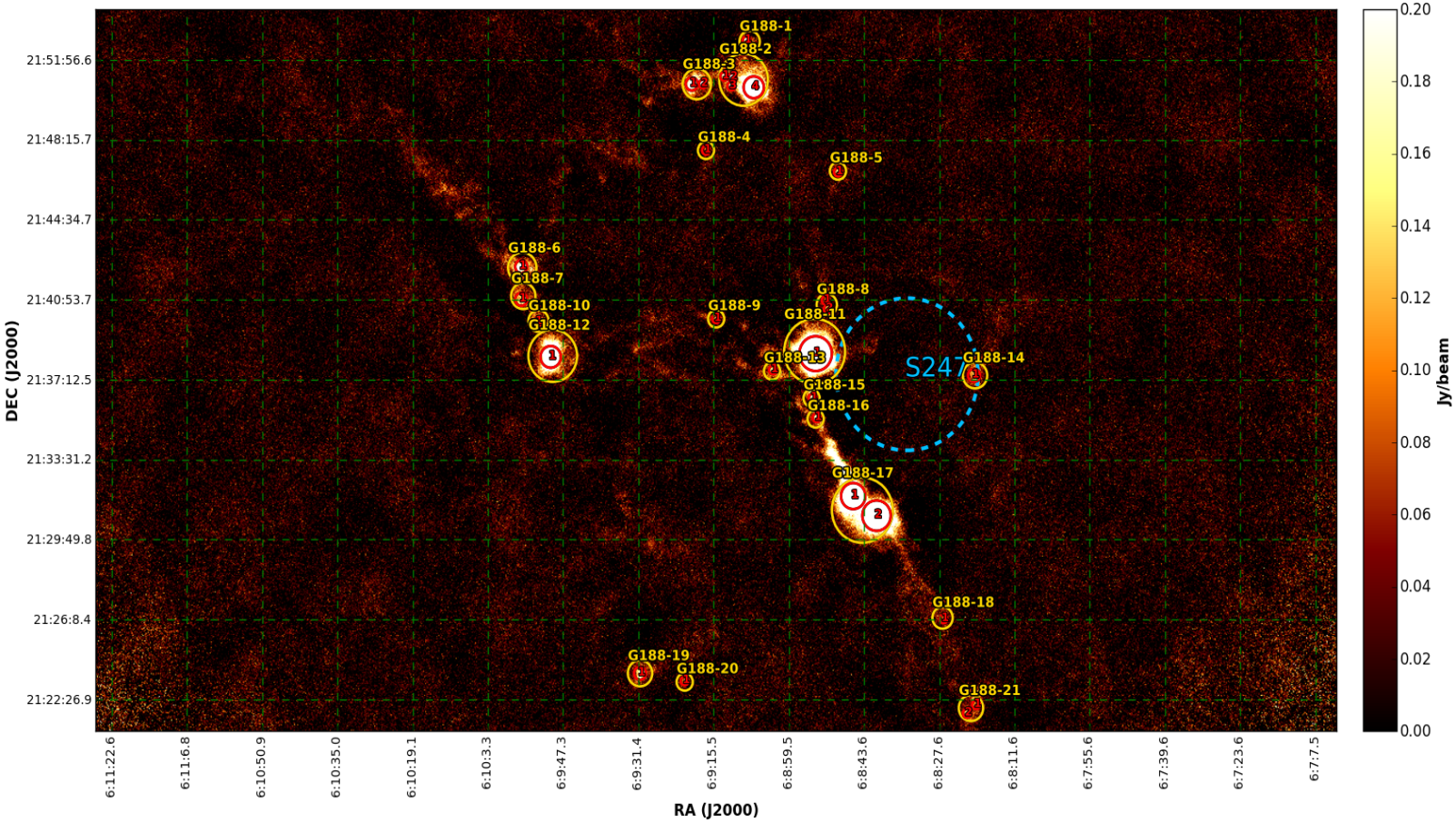

Figure 19: 850μm image of object G188. This object contains HII Region "S247" as well as 21 clump composites which host a total of 28 cores.

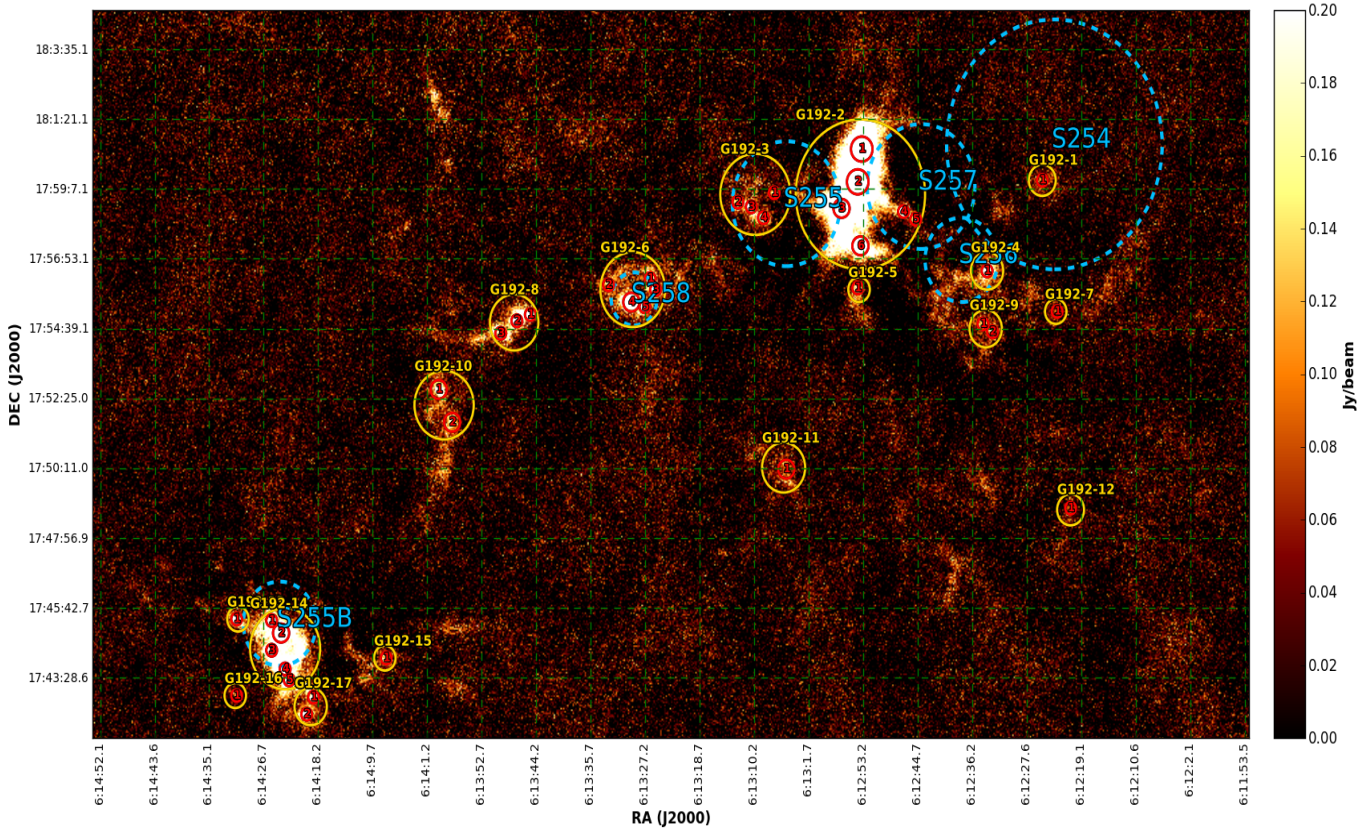

Figure 20: $850\mu m$ image of object G192. This object contains HII Regions "S254", "S255", "S255B", "S256", "S257", "S258" as well as 17 clump composites which host a total of 38 cores.

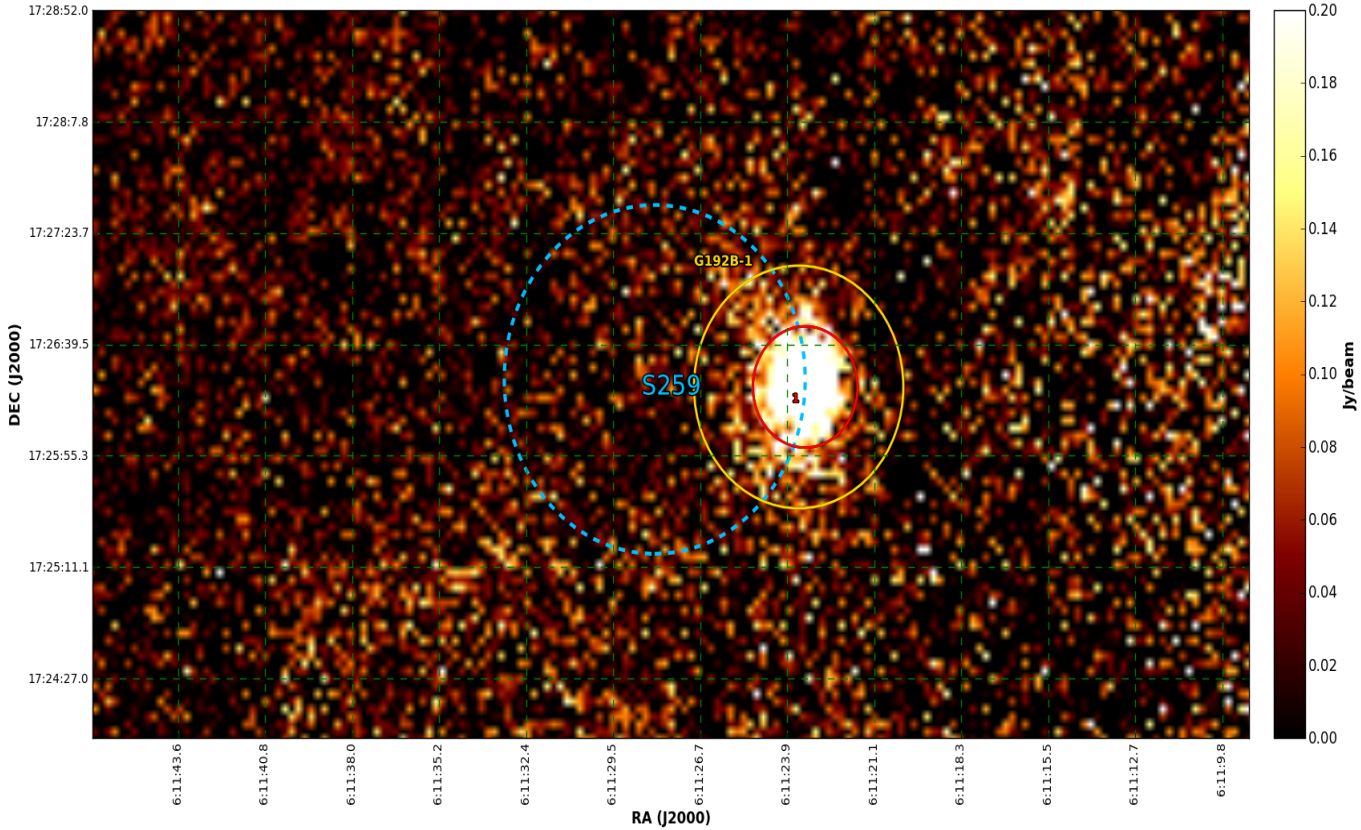

Figure 21: $850\mu m$ image of object G192B. This object contains HII Region "S259" as well as 1 clump composite which hosts 1 core.

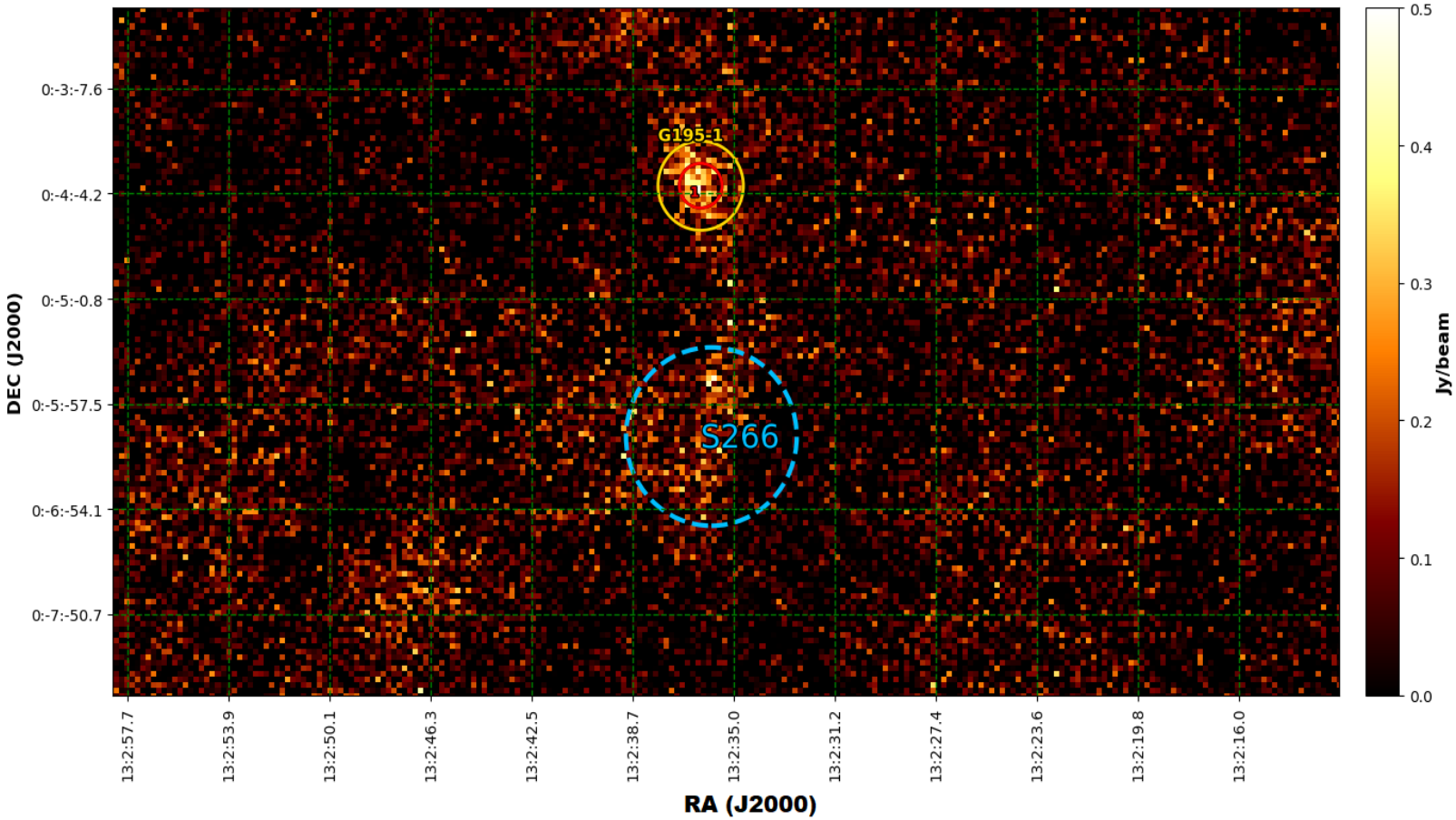

Figure 22: $850\mu m$ image of object G195. This object contains HII Region "S266" as well as 1 clump composite which hosts 1 core.

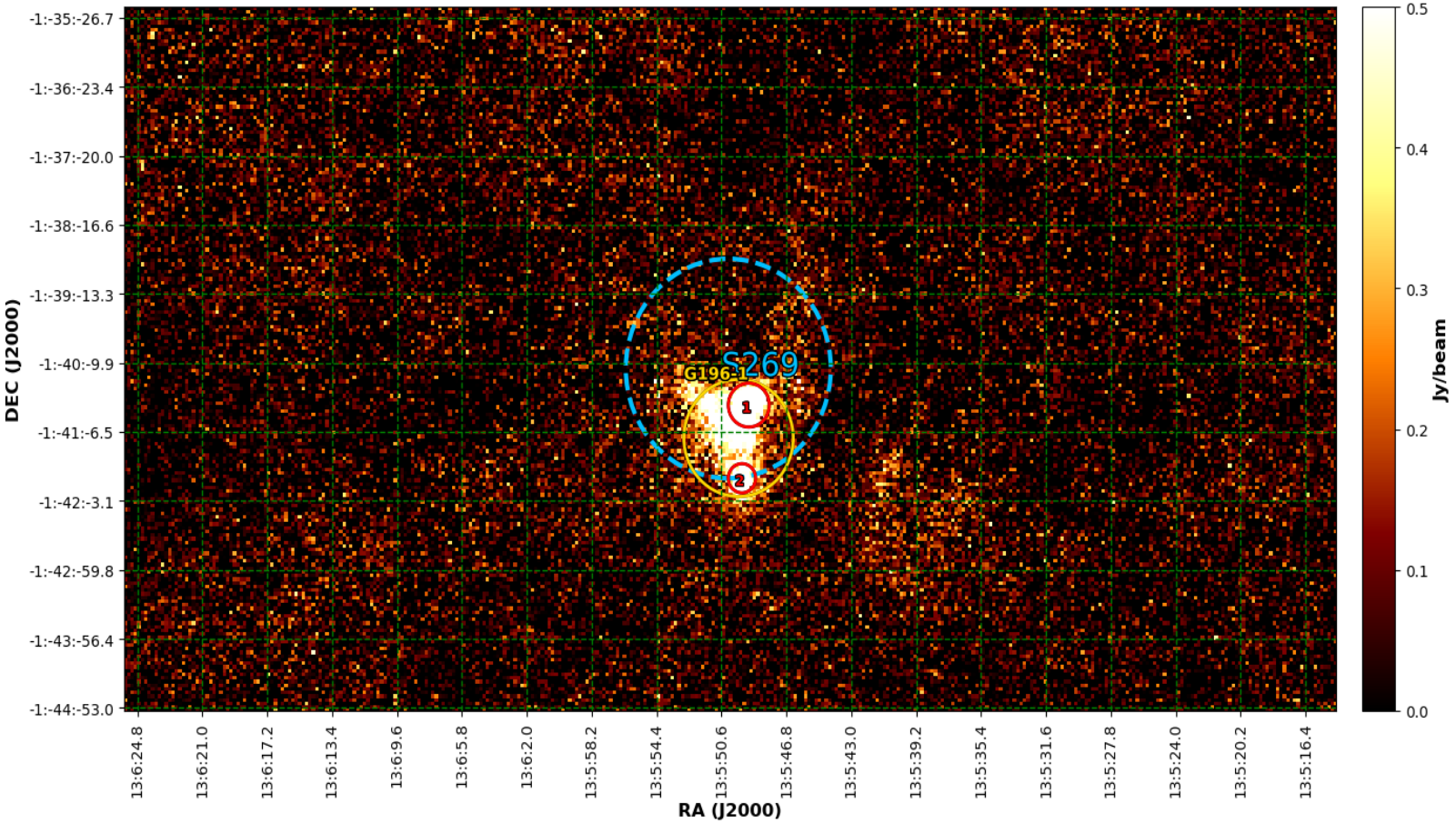

Figure 23: 850μm image of object G196. This object contains HII Region "S269" as well as 1 clump composite which hosts 2 cores.

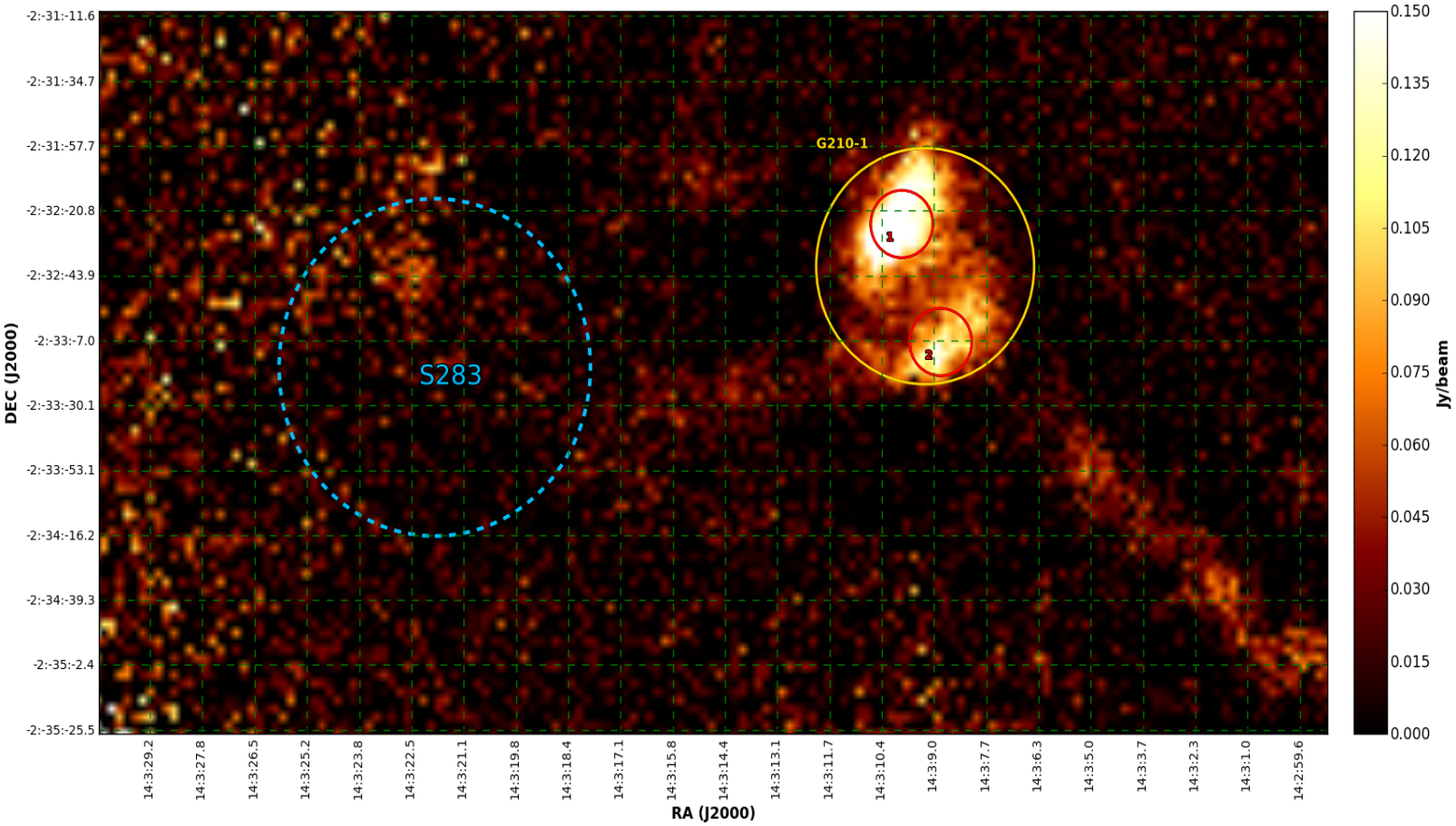

Figure 24: $850\mu m$ image of object G210. This object contains HII Region "S283" as well as 1 clump composite which hosts 2 cores.

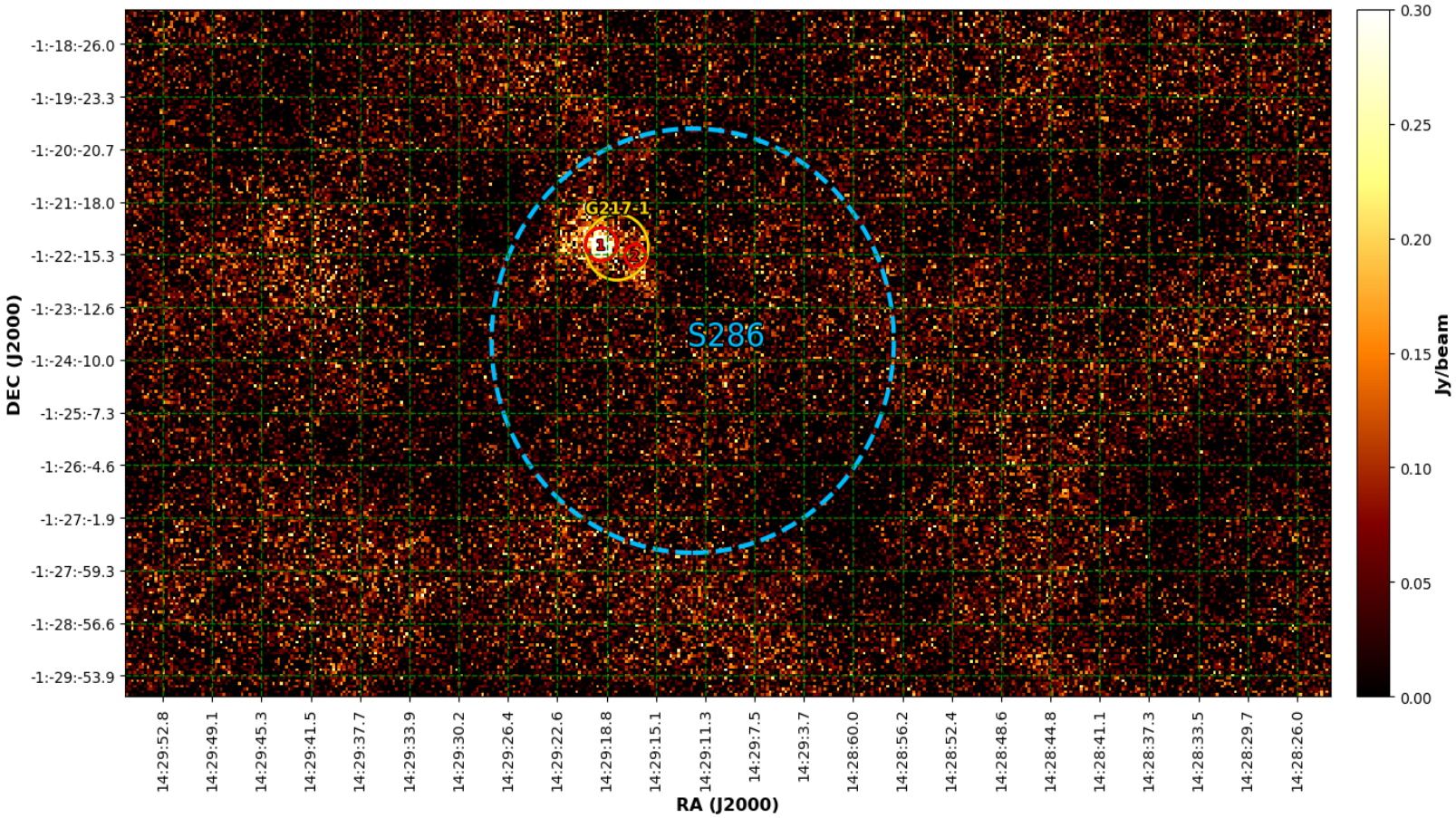

Figure 25: 850μm image of object G217. This object contains HII Region "S286" as well as 1 clump composite which hosts 2 cores.

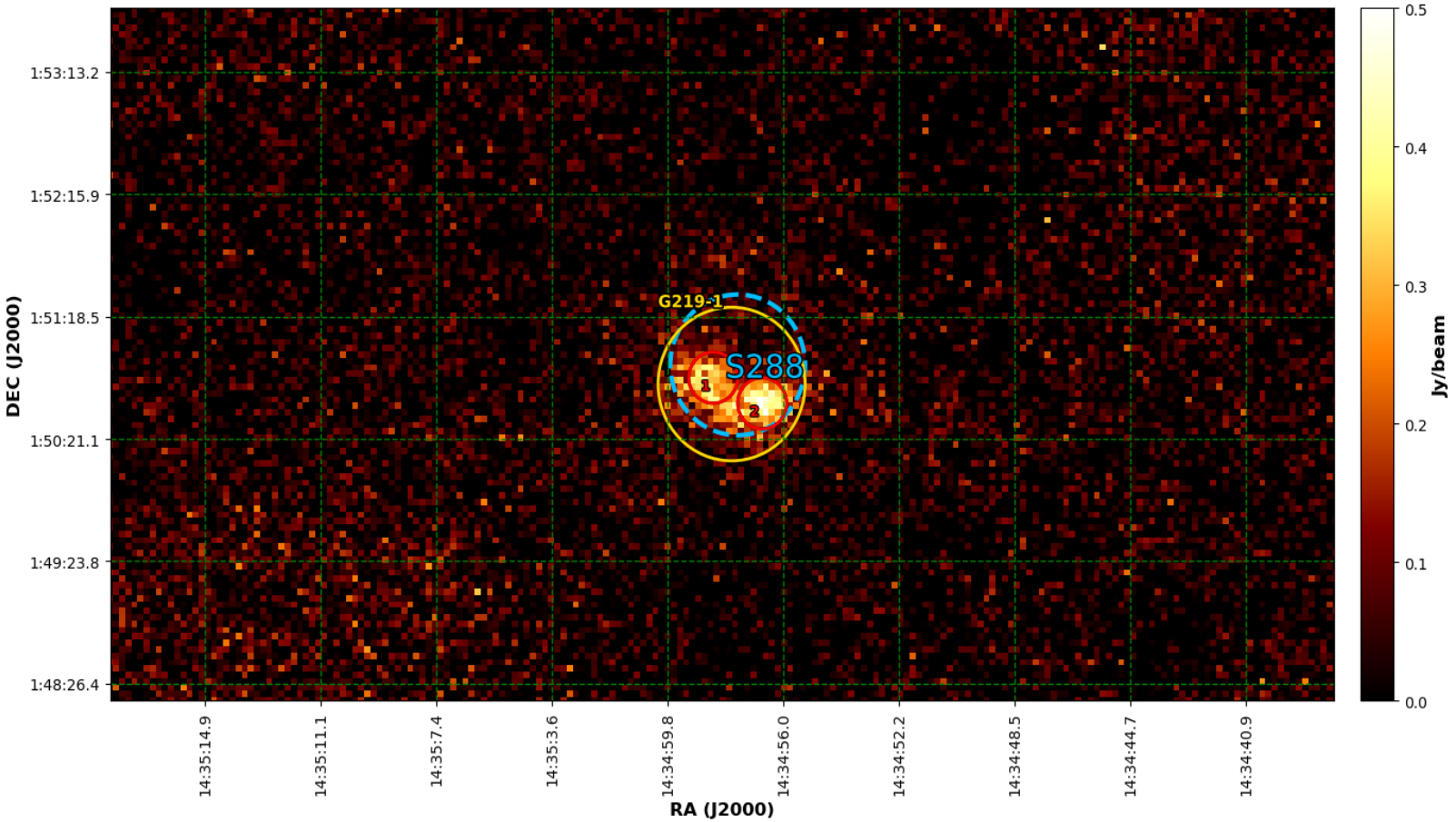

Figure 26: 850μm image of object G219. This object contains HII Region "S288" as well as 1 clump composite which hosts 2 cores.

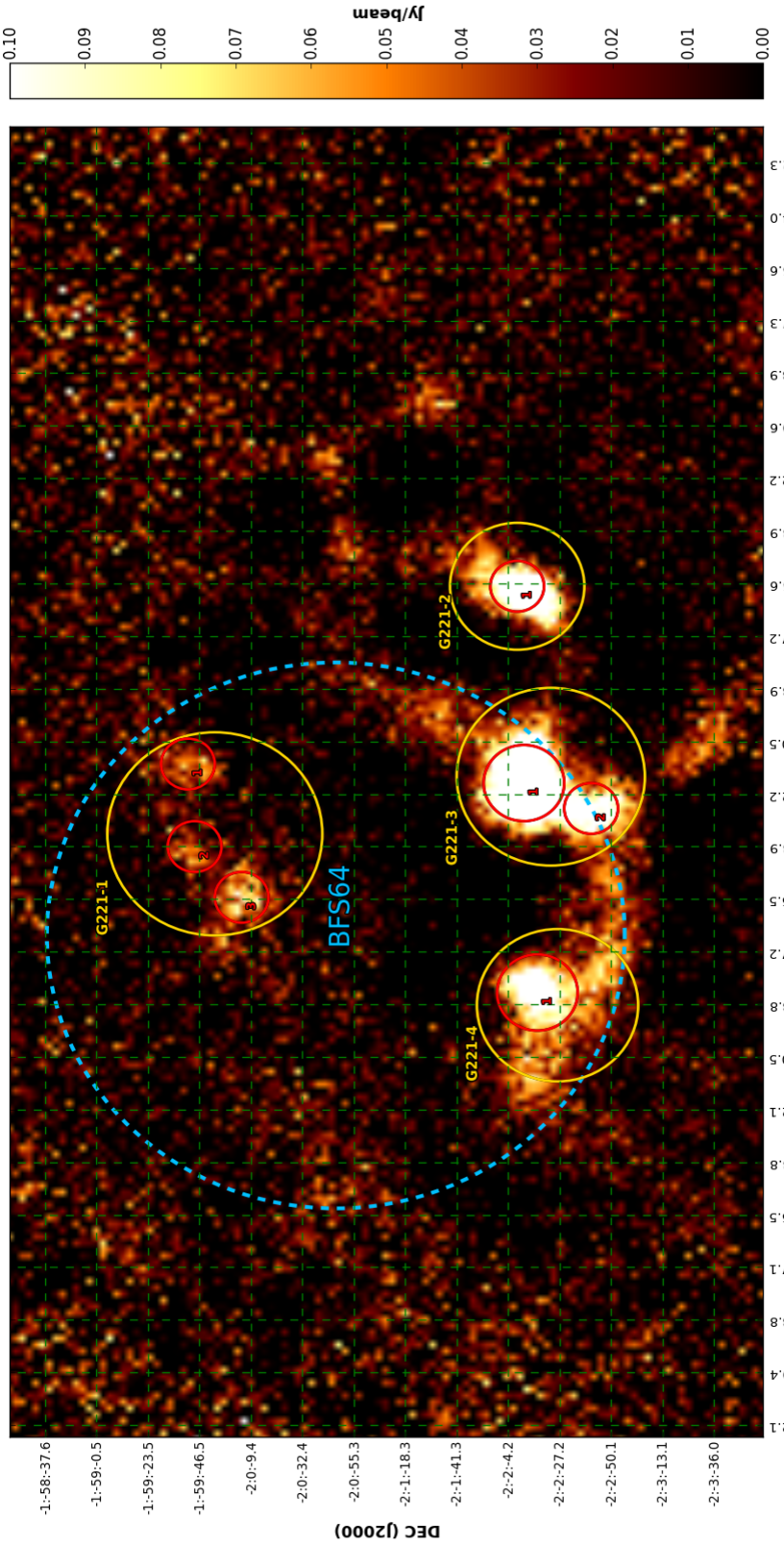

Figure 27: $850\mu m$ image of object G221. This object contains HII Region "BFS64" as well as 4 clump composites which host a total of 7 cores.

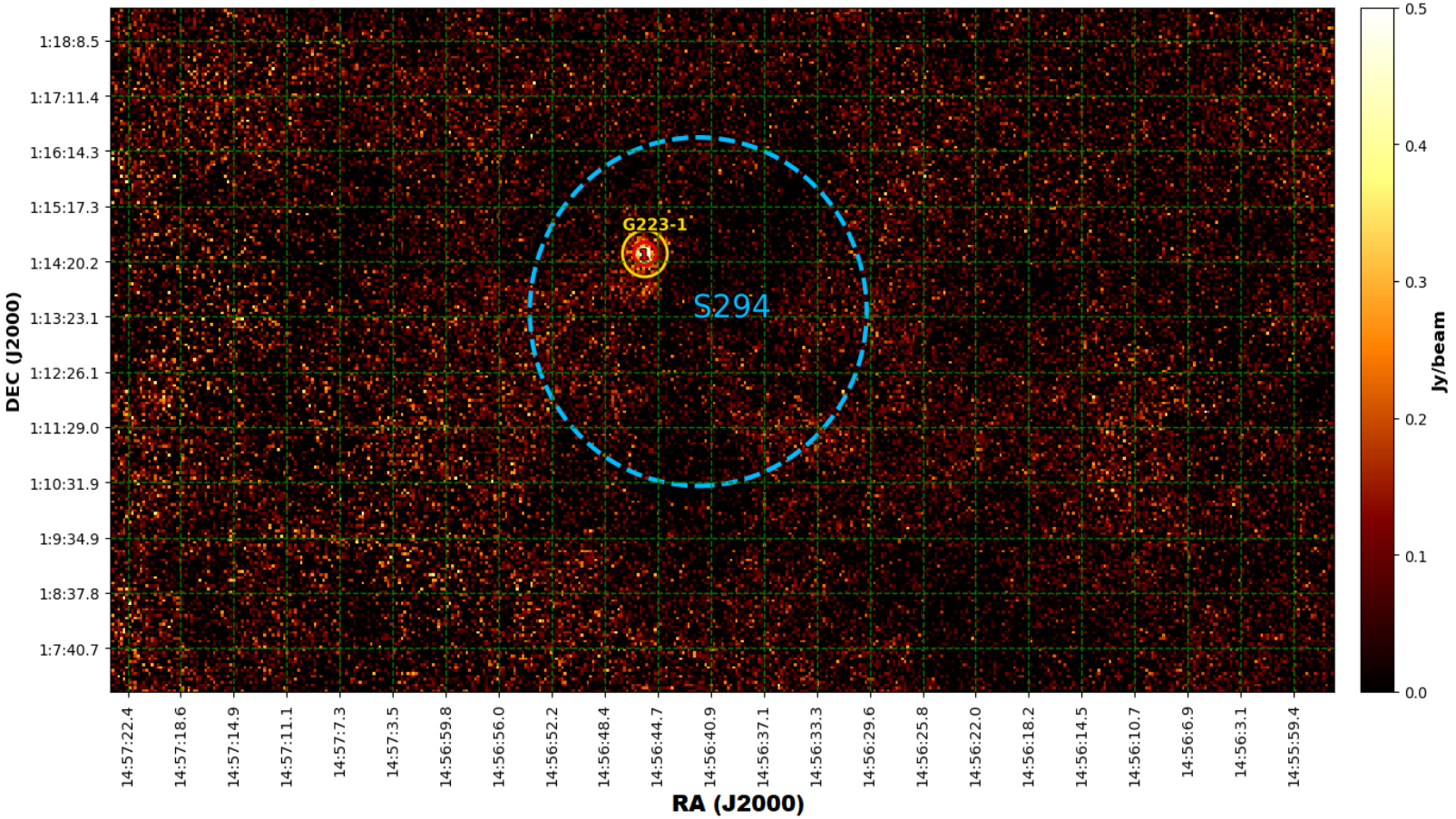

Figure 28: 850μm image of object G223. This object contains HII Region "S294" as well as 1 clump composite which hosts 1 core.

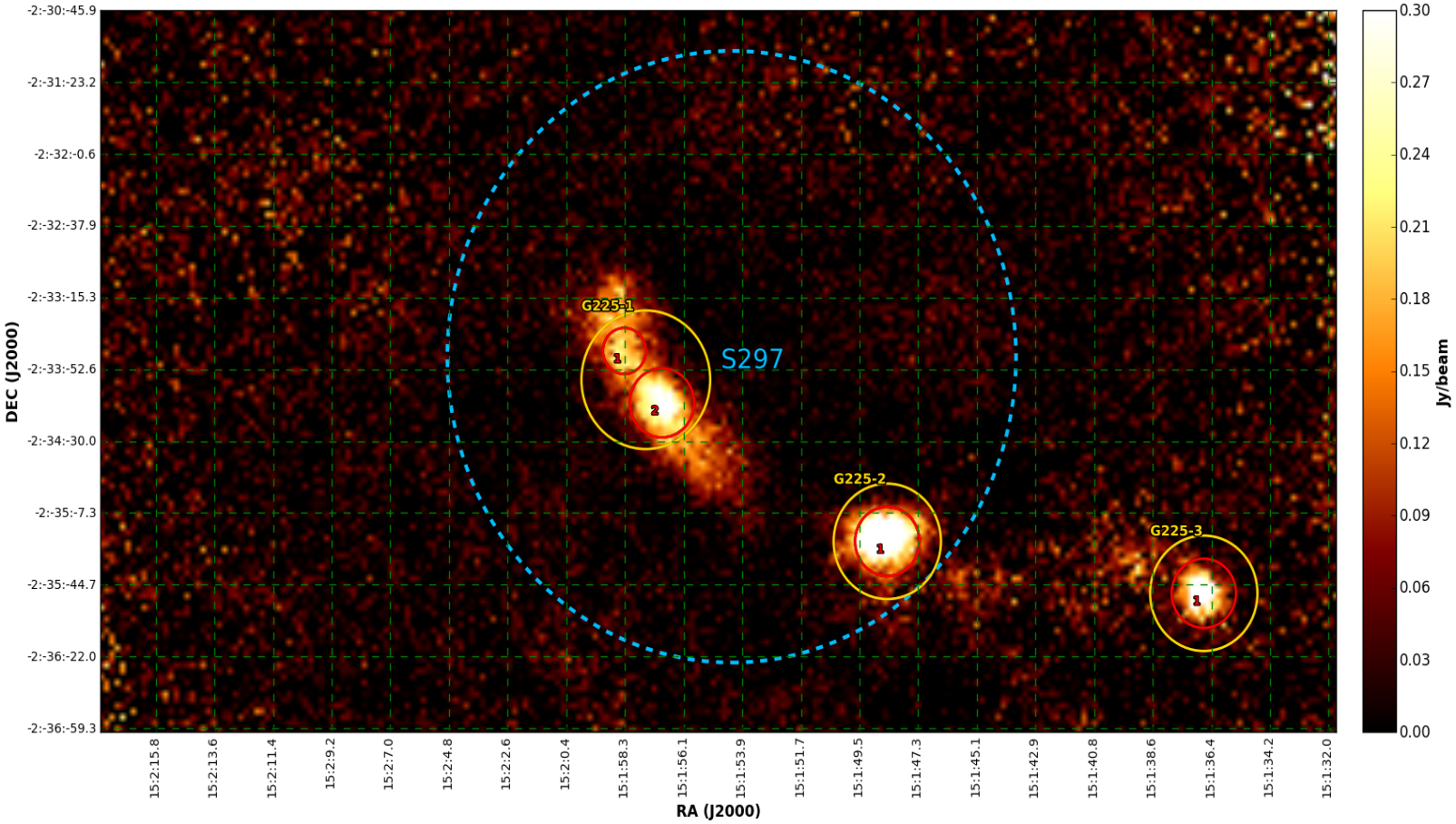

Figure 29: $850\mu m$ image of object G225. This object contains HII Region "S297" as well as 3 clump composites which host a total of 4 cores.

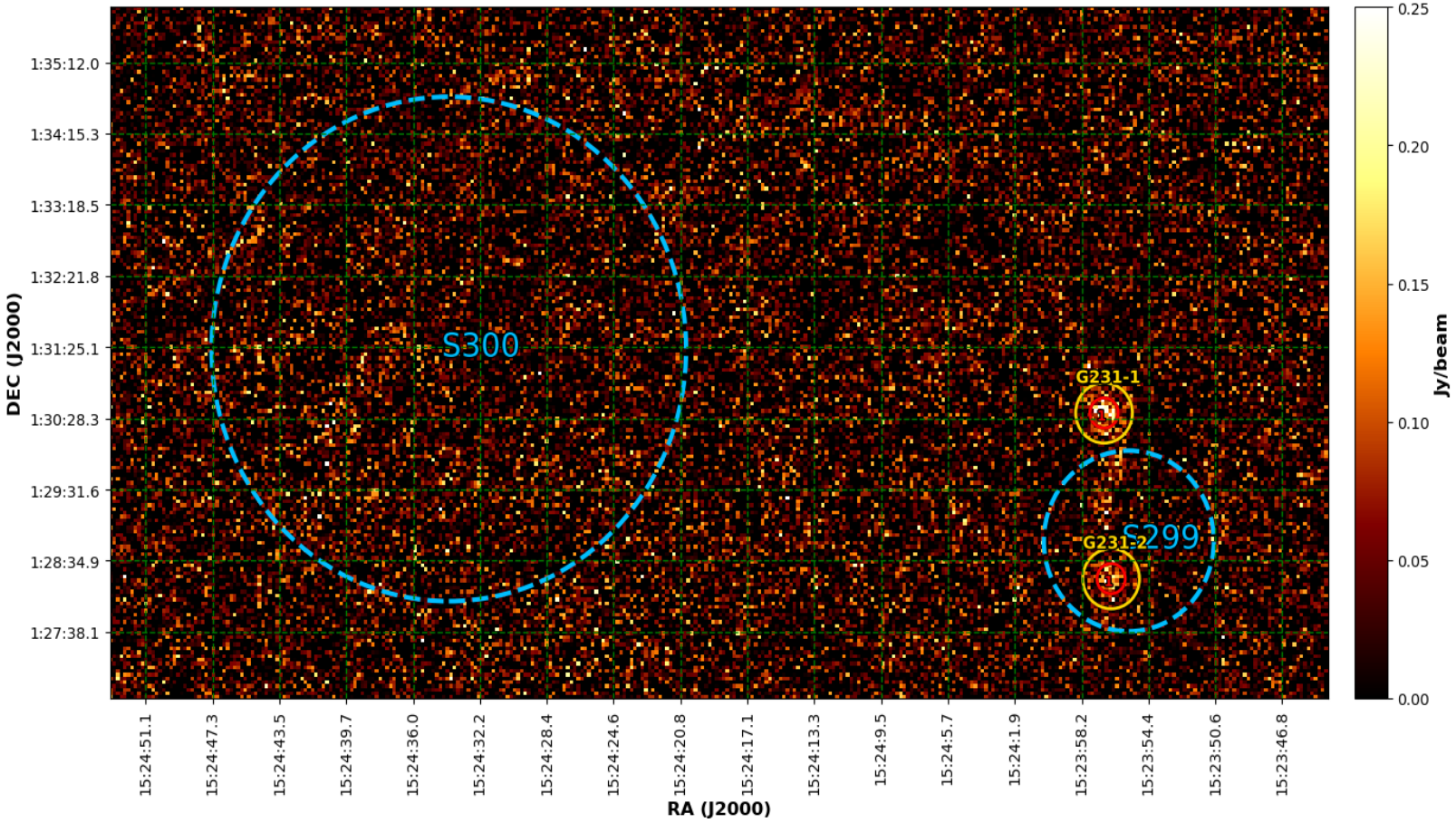

Figure 30: 850μm image of object G231. This object contains HII Regions "S299" and "S300" as well as 2 clump composites which host a total of 2 cores.

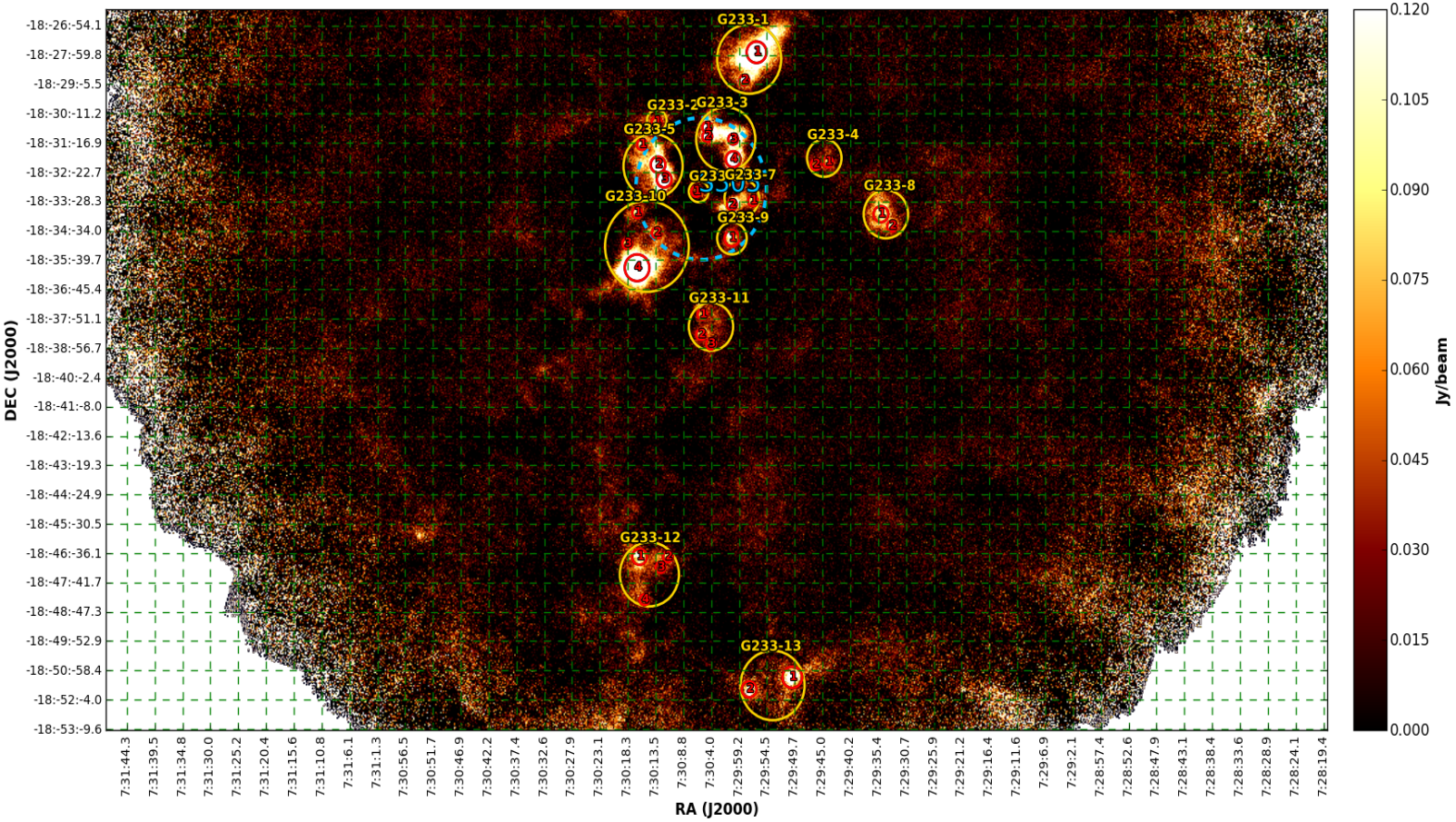

Figure 31: $850\mu m$ image of object G233. This object contains HII Region "S305" as well as 13 clump composites which host a total of 31 cores.

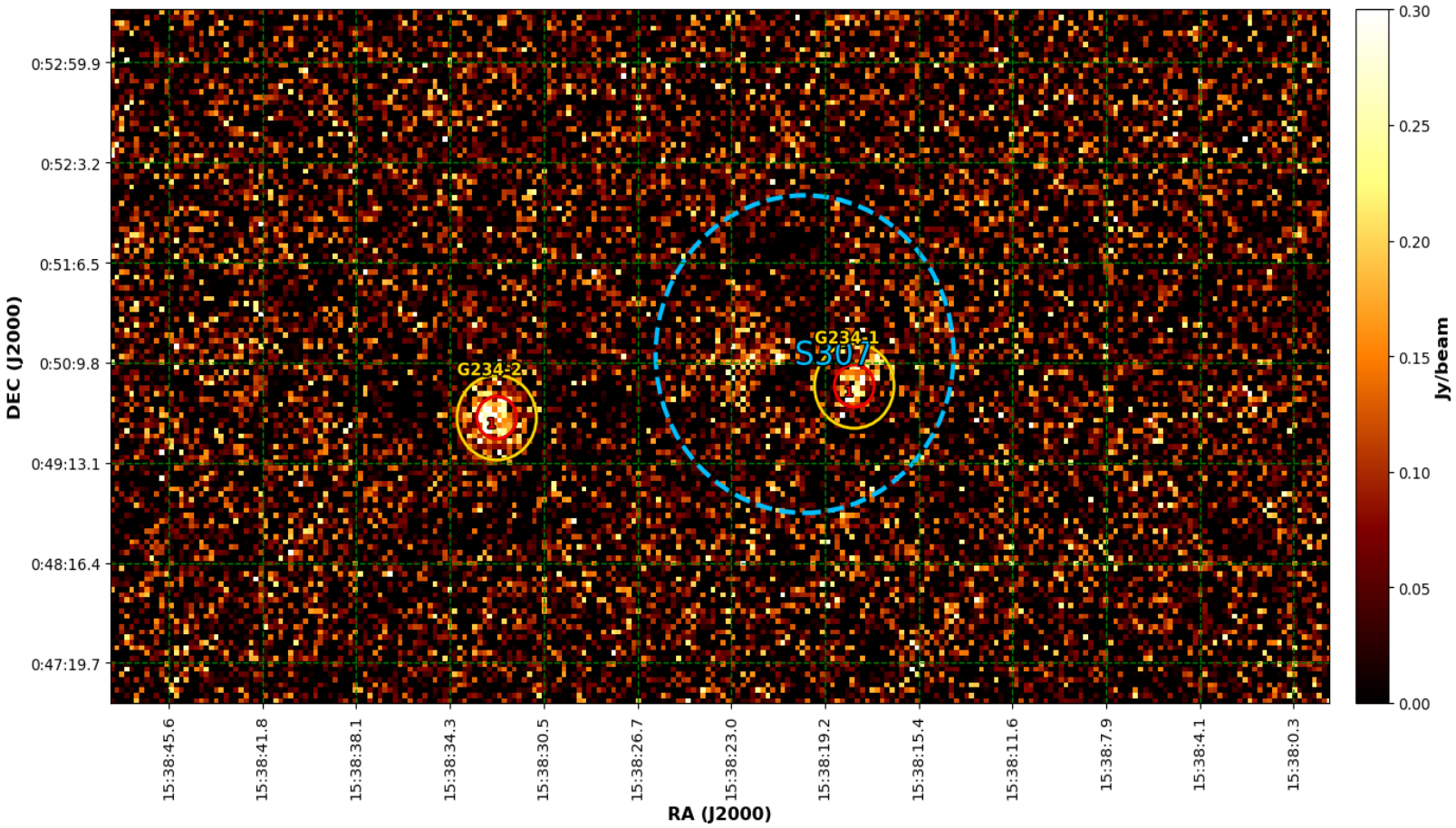

Figure 32: $850\mu m$ image of object G234. This object contains HII Region "S307" as well as 2 clump composites which host a total of 2 cores.